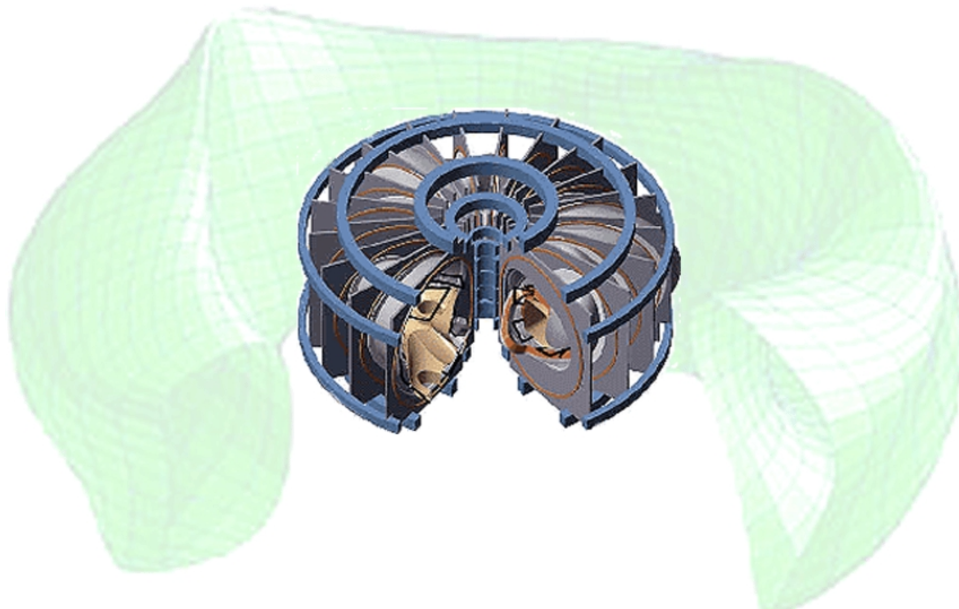

National Compact Stellarator Experiment

Physics Validation Report

by

The National Compact Stellarator Team

Princeton Plasma Physics Laboratory
Oak Ridge National Laboratory
The University of Texas at Austin
Columbia University
Lawrence Livermore National Laboratory
The University of California at San Diego
Sandia National Laboratory - Albuquerque

March, 2001

The National Compact Stellarator Team

A. Brooks, T. Brown, J. Chrzanowski, F. Dahlgren, L. Dudek, H. Fan, E. Fredd, E. Fredrickson, G. Fu, A. Georgievskiy, R. Goldston, R. Hatcher, R. Hawryluk, P. Heitzenroeder, S. Hudson, D. Johnson, J. Johnson, C. Jun, C. Kessel, A. Klink, L.-P. Ku, H. Kugel, J. Lewandowski, Z. Lin, R. Majeski, D. Mikkelsen, D. Monticello, H. Mynick, G. Neilson, C. Neumeyer, G. Oliaro, A. Pletzer, N. Pomphrey, S. Ramakrishnan, M. Redi, W. Reiersen, A. Reiman, P. Rutherford, J. Schmidt, R. Simmons, D. Stotler, R. White, R. Woolley, M. Zarnstorff,
Princeton Plasma Physics Laboratory, Princeton, NJ 08543

R. Benson, L. Berry, M. Cole, P. Goranson, S. Hirshman, W. Houlberg, E. Lazarus, J. Lyon, P. Mioduszewski, B. Nelson, D. Rasmussen, D. Spong, P. Strand, D. Strickler, D. Williamson,
Oak Ridge National Laboratory, Oak Ridge, TN 37831

W. Miner, D. Ross, P. Valanju, *The University of Texas at Austin, Austin, TX 78712*

A. Boozer, *Columbia University, New York, NY 10027*

M. Fenstermacher, T. Rognlien,
Lawrence Livermore National Laboratory, Livermore, CA 94551

A. Grossman, *University of California at San Diego, San Diego, CA 92093*

M. Ulrickson, *Sandia National Laboratory, Albuquerque, NM 87185*

In collaboration with:

D. Anderson, J. Talmadge, *The University of Wisconsin, Madison, WI 53706*

S. Knowlton, *Auburn University, Auburn, AL 36849*

P. Garabedian, *New York University, New York, NY 10012.*

B. Blackwell, R. Dewar, *Australian National University, Canberra, Australia*

W. Cooper, *Ecole Polytechnique Federale de Lausanne, Switzerland*

M. Drevlak, P. Merkel, C. Nuehrenberg, R. Schneider, E. Strumberger,
Max Planck Institute for Plasma Physics, Greifswald, Germany.

M. Isaev, M. Mikhailov, A. Subbotin, *Kurchatov Institute, Moscow, Russia.*

W. Kernbichler, V. Nemov, *Austria*

N. Nakajima, M. Okamoto, K. Watanabe, *National Institute for Fusion Science, Japan*

R. Sanchez, *Universidad Carlos III de Madrid, Spain.*

Glossary and Definitions

- $\beta = 2\mu_0 \langle p \rangle / \langle B^2 \rangle$, where p is the pressure and $\langle\ \rangle$ denotes volume average.
- Aspect ratio $A = R / \langle a \rangle$, where $\langle a \rangle$ is the average minor radius, from the cross-sectional area
- Iota (ι) and iota-bar (ɨ = 1/q) are used interchangeably for the magnetic rotational transform.
- Unless otherwise specified, all equilibria, both fixed- and free-boundary, shown are calculated by the VMEC 3D equilibrium code, see Section 4.1. VMEC is an 'inverse' equilibrium solver, which solves directly for the shape of the flux surfaces. Thus its representation presumes that the flux surfaces are simply connected, without islands or stochastic regions.
- Unless otherwise specified, all Poincare plots shown are calculated by the PIES 3D equilibrium code, see Chapter 4.3. PIES is a 'forward' equilibrium solver, directly calculating the full three-dimensional magnetic field and current distribution, including simulating the effect of islands and stochastic regions by flattening the local pressure gradient. It determines the flux surface topology and shape by directly integrating the field-line orbits.
- Unless otherwise specified, all low-n stability calculations shown are calculated by the TERPSICHORE stability code, see Chapter 5.
- Unless otherwise specified, all infinite-n ballooning calculations discussed are calculated by the COBRA code, see Chapter 5.

Executive Summary

Magnetic plasma confinement in toroidal geometries is a proven approach for advancing the science of fusion energy and is promising as a basis for future fusion power plants. Most of the research to date has concentrated on two types of configurations, tokamaks and stellarators. Tokamaks, which produce the confining poloidal magnetic field by toroidal currents in the plasma, have demonstrated excellent short-pulse plasma performance in “compact” geometries, with aspect ratios (ratio of the plasma major radius to the average minor radius) usually less than 4. Stellarators use three-dimensional magnetic fields generated by coils to produce some or all of the confining poloidal magnetic field. Stellarators have demonstrated levels of performance approaching those of tokamaks, generally at aspect ratios in the range of 6-12.

Since stellarators can produce all components of the magnetic field directly from external coils, they are intrinsically well suited for steady state operation and do not require external current drive systems. The physics properties of toroidal plasmas are determined by the shape of the MHD equilibrium, and the stellarator’s three-dimensional shaping offers many more degrees of freedom than are available with axisymmetric configurations. This additional flexibility can be used to tailor the equilibrium to obtain desired physics properties. Historically, it has been a challenge for stellarators to provide acceptable drift-orbit confinement, allowing adequate fast-ion confinement and low neoclassical transport losses. A strategy for 3D drift-orbit confinement is “quasi-symmetry”, which is based upon work by A. Boozer [1] showing that drift-orbit topology and neoclassical transport depends only on the variation of $|B|$ within a flux surface. This was used by J. Nuehrenberg [2] and P. Garabedian [3] to develop stellarators that, while three-dimensional in Euclidean space, have a direction (either helical or toroidal) of approximate symmetry of $|B|$ in (Boozer) flux coordinates. Quasi-symmetric configurations have drift-orbits similar to equivalent symmetric configurations, and thus similar neoclassical transport. Also, rotation in the quasi-symmetric direction is undamped, as in a symmetric configuration.

The Compact Stellarator Opportunity

The Compact Stellarator Opportunity is to build upon the advances in understanding of both stellarators and tokamaks and to combine the best features of both. We wish to use the stellarator’s externally generated helical field and 3D shaping to provide MHD stability without external current drive or feedback systems, designing plasmas that have the potential to be free of disruptions. From tokamaks, we wish to use the excellent confinement, ability to stabilize and manipulate turbulent transport, and lower aspect ratio (compared to classical stellarators) to reduce development costs and system size. Three-dimensional shaping is used to passively stabilize the modes that limit the β and pulse-length of toroidal plasmas (particularly the external kink and neoclassical tearing modes). Quasi-axisymmetric design provides good orbit confinement, allows undamped flows to stabilize turbulence, and is best suited for higher β limits and lower aspect ratio.

An experimental facility, the National Compact Stellarator Experiment (NCSX), is proposed to support the research needed to develop the compact stellarator through its proof-of-principle (PoP) stage. The NCSX is the principal element in a national proof-of-principle program, first proposed in 1998 [4], to develop the physics of compact stellarators. It will advance U.S. plasma science goals by broadening the understanding of turbulence and transport, macroscopic stability, wave-particle interactions, and plasma boundary physics, using its unique capabilities to vary configuration parameters. It will acquire the physics data needed to evaluate the attractiveness of the compact stellarator as a concept for fusion energy, a 10-year milestone established by the Fusion Energy Sciences Advisory Committee in 1999. The breadth of the questions proposed for study by NCSX, and particularly the study of high-β plasmas requires a proof-of-principle experiment, with sufficient size, magnetic field strength, heating power, power and particle handling capabilities, diagnostics, and flexibility.

NCSX Scientific Mission and Design Goals

The mission of the NCSX research is to investigate the effects of three-dimensional plasma shaping, of internally- and externally-generated sources of rotational transform, and of quasi-axisymmetry on the stability and confinement of toroidal plasmas. It will contribute to the national fusion program's MFE Goal #1 to advance understanding of plasma and enhance predictive capabilities. It will contribute in important ways to answering some of the major outstanding challenges in plasma science, as set forth in the Fusion Energy Sciences Advisory Committee report, "Opportunities in the Fusion Energy Sciences Program." [5]

Macrostability major challenge: What are the fundamental causes and nonlinear consequences of plasma pressure limits in magnetically confined plasma systems, and how can a fusion system's plasma pressure and hence power density be optimized, with minimum off-normal events?

In NCSX:

- What are the beta limits and limiting mechanisms in a low aspect-ratio stellarator? Can pulse-length-limiting instabilities, such as external kinks and neoclassical tearing modes, be stabilized by external transform and 3D shaping?
- How do externally-generated transform and 3D shaping affect disruptions and their occurrence?

Transport and Turbulence major challenge: What are the fundamental causes of heat loss in magnetically confined plasmas, and how can heat losses be controlled, in order to minimize the required size of a fusion power system?

In NCSX:

- Can the collisionless orbit losses typically associated with 3D fields be reduced by designing the magnetic field to be quasi-axisymmetric? Is flow damping reduced? Is the resulting transport and confinement similar to actually axisymmetric systems? How does the transport scale in a compact stellarator?
- Do anomalous transport control and reduction mechanisms that work in tokamaks transfer to quasi-axisymmetric stellarators? Do zonal flows saturate turbulent transport in a quasi-axisymmetric stellarator at levels similar to tokamaks?

Wave-Particle interactions major challenge: What are the fundamental causes and nonlinear consequences of wave interactions with non-thermal particles, which can be used both to *minimize any negative consequences of fusion products in magnetically confined plasmas, and ultimately to take advantage of the free energy represented by the fusion product population?*

In NCSX:

- How do the Alfvenic-eigenmode spectrum and stability of a quasi-axisymmetric stellarator differ from those of a tokamak or a non-symmetric stellarator?

Boundary Interactions major challenge: What are the fundamental mechanisms of parallel transport along open magnetic field lines, and how can the heat flux along these field lines be dissipated before its strikes material surfaces?

In NCSX:

- How do stellarator field characteristics such as islands and stochasticity affect the boundary plasma and plasma-material interactions? Are 3D methods for controlling particle and power exhaust compatible with good core confinement?

The compact stellarator offers innovative solutions to some of the critical problems that lie on the path to an attractive fusion power plant. A key challenge for magnetic fusion energy research is finding a compact, high-beta toroidal plasma configuration that can be efficiently sustained without disrupting. The compact stellarator complements the advanced-tokamak and currentless-stellarator strategies. It uses helical fields from external coils, combining three-dimensional plasma shaping and quasi-axisymmetric design to produce a moderate aspect ratio configuration. The NCSX will contribute to the understanding and improvement of toroidal confinement by using its unique capabilities to gain a better understanding of the physics:

- Beta limits and limiting mechanisms.
- Neoclassical transport reduction by quasiaxisymmetric design.
- Anomalous transport reduction by flow-shear control, using reduced flow damping by QA design.
- Stabilization of equilibrium islands and neoclassical tearing modes with stellarator magnetic shear.
- Power and particle exhaust with a compact stellarator boundary.
- Three-dimensional shaping effects on nonlinear magnetohydrodynamics.
- Conditions for disruption-free operation at high-beta with bootstrap current and external transform.

The physics benefits of the compact stellarator solution, passive stability and tokamak-like confinement including the ability to manipulate the turbulent transport with flows, could outweigh the additional costs associated with more complex coils. The NCSX will provide the data needed to make a proper assessment and accomplish program milestones.

Relationship to Other Programs

The U.S. stellarator program will complement the world stellarator program, producing results that are important for fusion science and that will not be obtained otherwise. The Japanese LHD and German Wendelstein programs feature large experiments with superconducting magnets that will advance stellarator core transport and stability physics, boundary physics, and long-pulse sustainment. However, the LHD and W7-X devices have plasma aspect ratios of 6 and 10.6, respectively. The drift-optimized W7-X was explicitly optimized to suppress the bootstrap current. Neither will test the effects of quasi-symmetry on the confinement physics, compatibility with the bootstrap current providing a significant fraction of the rotational transform in the design optimization, or reductions in the aspect ratio of stellarators down to values (~4) approaching those of tokamaks. The NCSX will address these issues, making unique contributions to world stellarator research.

A low-aspect-ratio quasi-axisymmetric experiment, CHS-qa, is being designed by a group at Japan's National Institute for Fusion Science (NIFS), though not yet formally proposed. The CHS-qa configuration design effort, so far, has evaluated plasma configurations assuming there is no net plasma parallel current [6]. The NCSX is optimized around a high-β configuration with self-consistent bootstrap current profiles, and targets the issues of β limits and high-β disruption avoidance. Thus the NCSX and CHS-qa would be complementary

The national compact stellarator program also couples to and builds upon the programs on existing or already-approved concept-exploration experiments at the University of Wisconsin (HSX) and Auburn University (CTH). The HSX will investigate transport reduction by quasi-helical (QH) symmetry, while the CTH will investigate low-beta stability issues in current-carrying stellarators. In addition, it is expected that a stellarator theory and experimental collaboration program will parallel the project's activities.

As part of the proposed U.S. compact stellarator program, a concept-exploration-level experiment, the QOS, is also being proposed by Oak Ridge National Laboratory as a complement to NCSX. The QOS experiment will investigate the confinement physics of quasi-poloidal (QP) symmetry. Since QP symmetry implies a large toroidal viscosity, the QOS experiment will investigate the role of poloidal flows in confinement enhancement, while NCSX with its low toroidal flow damping will focus more on flow-shear stabilization mechanisms. While the QOS will push down to very low aspect ratio (~2.6), where equilibrium quality is a key issue, the NCSX will push up in beta (4%), where the key issues are stability and disruption immunity. The scientific contributions and design characteristics of the QOS will complement those of the NCSX in order to broaden the knowledge base for compact stellarators.

The proposed NCSX program also complements the Advanced Tokamak (AT) and Spherical Torus (ST) programs, which are developing an approach to sustainment based on the use of nearby conducting walls and active feedback control of unstable modes and current profiles. The NCSX investigates an innovative alternative, where instabilities are stabilized by the design of the three-dimensional shape of the plasma and control is maintained using external coils to shape the plasma.

NCSX Physics Design

In order to carry out its research mission, the NCSX plasma and facility has been designed with the following goals:

- Passive stability to the external kink, neoclassical-tearing, ballooning, and vertical instabilities to $\beta \geq 4\%$, without the need for nearby conducting walls or feedback systems.
- Good quasi-axisymmetry to provide closed drift-orbits and low flow-damping, sufficient to allow balanced neutral-beam injection (for control of parallel flows and beam-driven currents).
- $\beta \approx 4\%$ stable equilibria consistent with steady state without the need for external current drive.
- Aspect ratio ~ 4
- Good flux surface quality at high beta, without taking into account island width reductions due to neoclassical effects.
- Experimental flexibility to vary the plasma shape, external transform, pressure, and current to carry out the research mission.

The NCSX is designed around a computed QAS plasma configuration (Figure 1) It has three periods, an aspect ratio $R/\langle a \rangle = 4.4$, and strong axisymmetric shaping, as well as the three-dimensional shaping that is clearly evident in the figure. The shape is optimized for minimum ripple and marginal stability to several modes at $\beta = 4\%$. The rotational transform profile (Figure 2) increases monotonically, except very near the edge, from about 0.4 ($q \approx 2.5$) to 0.65 ($q \approx 1.5$). The bootstrap current provides about one-fourth of the rotational transform at the edge, while the remainder is provided by coils. The plasma as designed has good magnetic surfaces all the way to the edge except for a small removable island chain at the $\iota = 0.6$ surface.

The main coils for NCSX are the modular coils shown in Figure 3. They resemble toroidal field coils with out-of-plane deformations. Three coils are extended radially to allow tangential access for neutral beams and diagnostics. Not shown but also included are toroidal field coils, poloidal field coils, and trim coils for configuration flexibility. The coils are designed to produce good magnetic surfaces and to reconstruct the physics properties of the reference plasma. The additional coils provide experimental flexibility to test the physics, for example the ability to vary the rotational transform, the shear, and the beta limit, while maintaining good quasi-symmetry. The design is robust in that the coils can provide good configuration properties over a wide range of β, I_P, and profile shapes.

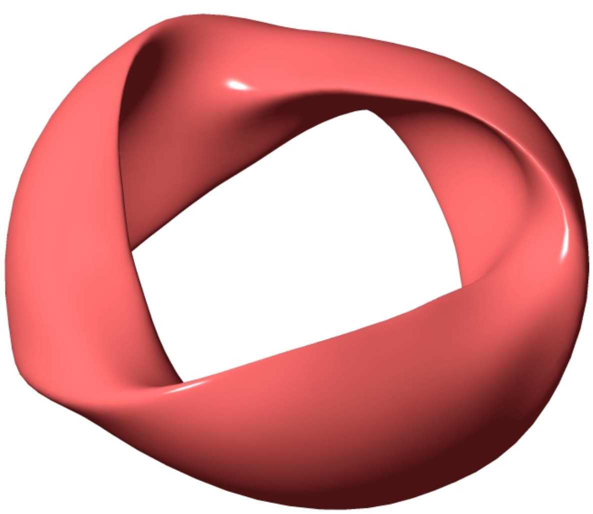

Figure 1. NCSX Reference Plasma Configuration

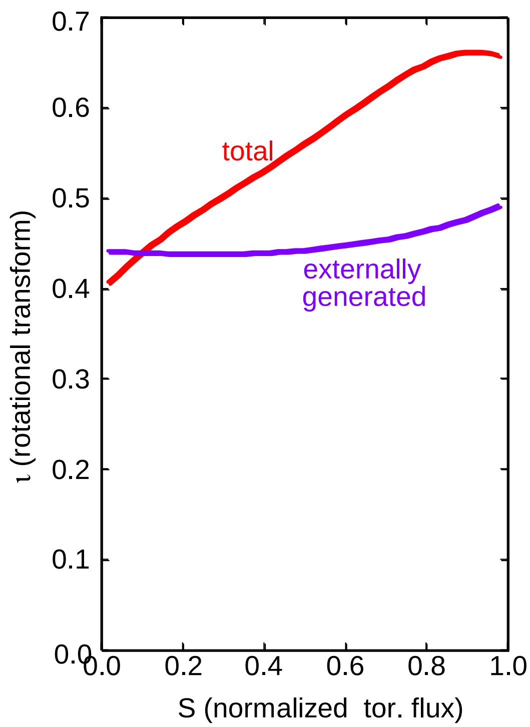

Figure 2. Rotational Transform Profile

The NCSX design is robust in its equilibrium evolution during a pulse. Startup simulations advancing from an initial vacuum state to a high-beta target state along a stable path, consistent with planned equipment capabilities, have been carried out. Free-boundary equilibrium calculations show that the coils produce good magnetic surfaces in the vacuum and high-beta states. This is a result of substantial improvements in design concepts and tools since robustness was identified as a technical issue by the Fusion Energy Sciences Advisory Committee in August, 1999. In sharp contrast to the reference plasma configuration presented in 1999, the present configuration has good magnetic surfaces out to the edge. Residual islands have been eliminated in the design by a newly-developed methodology which makes small resonant perturbations in the coil geometry to reduce island widths as calculated by the PIES free-boundary equilibrium code. A system of trim coils is included in the design to provide a capability for reducing islands over the range of equilibria needed for startup and flexibility. As a further measure the configuration is designed with “reversed shear” so that neoclassical effects should reduce the widths of any island.

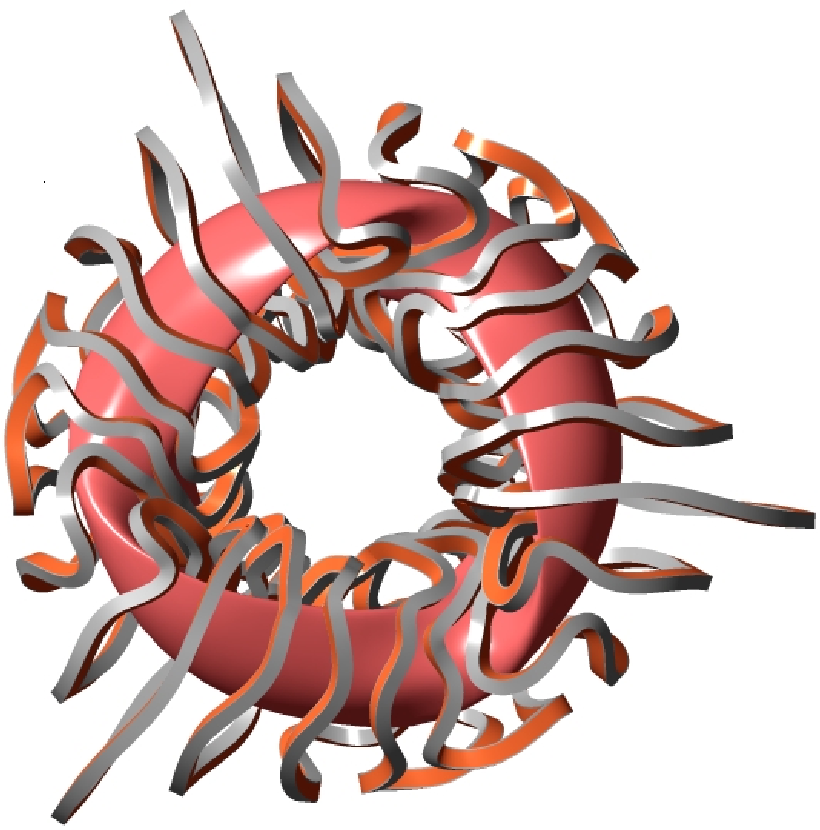

Figure 3. NCSX Modular Coils

The dimensions and performance parameters of NCSX are chosen to meet mission requirements at minimum cost:

Major radius R=1.4 m.

Magnetic field 1.2-1.7 T (>2 T at reduced rotational transform).

Magnet flattop pulse length 1 s at B = 1.2 T, 0.2 s at B = 1.7 T.

Neutral beam heating power 3 MW initially, upgradable to 6 MW.

Radiofrequency heating power: upgradable to 6 MW

Plasma-facing component are designed to remove plasma heat losses without overheating material surfaces, control neutral recycling, and minimize impurities. Because of the complexity of the three-dimensional magnetic field, it is expected that the design of the optimum power and particle handling system will be a long-term research program. The NCSX will use carbon as the material for plasma-facing components, which will be bakable in-situ to 350°C. A range of internal structure, including neutral beam shinethrough armor, limiters, baffles, divertors and pumps are expected to be implemented over the life of the experiment. Initially, an internal frame structure will be installed that can support graphite-weave panels in a range of shapes covering any part of the first wall. This design is robust and provides flexibility to modify the first-wall design to meet program needs. It will also allow plasma shape flexibility and experimental investigations of boundary physics issues, as well as other physics studies.

Fueling will be provided by a programmable multi-species gas injection system which can provide feedback control on the density. High vacuum will be provided by an existing turbomolecular pumping system

A total of 12 MW of auxiliary heating can be accommodated by the NCSX design, 6 MW of tangential neutral beam injection (NBI) and 6 MW of radio-frequency heating. Initially the facility will be equipped with 3 MW of tangential NBI using two of the four existing PBX-M neutral beamlines arranged in a balanced (1 co-, 1 counter-) configuration. The remaining two can be added to upgrade the NBI power to 6 MW. Two radiofrequency heating options are available as potential upgrades. High frequency fast wave heating utilizes fast magnetosonic waves at high harmonics of the ion cyclotron frequency, which minimizes ion damping while producing strong damping on the electron population. The operating frequency chosen for NCSX is 350 MHz. Ion Bernstein wave mode conversion heating uses a fast magnetosonic wave in the 20-30 MHz range, excited at the boundary of a multiple-ion species plasma. After conversion to the slow wave, damping can be on electrons or ions, depending on the ion temperature and species mix.

The facility will be equipped at first with the minimum set of diagnostics needed to support shakedown of major machine systems and the first few phases of physics operation, including first-plasma, electron-beam mapping of flux surfaces, Ohmic plasma experiments, and initial heating experiments. It is expected that an expanded diagnostic system will be necessary to achieve the full range of NCSX physics goals, and that these will be added during the operating life of the facility. Experimental results from the initial operating phases will help optimize the selection of new diagnostic systems and their design characteristics.

NCSX Engineering Design

A pre-conceptual design has been developed for NCSX. The NCSX design is built around the 3-period reference plasma configuration, with a major radius of 1.4 m. The plasma is surrounded by a vacuum vessel with an internal structure that can support molded carbon fiber composite (CFC) panels that are bakable to 350°C. The design features 21 modular coils, 21 toroidal field coils, and 4 pairs of poloidal coils located symmetrically about the horizontal midplane. The coils are pre-cooled to 80K. A cryostat encloses all of these coils. The modular coils, TF coils, and vacuum vessel are assembled in 120° segments. Each segment features ports for heating, pumping, diagnostics, and maintenance access. A cutaway view of the stellarator core assembly is shown in Figure 4.

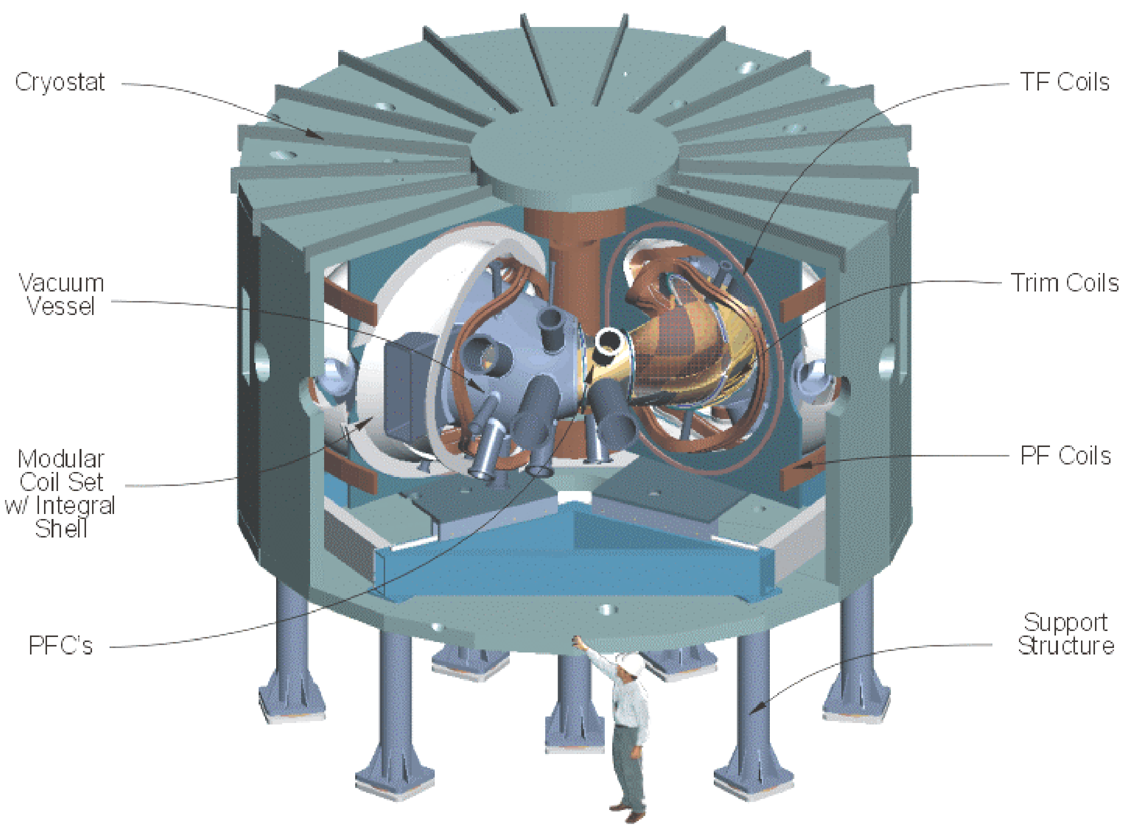

Figure 4. NCSX Stellarator Core

The NCSX will be assembled in the combined PBX/PLT test cell following removal of the PBX device. This location is well suited to NCSX. The test cell provides ample space for the device along with adequate crane capacity. The PBX/PLT computer and control rooms, which are contiguous to the test cell, will be refurbished and utilized. Many systems formerly used on

PBX including the neutral beam, vacuum pumping, power supplies, and water systems will be reused. Power supplies located at D-site will also be used.

Plans for Completing the Design, R&D, and Construction

Following the Physics Validation Review, the review findings and recommendations will be incorporated into the project's plans for developing the design. The next step will be to update the reference NCSX design by September, 2001, incorporating results of ongoing design improvement studies. That update will be the basis for developing the conceptual design. A conceptual design review (CDR) is currently planned for April, 2002. It is expected that the CDR will formally establish the baseline design, cost, and schedule for NCSX. Approval to construct NCSX would be expected following a successful CDR.

R&D and physics analyses will be important to support the design development. The R&D activities will range from small-scale tests to establish design criteria to large-scale prototypes to establish manufacturing approaches and costs. Manufacturability input from industry will continue to be a feature of the design process. Physics analyses (e.g., coil-set flexibility, operating scenarios, boundary physics) will continue in support of the design process. Detailed engineering design is proposed to begin in FY-2003 with fabrication activities starting in FY 2004. For planning purposes it is assumed that First Plasma would occur at the end of FY 2006.

Cost and Schedule

Cost has been a prime consideration in establishing the design parameters for NCSX. The machine size and maximum toroidal field were established to keep the project cost at a target value of $55M in FY 1999 dollars, including contingency, while meeting the mission objectives. Assuming a four-year project (FY 2003-06), the cost in as-spent dollars is projected to be about $65M. This project has been categorized by DOE as a Major Item of Equipment (MIE) activity and the project cost defined accordingly. The preconceptual design work done to date supports our expectation that the proposed project can be carried out for this cost. Non-project pre-operational costs for NCSX research preparation and planning during the project period are projected to be about $4M in FY 1999 dollars ($4.6M as-spent).

Management Arrangements

The NCSX is jointly proposed by Princeton Plasma Physics Laboratory and Oak Ridge National Laboratory in partnership. These laboratories will lead the design, construction, operation, possible enhancements, and physics research for the NCSX project. PPPL has the lead responsibility for project execution. A management organization for the Project is established within the PPPL organization, reporting to the Department of Energy through the PPPL Director. ORNL provides major support, including leadership in key physics and engineering areas.

In carrying out the design and construction phases of the NCSX, PPPL will lead the project management team while ORNL has the lead responsibility for designing the stellarator core. The project will apply the management approach that has been developed and refined during the execution of numerous successful fusion projects. This approach is consistent with DOE Project Management guidelines and directives.

The physics and concept development phase of the NCSX project has been carried out by an integrated national team, with numerous U.S. institutions collaborating. The work has benefited from collaborations with foreign stellarator researchers (in Australia, Austria, Germany, Japan, Russia, Spain, and Switzerland). This approach has facilitated cost-effective knowledge transfer and resource sharing within the DOE system of laboratories and been effective in broadening national participation in the program.

The national team model will be continued as the project moves forward. The NCSX will be a national facility that will provide research opportunities for collaborators from many institutions. Collaborators will have opportunities to lead research areas, install innovative diagnostics and other research tools, conduct student research, and represent the project in scientific conferences.

Conclusions

Compact stellarators provide an important opportunity for the fusion program, offering unique capabilities to advance fusion science and innovative solutions to making magnetic fusion energy more attractive. The quasi-axisymmetric stellarator builds upon the advances in both tokamaks and stellarators and combines the best features of both. A sound physics basis has been established for a proof-of-principle experiment, NCSX, to further develop the physics. Dramatic advances in several aspects of the design have resolved earlier technical issues associated with the robustness of the equilibrium as it evolves from vacuum to high beta. A machine concept has been developed that shows that the NCSX scientific mission can be carried out in a practical and affordable facility. Plans are in place to move forward with the next phase of the project, conceptual design.

References

[1] A. Boozer, Phys. Fluids (1983)
[2] J. Nuehrenberg and R. Zille, Phys. Lett. A **129** (1988) 113.
[3] P. Garabedian, Phys. Plasmas **3** (1996) 2483.
[4] 1998 Stellarator PoP Program proposal.

[5] Fusion Energy Sciences Advisory Committee, “Opportunities in the Fusion Energy Sciences Program,” June, 1999.
[6] S. Okamura et al, IAEA 2000.

Chapter 1 -- Motivation and Goals

1.1 Introduction

Magnetic plasma confinement in toroidal geometries is a proven approach for advancing the science of fusion energy and is promising as a basis for future fusion reactors. Most of the research to date has concentrated on two types of configuration, tokamaks and (to a lesser extent) stellarators. Tokamaks, and other axisymmetric configurations, produce the confining poloidal magnetic field by toroidal currents in the plasma, which are typically generated inductively. Tokamaks have demonstrated excellent short-pulse plasma performance in “compact” geometries, with aspect ratios (ratio of the plasma major radius to the average minor radius) usually less than 4. Stellarators use three-dimensional magnetic fields generated by coils to produce some or all of the confining poloidal magnetic field. Stellarators have demonstrated levels of performance approaching those of tokamaks, but generally at aspect ratios in the range of 6-12.

Since stellarators can produce all components of the magnetic field directly from external coils, they are intrinsically well suited for steady state operation, and do not require external current drive systems. In addition, stellarators typically,do not experience disruptive terminations (disruptions) of the plasma. For example, both the W7-A [1] and Cleo [2] experiments were able to eliminate disruptions at the density limit and when passing through edge q=2 (rotational transform $\iota\!\!\!-$ = 0.5) by the addition of small amounts of externally (coil) generated rotational transform to plasmas with substantial parallel plasma currents. Recent experiments on W7-AS [3] have generated disruptions at edge $\iota\!\!\!-$ ~ 0.5 (q~2) when the plasma current profile is analyzed to be unstable to global tearing modes (extending from center to edge). This instability is well understood in both stellarators and tokamaks, and is easily avoided either by design or care in experiment operation. Extending the study of stellarator stability and disruption avoidance to high-β and low aspect ratio awaits new experiments.

As in tokamaks, the physics properties of a 3D stellarator are determined by the shape of the MHD equilibrium. Three-dimensional equilibria offer many more degrees of freedom than are available for axisymmetric configurations, and this additional shaping flexibility can be used to tailor the equilibrium to obtain desired physics properties. This was first systematically exploited in the development of the “Advanced Stellarator” (AS) concept [4], in which a stellarator configuration was numerically optimized to realize good equilibrium, stability, and transport properties, using theoretical/numerical models. The AS optimization approach produced the designs for the Wendelstein 7-AS (operating since 1988) and Wendelstein 7-X [5] (under construction) experiments at the Max-Planck-Institüt für Plasmaphysik in Germany.

Historically, the major challenge for stellarators has been to provide acceptable drift-orbit confinement, allowing adequate fast-ion confinement and low neoclassical transport losses. This is due to the fully three-dimensional shape, which has no ignorable coordinates and thus no conserved canonical momenta for drift orbits. Thus, the radial excursion of drift orbits is not necessarily bounded, as it is in axisymmetric systems. In addition, a general 3-D magnetic field will have a strong modulation in the magnitude of B, |B|, in every direction, producing strong plasma flow damping in all directions. With the availability of numerical optimization, two strategies have been developed to provide adequate drift-orbit and neoclassical confinement. The first is ‘non-symmetric drift-orbit omnigeneity’, whereby the magnetic field structure is optimized to approximately align drift-orbits with flux surfaces by counteracting the toroidal drift-terms with the helical drift-terms. This is the strategy developed for the design of the superconducting Wendelstein 7-X under construction in Germany, with aspect ratio 10.6, where the orbit confinement was specifically optimized to minimize the bootstrap current. This strategy, partially optimized, also underlies the design of Wendelstein 7-AS, the new ‘shifted-in’ configuration in LHD [19], and the new experiment Heliotron-J [6].

The second strategy for 3D drift-orbit confinement is called ‘quasi-symmetry’, which is based upon work by Boozer [7] showing that drift-orbit topology and neoclassical transport depends only on the variation of |B| within a flux surface, not on the dependence of the vector components of B. This was used by J. Nuehrenberg [8,9] and P. Garabedian [10] to develop stellarators that, while three-dimensional in euclidian space, have a direction (either helical or toroidal) of approximate symmetry of |B| in (Boozer) flux coordinates. Quasi-symmetric configurations have drift-orbits similar to equivalent symmetric configurations, and thus similar neoclassical transport. Rotation in the quasi-symmetric direction is also undamped, as in a symmetric configuration. The first experimental test of quasi-symmetry is the Helically Symmetric eXperiment (HSX) now beginning operation at the University of Wisconsin.

In parallel, there has been a tremendous advance in the understanding of tokamak experiments and the ability to manipulate tokamak plasmas. There has been a general confirmation of ideal MHD equilibrium and stability theory (excepting Mercier stability) and neoclassical transport theory. Methods for stabilizing and manipulating turbulent transport (particularly for ions) have been developed, allowing the elimination of anomalous ion-thermal and particle transport, and reduction of anomalous electron thermal transport. There is a general understanding of the importance of flow-shear stabilization as a mechanism for stabilizing ion turbulence. In addition, there are a number of theoretical predictions that undamped turbulence-generated flows (zonal flows) are significant in saturating turbulent transport at the levels observed.

1.2 The Compact Stellarator Opportunity

The Compact Stellarator Opportunity is to build upon the advances in understanding of both stellarators and tokamaks and to combine the best features of both. We wish to use the stellarator's externally generated helical field and 3D shaping to enhance the MHD stability without requiring external current drive or feedback systems, designing plasmas that have the potential to be free of disruptions. From tokamaks, we wish to use the excellent confinement, ability to stabilize and manipulate turbulent transport, and lower aspect ratio (compared to classical stellarators) to reduce development costs and system size. We also wish to make use of some bootstrap current (driven internally by the pressure gradient) to relieve the coils of having to produce all the the magnetic rotational transform.

In detail, the opportunity is to use the three-dimensional shaping flexibility of stellarators to passively stabilize the modes that limit the β and pulse-length of toroidal plasmas (particularly the external kink and neoclassical tearing modes), thereby expanding the safe operating β range. Quasi-symmetric design provides good orbit confinement and allows undamped flows to saturate and stabilize turbulence. In our studies, we have found that quasi-axisymmetry is best suited for higher β-limits and lower aspect ratio.

1.3 NCSX Mission, Goals, and Unique Contributions to Fusion Science

The mission of the NCSX research is to investigate the effects of three-dimensional plasma shaping, of internally- and externally-generated sources of rotational transform, and of quasi-axisymmetry on the stability and confinement of toroidal plasmas. In particular,

- What are the beta limits and limiting mechanisms in a low aspect-ratio stellarator? Can pulse-length-limiting instabilities, such as external kinks and neoclassical tearing modes, be stabilized by external transform and 3D shaping?
- How do externally-generated transform and 3D shaping affect disruptions and their occurrence?
- Can the collisionless orbit losses typically associated with 3D fields be reduced by designing the magnetic field to be quasi-axisymmetric? Is flow damping reduced? Is the resulting transport and confinement similar to actually axisymmetric systems? How does the transport scale in a compact stellarator?
- Do anomalous transport control and reduction mechanisms that work in tokamaks transfer to quasi-axisymmetric stellarators? Do zonal flows saturate turbulent transport in a quasi-axisymmetric stellarator at levels similar to tokamaks?
- How do the Alfvenic-eigenmode spectrum and stability of a quasi-axisymmetric stellarator differ from those of a tokamak or a non-symmetric stellarator?

- How do stellarator edge-field characteristics such as islands and stochasticity affect the boundary plasma and plasma-material interactions? Are 3D methods for controlling particle and power exhaust compatible with good core confinement.

In order to carry out this research program, the NCSX plasma and facility has been designed with the following goals

- Passive stability to the external kink, neoclassical-tearing, ballooning, and vertical instabilities to $\beta \geq 4\%$, without the need for nearby conducting walls or feedback systems.
- Good quasi-axisymmetry to provide closed drift-orbits and low flow-damping, sufficient to allow balanced neutral-beam injection (for control of parallel flows and beam-driven currents).
- $\beta \sim 4\%$ stable equilibria consistent with steady state without the need for external current drive.
- Aspect ratio ~ 4
- Good flux surface quality at high beta, with no more than 10% of the toroidal flux in islands or stochastic regions.
- Experimental flexibility to vary the plasma shape, external transform, pressure, and current to carry out the research mission.

$\beta \sim 4\%$ was chosen as a goal to provide an unambiguous test of 3D shaping stabilization of the external kink-instability. While the tokamak (A>2) and spherical-torus (A<2) have achieved very high $\beta_T \sim 12\%$ and ~ 40% (respectively) with large amounts of external current drive (including inductive), the β-limit compatible with steady state operation and low external current drive is much lower. Advanced-tokamak stability studies have found that the ideal β -limit is ~ 2-3% [11,12,13,14,15] with external current drive supplying < 30% of the total magnetic transform and without wall stabilization, even for strong shaping (elongation up to 2, triangularity up to 0.8). The advanced tokamak program is working to raise this limit by a combination of conducting walls and active feedback on the resistive-wall instability. For NCSX, achieving $\beta \geq 4\%$ without significant current drive or wall stabilization would demonstrate that 3D shaping is effective at raising the sustainable β-limit. Aspect ratio ~ 4 was chosen to be substantially below existing designs for stellarators with optimized confinement and stability, yet not so low that the other goals cannot be attained.

Since the issues addressed by the mission questions (high-beta stability consistent with steady state, disruptions, transport, and boundary conditions) are critical for magnetic confinement concept improvement, the answers will have far-reaching scientific benefits. Because of its hybrid character, 3D shaping, quasi-axisymmetric design, and flexibility, the NCSX is uniquely capable of providing the answers.

Thus, NCSX will provide a data base for accomplishing the 10-year milestone established by the Fusion Energy Sciences Advisory Committee in 1999: "Determine attractiveness of a Compact Stellarator by assessing resistance to disruption at high beta without instability feedback control or significant current drive, assessing confinement at high temperature, and investigating 3-D divertor operation." This database will provide the basis for designing follow-on experiments, and determining the value of the compact stellarator opportunity.

The breadth of the questions proposed for study by NCSX, and particularly the study of high-β plasmas, requires substantial diagnostics, plasma heating, and power handling capabilities. Significant heating power is required for high-β studies since the predicted β scales as $P^{0.5}$ for most empirical confinement scalings. High heating-power is also required to study plasma wall interactions and edge solutions. Moderate plasma size (similar to PLT or D-III), in terms of poloidal flux or ion drift-orbit width divided by minor radius, is needed to obtain moderately collisionless plasmas for the studies of high-β stability and anomalous transport. The breadth of questions proposed and these required capabilities typify a 'Proof of Principle' experiment, as defined in the FESAC Report on Alternate Concepts, DOE/ER-0690. It is appropriate to address these questions and propose a Proof of Principle experiment, as NCSX builds upon the existing world stellarator program (which is already at the Performance Extension stage), the world tokamak program which has developed the physics of axisymmetric magnetic configurations, and upon HSX [16] which will experimentally test the principles of quasi-symmetry for the first time, at a Concept Exploration level. In addition,

The methods used to numerically design the NCSX plasma and coils have built upon established techniques developed to design W7-X [5] and used to design HSX [16] and previous design studies [9,10]. These techniques have been validated by the verification of fields and initial studies of HSX [17]. The methods have been extended to lower aspect ratio, to include the effects of the bootstrap current, and to address MHD stability in order to address the particular goals of NCSX. This has required significant enhancement of many of the numerical physics models, as discussed in Chapter 2. The codes used to evaluate the physics properties of NCSX and alternative configurations have been extensively benchmarked against both experiments and other codes, as discussed throughout this document.

1.4 Relationship to the World Stellarator Program

There is a strong world-wide program of stellarator research, due in part to their suitability for steady-state operation and stability against disruptions. Existing experiments range from the university scale up to the Performance Extension scale. This broad program has produced a physics and engineering knowledge base and experience that we have been fortunate to be able to build upon in our design studies for NCSX.

The Japanese LHD and German Wendelstein programs feature large experiments with superconducting magnets that will advance stellarator core transport and stability physics, boundary physics, and long-pulse sustainment. However, the LHD and W7-X devices have plasma aspect ratios of 6 and 10.6, respectively. W7-X was explicitly optimized to suppress the bootstrap current while LHD is expected to have relatively low bootstrap currents. Neither will test the effects of quasi-symmetry on the confinement physics, compatibility with the bootstrap current providing a significant fraction of the rotational transform, or reductions in the aspect ratio of stellarators down to values (~ 4) approaching those of tokamaks. These topics will be studied on NCSX as the core of its mission .

The world's largest existing stellarator, Japan's Large Helical Device (LHD), has already demonstrated significant confinement enhancement (up to 2.4 times the ISS95 [18] empirical stellarator confinement-time scaling) and β = 2.4% [19] and recently 3.5% [20] (heating-power-limited) in configurations with aspect ratio around 6. This β value is above the predicted ideal stability limit, yet no limiting instabilities are observed. Confinement times up to 0.3 sec and mid-keV peak temperatures have been obtained. With megawatt-levels of plasma heating, the LHD has operated for pulse lengths greater than 1 minute (recently > 2 minutes [20]).

The operating Wendelstein 7-AS experiment [21] is a partially optimized precursor to Wendelstein 7-X. It has demonstrated the effectiveness of the numerical optimizations in its design, and the benefit of using 3D shaping to control physics characteristics. It has observed enhanced confinement regimes and confinement up to ~2.5 times the ISS95 global scaling. In addition, there are a number of other international stellarator experiments exploring the physics of 3D confinement in a number of configurations at a variety of scales, including CHS[22], TJ-II[23], H-1[24], and Heliotron-J.

The NCSX is the centerpiece of a proposed U.S. compact stellarator proof-of-principle program. The U.S. program will complement the world stellarator program, producing results that are important for fusion science and that will not be obtained otherwise. The national compact stellarator program also couples to and builds upon the existing or already-approved concept-exploration experiments at the University of Wisconsin (HSX) and Auburn University (CTH). The HSX will investigate transport reduction by quasi-helical (QH) symmetry, while the CTH will investigate low-beta stability issues in current-carrying stellarators.

As a complementary part of the proposed U.S. compact stellarator program, a concept-exploration experiment, the QOS, is also being proposed by Oak Ridge National Laboratory. The QOS experiment will investigate the confinement physics of quasi-poloidal (QP) symmetry to reduce neoclassical losses. Since QP symmetry implies a large toroidal viscosity, the QOS experiment will investigate the role of poloidal flows in confinement enhancement, while NCSX with its low toroidal flow damping will focus on tokamak-like flow-shear stabilization. The QOS will push down to very low aspect ratio (<3), where equilibrium quality is a key issue, NCSX will push up in β to explore stability and disruptions. The scientific contributions and design characteristics of the NCSX and QOS will be complementary, in order to broaden the compact stellarator knowledge base.

A low-aspect-ratio quasi-axisymmetric experiment, CHS-qa, is being designed by a group at Japan's National Institute for Fusion Science (NIFS), and indicates the world-wide interest in compact stellarator concepts. The CHS-qa has not been formally proposed. The CHS-qa configuration design effort, so far, has evaluated plasma configurations assuming there is no net plasma parallel current [25], even though such currents are expected (via the bootstrap current) for quasi-axisymmetric configurations. In contrast, we have confronted the bootstrap current and its implications by designing the NCSX around a high-β quasi-axisymmetric configuration with self-consistent bootstrap current profiles. The NCSX design targets the issues of β limits and high-β disruption avoidance which are critical for the long-term attractiveness of the concept.

The scientific success of these experiments requires a continuing vibrant 3D theory and numerical modeling program. This is required in the near term to complete the design of NCSX and other new experiments, and in the longer run to enable interpretation and understanding of experimental results. General 3D topics of high importance include:

- Non-linear MHD stability analysis, including Alfvenic eigenmodes,
- Non-linear micro-stability and turbulence simulation, coupled with neoclassical transport effects,
- Edge modeling,
- Integrated discharge analysis and simulation,
- Faster 3D equilibrium calculations including islands, stochastic regions, and neoclassical effects,
- 3D equilibrium reconstruction and analysis,
- RF wave propagation and damping.

We will encourage and endorse efforts to address these issues, and we welcome collaborative approaches.

1.5 Relationship to Advanced Tokamak and Spherical Torus Programs

The physics challenge for the tokamak program is to integrate the recent advances in understanding to allow stable high-β_T (~5%) steady-state plasmas without disruptions, as indicated in the ARIES-RS study [26], for example. Sustainment of the plasmas should minimize the externally driven current, to minimize recirculating power. Meeting these challenges is the focus of the Advanced Tokamak and Spherical Torus research programs. As presently understood, this will require nearby conducting walls to stabilize the external kink instability, active feedback stabilization of the resistive wall instability, active feedback stabilization of neoclassical tearing modes, and current profile control using external current drive.

The proposed NCSX program complements this research by investigating an alternative innovative approach, where these instabilities are stabilized by the design of the three-dimensional shape of the plasma. Control of the equilibrium is maintained using the external coils to modify the plasma shape through the externally-generated poloidal magnetic field.

1.6 NCSX Contributions to Fusion Energy

If NCSX is successful, the compact stellarator will provide innovative solutions to some of the critical problems that lie on the path to an attractive fusion power plant. A key challenge for magnetic fusion energy research is finding a toroidal plasma configuration that has high power density, can be sustained with low power recirculation, and does not disrupt. The compact stellarator complements the present strategies based on advanced tokamaks, spherical torus, or currentless stellarators by combining helical fields and three-dimensional shaping from external coils at moderate aspect ratio to produce a configuration that could be passively stable and achieve tokamak-like power-densities without the need for external current drive. By optimization of the magnetic field structure, compact stellarators should have tokamak-like confinement, including the ability to manipulate the turbulent transport with flows. Thus, while compact stellarator research will surely broaden our understanding of magnetic fusion science, it may also provide an attractive[27] reactor solution, see Figure 1-1.

The NCSX will advance the compact stellarator as a fusion confinement concept by testing the understanding of the basic physics principles that govern its performance and ultimately will determine its attractiveness. The concept-improvement goals of NCSX are to:

- Determine conditions for high-beta disruption-free operation, compatible with bootstrap current and external transform in a compact stellarator configuration.
- Determine beta limits and limiting mechanisms.
- Demonstrate reduction of neoclassical transport by quasi- axisymmetric design.
- Demonstrate anomalous transport reduction by flow- shear control, using reduced flow damping of quasi-axisymmetry.
- Verify the stabilization of equilibrium islands and neoclassical tearing modes by design of magnetic shear.
- Test stability of Alfvenic modes and their coupling to fast ions in a 3D quasi-axisymmetric configurations
- Develop a power and particle exhaust solution compatible with a compact stellarator.

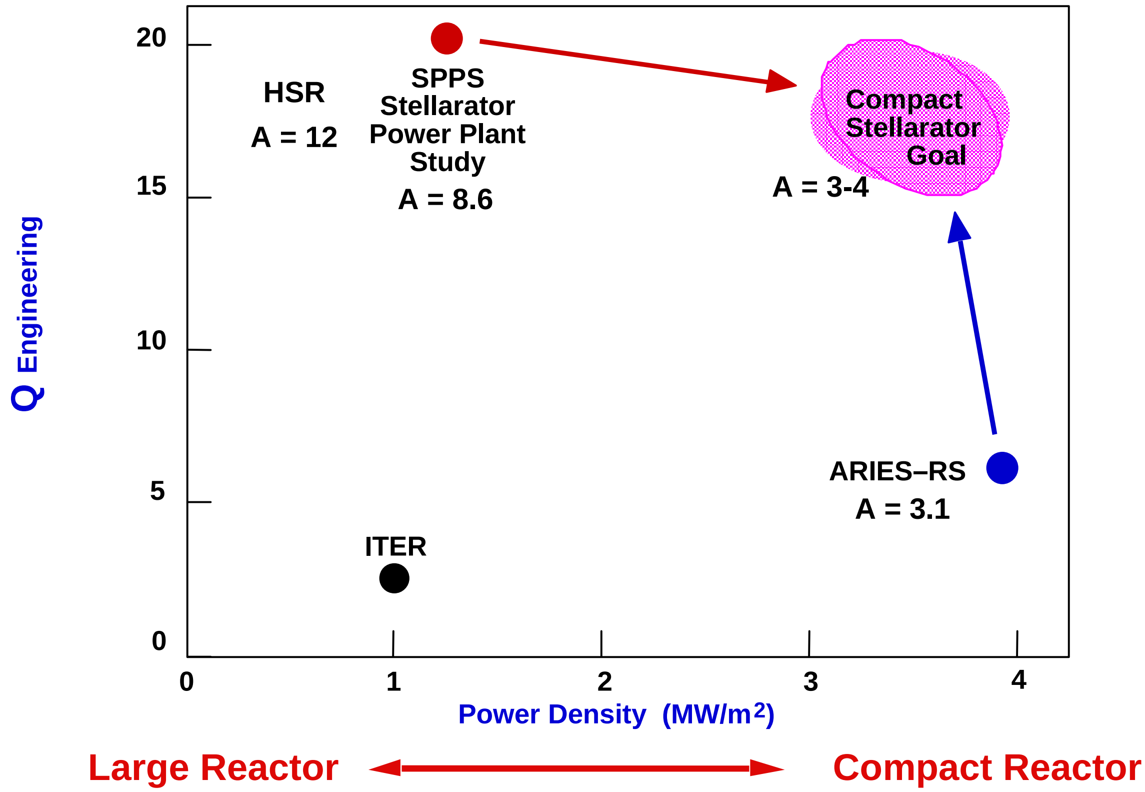

Figure 1-1. Compact stellarators, by combining the low recirculating power (high Q_{eng}) and disruption immunity of stellarators with the low aspect ratio and high power densities of tokamaks, could be attractive

This database, and the improved understanding of 3D plasma confinement that it will provide, will provide the basis for the design of follow on experiments and possible reactor design studies.

While the configurations investigated in the design of NCSX are not optimized as possible reactor designs, they do illustrate the advantages of compact stellarators in a reactor setting. Chapter 14 presents an initial analysis of the reactor implications of compact stellarator designs based upon NCSX-like configurations.

References

[1] W VII-A Team, Nucl. Fusion **20** (1980) 1093.
[2] D.C. Robinson and T.N. Todd, Phys. Rev. Letters **48** (1982) 1359.
[3] A. Weller et al, IAEA 2000; E. Sallander, A. Weller, and W7-AS Team, Nucl. Fusion **40** (2000) 1499.
[4] J. Nührenberg and R. Zille, Phys. Lett. A **114** (1986) 129.
[5] C. Beidler et al., Fusion Technol. **17** (1990) 148.
[6] T. Obiki et al., IAEA 2000 (Sorrento), paper EXP1/09.
[7] A. Boozer, Phys. Fluids 26 (1983) 496.
[8] J. Nührenberg and R. Zille, Phys. Lett. A **129** (1988) 113.
[9] J. Nührenberg, W. Lotz, and S. Gori, in Theory of Fusion Plasmas (E. Sidoni et al., Eds.) (SIF, Bologna, 1994)
[10] P. Garabedian, Phys. Plasmas **3** (1996) 2483.
[11] A. Bondeson et al., Nucl. Fusion **37** (1997) 1419.
[12] P.T. Bonoli et al., Plasma Phys. Control. Fusion **39** (1997) 223.
[13] KSTAR Physics Validation Review Documents, KBSI, 1997.
[14] S.C. Jardin et al., Fus. Eng. Des. **48** (2000) 281.
[15] C.E. Kessel, Jr., private communications.
[16] D.T. Anderson et al., Proc. J. Plasma Res. SERIES, Vol. 1 (1988).
[17] J.N. Talmadge et al., IAEA 2000 (Sorrento).
[18] U. Stroth et al, Nucl. Fusion **36** (1996) 1063.
[19] M. Fujiwara et al, IAEA 2000 (Sorrento), paper OV1/4.
[20] private communication.
[21] J.V. Hofmann et al., Plasma Phys. Control. Fusion **38** (1996) A193.
[22] K. Matsuoka et al., IAEA 1988 (Nice) (IAEA, Vienna, 1989), Vol. 2, 411.
[23] C. Alejaldre et al., IAEA 1998 (Yokohama) (IAEA, Vienna, 1999), Vol. 1, 303.
[24] S.M. Hamberger et al., Fusion Technol. 17 (1990) 123.
[25] S. Okamura et al, IAEA 2000 (Sorrento), paper ICP/16.
[26] F. Najmabadi et al., Fusion Eng. Des. **38** (1997) 1.
[27] R.A. Krakowski, Fusion Technol. **27** (1995) 135.

Chapter 2 — NCSX Physics Design

The National Compact Stellarator Experiment will be the primary research tool in the U.S. for understanding the physics of compact stellarators. Theoretical calculations have demonstrated the exciting promise of quasi-axisymmetric stellarators (QAS) for fusion science. They show that a high-beta, low-aspect-ratio three-dimensional plasma configuration can have the magnetic symmetry of a tokamak, with similar charged-particle drift orbits and plasma flows. Externally generated helical fields provide most of the rotational transform and shape the plasma so as to stabilize the limiting instabilities such as external kink, vertical, ballooning, and Mercier modes without requiring a conducting wall or feedback control. Its bootstrap current will provide a significant fraction of the rotational transform and prevent the unstable growth of magnetic islands. The potential benefits of such a configuration are large: a compact, easily sustained configuration with the good plasma performance of a tokamak.

2.1 Physics Design Overview

NCSX has been designed to accomplish the mission and goals presented in Chapter 1. It is designed around a computed QAS fixed boundary plasma configuration, shown in Figure 2-1. It has three periods, an aspect ratio $R/\langle a\rangle = 4.4$, and strong axisymmetric shaping (average elongation ~1.8), as well as the three-dimensional shaping that is clearly evident in the figure.

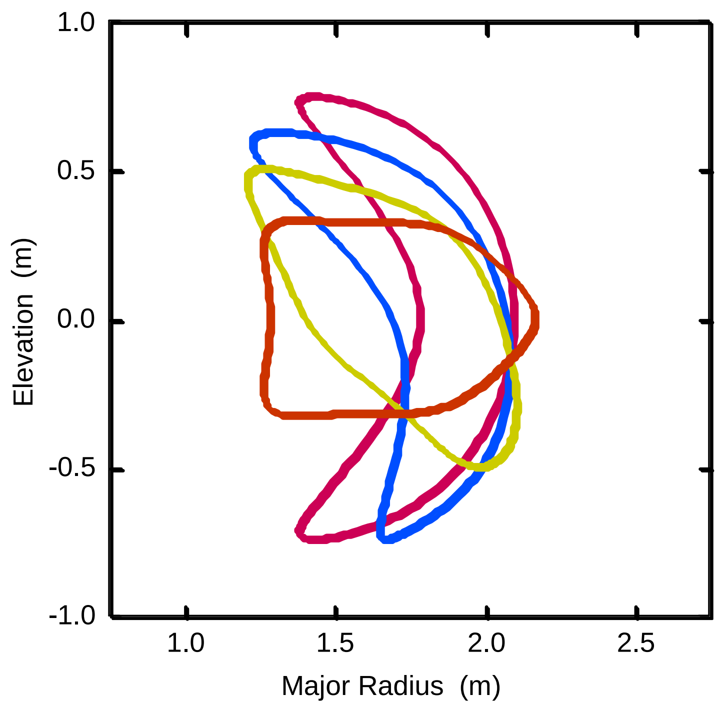

Figure 2-1 Plasma cross-sections at the symmetry planes (the bean- and bullet-shapes) and at equally spaced toroidal angles in between

The shape was optimized for stability and minimum ripple (good quasi-axisymmetry) at $\beta = 4\%$. The effective (for neoclassical transport) ripple is 0.6% at S = 0.5 (where S is the normalized toroidal flux) and about 3.4% at the edge. An axisymmetric configuration would be unstable without a conducting wall at this β value, so this design provides a clear test of the stabilizing effect of three-dimensional shaping. A moderately broad pressure profile, typical of stellarators, and the bootstrap current profile shown in Figure 2-2 were used in the optimization. The bootstrap current provides about one-fourth of the rotational transform at the edge (Figure 2-3), while the remainder is provided by coils. The rotational transform increases monotonically, except very near the edge, from about 0.4 ($q \approx 2.5$) to 0.65 ($q \approx 1.5$). Except for a small removable island chain at the $\iota = 0.6$ surface, the plasma has good magnetic surfaces all the way to the edge.

The NCSX uses modular coils (Figure 2-4) to provide the helical magnetic field. Modular coils resemble toroidal field coils with out-of-plane deformations. The three coils on the v=0 symmetry planes were extended radially to allow tangential access for neutral beams and diagnostics. The design also includes toroidal field coils, poloidal field coils, and trim coils for equilibrium flexibility. The coils are designed to produce good magnetic surfaces and to approximately reconstruct the physics properties of the reference plasma. The additional coils provide substantial experimental flexibility to test the physics while maintaining good quasi-axisymmetry and magnetic surfaces.

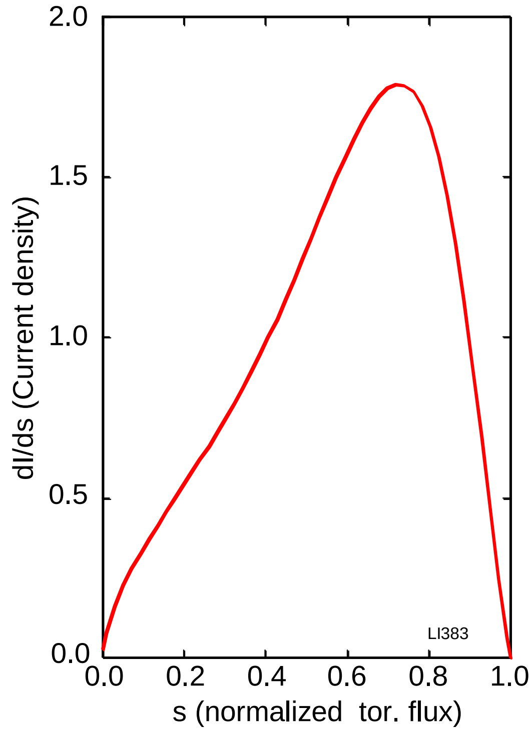

Figure 2-2 Current profile

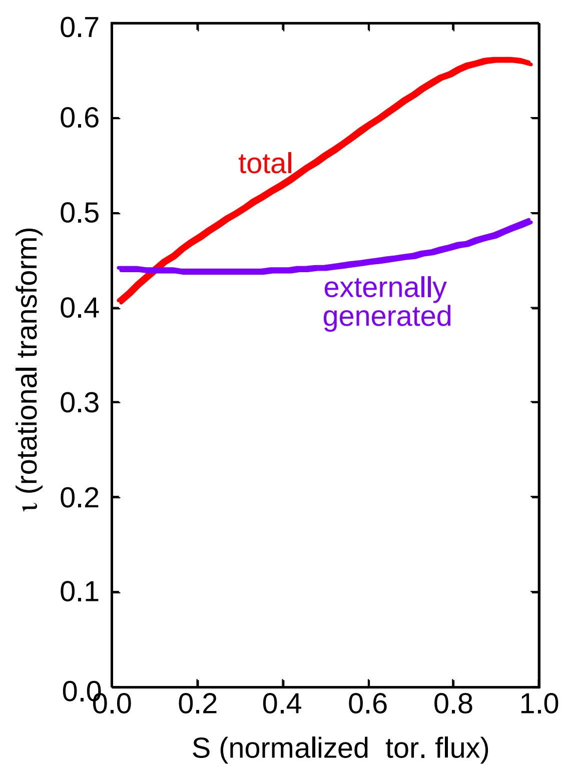

Figure 2-3 Rotational transform profile

Figure 2-4 1017 modular coil design

The NCSX design provides the physics properties and flexibility necessary to develop the physics of compact QA stellarators. The configuration physics design goals and achievements are:

- Reference beta high enough to demonstrate the success of three-dimensional shaping in stabilizing a sustainable toroidal configuration - achieved $\langle\beta\rangle = 4\%$.
- Aspect ratio ($A = R/\langle a\rangle$) substantially less than in existing drift-optimized stellarator designs - achieved A 4.4 (HSX: $A = 8$; W7-X: $A = 11$).
- Stellarator shear in the rotational transform profile - achieved $\iota(0) = 0.39$, $\iota(a) = 0.65$, monotonically increasing except very near the edge.
- At least half the rotational transform provided by coils, to be conservatively disruption-resistant - achieved ~3/4 from coils.
- Good magnetic surfaces – achieved by two independent means: via the application of island removal methods in the configuration design; and via “reversed shear” giving neoclassical island reduction and healing.

- Good quasi-symmetry – achieved an effective ripple of ~3.4% at the edge, helical ripple neoclassical transport low compared to toroidal, counter-injected beam-ion losses (30%) tolerable for beta experiments at B = 1.2 T.
- Stability to ballooning, external kink, vertical, and Mercier modes - achieved at $\langle\beta\rangle$ = 4%..

The key physics design goal for NCSX has been developing a flexible and robust coil design. Substantial advances in physics tools (e.g., equilibrium codes) and design methodologies have resulted in dramatic progress in this area beyond the interim NCSX design that was presented to the Fusion Energy Sciences Advisory Committee (FESAC) in mid-1999. New plasma design strategies have overcome the problem of edge stochasticity seen in the reference plasma in the 1999 design. Physics-based strategies for targeting surface quality as a coil design objective have been developed and applied. A different coil topology has been adopted. New tools for evaluating the flexibility of candidate coil designs, non-existent in mid-1999, have now achieved a high level of productivity.

The NCSX coil design now exhibits the flexibility needed to vary the equilibrium parameters, such as the external rotational transform profile, the shape, and the degree of quasi-axisymmetry, that determine plasma physics properties. The coils can support experiments to understand and control stability limits, transport, plasma-wall interactions, and conditions for disruption avoidance. They are compatible with a stable startup pathway from vacuum magnetic surfaces to a target high-beta equilibrium. They are robust so as to accommodate the anticipated range of variation of profile shapes, betas, and currents that will be encountered in startup and physics experiments, compatibly with good quasi-axisymmetry and magnetic surfaces. The coils can provide a wide range of plasma current (up to 420 kA) and ramp rates (up to 3 MA/s), background toroidal field (±0.3 T), axisymmetric poloidal fields from the PF coils, and helical fields from the modular coils. Coil designs have been generated with these physics capabilities:

- Good plasma physics performance (stability and low ripple) is achieved over a wide range of beta and plasma current values for fixed profile shapes.
- Stable paths from vacuum to high-beta conditions are available.
- Good plasma physics performance (stability at $\langle\beta\rangle$ 7 3% and low ripple) is achieved over a wide range of profile shapes for fixed plasma current values.
- Shape flexibility to vary the theoretical stability boundaries for fixed pressure and current profiles is available. The stability beta limit can be reduced to below 1% or, by trading quasi-symmetry for stability, it can be raised to at least 4%.
- Flexibility to vary ι up and down at fixed shear, to vary the shear at fixed $\iota(0)$ or at fixed $\iota(a)$ is available.

- Good magnetic surfaces are achieved, by design, in vacuum and in the reference high-beta state. Resonant trim coils are provided in case they are needed to maintain good surface quality in other configurations.

Machine size, heating power, and pulse length are set by a combination of physics and practical considerations, including cost. Here we describe the main parameters of the facility and their motivation.

- Major radius R=1.4 m. Since the machine cost increases strongly with size, we have sought to set the major radius at the minimum value compatible with NCSX physics goals. The limiting factor is access. At the chosen size, available neutral beam injectors can be accommodated with acceptable injection losses. Access for diagnostic viewing and for personnel entry to the vacuum vessel interior is critical for the repair and modification of in-vessel hardware. While such access is available in the design, it is marginal, so improving access at fixed overall machine size is a high priority goal for design optimization during conceptual design.

- Heating power: 3 MW initially, upgradable to 12 MW. The facility will be initially equipped with 3 MW of neutral beam heating from two tangential injectors, one co- and one counter-, using two of the four existing 50 keV neutral beams from PBX-M to minimize cost. The device will be designed with provision for up to 12 MW of auxiliary heating: all four PBX-M beams (6 MW total) as well as wave launchers for up to 6 MW of radio-frequency heating.

With the full complement of hydrogen neutral beams (6 MW), the reference beta value of 4% and a collisionality $\nu^*=0.25$ are predicted to be attained at B = 1.2 T, assuming an enhancement factor of 2.9 times the ISS95 stellarator confinement time scaling, or 0.9 times the ITER-97L tokamak scaling (i.e., close to L-mode).

With the initial 3 MW beam system and the same collisionality and enhancement assumptions, the predicted beta value is 2.5 – 2.8%. The 3 MW system provides balanced injection necessary for discharge control (Chapter 10) and enough power to investigate enhanced confinement regimes, assess confinement scaling, and acquire a database for deciding on the amount and type of any plasma heating upgrades that might be needed.

Further details on projected plasma parameters and profiles are provided in Chapter 8.

- Minimum magnetic field for good confinement of neutral beams: 1.2 T. A minimum product of magnetic field and major radius $B\times R$=1.7 T-m is required to keep the losses of tangentially counter-injected 40-keV hydrogen ions below 30%. For the R = 1.4 m design, the minimum magnetic field is 1.2 T.

- Maximum magnetic field at full external transform: 1.7 T; minimum heating pulse length: 0.3 s. The available heating systems can provide full heating power for 0.3 s pulse lengths initially. A cost-effective magnet design provides a 0.46 s flattop at 1.7 T, which allows 0.1 s for plasma initiation, 0.06 s for a rapid (3 MA/s) inductive current ramp (to produce bootstrap-like current profiles), 0.1 s to heat to full beta, and 0.2 s for the plasma to relax at full current and full beta.

The currently available range of magnetic fields (1.2-1.7 T) will support physics studies of low-collisionality transport and confinement scaling, although it is marginal for these purposes. A factor of 2 would be more desirable. Using the supplementary toroidal-field coils, the magnetic field can be increased to 2 T, but with reduced external rotational transform. Increasing the maximum magnetic field towards 2.4 T through modular coil design improvements is an objective for design optimization efforts in the conceptual design phase.

- Upgrade heating pulse length: 1.1 s. At B = 1.2 T the coils and power supplies are capable of 1.1 s heating pulses. Realistic upgrade paths are available to extend the heating pulse length to match this value, which would allow time for true equilibration of the configuration (flat voltage profiles). The priority of such upgrades, and the optimum path to take, will depend on experimental results from the initial phases of NCSX operations.

In the remainder of this chapter we describe the physics design of the NCSX facility. We describe the methods used to develop the reference plasma configuration and associated coils, which we have introduced in this section, and then evaluate them in terms of their physics properties and flexibility. Then we summarize power and particle handling capabilities, plasma heating, diagnostics, and the planned research program. Later chapters describe engineering solutions and physics analyses in greater detail.

2.2 Reference Plasma

The NCSX reference plasma configuration was designed through the use of an optimization code. The optimizer adjusts the values of about 40 parameters specifying the shape of the plasma boundary to attain stability and other targeted configuration properties. For this purpose, the value of $\langle\beta\rangle$ was fixed at 4.25%, the pressure profile was specified, and the current profile was taken as the calculated bootstrap current (see Chapter 4). Quantities targeted in the optimizer for this calculation included: a measure of quasi-axisymmetry (the sum of the squares of the non-axisymmetric Fourier components of B in Boozer coordinates, with an adjustable weighting of contributions from different flux surfaces); the eigenvalue of the most unstable external kink mode calculated by the TERPSICHORE [1] code; ballooning eigenvalues calculated by the VVBAL or the COBRA [2] codes; the rotational transform on one or two flux surfaces; the complexity and current density of an external surface current constructed by the NESCOIL [3] code representing a first approximation to a set of coils. (The surface-current coil solving method is described in the next subsection.) The properties of these MHD equilibrium configurations are completely determined by the current and pressure profiles, as well as the plasma boundary, which is represented as a finite sum of Fourier harmonics for R and Z. Varying the Fourier harmonics as independent variables in the optimizer allows us to seek stellarator configurations in which the various criteria are satisfied as well as possible. The VMEC code [4]

Table 2-1 Properties of the reference plasma configuration

Number of periods	3
R/⟨a⟩	4.4
⟨β⟩	4.1%
ι(0)	0.40
ι(a)	0.66
ι(0) vacuum	0.45
ι(a) vacuum	0.49
R (meters)	1.42
⟨a⟩ (meters)	0.33
w_{min} (meters)	0.13
I_P (kA) at B=1.7 T	175
ϵ_h effective	0.6%

is used to calculate the MHD equilibria needed to evaluate the physics targets for arbitrary values of the independent variables.

In the design process, candidate configurations generated through use of the optimization code were evaluated in more detail with an array of standalone codes that consume too much computer time to be practical to run as part of the optimizer. Ion thermal confinement times were estimated by Monte Carlo simulation using the GTC code to simulate the full ion distribution function [5]. The energy losses of neutral beam ions were also calculated using Monte Carlo simulations [6,7]. The CAS3D MHD stability code [8] was used to confirm the Terpsichore calculations, and to evaluate free-boundary kink and vertical stability without relying on currents in the wall to provide stabilization. (Terpsichore calculations had a conducting wall at about three times the minor radius, where it was calculated to have little impact on the stability.) The integrity of the flux surfaces was monitored with the PIES code [9], which solves the three-dimensional equilibrium equations using a general representation of the magnetic field, so that it can handle islands and stochastic regions. The results of the calculations by this array of codes were used to fine-tune the optimizer and to help steer the design process.

Table 2-1 tabulates the key properties of the NCSX reference plasma configuration, with a major radius of 1.4 m. The properties of the reference plasma configuration have been evaluated at a ⟨β⟩=4.1%, where it is designed to be marginally stable. Very recent high-resolution stability analyses have found that the plasma has a relatively high order (n = 11, m = 17) mode, localized near the edge (see Chapter 5). The values of ι at the magnetic axis and the plasma boundary are given for the full current, full ⟨β⟩ equilibrium, and for the vacuum stellarator field having the same boundary. The quantities w_{min} and I_P are, respectively, the minimum half-width of the cross-section and the total plasma current (evaluated for B= 1.7 T). The quantity ε_{h} is an effective ripple strength evaluated at a normalized toroidal flux S=0.5 (r/a≈0.7). It is calculated numerically to match the $1/\nu$ transport regime [10].

As initially generated by the optimizer, the plasma configuration was calculated to have a total island width of about 15% of the minor radius at $\langle\beta\rangle = 4\%$, dominated by a single island chain at $\iota = 0.6$ with an island width of about 10%. The islands have been removed, using a method based on the PIES code, either by a slight further adjustment of the boundary shape or by a slight perturbation of coils that have been designed based on the unmodified plasma configuration. The adjustment process, as well as the general subject of flux surface calculations, will be discussed in Chapter 4.

2.3 Helical-Field Coil Design Methodology

The design of coils for low aspect ratio stellarators presents new challenges due to the strong harmonic coupling between toroidal (1/R) and helical components of the field. In addition to preserving the good physics characteristics of the reference plasma, the coil set must be capable of satisfying engineering constraints. Feasibility constraints placed upon the coils include limitations on the allowable current density in the coils; lower bounds on the radius of curvature and wind-back characteristics (complexity) of the coils; separation of the coil winding surface from the plasma; and access through the coils for heating, diagnostics, and maintenance personnel.

The design methodology for obtaining coils for NCSX is based on the “reverse engineering” technique pioneered in the late 1980’s by the W7-X group under Nuehrenberg, *et al*. Earlier coil design efforts worked with direct parameterizations of helical coils to obtain large aspect ratio (A) configurations with certain basic physics properties. A dramatic departure from this approach was to realize that a much broader spectrum of configurations could be investigated by separating the plasma optimization process from the coil design. Not only does this allow better optimization of physics properties, it also makes available a much larger design space (*e.g.,* multiple topologies and geometrical properties) for finding suitable coils. At large A, the plasma and coil optimization could be done independently of each other. However, at the lower A of NCSX, it has been found beneficial to weakly couple these two optimization processes in such a way that certain coil properties, approximated via a surface-current representation, are included directly in the physics optimization procedure, as mentioned in Section 2.2. In this way, physics solutions can be guided toward regions of parameter space where realizable coils exist.

In finding NCSX coil solutions by the reverse engineering method, the boundary shape of the reference plasma is targeted by minimizing the root-mean-squared normal component of the total magnetic field on the plasma surface. The plasma boundary is prescribed by a fixed-boundary solution from the VMEC equilibrium code. Coil solutions typically reproduce the desired physics properties when the total residual B-normal is less than 0.6% (in units normalized to the local value of |B|) on average and less than 2.5-3% peak. The value of B-normal includes contributions from the plasma's internal currents (which are calculated using the BNORM code) and, optionally, from specified background coils as well as from the helical-field coils.

Filamentary helical-field coils are arranged on a coil winding surface (CWS) that approximately conforms to the reference plasma boundary, with enough separation (typically about 18 cm on the inboard and 28 cm on the outboard side) to allow space for plasma-facing components, the vacuum vessel, and finite coil cross section. The CWS shape can be fixed or it can be varied as part of the optimization process, which has the benefit of further improving the physics and engineering objectives. Two methods are used for finding an optimum filamentary coil set on the CWS. The first is to solve for a surface-current distribution on the CWS and then convert it to a discrete-filament representation. The second is to solve for the filament geometries directly using a parametric representation of their trajectory on the winding surface.

The first method (without the discretization of this continuous distribution into coil filaments) is incorporated in the NCSX physics optimization process. The Neumann Equation Solver code NESCOIL [3] is used to find the current distribution that minimizes B-normal. To improve the targeting of both physics objectives (represented by B-normal) and engineering objectives (*i.e.,* low current density, gentle bend radii of the coils) for NCSX, a singular value decomposition (SVD) technique was developed. The new code, NESVD, runs as fast as the original NESCOIL code, which enables it to be placed within an optimizer loop so that the shape of the coil winding surface can be adjusted to yield further improvements in the target criteria. A newly developed method based on a genetic algorithm (GA) is available, if desired, to convert surface current potentials computed in NESCOIL or NESVD to an optimized set of discrete coils.

The second method for determining coils, the direct-filament method, has led to the modular coil designs that are of most interest for NCSX. This method uses the COILOPT code, which optimizes the coil geometry on a toroidal winding surface that is well separated from the plasma boundary. A parametric representation of the filamentary coils is used, with constraints to ensure preservation of stellarator symmetry. In addition, parameters representing the winding surface geometry can be varied to further improve the optimization targets. Target functions in the optimization problem include the B-normal error, the lengths of individual coils, the minimum coil radius of curvature, the minimum separation between adjacent coils, and the minimum separation between the coils and the plasma. Geometric constraints are introduced in the form of weighted penalty functions.

Methods for targeting magnetic surface quality as a coil design objective have been investigated. To date, the most success has been achieved using the PIES code to compute small modifications to the modular coil geometry determined by COILOPT. Coefficients in the modular coil representation are adjusted to cancel the normal magnetic field components at the dominant resonant island chains in the plasma interior. The resulting modified plasma has significantly improved magnetic surface quality (residual islands widths are greatly reduced). This method is described in greater detail in Chapter 4. Other, less computationally intensive methods have also been explored. One approach is to use an estimated island width calculated from the resonant magnetic field component at rational surfaces, thereby avoiding the time-consuming PIES calculations. This approach has not yet been fully tested but appears promising. Another approach, implemented within the NESVD scheme, adds the ability to minimize the resonant field errors on the plasma surface. The square of the field line displacement from a nominal flux surface can be written as a linear function of the Fourier components (in a straight magnetic field line system) of the normal field error on that surface. This may provide an ability to further improve magnetic surface quality at the edge.

2.4 Helical-Field Coil Designs

Modular coils were selected as the reference coil concept for NCSX because they were found to provide the best physics properties of the various topologies that were studied. Coils of this type have operated successfully in the W7-AS and HSX stellarators and a superconducting version is being constructed for the W7-X stellarator. In this section we introduce the basic NCSX modular coil design which reproduces reference plasma physics properties and provides neutral beam access, and which has been adopted as the reference for engineering studies. In Section 2.7 we discuss the physics validation of the reference design as well as design variations that have been explored in efforts to understand potential improvement paths.

Modular coils were designed using the reference plasma configuration as a target equilibrium. An initial modular coil solution, designated 0907, contained 7 coils per field period (4 unique coil types) including a coil on the v = 0 symmetry plane (the bean-shaped cross section). The number of coils per period (7) was chosen because it resulted in very low error in B-norm on the plasma boundary. This solution was found with COILOPT, targeting the minimum coil-coil separation ($\Delta_{cc,min}$), minimum radius of curvature (ρ_{min}), and coil length; and allowing the winding surface to vary. As a final step in the optimization procedure, the length constraints were removed and a minimum plasma-coil separation ($\Delta_{cp,min}$) target was imposed. Results of the optimization are given in Table 2-2. As a preliminary check, a free-boundary

VMEC equilibrium was calculated using this modular coil solution and the reference plasma profiles, and it was found to closely match the original (fixed boundary) plasma configuration.

Table 2-2 Modular coil optimization results

Design	ID	N_c	δB_{avg}(%)	δB_{max}(%)	$\Delta_{cc,min}$(cm)	ρ_{min}(cm)	$\Delta_{cp,min}$(cm)
M2	0907	7	0.57	2.55	13.4	11.0	23.3
M3	1017	7	0.61	2.61	14.8	12.3	23.3

In order to achieve adequate access for the neutral beams, it was necessary to modify the 0907 coil set by extending the modular coils near the v = 0 symmetry planes in radius on the outboard side while preserving the low B-normal errors of solution 0907. Starting with the 0907 coil set, the coils were re-optimized using a modified winding law that imposes the radial

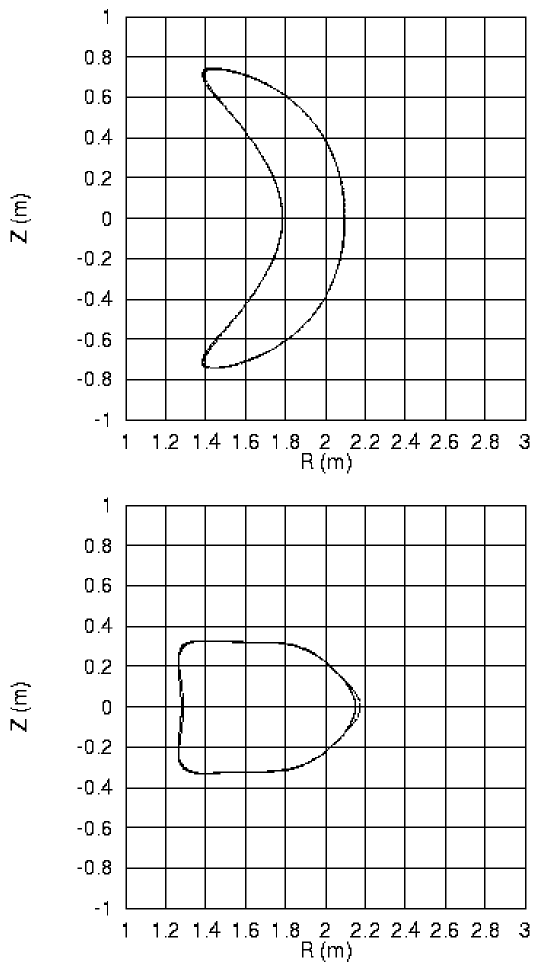

Figure 2-5 Free-boundary reconstruction (solid) with modular coil solution 1017, compared with the target (fixed boundary) plasma boundary (dashed), shown for the v=0 (top) and v=1/2 (bottom) toroidal planes

extension on the coils, while maintaining stellarator symmetry. The resulting solution, the 1017 coil set, is compatible with the engineering design of the neutral beam injection system and has field errors comparable to 0907. The 1017 coil configuration is displayed in Figure 2-4, and a free-boundary reconstruction of the plasma with these modular coils is shown in Figure 2-5.

Coil solutions are not unique, and thus there is freedom available to optimize the coils for given physics goals. The 1017 design was selected for engineering assessment and an attractive machine concept has been developed based on it. However, at this stage of the design it is important to continue trying to optimize the design for manufacturability, access, and physics performance. Therefore, alternatives to the 1017 design have been studied, with the aim of reducing current densities, reducing bend radii, increasing coil-to-coil spacing, and reducing the number of coils consistent with required physics properties. The final coil configuration for the conceptual design will be selected later in the design process.

2.5 Robustness and Flexibility

In order to achieve its scientific goals, the NCSX device must be capable of supporting a range of variations in plasma configuration. While the helical-field coils provide the physics properties required for a particular high-beta equilibrium as a minimum condition, the complete coil design must provide the flexibility and robustness necessary to meet the research needs of the program. In particular, the coils must be capable of:

- Providing access paths to high-beta states, starting from an initial vacuum state.
- Providing good physics properties over a wide range of plasma pressure and current profiles in order to be robust against physics uncertainties.
- Being able to vary the physics properties of the plasma configuration, including rotational transform and shear, so that the understanding of how the physics depends on configuration parameters can be tested experimentally.

To meet flexibility and robustness requirements, the basic NCSX modular coil design is augmented in several ways:

- The 21 modular coils are grouped into four circuits, one circuit for each distinct coil shape. The like-shaped coils are connected in series and circuit currents are controlled independently.
- A supplementary toroidal-field coil set provides a weak (±0.3 T) 1/R field that can be in either direction relative to the modular coils. It provides the capability to vary the external rotational transform at fixed shear.
- A poloidal field coil system provides inductive current drive (1.4 Wb of flux swing with low stray fields in the plasma region, and current ramp rates up to 3 MA/s) in either direction. It also provides low-order axisymmetric multiple fields (dipole, quadrupole,

hexapole, octupole) for plasma shape control. Several poloidal field coil design variants are analyzed in later chapters, including representation in terms of a toroidal multipole expansion. The final design of the poloidal field coils will be established during conceptual design.

- A trim coil system provides control of helical field components with poloidal mode numbers m = 5 and 6 and toroidal mode number n = 3 at specific resonant surfaces in the plasma. These provide capability for magnetic island width control over a wide range of plasma configurations, in case such control proves necessary to meet flexibility and robustness requirements. The chosen design approach allows the addition of trim coils for other poloidal modes if necessary. Trim coil design is described in more detail in Sect. 2.6 and the status of physics validation is given in Chapter 4.

Physics evaluations of NCSX flexibility and robustness are described in detail in Chapters 9 and 10.

2.6 Trim Coils for Maintaining Good Surfaces

The modular coils, in combination with a rich poloidal coil set plus a background 1/R field from a toroidal coil set provides the flexibility and robustness to reach a wide range of plasma states. This includes the time evolution of the discharge from vacuum to the high-beta

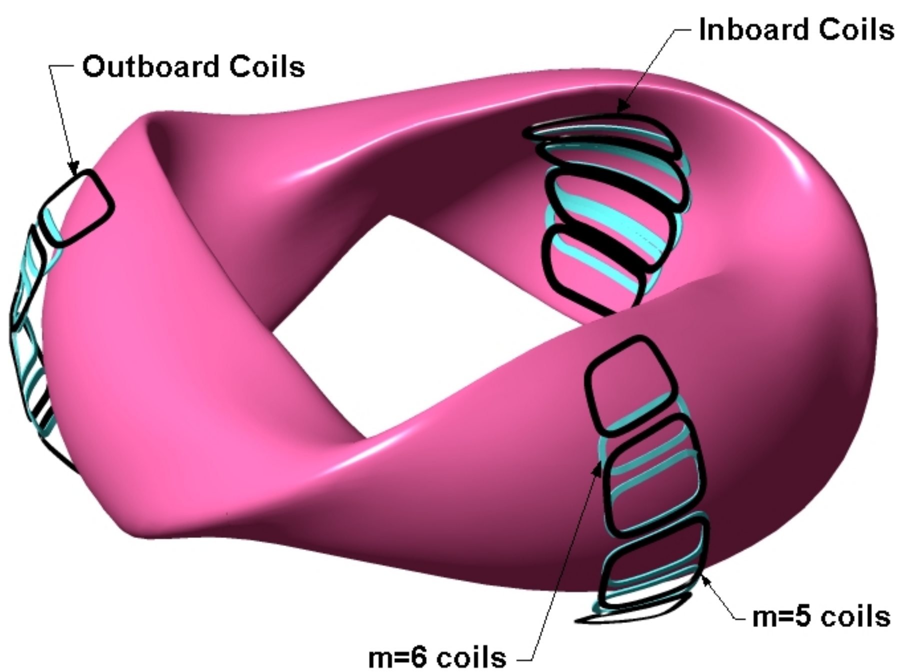

Figure 2-6 Resultant m=5 and m=6 trim coil sets

state. It includes operation with different current, pressure or iota profiles. Using the island healing method previously mentioned, the basic coil set is designed to produce good surfaces in the reference high-beta state but may not have sufficient control over island producing resonances for other plasma states. For that we introduce a trim coil set.

The trim coils were designed to target the specific resonances based on the range of iota encountered. Hence, the resonances were limited to the lower poloidal modes (m=5,6) for the n=1 toroidal mode, the dominant modes for the LI383 family. Trim coils for other modes will be added if found necessary.

The design goal for trim coils was to provide coil sets which strongly couple to the targeted resonances on interior plasma surfaces with minimum current demands and minimal impact on the radial field at the plasma boundary. The design was guided by an initial evaluation of where trim coils would be most effective, on a specified surface conforming to the plasma. It was found that the regions of strongest coupling occur around v=0 inboard and outboard. This is the banana or crescent section of the plasma. Not surprisingly, this is where the resonant interior surfaces are closest to the trim coil winding surface.

Trim coils were located in these regions of strong coupling, leading to a simple racetrack shape. Four coils inboard and four outboard (see Figure 2-6) at each period provide approximately 33% of the effectiveness of an ideal helical winding for the m=5 resonance, while covering only a much smaller portion of the surface. The m=6 winding is more than 40% effective. The coverage may need to be reduced further to avoid interference with neutral beams.

The offset of this surface was limited by engineering constraints. The current demands were seen to increase rapidly with distance from the resonant surface. This, plus accessibility to coils at the inboard side of the plasma, led to a selection of a surface inside the vacuum vessel behind the first wall. This also allowed locating trim coils between the co- and counter- neutral beams.

2.7 Physics Evaluation of Coil Designs

The main stellarator coils of NCSX are designed to reproduce the reference plasma configuration (LI383) at the state of full current and full beta, using the reverse engineering method discussed in Section 2.3. In this section, we discuss the physics validation of coil designs by evaluating the physics properties of free-boundary equilibria that are reconstructed from candidate coils. We make use of capabilities that are provided for flexibility: supplemental toroidal and poloidal field coils and the freedom to energize modular coils independently. These enable us to further improve and optimize plasma performance. Most of the physics and engineering analyses reported in this document are based on the 0907 or 1017 coil designs described in Section 2.4, but we also report on some more recent designs that indicate directions for improvement.

- **2.7.1 Modular coils for the reference plasma configuration**

Summarized in Table 2-3 are selected sets of coils that are discussed in this section. All have seven modular coils per period and four unique types of coils. All designs preserve stellarator symmetry and in each period have a coil on one of the symmetry planes, either at the bean-shaped cross-section (v=0) or the oblate cross section (v=1/2). The M2 (0907) is an early design which did not accommodate tangential access needed for the neutral beams, but is used in some of the physics analyses. The M3 (1017) coil set has the outer legs of two coil types extended to accommodate tangential access. The M3 is used as the reference for engineering studies and most of the physics analyses. The M8 and M7 are later designs exploring methods for improvement. In both of these design the coil currents were allowed to vary independently in the design process and, in the case of M8, the constraint on the minimum radius of curvature was relaxed to achieve a smaller fitting error. The M7 design explores placing the symmetry coil on v=1/2 cross section. While the M7 has not specifically been designed to meet tangential access needs, the coil modifications that would be required are much less than in designs with a v=0 symmetry coil.

Table 2-3 Definition and characteristics of modular coils

Physics Evaluation ID	M2	M3	M8	M7
Coil Design ID	0907	1017		
Use in design process				
Engineering reference		X		
Physics analyses	X	X		
Exploration			X	X
Extended coil for tangential access?	No	Yes	Yes	No
Symmetry coil position	v=0	v=0	v=0	v=1/2
Treatment of coil currents in design optimization.	Constrained to be equal	Constrained to be equal	Allowed to vary	Allowed to vary

- **2.7.2 Methodology of Evaluation and Optimization**

To evaluate the physics properties of plasmas reconstructed from coil designs, we represent each coil as concatenated line segments. Magnetic intensities inside the coil envelope for each design were calculated at 16 toroidal planes (per field period), with each plane further divided into 101 by 101 meshes in R and Z. This field map was used by the free-boundary VMEC [4] to construct equilibria consistent with the prescribed pressure and current profiles and the enclosed toroidal flux. In our evaluation, we used earlier machine parameters (R= 1.7 m, B = 2 T, and I_p = 250 kA) which differ from the current machine parameters (R = 1.4 m, B = 1.7 T, and I_p = 175 kA). The pressure and current profiles were the same as those in the reference configuration (Section 2.2).

As in the design of the reference plasma (Section 2.2), the VMEC code is the main tool used to calculate free boundary equilibria. These equilibria were evaluated by TERPSICHORE [1] and COBRA [2] for the kink and ballooning stability. The conducting wall, which was assumed to be conformal to the plasma boundary, was placed at a distance 2.5 times the minor radius from the plasma-vacuum interface. The NEO [10] was used for the effective helical ripple, $\varepsilon_{h,eff}$, in the asymptotic collisionless $1/\nu$ regime (the thermal helical transport scales as $\varepsilon_{h,eff}^{3/2}$). The ORBIT3D [11] code was used to evaluate the fraction of neutral beam energy loss. The nŒ0 components of the magnetic spectrum in Boozer coordinates were summed together as a simple figure-of-merit (χ^2_{Bmn}) for the quasi-symmetry of a configuration. In VMEC it is assumed that flux surfaces are nested without islands and stochastic regions. Equilibrium and flux surface analyses are discussed in Chapter 4, while the stability and transport codes are discussed in Chapters 5 and 8, respectively.

For the neutral beam loss calculation with ORBIT3D, hydrogen beam particles were launched at a toroidal plane corresponding to v=0 and at a tangency radius which was aligned with the magnetic axis. The beam particles had an initial energy of 40 keV and a deposition profile taken from a PBX high beta discharge. The background plasma was assumed to be H and had parabolic density and temperature profiles. The impurity species was assumed to be A=18 and Z=9, the density of which was 1/10 of the main ion species.

As in Section 2.2, a Levenberg-Marquardt technique was used to optimize coil currents to achieved desired physics properties, such as the quasi-symmetry, kink or ballooning eigenvalues. The pressure profile was not optimized, however, so further increases in beta are likely to be possible. Because the technique is a local gradient method and the topology of the optimization space is complex with abundant hills and valleys, further constraints, such as regularization of currents, or trials with different weighting may be needed in the search of the global optimum.

The results to be discussed below are mostly based on calculations with reasonable, but nevertheless limited resolutions. Detailed convergence studies, such as those shown in Chapter 5, are extremely time consuming and can only be done for the reconstructed cases at a later time. While results of some individual cases may change when the fine resolution calculation is eventually carried out, the general conclusions of the study presented below will remain valid.

- **2.7.3 Properties of Plasmas Reconstructed From Coils**

In Table 2-4, we show physics properties of plasma configurations reconstructed from these four coil designs. Each case represents a free-boundary equilibrium in which the coil currents were adjusted using the optimizer to target MHD stability and quasi-axisymmetry. In each case, the four modular coil group currents (one for each unique coil type) were allowed to vary independently. An additional PF coil set was used (except for M8, which used axisymmetric multipole fields instead) and a 1/R TF field was used in the plasma optimization. The properties of the reference plasma configuration are shown for comparison.

Table 2-4 Comparison of properties of optimized free-boundary reconstructed plasmas

Coil ID Case No.	Reference plasma (LI383)	M2 M2.3.Z07	M3 M3.3.Z03	M8 M8.3.K594	M7 M7.3.K03
A	4.36	4.25	4.16	4.17	4.37
β	4.19	4.24	4.10	4.09	4.18
R (m)	1.734	1.738	1.738	1.726	1.736
<a> (m)	0.397	0.408	0.418	0.414	0.397
R-min (m)	1.209	1.206	1.196	1.186	1.212
R-max (m)	2.173	2.186	2.208	2.176	2.163
Z-max (m)	0.764	0.772	0.775	0.774	0.756
Min plasma-limiter distance (cm)	1.14	0.36	-0.80	-1.26	0.98
$\iota(0)$	0.394	0.409	0.413	0.429	0.402
$\iota(a)$	0.655	0.655	0.653	0.648	0.653
ι, Max	0.662	0.663	0.659	0.656	0.662
λ, Kink ($x10^4$) [1]	Stable (3)	Stable (3)	Stable (3)	Stable (3)	Stable (3)
λ, Ballooning, ζ=60 [2]	0.91-0.96 (0.11)	0.92-0.96 (0.07)	Stable	Stable	0.91-0.96 (0.14)
χ^2 $_{Bmn}$ ($x10^4$)					
S=0.3	0.5	0.7	0.8	0.8	0.6
S=0.5	1.7	2.2	2.5	2.6	1.8
S=0.8	6.9	8.9	10.3	10.7	7.0
$\varepsilon_{h,eff}^{3/2}$ ($x10^4$)					
S=0.3	1.0	2.2	3.0	1.7	2.1
S=0.5	5.6	8.4	12	7.1	6.9
S=0.8	32	43	63	39	31
f_{NB} (%), 40KeV NBI, 2T, H	14.4	17.7	17.2	15.4	18.1

1. For kink unstable configurations, we give the eigenvalue followed by the most unstable mode in n/m, where n is toroidal mode number and m is the poloidal mode number.
2. For ballooning unstable configurations, we give the range of instability in s, the normalized toroidal flux, followed by the maximum eigenvalue in the unstable region.
3. Recent calculations with improved resolution indicate that these configurations may be unstable to localized kink-ballooning modes, such as m/n=11/17. See Chapter 5.

The coil designs reproduce the aspect ratio, rotational transform and beta of the reference plasma very well. Stability of the N=0 (periodicity-preserving) and N=1 families of external kink modes is preserved in the M3 design, but at the expense of quasi-symmetry.

The M8 and M7 designs explore avenues for improving the quasi-axisymmetry. The M8 design, in which the coil group currents were allowed to vary in the design process, has an improved effective ripple parameter and reduced neutral beam losses relative to the M3, while the stability properties are preserved. The plasma properties of the M7 design come close to those of the reference plasma configuration. Shape control at the outboard tip of the oblate cross section is important for maintaining a magnetic well, which in turn is important for stabilizing the pressure-driven kink mode, as explained in Chapter 5. Having a coil at the v=1/2 cross section is evidently beneficial for this; the benefit manifests itself in the form of better quasi-axisymmetry. In general, we find that the M7 gives the best reconstruction results. Although it would need to be modified to accommodate tangential access, the study shows the benefit of having the symmetry coil on the v=1/2 plane.

2.7.4 Summary

The performance of several modular coil designs has been analyzed in terms of the physics properties of the reconstructed plasmas. The coil design utilized for the initial engineering study (M3) has moderately good ripple characteristics, and the kink and ballooning modes can be stabilized. The freedom to independently vary the modular coil currents and the use of additional PF and TF coils are valuable design features in this regard. They allow us to find more MHD stable plasmas without losing beta or changing the aspect ratio at the full current state. Such modifications make configurations less quasi-symmetrical, with increased ripple along magnetic field lines, particularly inside 50% of the plasma radius. More optimized coil designs (M8) are able to reconstruct stable equilibria with favorable ripple and orbit confinement. There appears to be an advantage to placing a coil at the symmetry plane v=1/2, which results in a more MHD stable plasma. This will be further explored during conceptual design.

Further improvement may be possible by incorporating TF biasing in the design optimization process. Coupling physics optimization directly to the coil optimization could streamline the present design process and open a wider design space. Developing such a tool in the next phase of the NCSX project, thus, may lead us to even better coils.

2.8 Reference Scenarios

To implement coil physics requirements in the engineering design process, a set of reference scenarios is defined. These are idealized representations of real machine operation that establish a basic performance envelope for the coils and power systems. The machine capabilities so defined are then compared with the requirements derived from detailed physics evaluations of startup (Chapter 10) and flexibility and robustness (Chapter 9). Coil designs are modified as needed to meet these physics requirements. This iterative process leads to a machine design that is optimized to provide the required physics capabilities at minimum cost.

The reference scenarios consist of sequences of three equilibrium states with boundary shapes matching that of the reference high-beta plasma:

- S1 state: zero current, zero beta (i.e., vacuum). Provides large volume of closed vacuum magnetic surfaces for plasma initiation.
- S2 state: full current, zero beta (nominally end of current ramp, start of heating). Provides a hollow current profile setup by rapid current ramping before introducing plasma heating.

- S3 state: full current, full beta (reference high beta equilibrium). The target state.

The reference scenarios are defined by a sequence of phases with specified time intervals, as shown in Table 2-5. Machine design implications will be addressed in the next chapter, Chapter 3.

Table 2-5 Reference scenarios for initial coil design

	Units	Low Field Scenario	High Field Scenario
Maximum magnetic field at R=1.4 m	T	1.2	1.7
Maximum plasma current	kA	125	175
Initiate plasma	s	0.1	0.1
Ramp current to full current (S1 to S2 state)	s	0.041	0.058
Current ramp rate	MA/s	3	3
Heat to full beta (S2 to S3 state)	s	0.1	0.1
Maintain constant current, beta, and magnetic field	s	1.0	0.2

2.9 Electromagnetic Requirements

An important physics goal of the NCSX will be the demonstration that the NCSX target equilibrium is intrinsically stable to the external kink mode in the absence of a close fitting conducting wall. The NCSX is designed to minimize the influence of the vacuum vessel and other close fitting structure on the growth rate of the external kink. This can be achieved by keeping conducting structures beyond the critical plasma-wall separation, where the wall begins to have a significant effect on the mode, or by keeping the effective time constant for these structures short compared to plasma evolution time scales.

Design criteria are developed by performing stability calculations with the TERPSICORE 3-D ideal stability code. The reference plasma configuration, which is marginally kink stable at its design beta (~4%) without a wall, is used. To destabilize the kink, the beta is artificially increased. A conformal conducting wall is placed around and at some distance from the plasma. When the effective beta is increased by ~5%, the critical wall-plasma separation is reduced to about 5 cm, or $b/a \approx 1.13$. The NCSX vacuum vessel lies outside this layer over most of the surface, but is close to it on the inboard side, so it might be expected to modify the mode growth rate. However, the wall time constant for the vacuum vessel is much shorter than the pulse length. Thus, although the vacuum vessel may be close enough to affect the mode growth rate, it should not affect the ability to determine experimentally the intrinsic external kink stability of the NCSX plasma.

2.10 Power and Particle Handling

The plasma conditions needed to achieve the NCSX research goals require a level of plasma performance that may be achievable only with good control of neutrals and impurity influx. A power and particle handling program is planned to develop a heat removal and particle control capability consistent with the needed enhanced plasma performance. The goals for plasma-facing component design are to minimize the impact on plasma performance:

- Heat removal must be accomplished in a way that avoids excess temperatures on the material surfaces.
- Neutrals from recycling must be controlled so as to minimize their effect on plasma performance.
- Plasma-surface interactions must be designed for minimum impurity generation.

The design of stellarator power and particle handling hardware is strongly affected by the three-dimensional geometry and by the potentially complex topology of the magnetic field-line structure outside the last closed magnetic surface. Islands, ergodic regions with short and long field-line connection lengths, and ordered-layer structures are all possible. Hardware components, including limiters and divertors, can be localized both toroidally and poloidally, can follow the helical twist of the plasma for a distance, and can be contoured to meet specific performance objectives. For these reasons, the design of the optimum power and particle handling system will be a long-term program, based on the ongoing LHD and W7-AS experiments and on modeling studies now under way. The design of the plasma facing hardware will be iterated during operation to incorporate new experimental results and ideas.

2.10.1 Physics Modeling

Modeling studies that are under way or planned to support the physics design of NCSX power and particle handling systems, described in detail in Chapter 11, are summarized as follows:

- The magnetic field-line topology outside the last closed magnetic surface (LCMS) of NCSX plasmas are being studied with codes developed for Wendelstein 7-X and made available by stellarator researchers at Germany’s Max Planck Institute for Plasma Physics. The codes have been modified to handle the large internal currents associated with quasi-axisymmetric stellarator plasmas. Field-line analyses for the NCSX modular coils exhibit an ordered-layer structure similar to that of an axisymmetric tokamak outside the LCMS.
- The spatial loss pattern of energetic ions from neutral beam injection is analyzed using the same Monte Carlo slowing-down model used to estimate beam heating efficiencies. The losses are found to be concentrated in helical stripes either above or below the midplane, depending on the ∇B drift direction.

- The heat flux profiles on plasma-facing component surfaces that intersect open field lines will be estimated using a technique that couples field line tracing with a model for transverse "diffusion" of the field lines. The field line diffusion simulates the effects of cross-field energy transport and has the effect of broadening the heat deposition profiles on target surfaces. These calculations will utilize codes provided by German colleagues, adapted for the NCSX application.
- Guidance on the placement of plasma-facing components for minimum neutral influx is being developed using the DEGAS 2 Monte Carlo neutral transport code. The volume distribution of neutrals inside the plasma is calculated for potential recycling sources. Initially, two-dimensional geometries based on axisymmetrized NCSX cross sections are being analyzed to obtain preliminary guidance.
- On a longer time scale, the project will move to more sophisticated edge-plasma transport models that self-consistently treat plasma-neutral interactions and couple to plasma edge turbulence models. These models could contribute to hardware upgrade decisions including the most effective location of baffles to control fueling, the type and position of edge-plasma diagnostics, and the level of impurities that can enter the core.

2.10.2 Physics Design of Power and Particle Handling System

The NCSX machine requires an initial system of power and particle handling hardware that supports plasma shape flexibility and experimental investigations of boundary physics issues. It will be upgradable to support the planned phased implementation of power and particle handling systems. The design must be robust against the physics uncertainties that exist in the distribution of heat and particle fluxes on the wall, although cost considerations limit the amount of area that can be covered with expensive material.

- Materials: the vacuum vessel material is Inconel and the plasma-facing components are made of graphite or carbon-fiber composite material. Because of the short heating pulse length, the allowable peak heat flux is quite high, up to 30 MW/m^2, and wall pumping can be used for particle removal.
- Configuration: The baseline design utilizes a contoured liner constructed of molded carbon fiber composite (CFC) panels mounted on a frame of poloidal rings. The molded panels form a continuous shell around the plasma with penetrations for diagnostics, heating, and personnel access. The continuous shell can meet the requirements of the plasma-facing surface, providing a high heat flux capability in the divertor region; providing an inboard belt limiter; providing a high heat flux surface for energetic ions from neutral beam injection; and providing armor for neutral beam shinethrough. During conceptual design, adding baffling in the divertor region will be investigated. The plan is to stage the installation of the liner, with limited wall coverage during initial operation, perhaps limited to covering the frame of poloidal rings with low-Z tiles.

- Vacuum pumping and wall conditioning: four 1500 l/s pumps will be provided using existing pumps. Base pressures of about 2-3×10^{-8} torr are expected, based on previous experience with this same equipment. The graphite PFCs will be bakable to 350ºC to expedite the transport of hydrogen and impurity gasses out of the material. The vacuum vessel will be kept at 150ºC to facilitate diagnostic interfaces. Glow discharge cleaning and boronization will be provided for wall conditioning initially. Lithium deposition is of interest and the port space will be provided to accommodate various implementation options as upgrades.
- Fueling: A programmable multi-species gas injection system based on the existing PBX-M equipment will be provided. It will be capable of real-time feedback control based on a density measurement. High-field-side pellet injection may be added as an upgrade, to provide a tool for accessing enhanced confinement modes. The PBX-M pellet injector is available and any necessary guide tubes will be pre-installed in the device to ensure that high-field-side launch capability can be accommodated.

Further details about the design of power and particle handling systems and capabilities are provided in Chapter 11.

2.11 Plasma Heating

Auxiliary heating is required to achieve the plasma conditions (high $\langle\beta\rangle$ at collisionalities ν^*70.25) needed to accomplish the NCSX research goals. A total of 12 MW can be accommodated by the device design, 6 MW of tangential neutral beam injection (NBI) and 6 MW of radio-frequency heating. Initially, the facility will be equipped with 3 MW of tangential NBI using two beamlines arranged in a balanced (1 co-, 1 counter-) configuration. The initial system provides balanced injection for discharge control (Chapter 10) and enough power to investigate enhanced confinement regimes, assess confinement scaling, and acquire a database for deciding on the amount and type of any plasma heating upgrades that might be needed. Detailed analyses of NCSX plasma heating capabilities and options are explained in Chapter 7.

Neutral beams are attractive because they have been successful over many decades as a tool for confinement physics experiments, particularly those addressing high-beta issues. They are flexible because they provide effective coupling and heat deposition over a wide range of plasma configurations and parameters. The availability of the existing 6 MW NBI system from PBX-M, developed in the 1970s by Oak Ridge National Laboratory and consisting of four beamlines and the associated controls and power systems, presents a cost-effective design solution. They have a maximum beam energy of 50 keV and a pulse length of 0.3 s, and can inject hydrogen or deuterium. The NBI system supports plasma startup by heating the plasma. Tangential injection and hydrogen neutrals are used to reduce beam ion losses. A balanced configuration is chosen to provide the control capability required to null the beam-driven currents, as explained in Chapter 10. The neutral beams provide a range of useful physics capabilities, such as ion heating, current drive (for flexibility), pressure profile control, and ExB shear control. Increasing the pulse length beyond 0.3 s is of interest, as explained in Sect. 2.1, to study fully equilibrated current profiles. It is likely that the pulse lengths can be extended to 0.5 s with no modification and little power degradation. The MAST program in the United Kingdom uses the same type of ORNL beamlines and is developing technology to extend their pulse lengths to >1 s. The NCSX program can take advantage of those developments to extend its neutral beam pulse lengths in the future.

The RF heating system for NCSX will be designed to deliver 6 MW of radio frequency (RF) power to heat the plasma. If current drive were desired, the available heating techniques could provide it with minor modifications to the system. Two options are available, high frequency fast wave (HFFW) and mode conversion heating.

High frequency fast wave heating utilizes fast magnetosonic waves at high harmonics of the ion cyclotron frequency, which minimizes ion damping while producing strong damping on the electron population. The operating frequency chosen for NCSX is 350 MHz. This choice of frequency dictates the use of klystrons for power sources, and folded-waveguide launchers for coupling RF to the plasma. The attractions of HFFW heating include insensitivity to the magnetic field, strong damping, and no significant damping on the neutral beam ions.

In ion Bernstein wave mode conversion heating, a fast magnetosonic wave, excited at the boundary of a multiple-ion species plasma, propagates to the ion-ion hybrid layer where it undergoes conversion to the slow wave. Damping can be on electrons or ions, depending on the ion temperature and species mix. Modeling of NCSX plasmas has indicated that a high field side fast wave launch is necessary to efficiently access the mode conversion surface. The modular coil design permits installation of a high field side “combline” antenna. This type of antenna can be constructed with a very small radial build, which lends itself to installation in a shallow "pocket" in the vacuum vessel, on the high field side.

Electron cyclotron heating has not been analyzed in detail, but because of its modest port requirements, it is expected that up to 2 MW can be accommodated as a future upgrade, if desired.

2.12 Diagnostics

A capable array of diagnostics is planned to make the plasma physics measurements necessary to accomplish program goals. The facility will be equipped at first with the minimum set of diagnostics needed to support shakedown of major machine systems and the first few phases of physics operation, including first-plasma, electron-beam mapping of flux surfaces, Ohmic plasma experiments, and initial heating experiments. It is expected that an expanded diagnostic system will be necessary to achieve the full range of NCSX physics goals, and that these will be added as upgrades during the operating life of the facility. Experimental results from the initial operating phases will help optimize the selection of upgrade systems and their design characteristics. Nonetheless, an implementation plan for upgrade diagnostics has been developed for use as a reference for design purposes. It is used in the ongoing design process to set port access requirements and ensure that a feasible solution exists for all required measurements. The diagnostic program is described in greater detail in Chapter 12.

2.12.1 Baseline Diagnostics

The initial complement of diagnostics includes the following:

- Magnetic sensors: a diamagnetic loop and arrays of flux loops, Rogowski loops, and B-field probes will provide signals to determine the plasma magnetic configuration with the aid of an equilibrium reconstruction code. Because of the strong shaping in NCSX plasmas, such a magnetic reconstruction can provide important information on profiles of plasma pressure and toroidal current.
- Visible cameras: tangential views of the plasma will provide a convenient monitor of the plasma discharge evolution and plasma-wall interactions.
- Interferometer: a single line of sight will provide a monitor of the line density through the core of the plasma during the initial plasma run.
- Vacuum ultraviolet survey spectrometer: This instrument will survey impurity emission from the VUV part of the spectrum, along a single sightline. This diagnostic, as well as the visible spectroscopic diagnostics listed below, are needed to look for signs of impurity contamination problems. This is a common concern in the shakedown phase of any device, when plasma control may be poor and internal hardware problems can be expected. Either can lead to unplanned plasma-material contact, resulting in impurity influx and an increase in radiated power. Detecting such radiation, most of which is in the vacuum ultraviolet, can aid in diagnosing and correcting such problems.
- Visible survey spectrometer: This instrument will monitor the plasma along several lines of sight. At one location, a special detector system will be provided, capable of monitoring selected impurity and hydrogen/deuterium recycling lines with high time resolution.
- Soft x-ray imaging array: This system will measure x-ray emissivity along a fan array of sightlines to detect internal magnetohydrodynamic (MHD) activity. Since such activity can greatly influence the behavior of the plasma particularly as plasma startup control is first being established, these measurements will be valuable in establishing good plasma control in the initial Ohmic experimental phase. The same array can provide other data useful for early NCSX operation, besides MHD. Significant bounds can be placed on the

electron temperature; this is especially valuable since, at the low magnetic fields and high densities expected for early NCSX operation, electron-cyclotron emission measurements of electron temperature may be precluded. Finally, the soft x-ray array may be able to support rough measurements of the total radiated power profiles.

- Electron-beam field mapping apparatus: An electron gun and a fluorescent screen will be provided to investigate the magnetic flux surface quality of the device as constructed and to test the effects of coil-current variations on the magnetic configuration geometry.

2.12.2 Upgrade Diagnostics

After initial shakedown of the NCSX equipment is completed and control of the plasma becomes more routine, it is expected that attention will shift toward the research goals and progressively more diagnostic capability will be required. Diagnostic emphasis will shift from basic monitoring of global quantities and impurities to local measurements of plasma parameters in the core and edge and, later, to more detailed profile measurements. Diagnostics for measuring MHD activity, fast ion behavior, edge and divertor characteristics, and turbulence will see a steady improvement in capability.

Among the upgrade diagnostics, beam-based spectroscopy diagnostics (known as CHERS and MSE) will be used to obtain profile information on ion temperature, rotation velocity, magnetic field pitch angle, radial electric field, and current density. A multi-pulse Thomson scattering system will provide multiple snap shots, during a pulse, of the electron temperature and electron density profiles along a laser beam. Some of the diagnostics upgrades will be augmentations of the initial systems. For example, magnetic sensors will be added or improved through the life of the project, as experience is gained and as new physics or control needs arise. Multiple sets of soft x-ray arrays for monitoring MHD activity, and bolometer arrays to measure radiated power are similarly staged in the plan.

2.12.3 Diagnostic Access

During conceptual design, the project emphasis will be on the design of the stellarator core device, including the coils, vacuum vessel, and plasma-facing components. A systematic analysis of the access constraints and tradeoffs for both baseline and upgrade diagnostics will be an important element of the conceptual design activity. Diagnostic considerations have played a prominent role in the pre-conceptual design development of the NCSX. As a result, a large number of ports (about 87) is provided and many specific diagnostic needs have been taken into account, however the task of providing adequate diagnostic access has only begun. At this stage, the available access is marginal, and providing good diagnostic access will be an important design goal for the conceptual design phase.

2.13 Research Plan, Operation Requirements

The research plan for NCSX will be carried out in a sequence of experimental campaigns:

- First plasma operation: Short Ohmic pulses will be used to achieve the first-plasma milestone and carry out a brief campaign intended to test the ability to initiate and control the plasma and the operation of the initial diagnostics.
- Field-line mapping: This campaign will test the accuracy of the stellarator magnetic field generation by measuring properties of the magnetic surface configuration in vacuum.
- Initial Ohmic experiments: This campaign will establish good control of the magnetic configuration as well as good vacuum and wall conditions. Physics results on global confinement scaling, density limits, vertical stability, effects of low-order rational surfaces on stability and disruptions, and plasma-wall interactions, all at low beta, will be produced.
- Initial plasma heating and transport experiments. This campaign will explore the flexibility, plasma confinement, and stability of the stellarator experiment, starting at the initial heating power (3 MW from two neutral beams), magnetic field (at least 1.2 T) and pulse length (at least 0.3 s). The ability to control the discharge evolution to produce current profiles approximating the bootstrap profile will be tested. Physics results on the adequacy of neoclassical transport optimization, density limits, confinement scaling, and enhanced confinement regimes will be produced. Conditions for avoiding density-limit disruptions will be investigated. Boundary plasma conditions and plasma-wall interactions will be studied. This campaign will develop a database for deciding on the amount and type of any plasma heating upgrades that might be needed and for next steps in the implementation of plasma-facing components. In addition, this campaign will likely commission new diagnostics systems.
- Confinement optimization and increasing beta: This campaign will attempt to extend enhanced confinement regimes and investigate high-beta stability issues with a full neutral-beam complement (6 MW from four beams) and/or megawatt-level radio--frequency heating. Enhanced confinement will be pursued using the techniques developed on tokamak experiments, including sheared rotation from NBI, reduced recycling by wall coating (B, Li) and conditioning, by edge radiation (RI-mode), and by pellet fueling. The dimensional and non-dimensional scaling of confinement will be determined and compared to other configurations. These plasmas will then be used to test directly the predicted beta-limit and the predicted beta-limiting mechanisms. The configuration requirements to avoid disruptions and the disruption-free operating area at high beta will be documented.
- Long-pulse upgrade: This campaign will be preceded by an upgrade to the heating systems (to allow pulse lengths of ~1 sec, and power of as much as 12 MW) and a possible upgrade of the plasma-facing components for improved power and particle exhaust handling for long pulse. These upgrades will allow equilibration of the current profile to the bootstrap current, and will be used to document the high-beta disruption-free operating area in long-pulse operation (compared to the current-profile relaxation time).

These campaigns could be carried out in as little as four years with adequate operating time, diagnostics, and needed facility upgrades. All NCSX research goals could be accomplished in that time. The facility is designed for a 10-year operating life, which is typical for experimental facilities of this class. The design provides for a maximum number of pulses, based on operation in the reference scenario, of 100 per day, 13,000 per year, and 130,000 over the life of the experiment. The device and beams can be operated either in hydrogen or deuterium, with deuterium operation administratively limited by biological shielding capability as on PBX-M.

References

[1] D.V. Anderson, A. Cooper, U. Schwenn and R. Gruber, *Linear MHD Stability Analysis of Toroidal 3D equilibria with TERPSICHORE* in "Theory of Fusion Plasmas," J. Vaclavik, F. Troyon and E. Sindoni eds. (Soc. Ital. Fisica -- Editrice Compositori, Bologna, 1988) pp. 93-102.

[2] R.Sanchez, S.P.Hirshman, J.C.Whitson and A.S.Ware, Journal of Computational Physics **161** (2000) 589.

[3] P.Merkel, Nucl. Fusion **27** (1987) 867; P.Merkel and M. Drevlak, Proceedings, International Congress of Plasma Physics and 25th EPS Conf. Control. Fusion and Plasma Phys, Prague 1998, edited by P.Pavlo. (Europ.Phys.Soc., Geneva, 1998) ECA 22C, 1745.

[4] S. P Hirshman, W. I. van Rij, and P. Merkel, Comput. Phys. Commun. 43, 143 (1986).

[5] Z. Lin, W. M. Tang, and W. W. Lee, Phys. Plasmas **2** (1995) 2975.

[6] D. A. Spong, S. P. Hirshman, J. C. Whitson *et al.*, Proceedings, 17th IAEA Fusion Energy Conference, Yokohama, 1998 (International Atomic Energy Agency, Vienna, 1998) paper IAEA-F1-CN-69/ICP/07, to be published in Nucl. Fusion Supplement, 1999.

[7] M. H. Redi, H. E. Mynick, M. Suewattana, R. B. White, and M. C. Zarnstorff, Phys. Plasmas **6** (1999) 3509.

[8] C. Nuehrenberg, Phys. Plas. 3, 2401 (1996); C. Schwab, Phys. Fluids B5, 3195 (1993).

[9] A. H. Reiman and H. Greenside, Compt. Phys. Commun. **43**, pp. 157-167 (1986).

[10] V. V. Nemov, S. V. Kasilov, W. Kernbichler, and M. F. Heyn, Phys. Plasmas **6** (1999) 4622.

[11] R. B. White and M. S. Chance, Phys. Fluids 27(10), 2455 (1984).

[12] G. Y. Fu, L. P. Ku, M H. Redi, et. al., “Recent Progress in MHD Stability Calculations of Compact Stellarators,” 18th IAEA Fusion Energy Conference, Sorrento, Italy, Oct. 4-10 (2000).

Chapter 3 - Engineering Design

Development of the NCSX engineering design was an iterative process that involved:

- Defining physics requirements and design criteria,
- Developing the stellarator core configuration,
- Developing cost estimates and scaling algorithms, and
- Exploring design alternatives.

The NCSX design is built around the 3-period reference plasma configuration, scaled to a major radius of 1.4 m. A cut-away view of the stellarator is provided in Figure 3-1. The machine parameters are presented in Table 3-1. The plasma is surrounded by a vacuum vessel with an internal liner of molded carbon fiber composite (CFC) panels that are bakeable to 350ºC. The design features 21 modular coils, 21 TF coils, and 4 pairs of PF coils located symmetrically about the horizontal midplane. The coils are pre-cooled to 80K. A cryostat encloses all of these coils. The modular coils, TF coils, and vacuum vessel are assembled in 120° segments. Each segment features ports for heating, pumping, diagnostics, and maintenance access.

NCSX will be assembled in the combined PBX/PLT test cell following removal of the PBX device. Figure 3-2 shows a plan view of NCSX inside the test cell. This location is well suited to NCSX. The test cell provides ample space for the device along with adequate crane capacity. The PBX/PLT computer and control rooms, which are contiguous to the test cell, will be refurbished and utilized. Many systems formerly used on PBX including the neutral beam

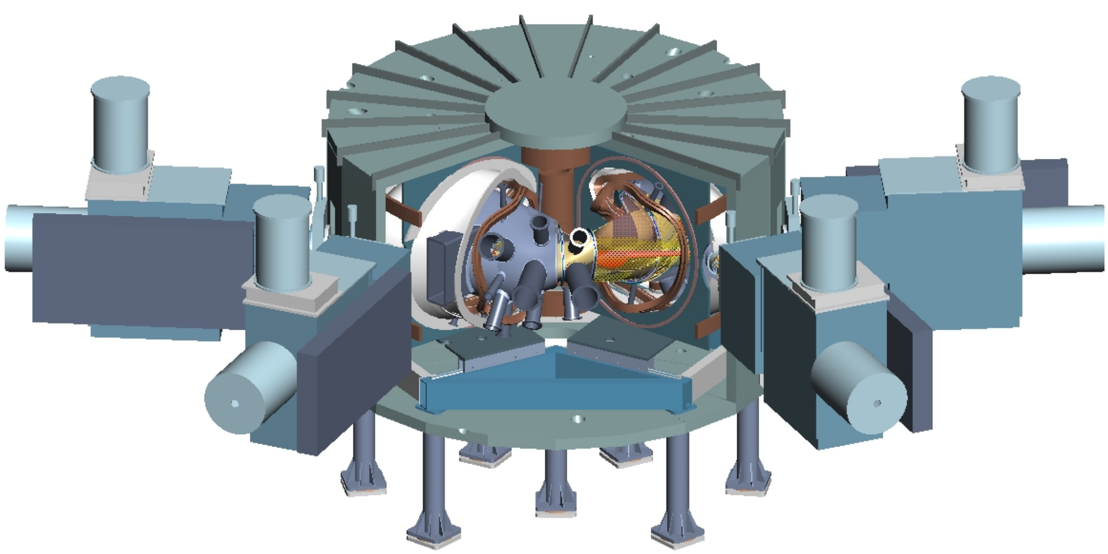

Figure 3-1 NCSX machine configuration

NCSX will be assembled in the combined PBX/PLT test cell following removal of the PBX device. Figure 3-2 shows a plan view of NCSX inside the test cell. This location is well suited to NCSX. The test cell provides ample space for the device along with adequate crane capacity. The PBX/PLT computer and control rooms, which are contiguous to the test cell, will be refurbished and utilized. Many systems formerly used on PBX including the neutral beam (NB), vacuum pumping, power supplies, and water systems will be reused. Power supplies located at D-site will also be used.

Table 3-1 NCSX machine parameters

Major radius	m	1.4
Aspect ratio		4.4
Volume	m3	3.0
Surface Area	m2	23.9
Maximum plasma current	kA	420
Maximum toroidal field	T	2

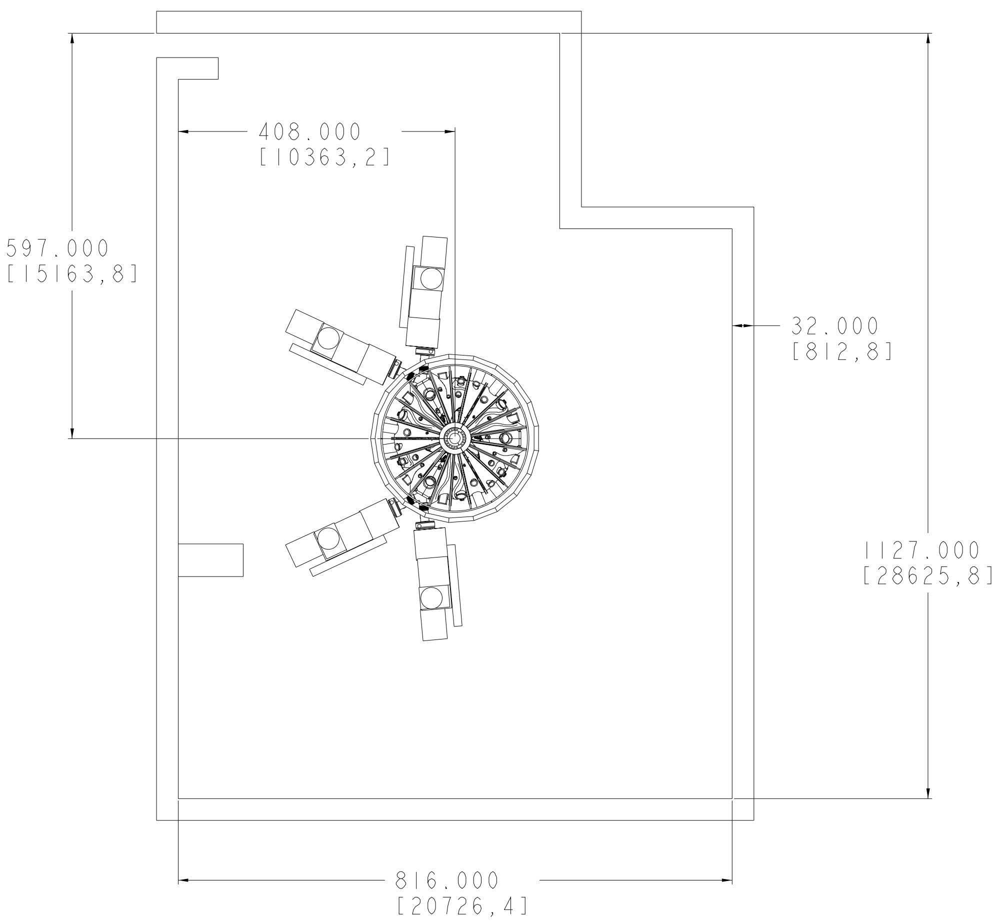

Dimensions are in inches (millimeters)
Figure 3-2 Plan view of NCSX in combined PBX/PLT test cell

3.1 Stellarator Core

The stellarator core is a complex assembly of four magnet systems that surround a highly shaped plasma. The coils provide magnetic field for plasma shaping and position control, inductive current drive, and field error correction. The vacuum vessel and plasma facing components are designed to produce a high vacuum plasma environment with access for heating, pumping, diagnostics, and maintenance. The entire system is surrounded by a cryostat to permit operation of the coils at liquid nitrogen temperature. Figure 3-3 shows a cutaway view of the stellarator core assembly.

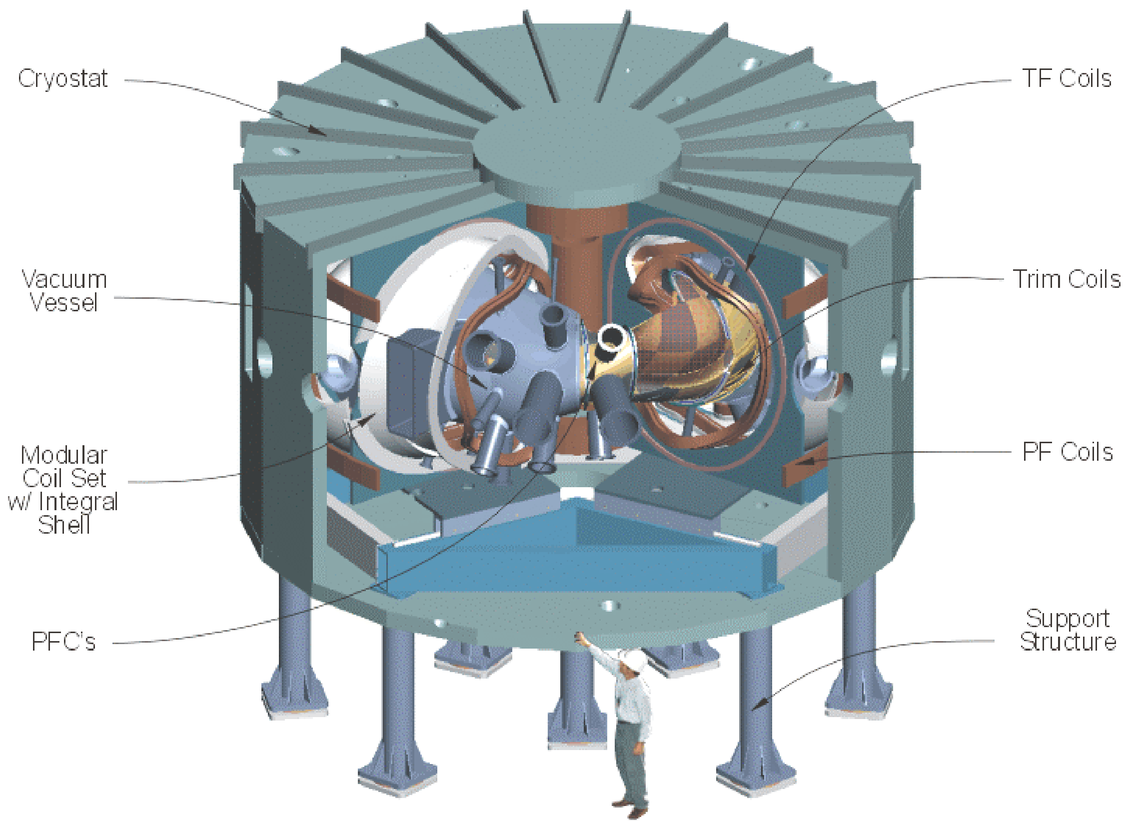

Figure 3-3 NCSX stellarator core

3.1.1 Plasma facing components

The baseline design utilizes a contoured liner, shown in Figure 3-4, constructed of molded carbon fiber composite (CFC) panels mounted on a frame of poloidal rings. When the full complement of panels is installed, they will shield the entire interior surface of the vessel. The plan is to stage the installation of the liner, with very limited wall coverage during initial operation, and the addition of the remainder of the liner during later operation. Having an

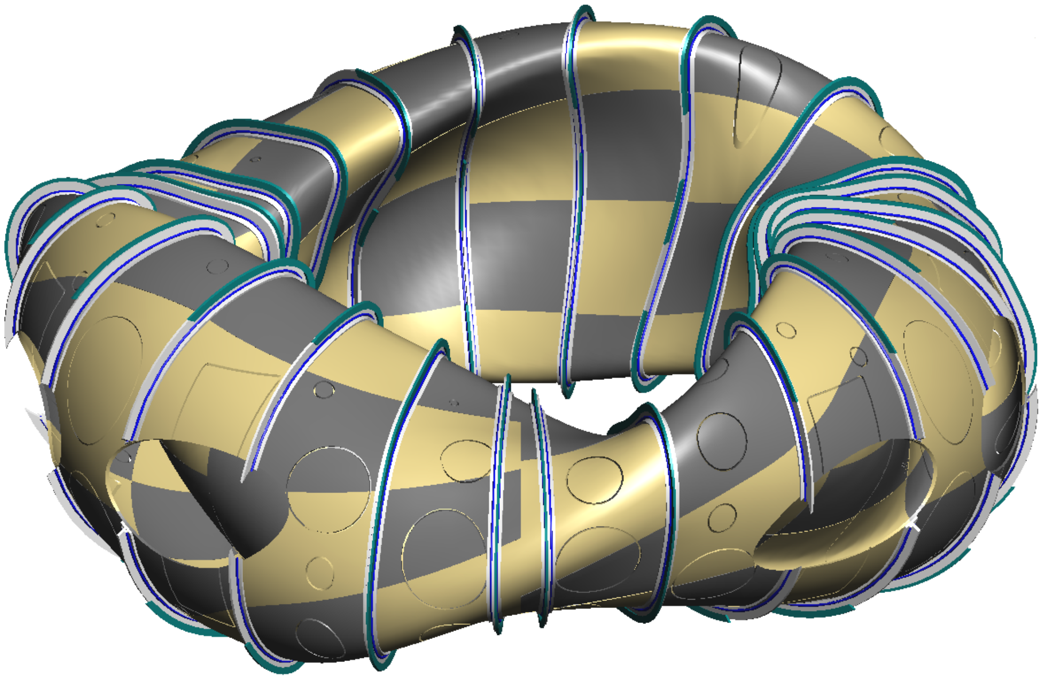

Figure 3-4 Internal liner with full complement of formed panels

independently supported, bakeable liner avoids the need to design the vacuum vessel and the in-vessel components mounted on the vessel for baking at 350ºC and reduces the heat loads to the cold mass during bakeout. The liner is baked at 350ºC while maintaining the vessel at 150ºC. Radiation heat loads to the vacuum vessel and in-vessel components are reduced by thermal shields mounted on the backside of the panels. During normal operation, the liner will have a lower pre-shot temperature in the range of 20ºC to 150ºC.

The molded panels form a continuous shell around the plasma with penetrations for diagnostics, heating, and personnel access. This shell serves many functions. It provides a high heat flux surface in the regions of sharp curvature where the heat flux from the plasma is expected to be highest. It can act as a belt limiter on the inboard midplane. On the lower half of the shell, it will absorb the power deposited by the beam ions that are promptly lost from the plasma. On the outboard side, the shell serves as armor to protect the vacuum vessel and in-vessel components from heat loads due to neutral beam shinethrough. The shell also protects in-vessel components mounted on the vessel, e.g., trim coils and magnetic diagnostics, from heat loads from the plasma.

The continuous shell allows great flexibility in plasma shaping because any surface that the plasma impinges on can act as a limiter and be resistant to damage from plasma heat loads. The properties of the CFC panels will be tailored to the local heat loads. More expensive panels with high thermal conductivity will be used in regions of higher heat loads. Less expensive panels with modest thermal conductivity will be used in regions of lower heat loads.

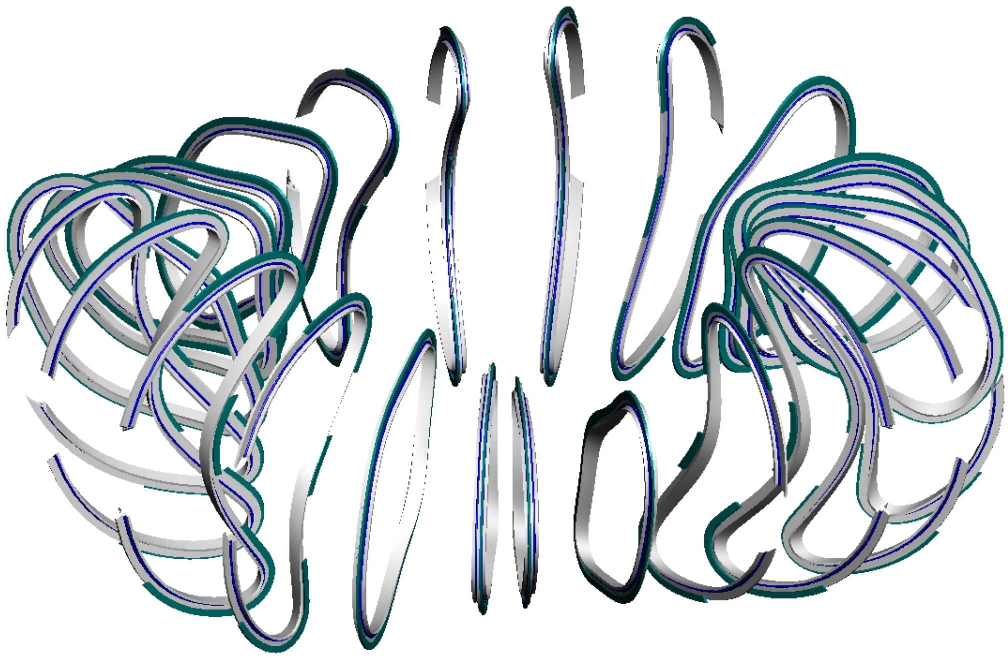

Figure 3-5 Support structure for formed panels

The panels are attached to 24 stainless steel ribs, which are traced to provide heating for the carbon liner during bakeout and cooling between shots. They also serve as thermal isolation members that maintain alignment of the liner during thermal cycling. For initial operation, there will be very limited wall coverage with CFC panels. The 24 ribs will act as a set of poloidal limiters. U-shaped sheet metal clips will protect rib surfaces not covered by CFC panels. The plasma facing surfaces of these clips are flame coated with boron carbide or other low-Z material. Figure 3-5 shows the general arrangement of the panel ribs. Bake out of the liner is provided by circulating heated gas through the tracing on the mounting ribs. The tracing also serves to remove the heat deposited in the PFCs during normal operation. Helium gas will be the working fluid for heating and cooling.

In the present design, the plasma-facing surface is located 2 cm off the nominal plasma surface on the inboard side and 10 cm on the outboard side. During conceptual design, options for expanding the plasma-facing surface away from the plasma and adding a baffled region at the tips of the plasma (akin to a divertor in a tokamak) will be investigated.

3.1.2 Vacuum vessel

The vacuum vessel is a complex, three-period structure with a geometry that repeats every 120º toroidally. The geometry is also mirrored every 60º so that the top and bottom sections of the first (0º to 60º) segment can be flipped over and serve as the corresponding sections of the adjacent (60º to 120º) segment. Table 3-2 lists the main vacuum vessel parameters.

Table 3-2 Vacuum vessel parameters

Physical parameters	
Material	Inconel 625
Thickness	0.95 cm (3/8 in)
Time constant	<10 ms
Inside surface area (without ports)	27.6 m^2
Inside surface area (with ports)	57.6
Enclosed volume (without ports)	8.69 m^3
Enclosed volume (with ports)	11.0 m^3
Weight with ports (without PFC's)	5375 kg
Operating parameters	
Liner bakeout temperature	350ºC
Vessel bakeout temperature	150ºC
Vessel operating temperature	20ºC
Heating pulse duration (max)	1.2 seconds
Cool down time between shots	
Short pulse operation	5 minutes
Long pulse operation	15 minutes

The vessel will be baked to 150ºC and operate at 20ºC. The vessel is maintained at temperature by helium gas circulated through tracing lines attached to the vessel exterior. The vessel is insulated on its exterior surface to provide thermal isolation from the modular coils, which operate at cryogenic temperature. When the vessel is being baked at 150ºC, the conductive heat loss through 2 cm of insulation to the cryogenic system will be 21 kW. Conductive heat losses drop to 13 kW during normal operation. In conceptual design, the insulation thickness will be increased where space allows, substantially reducing the conductive heat loss.

Inconel 625 is the material chosen for the vessel shell. It was selected over stainless steel primarily because of its low permeability and high electrical resistivity. The electrical resistivity of Inconel 625 is 70% higher than for 304SS. Higher resistivity results in a shorter vessel time constant, which is beneficial for plasma current profile control.

Using Inconel avoids the permeability issues associated with stainless steel. Stainless steel is prone to have elevated permeability when subject to severe cold working or when welded. Furthermore, the regions of elevated permeability are not necessarily uniform from one period to the next. Non-uniform regions of elevated permeability are a concern because they are a potential source of field errors.

The device will be fabricated in three subassemblies that are bolted together, complete with the vacuum vessel, modular coils, and TF coils. The ports will already be installed. The preliminary port configuration may be seen in Figure 3-6. Several sizes of radial and vertical ports are used to best utilize the limited access between modular coils. The large neutral beam ports are designed to permit personnel access into the liner for final assembly of the three vessel subassemblies and maintenance of diagnostics and liner panels. Most of the ports must be welded onto the three liner sub-assemblies after installation of the modular coils and prior to final assembly. Port stubs are provided on the vessel to permit the modular coils to slip on first, followed by welding of the port extensions from the outside using an automatic pipe welder inserted down into the port extensions.

The vessel will be supported from the modular coil structure via hangers for ease of adjustment and to minimize heat transfer between the two structures. Significant thermal growth must be accommodated when the modular coils are cooled to cryogenic temperatures or when the vacuum vessel is heated for bakeout.

Fabrication is a significant challenge, since the vessel has a contour closely conforming to the plasma on the inboard side. The vessel shell may be formed by pressing, explosive forming, or possibly casting sections of the vessel and welding them together to form the finished shape. Embossments can be incorporated to locally strengthen the wall thus permitting thinner gauge material and fewer piece parts and seams. The pressing option presently being explored is hydrostatic rubber forming. In this process, a male die is used in conjunction with a thick rubber platen that roughly approximates the contour of the liner. This reduces the tooling requirements since both male and female dies are not required. Segmentation of the vessel is driven by assembly requirements and inherent fabrication limitations. Fabrication by pressing requires the panel sections to be removable from the tooling dies. This requirement must mesh

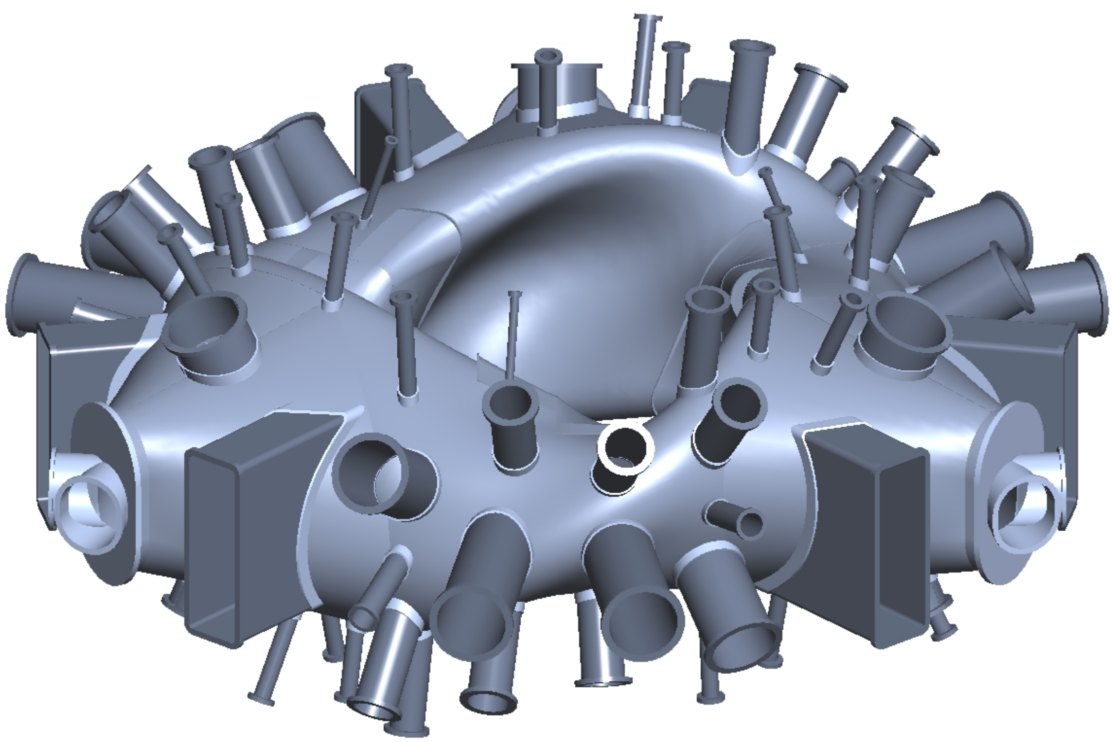

Figure 3-6 Vacuum vessel with port extensions

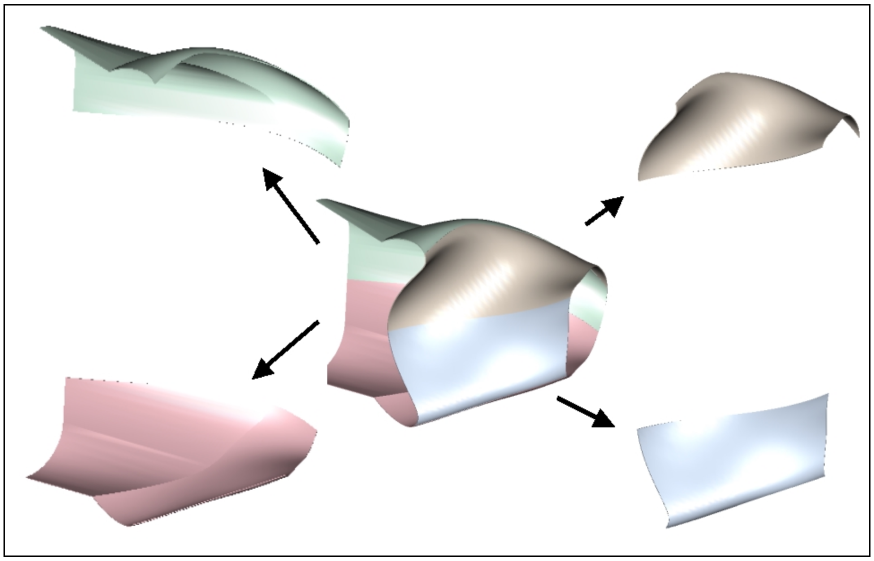

Figure 3-7 Vacuum vessel shell segmentation

with the desire for half-period segments. The result is that the number and geometry of poloidal segments is dictated by the die contour. A first cut at the segmentation indicates that the half period can be formed with as few as three poloidal sections, but more probably four as shown in Figure 3-7**.** For practicality, die size limitations may require more sections than this.

After each field period of the shell is constructed and port stubs welded in place, coolant tracing is installed on the outside surface on approximately 20 cm centers. To minimize distortion of the vessel, these lines are not skip welded or brazed, but are attached by clips and compression gaskets, bolted to the vessel, on approximately 15 cm centers.

The final assembly requires a precise fit. To accomplish this, the welding of the field period sections to their respective end flanges is done with the components all pre-assembled on a fixture into a complete torus. This forces a good fit during the final field assembly.

The next assembly step is installation of the port extensions. This requires that the vacuum vessel be placed inside the modular coils, by sliding the coils over each end of the vessel subassembly. The port extensions are then slipped into the port stubs and welded on from inside. The three sub-assemblies (periods), complete with coils, are bolted internally into a final torus at the oblate (wide) sections. The torus sections are provided with internal, machined end flanges that provide a double o-ring, bolted assembly. The o-rings will be metal or Viton. The space between the seals will be differentially pumped. The alternative, welding the period sections together, would be very difficult. There is also no access from the outside to reach an external weld joint. Achieving quality welds by welding on the inside would be very difficult due to the tight space constraints and contorted geometry inside the vessel. A bolted joint facilitates pre-installation of in-vessel components and assembly of the vacuum vessel. Figure 3-8 illustrates three segments being brought together to complete assembly of the vacuum vessel. The bolted joint feature also makes disassembly possible for major modifications of the device in the future.

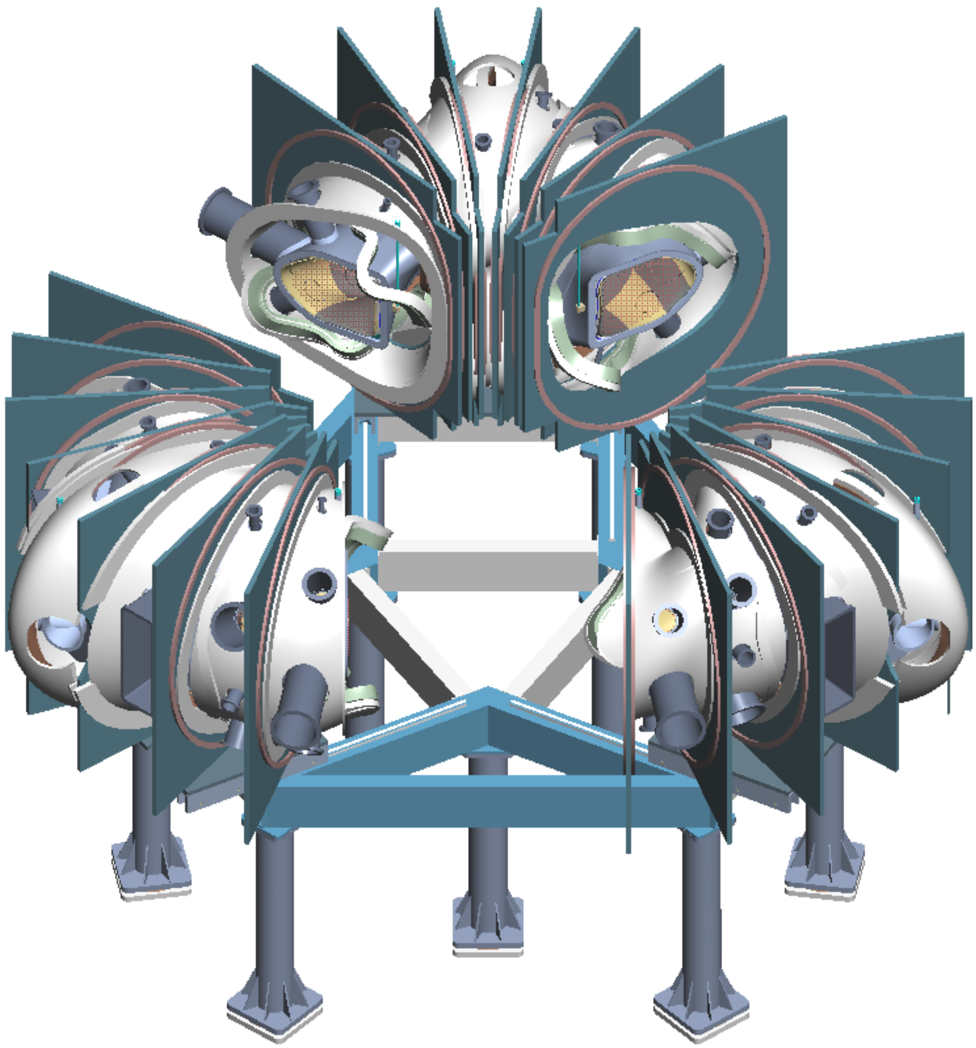

Figure 3-8 Final assembly of vacuum vessel

3.1.3 Modular coils

The modular coil set consists of three field periods with 7 coils per period, for a total of 21 coils. Due to symmetry, only four different coil shapes are needed to make up the complete coil set. The coils are connected electrically with 4 circuits in groups of 3 or 6, according to type. Each circuit is independently powered to provide maximum flexibility. The maximum toroidal field at 1.4 m produced by the modular coils with a flattop of 0.5s is 1.7 T. The toroidal field on axis can be raised to 2 T by energizing the TF coils, which can add ±0.3 T to the field generated by the modular coils.

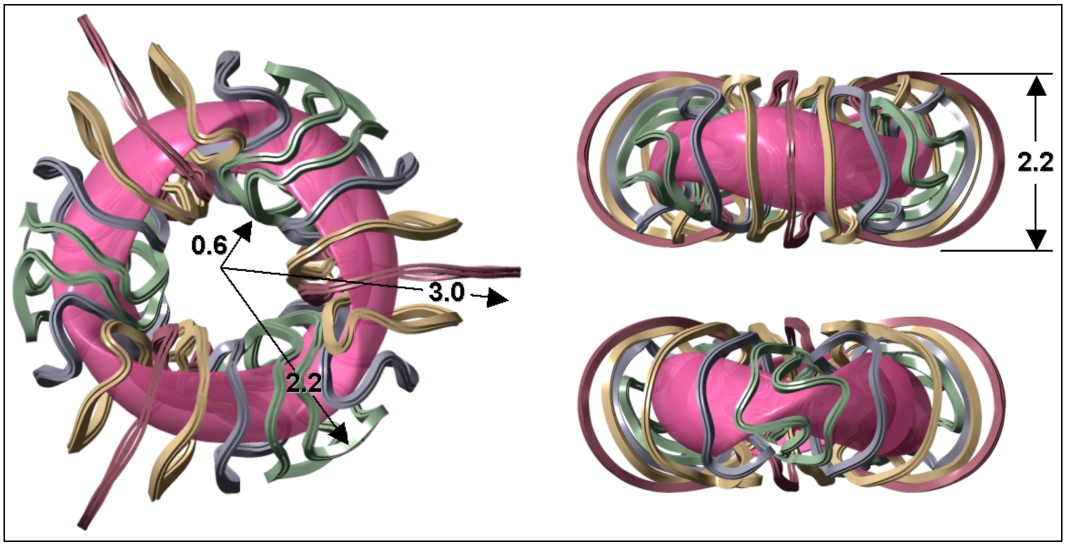

Figure 3-9 General arrangement of modular coil set

The modular coils are pre-cooled to 80K because of the high current density in the coils. In order to avoid two-phase flow in the cooling tubes or excessively high pressures, the windings are cooled with helium gas. Heat is removed from the helium gas through a heat exchanger with liquid nitrogen on the secondary side. The modular coil structure is cooled directly with liquid nitrogen vapor.

Figure 3-9 shows the general arrangement of the coil set. It may be seen that the outer leg of the coil on the v=0 symmetry plane is pulled out for neutral beam access. The other coils are wrapped more tightly around the plasma. The coils on either side of the v=0.5 symmetry plane (60º away from the v=0 symmetry plane) exhibit the largest toroidal excursion and are the most difficult to fabricate. Table 3-3 summarizes the main modular coil parameters.

Table 3-3 Modular coil parameters

Parameter	Unit	Value	Remarks
Number of field periods		3	
Number of modular coils		21	
Number of turns per coil		32	
Maximum toroidal field at 1.4 m	T	1.7	Modular coils only
	T	2.0	Modular plus TF coils
Winding length along winding center	m	6.0-7.6	
Winding cross-section	cm^2	67	
Winding accuracy	mm	±1	

The winding center for each modular coil is specified through a physics optimization process that emphasizes both plasma properties and geometric constraints, such as coil-to-coil spacing (a key factor determining the current density) and minimum bend radius. From this data, a cross-section is developed that is normal to the winding surface, except in regions where there are sharp bends or the coils are very close together. Twisting in these areas has been adjusted so as to avoid crimps and maximize the available conductor space. A study of the effect of finite-build coils on plasma reconstruction indicates that these small coil adjustments do not significantly affect the plasma properties.

The design concept uses flexible, copper cable conductor. The primary advantage of the flexible cable design is low cost, both to purchase the conductor and to wind it. The primary disadvantage is the loss of copper area compared to a solid conductor. A packing fraction of only 75% can be assured, although 80% is theoretically possible. The design is based on a packing fraction of 70%. The conductor is purchased as a round cable that has been compacted into a rectangular cross-section. Turn-to-turn insulation is then applied. Even after compaction, the conductor is flexible and easy to wind. A picture of the conductor before and after compaction is provided in Figure 3-10. Once wound, the conductor is vacuum impregnated with epoxy. The epoxy fills the voids within the cable conductor so the winding pack becomes a monolithic copper-glass-epoxy composite.

Table of Conductor Parameters

Parameter	Unit	Value
Maximum current	kA	20.3
Pulse length (ESW)	s	~1
Repetition rate	min	10
Total number of cycles	-	130,000
Conductor width	mm	16
Conductor height	mm	13
Max continuous length	m	130
Copper strand size	AWG	36
Conductor packing fraction	%	70-75
Insulation thickness	mm	0.8
Insulation rating	kV	> 3
Minimum bend radius	cm	> 4

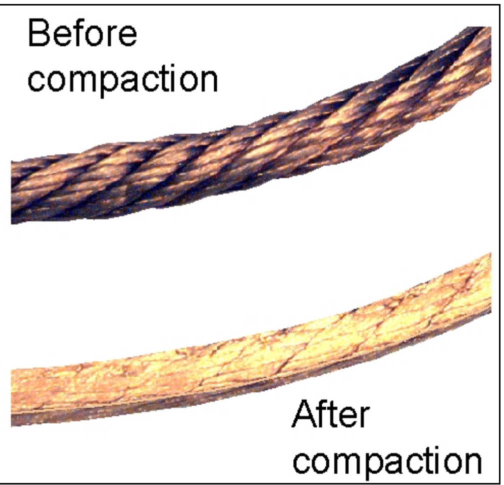

Figure 3-10 Cable conductor

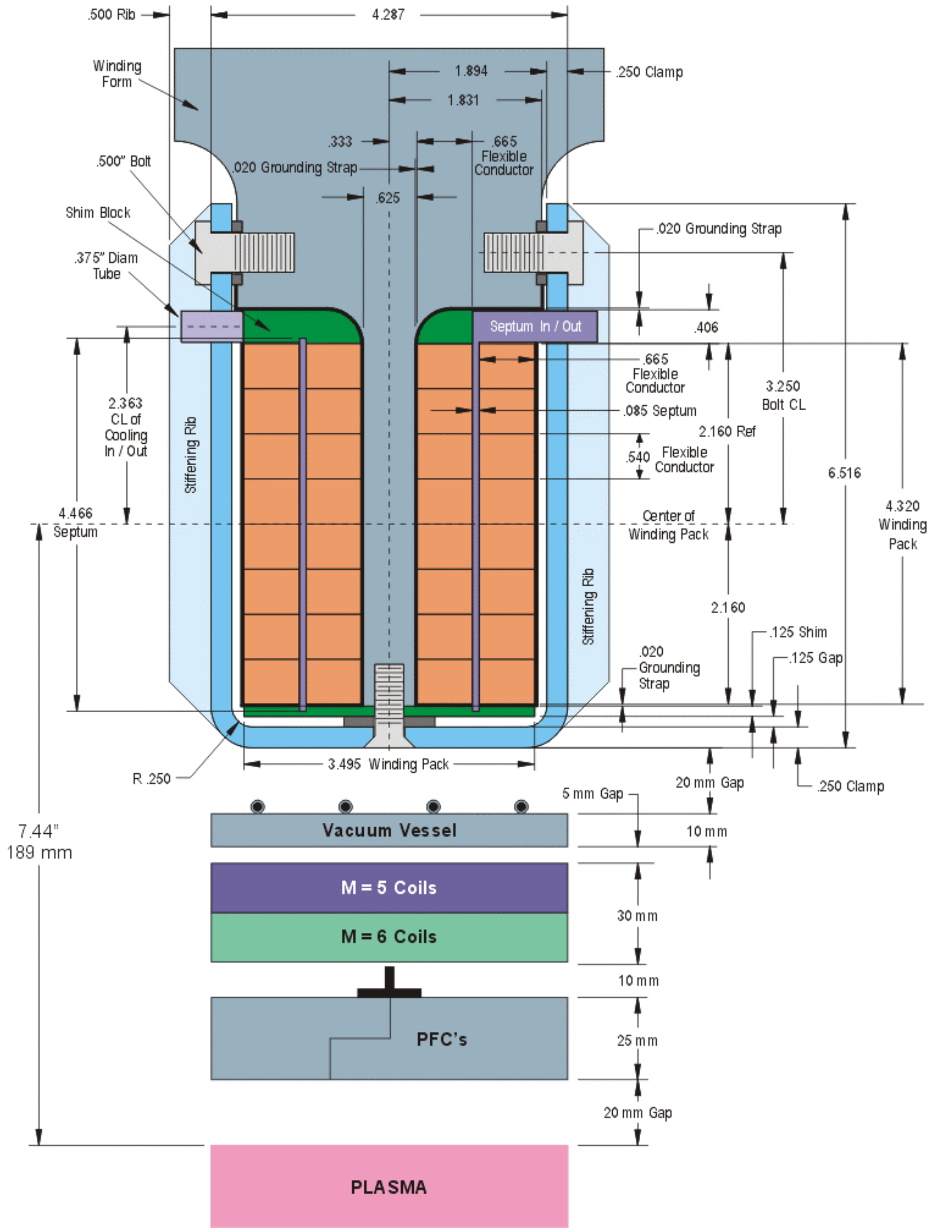

Figure 3-11 Modular coil cross-section

The cross-section dimensions of each coil are 10.9 cm x 16.5 cm, as shown in Figure 3-11. Within this envelope is a 16 mm thick, tee-shaped member that supports two multi-turn winding packs. Each winding pack is a double-layer pancake with 8 turns per layer. A crossover between layers occurs at the top of the tee. The leads extend from the bottom of the winding pack in a coaxial arrangement. Between the layers there is a thin plate through which gas cooling flows. The winding packs are clamped in place by discrete u-shaped brackets that provide support in areas where the electromagnetic force is away from tee structure.

In order to avoid unwanted field errors, the position of the winding current center must be tightly controlled. The true position tolerance (TPT) for the winding current center is ±1 mm. In order to achieve this tolerance, the conductor will be wound on a precision surface on each side

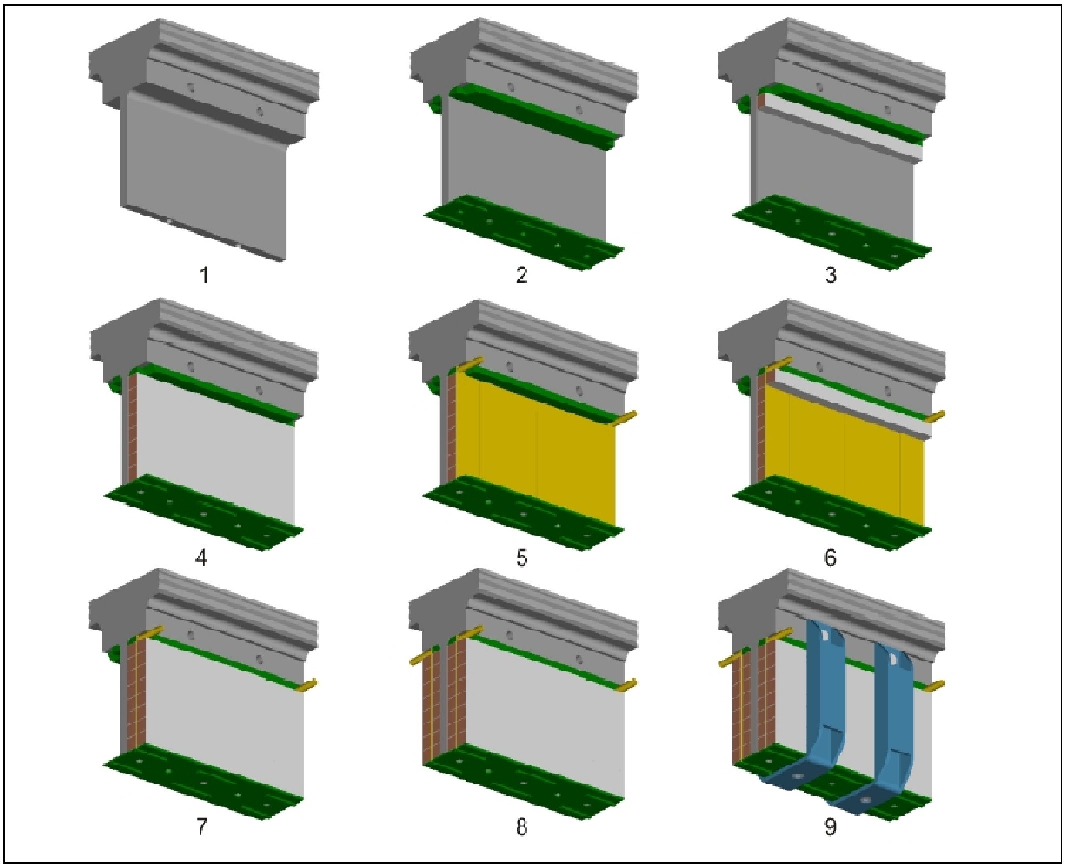

Figure 3-12 Coil winding process

of the structural tee, which is part of the winding form. The winding process is illustrated in Figure 3-12. The conductor is wound in a double pancake on each side of the tee. When the first pancake has been wound, a chill plate is placed against the first pancake. The chill plates consist of a copper sandwich containing a serpentine cooling passage with inlet and outlet pipes for the gas cooling. The chill plates avoid the need for cooling the conductor internally, which would reduce the achievable current density. Then the second pancake is wound. After winding is complete, the final geometry is verified and the assembly is vacuum pressure impregnated with epoxy to complete the insulation system. Support brackets are then installed. An illustration of a completed modular coil in the winding form is shown in Figure 3-13.

The winding form is fabricated as a casting. Due to the complexity of the shape, the pattern geometry will likely be developed through several iterations by a pattern maker. In order to minimize machining, the as-cast part must be within 5 mm of the true shape anywhere in the section. After stress relieving in a fixture, the casting would be re-measured and have all structural interface features machined.

Instead of making the winding cavity undersized and contour machining it to the required size and accuracy, it is proposed to make the cavity *oversized* in most areas. A very accurate, multi-part set of patterns would be created using rapid prototyping techniques (such as stereolithography or laminated object modeling) and accurately positioned in the casting. The space between the winding pattern and the structure would be filled with an epoxy grout. The

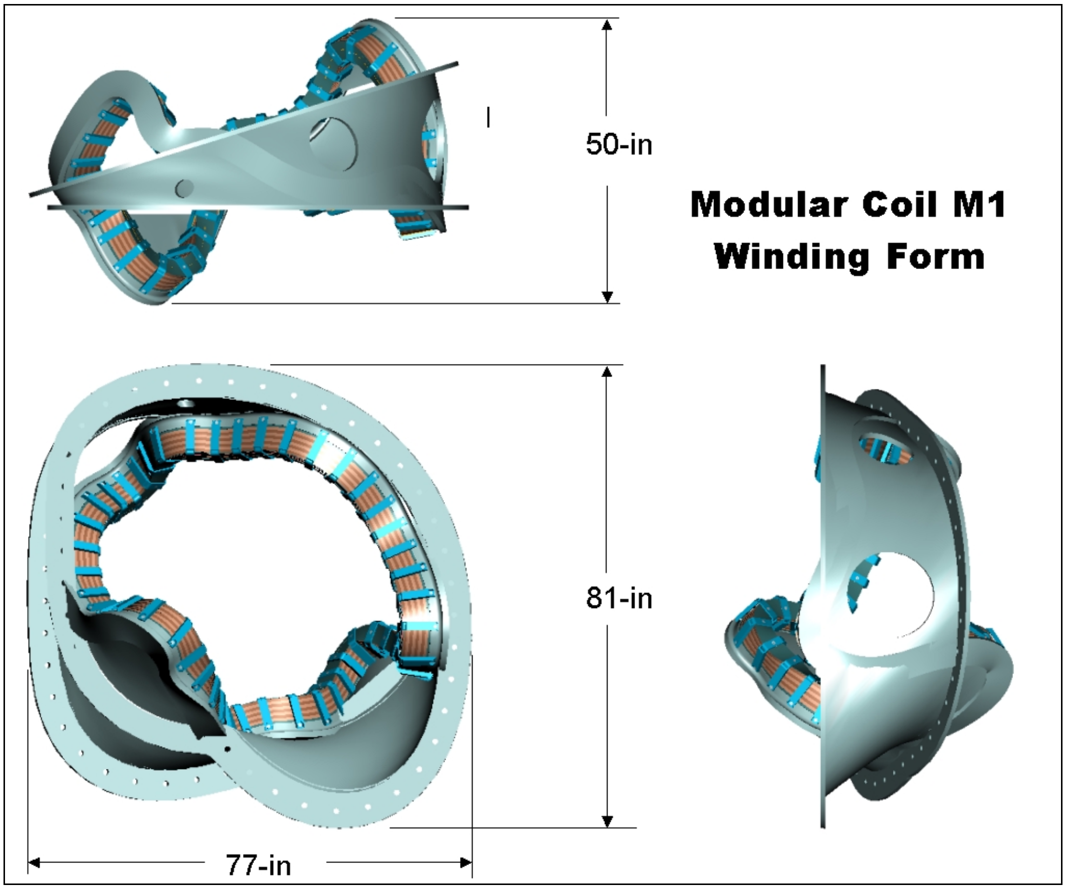

Figure 3-13 Completed modular coil in the winding form

pattern would be removed leaving a very accurate, molded winding cavity. In some areas, where the windings are very close together, there may not be room for the epoxy grouting. In these areas the structural tee would be locally machined to exact size. Of course, a fully machined winding cavity would be considered if the cost was favorable.

The modular coil windings will be cooled with helium gas at 80K. Figure 3-14 illustrates the current waveforms and temperature response of the modular coil windings for the two reference scenarios: 1.2 T with a 1.2 s flattop and 1.7 T with a 0.45 s flattop. The temperature rise in the 1.7T scenario is the higher of the two. The temperature rise is 26 K at the end of flattop and 36 K at the end of the pulse. The allowable temperature rise will be determined by thermal stress considerations. A limit of 40 K has been imposed pending more detailed analysis and testing.

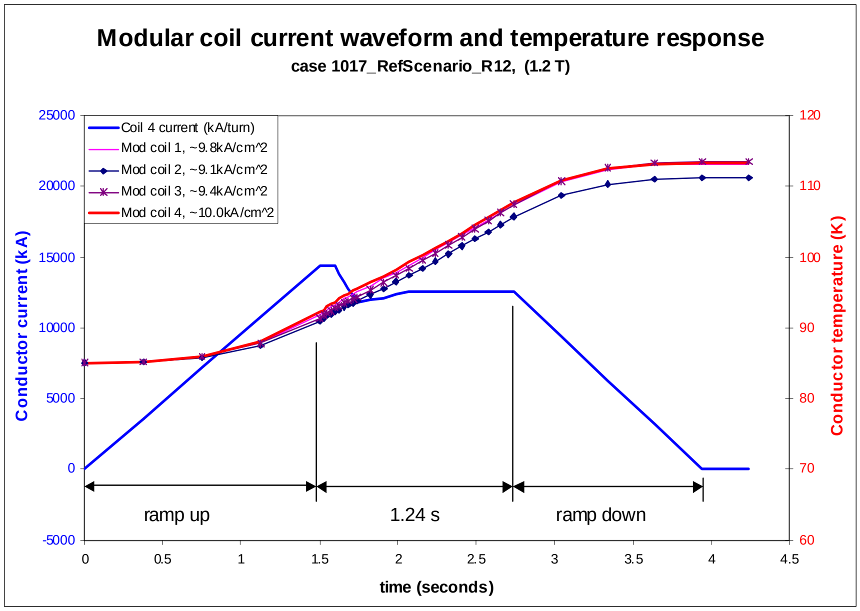

1.2 T

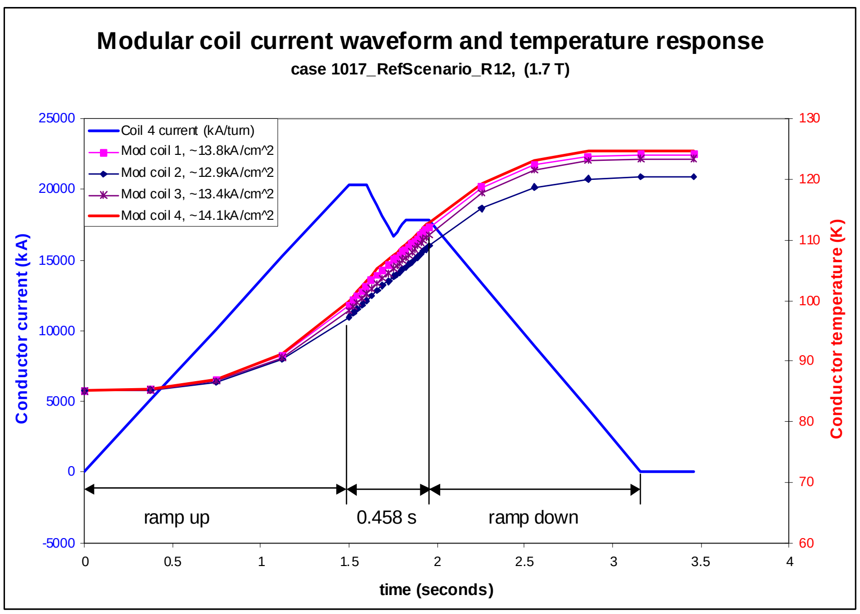

1.7 T

Figure 3-14 Modular coil current waveforms and temperature response

The temperature rise in an adiabatic copper coil is governed by the current density, equivalent square wave time (ESW), and initial temperature. In the 1.7 T reference scenario, the highest copper current density in the modular coils is 14 kA/cm^2, with an ESW of 1.2 s. Lower current density would translate into longer flattop times and perhaps higher toroidal field capability. Analysis indicates that cooldown within 15 minutes can be accomplished by cooling by gaseous helium at 80 K.

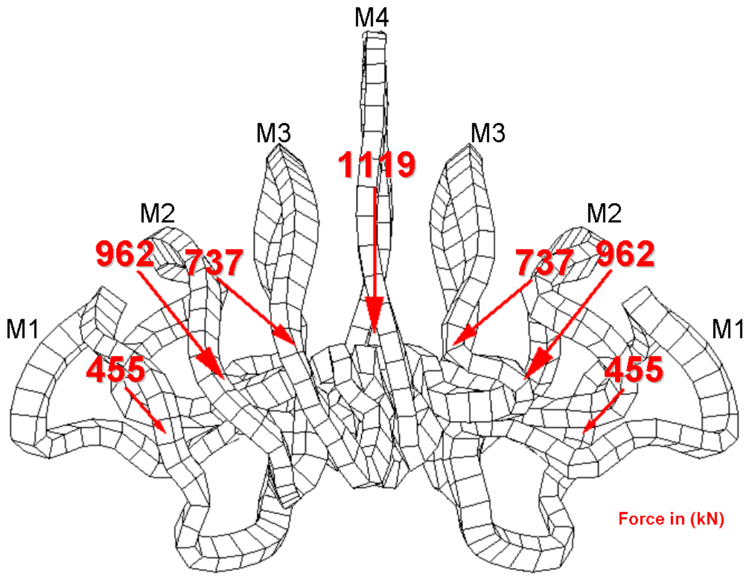

Figure 3-15 Net radial forces on modular coils

A preliminary analysis of the stresses in the coil structure has been completed. The structure has been evaluated for a "worst case" operating point, which occurs when the modular and PF coils are at their largest currents (based on the 1.7 T reference scenario) and the TF coils are providing an additional 0.3 T. The magnitude and direction of the net forces on the modular coil forces are shown in Figure 3-15. The stresses are calculated using a finite element model of the shell and web structures, with all the modular coil loads applied to the midpoint of the coil web structure. In this way the global response of the shell as well as the local bending in the web due to lateral loads can be determined. The TF coil loads are applied to the radial plates, which in turn are connected to the appropriate regions of the modular coil shell.

As shown in Figure 3-16, the analysis results indicate the stress in the structural shell is between 50-100 MPa throughout most of the structure. There are some areas in the inboard "trough" region that peak around 200 MPa. The stresses in the web portion of the structural tee are between 60 and 120 MPa, with very localized peaks up to 300 MPa due to bending. The allowable stress for membrane plus bending is about 180 MPa for a typical cast austenitic alloy.

Although the peak stresses from this first analysis exceed the allowable limit in localized areas, the shell thickness and shape can be optimized to reduce these localized stresses. The primary reason for selecting the shell concept for structural support is to have a robust structure that can be easily optimized to reduce stress peaking. At the same time, there is maximum flexibility for providing local holes and cutouts for diagnostic and heating access.

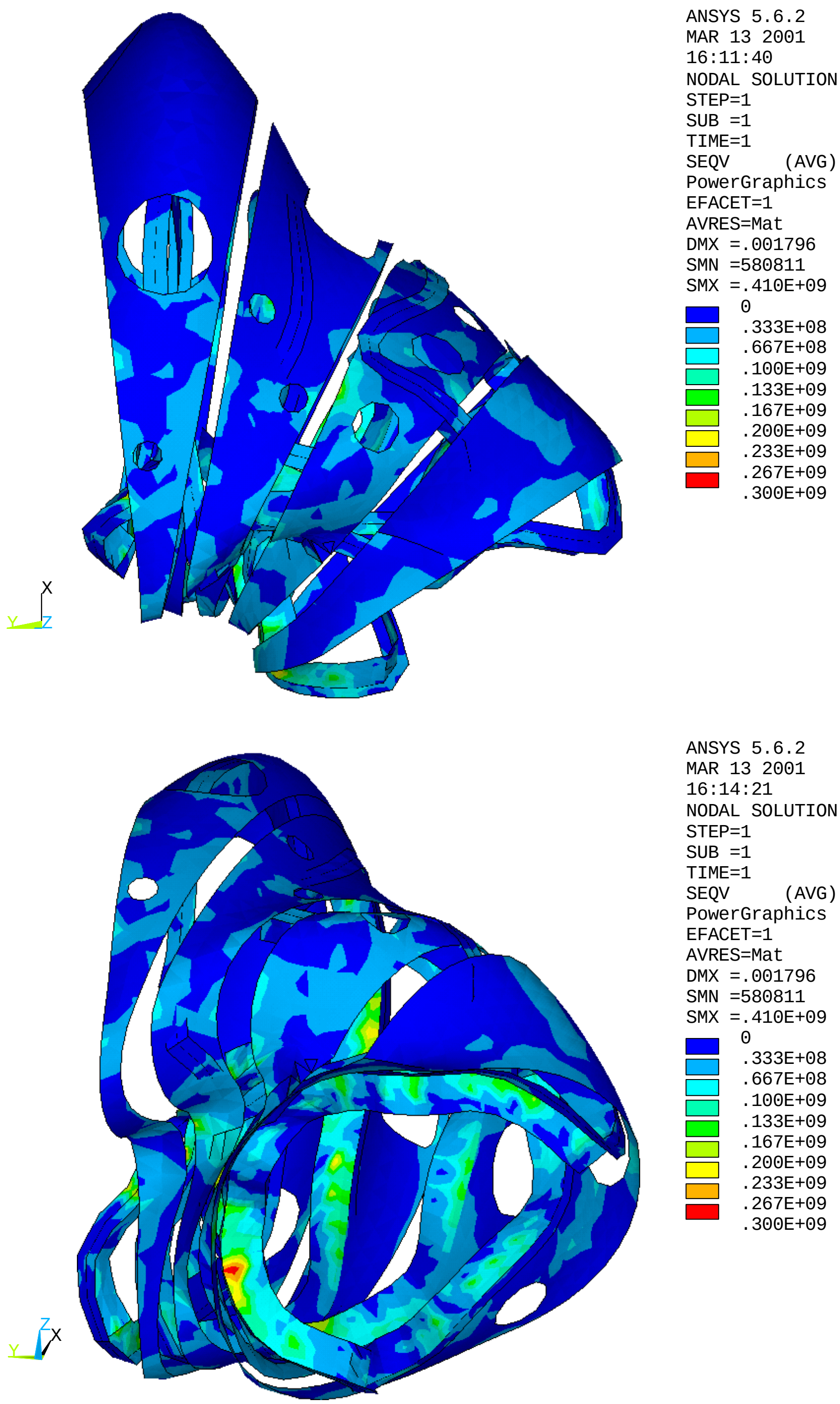

Figure 3-16 Stress pattern in modular coil structure for "worst case" operating loads (1.7 T from modular coil set, peak PF currents, 0.3T from TF coil set)

There are a number of improvements that will be sought in conceptual design. These include:

- Lowering the copper current density for longer flattop times and higher field capability,
- Reducing the number of modular coils for improved access and reduced cost, and
- Modifying the winding shape to make it easier and less expensive to manufacture.

Contracts will be placed with potential vendors to conduct manufacturing studies and provide feedback on how the coil design should be changed to improve fabricability and reduce cost.

3.1.4 Toroidal field coils

A set of toroidal field coils is included to provide flexibility in the magnetic configuration. Adding or subtracting toroidal field is an ideal "knob" for lowering and raising iota. There are 21 identical, equally spaced coils providing a 1/R field at the plasma. The TF coils are mounted on flat, radial plates that are bolted between adjacent modular coil winding forms. In addition to supporting and locating the TF coils, the radial plates provide structural support to the modular and PF coils. The TF coils are located at these radial locations for symmetry and to avoid introducing additional obstructions to access. All of the coils are connected in a single circuit. Each coil consists of a pair of windings, one on either side of radial support plates as shown in Figure 3-17. The windings are split about the plate for structural,

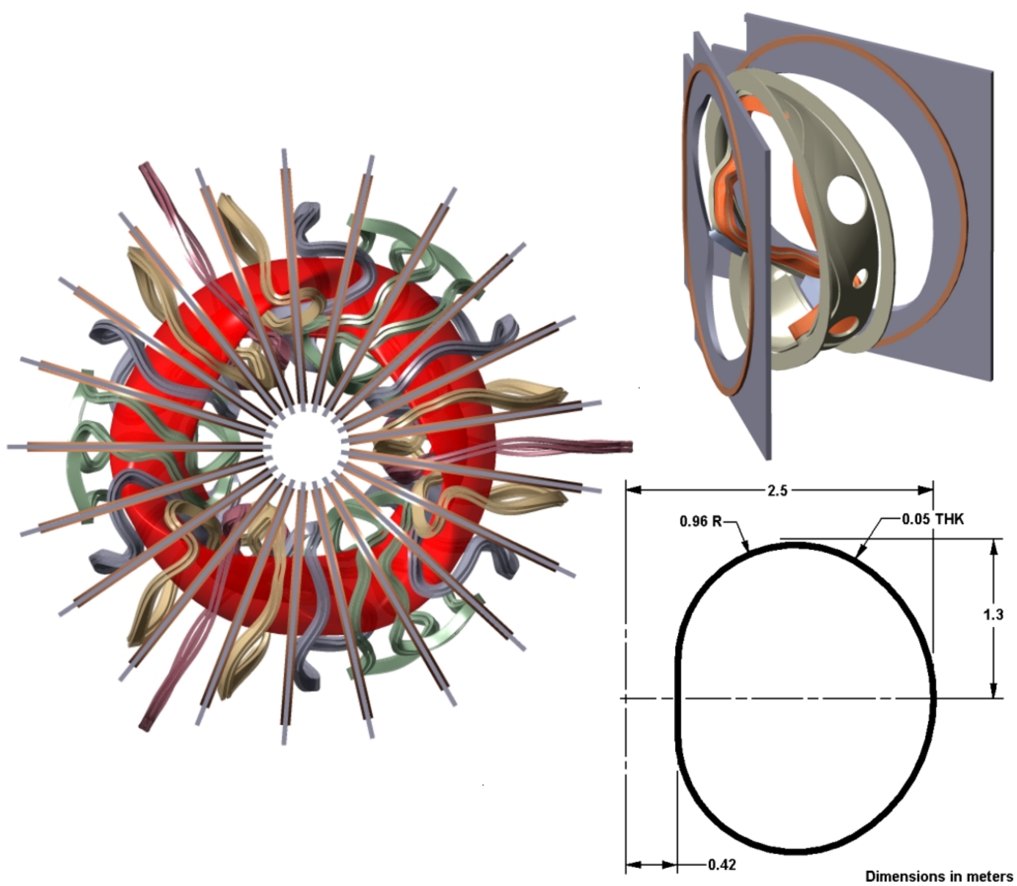

Figure 3-17 TF coil geometry and support

Table 3-4 TF coil parameters

Parameter	Unit	Value	
Number of TF coils		21	
Number of turns per coil		6	
Maximum toroidal field at 1.4 m	T	±0.3	TF coils only
Maximum current per turn	kA	17	
Winding length along winding center	m	9.5	
Winding cross-section	cm^2	21	
Maximum copper current density	kA/cm^2	9.6	

magnetic, and geometric symmetry, for improved accuracy, and for ease of mounting. The coils are wound from hollow copper conductor and insulated with glass-epoxy. They operate at the same temperature as the modular coil set - nominally 85K (cooled by 80 K helium) - and are connected in series. The leads consist of coaxial conductor to minimize field errors. The nominal TF coil parameters are listed in Table 3-4.

The modular coils were designed for the reference plasma configuration *in the absence of TF coils*. TF coils were added for flexibility. Design studies are being conducted to determine if the design of the modular coils could be improved by assuming a background 1/R field when designing modular coils for the reference plasma configuration.

The 1/R nature of the TF field was adopted based largely on precedent in other stellarators, which were largely high aspect ratio, many field period designs. The magnetic axis in these machines could be approximated by a circle, the shape of a field line in a 1/R field. However, in a low aspect ratio, 3-period stellarator like NCSX, it is not clear that a 1/R background field is optimal with a highly non-circular magnetic axis. In conceptual design, a study will be performed to optimize the field distribution from the TF coils.

3.1.5 Poloidal field coils

A set of poloidal field coils is provided for inductive current drive and plasma shape and position control. The basic coil geometry is shown in Figure 3-18. The coil set consists of two inner solenoid pairs (PF 1 and PF 2), a mid coil pair (PF 3) and an outer coil pair (PF 4). Coil pairs are symmetric about the horizontal midplane. The coils are of conventional construction, wound from hollow copper conductor and insulated with glass-epoxy. The PF coils operate at the same temperature as the modular and TF coil sets - nominally 85K (cooled by 80 K helium). The leads consist of coaxial conductor to minimize field errors. PF coil parameters are listed in Table 3-5. The coils are supported via adjustable clamps to the radial support plates.

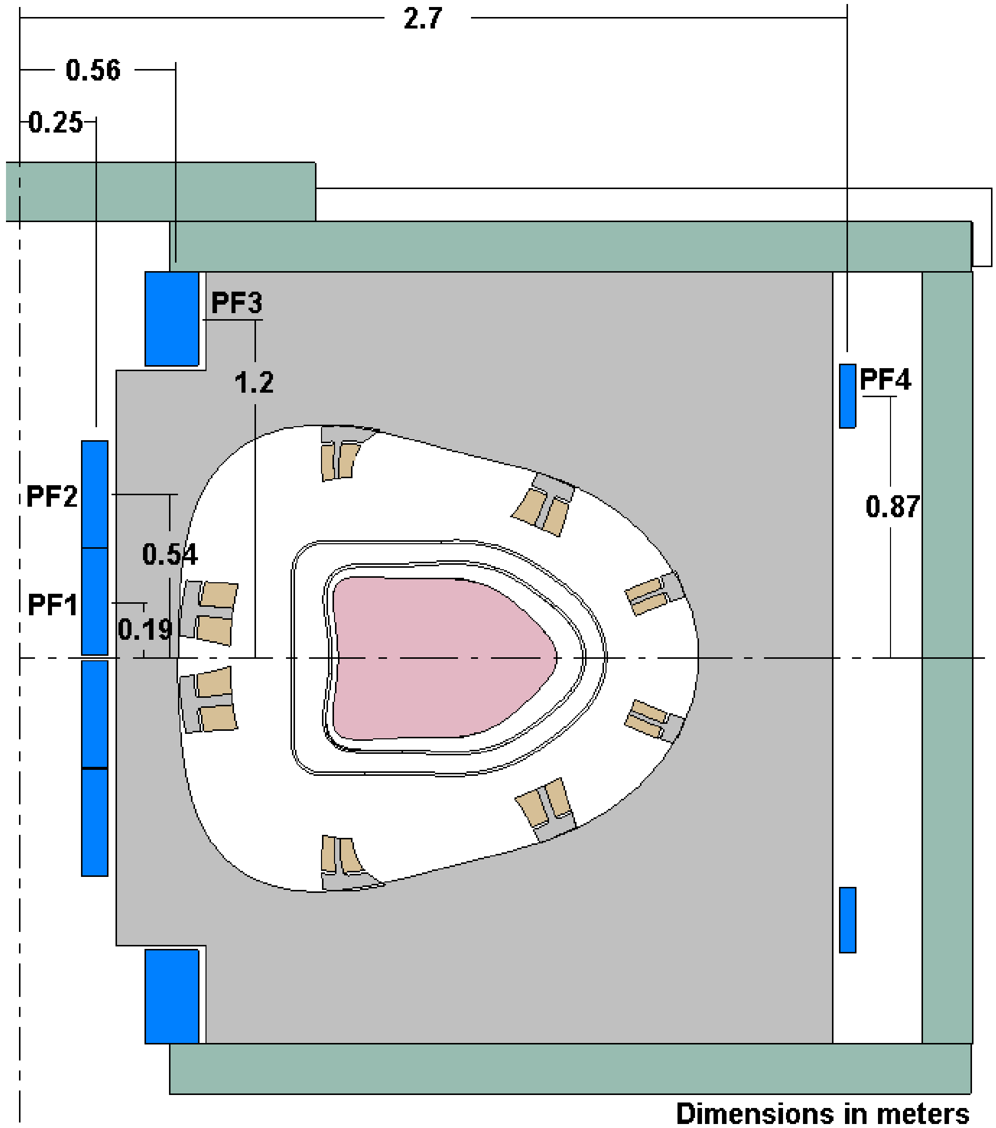

Figure 3-18 PF coil layout

Upper and lower PF coils in a given pair are connected in series. Thus, there are four independent electrical circuits. The PF coils, when independently driven, provide much flexibility for plasma shaping and position control. With an OH (nullapole) distribution in the PF coils, the coil set can provide 1.5 Wb (single swung) or 3 Wb (double swung). This capability should be adequate, even for the maximum plasma current of 420 kA, provided that the coil currents required for shaping are not too extreme.

The present design features four pairs of PF coils. This is the minimum number that might be acceptable for performing all of the required functions. During conceptual design, PF coil requirements for the full range of flexibility space will be investigated, including reproduction of the desired physics properties and surface quality. As a result of those investigations, the number and placement of the PF coils may change.

Table 3-5 PF coil parameters

Parameter	Unit	Total	PF 1	PF 2	PF 3	PF 4
Winding radius	m		0.25	0.25	0.556	2.745
Winding elevation	m		±0.188	±0.543	±1.155	±0.868
Winding width, dr	cm		9.02	9.02	17.88	5.41
Winding height, dz	cm		35.4	35.4	31.16	21.16
Number of turns per coil			76	76	80	12
Volt-seconds [a]	Wb	3				

[a] OH (nullapole) current distribution in PF coils, double swung

As with the TF coils, the modular coils were designed for the reference plasma configuration in the absence of PF coils. PF coils were added for flexibility and for inductive current drive. In conceptual design, studies will be conducted to determine if the design of the modular coils could be improved by taking advantage of the PF coils when designing modular coils for the reference plasma configuration. Studies will also be conducted to determine if the design could benefit by allowing the PF coils to be non-circular and non-planar.

3.1.6 Trim coils

Trim coils are provided to mitigate field errors, in particular the errors on m=5 and m=6 resonant surfaces. The coils are configured in a saddle geometry as shown in Figure 3-19, and are located inside the vacuum vessel on the inboard and outboard regions of the v=0 (bean-shaped) plasma cross-section based on a study to determine where the coupling with the plasma was best. The m=5 coils are on a surface that is offset 63 mm from the plasma on the inboard and 143 mm from the plasma on the outboard side. The m=6 coils are in a layer offset 15 mm farther out from the plasma. The present coil geometry interferes slightly with the beam lines near the outboard midplane, so the geometry of the saddle coils will have to be adjusted slightly during conceptual design.

The coils should require less than 10 kA-turns per coil. To provide this, five turns are envisaged in a 5 cm x 1 cm winding pack. Since the coils are located in the vacuum vessel, they must be vacuum tight (canned). High temperature electrical insulation will be required. The present concept for the coils is to provide a formed and embossed stainless steel panel into which the four saddle coils would be wound, with a second panel seam welded over the coils to provide the vacuum closure. Special tooling will be required to provide an accurate, contoured shape. The completed panels can be fully supported by the vacuum vessel on the inboard side, but will cantilevered from the top and bottom on the outboard side.

There are six panels (3 periods, each with an inboard panel and an outboard panel) for the m=5 resonance and six for the m=6 resonance. Coaxial leads from each panel will be routed to the outside through continuous conduit. There, the coils in each group will be connected in series and connected to power supplies in the ESAT building at C-site.

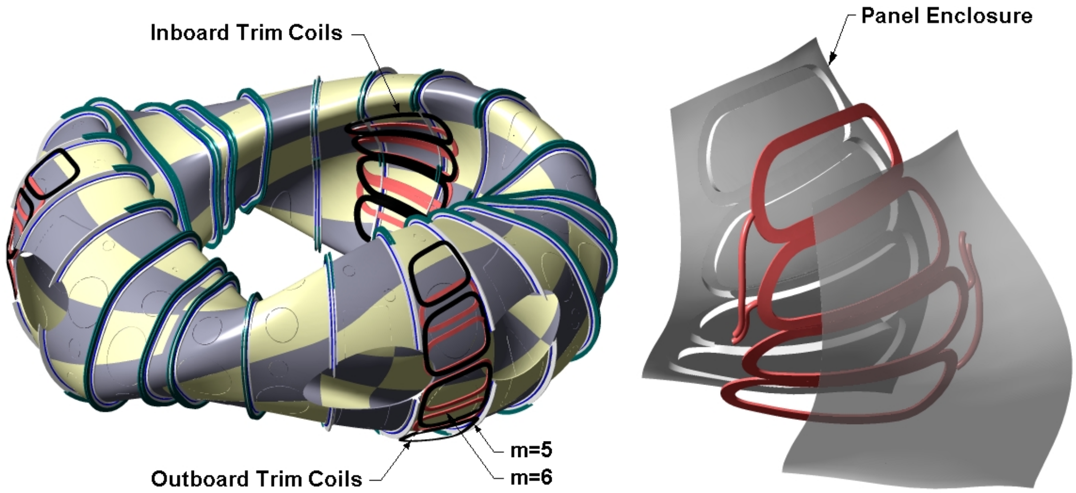

Figure 3-19 Trim coil configuration

To date, only the trim coils for symmetry preserving field errors have been investigated. In addition, it is anticipated that trim coils for symmetry breaking field errors, e.g., n/m=½ and n/m=⅔ resonant errors, might be desirable. The design of these trim coils will be investigated during conceptual design.

3.1.7 Machine support structure

The machine support structure consists of the base columns, support beams, and radial support plates. These components provide mounting points for all the other components and support the gravity and seismic loads on the device. The base columns and support beams are illustrated in Figure 3-20. The columns are tall enough to provide headroom under the machine. Rails mounted on top of the columns provide a means of assembling the machine in three field periods. The columns will be covered with thermal insulation to provide a long conduction path for reducing heat leakage to the machine.

The radial support plates provide a set of interface planes for the modular coils as well as convenient support structure for accurately locating and mounting the TF and PF coils. Shims can be used if necessary between the support plates and the modular coil structure for minute adjustments in coil position and to avoid tolerance buildup of the whole assembly. Adjustable brackets will provide the interface between the support plates and the PF coils to accurately align the coils with respect to the modular coils and TF coils. Since large ring coils are often out-of-round, these brackets will also serve to bring the coils into an acceptably round shape.

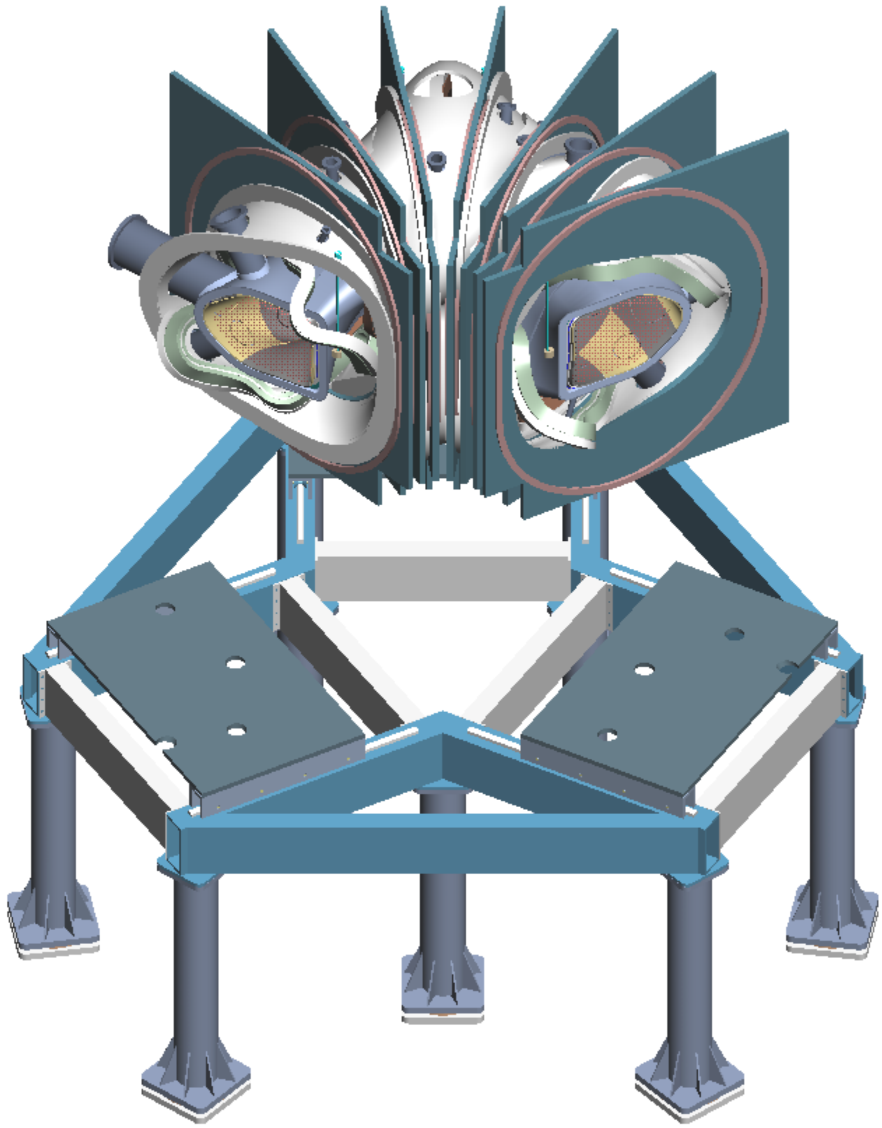

Figure 3-20 Support structure

3.1.8 Cryostat

Since the coils and structure operate at cryogenic temperatures, a cryostat is provided for thermal isolation. The cryostat must also seal the coil space from the outside air to prevent condensation on the cold surfaces and to provide a means for circulating dry nitrogen inside the cryostat to cool down and maintain the temperature of the interior structures.

The baseline concept consists of a simple frame and panel design covered with urethane insulation as illustrated in Figure 3-21. The frame consists of fiberglass channels mounted along the edges of each of the radial TF coil support plates. Fiberglass panels are attached to the frame to form a surface for the urethane. Fiberglass dams are positioned around each vacuum vessel port, coil lead, or utility penetration. A flexible silicone rubber boot is used to provide a seal. Urethane is then sprayed on the fiberglass panels using a commercial process typically used for

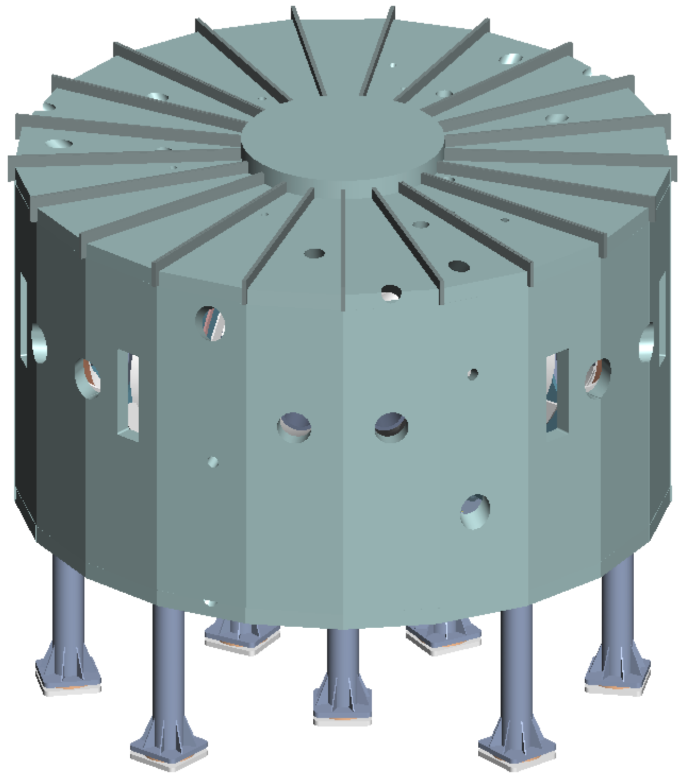

Figure 3-21 Cryostat configuration

large stationary cryogenic tanks. The exterior surface of the urethane is then sprayed with a butyl rubber coating for an additional gas seal and to provide a durable surface. For access to interior components, a few removable panels (including the top and bottom central openings) would be provided, but in general, the urethane would simply be removed and a hole cut in the panel where access is desired. The hole would be repaired by patching the panel and re-foaming. This process is analogous to accessing plumbing by cutting holes in a sheet rock wall.

The urethane insulation is approximately 8 inches thick, which provides good thermal isolation for the cold components (~ 2 kW heat leak), but is probably not sufficient to prevent condensation on the outside of the cryostat. For this reason, heaters and blowers will be used to control the outside surface temperature and prevent condensation. Flexible insulation must also be stuffed around the penetrations outside the boots.

3.2 Access and Maintenance

3.2.1 Diagnostic access

Port locations were defined based on available space between modular coils, trim coils, PF and TF coils, and structure, and are shown in Figure 3-22. Table 3-6 shows the size and total number of ports. The sizes and numbers of ports appear well matched to our needs for diagnostic access. However, the all-important task of matching the view angle to the geometric requirements remains to be done in conceptual design. A description of the NCSX diagnostics can be found in Chapter 12.

3.2.2 Access for plasma heating

The requirement for neutral beam access is to be able to accommodate two of the PBX-M neutral beams in the initial configuration. These beams must be oriented for tangential injection with one co-injected beam and one counter-injected beam. In addition, the device must be able to accommodate the two remaining PBX-M neutral beams as a future upgrade. One of these beams must be oriented for tangential co-injection. The other beamline must be capable of being oriented for either tangential co- or counter-injection.

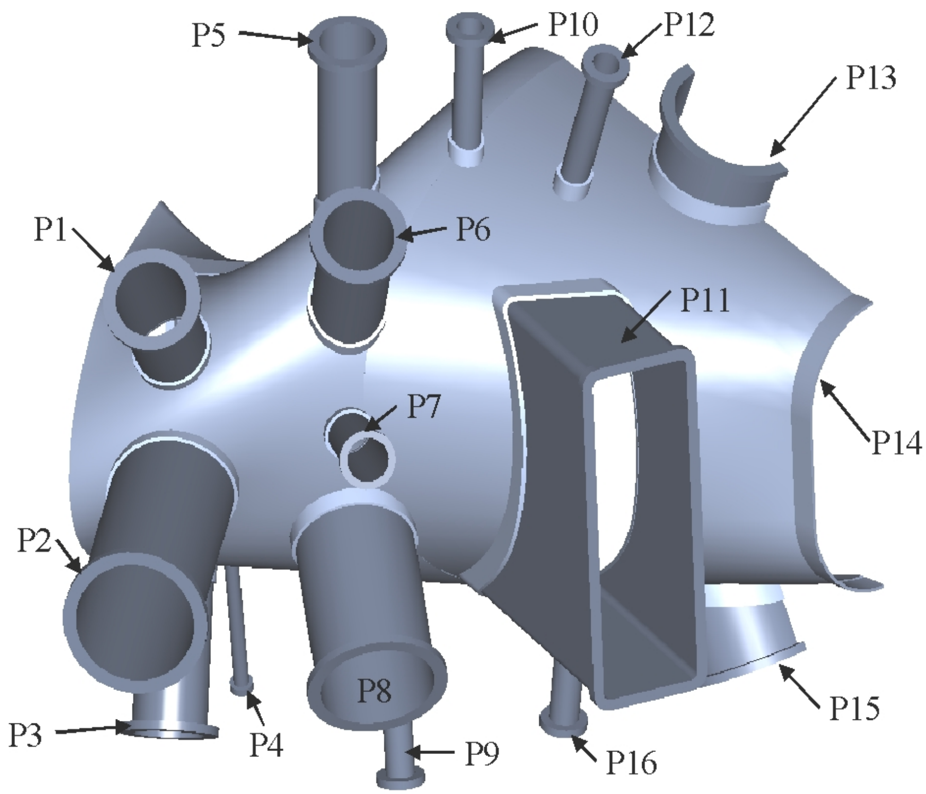

Figure 3-22 Vacuum vessel with ports for diagnostic access

Table 3-6 Port sizes and numbers

Port ID	Port size (inside diameter in inches)	Number of ports per half period	Total number of ports
P1, P3, P6	8.0	3	18
P2, P8	13	2	12
P4	1.5	1	6
P5	6.0	1	6
P7	4.5	1	6
P9, P10, P12, P16	3.0	4	24
P11	36 X 12	1	6
P13, P15	14.5	2	6
P14	31 X 20	1	3
Total			87

The neutral beams will be injected through a port centered on the v=0 (bean-shaped) cross-section. The outer leg of the modular coil has been moved to accommodate tangential injection. Figure 3-23 shows the device configured for two co- and two counter-injected neutral beams. If the fourth beamline was configured for co-injection, it would be located at the remaining v=0 plane.

NCSX is being designed to accommodate 6 MW of ion cyclotron resonant frequency (ICRF) heating in addition to neutral beams. The leading candidate for ICRF heating is a 20-25 MHz system that employs a combline antenna inboard of the plasma at the v=0.5 (the oblate or bullet-shaped cross-section). This size of the antenna is approximately 10 cm deep x 50 cm wide x 50 cm tall. This option is attractive because of the physics advantages derived and because it makes use of existing RF sources at PPPL. Design studies are currently underway to accommodate this plasma heating option.

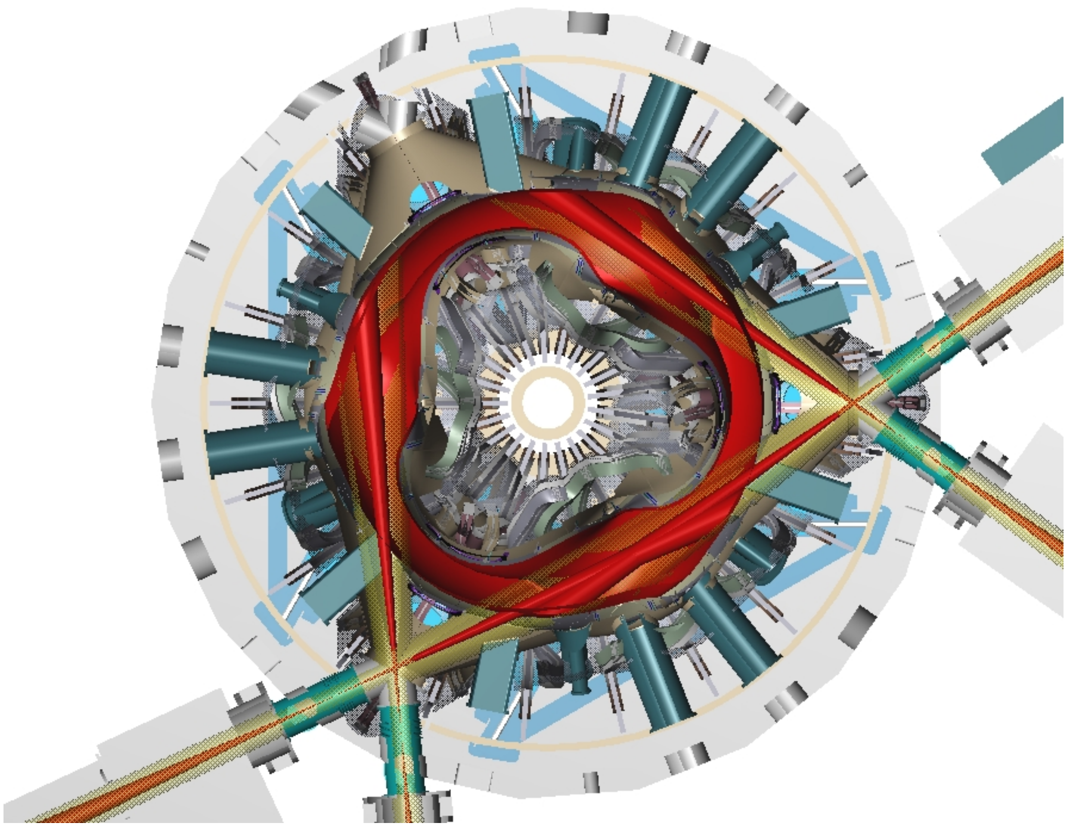

Figure 3-23 Plan view showing neutral beam access

3.2.3 Personnel acess

Personnel access requirements for different stages of fabrication and operation were considered. Several of the requirements are listed below:

- During manufacture – measure, inspect, assemble, and install components
- During field period subassembly – weld/inspect ports; leak check and repair welds; install trim coils, magnetic diagnostics, and PFC's
- During final assembly of vessel – connect vessel segments; clean, leak check, and inspect; complete installation of in-vessel components
- After final assembly of vessel – maintenance and reconfiguration of internal components

Port access is limited because of the modular coils, PF coils, TF coils, and structure supporting the modular coils. The three large ports through which the neutral beams are injected are adequate for personnel access. These ports have an opening of 32 inches tall by 20 inches wide. Plan and elevation views are provided in Figure 3-22.

These ports have ample size for allowing personnel access into the vacuum vessel. However, they are less than ideal because the outboard trim coils are located in front of them, blocking immediate access into the vessel interior. The trim coils and molded panels in front of the trim coils would likely have to be removed to allow entry into the vessel interior. Although in the initial configuration only one of the three ports would have neutral beams installed, it is

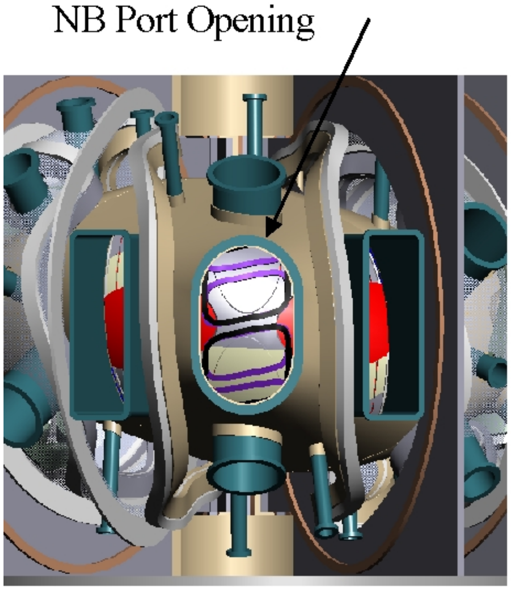

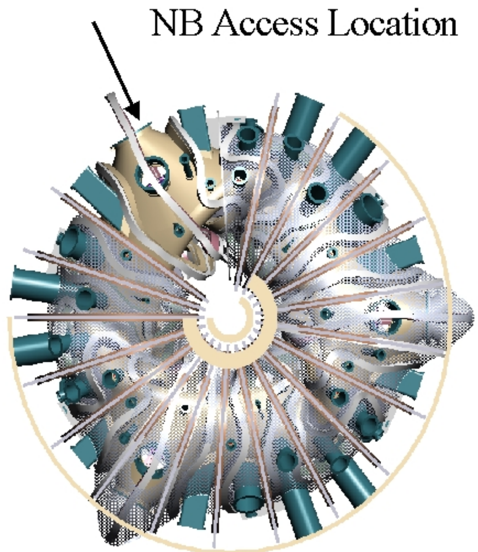

Figure 3-24 Elevation and plan views of personnel access port

anticipated that ultimately two or perhaps all three would have equipment installed that would block ready access to the vessel interior. For this reason, alternative routes for personnel access (perhaps through the ports adjacent to the neutral beam ports, which are also large enough to permit personnel access) will be investigated during conceptual design. In addition, NCSX engineers will work with PPPL machine technicians to incorporate features inside the vacuum vessel to improve maintainability.

3.3 Machine Assembly

Machine assembly includes all activities in the assembly of the individual field periods (one-third segments of the overall machine) plus the overall machine assembly. These activities can be divided into three areas, which include:

- Planning and oversight
- On-site pre-assembly
- Test cell and basement assembly activities

3.3.1 Planning and oversight

A Construction Manager will be appointed and will be responsible for planning and supervising all assembly activities in the NCSX test cell and test cell basement. Engineering will support field activities. The oversight and planning responsibilities will also include the pre-assembly of the three field periods in the TFTR test cell. A full time Construction Safety Representative along with Industrial Hygienist and Quality Control will support all field activities.

Special tooling will be designed and fabricated to support the field period and machine assembly activities. This tooling will include lifting, assembly and alignment fixtures and jigs.

A platform will be designed and fabricated which will surround the NCSX device and provide support for diagnostics and improve access to the machine. This platform will be modular in design, similar to the NSTX platform, allowing for fabrication of standard parts and minimizing costs during future expansion.

3.3.2 On-site pre-assembly

The vacant TFTR test cell will be utilized for the assembly of the three field periods. The area has sufficient floor space, crane capacity, and electrical power to allow for the assembly of all three field periods in parallel. The area will also have a line from the NSTX helium bakeout system so that the individual vacuum vessel sections can be baked to 150ºC.

The modular and TF coils will be completely pre-assembled at the factory for fit-up, inspection, and testing prior to shipping. They will then be delivered to the assembly area. The Inconel vacuum vessel will be delivered in three sections plus the port extensions.

Each field period is comprised of one third of the Inconel vacuum vessel, TF and modular coils, PFC support rings, trim coils and in-vessel diagnostics. The TF and modular coils will first be assembled over the vacuum vessel (VV) segment. The vacuum vessel will then be supported (hung) from the modular coil structure. Once assembled, the port extensions will be welded onto each VV segment. PFC support rings will then be installed inside of the vacuum vessel to support the PFCs. In the initial configuration, these rings will be covered with low-Z tiles with minimal coverage of molded CFC panels.

The vacuum vessel segment will then be baked out to 150ºC and a vacuum leak check will be performed to verify the integrity of the newly welded port extensions. Following the leak check, some of the in-vessel diagnostics along with the trim coils will be installed. The field period is now ready for delivery to the NCSX test cell.

3.3.3 Test cell and basement assembly activities

The plan is to pre-assemble as many components as possible outside of the test cell. This will minimize congestion in the NCSX test cell and should decrease the assembly schedule. The machine components will be delivered to the NCSX test cell and unloaded using the 30 Ton overhead crane.

The general assembly plans are to first install and level the machine support columns. This will be followed by installing the lower support ring segments (with a fiberslip surface) and lower cryostat floor. Prior to delivering the field periods, the lower PF 3 and PF 4 coils will be positioned onto the top of the support rails.

Each of the three field periods will be delivered and positioned onto the lower support rails, which allow the field periods to be moved radially together for final fit up. The three field periods will then be carefully slid together and their vacuum vessel segments bolted together using either a Helicoflex or Viton seal.

The vacuum pumping duct will then be connected to the vessel so that the pre-operational test procedures (PTP) for pumpdown can be performed. These tests will verify the integrity of the vacuum boundary. Once these tests have been completed, the remaining components can be assembled. The lower PF 3 and PF 4 coils will be raised into position followed by the installation of the upper PF 3 and PF 4 coils. The solenoid assembly (with the PF 1 and PF 2 coils) will then be placed in position.

The remaining elements of the cryostat will then be assembled. Bus and cable runs, water-cooling lines, helium gas lines along with the liquid nitrogen lines will also be installed and connected at this time.

The machine platform will be installed in stages around the machine. Once the major machine components have been installed, the platform will quickly grow around the device to make access easier and to support auxiliary lines that will interface with the machine. In conjunction with the platform installation lighting, fire detection and fire suppression systems will be installed under the platform.

The final installations will include the neutral beams and external diagnostics, which will be installed following the completion of the platform. The radiation shield wall that surrounds the delivery area will be completed once all of the major elements of the machine have been delivered to the test cell.

3.4 Neutral Beam Heating

NCSX will re-use two of the four PBX-M neutral beamlines in its initial configuration. NCSX will be able to accommodate the other two as an upgrade. Prior to clearing the test cell, the four beamlines will be relocated to the Neutral Beam Power Conversion building at D-site for refurbishment. Upon completion of the machine assembly, two beamlines will be installed on the machine.

The beamlines will re-use existing support subsystems (power, vacuum, cryogenic, water, air, instrumentation, control, diagnostic, and computer archiving subsystems). These subsystems have not been maintained since PBX-M was last operated in FY93. In order to startup these subsystems, maintenance, repair, and integrated subsystem testing must be performed.

There is concern about starting up the neutral beam accel power rectifier and modulator. This equipment was designed in the 1970's and is based on 1950's technology. It is difficult to impossible to procure spares. Starting up two of the beamlines by cannibalizing parts from the accel power supplies for the unused beamlines appears feasible. However, the long-range plan is to use a modern accel power supply for the third and fourth beamlines and ultimately, for the first two as well.

3.5 Fueling, Vacuum Pumping, and Conditioning

Fuel gas can be puffed into NCSX using the legacy PBX-M gas puffing system, which includes a hydrogen purification system. The legacy PBX-M pellet injection system will be installed later, as an upgrade after first plasma. Special guide tubes will be installed for injection from the high field side during the initial machine assembly.

NCSX will also re-use the torus vacuum pumping system from PBX-M. This system consists of:

- 4 Leybold Heraeus TMP 1500 turbo-molecular pumps (TMPs)
- 4 Model 1398 belt driven backing pumps
- 1 Kinney KT 500 belt driven roughing pump

The four TMPs will initially be mounted on the two neutral beam drift ducts. A new Residual Gas Analyzer (RGA) will be installed. Routine scheduled maintenance has not been performed on these systems since CY93 and will be required prior to startup. The legacy controls will be replaced with a PLC based system.

NCSX will also provide capability for wall conditioning with glow discharge cleaning (GDC) and boronization using Trimethylboron (TMB).

3.6 Electrical Power

Electric power systems includes all work required to supply AC power to all NCSX systems. The largest component of the work is the supply of controllable DC power to the modular, TF, and PF magnets. Preliminary design studies considered many approaches, including the following:

Option 1: Use of C-site MG sets and C-site Robicon AC/DC converters;

Option 2: Relocation of existing Transrex AC/DC converters from D-site to C-site, and supply of power to same via new AC transmission from D-site to C-site;

Option 3: Procurement of new AC/DC converters for C-site, and supply of power to same via new AC transmission from D-site to C-site;

Option 4: Use of existing Transrex AC/DC converters at D-site with DC transmission from D-site to C-site:

a) Segregated completely from NSTX, no shared power supplies

b) Use of C-site MG and Robicon equipment where possible

c) Sharing of power supplies with NSTX

After careful study, Option 4c was identified as the most cost effective and technically attractive option. It was determined that sufficient D-site power supplies were available, with some sharing with NSTX, such that all of the three reference scenarios (the Day One, 1.2T, and 1.7T reference scenarios) can be supplied with the baseline design. Switchover of systems shared between NSTX and NCSX can be accomplished in a matter of minutes, but must be limited to, nominally, one operation per day in order to limit the number of times that the isolating switches are cycled. Ratings of the AC/DC converter systems supplied are provided in Table 3-7.

Table 3-7 Ratings of the AC/DC converter systems

Circuits	Full Load Current (kA)	No-Load Voltage (kV)	Comments
M1, 2, 3, 4	+24	+/-2	Each circuit independently controllable; shared with NSTX TF
PF1	+/-24	+/-8	Shared with NSTX OH
PF2	+/-24	+/-2	
PF3	+24	+/-2	
PF4	+24	+/-2	
TF	+/-24	+/-2	
Trim1,2,3,4	+5	+/-0.3	

3.7 Central I&C and Data Acquisition

Central I&C and Data Acquisition provides the global man-machine interface for all facility and physics subsystems such as:

- High energy subsystems
- Safety systems
- Facility timing and synchronization system
- Power conversion feedback control systems
- Cooling systems
- Diagnostic systems
- Auxiliary heating subsystems

The Experimental Physics and Industrial Control System (EPICS) will be the software base for this function. Also provided will be a convenient interface to the data acquisition and data management systems, allowing the acquisition, display, analysis, archival, and restoration of NCSX shot data. The MDSplus software from MIT will be used for data acquisition functions. This work package will also provide the physical control room environment, which will include the workstations and furniture for physics, engineering, and operations staff.

The communications backbone will be an extensive TCP/IP network infrastructure running at a minimum of 100Mbps. All NCSX facilities and physics subsystems will use this common communications highway. Several classes of networks will be deployed which will provide varying degrees of security depending on the importance of the connected subsystems. A new timing and synchronization system, with the flexibility of the old TFTR system, will be designed and deployed for all machine timing requirements. All instrumentation will be based on modern PC technology and the PCI bus in the form of Compact PCI (CPCI), PXI, and some VME. All the instrumentation electronics and computers required for diagnostic subsystems will also be provided.

Site and Facilities

3.8.1 Site preparation

Site preparation includes all activities associated with the preparation of the NCSX test cell and those areas that will be required to support the operation of the NCSX device, including:

- Facility modifications outside of the test cell
- Preparation of the test cell
- Seismic reinforcement of the test cell shield walls.

3.8.1.1 Facility modifications outside of the test cell

The vacant PBX/PLT control rooms will become the home of the new NCSX control room. The existing facilities will be cleared. All of the wiring systems will be electrically safed, followed by the removal of wiring, cables, trays, control consoles, etc. Both the ceiling and raised floor will also be discarded and replaced, including new lighting and electrical panels throughout the control room. The adjacent PBX computer room will also be cleared and the walls separating the computer and control rooms removed. Once the walls have been reconfigured and the ceiling and floor replaced, the control room will be refurbished.

Other areas outside of the test cell, which will be modified, include the 2nd floor of the D-site FCPC building and the vacant TFTR test cell. A great deal of activity will occur in the 2nd floor of the FCPC building at D-site. It is from this area where the power required by the NCSX coil systems will originate. The 2nd floor presently houses a number of occupied offices plus the vacuum prep laboratory. The laboratory will remain in its present location. However, the offices along with the personnel will have to be relocated. The office walls will be removed. Twenty 6" diameter penetrations will have to be added through the FCPC concrete floor along with a large weatherproofed wall penetration for the exiting power cables.

The field period assemblies will be assembled in the vacated TFTR test cell at D-site. The facility already has sufficient floor space, lighting, power and crane capacity. However, it will be necessary to bakeout each of the vacuum vessel segments during the assembly of the field periods. The NSTX Helium Bakeout System will be utilized for bakeout. It will be necessary to extend the bakeout lines approximately 100 feet to the field period assembly area.

3.8.1.2 Preparation of the NCSX test cell

The NCSX test cell is the location of the combined PLT and PBX test cells at C-site. The PLT device has already been removed, but the PBX machine along with its diagnostics and neutral beams, remains intact. The area will first be electrically safed by PPPL or electrical contract personnel. Major electrical components such as panels and circuit breakers will be salvaged for future use on NCSX. The bulk removal of the cables and trays will be performed later as part of a bulk removal operation. Prior to bulk removal of the PBX device, all lead and hydraulic fluids will be removed. There is presently approximately 16,000 pounds of lead shielding which will be removed by PPPL personnel along with all of the hydraulic fluids from pumps along with the TF hydraulic joint clamps.

Once these operations have been completed, the PBX device along with remaining diagnostics, bus systems, coils, structure, vacuum vessel, cables, and trays will be removed by a contract salvage firm. Preliminary indications are that the contractor will perform these activities at no cost to PPPL, as was done for PLT.

The existing radiation shield walls between the PLT and PBX test cells will be removed, which will increase the size of the NCSX test cell. Additional shielding around the delivery high bay area will also be removed to expedite the removal of the PBX device along with assembly of the NCSX.

3.8.1.3 Seismic reinforcement of the test cell shield walls

Once the PLT and PBX test cells have been cleared, and prior to starting the assembly of NCSX, the remaining shield walls will need to be seismically reinforced. It may also be necessary to increase the height of the shield walls on the East, West and South walls to reduce shine associated with operations. The shield wall surrounding the delivery area will be completed once the major components for the NCSX device have been delivered.

3.8.2 Heating, cooling, and utility systems

The vacuum vessel is bakeable to 150ºC with a nominal operating temperature of 20ºC. Inside the vacuum vessel is a stand-alone liner that ultimately will be covered with molded CFC panels. The liner is bakeable to 350ºC with a nominal operating temperature in the range of 20ºC to 150ºC. The vacuum vessel and liner will be connected to helium systems capable of independently controlling their temperature. This requires that the systems have both a heating capability (for bakeout and to maintain the temperature during standby operation) and a cooling capability (to remove heat deposited by the plasma between pulses).

Cooling water is required by numerous systems, including:

- Neutral beams
- Vacuum pumping
- Diagnostics
- Vacuum vessel and liner heating and cooling systems

Each of these cooling loops will be connected to the existing C-site water system.

3.8.3 Cryogenic systems

The modular, TF, and PF coils on NCSX are located within a common cryostat and pre-cooled to liquid nitrogen temperature (80K) before operation. A liquid nitrogen supply system is provided to remove heat from the structure and from the nitrogen environment within the cryostat. The coils within the cryostat will be cooled by helium gas. The helium gas will be pre-cooled to 80K in a liquid nitrogen heat exchanger.

The liquid nitrogen system is a once through system. Upon vaporization, the nitrogen exhaust will be heated and vented to the atmosphere. A 15,000-gallon tank will be installed at C-site for storage of liquid nitrogen. If required, a second 15,000-gallon tank can be installed at a later date.

3.8.4 Utility systems

Compressed air, gaseous nitrogen, and vacuum venting systems will be provided in the NCSX test cell. Manifolds will encircle the machine to provide access to these systems at each bay. The vacuum vent will connect to the vacuum pumping system, which is in the basement beneath the experiment.

Chapter 4 – Equilibrium and Flux Surface Integrity

This chapter discusses the NCSX equilibrium calculations, including the issue of flux surface integrity. The VMEC equilibrium code has been used for the routine generation of three-dimensional equilibria for stability and transport studies, and it has been incorporated in the optimizer for generating candidate NCSX configurations and assessing coilset flexibility. The code is described in Section 4.1. Equilibrium calculations have been done with bootstrap-consistent current profiles, and the calculation of the bootstrap current is discussed in Section 4.2. Calculation of three-dimensional equilibria with islands and stochastic regions has been done with the PIES code, and the code is described in Section 4.3. Section 4.4 discusses the evaluation of flux surfaces for candidate configurations generated by the optimizer. Section 4.5 describes a method that has been used to make small modifications to the NCSX configuration to heal residual magnetic islands. A set of trim coils provides flexibility in the experiment to adjust resonant field components for a range of configurations. The calculations described in sections 4.3-4.5 do not include neoclassical effects, which reduce island widths, and the likely consequences of these effects are estimated in Section 4.6.

4.1 VMEC

The VMEC code[1] solves the three-dimensional equilibrium equations using a representation for the magnetic field that assumes nested flux surfaces. VMEC uses an inverse moments method, in which the geometric coordinates R and Z are expanded in Fourier series in both a poloidal angle variable and the toroidal angle(for three dimensions). The coefficients Rmn, Zmn in this series expansion are functions of the normalized toroidal flux s, where s = 0 is the magnetic axis (which can be a helical curve in three dimensions) and s = 1 is the plasma boundary. Here, m is the poloidal and n is the toroidal Fourier mode number. The boundary Fourier coefficients Rmn(1) and Zmn(1) can either be constant (corresponding to a "fixed-boundary" equilibrium calculation), or they may be self-consistently computed from the MHD force balance equation at the plasma-vacuum boundary (for a "free-boundary" calculation[2]). Internally, VMEC computes an addition "renormalization" stream function (λ) which is used to optimize, dynamically and at every radial surface, the convergence rate in Fourier space for the spectral sum Σ(Rmn**2 + Zmn**2). In the original VMEC, radial mesh gridding is staggered, with the Rmn(s) and Zmn(s) coefficients defined on integral radial mesh points sj = (j-1)/(Ns-1) [where Ns is the number of radial nodes] and the lambda coefficients on half-integer mesh points interleaving the Rmn, Zmn mesh. This scheme has been proven to lead to excellent radial resolution as well as minimal mesh separation (at least for large aspect ratio plasmas and with limited angular resolution meshes).

Significant improvements have been made to the VMEC code in the context of the NCSX design effort. It has been redifferenced to improve the convergence both on finer angular and radial meshes as well as for equilibria with a wide range of rotational transform profiles. In VMEC, the inverse equations are cast as second order equations (in radius) for the Fourier components of R, Z, and λ. As noted above, λ has been previously differenced radially on a mesh centered between R, Z nodes, which greatly improved the radial resolution. This could be done to second order accuracy (in $h_s = 1/[N_s\text{-}1]$) since no radial derivatives of λ appear in its defining equation, $J^s = 0$ (here, J^s is the contravariant radial component of the current). Near the magnetic axis, however, a type of numerical interchange instability (mesh separation) has been observed as the angular resolution is refined. This behaviour has prevented the temporal convergence of 3D solutions with large numbers of poloidal (m) and toroidal (n) modes (typically, $m \sim 6\text{-}8$ was the practical limitation). It has also produced convergence problems for equilibria with low ι (<<1) where field lines must encircle the magnetic axis many times to define magnetic surfaces. The new differencing scheme computes the stream function on the same mesh as R and Z (although the output values of λ continue to be on the centered-grid for backwards compatibility), which leads to numerical stabilization of the origin interchange. To avoid first order errors (in h_s) near the plasma boundary resulting from the new representation of λ, the radial current J^s continues to be internally represented (in terms of λ) on the interlaced-grid. This maintains the good radial spatial resolution associated with the original half-grid representation for λ. As a result, computation of accurate, convergent solutions with substantially higher mode numbers is now possible using VMEC ($m < 20$). This corresponds to much finer spatial resolution and significantly improved force balance in the final equilibrium state. It also allows the calculation of equilibria with lower values of ι, which were difficult to obtain with the previous differencing scheme.

An additional improvement in the output from VMEC includes a recalculation (once the VMEC equilibrium has been obtained) of the magnetic force balance $\mathbf{F} \equiv \mathbf{J}\text{x}\mathbf{B} - \nabla p = 0$. The radial ($\nabla s$) component of $\mathbf{F}$ is solved in terms of the non-vanishing contravariant components of B (B^u and B^v) and the metric elements determined by VMEC, as a magnetic differential equation for B_s. An angular collocation procedure (with grid points matched to the Nyquist spatial frequency of the modes) is used to avoid aliasing arising from nonlinear mode coupling of the Fourier harmonics of R and Z in the inverse representation of the equilibrium equation. The accurate determination of B_s, together with the higher angular resolution afforded by the larger limits on the allowable m,n spectra in VMEC, permits an accurate assessment for the parallel current (which contains angular derivatives of B_s) as a function of poloidal mode number, to be performed.

4.2 Bootstrap Current Profile

The current profiles for the NCSX design have been determined by a bootstrap current calculation using VMEC equilibria. Axisymmetric calculations using the bootstrap module in the jsolver code [3-5] have been used for this purpose. For perfect quasi-axisymmetry, the bootstrap current is identical to that in an equivalent tokamak, because the bootstrap current is determined by the Fourier components of mod(B) in Boozer coordinates. In practice, the quasi-axisymmetry condition is satisfied approximately. Fully three-dimensional Monte-Carlo-δf bootstrap calculations have been done for an earlier NCSX reference configuration, configuration C82, using the ORBIT code [6, 7] to quantify the errors introduced by the residual nonquasisymmetric ripple. These calculations have verified that the bootstrap current is given to a good approximation by the axisymmetric terms alone. The Monte-Carlo simulations for the non-axisymmetric case have been further benchmarked against calculations with the DKES

(Drift Kinetic Equation Solver) code [8]. In calculating the bootstrap current with the jsolver code, the density profile has been taken to be $n(s) = n(0)(1-s^{2.3})^{0.1}$, where $n(0) = 0.54 \times 10^{20}$ m^{-3}. The corresponding temperature profile for the full, 4% β, li383 case is $T(s) = T(0)(1-s^{2.3})^{1.9}$, where T(0) = 2.14 kev.

4.3 The PIES Code

Three-dimensional magnetic fields have magnetic islands and regions of stochastic field lines. The VMEC code uses a representation of the magnetic field that assumes nested flux surfaces. The PIES code is a three-dimensional equilibrium code that uses a general representation for the field, and is therefore capable of calculating islands and stochastic field line trajectories. There is an extensive set of publications on the algorithm, implementation, validation, convergence properties and applications of the PIES code. [9-13, 16-40]

The PIES code solves the MHD equilibrium equations using a Picard iteration scheme,

$$\nabla \times \mathbf{B}^{\mathbf{n}+1} = \mathbf{J}(\mathbf{B}^{\mathbf{n}}),$$

$$\nabla \cdot \mathbf{B}^{\mathbf{n}+1} = 0,$$

where $\mathbf{B}^{\mathbf{n}}$ is the magnetic field at the start of the n^{th} iteration, and $\mathbf{J}(\mathbf{B}^{\mathbf{n}})$ is the current found from the force balance equation, $\mathbf{J} \times \mathbf{B} = \nabla p$, and the constraint $\nabla \cdot \mathbf{J} = 0$. This scheme is closely related to the Picard algorithm widely used to solve the axisymmetric Grad-Shafranov equation in the form $\Delta^* \psi_{n+1} = j_\phi(\psi_n)$. As with the Picard iteration scheme for the Grad-Shafranov equation, underrelaxation is used to extend the domain of convergence of the Picard iteration.

An advantage of the Picard scheme is that it provides an accurate calculation of resonant pressure driven currents, which are believed to play an important role in determining island widths At each iteration, the code solves for the current from the force balance equation. Writing $\mathbf{J} = \mu \mathbf{B} + \mathbf{J}_\perp$, $\mathbf{J}_\perp = \mathbf{B} \times \nabla p / B^2$ gives, $\mathbf{B} \cdot \nabla \mu = -\nabla \cdot \mathbf{J}_\perp$. Integration of this magnetic differential equation gives an accurate method for determining the currents. (Following the work of Gardner and Blackwell [41] demonstrating the importance of using an accurate solution for the currents in stability studies, it is now in fact routine in Mercier and global stability studies for stellarators to recalculate the current from three-dimensional equilibrium solutions in this way.) In implementing a numerical scheme for solving the magnetic differential equation, explicit upper bounds on the associated numerical errors were derived and are used to allow the specification of required tolerances in the code.[10]

As the PIES code iterates, the pressure and current are flattened in islands and stochastic regions. Several numerical diagnostics in the code allow the determination of the location of these regions. The PIES algorithm is described in detail in the references [9-13, 19].

The PIES code has been validated by testing of the individual components, by internal checks in the code that monitor the accuracy with which the equilibrium equations are satisfied, and by comparison with analytic solutions and with other codes. Analytic solutions against which the code has been compared have included Soloveev equilibria[11], large aspect ratio stellarator expansions[11], helical force-free Bessel function equilibria with islands[19], and the analytic solutions of White et al for saturated tearing modes with narrow islands. Comparison of PIES with other codes has included: comparison with axisymmetric j-solver[14] equilibria for TFTR and DIII-D; comparison with Biot-Savart vacuum field solvers; comparison with marginal stability for tearing modes calculated by the linearized resistive time-dependent code of Hughes; and comparison with VMEC[16]. Ref. [16] contains a careful comparison between the VMEC code and the PIES code solutions. The devices modeled were the ATF and TJ-II stellarators, for transforms where low order rationals were absent. The flux surface shape, location of the magnetic axis and the value of iota as a function of flux surface were monitored as a function of β and radial resolution. An extrapolation in radial resolution was used to verify the quantitative agreement of the codes. The comparison with VMEC was continued in reference [18]. Here, the rotational transform as a function of radius was in excellent agreement between the two codes for the W7-X stellarator, at $< \beta > = 5\%$.

Many stellarators, for example ATF, TJ-II, W7-AS, W7-X and LHD have been modeled by the PIES code [11,16,18,20]. Present day experiments have not reached the predicted equilibrium beta limit, and no experimental study of this issue has therefore been possible.

In the context of the NCSX design effort, several modifications have been made to the PIES code that have increased its speed by about an order of magnitude, allowing routine application of the code to evaluate flux surfaces in candidate NCSX configurations. The speed of the code was improved by modifications to use an improved method for PIES initialization with a VMEC solution, to convert to a spline representation for field line following, and to store matrix inverses.

Compared with VMEC, the PIES code has a more time-consuming algorithm, which is needed for a general representation for the magnetic field. Time is saved by initializing PIES using a converged VMEC solution. For this purpose, the under-relaxation scheme in PIES has been modified to provided an improved coupling to the VMEC solution. This involves blending with the VMEC field in the first PIES iteration. The previous under-relaxation scheme blended the current rather than the fields. The under-relaxation was skipped in the first PIES iteration, allowing a large step from the VMEC field, and slowing the ultimate convergence. The PIES code follows magnetic field lines as a preliminary step to solving the magnetic differential equation determining the Pfirsch-Schlueter current. Conversion from a Fourier representation to a spline representation of the field has speeded ups the code by about a factor of two.

In each iteration of the PIES code, a discretized Ampere's law is solved by the inversion of a block-tridiagonal matrix. The elements of the blocks are determined by metric elements of a ``background coordinate system'' that does not change from one iteration to the next, allowing time to be saved by storing the inverses of the blocks. For high resolution calculations, this changes the scaling of the code's execution time from m^3n^3k to a much more favorable m^2n^2k where m and n are the number of the poloidal and toroidal modes retained, and k is the number of radial grid surfaces.

4.4 Flux Surface Integrity

Three-dimensional magnetic fields have magnetic islands and regions of stochastic field lines. It is desired to minimize the size of these regions in NCSX to obtain nested flux surface across at least 90% of the cross-section. As a first step, a fixed boundary reference equilibrium with good flux surfaces was identified. Coils were reverse engineered to produce this configuration, and free-boundary evaluation with the PIES code was incorporated in the coil design process to ensure that flux surfaces were preserved. Trim coils have been added to the design to provide flexibility, preserving the flux surfaces for a range of configurations.

The configuration optimizer used to generate candidate configurations for the NCSX design study did not include a measure of flux surface integrity. Flux surface calculations for the various candidate configurations have found significant differences in the extent of islands and stochastic regions. This is illustrated by the calculations described in this section. The earlier reference configuration, C82, was found to have a large region of stochastic field lines at beta values of interest. This was typical of several types of configurations that were studied. In contrast, the flux surfaces of the NCSX reference design Configuration 383 and similar configurations were nearly adequate even before the application of any flux surface optimization. The residual islands could be removed by a small adjustment of the boundary shape which had little impact on the other physics propterties. Section 4.5 discusses the adjustment of the fixed boundary configuration and of the coils for healing the flux surfaces.

In regions where $d\iota / ds > 0$, perturbed bootstrap current effects are predicted to lead to substantially decreased magnetic island widths in configurations of the type studied here.[42] This is the inverse of the neoclassical tearing mode that has been observed in tokamak experiments. This neoclassical effect is being incorporated in the PIES code, but has not been included in any of the calculations reported here. The calculations are therefore conservative in that the calculated island widths are likely to be larger than would be observed in an experiment operated in a collisionless regime. Section 4.6 gives an estimate of the neoclassical effect on the island widths.

The PIES calculations discussed in this section are all fixed boundary, and used 143 Fourier modes, $0 \leq m \leq 11$, $-6 \leq n \leq 6$, and 60 radial zones.

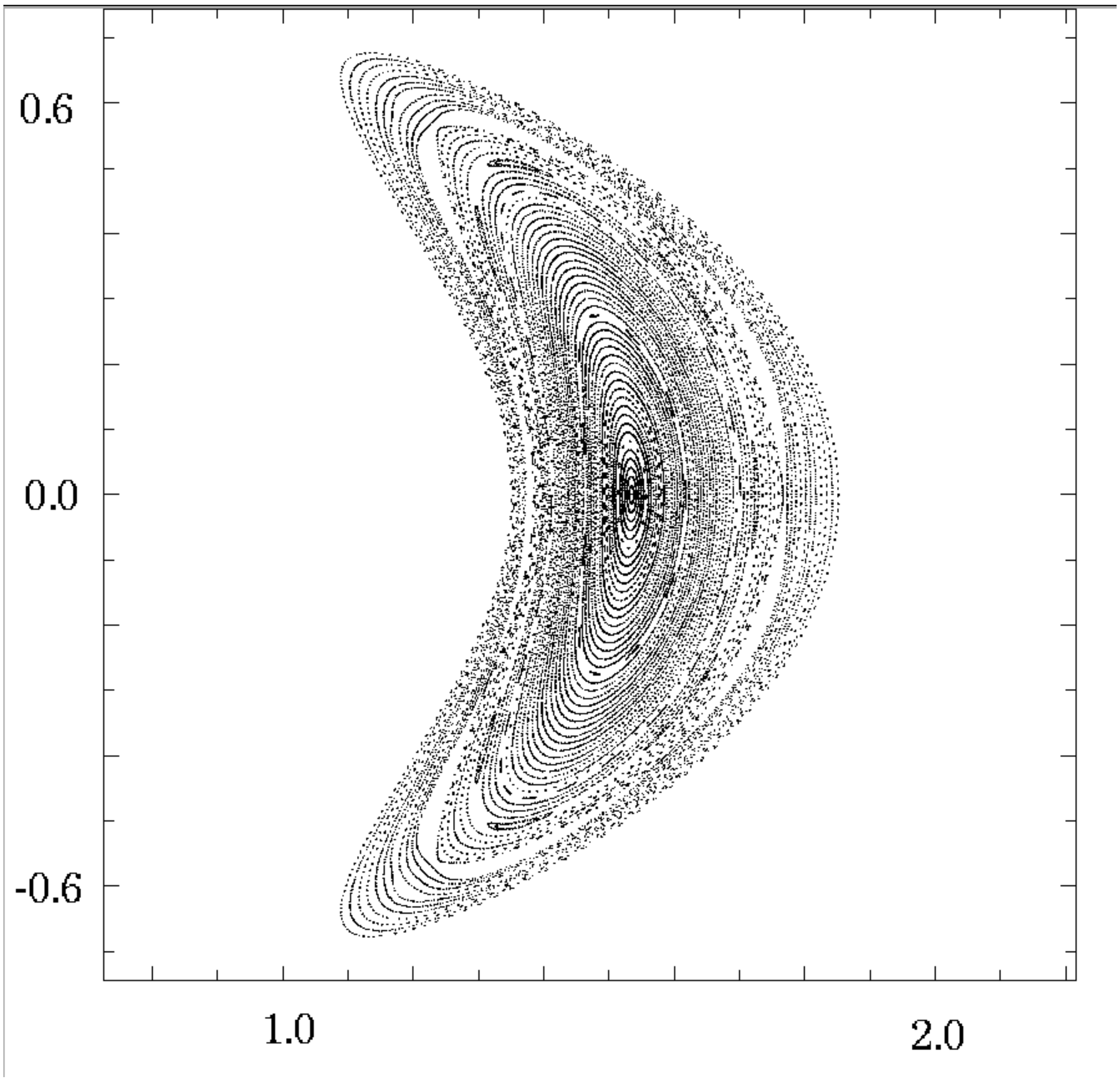

Figure 4-1. Poincare plot for configuration c82 at full current, β = 0

Figure 4-1 shows a Poincare plot of a fixed-boundary PIES equilibrium for Configuration C82 at full current, $\beta = 0$. Magnetic islands occupy about 10% of the cross-section. The islands are more readily visible if the Poincare plot uses a polar (ρ, θ) coordinate system, as in Figure 4-2. Here, the coordinate ρ is taken to be constant on VMEC flux surfaces, and to measure the distance of the VMEC flux surface from the magnetic axis along the $\theta = 0$, $\phi = 0$ line. The angular coordinate θ is identical to the VMEC angular coordinate. When plotted in these coordinates, the Poincare plot gives straight lines when the VMEC and PIES solutions coincide.

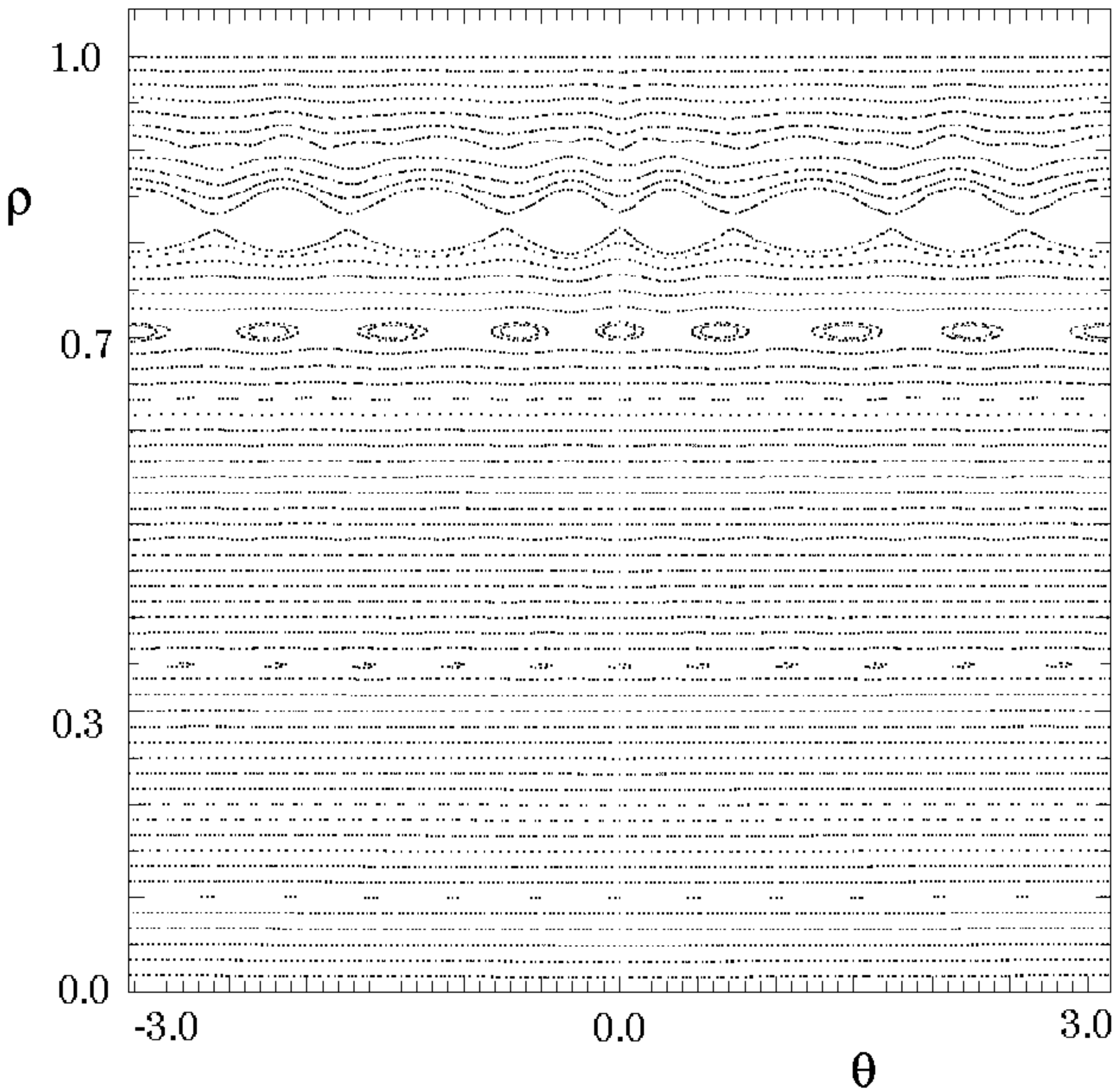

Figure. 4-2. Poincare plot for configuration c82 in VMEC coordinates, full current, β = 0

When β is raised to 3%, the PIES calculations find that a substantial fraction of the flux surfaces are lost (Figure 4-3). The equilibrium solution shown is not fully converged. The

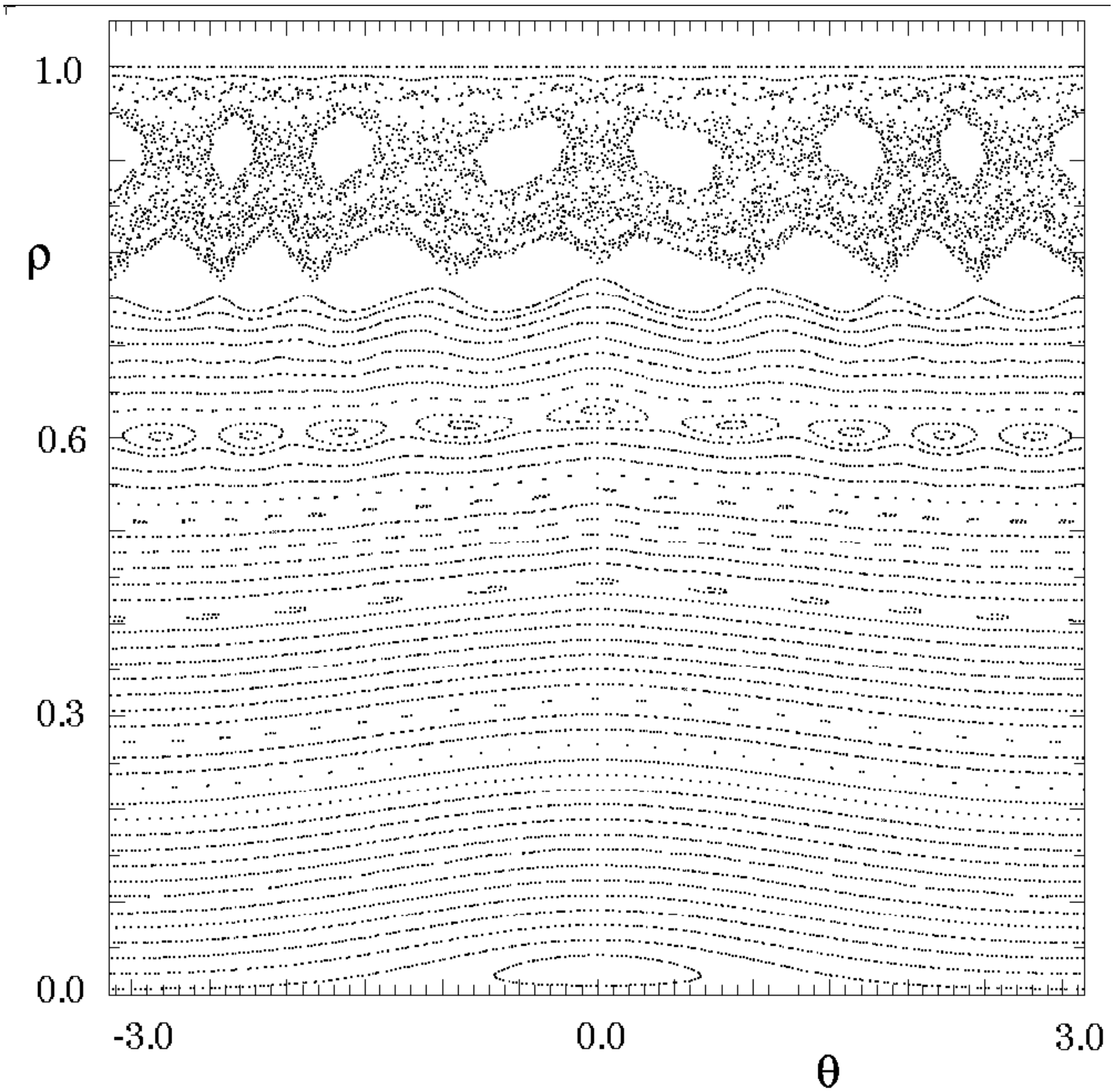

Figure 4-3. Poincare plot for earlier configuration, c82, at full current, β = 3%

outer surfaces continue to deteriorate as the calculation progresses, so that further computation is of limited interest. Flux surface integrity is a problem for configuration c82 in the absence of stabilizing neoclassical effects.

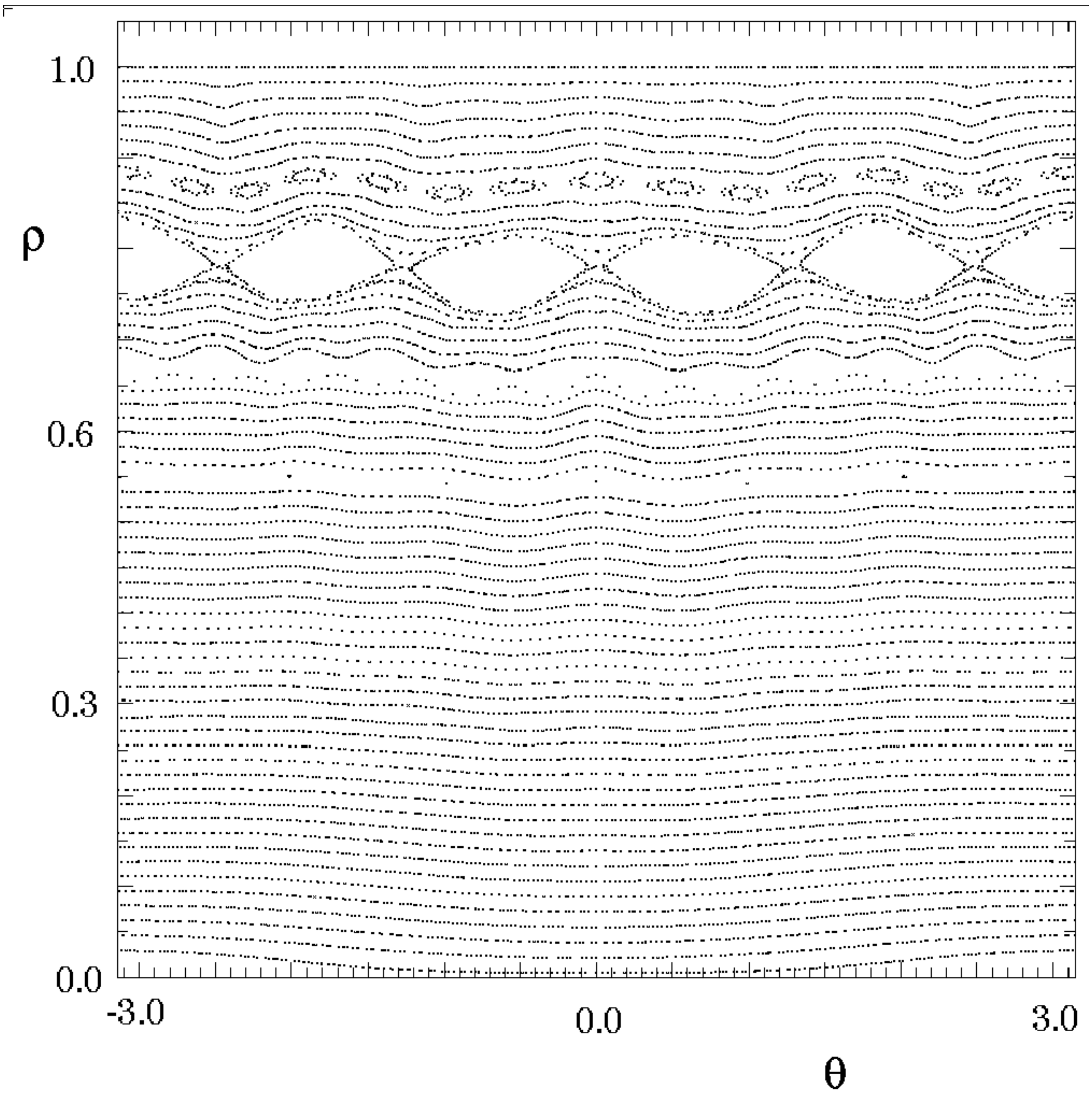

Figure 4-4. Poincare plot for configuration 383 at full current, □ = 4.2%

Figure 4-4 shows the result of a PIES calculation for configuration 383 as originally generated by the optimizer at full current, β = 4.2%. The flux surfaces are greatly improved relative to those of configuration c82. The total island width is about 15%, and is dominated by a single island chain at ι = .6 having poloidal mode number m = 5 and toroidal mode number n = 3.

The fact that the flux surface loss in the original configuration 383 is dominated by a single island chain indicates that this can be further improved by adjusting the amplitude of the corresponding resonant Fourier mode in the specification of the boundary shape. This has been demonstrated, and is discussed in the next section.

4.5 Healing of Flux Surfaces

In this section we consider manipulation of the width and phase of magnetic islands in finite β stellarator equilibria by making small variations to the boundary or the coils. Computation of the MHD equilibrium is provided by the PIES code. Magnetic islands are controlled by controlling the resonant fields at the rational surfaces, and the resonant fields are calculated via construction of quadratic-flux-minimizing surfaces [43].

Magnetic islands are caused by resonant radial magnetic fields where the rotational transform is a rational value. The continuous one-dimensional family of periodic orbits that form a rational rotational transform flux surface in the absence of resonant fields will be reduced to a finite set of periodic orbits by the resonant field, and an island chain will form. The periodic orbits surviving perturbation will typically be the stable and unstable periodic orbits, which correspond to the O and X points on Poincare plots of the magnetic field. In the small island approximation, where the shear, ι', is assumed constant across the island, the width of the island is given [44] as $w \propto \sqrt{\{|B_{nm}|/ \iota\!\!-' m\}}$, where $B_{nm} = (\mathbf{B} \cdot \nabla s \,/\, \mathbf{B} \cdot \nabla\phi_{nm}$ is the resonant Fourier component of the radial field at the $\iota\!\!- = n/m$ rational surface, s is the radial coordinate, and the prime represents derivative with respect to s. The phase of the island chain is determined by the sign of B_{nm} and the sign of the shear. The manipulation of island width and phase is enabled via control of the magnitude and sign of the resonant field.

A method for calculating resonant fields at rational surfaces has been incorporated into PIES. This method is based on the construction of quadratic-flux-minimizing surfaces. The construction of these surfaces has been presented in Ref. 43, and for the purposes of this discussion it is sufficient to note that a rational quadratic-flux-minimizing surface passes directly through the corresponding island chain, and may be considered as a rational flux surface of an underlying unperturbed magnetic field. The resonant radial field is constructed as the field normal to the quadratic-flux-minimizing surface. In the following, the term 'resonant field' shall refer to the action gradient [2] as calculated during the construction of a given quadratic-flux-minimizing surface.

A set of islands that we wish to control is selected. Generally the lowest order resonances present will produce the largest magnetic islands. A convenient method of selecting the lowest order rationals is guided by the Farey Tree construction [45]. The corresponding set of resonant fields that need to be controlled is represented by $\mathbf{B} = (B_{n1m1}, B_{n2m2}, ...)^T$.

We expect that an (n,m) island width will be strongly affected by an (n,m) resonant deformation of the plasma boundary in magnetic coordinates and perhaps through coupling to neighboring modes, so a set of independent boundary variation parameters is constructed as follows. We consider the minor radius $r = \sum r_{nm} \cos(m\theta - nN\phi)$ of the plasma boundary to be a Fourier series in the cylindrical toroidal angle and the poloidal angle used in VMEC to construct the input R and Z harmonics. The conversion to cylindrical space is given as $R = r\cos\theta$, $Z = r\sin\theta$. For a change $r \rightarrow r + \delta r_{nm} \cos(m\ \theta - n\ N\ \phi)$, the input Fourier harmonics for the VMEC code change according to $R_{m-1,n}\rightarrow R_{m-1,n}+\delta r_{nm}/2, R_{m+1,n}\rightarrow R_{m+1,n}+\delta r_{nm}/2$, $Z_{m-1,n}\rightarrow R_{m-1,n}-\delta r_{nm}/2, Z_{m+1,n}\rightarrow R_{m+1,n}+\delta r_{nm}/2$. In principle we may change infinitely many boundary harmonics r_{nm}, but a small set is chosen to match the islands that will be targeted and this becomes the vector of independent parameters $\mathbf{r} = (r_{n1m1}, r_{n2m2},...)^T$.

Now the problem is amenable to standard treatments where the functional dependence of **B** on **r** is represented

$$\mathbf{B}(\mathbf{r}_0+\delta\mathbf{r}) = \mathbf{B}(\mathbf{r}_0) + \mathbf{C}\cdot\delta\mathbf{r} + \ldots , \qquad (4\text{-}1)$$

where $\mathbf{r}_0 = 0$ is the initial boundary shape and $\delta\mathbf{r}$ is a small boundary variation. The coupling matrix **C** represents derivative information and will in general be an M ×N matrix, where M is the number of resonant fields, and N is the number of independent boundary variations. The jth column of the coupling matrix is determined through a VMEC/PIES run by making a small change δr_{njmj} and taking the difference in the resonant fields from the original equilibrium, divided by the change. Hence, N+1 VMEC/PIES runs are required to determine the coupling matrix.

The coupling matrix is inverted using the singular value representation [46], $\mathbf{C} = \mathbf{UwV}^T$, where U and V are ortho-normal and **w** is the diagonal matrix of singular values. If there are more variables than equations more than one solution may exist and the nullspace is spanned by the columns of U corresponding to zero singular values, of which there will be at least N-M.

Islands are removed if $\mathbf{B} = 0$, so by choosing a correction to the boundary $\delta\mathbf{r}$ according to

$$\delta\mathbf{r}_{i+1} = -\,\mathbf{V}\mathbf{w}^{-1}\,\mathbf{U}^T\,\mathbf{B}_i, \qquad (4\text{-}2)$$

where as in standard singular value decomposition techniques the zero, and if desired the small, eigenvalues are ignored in the inversion of **w**, and $\mathbf{B}_i$ is the vector of resonant fields at the ith iteration. In practice, several iterations will be required to achieve a desired accuracy.

This technique was applied to Configuration 383 A Poincare plot Figure 4-5 of the PIES field after 32 iterations shows island chains and the $\iota = 3/5$ island is quite large. In this and the other Poincare plots to be shown, the Poincare section is the $\phi = 0$ plane and 50 field lines are followed starting along the $\theta = 0$ line. In addition, field lines at the X points of several low order island chains are followed and the quadratic-flux minimizing surface and an estimated separatrix has been plotted over one period of each island chain. The separatrix of the island chains has been calculated using the resonant radial field and the shear at the rational surface of the VMEC equilibrium. PIES has not yet converged for this case, but the information about the island width is still useful for construction of the coupling matrix.

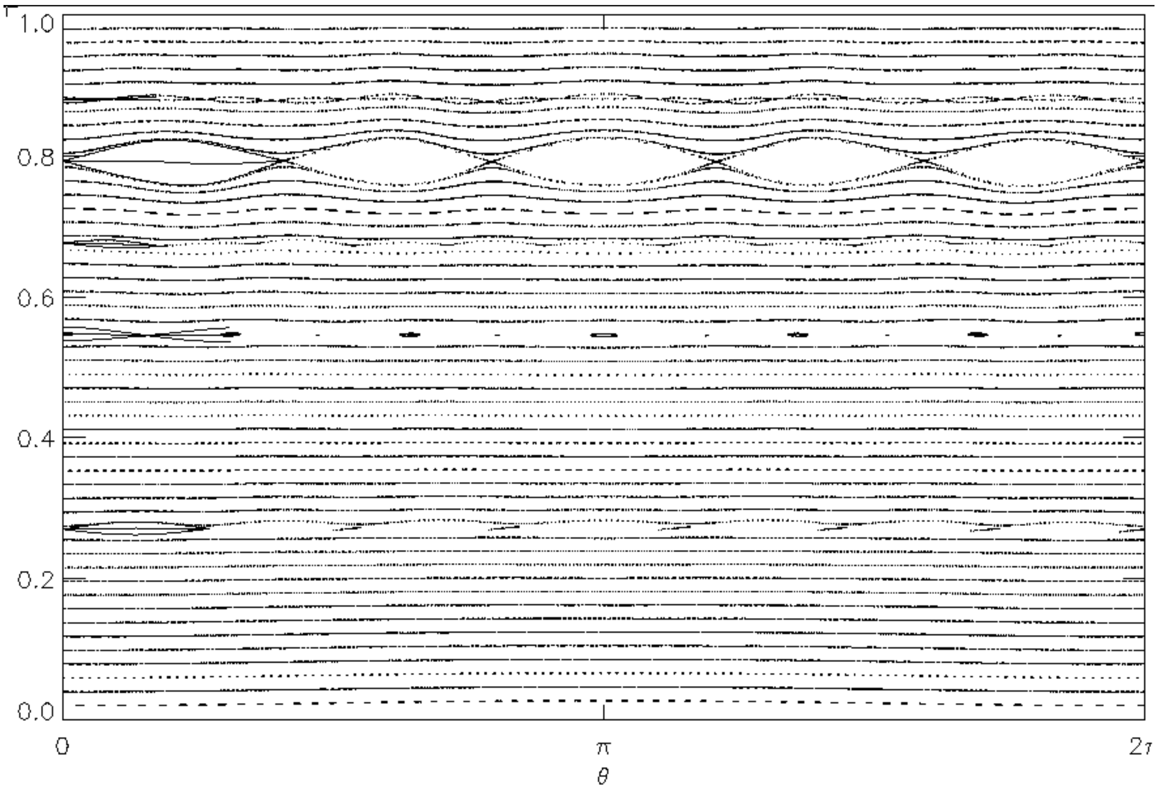

Figure 4-5. Poincare plot of initial li383 configuration after 32 PIES iterations

In this application of the island reducing technique, the (3,5),(6,10),(3,6) and (6,12) resonances are targeted, and the (3,9),(3,8),(3,7),(3,6),(3,5) and (3,4) boundary harmonics are varied. The (3,7) resonance is also present in the configuration, but this has not been targeted. The (6,10) resonance produces an island at the same rational surface as the (3,5), namely at $\iota\!\!\!-$ = 3/5, and may be considered as the second harmonic of the (3,5) resonance. If the (6,10) resonant field is not targeted, this may cause an island of distinct topology from the (3,5). For this set of resonant fields and independent boundary variation parameters, the coupling matrix is shown.

$$\begin{pmatrix} \delta B_{3,5} \\ \delta B_{6,10} \\ \delta B_{3,6} \\ \delta B_{6,12} \end{pmatrix} = \begin{pmatrix} -0.15603, & 0.94645, & -0.73397, & -1.13506, & -0.17282 & -0.30578 \\ 0.12627, & 0.17790, & 0.02146 & 0.19875, & -0.07025, & 0.01394 \\ -0.05487, & -0.22773, & -0.50056, & 0.24140, & -0.30079, & 0.01531 \\ -0.00874, & 0.03067, & -0.00351, & 0.00827, & -0.00327, & -0.00083 \end{pmatrix} \begin{pmatrix} \delta_{3,9} \\ \delta_{3,8} \\ \delta_{3,7} \\ \delta_{3,6} \\ \delta_{3,5} \\ \delta_{3,4} \end{pmatrix} \quad (4\text{–}3)$$

On performing the Newton iterations, the following reduction is observed.

iteration	$\lvert B_{3,5} \rvert$	$\lvert B_{6,10} \rvert$	$\lvert B_{3,6} \rvert$	$\lvert B_{6,12} \rvert$
0	1.8×10^{-3}	1.6×10^{-4}	1.3×10^{-4}	1.4×10^{-5}
1	1.3×10^{-4}	3.4×10^{-5}	1.0×10^{-4}	2.4×10^{-6}
2	6.7×10^{-5}	3.4×10^{-5}	5.1×10^{-5}	1.9×10^{-6}
3	2.4×10^{-5}	6.7×10^{-5}	4.0×1^{-16}	5.4×10^{-7}

(4-4)

The Newton iterations are terminated after four steps as this provides sufficient reduction of the islands as seen in Figure 4-6. In a true Newton iteration procedure, the coupling matrix would be re-calculated at every iteration. In this application such a procedure is too slow and the coupling matrix is not changed; nevertheless, the convergence is satisfactory. The total change in the boundary variation parameters is

$$\delta \mathbf{r} = (-0.00184,-0.00026,0.00056,0.00300,0.00012,0.00064)^T. \quad (4\text{-}5)$$

These variations are several millimeters in magnitude and generally have little impact on stability and other physics. However, the case shown does destabilize the ballooning modes on some surfaces. This would be expected to relax the pressure gradient slightly on those surfaces.

This is not surprising considering that the li383 configuration has been optimized to provide marginal ballooning stability at full pressure.

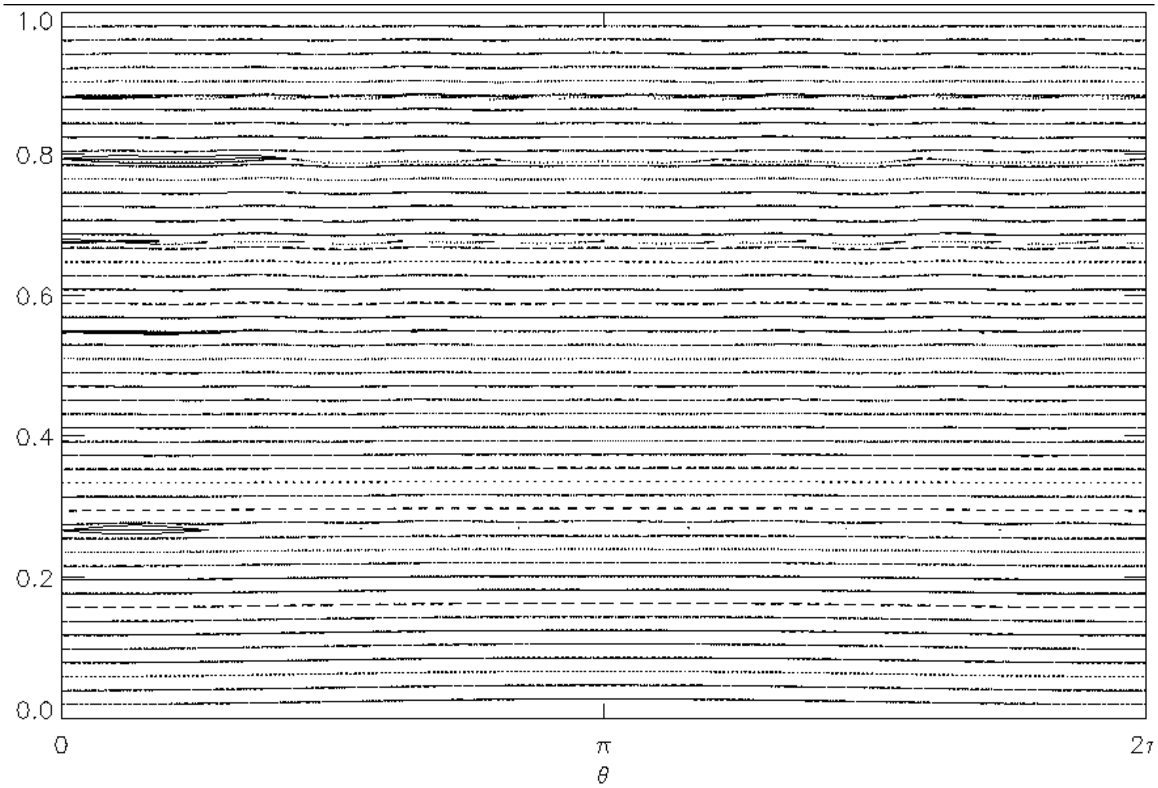

Figure 4-6. Poincare plot of full-beta island-reduced li383 configuration

The healed configuration has converged after 32 iterations. As mentioned, if the equilibrium has no islands, or if the width of the islands is less than the radial grid used in PIES, then PIES and VMEC will agree and PIES will rapidly converge. If the equilibrium displays islands and PIES is not fully converged, the island width after a given number of iterations is still sufficient for calculation of the coupling matrix and for the success of the Newton procedure in removing islands.

A similar procedure may be used to ensure coil designs are consistent with negligble island widths. A free-boundary implementation of PIES and a suitable parameterization of the coil geometry is used to optimize the coil design with respect to magnetic islands as follows.

A healed fixed boundary configuration is obtained as described above. It is important to note that such a boundary is consistent with there being no islands. Coils are designed to reconstruct a given boundary, but in general there will be some error - small but sufficient to excite islands at rational rotational transform surfaces. The free-boundary island healing approach will make small variations to the coil parameterization and examine the response of a chosen set of islands using free-boundary PIES calculations. The process is similar to the fixed boundary application, with the following differences.

The independent parameters that are varied alter the coil geometry, rather than the Fourier representation of the boundary, and optionally the coil currents. Also, in addition to eliminating resonant fields at rational rotational transform surfaces, it is convenient to require the plasma boundary created by the coils match the healed fixed boundary solution. To enable this, several Fourier modes representing the difference between the edge in free boundary calculation and the healed fixed boundary configuration are included in the target function to be zeroed.

The coils are represented by the following. The coils lie on a winding surface :

$$R = \sum_i r_i \cos(m_i \theta + n_i N \phi), \tag{4-8}$$

$$Z = \sum_i z_i \sin(m_i \theta + n_i N \phi), \tag{4-9}$$

and each coil has toroidal variation :

$$\phi_i = \phi_{i0} + \sum_k [\, \phi_{i,k,c} \cos(k\, \theta') + \phi_{i,k,s} \sin(k\, \theta')] \tag{4-10}$$

$$\theta' = \theta + \sum_j \theta'_j \sin(j\, \theta). \tag{4-11}$$

Typically a subset of the $\phi_{i,k,c}$ and $\phi_{i,k,s}$ modes is chosen to be the independent parameters.

The 0907 coils are considered. After 20 iterations the PIES field is shown in Figure 4-7. Varying only the $\{\phi_{i,k,c},\phi_{i,k,s};\ i = 1,2,3,4; k = 5,6,10\}$ modes and targeting the (1,5), (1,6) resonances, the magnitudes of the resonant fields are reduced by several orders of magnitude, and the resulting 'healed' configuration is shown in Figure 4-8. To ensure that this results in a converged PIES equilibrium with small islands a fully converged PIES run is performed. Figure 4-9 shows the equilibrium after 400 iterations, after which it is well converged. As discussed in section 4.6, the small residual islands remaining in Figure 4-9 should be inconsequential.

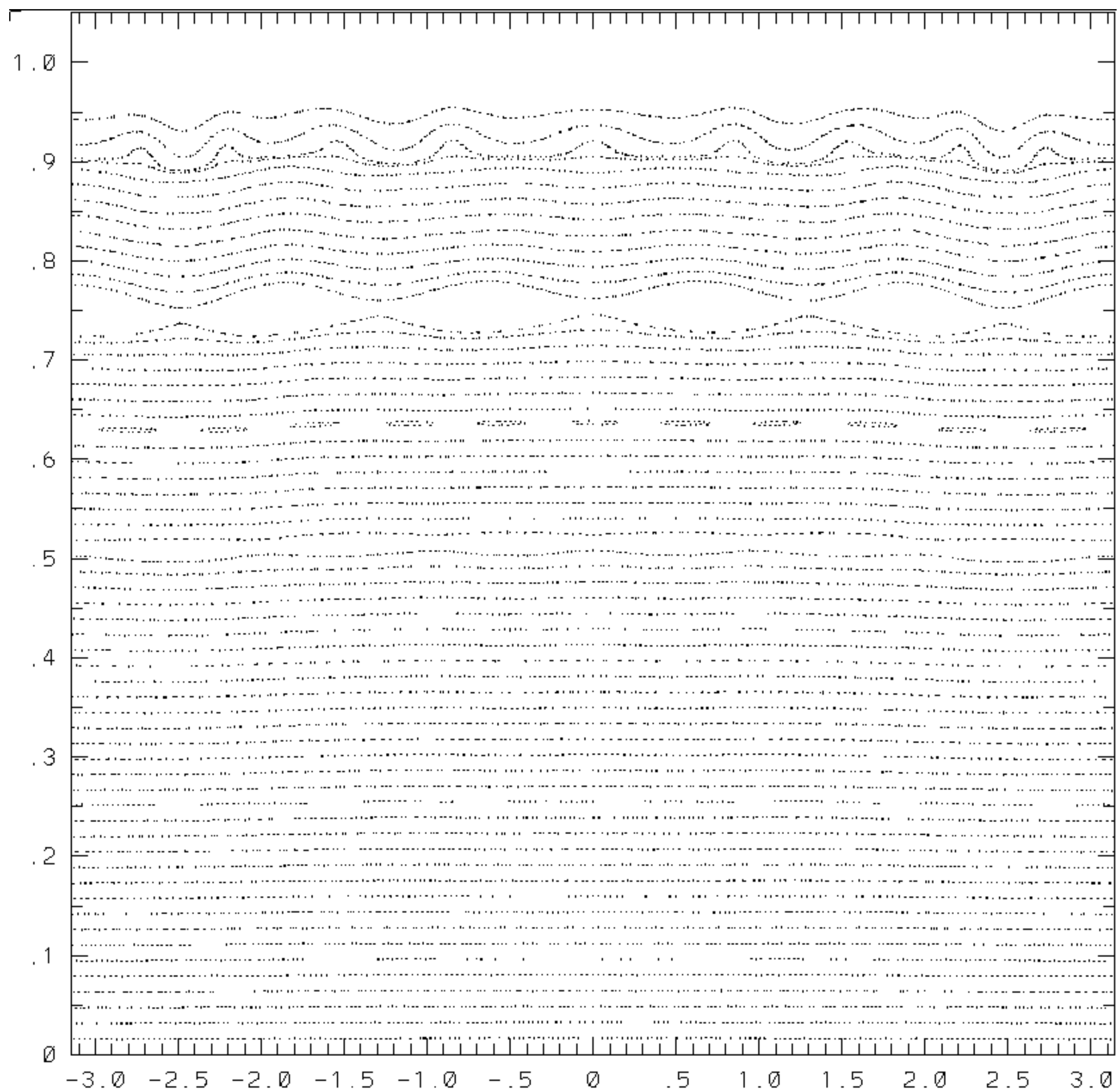

Figure 4-7. Poincare plot of free-boundary equilibrium with 0907 coil set after 20 iterations

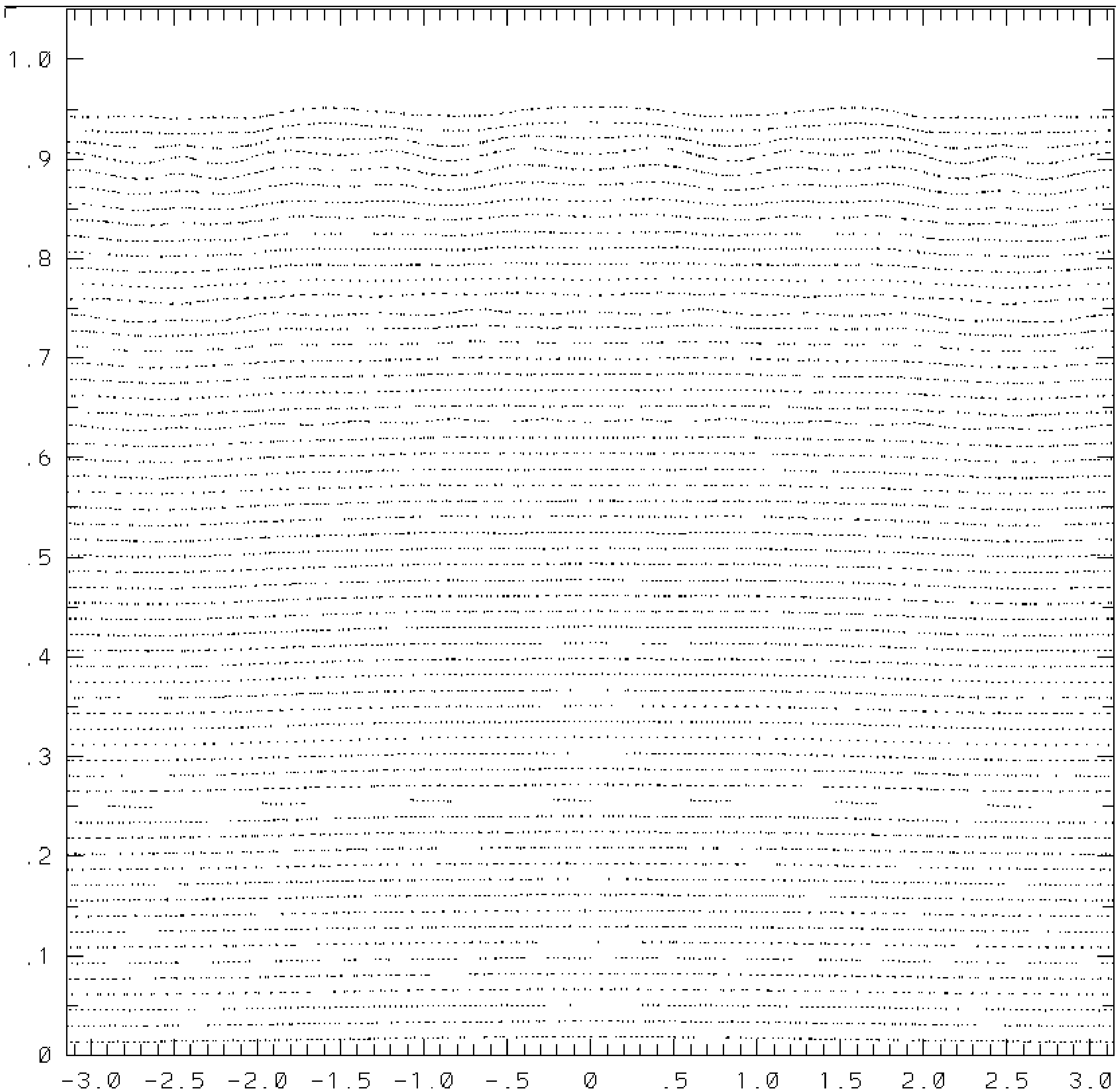

Figure 4-8. Poincare plot of free-boundary equilibrium with 0907 'healed' coil set after 20 iterations

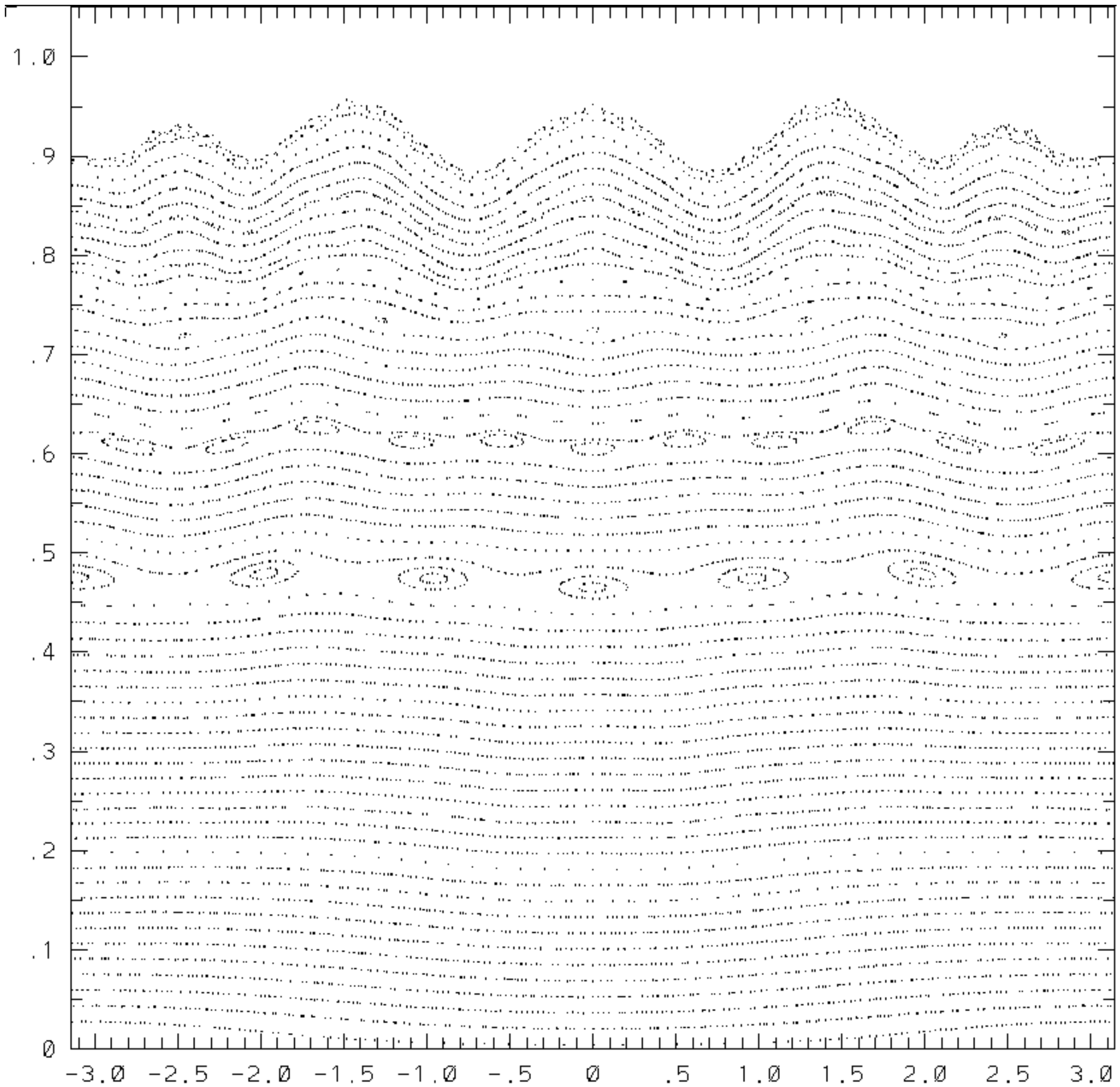

Figure 4-9. Poincare plot of converged free-boundary equilibrium with 0907 'healed' coil set

Figure 4-10 is a Poincare plot for the vacuum field produced by the 0907 "healed" coil set. The flux surfaces are regarded as quite adequate for startup.

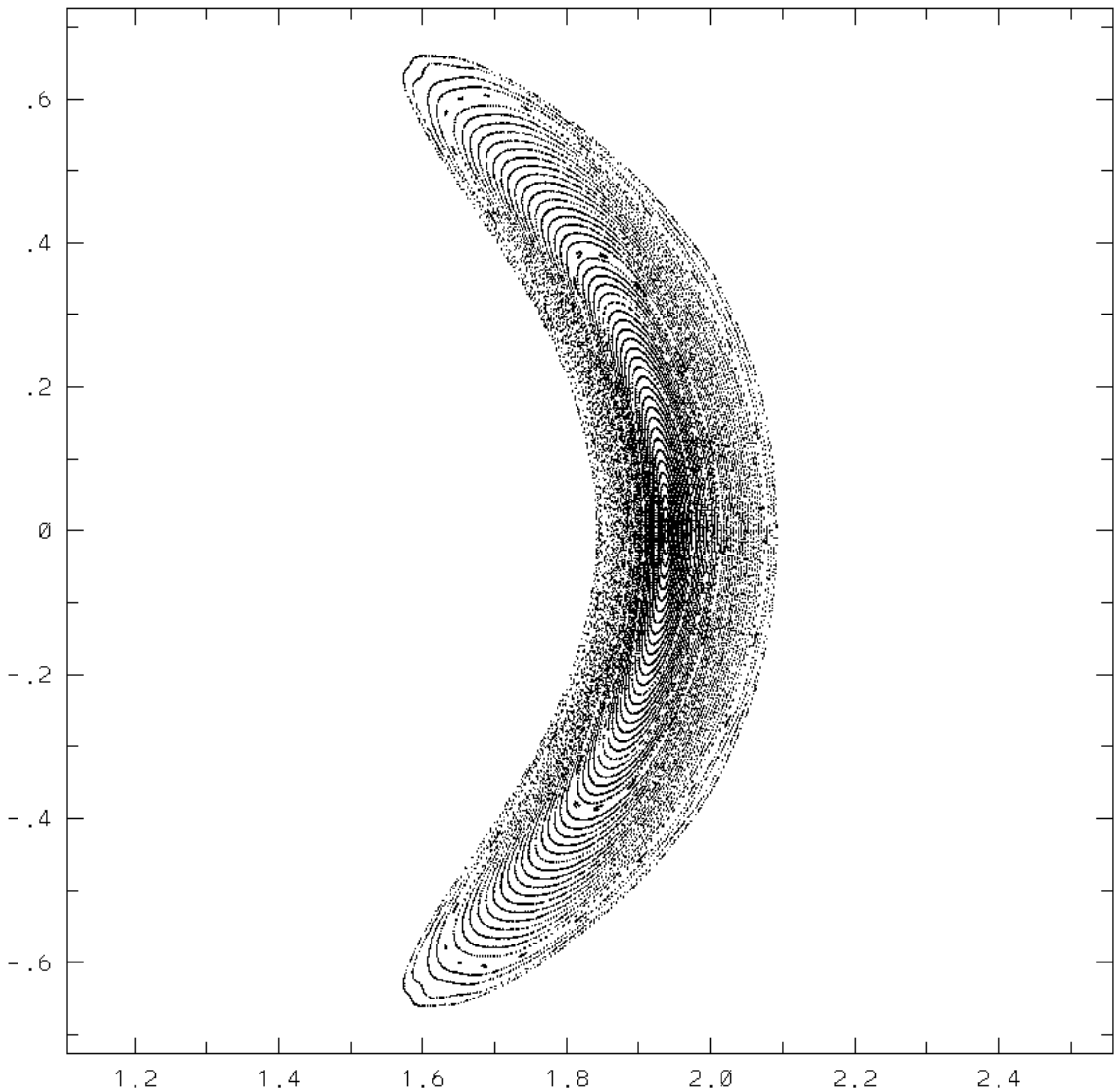

Figure 4-10. Poincare plot for the vacuum field produced by the "healed" 0907 coils

4.6 Neoclassical Healing of Magnetic Islands

4.6.1 Introduction

The purpose of this section is to estimate the effect of the neoclassical bootstrap current in reducing the width of magnetic islands produced by non-symmetric external field components in a quasi-axisymmetric stellarator such as NCSX. It has been recognized for some time [47] that the bootstrap current, which can destabilize "neoclassical tearing modes" in tokamaks, is stabilizing in a quasi-axisymmetric stellarator with outwardly increasing transform, i.e., positive

$d\iota/dr$. The magnitude of this effect depends on plasma collisionality, both through the dependence of the bootstrap current on the parameter ν_{*e} and through the role of finite parallel thermal conduction in limiting temperature flattening across the island.

In the present analysis, we employ the formalism of tokamak theory: the only stellarator-specific effect is an externally-imposed chain of magnetic islands with mode numbers corresponding to the dominant non-symmetric field "perturbation" in the NCSX configuration. For simplicity, we neglect two other effects, namely resonant Pfirsch-Schlueter currents and stabilizing resistive-interchange contributions, which are expected to be less important than the bootstrap current effect in the cases considered here.

4.6.2 Bootstrap Current Effect on Magnetic Islands

For cylindical tokamak geometry, including the bootstrap current density j_{bs}, the island width w in the weakly nonlinear regime [48,49,50] grows according to

$$(\mu_0/1.2\eta)\, dw/dt \;=\; \Delta' \;+\; 6.4\,(\mu_0 L_q/B_\theta)\, j_{bs}/w \tag{4-12}$$

where Δ' is the usual tearing-mode stability quantity and $L_q = q/q'$. The numerical coeffficient 6.4 arises from calculating the applicable Fourier component of the current perturbation caused by zeroing the bootstrap current inside the magnetic island, i.e., within the area bounded by the island separatrix [51]. Writing

$$j_{bs} \;=\; -\; C_{bs}\,(\varepsilon^{0.5}/B_\theta)\, dp_e/dr \tag{4-13}$$

where $\varepsilon = r/R$ and C_{bs} is a numerical coefficient of order unity which describes the dependences of the bootstrap current on the density and temperature profiles and on the collisionality parameter ν_{*e}, we obtain

$$(\mu_0/1.2\eta)\, dw/dt \;=\; \Delta' \;+\; 3.2\, C_{bs}\,\varepsilon^{0.5}\,\beta_{\theta e}\,(L_q/L_{pe})/w \tag{4-14}$$

where $L_{pe} = -\, p_e/p_e'$. For the tokamak ($q' > 0$), the bootstrap current term is positive and can overcome a negative Δ' to produce unstable neoclassical tearing modes. Comparisons with experimental data from tokamaks have generally suggested a numerical coefficient somewhat smaller than 3.2 in this equation; for example, analysis of neoclassical tearing modes in TFTR gave a coefficient of 2.6 [52]. For present purposes, however, we will retain the somewhat larger theoretical coefficient.

The case of an island produced by the vacuum magnetic fields in a quasi-axisymmetric stellarator may be considered analogous to the case of a tokamak in which an island is produced by superimposing an external helical magnetic perturbation that is resonant on a magnetic surface within the plasma. If such a perturbation were imposed dynamically, then the plasma would respond initially (i.e., within ideal-MHD theory) by forming a helical sheet current on the resonant surface. This sheet current would then decay resistively, producing a magnetic island; when the width of this island exceeds the very narrow resisitive layer of linear tearing-mode theory, it will be described by an appropriate generalization of the slow-growing tearing-mode theory. In the present context, we are interested in the case where the resonant helical perturbation has mode numbers m and n for which the tearing mode would be stable, i.e., for which Δ' is negative. (Accordingly, we henceforth write $\Delta' = -|\Delta'|$.)

It is straightforward to extend the theory of weakly nonlinear tearing modes [47] to include an externally driven island. Rather than introducing the external perturbation explicitly, it is more convenient simply to describe it in terms of the island width w_{ext} that would be produced after resistive relaxation of the currents on the scale-length of the island but <u>without</u> the bootstrap current effects. Adding the bootstrap current term as before, the island is found to evolve according to

$$(\mu_0 / 1.2\eta)\, dw/dt \;=\; -\, |\Delta'|\, (1 - w_{ext}^2/w^2) \;-\; 3.2\, C_{bs}\, \varepsilon^{0.5}\, \beta_{\theta e}\, (L_\iota / L_{pe})\, /w. \qquad (4\text{-}15)$$

Here we have also written $L_q = - L_\iota = - \iota'/\iota$, in order to use the quantity $\iota = 1/q$ that is more appropriate to a stellarator and to indicate that in this case the bootstrap term is stabilizing. For a high-m mode, to a very good approximation, we may use

$$\Delta' \;=\; -\, 2m / r\, . \qquad (4\text{-}16)$$

The "skin time" for resistive relaxation of w toward w_{ext} without bootstrap effects may now be estimated, namely $\tau_s = (\mu_0 / 1.2\eta)\, (2 w_{ext}\, r/m)$.

The bootstrap current term is seen to be inversely proportional to the island width w. This arises from the implicit assumption that density and temperature gradients are completely flattened across the magnetic island, thereby zeroing the bootstrap current within the island. Since electron thermal conduction is by far the fastest process of equilibration along field lines in high-temperature plasmas, bootstrap-current drive (or healing) of magnetic islands arises most effectively from the flattening of the electron temperature gradient, with flattening of the density gradient being less effective. Since in most practical cases (including the cases considered here) the electron temperature gradient provides the dominant contribution to the bootstrap current anyway, because the density profile is relatively flat, it is not unreasonable to employ the full bootstrap current in calculations such as these, but it should be recognized that this may give an over-estimate of the bootstrap-current effect on magnetic islands in some cases.

For very narrow islands, however, the path length along the helical field lines becomes very long, and finite (as distinct from effectively infinite) electron thermal conduction along the field lines will prevent the electron temperature from flattening fully across the island, thereby reducing even the most effective process of bootstrap-current island drive or healing. This effect is introduced into the theory [51] by modifying the bootstrap current term as follows:

$$1 / w \;\Rightarrow\; w / (w^2 + w_0^2) \qquad (4\text{-}17)$$

where we have defined a "critical island width" w_0, namely

$$w_0 \;=\; 5.1\, (\chi_\perp / \chi_{//})^{0.25}\, (R L_\iota / m\iota)^{0.5}. \qquad (4\text{-}18)$$

Here, $\chi_\perp$ and $\chi_{//}$ are the perpendicular and parallel thermal diffusivities, which control the degree to which the temperature is flattened across the island.

Setting $dw/dt = 0$, we then find the following relation to describe the actual island width w in terms of w_{ext} with bootstrap current effects included:

$$w_{ext}^2 / w^2 \quad = \quad 1 \; + \; 2 w_{bs}\, w / (w^2 + w_0^2), \qquad (4\text{-}19)$$

where we have introduced an island width characterizing the bootstrap current effect, namely

$$w_{bs} \quad = \quad 1.6\, C_{bs}\, \varepsilon^{0.5}\, \beta_{\theta e}\, (L_\iota / L_{pe}) \,/\, |\Delta'|. \qquad (4\text{-}20)$$

4.6.3 Assumed NCSX Parameters and Profiles

We have assumed the following parameters for the reference NCSX high-beta plasma:

$$\begin{aligned} &R \; = \; 1.4 \;\; \text{m} \\ &a \; = \; 0.32 \;\; \text{m} \;\; \text{(average)} \\ &\langle\beta\rangle \; = \; 4.2\,\% \\ &B_0 \; = \; 1.2 \; \text{T} \\ &\langle n_e \rangle \; = \; 5.8 \times 10^{19} \;\; \text{m}^{-3}. \end{aligned} \qquad (4\text{-}21)$$

We have used density and temperature profiles that correspond very closely to those resulting from transport calculations for NCSX [53], namely:

$$\begin{aligned} &n_e(r) \; = \; 7.8\, (1 - r^2 / a^2)^{0.35} \qquad (10^{19}\ \text{m}^{-3}) \\ &T_e(r) \; = \; 2.8\, (1 - r^2 / a^2)^{1.35} \qquad (\text{keV}) \\ &T_i(r) \; = \; 1.9\, (1 - r^2 / a^2)^{0.75} \qquad (\text{keV}). \end{aligned} \qquad (4\text{-}22)$$

The use of profiles that are parabolas raised to exponents α_n and α_T facilitates the calculation of the bootstrap current from the relevant theory. We have used an iota profile for the reference configuration for which the iota = 0.6 surface falls at r/a = 0.8 (see Section 3.1). The only other quantity needed from the iota profile is the local shear length, which for this profile is given by $L_\iota / a \; = \; 0.7$. It should be noted that the shear length L_ι may be longer for iota profiles that flatten or decrease toward the plasma edge.

4.6.4 Bootstrap Current Magnitude

To evaluate the bootstrap current term, i.e., the characteristic island width w_{bs}, it is essential to have a good estimate for the constant C_{bs}, since this can vary appreciably depending on profiles and on plasma collisionality. For present purposes, we have assumed the profiles given above and have employed the Hinton-Rosenbluth neoclassical theory for the "banana/plateau transition" [54], taking Z_{eff} = 1.5. We have allowed for T_i C T_e and have included both the ∇T_e and ∇T_i contributions to the bootstrap current. We obtain collisionality parameters (at the resonant surface r/a = 0.8) given by $\nu_{*e} = 0.49$ and $\nu_{*i} = 0.27$. For the profiles assumed and for these collisionality parameters, we than obtain $C_{bs} = 1.37$, which gives

$$w_{bs} / a = 0.28 . \tag{4-23}$$

In practical units, the value of C_{bs} found here corresponds to a bootstrap current density at the resonant surface r/a = 0.8 given by $j_{bs} = 60$ A/cm^2. This value is close to the peak of the bootstrap current density profile in this case, because of the strong local pressure gradient and modest collisionality in the region of the resonant surface. This value agrees reasonably well with other calculations of the bootstrap current density in the NCSX reference configuration (see Section 4.3).

For the case considered here, the major contribution to the bootstrap current arises from the electron temperature gradient. This is partly because the density gradient is relatively small and partly because the coefficient in the transport matrix that multiplies the electron temperature gradient falls off less strongly with collisionality than does the coefficient multiplying the density gradient. The ion temperature gradient is found to make only a small contribution to the bootstrap current.

4.6.5 Critical Island Width w_0

To evaluate the critical island width, w_0, we need estimates for the perpendicular and parallel electron thermal diffusivities. We obtain an estimate for $\chi_\perp$ from its relation to the energy confinement time τ_E. Using $\tau_E \approx a^2 / 4\chi_\perp$ together with the empirically projected energy confinement time in NCSX of 25 msec, we obtain an estimate $\chi_\perp \approx 1.0$ m^2/s.

Obtaining a good estimate for $\chi_{//}$ is trickier. We start by calculating the Spitzer parallel electron thermal diffusivity at the resonant surface; this gives $\chi_{//}^{Sp} \approx 2.9 \times 10^9$ m^2/s. If we use this value in the expression for w_o, we would obtain $w_0 / a \approx 0.02$. However, at low collisionality, the electron mean-free-path typically exceeds the parallel wavelength along the helical perturbations. In such cases, the use of Spitzer thermal diffusivity may lead to unphysically large parallel heat fluxes, and thermal diffusion must effectively be replaced by thermal convection, according to the relationship $\chi_{//} \nabla_{//}^2 T_e \Rightarrow v_{the} \nabla_{//} T_e$, where v_{the} is the electron thermal velocity. The quantity $\nabla_{//}$ is the inverse parallel wavelength along the helical perturbation, which depends on the island width w and can be estimated as $\nabla_{//} \approx (mw/R)\, d\iota/dr = m\iota w/RL_\iota$. Since $\chi_{//}$ appears only to the one-quarter power, it is not necessary to retain this explicit dependence on the island width w and so, for present purposes, we simply estimate it as $w/a \approx 0.05$. For the "effective" thermal diffusivity in this convection-limited regime, we obtain $\chi_{//}^{eff} \approx 7.2 \times 10^7$ m^2/s. If we use this value in the expression for w_0, we would obtain $w_0 / a \approx 0.05$ (validating our estimate used to obtain $\chi_{//}^{eff}$).

Without more theoretical work, it is not obvious which value to use for w_0. Almost certainly, the Spitzer thermal diffusivity will overestimate parallel heat transport at low collisionality. On the other hand, fast electrons may still be able to equilibrate the temperature at a rate faster than that given by convection at the thermal speed. Accordingly, it might be appropriate to take a range $w_0/a = 0.03 - 0.04$. In the calculation of the bootstrap island effect given below, we have simply chosen an intermediate value, namely:

$$w_0/a \approx 0.035. \tag{4-24}$$

It has been pointed out [55] that islands of width less than w_0 would not be expected to have a seriously deleterious effect on confinement because transport from one side of the island to the other along the direct path is already larger than transport along the path that follows the helical field lines. For the high-β NCSX reference case, this effect would apply only to islands with widths less than about 1 cm. However, the effect (unlike the bootstrap current) does not depend on the plasma beta-value and it increases strongly with higher collisionality, so it should apply particularly to low-temperature pre-heated plasmas. The Spitzer parallel thermal diffusivity scales as $T_e^{2.5}$, so a reduction in the temperature at the resonance surface to 100 eV (from 700 eV in the high-β plasma) would result in an increase in w_0/a to about 0.8. (Since parallel thermal convection scales much more weakly with electron temperature than thermal diffusivity, we find that the Spitzer diffusivity would be the operative process in this case.) This result suggests that in low-temperature ohmic plasmas in NCSX, islands at the iota = 0.6 surface as large as about 2.5 cm may not have a seriously detrimental effect on confinement.

4.6.6 Results for NCSX Reference Case

The actual island widths w for a range of possible "externally-produced" island widths w_{ext} are given in Table 4-1. For this calculation, we have taken $w_{bs}/a = 0.28$ and a value $w_0/a = 0.035$ (see the preceeding discussions). For external islands with widths in the range 2 - 6 cm (i.e., 6 - 18 % of the minor radius), the bootstrap current reduces the island width by almost a factor-of-three.

w_{ext} (cm)	w (cm)
1.0	0.41
2.0	0.70
3.0	1.00
4.0	1.34
5.0	1.73
6.0	2.19

Table 4-1. Neoclassical bootstrap-healed island widths w for various externally-generated island widths w_{ext} at the iota = 0.6 surface in the reference NCSX high-□ configuration

4.6.7 Conclusions Concerning Neoclassical Healing

The depletion of bootstrap current within the island causes a substantial reduction in the width of the magnetic island caused by the dominant non-symmetric field "perturbation" in NCSX. Specifically, for the 4%-beta reference NCSX configuration, the bootstrap current should reduce the width of the m/n = 5/3 islands at the iota = 0.6 surface by almost a factor-of-three.

The bootstrap current in NCSX is sufficient for this purpose despite the relatively high collisionality of the plasma, which puts the island region (where $\nu_{*e} \approx 0.5$) in the "banana-plateau transition", rather than "pure banana", regime of neoclassical transport. For the cases considered, the main contribution to the bootstrap current comes from the electron temperature gradient, rather than the density gradient. The key element in ensuring sufficient bootstrap current is a relatively high value of the local $\beta_{\theta e}$ at the resonant surface together with a relatively steep local electron pressure gradient.

4.7 Conclusions

The VMEC code has been used for the routine calculation of three-dimensional equilibria for stability and transport studies. The PIES code has been used to calculate three-dimensional equilibria with islands and stochastic regions. Critical improvements have been made to both codes during the course of the NCSX design study. PIES calculations have found significant differences in the flux surface quality of candidate NCSX configurations, with the reference configuration, LI383, having particularly good flux surfaces. Judicious adjustment of the resonant field components has been used to heal the residual islands in this configuration. A set of trim coils provides the flexibility to generate a range of configurations with good flux surfaces. Neoclassical effects are estimated to provide additional suppression of magnetic islands.

References

[1] HIRSHMAN, S.P., Lee, D.K., Comput. Phys. Comm. **39** (1986) 143.

[2] HIRSHMAN, S.P., Van Rij, W.I. and MERKEL, P., Comp. Phys. Commun. **43** (1986) 143.

[3] KESSEL, C. E. Nuc. Fus., **34**, (1994) 1221.

[4] HIRSHMAN, S. Phys. Fluids, **31**, (1988) 3150.

[5] HARRIS, G. R. EUR-CEA-FC-1436, (1991).

[6] WHITE, R. B. AND CHANCE, M. S. Phys. Fluids **27**, (1984) 2455.

[7] WHITE, R. B. Phys. Fluids B **2**, (1990) 845.

[8] SPONG, D. http://www.pppl.gov/ncsx/Meetings/Physics_Mtgs/1999/June/june.html.

[9] REIMAN, A., and Greenside, H. S., Comput. Phys. Commun. **43** (1986) 157.

[10] REIMAN, A., and Greenside, H. S., J. Comput. Phys. **75** (1988) 423.

[11] GREENSIDE, H., REIMAN, A., and SALAS, A., J. Comput. Phys. **81** (1989) 102.

[12] Reiman, A. and Pomphrey, N. J. Comput. Phys. **941** (1991) 225.

[13] MONTICELLO, D. A., MERKEL, P., JOHNSON, J. L., and REIMAN, A. H., Proceedings of Tenth International Conference on Stellarators, Madrid (1995).

[14] DELUCIA, J., JARDIN, S. C., and TODD, A. M. M., J. Comput. Phys. **37** (1980) 183.

[15] CHODURA, R. and SCHLUTER, A., J. Comput. Phys. **41** (1981) 68.

[16] JOHNSON, J. L., MONTICELLO, D. A., REIMAN, A. H., et al., Comp. Phys. Commun. **77** (1993) 1.

[18] MERKEL, P., JOHNSON, J. L., MONTICELLO, D. A., et al., Proceedings of the Fourteenth International Conference on Plasma Physics and Controlled Nuclear Fusion Research paper IAEA-CN-60 | D-P-II-10 (1994).

[19] REIMAN, A. H. and GREENSIDE, H. S., J. Comput. Phys. **87** (1990) 349.

[20] JOHNSON, J. L., MONTICELLO, D. A., and REIMAN, A. H., Proceedings of the 15th International Conference on the Numerical Simulations of Plasmas (1994).

[21] A. H. Reiman and H. S. Greenside, J. Comput. Phys. **87** (1990) 349.

[22] A. H. Reiman and D. Monticello, Phys Fluids B **3** (August 1991) 2230.

[23] A. H. Reiman and D. Monticello, Nucl. Fusion **32** (1992) 1341.

[24] R. J. Goldston, et al Fusion Technol. **21** (May 1992) 1039.

[25] A. Lopez Fraguas, A. Salas, A. H. Reiman, D. A. Monticello, and J. L. Johnson, in Proceedings of the Ninth Kiev International Conference on Plasma Theory, July, 1992, p. I-577.

[26] S. C. Jardin, et al in Proceedings of the Fourteenth International Conference on Plasma Physics and Controlled Nuclear Fusion Research, (Wurzburg, Germany, September 1992) (International Atomic Energy Agency, Vienna, Austria), Paper IAEA-CN-56/D-4-13.

[27] D. A. Monticello, A. H. Reiman, and C. Y. Wang, in Proceedings of the Ninth International Workshop on Stellarators, (International Atomic Energy Agency, Vienna, Austria, 1993), p. 114.

[28] A. Salas, A. Lopez Fraguas, A. H. Reiman, D. A. Monticello, and J. L. Johnson, in Proceedings of the Ninth International Workshop on Stellarators, (International Atomic Energy Agency, Vienna, Austria, 1993) p.127.

[29] P. Merkel, J. L. Johnson, D. A. Monticello, and A. H. Reiman, in Proceedings of the Ninth International Workshop on Stellarators, (International Atomic Energy Agency, Vienna, Austria, 1993), p. 133.

[30] J. L. Johnson, D. A. Monticello, A. H. Reiman, and C. Wang, in Proceedings of the Ninth International Workshop on Stellarators, (International Atomic Energy Agency, Vienna, Austria, 1993), p. 121.
[31] J. L. Johnson, D. A. Monticello, A. H. Reiman, A. Salas, A. L. Fraguas and S. P. Hirshman, Comp. Phys. Commun. **77** (September 1993) 1.
[32] J. A. Schmidt, et al, J. Fus. Energy **12** (1993) 221.
[33] J Nuhrenberg, et al, Plasma Physics and Controlled Fusion, **35** Supplement (December 1993) B115.
[34] J. Manickam, et al, Phys. Plasmas **1** (1994) 1601.
[35] P. Merkel, J. L. Johnson, D. A. Monticello, A. H. Reiman, A. Salas, and A. L. Fraguas, Proceedings of the Fifteenth International Conference on Plasma Physics and Controlled Nuclear Fusion Research, (International Atomic Energy Agency, Vienna, Austria, September 1994).
[36] D. A. Monticello, J. L. Johnson, A.H.Reiman, and P.Merkel, in Proceedings of the Tenth International Workshop on Stellarators, EUR-CIEMAT **30** (1995) p. 45.
[37] R. J. LaHaye et al, in Proceedings of the Sixteenth IAEA Fusion Energy Conference, (International Atomic Energy Agency, Vienna, Austria, 1996) Paper F1-CN-64/AP1-21.
[38] A. Reiman, L.P. Ku, D. Monticello, C. Nuehrenberg, and W. Cooper, Plasma Physics Reports **23** (1997) 472.
[39] S. Arndt, P. Merkel, D. A. Monticello and A. H. Reiman, Phys. Plasmas **6** (1999) 1246.
[40] A. Reiman, et al, Phys. Plasmas **8** (2001).
[41] H. Gardner and B. Blackwell, Nucl. Fusion **33** (1993).
[42] C. C. Hegna and J. D. Callen, Phys. Plasmas **1** (1994) 3135.
[43] S.R. Hudson and R.L. Dewar. Analysis of perturbed magnetic fields via construction of nearby integrable field. *Phys.Plasmas*, **6(5)** (1999) 1532.
[44] A.J. Lichtenberg and M.A. Lieberman. *Regular and Chaotic Dynamics, 2nd ed.* Springer-Verlag, New York, 1992.
[45] J.D. Meiss. Symplectic maps, variational principles & transport. *Reviews of Modern Physics*, **64(3)** (1992) 362.
[46] W. H. Press, B. P. Flannery, S. A. Teukolsky, and W. T. Vetterling. *Numerical Recipes in Fortran 77 : The art of scientific computing*. Cambridge University Press, Cambridge, U.K.
[47] C. C. Hegna and J. D. Callen, Phys. Plasmas **1** (1994) 3135.
[48] P. H. Rutherford, Phys. Fluids **16** (1973) 1903.
[49] J. D. Callen, et al., in "Plasma Physics and Controlled Nuclear Fusion Research", Kyoto (IAEA, Vienna, 1987). **2**, p. 157.
[50] C. C. Hegna, et al., Plasma Phys. Controlled Fusion **35** (1993) 987.
[51] R. Fitzpatrick, Phys. Plasmas **2** (1995) 825.
[52] Z. Chang, et al., Phys. Rev. Lett. **74** (1995) 4663.
[53] D. R. Mikkelson, NCSX Project Meeting (January, 2001); see also Section 8.
[54] F. L. Hinton and M. N. Rosenbluth, Phys. Fluids **16** (1973) 836.
[55] R. J. Goldston, private communication (June, 2000).

Chapter 5 -- Ideal Magnetohydrodynamics Stability

5.1 Overview

In this chapter, we consider ideal stability of various MHD modes ranging from low mode number (vertical modes, external kink modes) to infinite n (ballooning modes, Mercier modes). We will discuss general MHD stability properties of compact QAS with finite plasma current and various stabilization mechanisms. We will present details of stability results for the NCSX reference configuration. Much of the results have already been published [1,2,3,4,5,6].

In our design study, we have used the most advanced 3D MHD stability codes available, such as Terpsichore-VVBAL [7] and COBRA [8,9] for infinite-n ballooning modes, Terpsichore [10] and CAS3D [11] for global moderate-n external kink modes. These codes are essential for self-consistent stability prediction of beta limits in stellarators. Extensive work has been done to benchmark these stability codes.

The NCSX configuration is closely related to advanced tokamaks with reversed shear. In fact, the initial design of NCSX started from an optimized reversed shear tokamak (ARIES design) by adding appropriate 3D shaping which generates external rotational transform while maintaining quasisymmetry. Due to quasi-axisymmetry, the bootstrap current in NCSX is similar to that in an equivalent tokamak. Therefore, like in a tokamak, both the plasma current and pressure drive MHD instabilities in the NCSX [3]. However, the MHD stability in the NCSX differs significantly from an advanced tokamak due to stabilizing influences of 3D shaping. As a result, the external kink modes are much more stable as compared to an advanced tokamak.

3D shaping of a QAS can influence the MHD stability in several ways as compared to an advanced tokamak. 3D shaping generates external rotational transform. This is stabilizing for both vertical and external kink modes because a smaller plasma current is present to drive instability at fixed edge iota. 3D shaping also modifies iota profile that affects MHD stability strongly. 3D shaping also strongly affects local magnetic shear and curvature that are important to MHD stability. Our optimization experience shows that 3D shaping can be used effectively to enhance MHD stability of a compact QAS. The NCSX reference configuration (LI383) is a product of such an optimization via 3D shaping.

This chapter is organized as follows. Section 5.2 describes the main stability codes used in this work and their benchmarks. Secdtion5.3 discusses general stability properties of compact QAS. Secyion 5.4 presents detailed stability analysis of the NCSX configurations for external kink modes and vertical modes as well as ballooning modes. Section 5.5 discusses the effects of wall on external kink stability. Section 5.6 discusses the Toroidal Alfven Eigenmodes in the NCSX. Finally, a summary is given in Section 5.7 .

5.2 Numerical Codes and Benchmarks

The NCSX design uses the most advanced codes for its stability calculations. Among them, the ballooning stability is calculated using two codes: Terpsichore-VVBAL [7] and Cobra [8,9]. The global kink and vertical mode stability is calculated using both Terpsichore [10] and CAS3D [11]. All these stability codes are based on numerical equilibria as computed by the 3D code VMEC [12].

- 5.2.1 Equilibrium code VMEC

The 3D equilibrium code VMEC [12] solves for 3D equilibria by minimizing plasma potential energy. A key assumption of the code is that the flux surfaces are closed. As a result, magnetic islands are not allowed. Our stability calculations are also based on this assumption. We expect that the VMEC solutions are good approximations of real equilibria when magnetic islands are small and the stability results should be reliable especially for global kink modes that are largely determined by global equilibrium profiles.

- 5.2.2 Ballooning codes Terpsichore and Cobra

The Terpsichore-VVBAL ballooning code [7] solves the standard ballooning mode equation in Boozer coordinates [13]:

$$\rho\gamma^2 \left(\mathbf{k}_\perp{}^2/B^2\right) \Phi - \mathbf{B} \bullet \nabla\left(\mathbf{k}_\perp{}^2/B^2\right)\mathbf{B} \bullet \nabla\Phi - p'/B^2 \left(\mathbf{k}_\perp \times \mathbf{B}\right) \bullet \kappa\Phi = 0 \qquad (1)$$

where $\mathbf{k}_\perp = \nabla\phi - q(\psi)\nabla\theta - q'(\theta - \theta_k)\nabla\psi$ with θ_k being the radial wave number. In Eq. (1), the first term is from the kinetic energy, the second term corresponds to the field line bending energy, and the last term corresponds to the destabilizing drive due to bad curvature and pressure gradient. A major part of the code is mapping from VMEC coordinates to straight field line Boozer coordinates. The ballooning equation is solved using a shooting method and the eigenvalue is a function of s, θ_k, and $\alpha = \phi - q\theta$ where α is the field line variable. Note that unlike in tokamaks, the local ballooning eigenvalues also depend on α in stellarators due to 3D geometry. The most unstable eigenvalue in the space of (s,θ_k,α) determines the beta limit. Instead of solving for eigenvalue ω^2 in Eq. (1), the following marginal equation is solved with λ as an eigenvalue:

$$\mathbf{B} \bullet \nabla \left(\mathbf{k}_\perp{}^2/B^2\right) \mathbf{B} \bullet \nabla\Phi + (1 - \lambda) \left(p' / B^2\right) \left(\mathbf{k}_\perp \times \mathbf{B}\right) \bullet \kappa\Phi = 0 \qquad (2)$$

where $(1-\lambda)$ is a multiplier to the destabilizing curvature term. Note that $\lambda > 0$ for instability. This method is advantageous over solving for ω^2 because the eigenvalue λ is well defined for both unstable and stable cases. In contrast, the eigenvalue γ^2 is a continuous spectrum for stable cases in Eq. (1) and is not well defined numerically.

The ballooning code COBRA [8] solves the ideal ballooning equation for the growth rate using finite element method. Eq. (1) then becomes a matrix equation. The computation can be done in an extremely efficient and accurate way by taking advantage of the Stürm-Lioville character of the ballooning equation. This property allows to estimate the growth rate to 4th order on the mesh step size along the magnetic field line by variationally refining a previous 2nd order estimated obtained from a standard matrix method. Fast evaluation is made possible by coupling this evaluation process to a Richardson's extrapolation scheme, that will extrapolate to zero mesh step size from a few previous evaluations of the growth rates computed on very coarse (and therefore easy to evaluate) meshes. Important speed enhancements (of hundreds of times) relative to standard codes can be achieved in this way [8]. Recently, a VMEC-based version of COBRA [9] has been developed as a result of several convergence problems appearing on the Boozer-coordinate-based COBRA (namely, the growth rate would sometimes change when the number of Boozer modes included in the equilibrium mapping from the VMEC equilibrium solution, turning unstable previously ascertained stable cases). In this latest version, the magnetic field line must be numerically followed at the same time that the ballooning equation is solved in a way that does not interfere with the Richardson's scheme. This has been achieved by locating the magnetic field line at each mesh point via a Newton-Raphson scheme [9].

We have used both Terpsichore-VVBAL and Cobra in our configuration design. The Terpsichore ballooning code was exclusively used in the past until Cobra became available recently. Since Cobra is a much faster code, we have used it extensively in the search of plasma configurations that are stable to ballooning modes at high beta.

To validate these two ballooning codes, we have made benchmark comparisons between them. The first case of comparison is a QHS configuration that is unstable to ballooning modes at β as low as 2%. At this beta, the configuration is Mercier stable so that the ballooning stability results are not sensitive to the length of integration. Figure 5-1 on the left shows the comparison of the eigenvalues as a function of the normalized toroidal flux (Note that the normalization for eigenvalues of the two codes are different). Good agreement of the unstable region is evident in the figure. It should be noted here that The definitions of the eigenvalue are different in the two codes so that the absolute size of the eigenvalue does not agree. We have also compared the results of the two codes for the QAS configuration C82, which was the reference configuration for NCSX a year ago. A comparison of a 4% beta case is shown in Fig. 5-1 on the right. Again, the region of ballooning instability matches well in two codes. The fluctuation in eigenvalue in the stable region calculated by Terpsichore is due to the resonances and the broadening of the eigenfunction which requires even larger boxes of integration to obtain better solutions. The important conclusion, however, is that the unstable region agrees well.

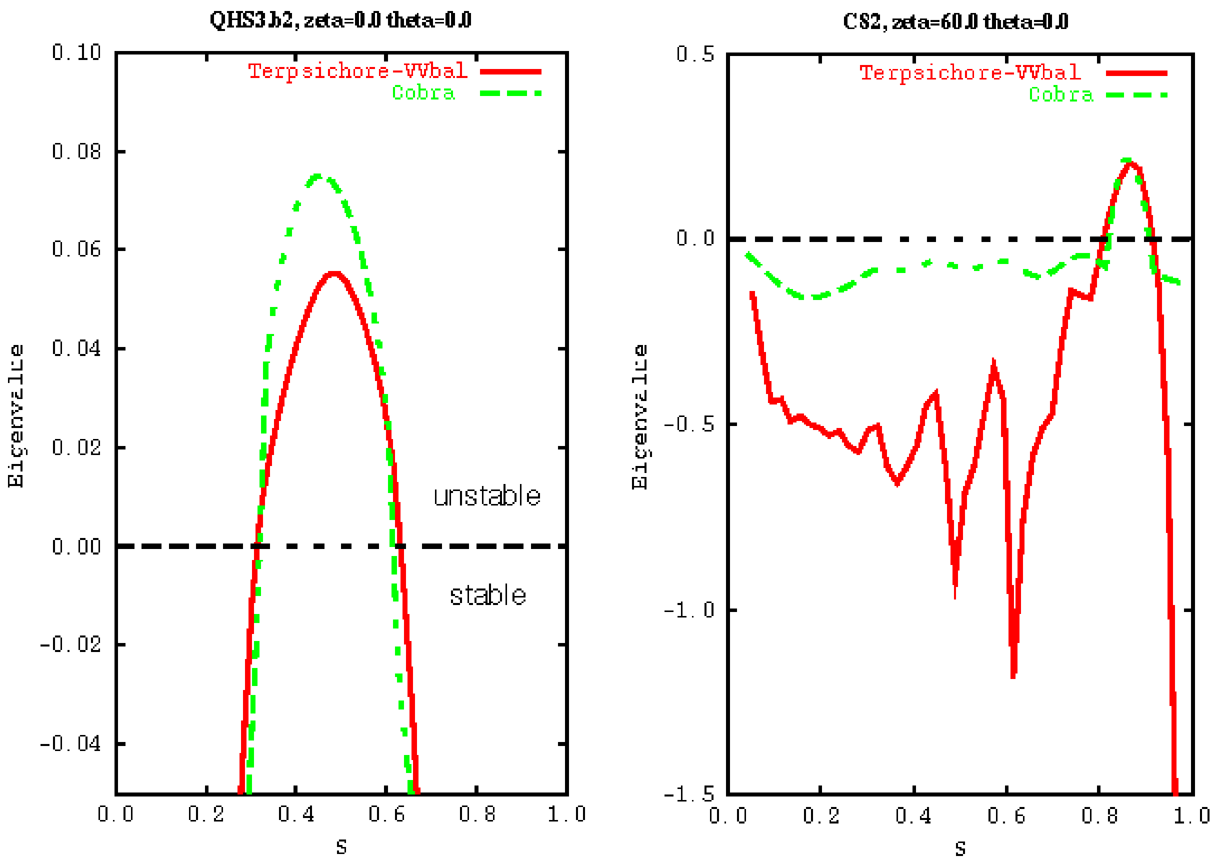

Figure 5-1: Ballooning eigenvalues obtained with Terpsichore (red) and COBRA (green) as function of normalized toroidal flux S for a QHS stellarator (left) and a QAS stellarator (right)

- 5.2.3 Global 3D codes Terpsichore and CAS3D

The three dimensional ideal MHD stability code Terpsichore [10] is used to calculate the stability of global MHD modes. The code determines the eigenvalues of the ideal MHD equations by minimizing the plasma potential energy as defined in the energy principle [14]:

$$\omega^2\ \delta W_k = \delta W_p + \delta W_{vac} \tag{3}$$

where $-\omega^2\ \delta W_k$ is the kinetic energy, δW_{vac} is the magnetic energy in the vacuum region between plasma and conducting wall, and δW_p is the plasma potential energy written as

$$\delta W_p = 1/2 \int d^3x\ \{\ \delta \mathbf{B}_{\perp}{}^2 + [\delta \mathbf{B}_{||} - \mathbf{B}\ (\xi \bullet \nabla\ p/B^2)]^2$$

$$+\ \Gamma(\nabla \bullet \xi)^2 + \mathbf{j}_{||} \bullet \xi \times \delta\mathbf{B} - 2\ \xi \bullet \nabla p\ \xi \bullet \kappa\} \tag{4}$$

where $\delta\mathbf{B}$ is the perturbed magnetic field, ξ is the plasma displacement vector, Γ is the coefficient of specific heat, $\mathbf{j}_{||}$ is the parallel equilibrium current along the field line, and κ is the magnetic curvature. The displacement vector is written as

$$\xi = \sqrt{g}\ \xi^s\ \nabla\theta \times \nabla\phi + \eta(\mathbf{B} \times \nabla s/B^2) \tag{5}$$

where s, θ, and ϕ are radial, poloidal and toroidal variables in Boozer coordinates. Note that $\delta\mathbf{B} = \nabla\times(\xi\times\mathbf{B})$ in ideal MHD. In Eq. (4), the first and second terms in the integrand are the stabilizing field line bending energy and the magnetic field compression energy respectively, the third term is the fluid compression energy, the fourth term is destabilizing due to parallel current and is responsible for kink instabilities. Lastly, the fifth term is usually destabilizing due to unfavorable curvature and pressure gradient.

It should be pointed out that for most of our results an artificial kinetic energy is used for simplicity. This artificial kinetic energy is given by $\delta W_k = (1/2)\int d^3x\ [(\xi^s)^2 + (\eta)^2]$. As a result, the plasma displacement is incompressible since the parallel component only appears in the fluid compression term. Although the calculated eigenvalue does not correspond to the physical growth rate, the marginal stability boundary remains the same. Recently, a new version of Terpsichore becomes available which uses physical kinetic energy and can calculate physical growth rate at $\Gamma = 0$.

The Terpsichore code uses Fourier decomposition in poloidal and toroidal angles and a finite element method for radial discretization The radial and surface component of the plasma displacement vector are represented by sums of Fourier series:

$$\xi^s(s,\theta,\phi) = \sum \xi_l(s) \sin(m_l\,\theta - n_l\,\phi + \Delta)$$

$$\eta(s,\theta,\phi) = \sum \eta_l(s) \cos(m_l\,\theta - n_l\,\phi + \Delta) \qquad (6)$$

where Δ is a phase factor and the subscript l is an index for each pair of poloidal and toroidal mode numbers (m,n). The radial dependence is represented by piece-wise linear elements for ξ_l and piece-wise constant elements for η. After minimization of the plasma potential energy, the problem reduces to an eigenvalue problem of a linear matrix equation. The eigenvalue system is solved by an inverse iteration method that can converge towards the most unstable eigenvalue. An accurate eigenvalue requires sufficient radial grid points and poloidal/toroidal modes for both the equilibrium and the perturbation.

The Terpsichore code uses a pseudo-plasma method for evaluation of the magnetic perturbation in the vacuum. In this method, the perturbed magnetic field in vacuum is written the same way as in plasma: $\delta B = \nabla\times(\xi\times\mathbf{B_v})$, but here B_v is a shearless pseudo-magnetic field. It can be shown that this representation is general as long as B_v is shearless. In this way, the vacuum region can be treated as a pressureless and currentless plasma and can be solved in the same way as in plasma.

The CAS3D [11] code is similar to Terpsichore in many aspects. It uses the same representations of the equilibrium and the perturbation as in Terpsichore and solves the same type of matrix equation for unstable eigenvalue. However, it differs significantly from Terpsichore in the treatment of vacuum. The CAS3D uses a Green function method in calculating the vacuum magnetic energy. Thus it can compute free boundary stability without a conducting wall. In contrast, a conducting wall is necessary present in Terpsichore model because it uses a finite grid for the vacuum. In practice, the conducting wall can be put far away so that the effects of the wall is minimal on the stability of external kink modes and the associated beta limits.

The Terpsichore code has been used for most of MHD calculations in the NCSX project for the sake of code speed. The CAS3D is used to benchmark the Terpsichore results and for some of the stability analysis.

The MHD calculations in stellarators differ from axisymmetric tokamaks in several ways. A key difference lies in Fourier mode selection for the perturbation. Unlike in tokamaks, different toroidal modes are coupled together due to 3D geometry. For stellarators with field period N_p, Fourier harmonics with toroidal mode number n are coupled to $n+kN_p$, where k is an arbitrary integer. There are $N_p/2+1$ families of modes for even N_p and $(N_p-1)/2+1$ families for odd N_p. For example, there are two families (N = 0, N = 1) for both $N_p = 2$ and $N_p = 3$ and there are three families (N = 0, N = 1 and N = 2) for $N_p = 4$. Within one family of modes, there are infinite number of eigenmodes with different mode spectra. Typically, the external kink modes have low toroidal mode numbers for the dominating harmonics. The vertical mode in stellarators belongs to the N = 0 family which preserves the stellarator periodicity. However, an eigenmode of the N = 0 family can have characteristics of a kink or ballooning mode when the dominating toroidal mode number is not zero.

A subtle issue of 3D stability calculations is the phase dependence. In tokamaks, the stability is independent of the phase due to axisymmetry. This is not so for the N = 0 family in stellarators. The stability also depends on the phase for the $N = N_p/2$ family when N_p is even. Assuming stellarator symmetry for the underlying equilibrium, only two values of the phase, $\Delta = 0$ (sin phase) and $\Delta = \pi/2$ (cos phase), are meaningful because the modes with sin phase are decoupled from the modes with cos phase. The phase should be zero for the N = 0 vertical mode.

The Terpsichore code has been benchmarked extensively. Earlier it was shown [15] that the Terpsichore's stability results agree well with 2D stability codes for growth rates of fixed boundary MHD modes in 2D analytic Solov'ev equilibria. In the present work, we have benchmarked Terpsichore against the 2D stability code PEST[16] and the 3D code CAS3D [11] for external kink modes for an optimized reversed shear tokamak equilibrium from the ARIES studies [17]. The calculated beta limit of the n = 1 external kink mode using Terpsichore is 2.34%, which agrees well with the PEST result of 2.4% and the CAS3D result of 2.3% [20]. We have also benchmarked the code for the n = 0 vertical mode in a large aspect ratio tokamak.

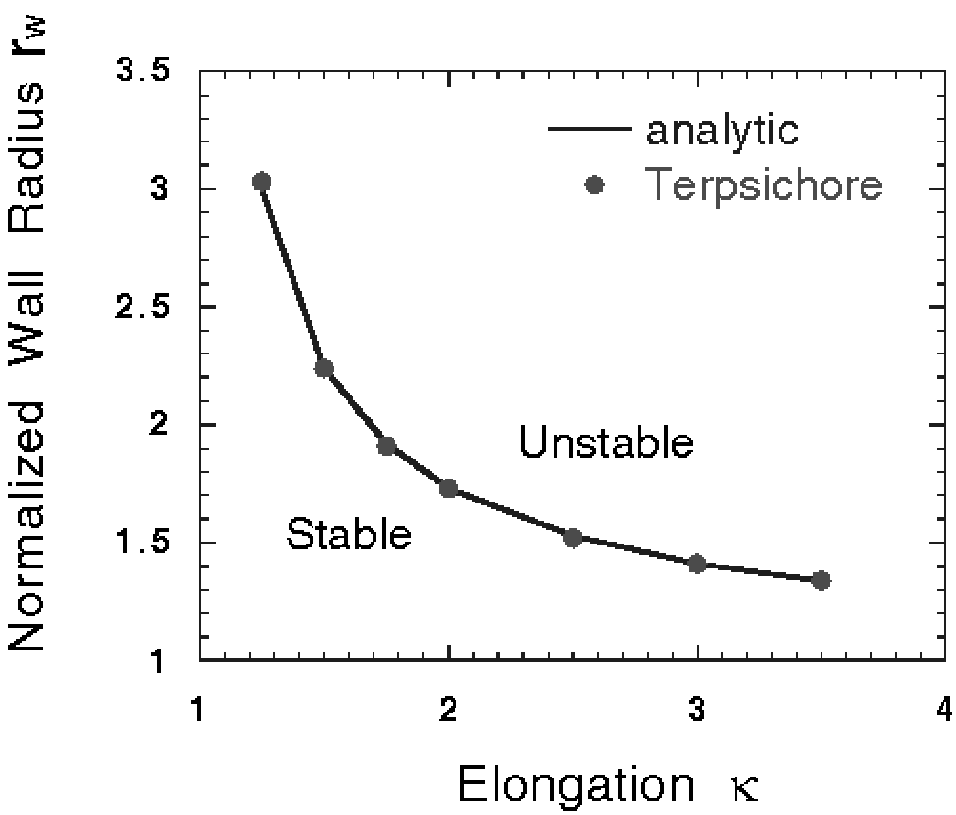

Figure 5-2: The critical normalized wall radius versus elongation for a elliptical plasma

Figure 5-2 plots the critical wall radius as function of ellipticity for the stability of the n = 0 vertical mode in an elliptical plasma with constant current density profile and zero beta. The Terpsichore results (shown in dots) agree well with the analytic stability criterion [18] (solid line) give by

$$r_w = \sqrt{\frac{\kappa+1}{\kappa-1}} \tag{7}$$

where the normalized wall radius is defined by $r_w = (a' + b')/(a+b)$ with a and b (a' and b') being the radius of the elliptical plasma (a confoncal wall) along the horizontal and vertical direction respectively. Here, $\kappa = b/a$. Most recently, we have compared stability results of Terpsichore with those of CAS3D for a real 3D stellarator equilibrium with finite beta and current [19]. Figure 5-3 shows the growth rates of the N = 1 external kink mode obtained by Terpsichore and CAS3D as function of plasma beta for the previous NCSX configuration C82. The results are obtained with 108 pairs of (m,n) for the kink mode and are converged in radial grid points and equilibrium Fourier modes. The CAS3D results are obtained without a conducting wall. The Terpsichore results are obtained with a conducting wall 2.5a away from the plasma edge so that the effects of wall on the beta limit should be negligible. We can then conclude that the Terpsichore's stability thresholds agree fairly well with those of CAS3D, at least for C82.

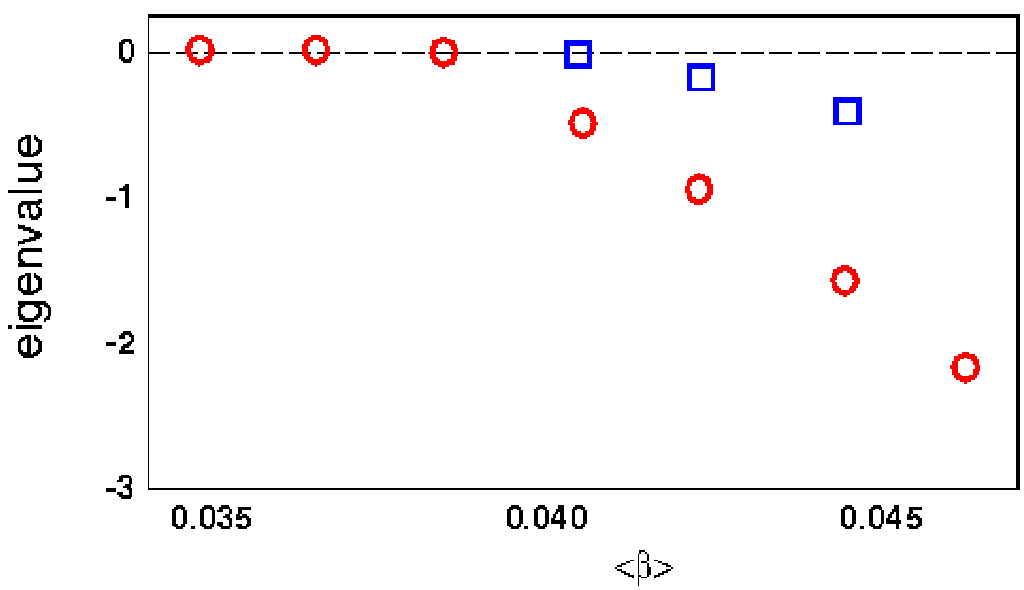

Figure 5-3: The N = 1 external kink eigenvalues as function of plasma beta obtained with CAS3D (open circles) and Terpsichore (open squares)

5.3 Kink and Vertical Mode Stability

Here we present general features of kink and vertical stability in a current-carrying finite beta compact QAS [4,6] and specific results for NCSX reference configuration. As described in the previous sections, the NCSX design point was initially obtained by shaping a reversed shear advanced tokamak (ARIES design) three dimensionally. The 3D shaping generates external rotational transform while maintaining quasi-axisymmetry. As a result, the iota profile is monotonically increasing until near the edge of plasma (or reversed shear for most of the minor radius in tokamak sense). We will show that stability of external kink modes and the vertical mode can be improved over those of advanced tokamaks by external rotational transform and pure 3D geometric effects.

First we consider the effects of external rotational transform on kink and vertical stability. Compared to advanced tokamaks, QAS configurations have lower plasma current because the external rotational transform replaces part of current-generated transform in tokamaks (at fixed edge iota or q). As a result, the external kink and vertical mode stability is improved in QAS due to lower current. We find that find that the vertical mode (of n = 0 family) can be much more stable in QAS devices than in tokamaks [4]. The QAS configuration C82 is calculated to be robustly stable to the vertical mode at a high averaged elongation ($\kappa \sim 2$).

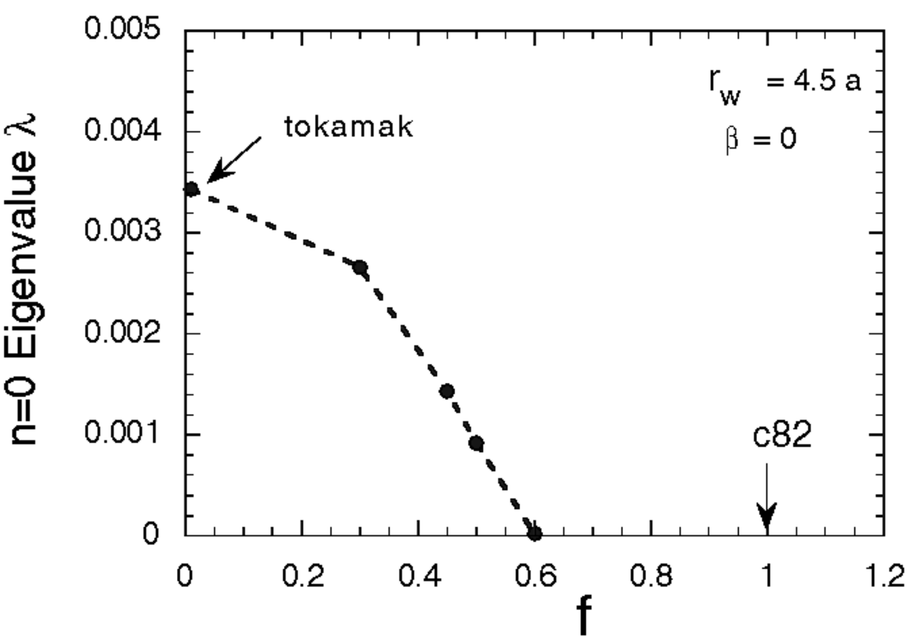

Figure 5-4: The eigenvalue of the vertical mode versus fraction of c82's nonaxisymmetric shape

Figure 5-4 shows the eigenvalue of the vertical mode as function of the fraction of nonaxisymmetric shape, f, at fixed current profile and zero beta. Here f = 1 corresponds to the full C82 shape and f = 0 corresponds a tokamak with the axisymmetric shape of C82. Equilibria are obtained by linear interpolation of the tokamak shape and the C82 shape (i.e., $R_{m,n}(f) = fR_{m,n}$, $Z_{m,n}(f) = fZ_{m,n}$ for $n \neq 0$, where $R_{m,n}$ and $Z_{m,n}$ are Fourier coefficients of the C82 shape). We observe that there is a large stability margin for the vertical mode in C82 with the marginal point at f = 0.6. The results of Fig. 5-4 are obtained with zero beta because of equilibrium convergence problem due to low ι at small f. At finite f, the effects of beta are found to be stabilizing. Thus, an even larger margin is expected at finite beta. This robust vertical stability is mainly due to effects of the external rotational transform. We have derived an analytic stability criterion for vertical mode in a large aspect ratio QAS with constant current density and constant external rotational transform [3]. The external rotational transform needed for stability is given by:

$$F_i = \frac{\kappa^2 - \kappa}{\kappa^2 + 1} \tag{8}$$

where $F_i = \iota_{ext} / \iota_{total}$ is the fraction of external rotational transform and κ is the axisymmetric elongation. This criterion has been confirmed by the Terpsichore code, as shown in Fig. 5-5. The calculated critical external transform (solid dots) agrees reasonably well with the analytic result (solid line). Physically, the external transform is stabilizing because the external poloidal flux enhances the field line bending energy relative to the current-driven term for the vertical instability. We note that F_i = 0.5, κ = 1.9 for C82 and Fi = 0.75 and κ = 1.8 for NCSX. Thus, both C82 and NCSX are very stable to the vertical mode according to this analytic criterion.

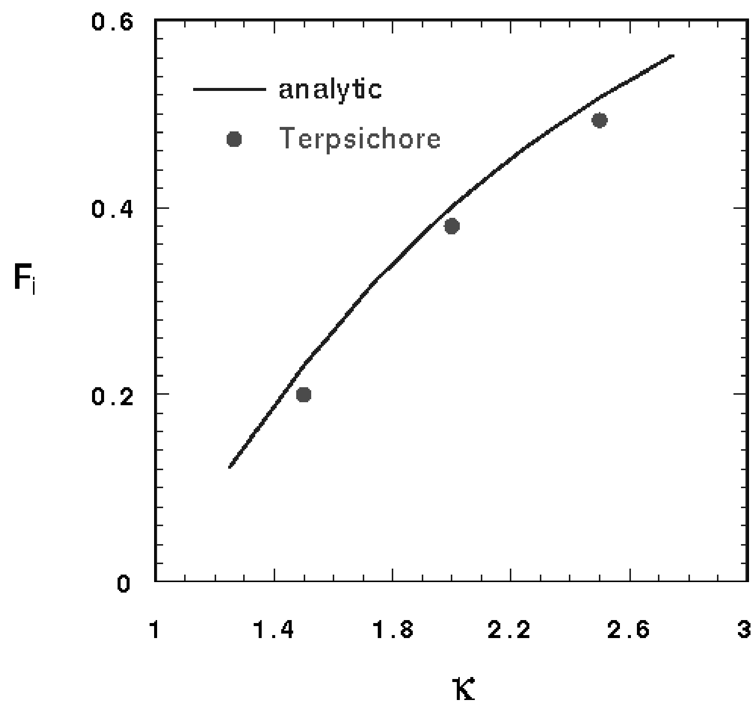

Figure 5-5: The critical value of fraction of external transform as function of axisymmetric elongation

Second, we show that external kink stability can be enhanced in QAS by controlling the iota profile via 3D shaping. Specifically, it is found that the edge magnetic shear is stabilizing for external kink modes [4]. Figure 5-6 shows the calculated N=1 external kink mode eigenvalue $\lambda = -\omega^2$ as a function of global magnetic shear near the edge defined by $\iota(1) - \iota(0.75)$ at $\iota(1) = 0.46$. These results are obtained for a $N_p = 4$ QAS with R/a = 2.1 and $\beta \sim 6.3\%$. The variation of shear is controlled entirely by 3D plasma boundary shape while keeping the current and pressure profiles fixed. We observe that the external kink mode is stabilized by edge magnetic shear. Physically, the shear is stabilizing because it enhances the field line bending energy.

Third, we show that external kink stability can also be enhanced in QAS by pure 3D geometry effects at fixed iota profile [4]. 3D shaping can affect important magnetic field properties in such a way so the MHD stability is favorable. In practice, favorable 3D shaping can be found by using a numerical optimizer that uses kink stability as a target function. Two examples are shown here to illustrate the pure geometry effects on MHD stability. The first example is an external kink stabilized by local magnetic shear controlled by 3D shaping. Figure 5-7 shows plasma cross-sections of a three field period R/a = 3.5 QAS before (left) and after (right) the stability optimization. The corresponding rotational transform profiles are shown in Figure 5-8.

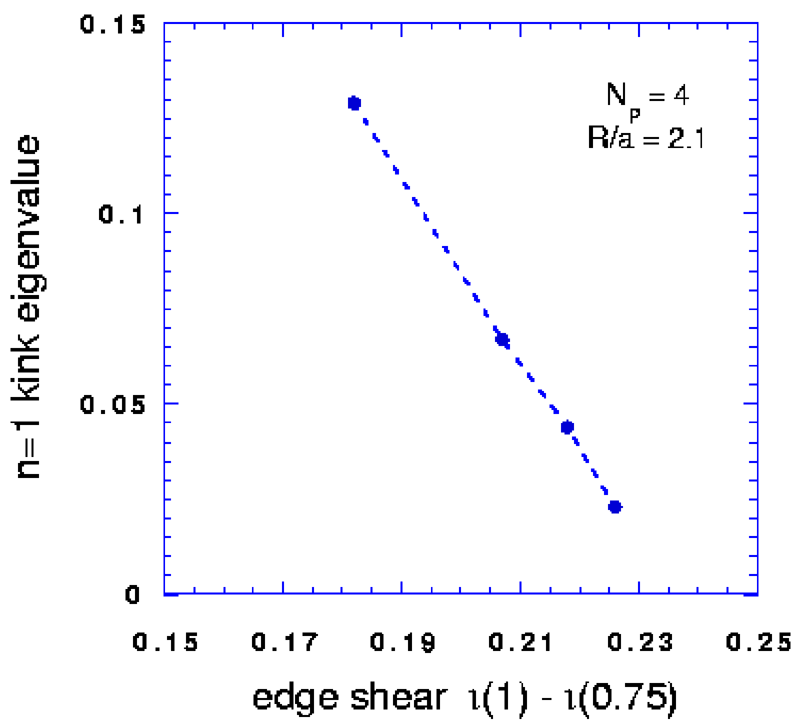

Figure 5-6: The n = 1 external kink eigenvalue versus edge magnetic shear for a four field period QAS with R/a = 2.1 and $\beta \sim 6.3\%$

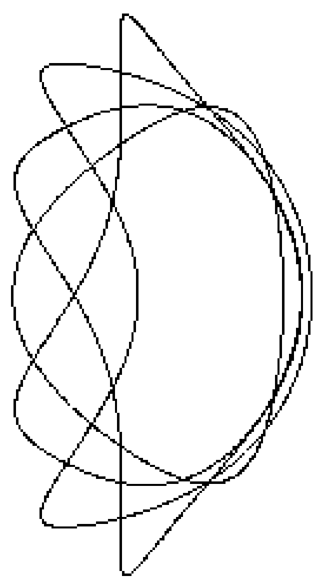

Figure 5-7: Plasma cross-sections of a three field period QAS before optimization (left) and after optimization (right)

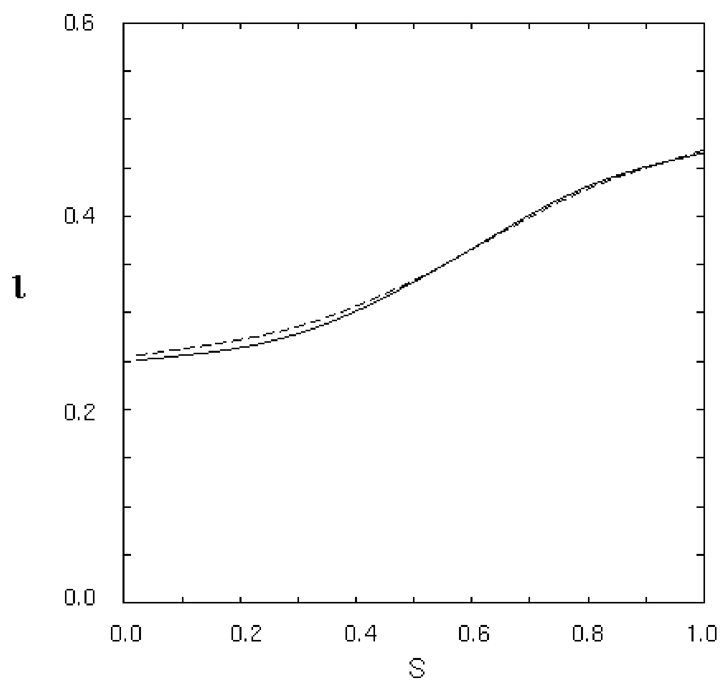

Figure 5-8: Iota profiles of a three field period QAS before optimization (solid line) and after optimization (dashed line)

The initial configuration (C3m) is unstable to an n=1 kink with eigenvalue of $\lambda = 1.8\times10^{-3}$. Figure 5-9 plots the perturbed pressure contour of the corresponding eigenmode at the two symmetric cross-section (at $\phi = 0$ and $\phi = \pi/3$). The unstable mode peaks on the outboard side of the plasma (i.e., ballooning) due to destabilizing bad curvature. The final configuration after optimization (called C82) is marginally unstable with an eigenvalue of $\lambda = 2.6\times10^{-5}$ at $\beta = 3.9\%$. We note that the change in the iota profile from C3m's to C82's is minimal and the two order of magnitude reduction in kink eigenvalue can only be attributed to pure geometry effects due to 3D shaping. The major change in shaping from C3m to C82 is an indentation of plasma boundary on the outboard side at the half-period cross section that is found to be most effective for stabilization. To understand the 3D shaping effects on stability, we have evaluated changes in stabilizing and destabilizing terms from C3m's to C82's. Table 5-1 list the relative contributions of these terms normalized by the vacuum magnetic energy for both C3m and C82.

Table 5-1: The breakdown of stabilizing and destabilizing terms in the plasma potential energy normalized by the vacuum energy for the most unstable n = 1 external kink mode in C3m and C82

	Vacuum	line bending	kink	ballooning
c3m	1.00	4.05	-3.98	-1.72
c82	1.00	4.51	-3.87	-1.64

The line bending column in Table 5-1 corresponds to the sum of first and second terms in δW_p [Eq. (4)], while the kink and ballooning columns correspond to the third and the forth term respectively. We note that the parallel current term (kink column) contributes about 70% of the total destabilizing sum for both cases and is thus the main destabilizing mechanism for the n = 1 external kink modes, in accordance with usual expectation. However, the ballooning term also contributes significantly to the instability. This is the reason the mode exhibits the strong ballooning feature shown in Fig. 5-9. Thus, the unstable mode should be called kink-ballooning mode. The pressure also contributes indirectly to the kink term through the parallel Pfirsch-Schluter current. For both cases, the Pfirsch-Schluter current contributes about 57% of the kink term. Thus, the pressure-induced Pfirsch-Schluter current is actually more important than the volume-averaged parallel current for these two configurations. We now discuss why the 3D shaping change from C3m to C82 stabilizes the external kink mode. We observe from Table 5-1 that the main difference between C3m and C82 is the field line bending term. This suggests that the effects of shaping on local magnetic shear play a significant role. Figure 5-10 shows the contours of local magnetic shear $\hat{S}$ of C82 on the s = 0.63 flux surface (the δW_p peaks approximately at this surface). Here, the local magnetic shear $\hat{S}$ is defined by $\hat{S} = -(\sqrt{g}/\Psi'^2)\ \mathbf{h} \cdot \nabla\times\mathbf{h}$ with $\sqrt{g}$ being the Jacobian and $\mathbf{h} = \mathbf{B} \times \nabla s / |\nabla s|^2$. Note that the global magnetic shear dq/ds is a surface average of $\hat{S}$ where $q = 1/\iota$. The value of local magnetic shear in Fig. 5-10 ranges from -74.3 to 28.6, while the global shear is dq/ds = -2.4. This shows that the local magnetic shear is dominated by helical contribution and is much larger than the global shear. Figure 5-11 compares the local magnetic shear of C3m with that of C82 on the outboard side at s = 0.63. Indeed we find that the local shear of C82 is substantially larger than that of C3m on the outboard side. This indicates that the local shear is responsible for the change in the field line bending energy and the stability between these two configurations.

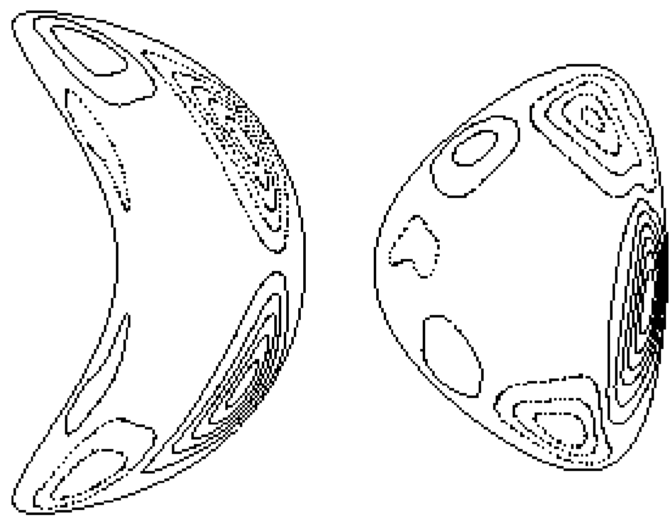

Figure 5-9: contours of perturbed pressure at the two symmetric cross-sections for C3m

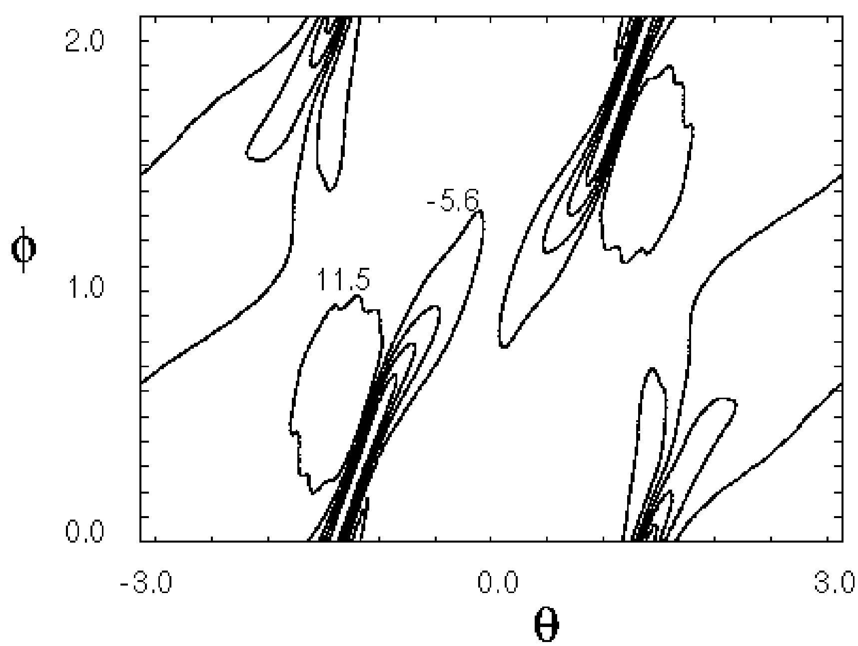

Figure 5-10: The contour plot of the local magnetic shear of the configuration c82 on the s = 0.63 flux surface for one field period ($0 \le \phi \le 2\pi/3$). The local shear value for some contours is marked

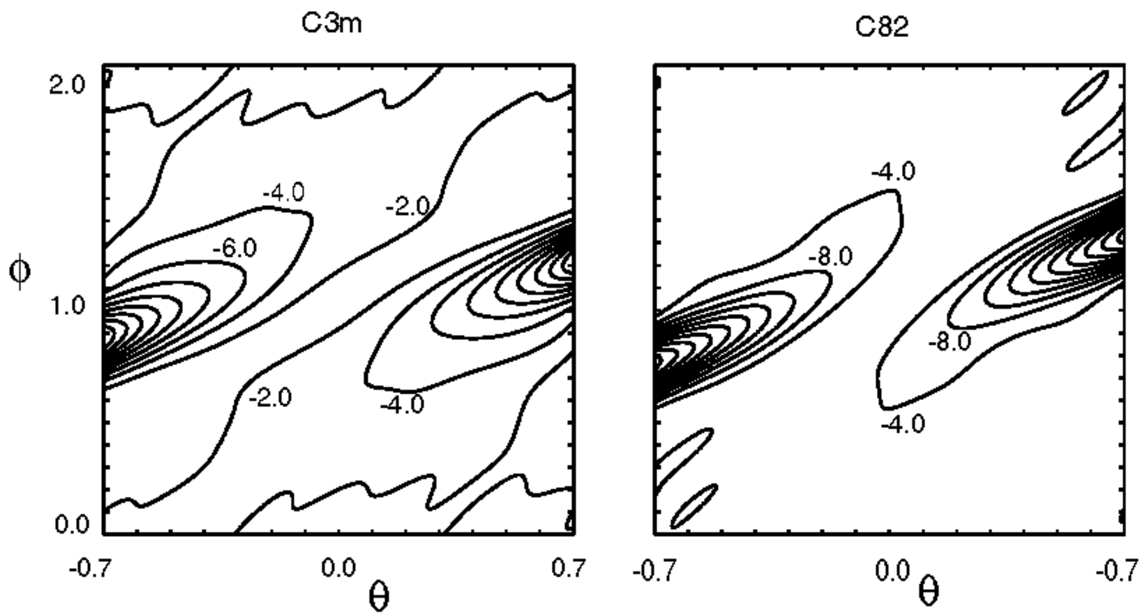

Figure 5-11: The contour plot of the local magnetic shear for the configuration C3m (left) and C82 (right) on the s = 0.63 flux surface on the outboard side of the torus (-0.7 < θ < 0.7). The local shear value for some contours is marked

We now discuss effects of magnetic well, which is a function of the 3D geometry. In our search for more robust configurations with good coil characteristics, we observed the importance of externally generated magnetic well on global MHD instability, especially the external kinks. Specifically we showed that the external kink stability is strongly correlated with the size of magnetic well. To isolate the effects of magnetic well, we generated a series of four QAS configurations with different magnetic wells. The shapes of last closed flux surfaces for each of the four configurations (labled KG7a, KG7b, KG7c and KG7d) are shown in Figure 5-12. The corresponding external magnetic well profiles, defined as $(1-V'(s)/V'(0))$ in the absence of the plasma current and pressure, are plotted in Figure 5-13. This series is generated by varying only a single term in the boundary harmonics, i.e., $Z(m,n) = Z(2,1)$., at fixed current and pressure profiles. By modifying this single term, we are able to change the magnetic well from a depth of 7% to 4%, 0%, and then -10% while maintaining approximately the same external iota profile (from 0.12 at center to 0.33 at the edge). The results of the N = 1 external kink stability from Terpsichore are shown in Figure 5-14 which plots the kink eigenvalue as function of plasma beta for each of the configurations. We observe that the beta limit increases from 2.2% (KG7e) to 5.2% (KG7a) as the corresponding magnetic well varies from -10% (magnetic hill !) to 7%. The calculations for the N = 0 family showed that the critical beta is always higher than those for the N = 1 instability. Since the rotational transform profiles of these cases are similar for these configurations, the difference in the kink stability can be attributable to the difference in the magnetic well. Physically, a strong magnetic well reduces the pressure gradient drive (ballooning term) and enhances the stability of global kink modes.

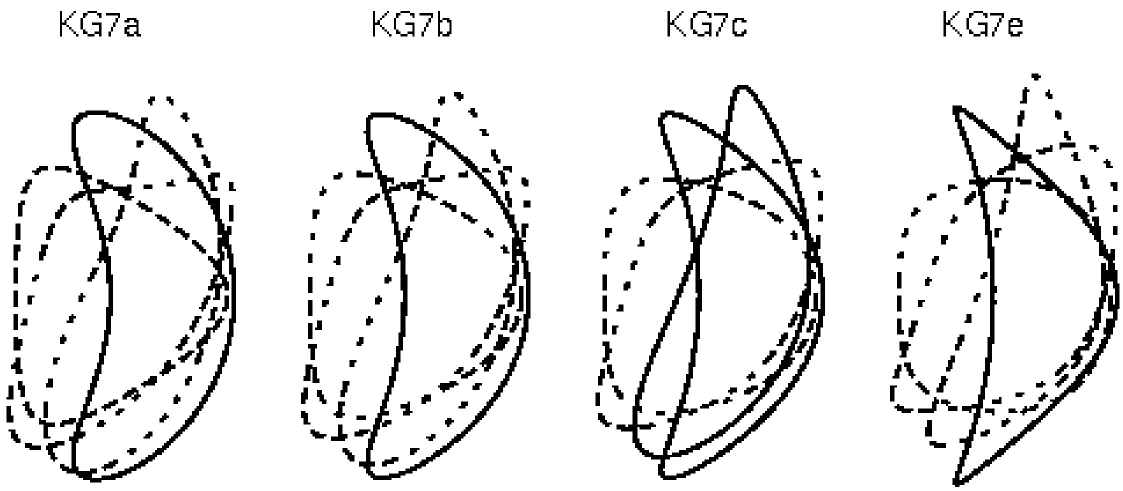

Figure 5-12: Poincare sections equally spaced over half a field period for four configurations with decreasing depths of externally generated magnetic well

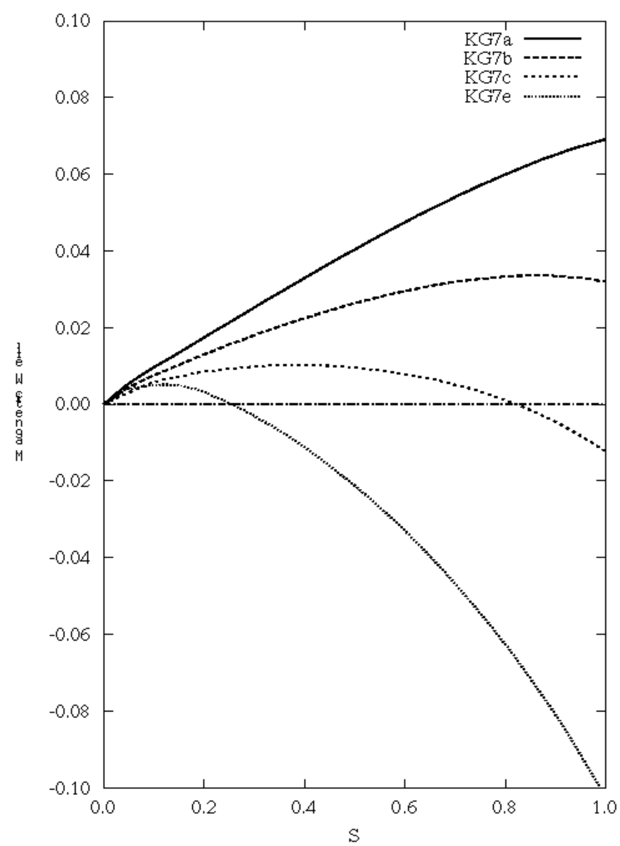

Figure 5-13: Vacuum magnetic well as a function of s

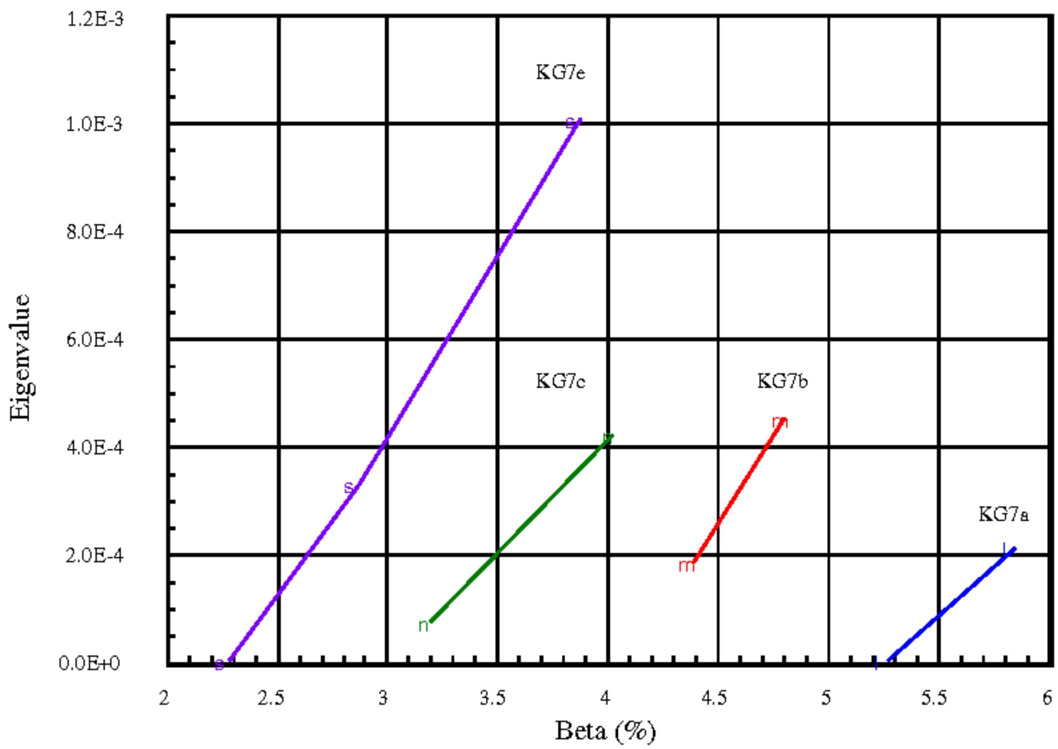

Figure 5-14: Eigenvalue of the N = 1 external kink mode versus averaged plasma beta for four configurations with increasing depths of magnetic well

5.4 Stability of NCSX configuration

Here we will present stability results for the NCSX reference configuration (LI383) in terms of Mercier stability, ballooning stability and, external kink and vertical mode stability. The NCSX configuration was found by optimizing the MHD stability of Mercier, ballooning and external kink modes along with quasi-symmetry and other desired targets. Thus, the configuration is designed to be stable (marginally) to all these modes. However, absolute stability is not guaranteed for several reasons. First, the stability evaluations in the optimizer are not complete. For example, the N = 0 family of modes were not included in the original optimization, but were checked afterwards. Similarly for ballooning stability, only two field lines are calculated at each flux surface. Second, the numerical resolutions used are fairly crude for the sake of speed and available memory. Here, we show a more complete stability analysis and convergence study to validate the optimization results.

- 5.4.1 Mercier Stability

Figure 5-15 shows the Mercier criterion (> 0 for stability) as a function of the normalized toroidal flux s. It is evident that Mercier modes are stable over the whole radii of the plasma. As stated in the preceding sections, the NCSX configuration was designed to have magnetic well in vacuum. The magnetic well is maintained in the full beta full current reference configuration. Thus, the favorable Mercier stability is not surprising.

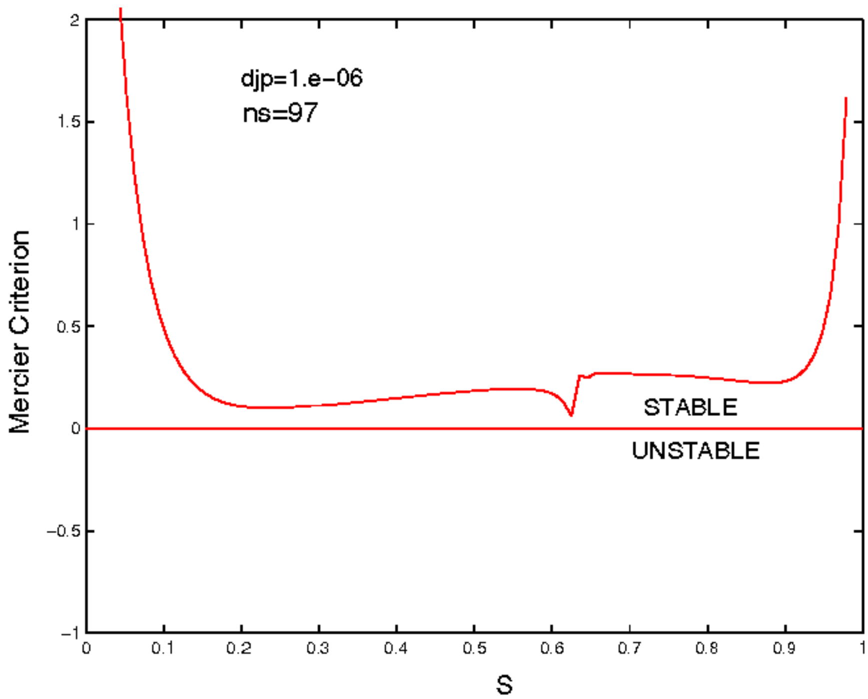

Figure 5-15: Mercier criterion for the NCSX reference configuration

- 5.4.2 Ballooning Stability

Figure 5-16 plots the ballooning eigenvalue (> 0 for instability) versus S calculated with the Terpsichore-VVBAL (solid line) and COBRA (solid star). We note that two codes give same marginal points (The absolute values of the eigenvalue differ because different definitions of the eigenvalue are used in the two codes). The results are obtained using parameters of $\theta_k = 0$ and $\alpha = \pi/3$ for which the ballooning modes are determined to be most unstable. The results are converged in terms of number of radial grid points and the number of Boozer modes for the equilibrium mapping. Figure 5-17 shows that the Terpsichore-VVBAL ballooning eigenvalue does not change when the number of Boozer modes is increased from 715 to 853. These results show that the NCSX configuration is ballooning stable over most of the plasma radii except in a small region near the edge. This weak ballooning instability can easily be re-stabilized by a slight change in the 3D boundary shape or by local flattening of the plasma gradient. Therefore, the NCSX configuration can basically be regarded as ballooning stable.

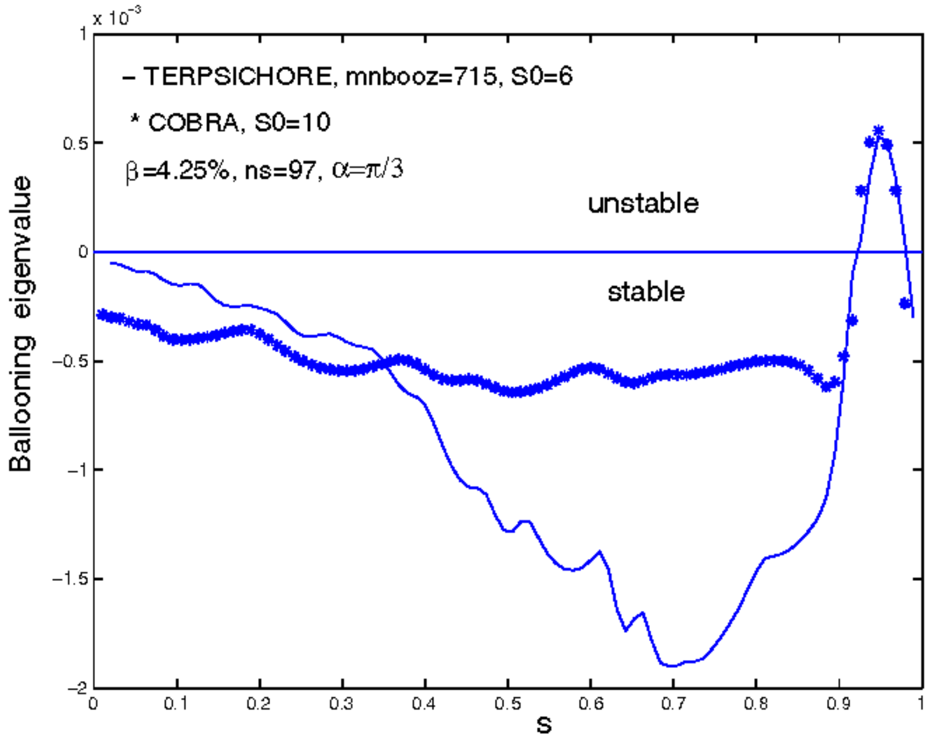

Figure 5-16: Ballooning eigenvalue as a function of S for the NCSX reference configuration

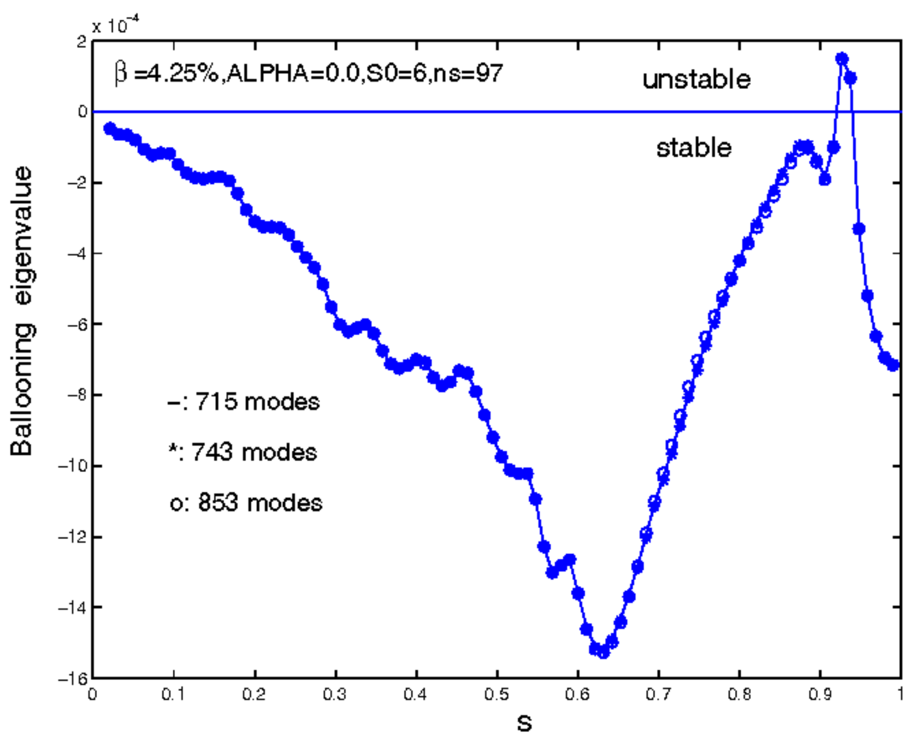

Figure 5-17: Ballooning eigenvalue as a function of S for the NCSX reference configuration

The stability results presented here are valid for infinite-n ideal modes. In practice, only finite-n modes can be unstable due to Finite Ion Larmor Radius (FLR) stabilization. Thus, an important issue is the stability of finite n ballooning modes and associated beta limits. We had carried out finite-n ballooning mode stability calculations using the global code Terpsichore for the configuration C82. The results showed that the finite n ballooning modes ($n \sim 20$) are significantly more stable than the Infinite-n results [6]. Work is in progress [21] to study the FLR stabilization of finite n ballooning modes by applying the WKB ballooning formalism and the quantum chaos theory [22].

5.4.3 External Kink and Vertical Stability

As mentioned before, the NCSX configuration was optimized to be marginally stable to the $N = 1$ family of external kink modes using a low resolution. Typically 49 radial grid points, 94 VMEC modes, 264 Boozer modes for mapping, and 91 modes ($n > 7$) for perturbation are used with Terpsichore in the optimization. Here we show a more complete stability analysis for both the $N = 1$ and the $N = 0$ families using higher resolutions.

We have carried out a systematic convergence study for the stability of global MHD modes in the NCSX configuration using Terpsichore. Up to 300 radial grid points, 218 VMEC modes, 414 Boozer mapping modes, and 361 modes ($n > 26$) for perturbation are used. We found that the stability is most sensitive to number of perturbation modes. Since the NCSX configuration is optimized to be marginal to the external kinks, we use two artificial multipliers, coec and coep for the kink and ballooning terms in δW respectively, to adjust the size of the two destabilizing terms. In this way, we can determine how far an equilibrium is from marginal stability boundary by varying these two coefficients.

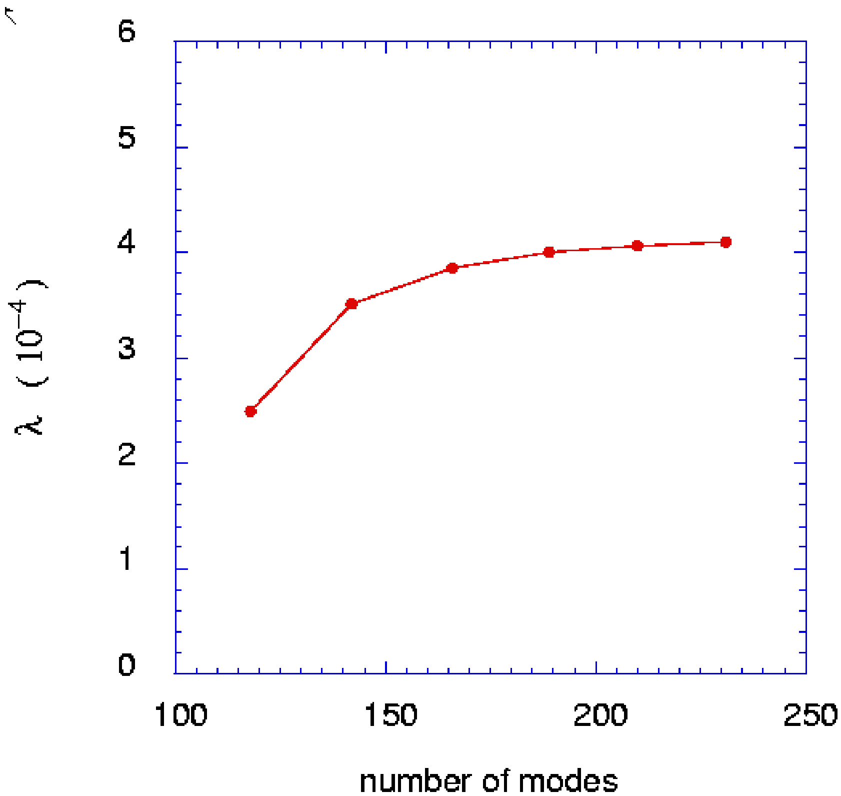

Figure 5-18: The N = 1 kink eigenvalue as function number of perturbation Fourier modes for the NCSX reference configuration.

Figure 5-18 shows the N = 1 kink eigenvalue λ as a function of number of the perturbation modes (at coep = coec = 1.025) for the mode with (m,n) = (17,11) being the largest harmonic. We observe that the eigenvalue converges for > 190 modes. Figure 5-19 shows the kink eigenvalues as function of coep (coec = coep) for the three most unstable modes of the N = 1 family. Note that in general there are many eigenmodes for the same mode family with different harmonic distribution. In Figure 5-19, the largest harmonic for each of the three eigenmodes are (17,11) (solid diamonds), (2,1) (solid dots), and (8,5) (solid square) respectively. The corresponding normal component of plasma displacement vector (versus radius) is shown in the Figure 5-20 on the left for the most unstable eigenmode. We observe that the eigenmode with the dominant (17,11) is the most unstable and yields a critical value of coep = coec = 0.925. This shows that, at β = 4.25%, the NCSX configuration (fixed boundary VMEC equilibrium) is weakly unstable to the N = 1 external kink with a small growth rate on order of 10^{-4}. This weak instability can be easily stabilized by modifying the 3D shape slightly as shown at the end of this subsection.

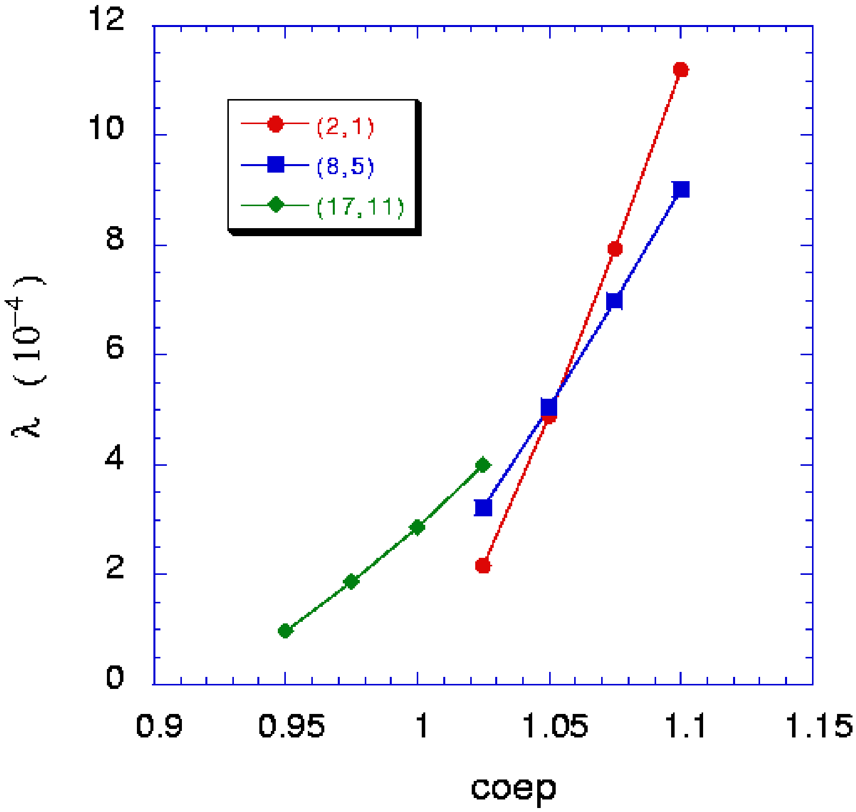

Figure 5-19: The N = 1 eigenvalues versus coep for the three most unstable modes

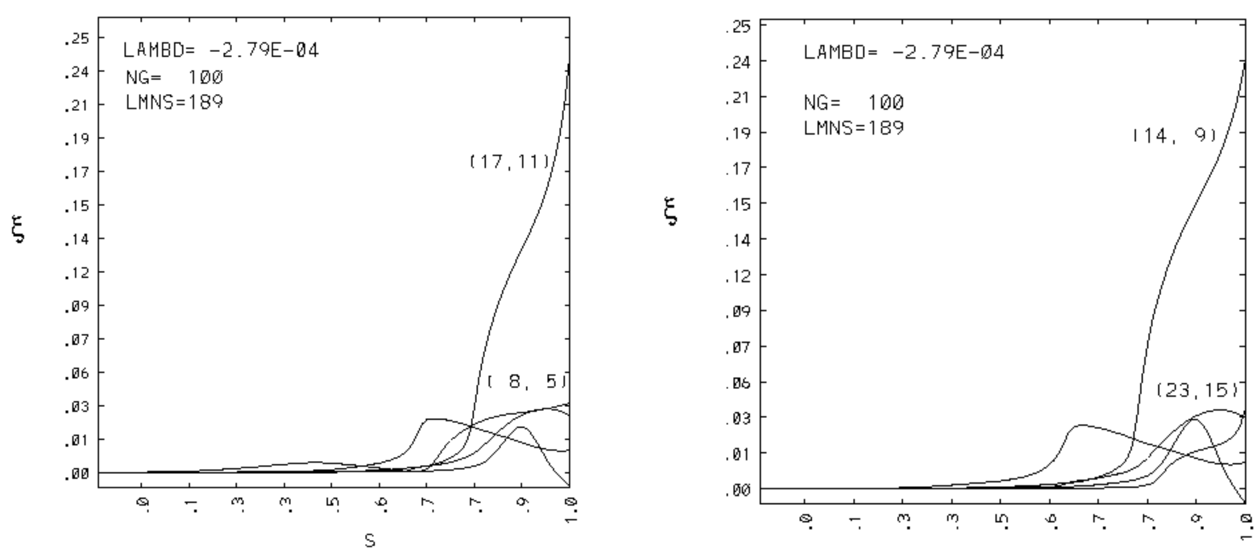

Figure 5-20: The radial displacement of the N = 1 (left) and N = 0 (right) most unstable eigenmode at coep = coec = 1.0

We now show results for the N = 0 family of modes, including the vertical mode for which the (1,0) harmonic is dominant. Figure 5-21 on the left shows the most unstable eigenvalue of the N = 0 family versus coep = coec with (m,n) = (14,9) being the dominant harmonic. The corresponding eigenfunction is shown in Figure 5-20 on the right. We observe that this mode yields a similar critical coep as compared to the N = 1 family. The stability of the vertical mode with dominant (1,0) is shown in Figure 5-21 on the right. The results are obtained at fixed coep = 1 and only the flux-averaged part of the parallel current in the kink term is being changed by coec. The corresponding eigenfunction at coec = 2.2 is shown in Figure 5- 22. The (1,0) harmonic is clearly dominating, as it should be for a vertical mode. We observe that the vertical mode would become unstable if the plasma current were raised by a factor of two. Thus, the NCSX configuration is robustly stable. This is expected from our simple analytic results due to a large external rotational transform.

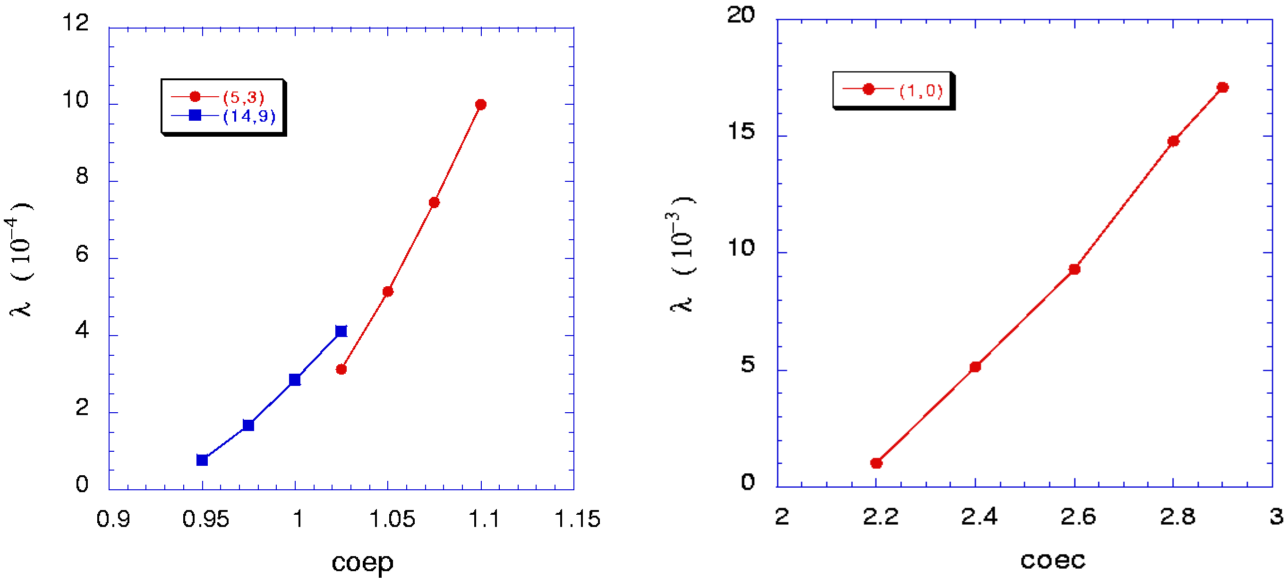

Figure 5-21: The N = 0 eigenvalue versus coep for the most unstable mode (left) and the vertical mode (right)

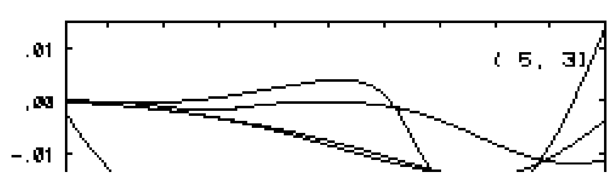

ξ

Figure 5-22: The radial displacement versus radius for the vertical mode

Finally, we demonstrate here that the weak high-n kink instabilities of the NCSX configuration (LI383) can be easily re-stabilized with a small change in the boundary shape. Figure 5-23 shows the cross-sections of the original LI383 (black) and the modified configuration LI383_B (red) that has been re-optimized for kink stability. The new configuration is calculated to be robustly stable to both N=1 and N=0 families of external kink modes with up to 201 perturbation modes (toroidal mode number up to 20). We observe that the shape change from LI383 to LI383_B is minimal.

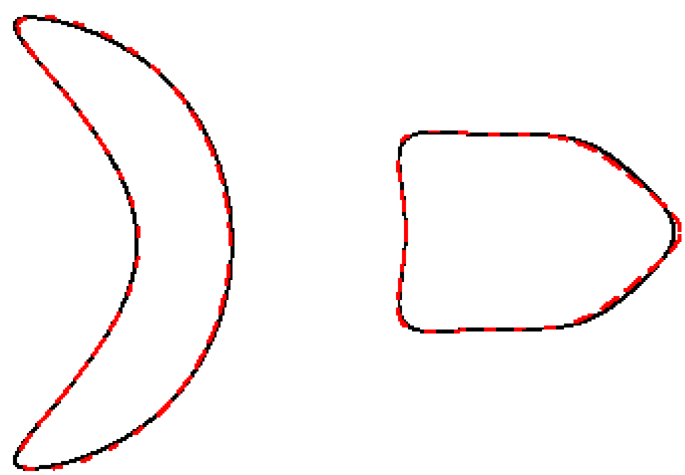

Figure 5-23 The comparison of cross-sections of the original LI383 configuration (black solid line) and the modified LI383 configuration (red dashed line) which is re-optimized to be stable to external kink modes

5.5 Effects of Wall on Kink Stability

In the preceding section, the wall is prescribed to be more than twice the minor radius away from the plasma edge so that the effects of wall on the kink stability is negligible. Here we investigate whether a much closer wall (say $d_{wall} \sim 0.3 < a >$) could have a significant effect on the beta limit. This is motivated by the fact that in an actual experiment, the vacuum vessel is close to the plasma over a significant fraction of the surface and they could influence the stability of external kink modes.

Figure 5-24 shows the most unstable eigenvalue of the N = 1 family as a function of the wall distance from the plasma edge, d_{wall} for the LI383 configuration. The plasma beta is raised from the baseline β = 4.25% to β = 5.0% with fixed plasma boundary shape in order to have instability with a close wall. The solid dots correspond to a fixed baseline plasma current whereas the solid square correspond to an enhanced plasma current proportional to the plasma beta. A conformal conducting wall is prescribed for these results. We observe that for both cases, stabilization of the external kinks (at β = 5%) requires a very close fitting wall at about $d_{wall} \sim 0.05$ or $d_{wall}/ < a > \sim 0.1$. This means that both the vacuum vessel and the conducting structures are not expected to affect the kink stability significantly in a real discharge of NCSX.

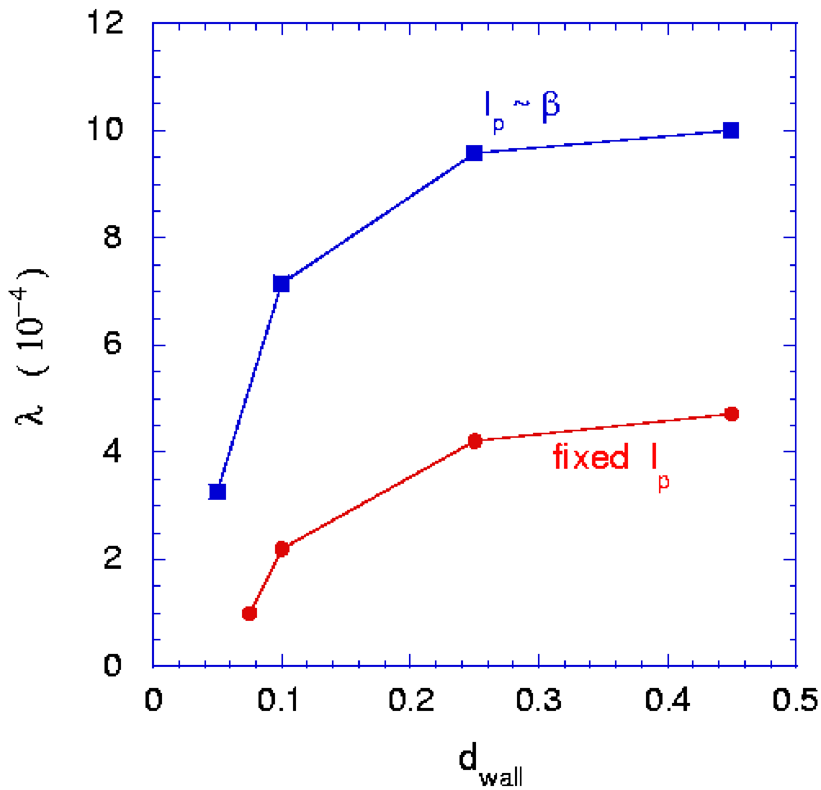

Figure 5-24: The N = 1 eigenvalue as function of wall distance for the NCSX configuration at β = 5%

5.6 Alfvén Mode Stability

It is known that energetic particles can resonantly destabilize shear Alfvén waves, such as Toroidal Alfvén Eigenmode (TAE), by tapping the free energy associated with their pressure gradient. TAEs are stable discrete shear Alfvén modes formed as a result of mode coupling of neighboring poloidal modes. Because TAEs are weakly damped, they are most susceptible to energetic particle destabilization. Since their discovery in 1985, TAEs have been routinely observed in NBI-heated tokamak plasmas (TFTR, DIIID, JT-60U) driven by fast neutral beam ions and in ICRH-heated plasmas driven by fast minority ions (TFTR, JT-60U, JET) [23]. Alpha particle-driven TAEs were first observed in the TFTR DT experiments [24]. NBI-driven TAEs have also been observed in stellarators (W7-AS [25], CHS and LHD [26]). TAE instability can sometime cause large losses of energetic ions, resulting in low heating efficiency.

In NCSX, the plasma is heated by neutral beam heating. Thus, questions naturally arise: can TAEs be destabilized in NCSX? If so, is there significant beam ion loss due to the instability?

A necessary condition for TAE instability is to satisfy the wave particle resonances (either $v_{||} = v_A$ or the sideband $v_{||} = v_A/3$.). For the NCSX standard high-beta operation, the main parameters at β = 4% are: B_0 = 1.2T, R_0 = 1.4m, the central electron density $n_e(0) = 7.7\times10^{13}$ (cm^{-3}), and $\beta_{beam} \sim 0.5\%$. The neutral beam ions (hydrogen) are injected tangentially into hydrogen plasmas at 50kev. Thus, we have $v_{||} / v_A \sim 1.0$ and the resonance condition can easily be met.

The TAE stability in NCSX, on the other hand, is subtler. To excite TAEs, the beam ion drive must exceed the mode damping. However, both the drive and the damping are sensitive function of plasma parameters and profiles. Furthermore, the 3D geometry of NCSX introduces another variable in this equation. Thus, there is no reliable ways to predict the TAE stability threshold without a systematic numerical modeling.

In actual tokamak experiments, the critical beam ion beta for instability varies widely, from $\beta_{beam,crit} \sim 0.1\%$ in the NNBI-heated JT-60U plasmas to $\beta_{beam,crti} \sim 0.5\%$ in the NBI-heated DIIID plasmas. Since $\beta_{beam} \sim 0.5\%$ at 5MW of beam heating power in NCSX, the TAE instability is possible in this device.

Although we expect the physics of TAE stability and related transport in QAS to be similar to that in tokamaks, the 3D geometry of NCSX does introduce important new physics effects. Because the mode coupling and Alfvén spectrum depend not only on the magnetic field strength but also on 3D geometry, significant mode coupling between different toroidal mode numbers is expected especially for high-n modes. This would result in additional continuum damping. This new mode coupling would also produce new types of Alfvén eigenmodes with their frequencies typically higher than TAE's. Another important difference is in q profiles (or iota profiles). Unlike in tokamaks, the NCSX has a q profile monotonically decreasing in radius until the very edge of the plasma. Thus, the Alfvén continuum gaps are not aligned over the whole plasma. This implies that the continuum damping is expected to be significant for global TAEs and the TAE instability is most likely to be located near the center of plasma, as observed in LHD [26].

In NCSX, the linear stability and nonlinear dynamics of TAE or other type of Alfvén Eigenmodes can be studied systematically over wide range of parameter space. In particular, the new physics introduced by the 3D geometry can be studied by varying the 3D shaping via coil currents. In this regard, we anticipate adding a set of coils to excite Alfvén eigenmodes externally, as has been done in JET using its saddle coil system [27]. This capability will allow measurement of Alfvén eigenmode frequencies and their damping rates and thus a systematic study of 3D effects on TAE stability.

5.7 Summary

We have presented the physics basis for ideal MHD stability in NCSX. The highlights of this chapter are as follows.

The most advanced MHD stability codes were used in the design of NCSX. We have validated these modern codes by benchmarking two independent local stability codes for infinite-n ballooning modes (Terpsichore-VVBAL and Cobra) and two independent global MHD stability codes for external kink modes (Terpsichore and CAS3D).

We have identified four physical mechanisms for stabilization of external kink modes and the vertical mode via 3D shaping. It was shown that 3D shaping can stabilize the vertical mode via external rotational transform and that 3D shaping can stabilize the external kink modes via magnetic shear (both global and local) and vacuum magnetic well.

Extensive convergence study has been done for both ballooning modes and external kink stability in the NCSX reference configuration (fixed boundary LI383 at $\beta = 4.25\%$), which was optimized to be marginally stable. A weak high-n external kink instability was found at higher numerical resolutions and was re-stabilization by a small change in the 3D shape.

References

[1] G. Y. Fu, L. P. Ku, N. Pomphrey *et al*., in the 17th IAEA Fusion Energy Conference, Yokohama, Japan, 19-24 October 1998 (International Atomic Energy Agency, Vienna) paper THP1/07.

[2] A. Reiman, G. Fu, S. Hirshman *et al.*,Plas. Physics and Contr. Fusion **41**, B273 (1999).

[3] G. Y. Fu, Phys. Plasmas **7**, 1079 (2000).

[4] G. Y. Fu, L. P. Ku, W. A. Cooper *et al.*, Phys. Plasmas **7**, 1809 (2000).

[5] M. H. Redi, A. Diallo, W. A. Cooper *et al.*, Phys. Plasmas **7**, 2508 (2000).
[6] G. Y. Fu *et al.*, the 18th IAEA Fusion Energy Conference, Sorrento, Italy, 4-10 October 2000 (IAEA, Vienna) paper TH3/2.
[7] W. A. Cooper et al., Nucl. Fusion **29**, 617 (1989).
[8] R.Sanchez, S.P.Hirshman, J.C.Whitson and A.S.Ware, JCP **161** (2000) 589.
[9] R. Sanchez et al., CPC, 2001.
[10] D. V. Anderson, W. A. Cooper, R. Gruber, S. Merazzi, and 115 U. Schwenn, Scient. Comp. Supercomputer II, 159 (1990).
[11] C. Nuehrenberg, Phys. Plas. **3**, 2401 (1996).
[12] S. P. Hirshman and J. C. Whitson, Phys. Fluids **26** 3553 (1983).
[13] ref for Boozer coordinates.
[14] I. B. Bernstein, E. A. Frieman, M. D. Kruskal and R. M. Kulsrud, Phys. Fluids, Proc. R. Soc. London Ser. A **244**, 17 (1958).
[15] G. Y. Fu, W. A. Cooper, R. Gruber, U. Schwenn, D. V. Anderson, Phys. Fluids B**4**, 1401 (1992).
[16] R. C. Grimm, J. M. Greene, J. L. Johnson, Methods Comput. Phys. **16**, 273 (1975).
[17] S. C. Jardin, C. E. Kessel, C. G. Bathke et. al., Fusion Engr. and Design **38**, 27 (1997).
[18] D. Dobrott and C. S. Chang, Nuclear Fusion **21**, 1573 (1981).
[19] M. H. Redi, et al., EPS, Budapest, Hungary (2000).
[20] M. H. Redi, C. Nuehrenberg, W. A. Cooper, G. Y. Fu, C. Kessel, L. P. Ku, the 26th EPS Conference on Controlled Fusion and Plasma Physics, Maastricht, Netherlands, 1999 (The European Physical Society) Paper P4.085.
[21] M. H. Redi et al., “Ballooning Mode Instability of Compact Quasiaxially Symmetric Stellarators”, in preparetion (2001).
[22] R. L. Dewar, P. Cuthbert, R. Ball, Phys. Rev. Lett. 86, 2321 (2001)
[23] K. L. Wong, Plasma Phys. Controlled Fusion 41, R1 (1999).
[24] R. Nazikian, G. Y. Fu, S. H. Batha et al, Phys. Rev. Lett. 78, 2976 (1997).
[25] A. Weller et al, in the 17th IAEA Fusion Energy Conference, Yokohama, Japan, 19-24 October 1998 (International Atomic Energy Agency, Vienna) paper EX2/1
[26] K. Toi, M. Takechi, M. Isobe et al, Nucl. Fusion 40, 1349 (2000).
[27] A. Fasoli, D. Borba, B. Breizman et al, Phys. Plasmas 7, 1816 (2000).

Chapter 6 -- Resistive Stability

The NCSX stellarator will have a substantial amount, ≈ 100 - 200 kA, of plasma current driven inductively or by the bootstrap effect. The presence of plasma current provides a potential source of free energy which can then drive MHD instabilities such as tearing modes [6.1]. Calculations of the non-linear evolution of tearing modes, including neoclassical effects [6.2] (bootstrap current) in the full 3-D geometry of NCSX is beyond the capability of present MHD codes. In the tokamak community, qualitative modeling of tearing modes has been successfully done using a simple, quasi-cylindrical, low beta model as described below [6.3-6.8]. The validity of the application of this model to stellarators is supported by experiments on W7-A and W7-AS where reasonable agreement between experiment and modeling was found [6.9, 6.10]. The calculations presented below suggest that the start-up, equilibrium, and high beta phases of the baseline NCSX plasma should be stable to internally driven tearing modes. Neoclassical effects are predicted to further enhance this stability.

6.1 Present Understanding vs. Experiments

The Δ' formalism used in the following analysis is derived in a zero beta, straight circular cylindrical geometry. Somewhat more refined formalisms (PEST III) allow for finite beta and shaping. However they are still constrained to axisymmetric equilibria and do not easily allow decoupling of ι (= 1/q) and J, nor do they calculate $\Delta'(w)$. Codes such as PIES or M3D can do a much more complete analysis, but are prohibitively expensive in terms of time to run. Tearing mode stability results found by application of the Δ' formalism to shaped, finite beta and toroidally asymmetric plasmas must be viewed with some skepticism.

The Δ' code used in the following calculations separates the ι(r) and J(r) profiles, necessary even in circular tokamaks such as TFTR, and particularly so in stellarators where a substantial fraction of the transform is not from the plasma current. The ι(r) and J(r) profiles are used in the standard differential equation governing the perturbed helical flux function [6.1]

$$[F^2/Fr^2 + 1/r\ F/Fr - m^2/r^2 - (FJ_0/Fr)/(F\psi_0/Fr)]\ \psi_{m,n} = 0 \qquad (6.1.1)$$

where ψ_0 is defined from ι(r) by

$$\psi_0(r) = B_0/R_0 \int_0^r (\iota(r) - m/n)\ r\ dr\ . \qquad (6.1.2)$$

The J(r) includes the bootstrap, beam driven and inductively driven currents. Equation 6.1.1 has a pole at the mode rational surface where ι(r) = n/m. In the boundary layer region near this surface a full fourth order differential equation must be used; however it has been shown that the mode stability is determined by matching the external solution across the boundary layer using the "constant – ψ" approximation. The matching condition yields a discontinuity in the first derivative, which is quantified in Δ'. A positive value for Δ' represents an unstable tearing mode, a negative eigenvalue stability.

This approach has been well studied and used extensively to analyze experimental tearing mode data in tokamak experiments. It provides both a basis for translating the measured external magnetic fluctuation levels into a measure of the island size as well as predictions of mode stability, growth rate and saturated island widths. In the circular cross-section TFTR tokamak this model found very good agreement between island widths predicted from edge magnetic fluctuation levels and island widths measured with the electron cyclotron emission temperature profile diagnostic [6.3].

Tearing modes have also been observed in stellarators such as the W7-AS and W7–A when net current is present. Simulations of the linear stability and non-linear evolution of the islands has been done, primarily with simple cylindrical Δ' models such as the one used here. In W7–A the analysis was also able to predict reasonably well the observed magnetic fluctuation level, *i.e.*, the saturated island width [6.9]. In the W7-AS experiment, these predictions were within an order of magnitude for the external magnetic fluctuation level and in reasonable agreement with the tomographically determined island size [6.10].

6.2 Δ' Analysis

Simulations of the start-up phase of the target NCSX plasma were done with the TRANSP code as described in Chapter 10. These simulations predict the evolution of the ohmic, beam driven and bootstrap current current profiles through the start-up phase to the target equilibrium. These time-dependent profiles have been analyzed for resistive stability to the (2/1), (5/3), (6/3), (7/3) and (7/4) tearing modes. The startup scenario has reversed shear (in the tokamak sense) and begins with $\iota(a) < 0.5$ [$q(a) > 2$]. As the plasma evolves the $\iota(a)$ drops until an m = 2, n = 1 rational surface enters the plasma from the edge at about 0.05 s.

The time dependent island width evolution is calculated by numerically integrating the generalized Rutherford equation [6.3, 6.5]

$$dw/dt = 1.22\ \eta / \mu\ [\ \Delta'(w) + \Delta_{nc}\ ]. \tag{6.2.1}$$

where η is the resistivity and μ is the magnetic permeability. The $\Delta'(w)$ is calculated numerically using the constant-ψ approximation [6.11] and Δ_{nc} is evaluated by using parameters calculated by TRANSP in the equation

$$\Delta_{nc} = (16\ \pi / 5)\ k_1\ R_0\ J_{bs} / (s\ \iota\ B_0\ w\ ). \tag{6.2.2}$$

Here J_{bs} is the local bootstrap current density, s is the local shear and w is the island width. The constant k_1 accounts for approximations made in deriving the effective perturbation in the bootstrap current due to the island. For the simulations shown here, the same $k_1 \approx 1$ was used as had been used to fit TFTR experimental data.

The results of such a calculation for the 2/1 mode are shown in Figure 6.-1. In this simulation the neoclassical term was not included. The plasma is stable or marginally unstable throughout the start-up phase. The island width remains less than 1% of the plasma minor radius, which is inconsequential. Inclusion of the neoclassical term, which is stabilizing, reduces the island size even further, as discussed in Section 4.6.

The next lowest order modes are the 4/2, 5/3, 6/3, 7/3, and 7/4 modes. The 4/2, 6/3 and 7/3 modes were calculated to be robustly stable. The stability calculations for the 5/3 and 7/4 modes were problematic. For these modes, located near the plasma boundary, the relatively large local edge current density introduces strong curvature in the radial eigenmode structure. The appearance of the eigenfunction shapes suggests that this formalism is not applicable. The failure could either result from the mapping of non-axisymmetric, finite beta and shaped equilibria to a circular cross-section, quasi-cylindrical, zero beta model or might indicate that the plasma was nearing the ideal stability marginal point (known to result in similar problems even in the simpler tokamak axisymmetric geometry).

The TRANSP time-dependent simulation analyzed above was meant to reach the NCSX target “li383” equilibrium in steady state. There are some differences in the pressure and current profiles between the li383 equilibrium and the 38381w47 TRANSP run. A Δ' analysis was also done of the single time point li383 equilibrium. In this analysis the saturated island width reaches about 3.6 % of the minor radius without inclusion of neoclassical effects. With neoclassical effects the saturated island width is inconsequential ($\approx$ 0.2 %).

6.3 Neoclassical Tearing

The inclusion of neoclassical effects, i.e., the modeling of the effect of the island on the bootstrap current density and the concomitant effect of the perturbed bootstrap current on the island, has very successfully reproduced some of the observed characteristics of tearing modes in normal shear high beta, low collisionality plasmas. This extensive experimental database [*e.g.*, 6.3-6.8] gives some credence to the neoclassical tearing mode model. However, neoclassical theory (applied to tearing modes) in the context of reversed shear plasmas has not been extensively tested. The W7-AS experiments in which tearing modes were observed were reasonably well modeled without the inclusion of neoclassical effects. Whether the neoclassical terms would have qualitatively changed the results is not clear. The conclusion of the authors was that, “*…, so far no direct evidence of neoclassical effects on the stability has been found*.” This statement could be interpreted as meaning there is no evidence either for or against the validity of the neoclassical theory of tearing modes. A study of double tearing modes in reversed shear plasmas in the TFTR tokamak also found no evidence for neoclassical modifications to the tearing mode stability in the negative shear regions [6.5]. However, in this case the analysis of double tearing modes was sufficiently unique that it is quite possible that the physics of the coupling in the double tearing modes was not adequately represented, leading to uncertainty in the conclusions. Further, single tearing modes were not observed in the reversed shear region of TFTR plasmas, consistent with the prediction of the neoclassical model that the bootstrap term is stabilizing in reversed shear.

6.4 Summary

The simulation of the NCSX start-up described in Chapter 10 has been analyzed for stability to tearing modes driven by ohmic, beam and bootstrap driven currents. The analysis has been done with a simple quasi-cylindrical Δ' code of the type used successfully in the analysis of tokamak plasmas. The plasmas are found to be stable to the low order tearing instabilities (4/2, 6/3, and 7/3 modes) and marginally stable to the 2/1 mode. The inclusion of neoclassical effects is generally believed to be stabilizing for plasmas with negative shear ($d\iota/dr > 0$, or $dq/dr < 0$), and the calculations suggest that the neoclassical terms result in a robustly stable 2/1 mode. The simple quasi-cylindrical stability calculations for the 5/3 and 7/4 modes located between $r/a \approx 0.85$ and the plasma edge did not give reasonable results, possibly indicating problems with the Δ' formulation or with the high local current density near the plasma edge.

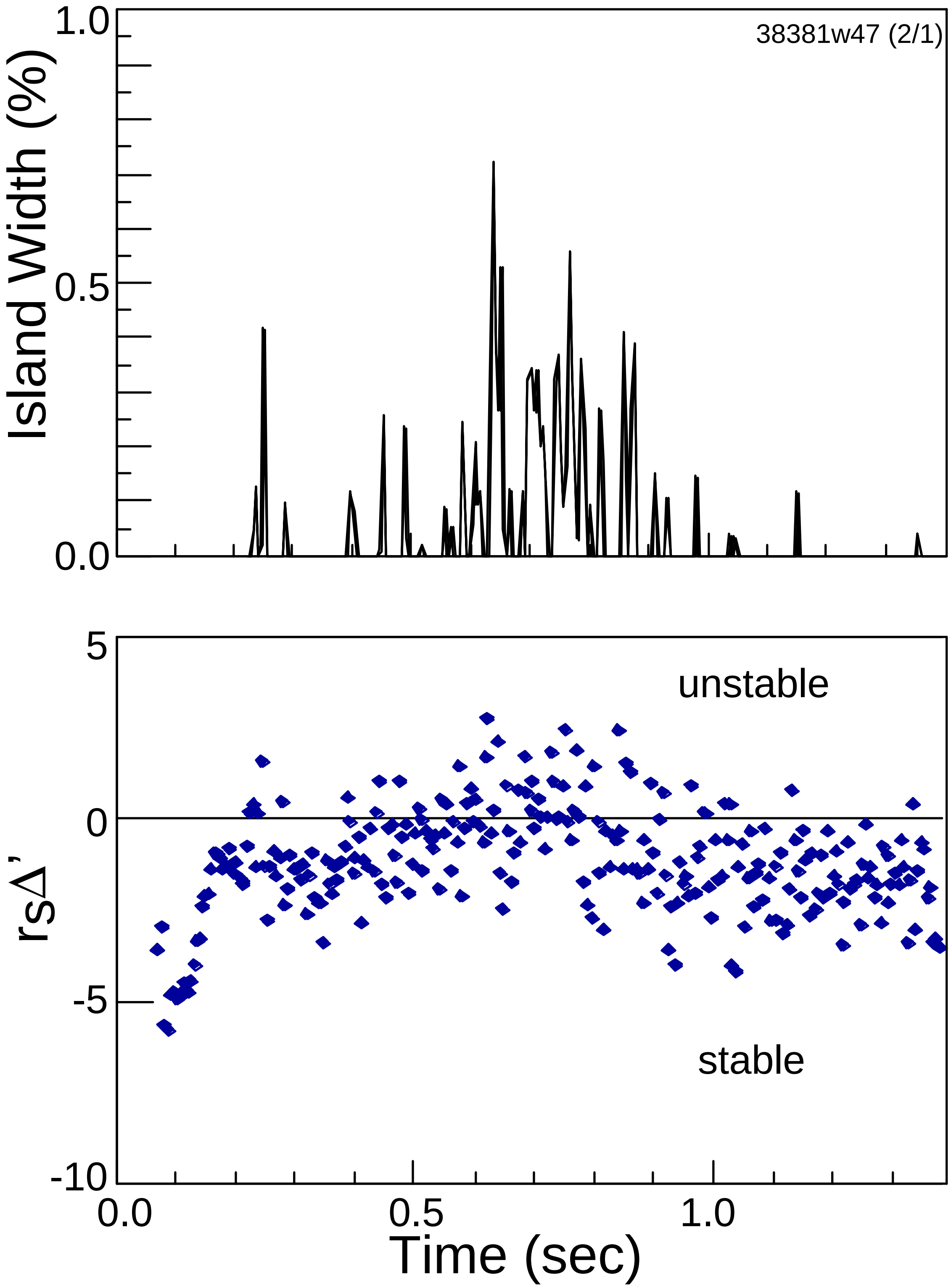

38381w47 (2/1)
Island Width (%)
1.0
0.5
0.0
unstable
stable
5
0
-5
-10
rsΔ'
0.0
0.5
1.0
Time (sec)

Figure 6-1

References

[6.1] H.P. Furth, J. Killeen, and M.N. Rosenbluth, Phys. Fluids **6**, (1963) 459.

[6.2] J.D. Callen, W.X. Xu, K.D. Siebert, B.A. Carreras, K.C. Shaing, and D. A. Spong, in *Plasma Physics and Controlled Nuclear Fusion Research* 1986, Kyoto (International Atomic Energy Agency, Viena, 1987), Vol. 2, p. 157.

[6.3] Z. Chang, J.D. Callen, E.D. Fredrickson, et al, Phys. Rev. Lett. **74**, (1995) 4663.

[6.4] Z. Chang, E. D. Fredrickson, S. H. Batha, M. G. Bell, R. V. Budny, F. M. Levinton, K.M. McGuire, G. Taylor, M. C. Zarnstorff and the TFTR Group, Physics of Plasmas **5**, (1998) 1076.

[6.5] E. Fredrickson, M. Bell, R.V. Budny, and E. Synakowski, Phys. of Plasmas **7**, (2000) 4112.

[6.6] D.A. Gates, B. Lloyd, A.W. Morris, et al., Nucl. Fusion **37** (1997) 1593.

[6.7] R.J. LaHaye, L.L. Lao, E.J. Strait, T.S. Taylor, Nucl. Fusion **37** (1997) 397.

[6.8] Q. Yu, S. Günter, Phys. of Plasmas **5** (1998) 3924.

[6.9] W VII-A TEAM, Nucl. Fusion **20**, (1980) 1093.

[6.10] E. Sallander, A. Weller, W7-AS Team, Nucl. Fusion **40**, (2000) 1499.

[6.11] P. H. Rutherford, Phys. Fluids **16**, (1973) 1903.

Chapter 7 -- Heating Methods

NCSX has been designed to accommodate a variety of heating systems, including ohmic heating, neutral beam injection, and two different strategies for ICRF. The plan is to initially provide ohmic heating and 3MW of balanced neutral beam injection for initial experiments. Subsequent upgrades could add an additional 6 MW of ICRF and 3 MW of neutral beam injection.

7.1 Ohmic Heating

The ohmic heating capability is implemented using the poloidal field coils, and provides inductive heating from up to 420 kA of ohmic current. This will be used for initial breakdown and formation of target plasma for neutral beam heating. It will also be used to manipulate the current profile shape, allowing relatively rapid equilibration with the bootstrap current, as discussed in Chapter 9.

7.2 Neutral Beam Injection Heating

7.2.1 Neutral Beam System Characteristics

7.2.1.1 Available Injection Power

NCSX will use the present PBX-M NBI system, consisting of 4 beamlines. The ion sources have 30 cm circular copper grids and a focal length of 440 cm. Each ion source was fabricated, tested, and fully qualified at ORNL in 1979-1980 to power levels of 1.5 MW, H^0 (@ 50 KV, 100A, 0.3 sec). In addition at ORNL, one ion source was demonstrated to yield 2 MW, D^0 (@ 50 KV, 70A, 0.3 sec). The injected power for a given species is proportional to the injection energy to the 5/2 power. Subsequent testing after installation on PDX demonstrated the capability to inject with four sources 8.3 MW D^0 in the absence of magnetic fields. The presence of stray magnetic fields and finite transition duct pressure reduced the available power to 6.5-7.0 MW D^0. This loss of reionization power of 12-18% will be regained by reinstalling the 100 kl/s cryopumping capability of the original design.

7.2.1.2 Pulse Length

The neutral beamline power handling surfaces are engineered to operate at a maximum of 500 msec pulse lengths at the full power peak power density of 3 kW/cm^2. In addition to power conditioning each of the ion sources at pulse lengths of 300 msec, ORNL in 1979-1980 demonstrated one ion source to operate at 500 msec pulse lengths using H^0 at about 50 KV, 90A. Similar results were obtained on PBX-M, where each of the 4 neutral beamlines was demonstrated to operate with D^0 at ~40 KV, 1 MW , to pulse lengths of 500 msec. Operation to higher powers at 500 msec seemed feasible for both H^0 and D^0 and should be considered available for NCSX. In addition, the MAST experiment, which is presently using similar ORNL style beamlines is planning to upgrade to 1.5-3 second pulse length capability. If this is successful, NCSX will be able to adopt this technology for long pulse NBI.

7.2.1.3 Control and Performance

After NBI installation, PPPL developed full computerization for the NBI system, including control of filament, arc, and accel conditioning, and fault response using an "artificial intelligence" or "expert rules" algorithm. One operator monitors all four systems in a “hands-off” manner. The computer control provided unforeseen benefits in operational reliability, reproducibility, and safety.

7.2.1.4 Ion Source Focal Length, Focusing, and Power Density Profiles

The PBX-M ion sources consist of 3 circular grids, 30 cm in diameter containing about 2000 circular holes for producing 2000 circular beamlets. The grids are shaped spherically concave to provide geometric focusing (aiming) with a focal length of 440 cm, which was the distance to the PDX torus port (Figure 7-1).

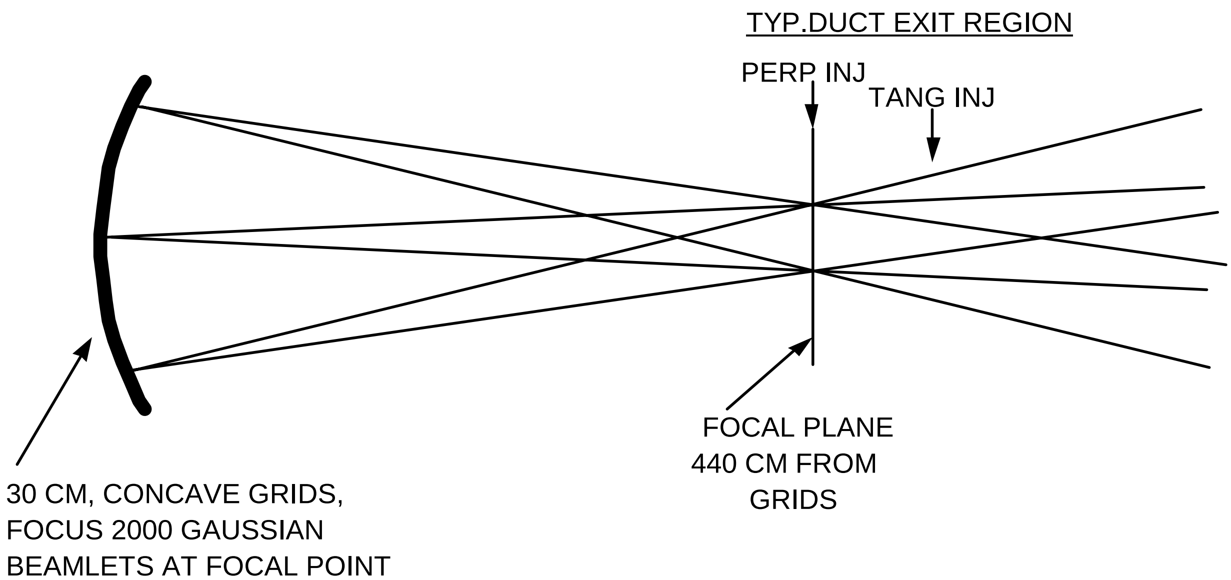

Figure 7-1. Schematic diagram of PBX-M ion source grid optics. The ion source grids are curved so as to focus 2000 Gaussian beamlets at a focal point 440 cm from the grids. Ion source optics determine the duct size and achievable aiming angles

The required grid curvature was modeled by J. Whealton (ORNL) using a Gaussian geometric optics code. Measurements of the respective as-built focal lengths and focusing were performed using a pinhole camera technique and power density profile measurements at the focal plane torus target. The final measured focal lengths were consistent with the design value of 440 cm. Table 7-1 gives the H^o angular divergences for each neutral beam at the torus target horizontal focal plane (440 cm). The results shown in Table 7-1 were obtained from measurements of the respective beam power density profiles measured along the horizontal axis in the focal plane at the torus target using a scanning water calorimeter behind pin-hole apertures (Figure 7-2). The semi-log plots exhibit Gaussian behavior down to about 10% of full power. Below the 10% power level, the profiles exhibit “wings” that have been characterized by asymmetric Gaussian, or polynomial least-squares fitting.

NBI System [a]	$\theta_{HW@HM}$ [b]	$W_{HW@HM}$ [c]	$\theta_{HW@1/e}$ [d]	$W_{HW@1/e}$ [e]
S	1.5°	11.58 cm	1.8°	13.9 cm
E	1.13°	8.75 cm	1.36°	10.5 cm
NW	1.2°	9.25 cm	1.44°	11.1 cm
SW	0.94°	7.25 cm	1.13°	8.7 cm

Table 7-1. Summary of NBI optics.

Notes
- [a] **NBI System listed in order of ion source fabrication and testing at ORNL.**
- [b] **Angular divergence from centerline to edge at one-half of full power.**
- [c] **Angular divergence from centerline to edge at 1/e of full power.**
- [d] **Beam half-width from centerline to edge at one-half of full power.**
- [e] **Beam half-width from centerline to edge at 1/e of full power.**

NCSX NBI access requirements depend on the desired injected power, which in turn depends on the effective focal length, focusing, and steering of the output neutral beam. These factors are essentially significant considerations in the design of long, tight, transition ducts for tangentially injecting beams. Preliminary NCSX neutral beam configurations and transition duct designs use the above results.

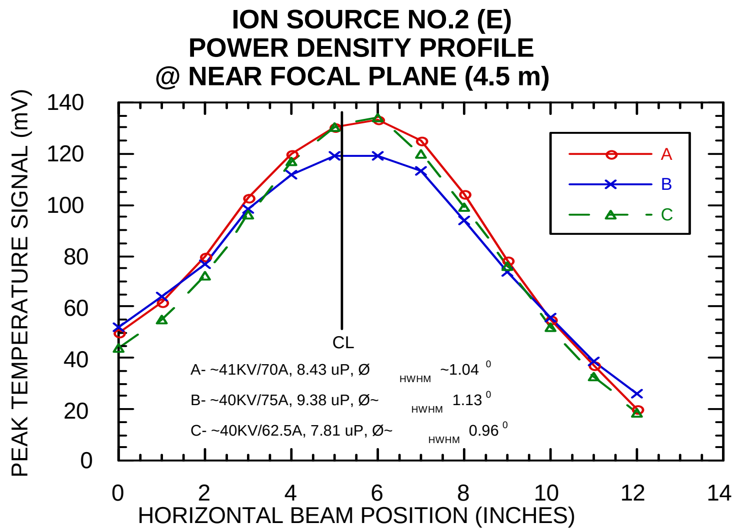

Figure 7-2. Power density profile measured at ORNL for PDX ion source No.2 (East NBI). Note that the resultant beam trajectory at the torus target at the exit of the transition duct is not entirely determined by simple, *apriori* mechanical alignment of the ion source. Measuring the actual bean position in the duct is important for proper beam alignment

The solid and dashed lines in Figure 7-3 show the simulated beam power density profile along the beam axis using the J. Whealton (ORNL) gaussian geometric optics code fit to the measurements given in Table 7-1.

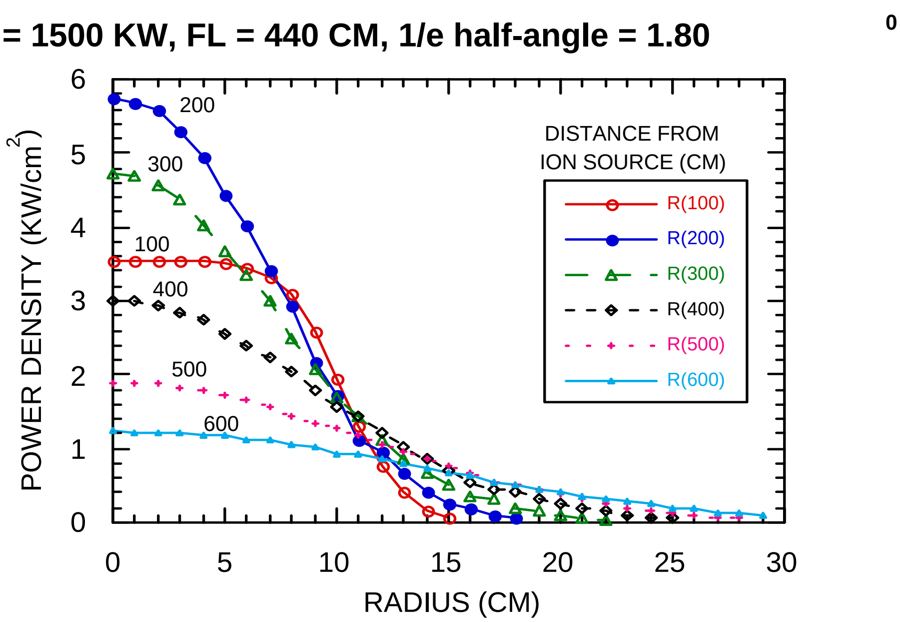

Figure 7-3. Simulated power density along beam axis. The beam port location should allow adequate duct width to avoid neutral and reionized power impingement on the duct walls

- **Maximizing Absorbed Power**

Injected Neutral Beam power is maximized by reducing system gas pressure in the transition duct which causes reionization and loss of neutral particles. The deflection of reionized beam particles into the duct walls by the fringe magnetic field causes additional gas load from out-gassing and an avalanching of reionized power loss. Reduction of transition duct neutral gas pressure to the ~10^{-5} torr regime significantly increases injected power. This is accomplished by optimizing the duct design and installing additional cryopumping in the front box of the beamline. Table 7-2 shows the NBI system injected power capability and the effects of fringe fields.

• PBX-M Injected Power Capability **• ORNL Qualification (No Fields)** $H^0 \rightarrow$ = 6 MW (4 x 1.5 MW) $D^0 \rightarrow$ = 8 MW (4 x 2.0 MW) **• PDX Testing (No Fields)** $D^0 \rightarrow$ 8.3 MW (4 NBI @ > 52 KV)
• Neutral Power Reionization Loss Fractions in PBX-M Due to Duct Neutral Gas (~1-4x10^{-4} T) • Perpendicular ducts $\rightarrow$ 0.88 P_0 (12% loss) • Tangential ducts $\rightarrow$ 0.83P_0 (17% loss)

Table 7-2. NBI power capability and reionization losses

7.2.1.6 Maximizing Desired Neutral Beam Species

Typically, neutral beamlines are operated with the neutralizer cell at ~90-95% equilibrium gas pressure to optimize the yield of the full energy component. Table 7-3 shows the measured NBI system neutral species yields. The additional gas target through the transition duct for different port access geometries can change the fractional ionic yield of the low energy components and produce small differences in the species ratios of injected beam. Small reductions in the percentage of the full energy component have been measured at the edges of beams in a narrow duct.

• Species Measurements
H^0 @40 keV
(ORNL, using ion dump yields)
• $H^0(E):H^0(E/2):H^0(E/3) = 63:20:17$
• $P^0(E):P^0(E/2):P^0(E/3) = 80:13:7$
D^0 @ 47 keV,100 ms, 1.6 MW
(PDX using RBS on injected neutrals)
• $D^0(E):D^0(E/2):D^0(E/3) = 53:32:15$
• $P^0(E):P^0(E/2):P^0(E/3) = 72:21:7$

Table 7-3. Species measurements for H^0 and D^0 using different methods

High duct pressure may change the species ratios measured upstream in the beamline and broaden the beam power profile. Direct species measurements of the output Neutral Beam reduce uncertainties in the analysis of experiments.

7.2.1.7 Power Transmission to the Far-Wall

Neutral Beam power transmission to the far-wall of the vessel ("shine-through") often requires at minimum sufficient armor to absorb a short full power pulse. This armor is usually designed to absorb at least a short full power pulse so as allow power and position calibration injections in the absence of plasma. Sometimes this armor is used to absorb short NBI conditioning pulses between discharges if the beamline calorimeter is not used. If far-wall armor cannot be installed, then suitable interlocks must be capable of stopping beam injection if sufficient plasma is not present. A useful formula for calculating the approximate fraction of beam that will "shine-through" a PDX plasma (R. Goldston) is:

H^0: 50 keV/nucleon ~ $3.4 \times 10^{-16}\ \mathrm{cm}^{-2}$

$$\text{Shine-thru} = \exp(-n_e \bullet 90 \bullet 3.4 \times 10^{-16}) = \exp(-n_e / 10^{13} \bullet 0.31)$$

D^0: 25 keV/nucleon ~ $7.4 \times 10^{-16}\ \mathrm{cm}^{-2}$

$$\text{Shine-thru} = \exp(-n_e / 10^{13} \bullet 0.67)$$

Figure 7-4 shows a plot of transmission through PDX plasmas *versus* density for H^0 and D^0 at 40 and 50 keV.

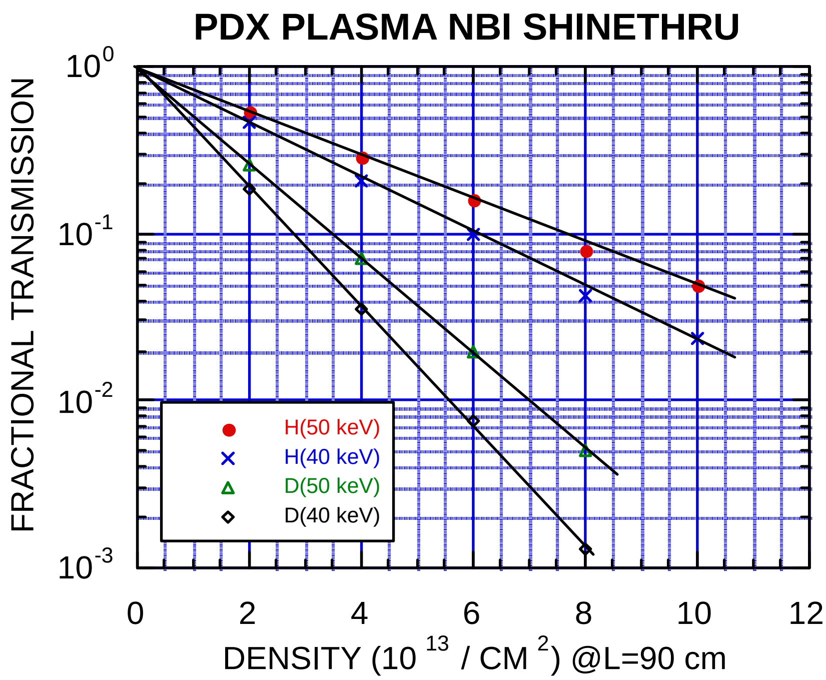

Figure 7-4. Plot of Neutral Beam power fractional transmission through a 90 cm thick PDX plasma *versus* density. This corresponds to the case of near-perpendicular injection (RTAN = 35 cm)

These results indicate that, for example, ATJ graphite at least 1.3 cm thick or the equivalent will be sufficient for wall armor tiles capable of absorbing the available peak NBI power densities of 3 kW/cm^2 for 500 msec in the absence of plasma. Thicker tiles with active cooler will be needed as an upgrade for longer NBI pulse lengths.

7.2.1.8 Minimizing Duct Wall Conditioning

Gas absorbed on and in duct walls is released (outgasses) under particle bombardment and heating. The reduction of duct outgassing by conditioning increases injected power and provides more reproducible results. Figure 7-5 shows the measured PDX East NBI system duct outgassing versus the cumulative power absorbed over several months. It is seen that, initially at the beginning of a 1-2 week Run, the duct outgassing was high but decreased steadily during the Run. Interruption of the Run for Maintenance resulted in the return of high outgassing rates due to fresh gas adsorbed on the duct walls from the vessel, and volume diffusion of fresh gas to the surface of the duct walls to replenish the outgassed surface region.

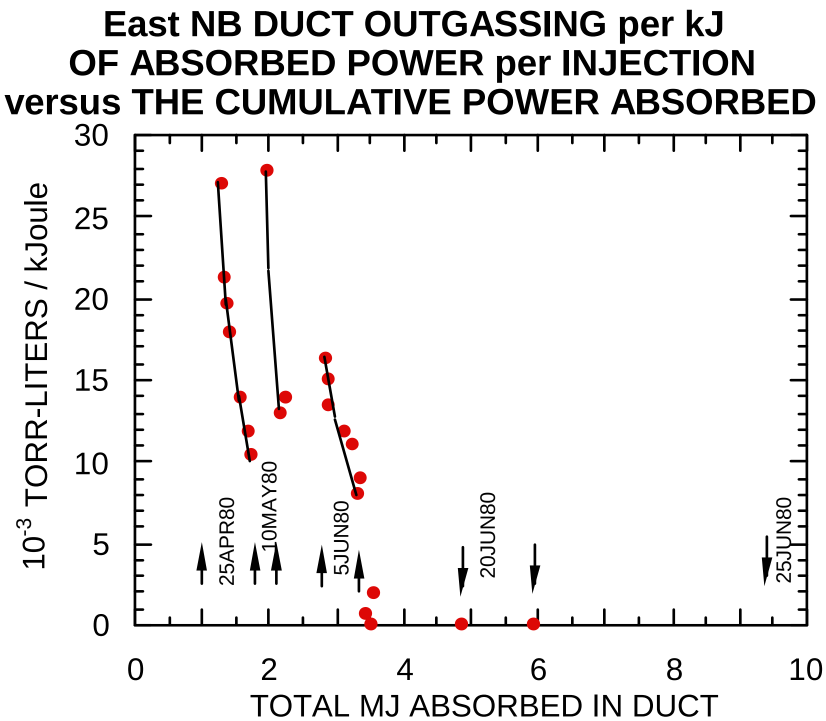

Figure 7-5. Measured duct outgassing during several months of operation. H2 Glow Discharge Cleaning (GDC) was used to clean the vessel immediately after pump-down from a vent. No H_2GDC or other GDC was applied thereafter. The application of HeGDC in the transition duct prior to NCSX daily operations and between discharges would reduce duct conditioning time significantly.

Duct outgassing can be reduced by high conductance geometry, with walls far from the beam, appropriate materials, baking, and HeGDC between discharges. The NCSX design will include the installation of high-speed cryopumping in the exit box of the beamlines at the entrance to the duct to significantly reduce or eliminate the effects of duct outgassing. This hardware will also accelerate NCSX pumpdown between discharges.

7.2.2.1 NCSX NBI Duct Design Optimization and Port Access Requirements

The NBI port access requirements discussed above can be summarized by reference to Figure 7-6, which shows a schematic diagram of the principal elements of a high conductance NBI transition duct. The beam, after passing through the beamline Torus Interface Valve (TIV), enters a rectangular section which is usually connected to a cylindrical section attached to the vessel. In the case of PBX-M, reionized power loss due to residual process gas in the duct is steered to the duct side wall by the predominantly vertical fringe field at the entrance to the duct, and eventually to the top of the duct by the predominantly horizontal fringe field at the vessel entrance. The duct has a ceramic break providing electrical isolation of about 3 kV, and a bellows at the vessel to decouple vessel motion during operation and bakeout. The bellows is shielded with a metal sheet fastened to the vessel and floating on the beam side. Diagnostic ports are provided to provide viewing of the beam in the duct for NBI and plasma related measurements (e.g., BES calibrations).

Optimization of the duct design consists in maximizing the width W, the height H, and the diameter D, while minimizing lengths Lr and Lc. The use of electropolished 304-SS (stainless steel) reduces the ratio of the atomic-to-geometric surface areas of the walls, which reduces outgassing. If possible, the use of a rectangular ceramic break and a rectangular bellows will maximize the vacuum pumping conductance. All vacuum seals will be bakeable to 150°C, to implement a 150°C bakeout capability, and possibly, to operate with the duct walls at 150°C. There will be a port for a duct ion gauge to monitor reionized power losses, and other diagnostic ports with spool pieces so as to avoid the direct impingement of reionized power on port flanges.

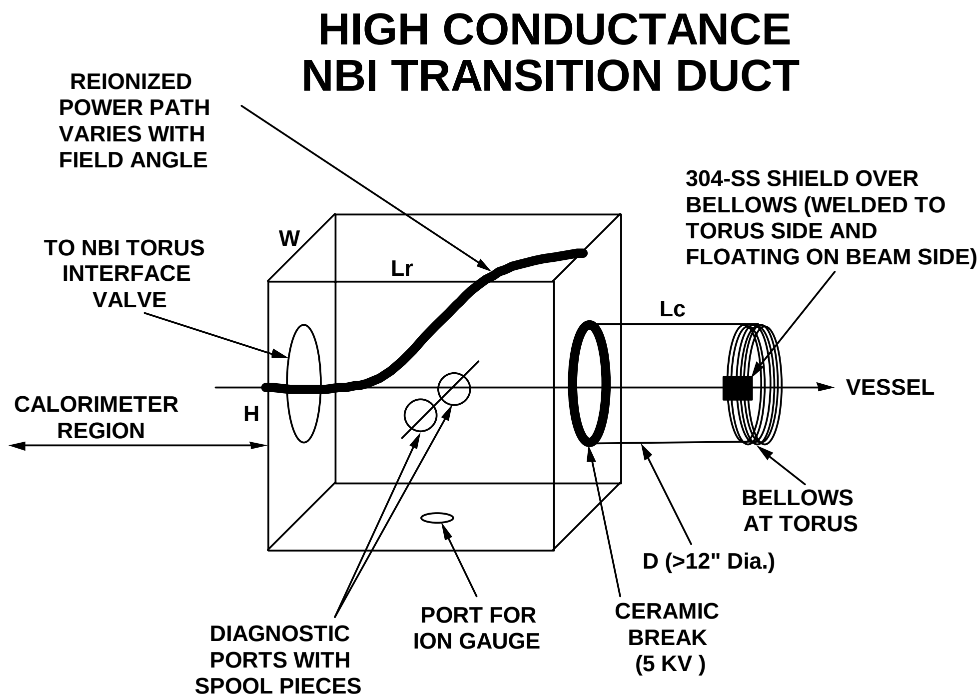

Figure 7-6. A partial schematic diagram showing the principal elements of a high conductance NBI transition duct

The NCSX design will include a duct port dedicated to a GDC electrode to facilitate duct conditioning. Table 7-4 gives a summary of the NBI transition duct and port requirements. The far-wall beam armor design will also include beam power and position diagnostics.

• Maximize dimensions W, H, and D (min. ~12”).
• Use electropolished 304-SS.
• If possible, use rectangular ceramic break and bellows to maximize conductance.
• All vacuum seals bakeable to 150°C.
• Provide 150°C bakeout capability.
• If possible, useful to operate at 150°C.
• Provide ion gauge port.
• Provide diagnostic ports with spool pieces.
• Provide port for GDC electrode.
• Far-wall beam armor should have beam diagnostics

Table 7-4. Summary of NBI transition duct design optimization and port access requirements

Hence, synergies accrue from combining duct requirements of the Neutral Beam and Torus Vacuum Pumping Systems. Figure 7-7 shows a schematic diagram of the principal

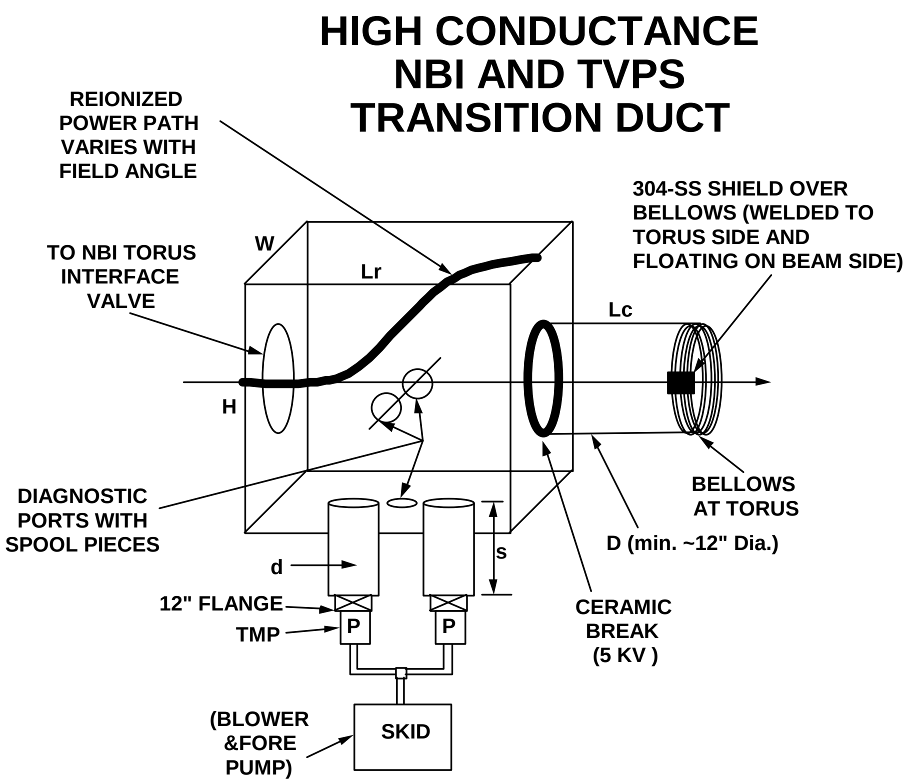

Figure 7-7. A partial schematic diagram showing the principal elements of a high conductance transition duct that combines the requirement of both NBI and TVPS requirements.

elements of a high conductance NBI transition duct that combines the design requirements for the Neutral Beam and Torus Vacuum Pumping Systems.

The proposed duct design (Figure 7-7) is essentially that discussed above with the addition of a Torus Vacuum Pumping System (TVPS) turbo molecular pumping station. It has maximized the width W, the height H, the diameter D and the diameter d, while minimizing lengths Lr and Lc. Length S is selected for high conductance reaching a fringe field region comparable to that at the pumps during their PBX-M service. In addition, S is sufficiently long to provide occlusion from beam sputtering. The other requirements discussed above are also applicable (electropolished 304-SS walls, 150°C bakeout capability). Table 7-5 gives a summary of the NBI transition duct, TVPS, and port access design optimization requirements.

• Port Access and external constraints need to be varied to: • Maximize dimensions of H,W, D • Minimize dimensions of Lc, Lr • Select S for high conductance, B-field operation, and occlusion from beam sputtering • Provide bakeability

Table 7-5. Summary of the NBI transition duct, TVPS, and port access design optimization requirements

7.2.2.2 NCSX NBI Design Maximizes Absorbed Power

The NCSX design locates the NBI ports so as to maximize the absorption of injected beam power over the desired plasma region. The absorbed power is determined by the beam focusing (perveance), the distance of the ion source from the deposition region, the aiming angle, and target plasma parameters.

7.2.2.3 NCSX NBI Design Maximizes the Desired Injected Species

The NCSX design locates the NBI ports so as to minimize effects on injected neutral particle species. Neutral Beam ion sources produce three ionic species [H^+(E), H^+(E/2), H^+(E/3), or D^+(E), D^+(E/2), D^+(E/3)]. The ion source and neutralizer, which are operated so as to maximize the full energy operation, determine the net neutral species fractions entering the transition duct [H^0(E), H^0(E/2), H^0(E/3), or D^0(E), D^0(E/2), D^0(E/3)].

7.2.2.4 NCSX NBI Design Allows Far-Wall Armor to Absorb Beam Shine-thru

The NCSX design locates the NBI ports so as to minimize beam power deposition on ports on the opposite wall. The port locations will allow the mounting of far-wall armor to absorb shine-through power and allow full-power, short-pulse beam injections in the absence of plasma for calibrations. Hence, far-wall armor provides wall protection and functions as an instrumented NBI diagnostic (IR Camera viewable, thermocouples, and/or water calorimetry).

7.2.2.5 The NSCX NBI Design Accommodates In-Vessel Constraints

The NCSX NBI port locations will allow for RF Antenna positioning requirements and special diagnostic location requirements. The requirements pertaining to the deposition of absorbed NBI power are addressed above. This will involve avoiding the direct NBI aiming at a port, but if this is not possible, the width of the required NB in-vessel armor can be extended into the duct entrance. Other constraints may pertain to toroidal location (e.g., plasma shape, Beam orbit loss deposition), and diagnostic relationships (*e.g.*, optical and IR views, the proximity to RF Antennas of magnetic diagnostics for control and MHD measurements, *etc*.).

7.2.2.6 NCSX Co & Counter NBI Configurations

Balanced co- and counter-tangential NB injection is needed to provide control of the neutral-beam driven currents, as discussed in Chapter 10, and to provide control of the driven rotation (and thus electric field) for transport studies. Configurations for 2 Co and 2 Counter NBI configurations have been studied using the constraints listed above in Sections 7.2.2.1 – 7.2.2.5. Figure 7-8 shows a candidate configuration for 2 Co and 2 Counter NBI system in the combined Test Cell. The planed site layout will also accommodate beam configurations with three co- and one counter-injected beam.

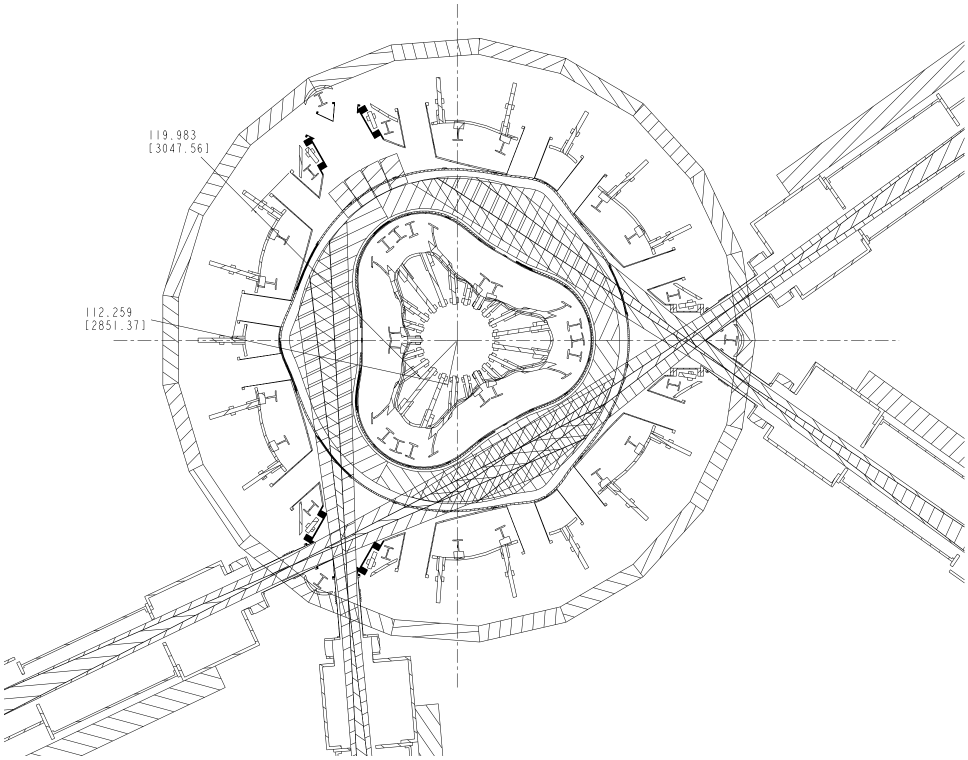

Figure 7-8. Candidate configuration for 2 Co and 2 Counter NBI system

A critcal element in this configuration is the transition duct region. Each transition duct region is shared by 2 beamlines ,and nearby walls receive power from an oppositely directed NBI. Figure. 7-9 shows one possible conceptual design of a transition duct region consistent with the principles given above.

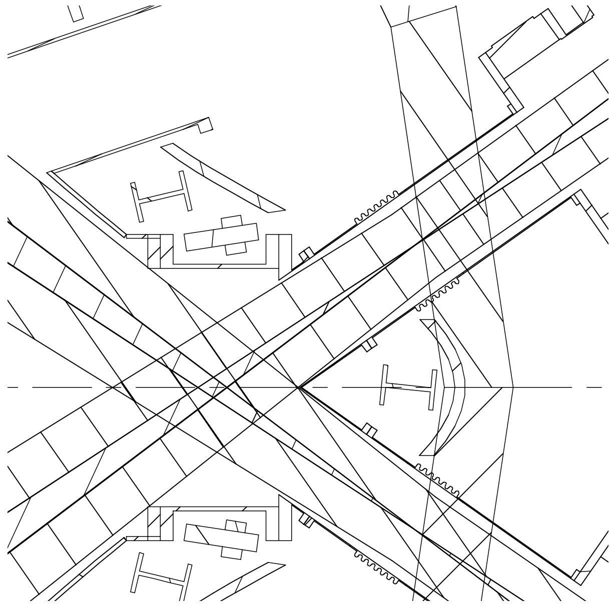

Figure 7-9. Conceptual design of a transition duct region

7.3 Fast Ion Confinement Analysis for NCSX

7.3.1 Introduction

Neutral beams will provide one of the primary heating methods for NCSX; up to 6 Mw of beam power will be available in the 40 to 50 keV energy range. These beams will be injected tangentially in both the co- and counter- directions in order to minimize beam driven currents. In addition to plasma heating, beams are also expected to provide a means for external control over the level of toroidal plasma rotation velocity and its profile.

NCSX has been designed to be as toroidally symmetric as possible in magnetic Boozer coordinates.[1] This leads to improved energetic beam ion confinement and higher predicted heating efficiencies in comparison to more conventional stellarators. However, even in such an optimized stellarator, there will remain some non-zero departure from perfect symmetry. These deviations will lead to somewhat enhanced levels of beam ion losses above those present in an equivalent symmetric tokamak. For example, localized magnetic wells in the stellarator can result in small fractions of locally trapped orbits that drift directly out of the plasma; this ripple can additionally cause banana orbits trapped in the 1/R wells to gradually leave the plasma due to the successive perturbations in their bounce points. Barely passing particle orbits are also perturbed by low levels of this ripple; their orbits can become stochastic over many toroidal transits and leave the plasma.

The above orbital effects require careful analysis for neutral beam heating since they are especially exacerbated by the nearly collisionless nature and high transit speed of the beam ions. This forms the motivation for the following set of calculations. The model described below is used for estimations of beam heating efficiencies (important for plasma performance estimations), scaling of heating efficiency with machine size and magnetic field level, parameter studies of the optimum beam injection tangency radius and toroidal injection location, and loss patterns of beam ions on the vacuum chamber wall (important for placement of wall armor and for minimizing the generation of impurities by the energetic beam ions).

- **Description of Model**

Our model (the DELTA5D[2] code) is based on the geometry shown in Figure 7-10. A pencil beam (zero width) is injected into the plasma on the equatorial plane ($\theta = 0$) aimed at a particular toroidal angle $\zeta_{inj.}$ and tangency radius, R_{tan} which can be varied. The deposition profile for the beam is externally specified and is obtained from the modeling of similar axisymmetric systems (using the cross-sectional shape at the $\zeta = \pi/3$ plane) using TRANSP[3]. Particles are initially distributed over flux surface locations in consistency with this deposition profile. Only flux surfaces having major radii (at $\theta = 0$) > R_{tan} are populated with beam ions. The initial beam ion pitch angle distribution in $v_{\|}/v$ is then determined by taking the ratio of the beam tangency radius to the local value of major radius where the particle is born.

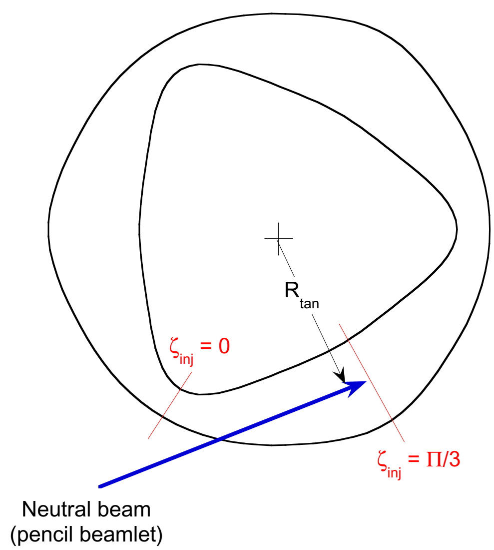

Figure 7-10. Geometry used for NCSX neutral beam calculations

From these initial conditions, the beam particle orbits are then followed by solving Hamiltonian guiding center equations which time advance the particles in the two angular coordinates (poloidal and toroidal angles in Boozer coordinates) and the conjugate momenta. Equilibrium magnetic fields are obtained from the VMEC stellarator equilibrium code[4] which are then transformed to Boozer coordinates.[1] Collisions with a static background plasma consisting of electrons and two background ion species (a main ion and one impurity component) are simulated using a Monte Carlo collision operator[5] based on pitch angle and energy scattering terms, taking into account the full velocity-dependent potentials[6] without assumptions regarding relative orderings of the electron, beam ion and impurity velocities. Collisions are allocated on a fixed time step Δt_{coll} which is chosen so as to maintain $\nu\Delta t_{coll} << 1$ and to allow a smooth granularity in modeling the collisional processes. The time integration step for the orbit integration is controlled by the ordinary differential equation solver LSODE[7] which internally choses an integration time step so as to maintain a prescribed accuracy level. The typical variation of the different beam ion collision frequencies with velocity and flux surface included in this model are shown, respectively, in Figures 7-11(a) and 7-11(b).

The subscripts on the collision frequencies denote the species (electrons, ions, impurities) which the beam is colliding with and whether the collision frequency pertains to pitch angle deflection (D) or energy scattering (E). Currently we do not include collisions with neutrals. Typically, the beam ions are injected at a velocity where they are slowing down somewhat more

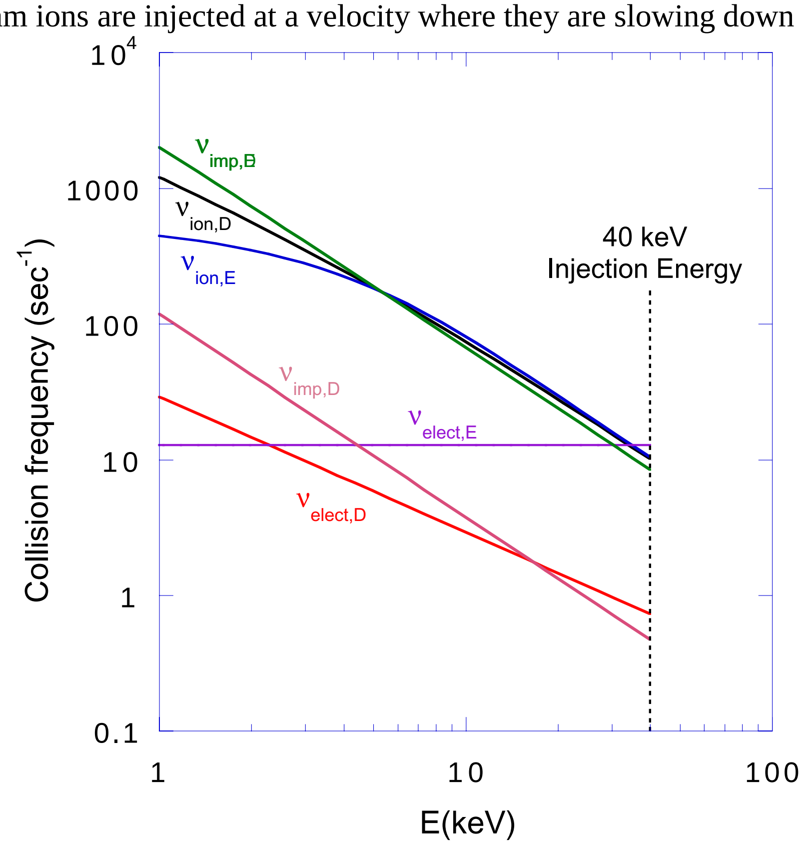

Figure 7-11(a). Collision frequencies vs. energy at r/a = 0.5 (collision frequencies with D/E subscripts denote pitch angle/energy scattering rates, respectiveley; ion, elect, imp subscripts denote beam collsions with plasmas ions, electrons, and impurities)

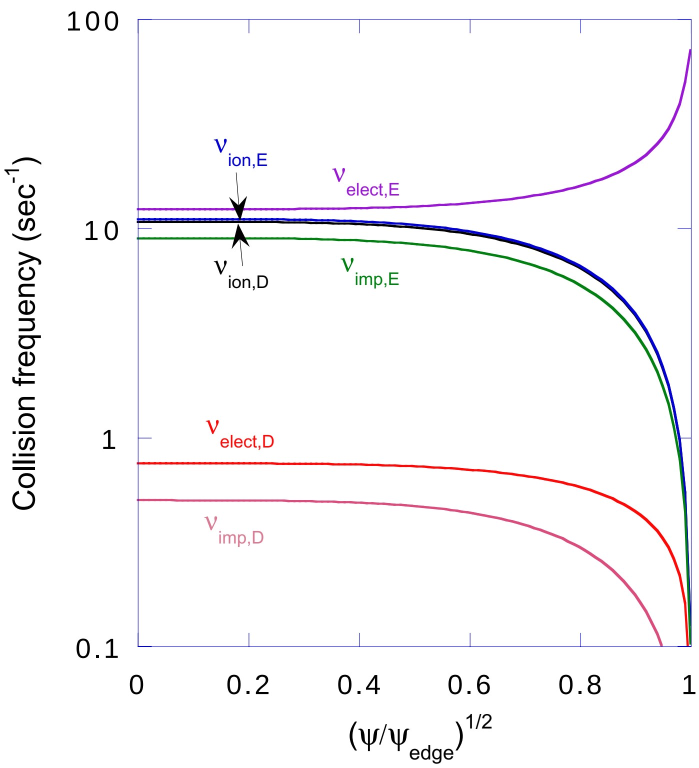

Figure 7-11(b). Collision frequencies vs. flux surface at E = 40 keV (collision frequencies with D/E subscripts denote pitch angle/energy scattering rates, respectiveley; ion, elect, imp subscripts denote beam collsions with plasmas ions, electrons, and impurities)

on electrons than ions, but they soon pass through the critical energy, below which they begin slowing down more on ions. Also as the beam ions pass through the critical energy, pitch angle scattering begins increasing; this can result in higher fast ion losses as the ions get scattered out of the passing region of velocity space. As the beam ions slow down to 3/2 kT_{ion} (with T_{ion} being the background field ion temperature), they are counted as part of the background plasma species. Beam ions that pass through the outer flux surface are removed from the distribution and not replaced; thus, the quoted loss rates may be a slight overestimate. Beam heating efficiencies are calculated by recording the losses of particles and energy out of the outer magnetic flux surface that occur during the slowing-down process. The DELTA5D[2] code follows groups of beam particles on different processors in parallel using the MPI language for inter-processor communication. It has been adapted to both the Cray T3E and IBM-SP computers. A variety of diagnostics of the escaping particles, such as pitch angle, energy and particle lifetime distributions, are retained to aid in understanding the loss mechanisms.

In Figures 7-12(a) and 7-12(b) we show some of the characteristics of a slowing-down beam for the parameters $n(0) = 6 \times 10^{19}$ m^{-3}, $T_e(0) = T_I(0) = 2.4$ keV. Figure 7-12(a) shows on the left-hand scale the time evolution of the percentage of energy lost from the beam averaged over the ensemble of 4,096 particles used here. We normally follow the distribution of beam particles until this energy loss fraction reaches a saturated plateau; this flattening is associated with the average beam ion slowing down to the 3/2 kT_{ion} energy level [shown on the right-hand scale in Figure 7-

12(b)]. Figure 7-12(a) also shows the time variation of the ensemble averaged ratio of magnetic moment to energy for the beam. Initially this ratio starts out small due to the anisotropic nature of the beam (i.e., composed mostly of passing orbits) and then increases as the beam pitch angle scatters and spreads out to become more isotropic. Finally, Figure 7-12(b) shows the decrease in time of the number of beam particles, indicating the degree to which particles are lost at times prior to that required for slowing down enough to join the background distribution.

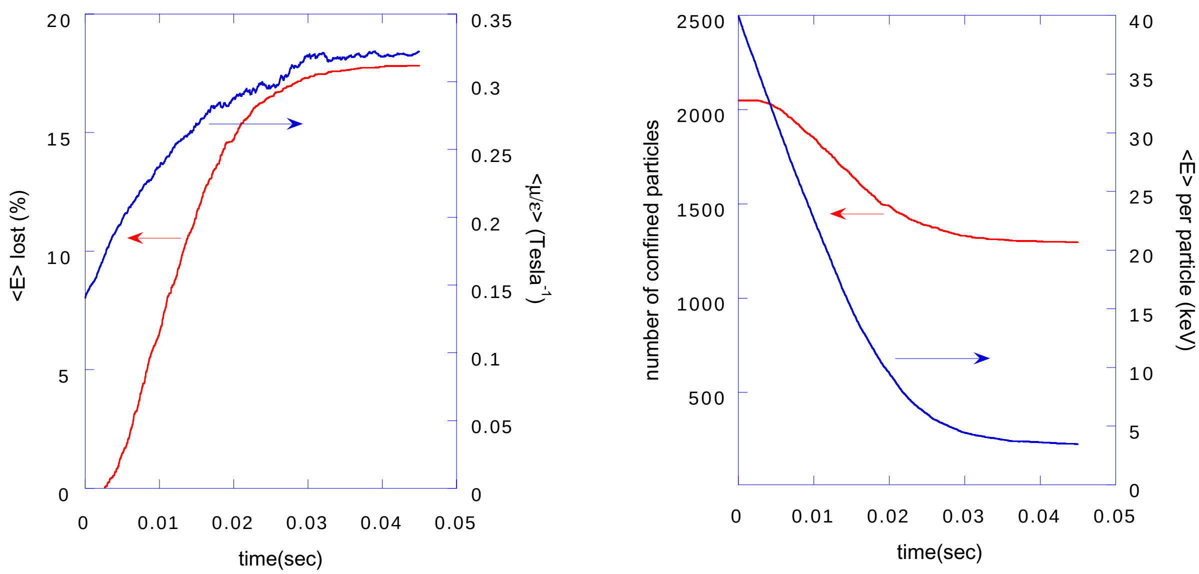

Figure 7-12(a). Typical evolution of ensemble averaged beam energy loss and <μ/ε>; (b). Decay in time of the number of confined beam particles and average energy per particle

Figures 7-13(a) and 7-13(b) show histograms of the energy and pitch angle distributions of the escaping beam ions for the case shown in Figure 7-12. As can be seen, the energy losses are characterized by a broad peak centered around 15 - 20 keV for both co- and counter- injection. The counter-injected ions also show a very sharp peak at the injection energy, presumably associated with prompt losses. The pitch angle distributions of escaping ions shown in Figure 7-13(b) are mostly peaked around the deeply trapped range of pitch angles with a secondary peak (for the co-injected ions) more in the transitional region. The counter-injected ions show a very sharp peak near $v_{||}/v$ = 0.6 - 0.7 which is close to the birth pitch angle, indicating a prompt loss component for the case of a tangency radius R_{tan} = 1.7 m.

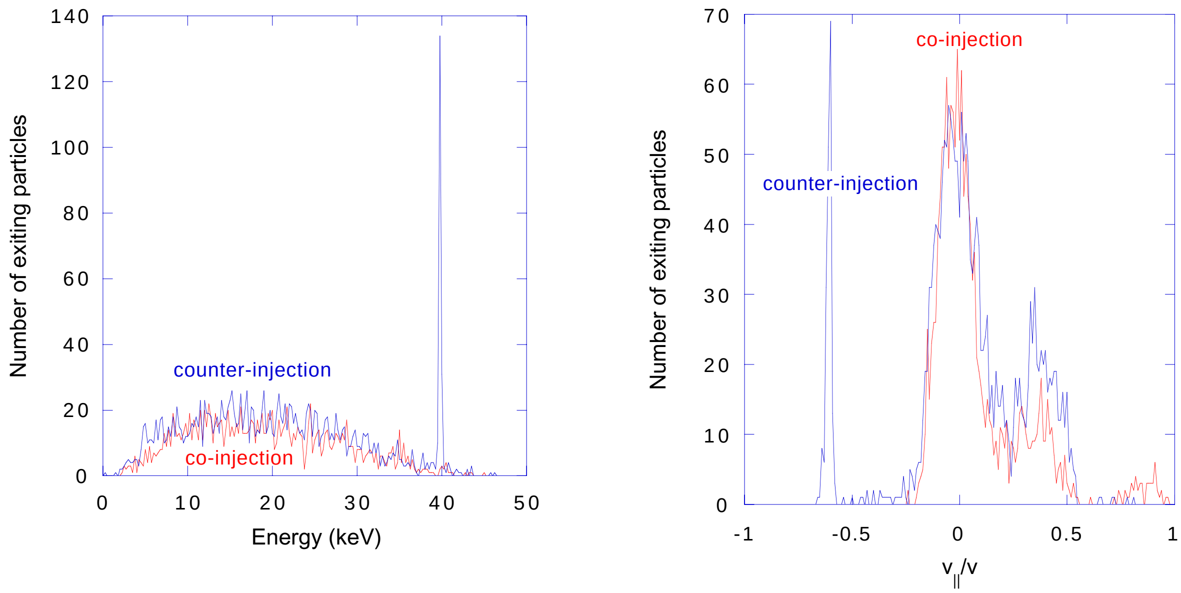

Figure 7-13(a). Energy spectrum of exiting beam particles; (b). Pitch angle spectrum of exiting beam particles

• Parameter Scans

We have used the model described above to study sensitivity to variations in configuration, beam and plasma parameters. In Figures 7-14, 7-17 through 7-19, we have used an earlier sizing of NCSX,[8] LI383, with a volume averaged magnetic field of 2 Tesla, and an average major radius of 1.7 meters. The central plasma density is nominally 6 x 10^{19} m^{-3} and the central ion and electron temperatures are set to 2.4 keV; the plasma species is hydrogen. An impurity species is present with Z = 18, A = 9, at 1% of the electron density, and a temperature equal to the background ion temperature. The beam is also taken as hydrogen and is monoenergetic at injection with an energy of 40 keV. The beam is initially deposited at $\theta_{inj} = 0$, $\zeta_{inj} = \pi/3$. Plasma profiles for temperature and density go as $1 - \psi^2$ and the ambipolar potential is set to zero. In the results for Figures 7-15 and 7-16 we have used the same configuration, although with design point parameters chosen for R_0 = 1.4 meters and <B> = 1.23 Tesla; temperatures and densities for these cases are based on transport modeling.

In Figure 7-14 the sensitivity of losses to the beam injection angle and tangency radius for co- and counter-injected beams in a <B> = 2T and R_0 = 1.73 m device is examined. In Figure 7-14(a) the toroidal angle at which the beam ions are initially deposited is varied, going from the beginning of the field period ($\zeta_{tan} = 0$ symmetry plane) to the half field period point ($\zeta_{tan} = \pi/3$); these two angles have been shown in Figure 7-10. Beam losses only depend weakly on the injection location due to the fact that most losses only occur after many transits around the stellarator after which collisions presumably will have spread out the beam distribution more uniformly in toroidal angle and erasing any memory of the initial particle loading. Nevertheless, there is some variation of losses with changes in ζ_{tan} and it appears that there is an optimum around $\zeta_{tan} = \pi/4$ for both co- and counter-injected beams. The reasons for this slight minimum in losses have not been investigated yet, but are expected to be caused by the dependencies of the first orbit losses on the injection angle.

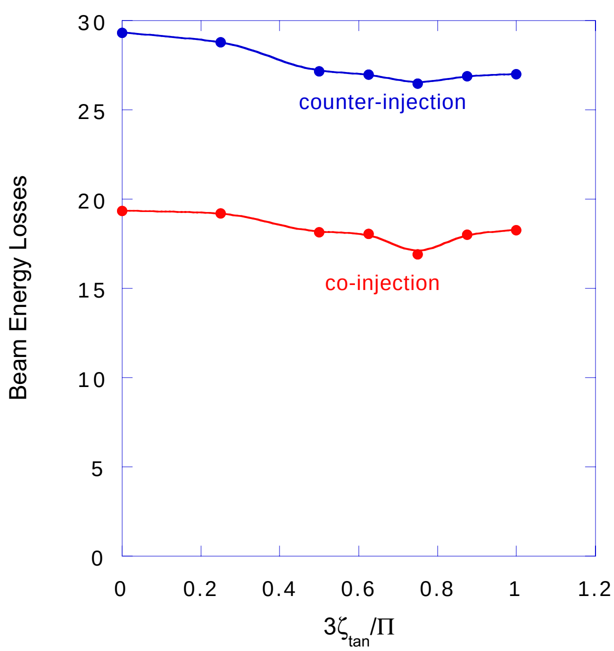

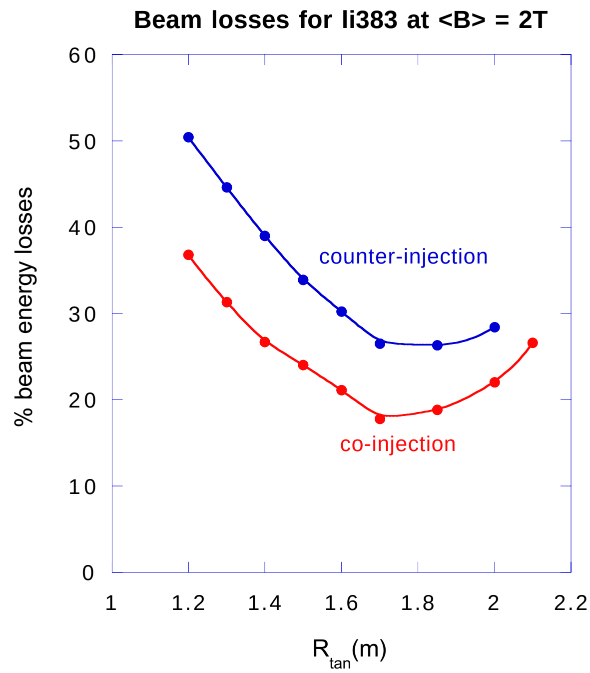

Figure 7-14(a). Dependence of beam losses on toroidal injection location; (b). Dependence of beam losses on beam tangency radius for a version of NCSX with R_0 = 1.73 m.

In Figure 7-14(b) the tangency radius for injection is varied. As the tangency radius is made smaller, the beams are initially launched onto larger pitch angles relative to the magnetic field (smaller $v_{\|}/v$). This puts them closer to the trapped-passing transitional regime of velocity space where orbits are more likely to experience prompt losses. As may be seen, the losses steadily increase for both co- and counter injected ions as R_{tan} is decreased. The minimum of these curves is close to the point where R_{tan} = the magnetic axis location. For this configuration the magnetic axis at the toroidal injection angle ($\zeta_{inj} = \pi/3$) was 1.68 m. As R_{tan} is increased beyond this point, losses again increase due to the fact that the beam ions are progressively being aimed further out in minor radius leading to hollow deposition profiles and increased fractions of prompt orbit losses. For subsequent analysis, the injection angle was chosen so that $\zeta_{tan} = \pi/3$ to best matches the beam and plasma cross section. The tangency radius is taken to be the magnetic axis location.

In Figure 7-15 we investigate the variation of beam losses with injection. Results presented in the previous Figures have been based on a 40 keV injection energy. The beams anticipated for NCSX will be capable of going up to 50 keV, but will also include lower energy components. For Figure 7-15, we have also shifted our plasma and machine parameters to the planned experiment with R_0 = 1.4 meters, <B> = 1.23 Tesla, average temperature for ions and electrons = 1.26 keV and average electron density = 6.8 x 10^{19} m^{-3}; these correspond to peak temperatures and densities of 1.58 keV and 8.5 x 10^{19} m^{-3} respectively (here we have used profiles that go as $1 - \psi^2$). Although the device size and magnetic field strength are smaller for this case, the beam losses are also lower due mostly to the fact that the slowing down time is shorter for these parameters. Another factor which keeps beam losses lower here is that the critical energy (E_{crit}) where the fast ions begin slowing down more on background ions than electrons is lower. For these parameters, it is around 23 keV while for the earlier parameters [$n(0) = 6 \times 10^{19}$ m^{-3}, $T_e(0) = T_I(0) = 2.4$ keV], E_{crit} was around 34 keV. This lower E_{crit} also is likely to account for the fact that beam losses seem to actually get slightly lower with increasing energy for the co-injected beams from 30 up to 50 keV. This is caused by the fact that below E_{crit} pitch angle scattering rapidly increases resulting in beam ions being scattered into the more lossy transitional and trapped orbits. As the initial beam energy is increased above E_{crit}, the beam ions can undergo more energy slowing down without as much pitch angle scattering, resulting in a smaller proportion of the initial beam energy being lost through scattering into unconfined orbits. In Figure 7-15 we show results both for (a) hydrogen beams injected into a hydrogen plasma, and (b) deuterium beams injected into a deuterium plasma.

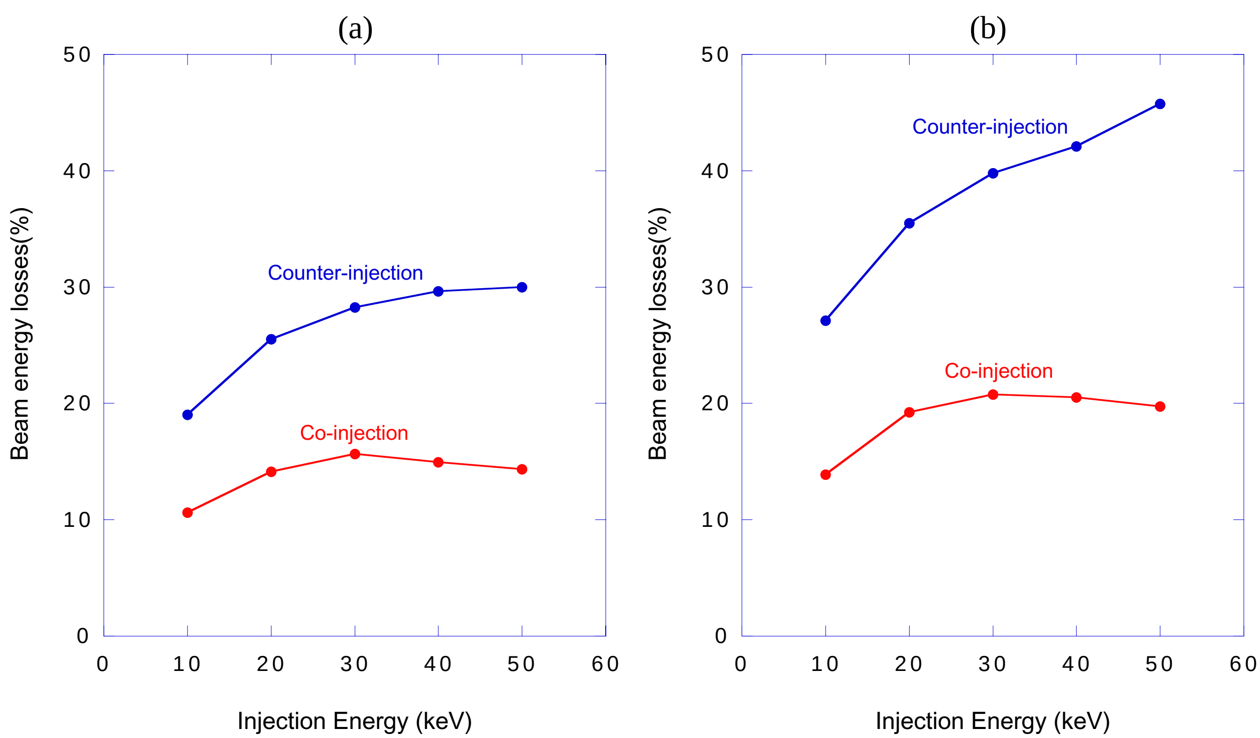

Figure 7-15. Variation of the beam energy losses with injection energy for a recent machine design point at R_0 = 1.4 m, <B> = 1.23 T, $n(0) = 8.5 \times 10^{19}$ m^{-3}, $T_e(0) = T_I(0)$ = 1.58 keV for (a) Hydrogen beams injected into a hydrogen plasma, and (b) Deuterium beams injected into a deuterium plasma

In Figure 7-16 we examine the variation of beam losses as the magnetic field is changed, using the R_0 = 1.4 m device and 40 keV beams. Here we have used profiles for temperature for temperature and density obtained from transport modeling with $n(0) = 8.1 \times 10^{19}$ m^{-3}, $T_i(0) = 1.9$ keV, $T_e(0) = 2.9$ keV.

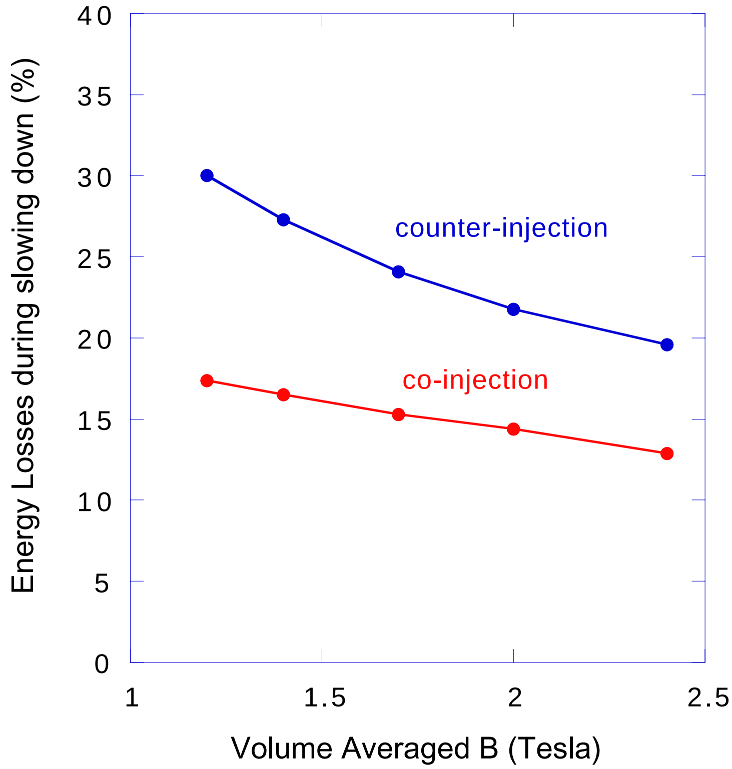

Figure 7-16. Variation of beam losses with magnetic field for 40 keV hydrogen ions for a device with R0 = 1.4 meters

The results shown in Figure 7-16 at <B> = 1.23 Tesla have also been used in the transport predictions of Chapter 8.

- **Loss Patterns of Beam Ions on Outer Flux Surface**

As indicated in Figure 7-13(a), a large fraction of the escaping beam ions leave the plasma with 1/3 to 1/2 of their initial injection energy. It is desirable to intercept this power deposition on the vacuum chamber wall by localized protective armor plating to minimize impurity generation and wall erosion. In order to design such structures, it is necessary to make estimates of the wall locations where the escaping beam ions will be deposited. Within the above Monte Carlo model, as the beam ions leave the outermost closed flux surface, their exit locations, exit times, pitch angles and energies are recorded. If it is assumed that beam ions then move rapidly through the unclosed outer flux region, this information can be useful in estimating power loading patterns on the vacuum chamber walls. More realistic models may eventually be developed which follow the fast ion trajectories in the outer region where flux surfaces no longer exist. Results based upon the current model are shown in Figure 7-17 for a typical case. Here the exit locations are plotted in Boozer poloidal and toroidal angle coordinates for the outermost flux surface. Colors are used to indicate the energy at which the fast ions leave the surface. As can be seen, most of the ions leave at intermediate energies from 10 - 20 keV, in similarity with Figure 7-13(a).

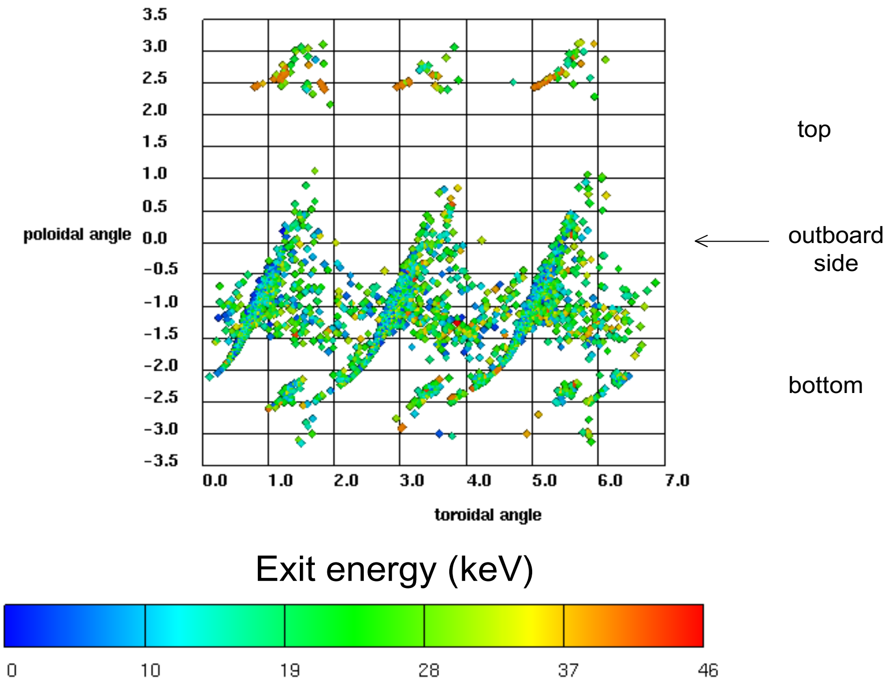

Figure 7-17. Location and energy spectrum of beam losses on outer surface in 2D Boozer coordinates

The fast ion losses are primarily concentrated in helical stripes on the bottom of the stellarator with one stripe per field period (this would presumably shift to the top of the stellarator with reversal of the magnetic field direction). We have also transformed this data into more geometric coordinates. In Figure 7-18 we plot the data of Figure 7-17 vs. the normal cylindrical azimuthal coordinate, $\phi_{cylindrical}$ and a poloidal angle, θ, which is equal to $\tan^{-1}[z/(R-R_0)]$.

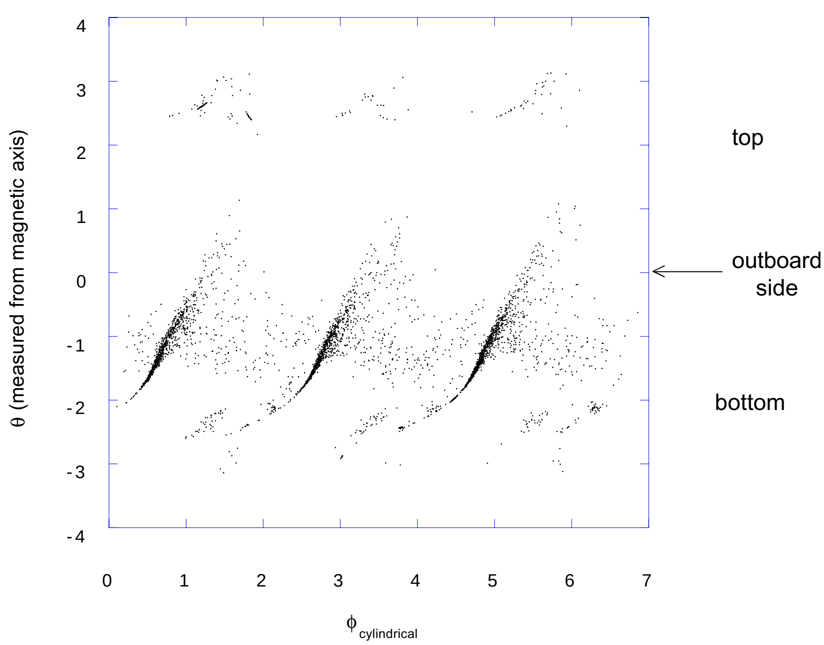

Figure 7-18. Location of beam losses on outer surface in 2D real space coordinates

Finally, we have plotted the ion loss locations on the three-dimensional outermost flux surface (Figure 7-19) as obtained from the VMEC stellarator equilibrium code. The flux surface is shown in red and the ion exit locations are color coded according to the ion's energy at the time it passes through the flux surface. Again, it can be seen that the losses are somewhat concentrated, motivating the design of protective structures at these locations. These issues will be further discussed in Chapter 11.

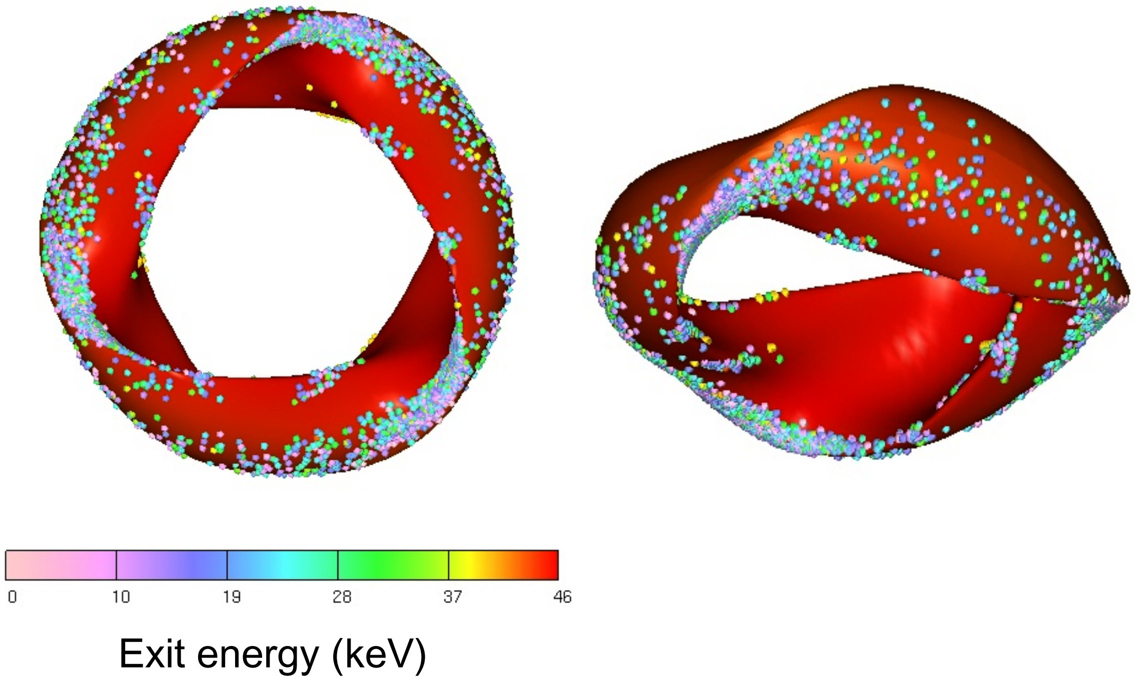

Figure 7-19. Location and energy spectrum of beam losses on outer surface in 3D

7.3.5 Suggestions for Future Work

The model described here has been developed for comparative studies of different NCSX configurations and to obtain approximate estimates of beam heating efficiencies and loss patterns. In order to develop an adequate physics understanding of fast ion confinement in a real experiment, a number of upgrades and new tools will need to be developed. Although many of these issues have already been thoroughly examined for tokamaks, the inherently 3D nature of the stellarator geometry will, in many cases, require a complete re-development of existing tools.

In the area of neutral beam deposition, finite width, multiple energy group beam models will need to be developed and their intersection with the 3D flux surface shapes taken into account. As the beam ions slow down, collisions with neutrals and multiple impurity species should be modeled; beam-beam self collisions and finite beam gyroradius effects may also be of relevance for some regimes. A number of additional physics diagnostics for beam ion effects can readily be included in the Monte Carlo calculations. For example, beam-driven currents and transfer rates of beam energy to the different plasma species can be obtained. Other diagnostics, such as predictions of the energy distributions of charge exchange neutrals escaping the plasma, can be useful in interpreting charge exchange measurements.

The beam slowing down model described here assumes nested, closed flux surfaces. Stellarators can develop magnetic islands and open field lines at some point near the plasma edge. In determining beam loss rates through these regions as well as beam loss patterns and heat loads on walls and divertors, it could be important to follow beam ion orbits into these regions by matching together Hamiltonian orbit models for the inner closed surface region with more conventional real space guiding center drift models for the regions outside the last closed flux surface.

7.4 High Frequency Fast Wave Heating

7.4.1 Introduction

The RF heating system for NCSX will be designed to deliver 6 MW of radio frequency (RF) power to the plasma. The baseline technique chosen for RF heating is High Frequency Fast Wave (HFFW) heating. HFFW is closely related to High Harmonic Fast Wave (HFFW) heating, which has recently been applied in the National Spherical Torus eXperiment (NSTX). HHFW, like HHFW, utilizes fast magnetosonic waves at high harmonics of the ion cyclotron frequency, which minimizes ion damping while producing strong damping on the electron population. However, because of the higher confining magnetic field in NCSX, compared to NSTX, operation at high harmonics in NCSX implies much higher absolute frequencies. The operating frequency chosen for NCSX is 350 MHz. This choice of frequency dictates the use of klystrons for power sources, and folded-waveguide launchers for coupling RF to the plasma.

One of the primary drivers for the choice of HFFW heating for NCSX was launcher accessibility to the plasma, compatible with the earlier coil designs. Accessibility restrictions have relaxed with the design change to modular coils. As a result, an alternative RF heating technique is now available - mode conversion heating with a high field side launch, discussed in the next section.

At present there is no projected need for current drive capability in order to cancel residual currents driven by neutral-beam injection during unbalanced injection, or to further tailor the equilibrium. However, the available heating techniques lend themselves to current drive, so that if current drive became desirable for any reason only minor modifications to the heating system described here would be needed.

7.4.2 Advantages of HFFW Heating

1) Insensitivity to the magnetic field. The absorption mechanism for fast waves on electrons is Landau damping, which is not dependent on cyclotron resonance effects. 2) Strong damping. NCSX is expected to operate at moderately high susceptibility ($\omega_{pe}^2/\Omega_{ce}^2 \sim 5$), which is a regime intermediate between conventional tokamaks and the spherical torus. High per-pass damping can be expected for a wide range of operating parameters. 3) Readily available sources and a coupling system which should be insensitive to minor variations in the plasma loading. 350 MHz 1 MW CW klystrons have been developed for particle accelerators. Isolators are available

which would allow the klystrons to operate into any load, reducing the risk of source arcs if the plasma edge, and the resultant load seen by the coupler, changes suddenly. 4) The ability to use compact, folded waveguide couplers. 5) If needed, the ability to drive current in a broad profile. 6) No significant heating of the bulk ions. No significant damping on the neutral beam ions, especially if no current drive is desired so that the launched parallel wavenumber can be relatively large (a slow parallel phase velocity inhibits current drive while increasing bulk electron damping).

7.4.3 High Frequency Fast Wave Heating in NCSX

In Figure 7-20 is shown a calculation of the per-pass absorption for HFFW for a model equilibrium with a peak density of 6×10^{19} m^{-3}, a launched $N_{\|}$ ($\equiv ck_{\|}/\omega$) = 6.8, central magnetic field of 1.2 T, in a hydrogen plasma with a density profile assumed to be (parabolic)$^{0.5}$. A 2% population of fast neutral-beam injected particles is assumed, to check damping on fast ions. Damping is seen to be adequate for central electron temperatures in excess of a few hundred eV.

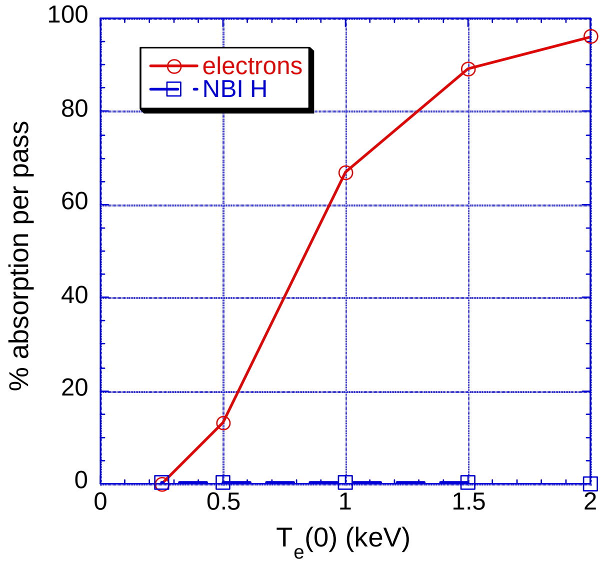

Figure 7-20. Per pass damping as a function of central electron temperature

In Figure 7-21 is shown the computed variation of per-pass damping with central magnetic field. Clearly this heating technique is largely insensitive to the operating field. The primary effect of lowering the field from 2T to 0.8T, for fixed $k_{\|}$ at the launcher, is to increase (ω/Ω_{ci}) and therefore increase $k_{\perp}$. Hence the integrated damping decrement increases slightly, as can be noted in Figure 7-21. In practice, reducing the field would be expected to decrease confinement, so that the target parameters would likely be reduced at lower field. The inverse scaling of $k_{\perp}$ with magnetic field would maintain strong damping at lowered field.

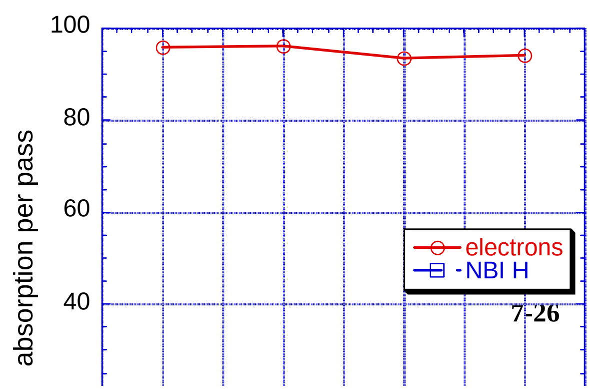

Figure 7-21. Per-pass damping for HFFW as a function of magnetic field

The modeling of HFFW absorption shown in Figures 7-20 and 7-21 was performed with the 1-D integral code METS95, which retains ion damping at high harmonic number.

7.4.4 HFFW Current Drive

Although there is no requirement at present that the HFFW system drive current, modeling has indicated that 6 MW of HFFW has appreciable current drive capability. In Figure 7-22 is displayed the results of a 2D axisymmetric calculation of the current drive efficiency as a function of launched $N_{||}$, using the TORIC code.

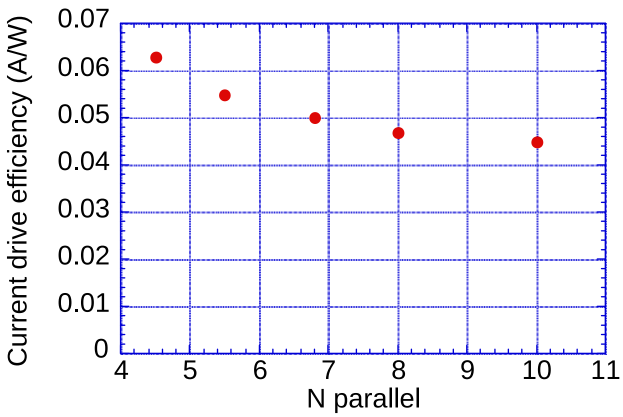

Figure 7-22. Current drive efficiency as a function of $N_{||}$

The highest current drive efficiency is obtained for low $N_{||}$ (or high v_ϕ/v_{Te}). At low $N_{||}$ coupling is primarily to superthermal electrons; hence a decrease in per-pass electron absorption is expected.

This decrease is displayed in Figure 7-23.

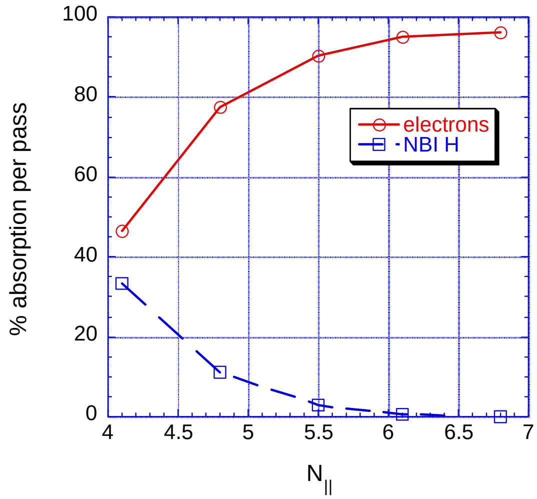

Figure 7-23. Per-pass absorption as a function of $N_{||}$, for 350 MHz HFFW incident on a plasma with $n_e(0)=6 \times 10^{19}$ m^{-3} (parabolic$^{0.5}$), $T_e(0) = T_i(0) = 2$ keV, 2% NBI H. Results from the METS95 code

From Figures 7-22 and 7-23 it is seen that reasonable current drive efficiency can be obtained with a launched $N_{||}$ which is strongly absorbed in a single pass. Therefore the 6 MW HFFW system should be capable of driving ~ 300 kA of noninductive current if needed.

7.4.5 Slow Wave Excitation

A possible concern with the use of fast waves at high frequencies is excitation of the slow or lower hybrid wave in the edge plasma. For 350 MHz the lower hybrid resonance occurs at a density of ~ 5×10^{18} m^{-3}. The right hand fast wave cutoff occurs at a density of ~ 3×10^{18} m^{-3}. In Figure 7-24 is displayed the hot plasma dispersion relation, calculated with the CRF code, for the NCSX model plasma used in conjunction with Figure 7-23. The only slow wave root in evidence is the ion Bernstein wave, which exists between ion cyclotron harmonics and does not couple to the fast wave (lower $k_\perp$) root. The lower hybrid root for these parameters occurs at extremely high $k_\perp$; greater than 10^4 m^{-1}. No coupling from the propagating fast wave to the slow wave would be expected in this case.

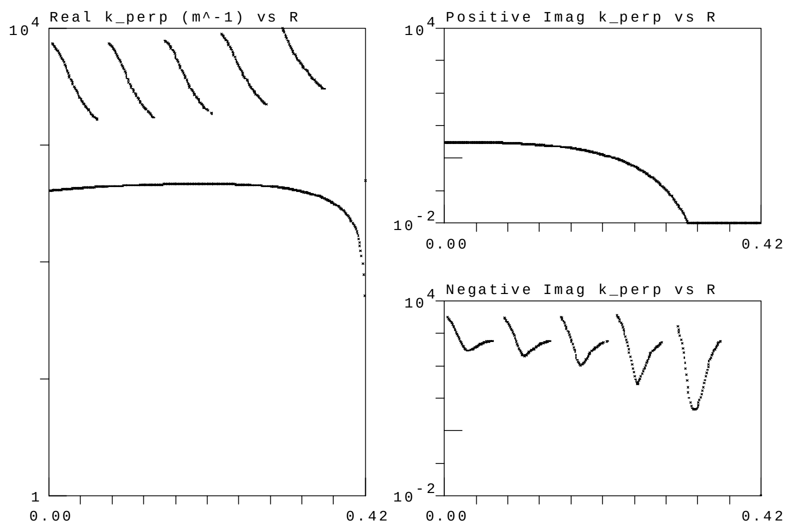

Figure 7-24. Hot plasma dispersion relation for 350 MHz HFFW. The near-vertical roots in the plot of Re($k_\perp$) vs. plasma position denote the ion Bernstein wave roots. The damping decrement for HFFW is given in the positive Im($k_\perp$) plot; the decrement associated with the Bernstein wave is given in the plot of negative Im($k_\perp$). The lower hybrid slow wave root is at $k_\perp > 10^4$ m^{-1}

It should be noted that experiments at 200 MHz in JFT-2M have seen no evidence of coupling to the lower hybrid root.

7.4.6 Launchers

At 350 MHz it is possible to utilize folded waveguide launchers. An example of a dipole folded waveguide launcher designed and built at ORNL as a prototype for installation on the FTU tokamak is shown in Figure 7-25.

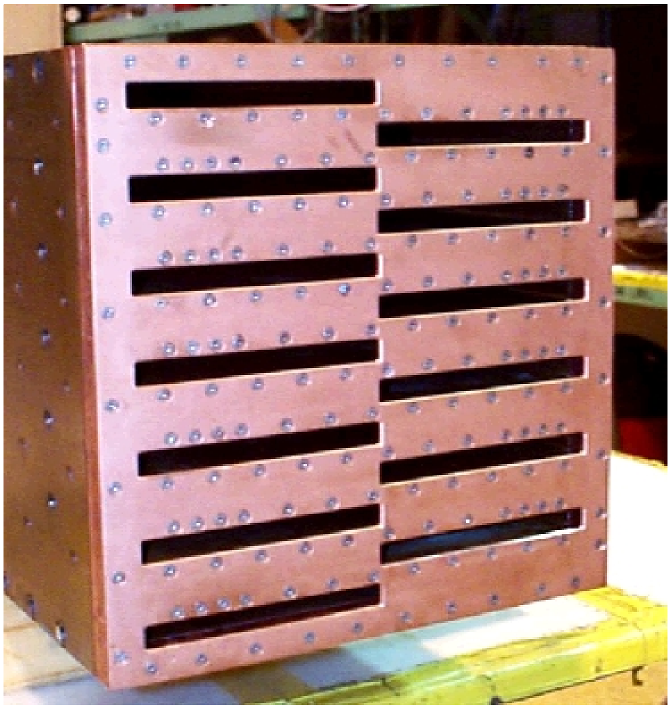

Figure 7-25. 440 MHz folded waveguide launcher, an ORNL prototype designed for FTU

A folded waveguide launcher capable of a directed launch for current drive would be somewhat more complex than a dipole launcher, with at least four apertures in the toroidal direction. Neighboring waveguide apertures would be phased to produce a directed launch of the fast wave.

Six sources (1.2 MW per source, 80% coupled) would be utilized to provide the required 6 MW of coupled power. The baseline design for the 350 MHz coupling system would therefore consist of four folded waveguide couplers, each 24 cm in toroidal extent $\times$ 44 cm in poloidal extent. Each coupler would consist of six apertures, each fed by one of the klystron sources through a four-way power splitter. This arrangement permits arbitrary phasing of the six neighboring waveguide apertures in each coupler, so that the launched $N_{||}$ can be varied in real time if necessary by adjusting the relative phase of the klystron sources. The total coupler area would be 0.42 m^2, which implies a power density at the coupler of approximately 14 MW/m^2 at full power. Folded waveguide couplers have demonstrated the capability of operating at high power density during test stand trials at ORNL. However, achieving this power density in NCSX would likely require that the coupler be closely coupled to the fast wave cutoff density, i.e. that the plasma density at the coupler be near 3×10^{18} m^{-3}.

7.5 Mode Conversion RF Heating

7.5.1 Introduction

In ion Bernstein wave mode conversion heating, a fast magnetosonic wave, excited at the boundary of a multiple-ion species plasma, propagates to the ion-ion hybrid layer where it undergoes conversion to the slow wave. Typically, the damping lengths for the slow ion Bernstein wave (IBW) are many times shorter than for the launched fast wave, so that power deposition occurs in a highly localized region near the hybrid layer. When the ion temperature is modest and the species mix is such that mode conversion takes place far from an ion cyclotron resonance, the IBW damps on electrons. For high ion temperatures, or modest concentration of one of the ion species so that the mode conversion layer is located close to a cyclotron resonance, ion damping can be produced.

Mode conversion heating was first successfully demonstrated using a high field side launch in the TFR tokamak[9]. Efficient, localized electron heating using mode conversion was demonstrated in TFTR[10] and more recently has been extensively utilized in C-MOD. In tokamaks, a low field side launch of the fast wave in D-^{3}He has been most commonly employed. Mode conversion with a high field side launch, which is efficient with a wider variety of ion species mixes, has now been utilized successfully in the LHD, WVII-AS, and CHS stellarators. Modeling of NCSX plasmas has indicated that a high field side fast wave launch is necessary to efficiently access the mode conversion surface. Although such a launch would have been exceedingly difficult or impossible to accommodate with the original saddle-coil design for NCSX, it now appears possible that the modular coil design will permit installation of a high field side "combline" antenna. This type of antenna can be constructed with a very small radial build, which lends itself to installation in a shallow "pocket" in the vacum vessel, on the high field side.

The METS 95 code, a 1-D hot plasma full-wave code which has been extensively benchmarked during mode conversion heating experiments in TFTR and C-MOD, has been employed to model mode conversion in NCSX. Mode conversion scenarios for NCSX have now been identified for D-H and D-^{3}He plasmas. Either ion or electron heating can be selected through an appropriate choice of the species mix and launched wavenumber.

7.5.2 Mode Conversion in D-H

The results of modeling D-H mode conversion are shown in Figure 7-26 (a & b). Figure 7-26a is a plot of the dispersion relation for 10% H in a D majority plasma, with a central magnetic field of 2T, a central electron density of 5×10^{19} m^{-3} (parabolic profile), for a fast wave excited at 25 MHz with a wavenumber of 9 m^{-1}. Note that this and all following modeling is largely invariant in (ω/Ω_i); if operation at a lower magnetic field is desired then the launch frequency must be reduced.

For the ion and electron temperatures chosen (T_e=T_i= 1 keV), METS 95 indicates that majority D/minority H mode conversion will produce relatively weak absorption, with a broad deposition profile on the electron population. Since absorption occurs well to the high field side of the hydrogen cyclotron resonance, a relatively high magnetic field is required to obtain core heating - at 20 MHz the magnetic field scales to 1.6T.

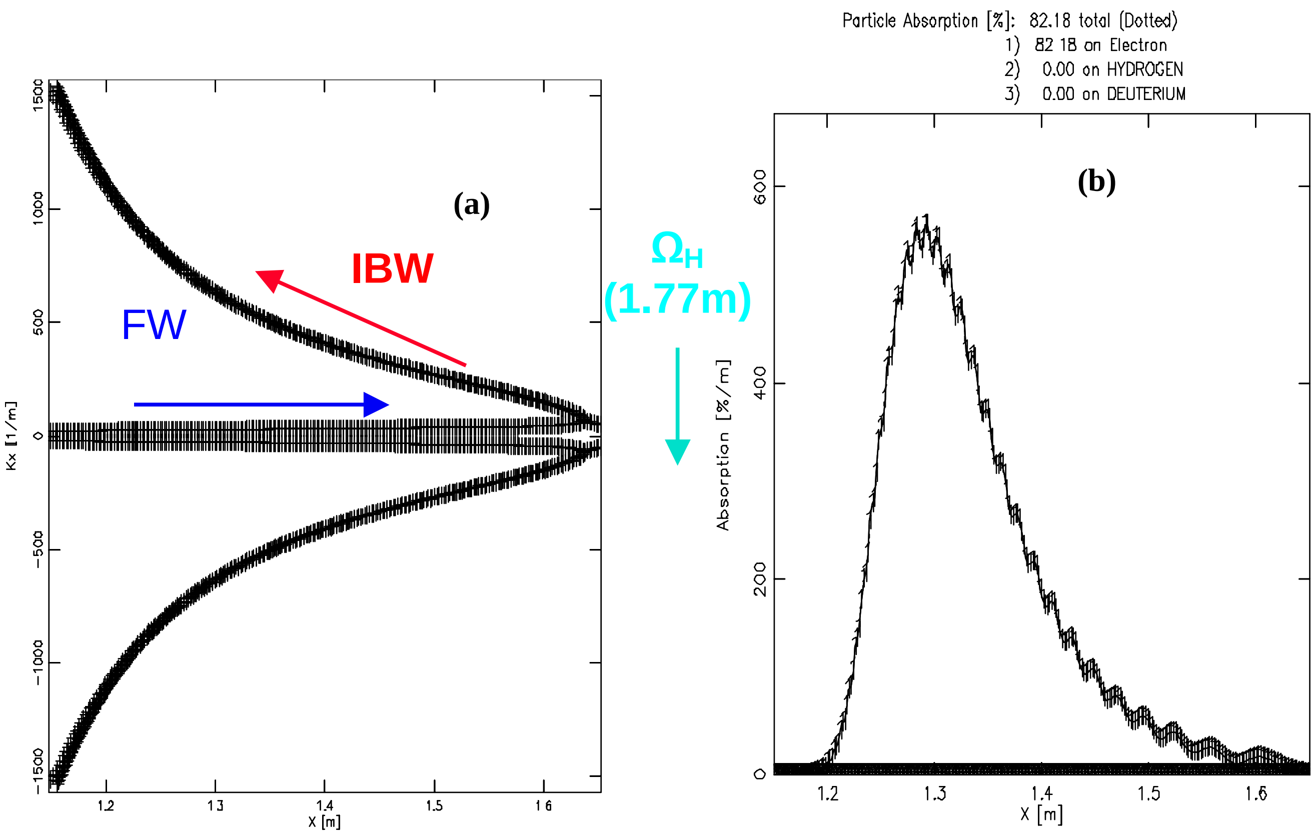

Figure 7-26. Dispersion relation for mode conversion in 10% H/90% D in NCSX (a), and power deposition profile (b). 82% of the launched power is deposited on electrons within the simulation window, with a full-width at half-max of ~15 cm. Central density for the simulation was 5×10^{19} m^{-3} (parabolic profile), central $T_e = T_i$ = 1 keV, 2T, with a launched frequency of 25 MHz and wavenumber of 9 m^{-1}

Although the option to use hydrogenic plasmas would permit access to possible low-recycling regimes, operation at the low toroidal field initially available on NCSX with core heating would require a prohibitively low operating frequency (~15 MHz). Finally, lower hydrogen concentrations (~5%) would allow experiments in conventional light ion minority heating, although the fast ion tail population is not expected to be well confined in NCSX.

7.5.3 Mode Conversion in H-^{3}He

The most promising and flexible ion system for mode conversion heating in NCSX H-^{3}He, which should permit localized ion or electron heating (or electron current drive), either on or off axis. With a transmitter frequency of 20 MHz (the lowest practical frequency for the existing PPPL sources), on axis heating can be obtained at central magnetic fields as low as 1.3T.

Localized electron heating can be produced in H-^{3}He for a wide range of species mixes and wavenumbers. However, ion heating is predicted for low concentrations of either hydrogen (light ion minority) or helium (heavy ion minority). In Figure 7-17 (a & b) the dispersion relation and deposition profile for 10%H in ^{3}He are shown. Deposition is predicted to be primarily on the hydrogen population. In order to produce ion heating it is necessary to launch the 25 MHz fast wave at high wavenumber (12 m^{-1}) in order to obtain Doppler-broadened Bernstein wave damping on the hydrogen..

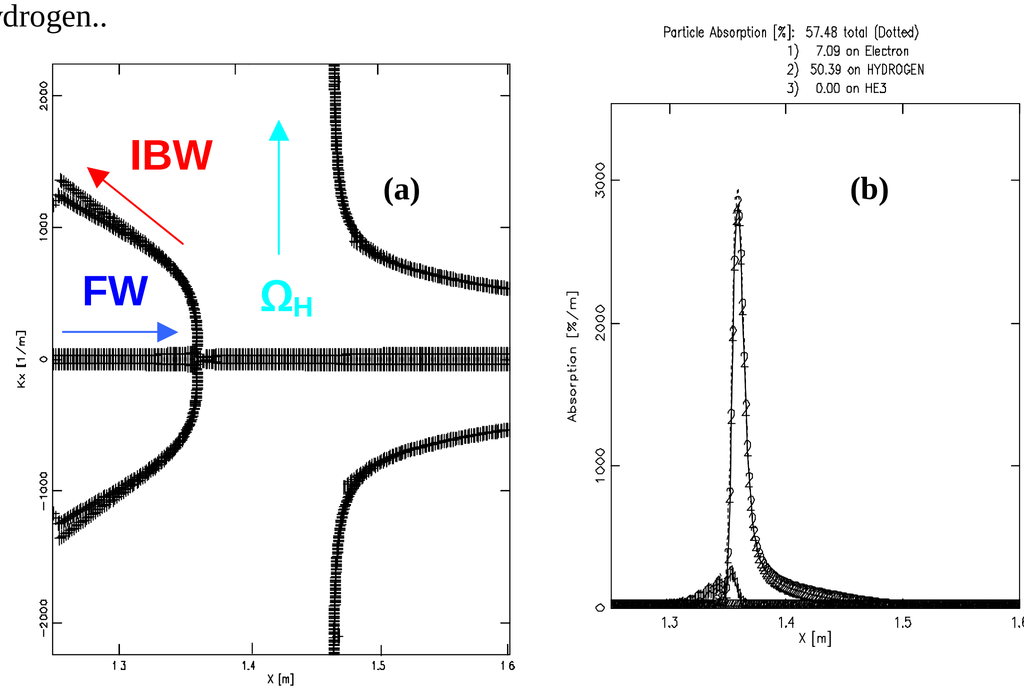

Figure 7-27 (a & b). Dispersion relation for mode conversion in 10% H, 90% ^{3}He plasmas. Excited frequency is 25 MHz at a wavenumber of 12 m^{-1}, with a central magnetic field of 1.6T, central density of 5×10^{19} m^{-3} (parabolic profile), central $T_e = T_i$ = 1 keV. 57% of the incident power is coupled to the hydrogen population via Doppler broadened cyclotron absorption

Ion tail formation under these conditions will be lessened due to the high hydrogen concentration. If a lower launched wavenumber or a higher hydrogen concentration is chosen, then localized electron heating rather than ion heating is predicted. The case modeled here corresponds to operation at 1.3T if the frequency is lowered to 20 MHz. Note that the deposition profile is extremely narrow, with a FWHM of approximately 2 cm. 3D effects will likely broaden the deposition profile, but insofar as the mod-B surfaces are also flux surfaces it is likely that very narrow power deposition profiles can be obtained.

At higher toroidal fields ion heating can be produced with a reduced ^{3}He fraction. In Figure 7-28 (a & b) is shown the dispersion relation and power deposition profile for 10% ^{3}He in a hydrogen minority, for 25 MHz operation at 2.2T.

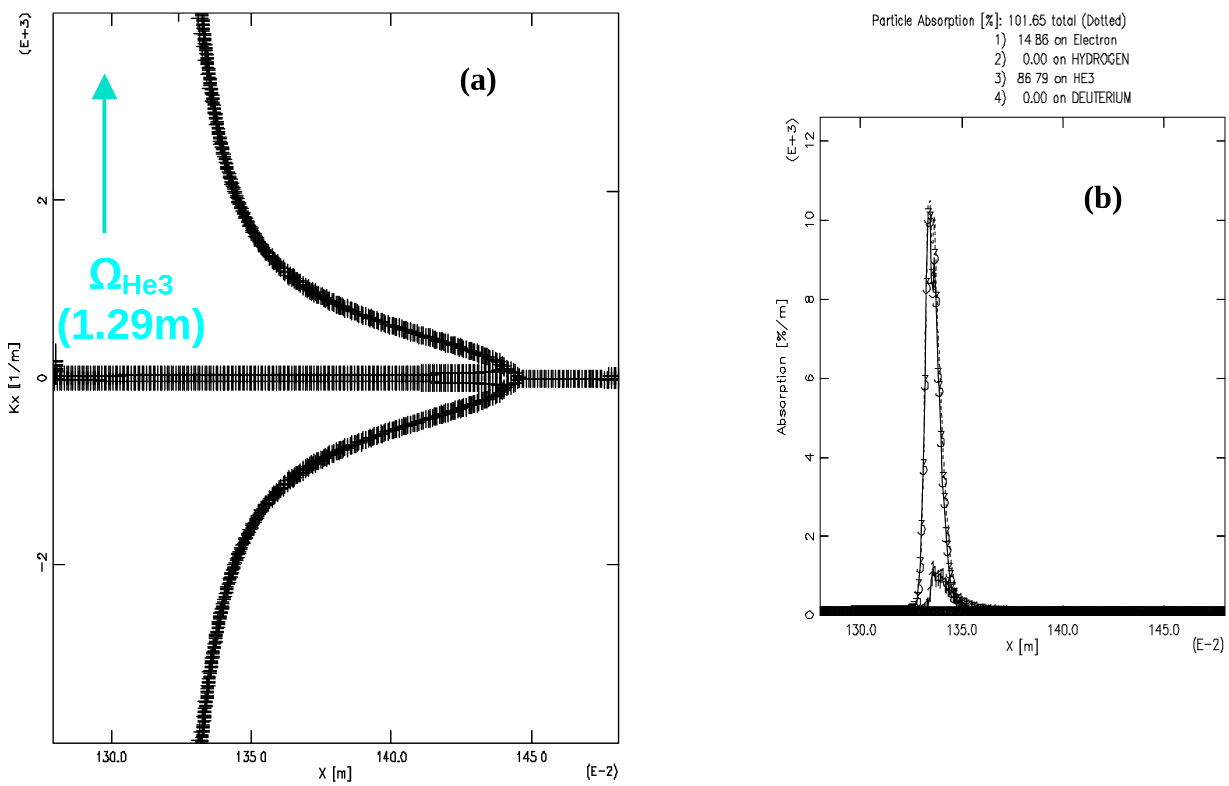

Figure 7-28 (a &b) Dispersion relation and power deposition profile for mode conversion in 10% ^{3}He, 90% H at 2.2T, 25 MHz, launched wavenumber of 6 m^{-1}, central density of 1×10^{20} m^{-3}, 1.0 keV ion and electron temperatures

In this example the magnetic field scales to 1.76T for 20 MHz operation. However, if deposition at the 2/3 radius is desired, then the field scales to 1.5T. Deposition at large minor radius may be acceptable here, since this case corresponds to IBW ion damping near a cyclotron resonance, which is desirable for rf shear flow generation. Note that the deposition layer (at least in this 1-D model) is extremely narrow, with a FWHM of about 1 cm.

For species mixes intermediate to the cases shown in Figures 7-27 and 7-28 (i.e. more nearly equal concentrations of H and ^{3}He), electron damping with a very narrow deposition profile is predicted. This can provide a localized heating source for measurements of the electron thermal diffusivity, or a localized current drive source for modification of the iota profile. Note that with two antennas iota profile modification can be accomplished with a minimal net current drive, by injecting both co- and counter- current.

These capabilities (localized or broad electron heating, localized current drive or current profile control, localized ion heating,, possible rf shear flow drive) combine to make mode conversion heating an attractive physics tool for NCSX.

7.5.4 RF Systems and Antennas for Mode Conversion

As stated earlier, the most attractive antenna for a high field side launch in NCSX is probably the combline, which utilizes "passive" excitation of a wide array of current straps. The combline was pioneered at GA[11] and has been tested on JFT-2M and to some extent on DIII-D. In order to provide the required 6 MW of RF heating, three antennas would be installed in NCSX, on the high field side of the device, with each antenna centered about the "bullet" plasma cross section.

The existing PPPL FMIT units could be used for mode conversion in NCSX, in a time-sharing arrangement with NSTX. An engineering study has determined that operation of two of the four FMIT sources over the frequency range of 20 - 30 MHz is feasible; this would provide 4 MW of rf source power. An additional 3-4 MW would be available from the remaining two sources, depending on the degree to which they were reconfigured. Although the sharing of sources precludes simultaneous RF heating of NSTX and NCSX, the transmitter modifications proposed would require minimal down time to change frequencies. A changeover from the NSTX operating frequency of 30 MHz to one of the NCSX operating frequencies (or the reverse) is expected to take a few days.

References

[1] A.H. Boozer, Phys. Fluids **24** (1981) 1999.

[2] D.A. Spong, J. Carlsson, D.B. Batchelor, et al., Bull. Am. Phys. Soc. **44** (1999) 215.

[3] R.V. Budny, D.C. McCune, M.H. Redi, J. Schivell, R.M. Wieland, Phys. Plasmas **3** (1996) 4583.

[4] S.P. Hirshman, J.C. Whitson, Phys. Fluids **26** (1983) 3553.

[5] A.H. Boozer, G. Kuo-Petravic, Phys. Fluids **24** (1981) 851.

[6] S.P. Hirshman, D.J. Sigmar, Phys. Fluids **19** (1976) 1532.

[7] A.C. Hindmarsh, "Odepack, a Systematized Collection of ODE Solvers, in Scientific Computing," R.S. Stepleman et al. (Eds.), North-Holland, Amsterdam, 1983, pp. 55-64.

[8] M. Zarnstorff, 2000 IAEA Fusion Energy Meeting, Sorrento, Italy (Oct. 2000).

[9] Equippe TFR, in Plasma Physics and Controlled Nuclear Fusion Research, Proc. 9th International Conf., Baltimore, 1982, Vol. 2, p. 17.

[10] R. Majeski et al., Phys. Rev. Lett. **76** (1996) 764.

[11] C. P. Moeller et al., in Radio Frequency Power in Plasmas, Proc. 10th Top. Conf., Boston, 1993 (AIP Conf. Proc. Vol. 289), p. 323.

Chapter 8 – Transport

There are three major transport issues that impact the NCSX design. First, is there sufficient energy confinement to test the MHD stability limit? Second, is the configuration sufficiently quasi-axisymmetric to reduce the neoclassical ripple transport to low levels, thereby allowing tokamak-like transport? Third, is the predicted pressure profile stable at high $<\beta>$?

The energy confinement needed to achieve the $<\beta>=4\%$ design goal is assessed chiefly through the required enhancement factor, H, over a standard stellarator scaling, ISS-95 [1], and the latest tokamak L-mode scaling, ITER-97P [2]. Comparison with tokamak scaling is warranted because the high degree of quasi-axisymmetry effectively eliminates ripple transport, thereby reducing the neoclassical transport to axisymmetric levels. As a result, NCSX may have tokamak-like transport and the ITER-97P L-mode scaling may be an appropriate predictor of the 'low' mode confinement in NCSX. The experimental basis for these scalings is briefly reviewed in Section 8.1.1. The experimental validation of neoclassical transport in stellarators is reviewed in Section 8.1.2; the local transport assessment in Section 8.3 is based on neoclassical predictions. Enhanced confinement (above the ISS-95 scaling) is seen in many stellarators, and is summarized in Section 8.1.3.

In Section 8.2 we present an overview of the confinement required for NCSX; this is assessed using a 0-D model (with fixed profile shapes) based on the profile predictions of a power balance code (Section 8.3). The global confinement scaling assessment is supplemented in Section 8.3 with temperature profile predictions based on solutions of the power balance equations using a combination of analytic neoclassical and anomalous transport. The predicted pressure profile shapes are within the range used in MHD stability studies. The power balance analysis finds that the NCSX design point is 'neoclassically accessible' and that the energy transport due to field ripple is much smaller than the axisymmetric neoclassical energy transport.

8.1 Experimental Basis for Projected Confinement

There are several ways to estimate the confinement of a new configuration. Empirical global scaling relations summarize a wide body of experience (but their extrapolability to a new type of device is unclear). Neoclassical transport theory is expected to set a lower bound on transport, but many stellarator plasmas are at, or near, this lower bound. There are no widely validated models for anomalous transport in stellarators, so the anomalous transport models we use in Section 8.3 are described there.

8.1.1 Global Energy Confinement

The ISS-95 [1] global confinement scaling represents typical confinement in unoptimized stellarators with H-mode discharges excluded. This scaling is based on the 'diamagnetic' stored energy (~total stored energy, including fast ions) and the estimated actual heating power (not the injected power), so we use the corresponding quantities in assessing $H_{ISS\text{-}95}$ for NCSX. The fast ion contribution to the stored energy can reach ~25-30% of the total in low collisionality

<β>=4% NCSX plasmas, which is similar to the fast ion stored energy fraction in neutral beam heated, low density stellarator (and tokamak) plasmas.

Plasmas heated by neutral beam injection and RF waves at the electron cyclotron resonance are included in the ISS-95 database. No confinement difference has been linked to the heating method, but in the database heating method and density are systematically correlated (higher density plasmas are heated predominantly by NBI). There is a further correlation between density and heating power (they rise together); it was possible to determine separate density and heating power dependences for only some of the devices.

Many NCSX parameters lie within the range of the stellarator experiments that make up the ISS-95 database. The exceptions are the minor radius, NCSX is nearly 20% larger than ATF, the aspect ratio, which is slightly lower than that of CHS, and the heating power, which is twice the maximum in the ISS-95 database.

Subsequent to the development of the ISS-95 scaling, LHD [3, 4] has provided confinement data for a much larger stellarator with a minor radius up to twice the size of NCSX (and 10 times its volume), and slightly more heating power than planned for NCSX. Energy confinement in LHD has ranged beyond twice the ISS-95 expectation [5, 6] even at high <β> [4, 7], and has no apparent dependence on heating method [8]. The enhanced confinement is attributed to an edge temperature pedestal [9, 10, 11], which is not generally observed in other stellarators but is not attributed to an H-mode in LHD. The pedestal may be associated with a chain of magnetic islands at or near the plasma edge [9]; island chains are associated with H-modes in W7-AS [12, 13].

The ITER-97P L-mode energy confinement scaling [2] is based on data from many tokamaks, and fits each tokamak individually as well or better than the earlier ITER-89P scaling [14]. Most parameter ranges (e.g., size, aspect ratio, B_o, density, P_{heat}, <β>) encompass the NCSX design point. The exceptions are that the magnetic shear differs dramatically from that in NCSX, q(a) is lower in NCSX, and in the tokamaks all the rotational transform is created by internal currents. In evaluating $H_{ITER\text{-}97P}$ for NCSX we use an effective plasma current, I_p^{eff}, which produces the same q(a) in an equivalent axisymmetric configuration. For the LI383 configuration I_p^{eff} =0.48 MA (R_o/1.4 m)(B_o/1.2 T).

The NCSX goal of <β>=4% with P_{heat}~4.6 MW (R_o=1.4 m, and B_o=1.2 T with the LI383 configuration) can be achieved with $H_{ISS\text{-}95}$=1.8 and $H_{ITER\text{-}97P}$=0.7 in a collsional high denisty plasma. (see Section 8.2). With an additional constraint that the minimum ν_i*=0.25, the required H factors are raised: $H_{ISS\text{-}95}$ to 2.9 and $H_{ITER\text{-}97P}$ to 0.9 (see Section 8.2). While the required confinement is quite unremarkable for an equivalent tokamak, it is slightly better than has been achieved to date in unoptimized stellarators. LHD has a number of nearly steady state discharges with <β>~2% and $H_{ISS\text{-}95}$ up to 2.0 ($H_{ISS\text{-}95}$ rises to 2.4 with dW/dt ~ 0.13P_{abs}). W7-AS reports $H_{ISS\text{-}95}$ up to 2.5 [15, 16] with low recycling conditions. NCSX is similar in size to the PBX-M tokamak, which achieved <β>=6.8% at B_o=1.1 T with 5.5 MW of neutral beam heating at $H_{ITER\text{-}97P}$ =1.7 and an estimated $H_{ISS\text{-}95}$~3.9 [17].

8.1.2 Experimental Confirmation of Neoclassical Predictions in Stellarators

Neoclassical theory sets a lower bound on the transport expected in NCSX, and provides an independent method of assessing the confinement required to achieve the design goals. In a number of instances stellarator experiments are in accord with neoclassical predictions, so they are of more than academic interest. The ambipolar radial electric field is reviewed first because the ion particle and energy ripple transport depends strongly on E_r.

The neoclassically predicted 'ambipolar' radial electric field (the E_r required to produce ambipolar particle flux) is generally in agreement with observations in the core of CHS [18] and W7-AS [19, 20, 21] in the 'ion root' regime. Agreement has also been obtained with net toroidal current and significant magnetic shear in W7-AS [22]. The general agreement even in plasmas with dominantly anomalous energy transport confirms the widespread assumption that anomalous transport is intrinsically ambipolar.

The widespread agreement with the neoclassically predicted electric field is very important because the neoclassical ripple transport is strongly dependent on E_r, particularly the ion channel. It may be possible to modify the radial electric field in NCSX with unbalanced momentum input from the neutral beams. This would allow enhancement of E_r (with little effect on ripple transport) or reduction in order to confirm theoretical predictions of enhanced transport with small E_r.

In the theoretically predicted 'electron root' regime [23] E_r is larger than in the 'ion root' (and of opposite sign), so the transport is correspondingly lower than with the ion root. With an ion root the $1/\nu$ regime helical energy transport scales as $T^{9/2}$, so the electron root would be especially valuable in reactors. W7-AS experiments confirmed that transport is reduced by either sign of E_r [21]. The electron root is frequently predicted, but not usually observed in low-density ECRH plasmas in W7-AS [21] and CHS [24].

Realization of the electron root regime has been experimentally elusive, but it may have been achieved in CHS [25] W7-AS [22, 26] and LHD [27]. The example from LHD is of special interest because there is no non-thermal electron flux involved. In all cases the reduction in transport is less than expected from naive application of the theory; this may be due to a non-diffusive flux of ripple trapped suprathermal electrons (driven by the ECRH absorption) which is outside the standard theoretical treatments [28]. The neoclassically driven E_r may also reduce anomalous transport as it does in tokamaks, but this has only scanty support in stellarators [29]. Manufacturing an 'electron root' with unbalanced neutral injection is also unlikely to achieve the full transport reduction that is produced by the ambipolar electron root E_r because any error in matching the ambipolar E_r is likely to result in increased transport.

In addition to confirmation of the predicted radial electric field, neoclassically predicted ion and electron energy transport is also frequently observed in the core of W7-AS plasmas [30, 22, 20, 21], and the core of ECRF heated CHS plasmas [24]. The transport due to ripple usually exceeds the axisymmetric component in existing stellarators [31, 24, 32]. Transport is greater than neoclassical predictions in the edge of W7-AS and ECRF heated CHS plasmas. Even the core of neutral beam heated CHS plasmas is usually anomalous, but ion confinement in the core of CHS hot-ion mode plasmas is close to neoclassical [33]. ATF reported anomalous electron energy transport even in the plasma core [34, 35], while observing the neoclassically predicted bootstrap current [36]. The anomalous transport in ATF was attributed to dissipative trapped electron mode turbulence, but these - even in combination with ion temperature gradient mode turbulence - do not explain the CHS data [24].

W7-AS has achieved up to $H_{ISS\text{-}95}$ ~2.5 [16], but these plasmas are consistent with neoclassical predictions for r/a<0.7, and the ‘ambipolar E_r’ is consistent with the measurements at all radii [21]. The unusually ‘narrow’ density profile (associated with the low-recycling conditions needed for this high confinement regime) is a key to the enhanced confinement, but not a departure from neoclassical behavior, because the steeper density gradient leads to higher electric fields.

Energy transport in dimensionless scaling experiments with matched CHS and LHD plasmas (with significant anomalous contributions in both devices) found that core transport follows gyro-Bohm scaling and the outer regions had scaling between Bohm and gyro-Bohm [11, 32]. In several cases the anomalous contribution to the ion energy transport in LHD is close to or smaller than the expected neoclassical contribution [11, 32].

In both CHS [18] and LHD [32] ‘inward shifted’ configurations with slightly smaller R_o have somewhat improved energy confinement relative to the standard R_o. The improvement is attributed to smaller neoclassical orbit drifts in these inward shifted configurations, but anomalous transport is significant for all R_o in both devices.

Generally speaking neoclassical theory is reliable for predicting the ‘ambipolar’ radial electric field in stellarators (false predictions of the ‘electron root’ are a notable exception), and the resulting reduction in neoclassical ripple transport (from its level with E_r=0) has been widely validated. Neoclassical predictions of energy transport are frequently accurate in the plasma core, but anomalous energy transport is usually significant or even dominant in the outer plasma and sometimes in the core. Unfortunately, there is no physical understanding of anomalous transport in stellarators that can indicate when it will be important.

8.1.3 Enhanced Confinement Regimes

A number of enhanced confinement regimes have been reported in stellarators; some of these appear to be similar to tokamak regimes; the H-mode is among them [37]. In stellarator H-modes the energy confinement is enhanced modestly (no more than 30%) in W7-AS [12, 13] and CHS [38, 39, 40. 41]. Access is typically restricted to narrow ranges in ɨ, which minimizes damping of poloidal rotation at the plasma boundary [42, 43] (in W7-AS the poloidal rotation is damped less than the toroidal rotation).

CHS reports two enhanced confinement regimes associated with a change in the radial electric field. One is a ‘high ion temperature mode’ [44] said to be similar to TFTR supershots and hot ion modes in JET and JT-60U; the similarity includes a peaked density profile, which is rare in stellarators. The other enhanced confinement regime is a dynamic E_r bifurcation regime [45, 46, 47] with rapid variations in the magnitude of the radial electric field driven by central ECH; these appear to confirm theoretical predictions of E_r bifurcation [48].

8.2 Global NCSX Model: confinement dependence on β and density

The relationship between several important plasma parameters is illustrated in Figure 8-1. Contours of the minimum ion collisionality and confinement H factors required for a given $\langle\beta\rangle$ and density are shown for two neutral beam power levels. Low ν_i^* is required for NCSX to test transport, stability, and bootstrap current at moderately low collisionality, but rasing the density reduces the $H_{ISS\text{-}95}$ needed to reach a given $\langle\beta\rangle$.

The results in Figure 8-1 are obtained from a '0-D model' which is based the LI383 configuration, with R_o=1.4 m, B_o=1.2 T, and with fixed profile shapes for density and temperature (those in Figure 8-5; note that the minimum ion collisonality is located at r~0.7a). The maximum density is at the Sudo limit [49]. The 0-D model is comprised of the following equations (powers are in MW, stored energy in MJ, B_o in Tesla, a and R_o in meters, $\langle\beta\rangle$ is not in %, $\bar{n}_e$ is in10^{19} /m^3):

Orbit losses reduce the heating power to $P_{heat}=P_{inj}(1-0.24/\mathrm{sqrt}\{(R_o/1.4\ \mathrm{m})(B_o/1.2\ \mathrm{T})\})$
Sudo density limit = $\{P_{heat}B_o/(R_o a^2)\}^{0.5}\ 2.5\times10^{19}\ /\mathrm{m}^3$
Based on Figure 8-5, the miminum $\nu_\iota^* = 0.027\{\bar{n}_e{}^3 R_o/(100\langle\beta\rangle)^2 B_o^4\}$
The stored energy (in MJ) is $W_{tot}=1.5\langle\beta\rangle(10B_o^2/2\pi)V_p$, where $V_p=2R_o(\pi a)^2$
The energy confinement time is $\tau_E=W_{tot}/P_{heat}$, and the H factors are
$H_{ISS\text{-}95}=\tau_E/a^{2.21}R_o^{0.65}P_{heat}^{-0.59}\bar{n}_e^{0.51}B_o^{0.83}\text{ƚ}(2a/3)^{0.43}\ 0.079$ sec
The effective plasma current needed for the ITER-97P confinement scaling is
Ip= $(B_o/1.2\ \mathrm{T})(R_o/1.4\ \mathrm{m})$ 0.48 MA, and for hydrogen plasmas (M_{eff}=1)
$H_{ITER\text{-}97P}=(W_{tot}/P_{inj})\ /(a/\sqrt{\kappa})^{0.31}R_o^{1.38}\kappa^{0.67}P_{inj}^{0.57}\ \bar{n}_e^{0.24}B_o^{0.2}I_p^{0.74}0.037$ sec, where "$a/\sqrt{\kappa}$" represents the tokamak definition of minor radius; the symbol "a" follows the stellarator definition.

The approximation for neutral beam orbit losses used above is based on the B_o and R_o scans in Chapter 7, which used the plasma parameters of Figure 8-5. Higher density, colder plasmas (as in Figure 8-6) will have less orbit loss because there is less time for stochastic diffusion and because the slowing down rate is increased more than the pitch angle scattering rate, but no 'credit' for this is taken in the orbit loss approximation used here.

As $\langle\beta\rangle$ is raised at a fixed density in Figure 8-1 the stored energy and H factors rise linearly with $\langle\beta\rangle$, and the collisionality drops as $1/\langle\beta\rangle^2$. The density dependence of the ISS-95 scaling lowers $H_{ISS\text{-}95}$ as the density rises, but the collsionality increases as $\bar{n}_e{}^3$ at fixed $\langle\beta\rangle$. At $\langle\beta\rangle$=4% and ν_ι^*=0.25, the required $H_{ISS\text{-}95}$=2.9 and $H_{ITER\text{-}97P}$=0.9. Raising the density to the Sudo limit reduces $H_{ISS\text{-}95}$ to 1.8 at $\langle\beta\rangle$=4%, but then $\nu_\iota^*>1$. With 6 MW of injected power and $H_{ISS\text{-}95}$=1, the achievable $\langle\beta\rangle$ is slightly above 2%.

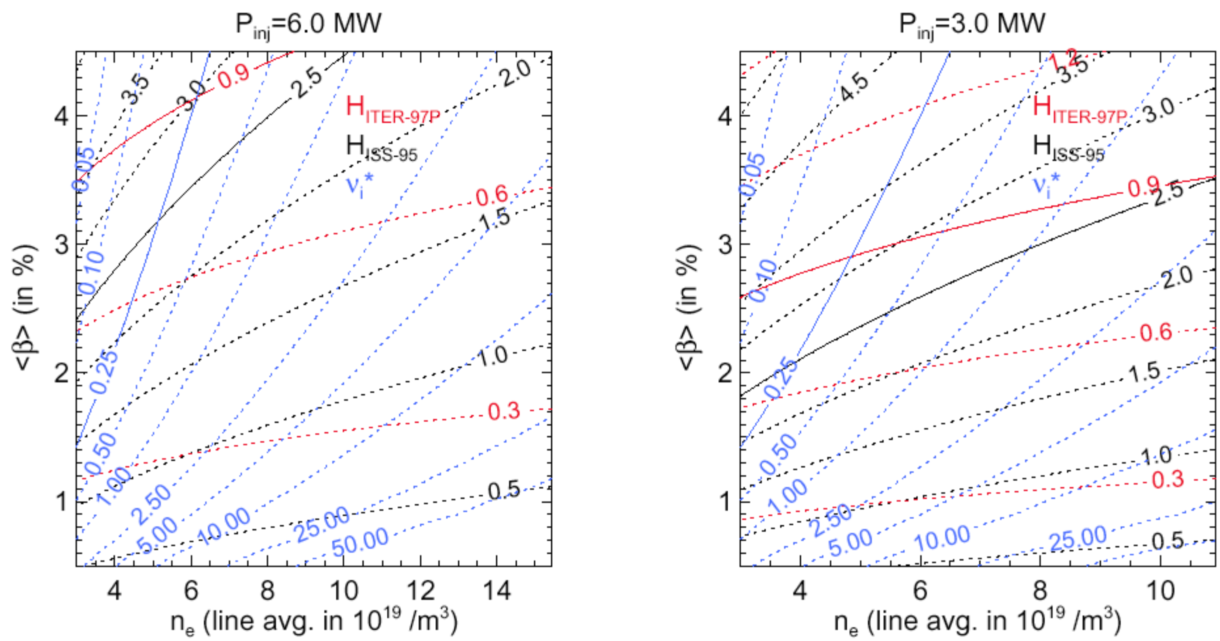

Figure 8-1. $H_{ITER-97P}$, H_{ISS-95} and the product B_oR_o for (a) ν_ι*=0.25, and (b) density at the Sudo limit

Note that with 6 MW, $H_{ITER-97P}$ is below 1 at <β>=4%, and even with only 3 MW injected <β>~3.5% can be achieved with $H_{ITER-97P}$=1. Finally, with 3 MW, H_{ISS-95}=2.9 and $H_{ITER-97P}$=0.9 are compatible with <β>~2.7% and ν_ι*=0.25 (these H factors produce <β>=4% and ν_ι*=0.25 with 6 MW).

8.3 Transport simulations of NCSX

One of the NCSX design goals is to reduce transport by producing a highly quasi-axisymmetric configuration with the transport of an equivalent axisymmetric device. With low 'effective' ripple the particle, energy, and momentum transport should all be reduced relative to unoptimized stellarator designs, and should be similar to tokamak transport. Anomalous transport may be reduced by the effects of flow shear and the rotational transform and magnetic shear, which are similar to those of the 'reversed shear' enhanced confinement regime in tokamaks.

The temperature prediction code described in this section also must determine the self-consistent radial electric field, E_r, which would be set up by ambipolar neoclassical ripple transport. The ion energy and particle transport are strongly dependent on E_r, so the self-consistent value must be used. The analytic estimate for E_r has been spot checked by a Monte Carlo transport calculation with GTC. With this ambipolar E_r the DKES code confirms that the energy transport due to field ripple is much smaller than the axisymmetric neoclassical energy transport. The benchmarks with GTC and DKES are presented in Section 8.3.2.

8.3.1 Methodology for local transport simulations

Temperature profile predictions for NCSX involve several steps:

1. estimate the E_r necessary for ambipolar particle flux,
2. estimate the ripple transport,
3. predict temperature profiles.

The temperature profile predictions are solutions of the coupled power balance equations for the electron and ion temperatures. The thermal diffusivities are made up of three parts: neoclassical ripple transport, neoclassical axisymmetric transport, and an anomalous transport model with an adjustable coefficient.

The ripple transport depends on the density and temperature – and their gradients - as well as the radial electric field which, in turn, depends on the helical particle transport. Consequently, everything must be solved for 'simultaneously', so an iterative procedure is used until the temperatures and transport fluxes have converged. By construction, the algorithm for finding the ambipolar electric field searches for the ion root.

The analytic model for neoclassical helical transport [50, 48, and earlier references therein] is based on a 'single helicity' magnetic configuration. Mynick [51] used a Monte Carlo transport simulation to approximately verify analytic transport expressions for a single helicity magnetic configuration.

The single helicity analytic model has been extended in the $1/\nu$ regime to more complex magnetic configurations [52] and benchmarked against a Monte Carlo calculation of transport. For NCSX simulations we incorporate this extension of analytic theory by using the 'effective helical ripple' (as calculated by the NEO code [52] for the LI383 configuration) for all transport regimes. The justification is twofold: 1) a successful benchmark with the GTC code, which makes no assumption concerning the collisionality regime (see next section), and 2) through the ambipolar E_r the electrons effectively set the overall level of transport and they are in the $1/\nu$ regime (see the benchmark discussion in the next section). The effective helical ripple for the LI383 configuration is shown in Figure 8-2. For comparison, the effective helical ripple of W7-X is close to 0.01 at all radii, and that of ATF ranged from 0.3 near the edge to ~0.1 deep in the core.

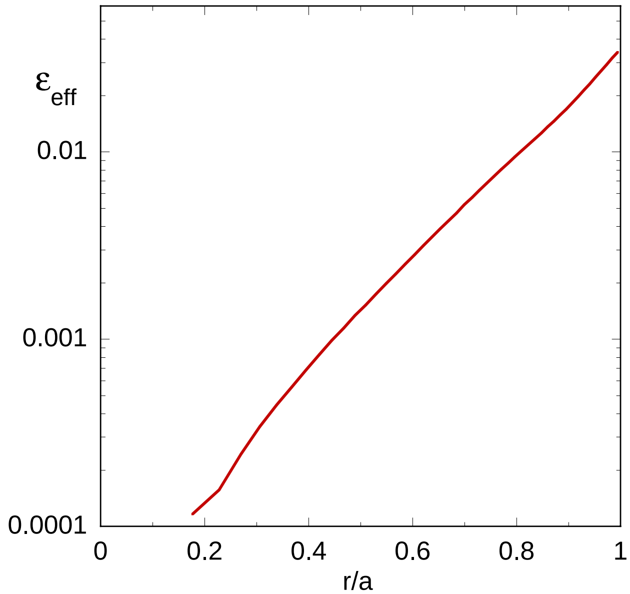

Figure 8-2. The effective helical ripple for the LI383 configuration vs the square root of the normalized toroidal flux

The neoclassical axisymmetric transport is given by the Chang-Hinton [53] formulation for a circular plasma cross section; the implementation was adopted from SNAP [54]. A calculation by THRIFT (based on profiles close to those in Figure 8-5) shows that the Chang-Hinton formulation of axisymmetric transport should be reduced by 35% for these conditions, so this correction factor was used in the calculation of the Figure 8-5 profiles. Other collisionality regimes, such as that in Figure 8-6, may require a different correction; no correction was used for Figure 8-6. In future, the neoclassical transport routines in THRIFT will be incorporated into the power balance code.

The anomalous diffusivity is adjusted in the predictions in order to match a target thermal $\langle\beta\rangle$ or H factor. The power conducted by the anomalous term can then be compared to the neoclassical conduction power as a measure of confinement 'robustness'. The simplest anomalous transport model is spatially uniform. Stellarators often have experimentally determined thermal diffusivities that are approximately radially constant (unlike many tokamaks). A local Lackner-Gottardi expression for anomalous transport can also be used. This anomalous transport model is based on one originally developed for ASDEX [55], with additional B_o and R_o scaling inspired by Lackner[56], and used to model a W7-AS discharge [57]:

$$\chi^{LG} = 1.5\ \mathrm{m^2/s}\ (1.6\ \mathrm{m}/R_o)(2\ \mathrm{T}/B_o)^2\ T_{e,keV}{}^{1.5}/(1.1-(r/a)^2)^4\ . \tag{8-1}$$

The multiplier is used here is the same for the electron and ion diffusivities, and only the temperatures near the edge are sensitive to which species is anomalous. This anomalous model increases strongly in the outer region of the plasma; as a result it is the dominant term near the edge and its contribution is insignificant in the plasma core with the multipliers used here (see Figure 8-5).

The ‘triangular’ heating profile used here is similar to those calculated by TRANSP (see Figure 10-28) for neutral beam injection into an axisymmetric torus with the oblate portion of the NCSX cross section. The orbit loss calculations (see Chapter 7) are carried out for the full 3-D geometry, and show relatively weak dependence on the injector’s toroidal location, so the heating calculation in axisymmetric geometry may be a good approximation to a 3-D heating calculation.

The power balance equations are solved with an assumed density profile shape, and assumed outer boundary temperatures. The results are not sensitive to variations in these assumptions, largely because the anomalous transport multiplier is adjusted until the predictions match a target (typically $\langle\beta\rangle$=4%). Where the anomalous multiplier goes to zero defines the boundary of the ‘neoclassically accessible’ region. For $\langle\beta\rangle$=4% the neoclassical boundary is beyond the maximum magnetic field of the R_o=1.4 m design.

The heating power is split between ions and electrons according to the Stix thermalization model [58].

8.3.1 Benchmarks of analytic and numerical neoclassical transport

Reality is more complex than the analytic neoclassical transport model used in the power balance solutions in several important ways. Real stellarators have multiple helicity components, and in some stellarators there is no single dominant component. In complex configurations there will generally be multiple trapped particle populations, and each can have transport resonances where the electric and magnetic contributions to the poloidal drift cancel (see Figure 1 of Ref. 30).

The most complete numerical simulations of neoclassical transport in multi-helicity magnetic geometry use Monte Carlo methods [59, 51, 60, 61] or are based on a drift kinetic equation solver, DKES [62, 63]. All of these codes have shown that analytic theory is reliable in simple magnetic geometry. Both kinds of codes have been used to show that the various analytic transport regimes can even frequently be identified in the mono-energetic diffusivities obtained for complex geometries, although the coefficients must be fitted to the numerical results [61, 64]. The coefficient for the $1/\nu$ regime can be evaluated for multi-helicity magnetic configurations by the NEO code [52], which provides an ‘effective helical ripple’ valid in the $1/\nu$ regime. Not all energies and species are in the $1/\nu$ regime, however, so we have carried out further benchmarks for NCSX.

The analytic transport model’s prediction of the electric field and the energy fluxes has been benchmarked against numerical transport simulations in the earlier C82 configuration. For this work we used a gyrokinetic particle simulation code, GTC [60], which has previously been extensively benchmarked against analytic predictions for axisymmetric neoclassical transport [60]. An ancestor of GTC was used to validate analytic expressions for helical neoclassical transport [51]. For this benchmark GTC used here simulates the full ion distribution function (f)

and the deviation of the electron distribution from a Maxwellian (δf). It uses a low-noise technique to calculate the particle fluxes from the toroidal variation of $p_{\|}+p_{\perp}$ due to Boozer [65]. The NCSX benchmark was carried out at a single flux surface (r=0.84 a) with PBX density and temperature profiles scaled to NCSX conditions.

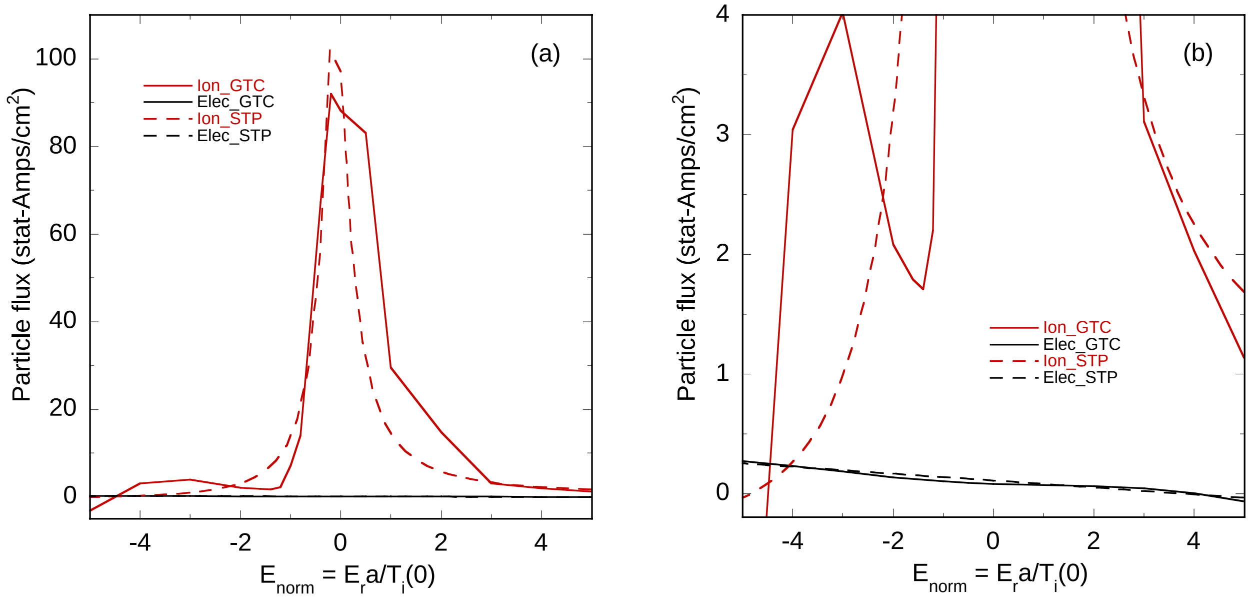

Figure 8-3. Comparison of analytic (STP) and full geometry (GTC) calculations of particle transport as a function of the radial electric field (for the configuration C82)

The radial electric field was varied, and the ion and electron particle fluxes calculated by GTC and the analytic prediction are compared in Figure 8-3. Note that the electron flux is relatively insensitive to the electric field (the dependence is less than proportional) so it sets the level of particle flux. The ion flux depends very strongly on electric field, and the particle flux becomes ambipolar close to the E_r that makes the ion flux vanish. In spite of the significant differences between the analytic and Monte Carlo ion particle fluxes, the 'ambipolar' electric field is well predicted. The analytic method is successful because the electrons are in the 1/ν regime (so the extension of the single helicity model is valid), and they effectively set the transport level because the electron flux is not very sensitive to the electric field (by definition, the ion flux must equal the electron flux at the ambipolar electric field). The numerical and analytic electron fluxes are in close agreement, and as a result the predicted analytic and Monte Carlo ambipolar fluxes are quite close.

Maassberg [28] used the DKES [62, 63] code to calculate the mono-energetic transport coefficients at r=a/2 for the LI383 configuration (see Figure 8-4). In the low collisionality regime, the normalized particle transport coefficient, $\Gamma_{11}{}^*$, approaches the equivalent axisymmetric result as the electric field is increased; the expected magnitude is $E_r/Bv>3\ 10^{-3}$ V/m (see Figure 8-4). With the electric fields required for ambipolar flux (as determined above) the transport will be very close to the axisymmetric result. The bootstrap coefficient, Γ_{31}, is not far from the axisymmetric result (although the latter is not the limit for large E_r).

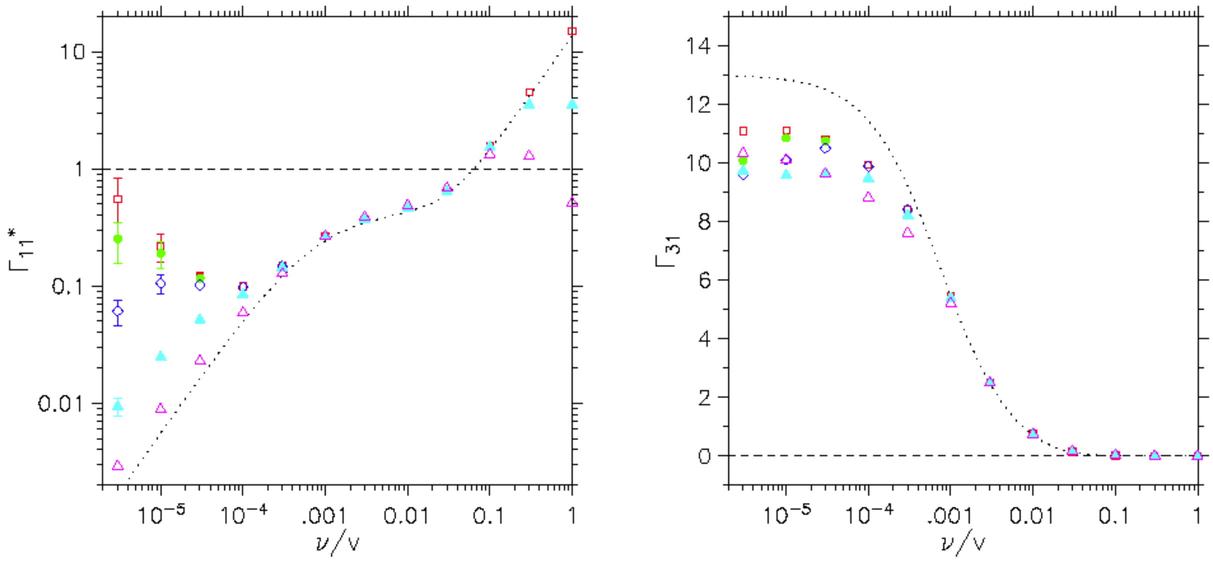

Figure 8-4. DKES results for NCSX (LI383) at r=a/2: (a) mono-energetic particle transport coefficient normalized to the plateau value of an equivalent elongated axisymmetric configuration, and (b) the bootstrap current coefficient. The abscissa is the inverse of the mean fre path. Radial electric field values: Er/(Bv)= 0 red squares, 1x10-4 green circles, 3x10-4 dark blue diamonds, 1x10-3 blue filled triangles, 3x10-3 pink open triangles. Dotted curve in (a) is the axisymmetric result

The GTC and DKES benchmarks thereby confirm that the ripple transport is expected to be insignificant in the planned NCSX conditions. This conclusion could become invalid if strong central electron heating were used in NCSX; the resulting high central electron temperatures would dramatically increase the ripple fluxes, but even in this case the ripple fluxes would be small in the cooler plasma outside the center.

8.3.2 Temperature Profiles for NCSX Scenarios

Figure 8-5 shows plasma profiles for the 'standard' high $<\beta>$ condition (P_{inj}=6 MW, B_o=1.2 T, R_o=1.4 m), where the density has been chosen so that the minimum ν_t*=0.25. Truly 'reactor relevant' collisionality values would require much higher H-factors (or B_o, or P_{inj}), but this plasma is expected to be in the relevant collisionality regime from the point of view of energy transport and bootstrap current generation. The pressure profile is within the range

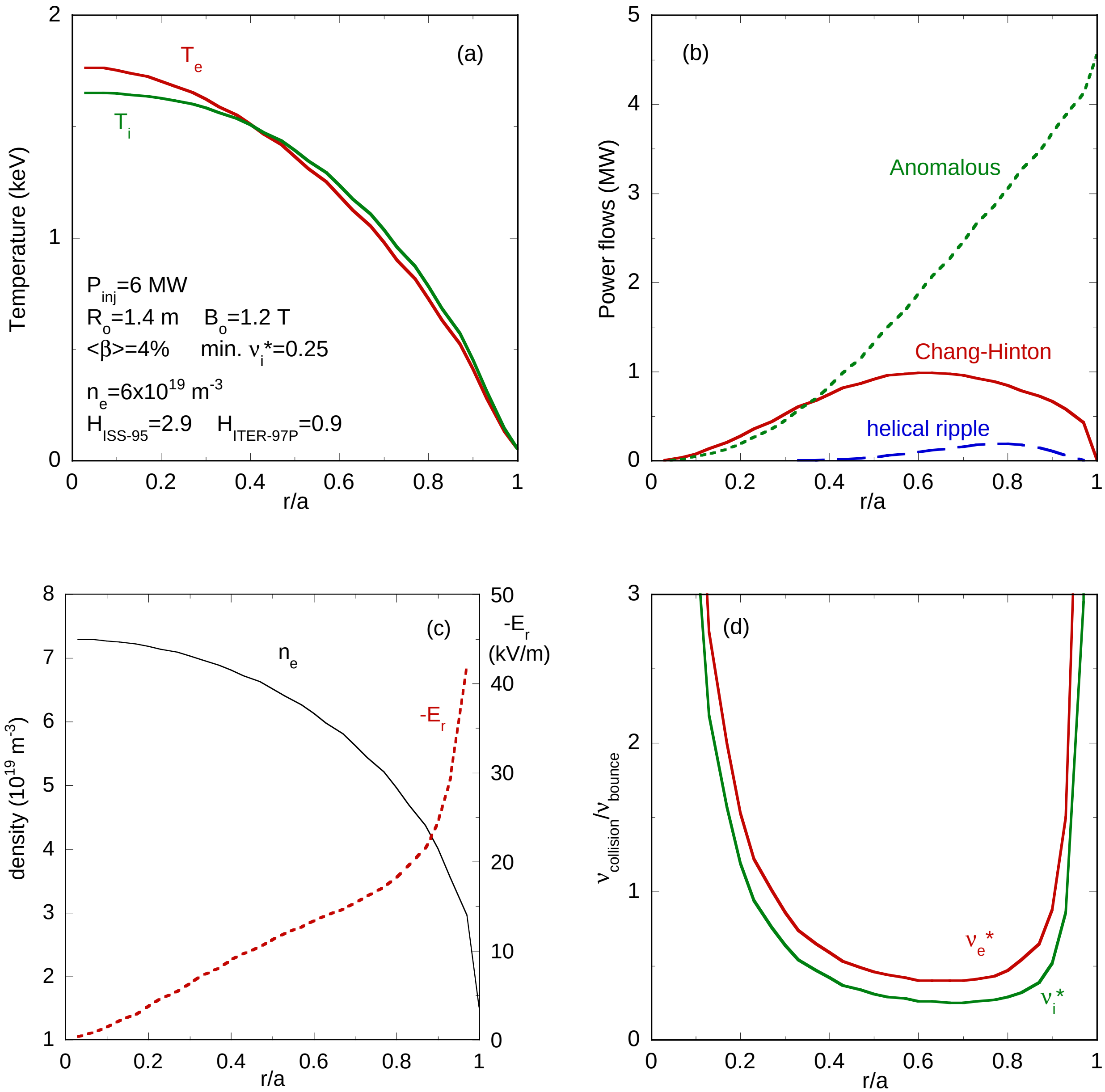

Figure 8-5. Profiles for standard high beta plasma.

used for MHD stability studies in chapter 5. With the highly quasi-axisymmetric magnetic geometry the ripple energy transport is negligible compared to the axisymmetric neoclassical transport, which has been normalized to a THRIFT calculation for these conditions. Thus, the transport is that of an equivalent tokamak. The radially constant anomalous trasnport model has been used to determine how much anomalous transport can be tolerated in the plasma core. The anomalous transport exceeds the neoclassical transport in the outer two thirds of the plasma. The radial electric field is in the ‘ion root’ regime everywhere. (The collisionality scaling used in Section 8.2 is based on this figure.)

When matching a target for <β>, $H_{ISS\text{-}95}$, or $H_{ITER\text{-}97P}$, the fast ion stored energy is not calculated by the power balance code. In plasmas with mininmum $\nu_i^*=0.25$ the fast ion stored energy is ~25% of the total, so the target for the thermal <β> is 3%. A separate calculation using the profiles of Figure 8-5 confirmed that the total <β>, including fast ions, is 4.1%.

While the neutral beams heat ions preferentially, the neoclassical losses are also larger in the ion channel so $T_e > T_i$ in the plasma center. At larger radii $T_e < T_i$ because we have assumed the electron and ion anomalous thermal diffusivities are equal. If all the anomalous transport is assigned to one channel then it becomes the colder species where anomalous transport is dominant.

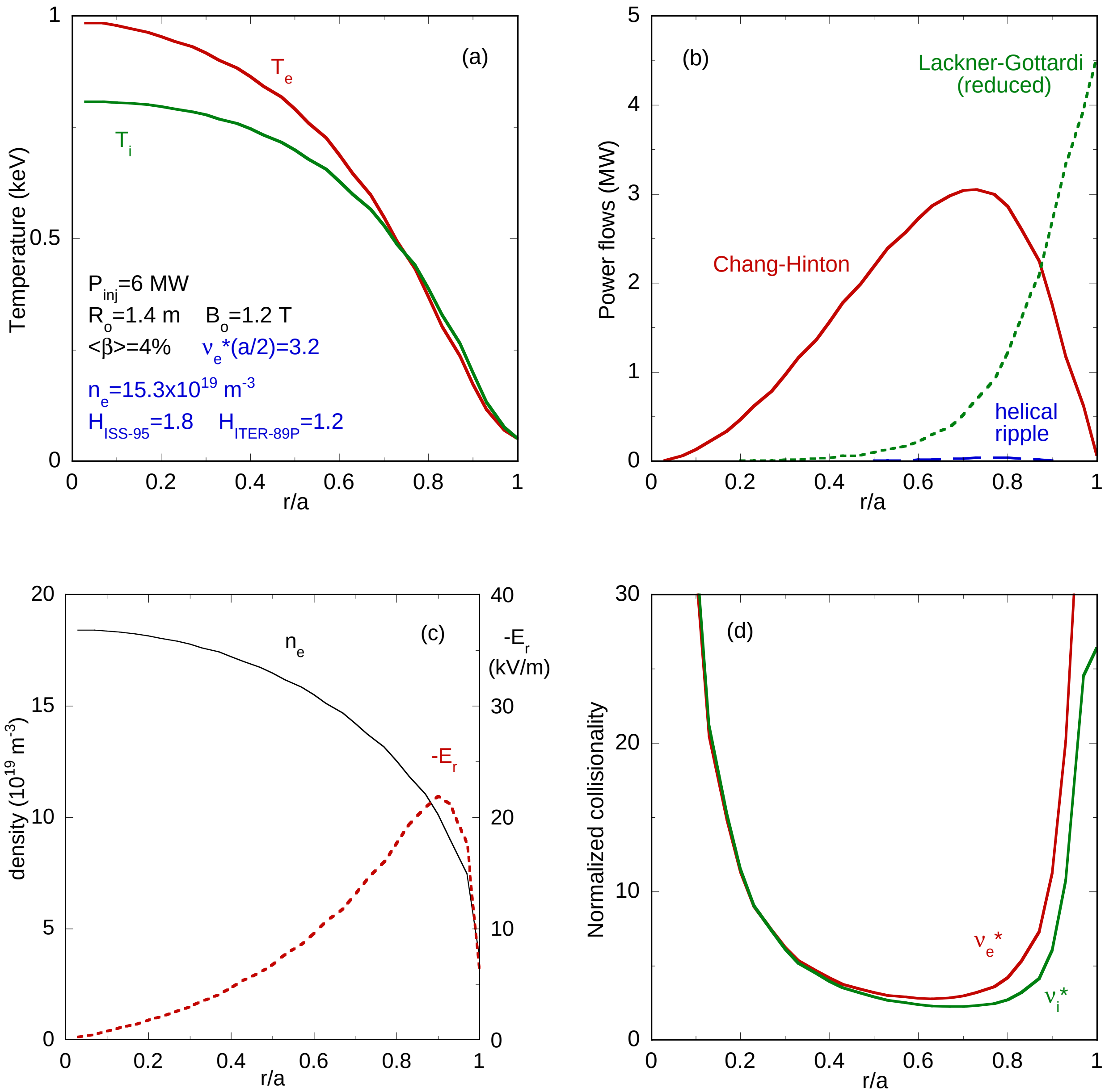

Figure 8-6. Profiles for high density, high beta plasma

The density dependence of the ISS-95 scaling favors operation at high density. Raising the density to the Sudo limit reduces the H_{ISS-95} needed to reach $<\beta>=4\%$ from 2.9 to 1.8 (see Figure 8-6). Ripple transport is even more unimportant at these lower temperatures because it has a stronger temperature dependence than axisymmetric transport. The Lackner-Gottardi transport model was used, so anomalous transport is important only in the outer part of the plasma. The thermal beta is fully 4%; the fast ion contribution will be much lower in this colder denser plasma. Note that the collisionality is now high, however. The results of the power balance code are similar to those from the 0-D model in Section 8.2.

If the anomalous transport is sufficiently high to reduce H_{ISS-95} to 1, then 6 MW injected into a plasma at the Sudo density limit produces $<\beta>=2.2\%$ - enough for tests of the lower $<\beta>$ limits with unoptimized shapes (see Chapter 5). At these colder temperatures the ripple transport is reduced further and the Lackner-Gottardi anomalous model is dominant in the outer 30% of the minor radius.

The initial complement of neutral beam injectors will generate 3 MW and would be expected to produce lower $<\beta>$ for a given H factor. Again choosing the density so that minimum $\nu_t^*=0.25$, we find that $H_{ISS-95}=2.9$ or $H_{ITER-97P}=0.9$ implies $<\beta>=2.5$-2.8%, respectively, at $B_o=1.2$ T. This would exceed the lower $<\beta>$ limits which are predicted for less optimized shapes.

8.6 Summary

We find that the high degree of quasi-axisymmetry of the LI383 configuration reduces the neoclassical ripple transport to a small fraction of the neoclassical axisymmetric transport. It is assumed here that the actual radial electric field (including any driven by unbalanced neutral injection) reduces the ripple transport at least as much as the 'ambipolar' electric field would. This means that NCSX is tokamak-like in the sense of being dominated by axisymmetric transport. Since the magnetic shear is similar to the 'reversed shear' enhanced confinement regime in tokamaks, it may have reduced levels of anomalous transport, as well.

Relative to the ISS-95 global energy confinement scaling, the confinement required to reach the high $<\beta>$ goal of 4% - and low collisionality, simultaneously - is only slightly higher than that already achieved in unoptimized stellarators. This level of confinement is ~10% lower than predicted by the ITER-97P tokamak L-mode scaling. By operating near the stellarator density limit, the required enhancement over the ISS-95 scaling is reduced by 35%.

A combination of neoclassical and anomalous transport models predict pressure profile shapes that are within the range of those used to study the MHD stability of NCSX. They also show that $<\beta>=4\%$ plasmas are 'neoclassically accessible', and can tolerate large levels of anomalous transport in the outer region of the plasma. Core temperatures of up to ~2 keV are expected in plasmas with moderate collisionality.

The high degree of quasi-axisymmetry in NCSX is expected to greatly reduce the rotation damping that is usually observed in stellarators. This may result in 'tokamak' levels of flow and the potential for highly sheared flows that could reduce transport (calculations of toroidal flow damping rates are in progress). With balanced co and counter beams it will be possible to vary the external momentum input and, hence, the flow shear, to study its effects on transport.

The initial complement of 3 MW of neutral beam injection power will be sufficient to produce $<\beta>$=2.5-2.8% at B_o=1.2 T (assuming H_{ISS-95}=2.9 or $H_{ITER-97P}$=0.9) at moderate collisionality. This would be sufficient to test the lower $<\beta>$ limits which are predicted for less optimized shapes (see Chapter 5).

Standard techniques for confinement enhancement in stellarators and tokamaks are planned. These include wall conditioning, control of wall recycling, unbalanced neutral beam injection, pellet injection, limiting regions of high flux expansion, and edge biasing.

References

[1] Stroth, U., et al., Nuclear Fusion **36** (1996) 1063.
[2] Kaye, S. (1997) (????)
[3] Iiyoshi, A., et al., Nuclear Fusion **39** (1999) 1245.
[4] Fujiwara, M., et al., 18th IAEA Fusion Energy Conference, Sorrento, 2000, OV1/4.
[5] Motojima, O., et al., Phys. Plasmas, **6** (1999) 1843.
[6] Yamada, H., 2001, private communication.
[7] Sakakibara, S., et al., submitted to Nuclear Fusion, 2000.
[8] Watari, T., et al., 18th IAEA Fusion Energy Conference, Sorrento, 2000, EX8/4.
[9] Ohyabu, N., et al., Phys. Rev. Letters, **84** (2000) 103.
[10] Narihara, K., et al., 18th IAEA Fusion Energy Conference, Sorrento, 2000, EXP5/28.
[11] Yamada, H., et al., Phys. Rev. Letters, **84** (2000) 1216.
[12] Erckmann, V., et al., Phys. Rev. Letters, **70** (1993) 2086.
[13] Hirsch, M., et al., Plasma Phys. Control. Fusion **40** (1998) 631.
[14] Yushmanov, P., et al., Nuclear Fusion **30** (1990) 1999.
[15] Kick, M., et al., 16th IAEA Fusion Energy Conference, Montreal, **2** (1996) 27.
[16] Stroth, U., et al., Plasma Phys. Control. Fusion **40** (1998) 1551.
[17] Sauthoff, N., et al., 13th IAEA Fusion Energy Conference, Washington, **1 (**1990) 709.
[18] Okamura, S., et al., Nuclear Fusion **39** (1999) 1337.
[19] Maassberg, H., et al., Plasma Phys. Control. Fusion **35** (1993) B319.
[20] Baldzuhn, J., et al., Plasma Phys. Control. Fusion **40** (1998) 967.
[21] Kick, M., et al., Plasma Phys. Control. Fusion **41** (1999) A549.
[22] Erckmann, V., et al., 16th IAEA Fusion Energy Conference, Montreal, **2** (1996) 119.
[23] Mynick, H. E., Hitchon, W. N. G., Nuclear Fusion **23** (1983) 1053.
[24] Yamazaki, K., Amano, T., Nuclear Fusion **32** (1992) 633.
[25] Fujisawa, A., et al., 16th IAEA Fusion Energy Conference, Montreal, **2** (1996) 41.
[26] Maassberg, H., et al., Phys. Plasmas, **7** (2000) 295.
[27] Ida, K., et al., 18th IAEA Fusion Energy Conference, Sorrento, 2000, EX9/4.
[28] Maassberg, H., 2000, private communication.
[29] Fujisawa, A., et al., Phys. Rev. Letters, **82** (1999) 2669.
[30] Maassberg, H., et al., Phys. Fluids, **B 5** (1993) 3627.
[31] Renner, H., et al., 13th IAEA Fusion Energy Conference, Washington, **2 (**1990) 439.
[32] Yamada, H., et al., 18th IAEA Fusion Energy Conference, Sorrento, 2000, EX6/7.
[33] Ida, K., et al., submitted to Nuclear Fusion**,** 2000.

[34] Murakami, M., et al., 13th IAEA Fusion Energy Conference, Washington, **2 (**1990) 455.
[35] Murakami, M., et al., Phys. Fluids, **B 3** (1991) 2261.
[36] Murakami, M., et al., Phys. Rev. Letters, **66** (1991) 707.
[37] Wagner, F., and Stroth, U., Plasma Phys. Control. Fusion **35** (1993) 1321.
[38] Toi, K., et al., 14th IAEA Fusion Energy Conference, Wurzburg, **2** (1992) 461.
[39] Toi, K., et al., Plasma Phys. Control. Fusion **36** (1994) A117.
[40] Toi, K., et al., 15th IAEA Fusion Energy Conference, Seville, **2** (1994) 331.
[41] Toi, K., et al., Plasma Phys. Control. Fusion **38** (1996) 1289.
[42] Hirsch, M., et al., Plasma Phys. Control. Fusion **42** (2000) A231.
[43] Jaenicke, R., et al., 18th IAEA Fusion Energy Conference, Sorrento, 2000, OV4/3.
[44] Ida, K., et al., Nuclear Fusion **39** (1999) 1649.
[45] Fujisawa, A., et al., Phys. Rev. Letters, **79** (1997) 1054.
[46] Fujisawa, A., et al., Plasma Phys. Control. Fusion **42** (2000) A103.
[47] Fujisawa, A., et al., 18th IAEA Fusion Energy Conference, Sorrento, 2000, EX6/6.
[48] Hastings, D. E., Houlberg, W. A., Shaing, K.-C., Nuclear Fusion **25** (1985) 445.
[49] Sudo, S., et al., Nuclear Fusion **30** (1990) 11.
[50] Shaing, K.-C., Phys. Fluids **27** (1984) 1567.
[51] Mynick, H. E., Phys. Fluids, **25** (1981) 325.
[52] Nemov, V. V., et al., Phys. Plasmas, **6** (1999) 4622.
[53] Chang, C. S., Hinton, F. L., Phys. Fluids, **29** (1986) 3314.
[54] Towner, H., et al., Rev. Sci. Instrum. **63** (1992) 4753.
[55] Lackner, K., et al., Plasma Phys. Control. Fusion **31** (1989) 1629.
[56] Lackner, K., Gottardi, N. A. O., Nuclear Fusion **30** (1990) 767.
[57] Karulin, N., "Transport modeling of stellarators with ASTRA", IPP 2/328, Max-Planck Institut fur Plasmaphsyik, Garching, Germany (December 1994).
[58] Stix, T. H., Plasma Physics, **14** (1972) 367.
[59] Boozer, A. H., Kuo-Petravic, G., Phys. Fluids **24** (1981) 851.
[60] Lin, Z., Tang, W. M., Lee, W. W., Phys. Plasmas, **2** (1995) 2975.
[61] Lotz, W.,Nuehrenberg, J., Phys. Fluids, **31** (1988) 2984.
[62] Hirshman, S. P., et al., Phys. Fluids, **29** (1986) 2951.
[63] van Rij, W.I., Hirshman, S. P., Phys. Fluids, **B 1** (1989) 563.
[64] Maassberg, H., et al., Plasma Phys. Control. Fusion **41** (1999) 1135.
[65] Lewandowski, J. V. L., et al., submitted to Phys. Plasmas, 2000.

Chapter 9 -- Configuration Flexibility and Robustness

9.1 Introduction

In order to achieve the scientific goals of the NCSX mission, the NCSX device must be capable of supporting a range of variations in plasma configuration about the reference baseline equilibrium. In the following sections we demonstrate the robustness and flexibility of NCSX.

As described in Chapter 2 the NCSX coil system was designed in a two-stage approach. In the first stage, a reference physics configuration was identified with attractive physics properties (the S3 state of li383). In the second stage, coils were reverse-engineered in such a way that the physics properties of the reference configuration were reproduced as accurately as possible, consistent with engineering constraints, in a free-boundary reconstruction of the plasma.

Figure 9-1 shows a top view of the modular coil set M1017 used for the flexibility and robustness studies presented here. There are 7 coils in each of the three periods of the machine. Stellarator symmetry implies that within any given period only 4 coil currents are independent. The independent coils are labeled “1”, “2”, “3” and “4”. Stellarator-symmetric partners are labeled with prime superscripts. The same numbering convention will be used to identify the coils when presenting coil current solutions in our flexibility studies.

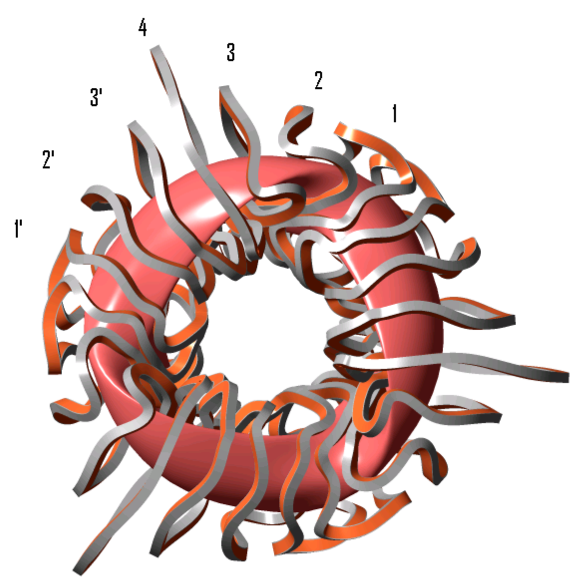

Figure 9-1. Modular coilset M1017 used for flexibility and robustness studies. Integers “1”, “2”, “3” and “4” label the four coils within each period whose coil currents are allowed to vary independently of one another. Coil k’ is the mirror symmetric partner of coil k

NCSX plans to allow the four modular coil currents to vary independently; thus the mean (toroidally averaged) toroidal magnetic field at a given radius will also vary. For systematic experiments it is advantageous to separate the provision of external transform by 3D shaping from provision by changes in the average toroidal field. In principle, the average toroidal field can be constrained to be a constant value by varying only three linear combinations of the four modular coil currents. However we have found that this leads to a considerable reduction in the flexibility of NCSX to control the external transform. For this reason NCSX plans to include an auxiliary TF coil system where the TF coil current is allowed to vary together with the four modular coil currents in such a way that the mean TF field remains constant.

In the flexibility calculations presented in this Chapter, the auxiliary toroidal field coil is modeled as a single vertical wire filament on the machine centerline (R=0). A filament current of $I_T = 7.0 \times 10^6$ Amps produces an auxiliary TF field of $B_T = 1.0$ T at the radius R = 1.4 m.

In addition to the five independent coil systems mentioned so far, a system of axisymmetric poloidal field currents is included for additional flexibility. For the flexibility studies presented here, the poloidal fields are included as a superposition of the lowest four axisymmetric multipoles (Dipole, Quadrapole, Hexapole and Octapole). Candidate poloidal field coilsets are evaluated by fitting to the multipole fields output by the free-boundary optimizer. Once the range of multipole fields required to produce configurations which span the desired operating space is known, a discrete poloidal field coil system will be designed where the coils are placed in optimal locations subject to the known accessibility constraints for diagnostics and beam access, etc. The expansion point for the multipole fields is R = 1.4 m, Z = 0.0 m, and units for these fields are such that $\mu_0 B_0 = 1$.

The reference li383 S3 plasma configuration (I_p = 174 kA, B_T = 1.7 T at R = 1.4 m) assumes bootstrap consistency between the current and pressure profiles. These ‘reference’ profiles are shown in Figure 9-2. The reference configuration shape was derived using a fixed-boundary optimizer. For fixed values of β, I_p and B_T, the optimizer adjusts the shape of the plasma boundary to minimize a physics objective function which includes measures of quasi-axisymmetry, and of kink, ballooning, and Mercier mode stability - see Chapter 2. For li383, the β-limit is 4.2%.

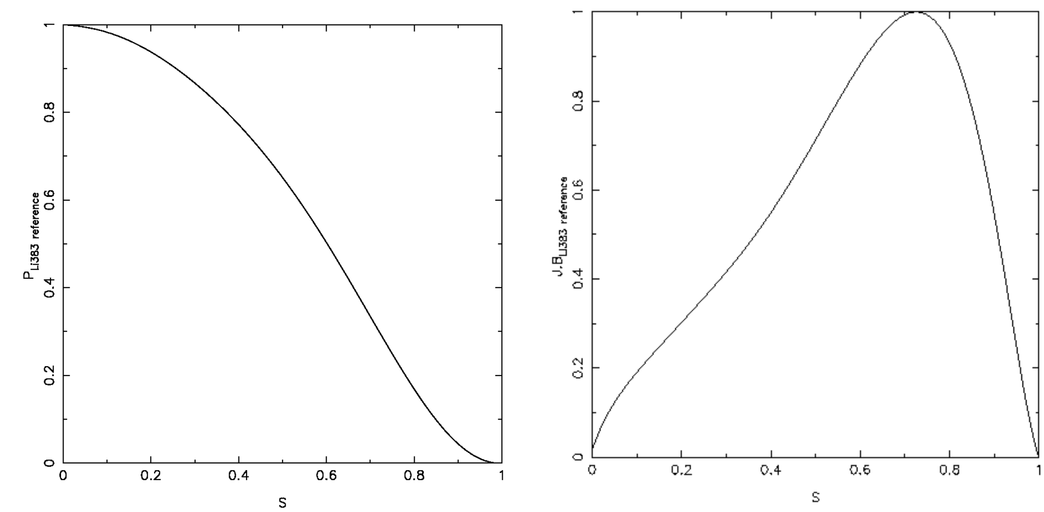

Figure 9-2. Baseline 'reference' current (J.B) and pressure (p) profiles as a function of normalized toroidal flux, s

The VMEC based free-boundary optimizer is used to determine coil currents which produce a free-boundary equilibrium consistent with a chosen set of plasma profiles. The cost function minimized by the optimizer is a weighted sum of $\chi^2_{Bmn} = \Sigma' B^2_{mn}/B^2_{00}$, a measure of the degree of quasi-axisymmetry of the plasma (the B_{mn} are Fourier components of the magnetic field analysed on the s=0.25, s=0.50, and s=0.75 magnetic surfaces evaluated in Boozer magnetic coordinates; the summation is over modes with n>0), $\chi^2_K = \lambda_K^2$ (the square of the unstable eigenvalue of the dominant kink instability evaluated by the TERPSICHORE stability code), and $\chi^2_B = \Sigma\lambda_B^2$ (the sum of squares of the maximum ballooning eigenvalue on any of the 49 magnetic surfaces used in the calculation of VMEC equilibria). Optimized equilibria are constrained to be tangent at some point to a three-dimensional first wall boundary whose normal separation distance from the plasma to the reference li383 plasma configuration is defined (as a function of poloidal angle u) by

$$\rho_{sep}(u) = \begin{cases} 10.0 - 20.0{*}u \text{ cm} & \text{for } 0.0 < u < 0.4, \\ = 2.0 \text{ cm} & \text{for } 0.4 < u < 1.0 \end{cases}$$

for all toroidal angles v. This limiter surface is a surrogate for the eventual plasma facing component boundary.

The reference profiles of current and pressure define a single point in the operating space of NCSX. In the following subsections we address the following questions on robustness and performance:

- How does the plasma performance change as profiles are changed from the reference?
- Is the operating space for configurations with adequate performance characteristics wide enough to allow fulfillment of the NCSX mission?
- Can the designed coils produce the magnetic fields required to support this range of plasma configurations?

9.2 Robustness of Plasma Shape and Position

Execution of planned experiments will require pre-programming of coil current (or voltage) waveforms. Accurate prediction of plasma profiles is unlikely during initial experimental campaigns, therefore pre-programmed coil currents will only be approximately consistent with actual profiles. Plasma shape and position will likely differ from expectation.

It is appropriate to ask whether equilibria obtained using estimated coil currents will have positions and shapes that are sufficiently close to the desired configuration that recovery by feedback control is possible. To address this question free-boundary equilibria were calculated for a variety of pressure and current profile shapes, net plasma toroidal current and plasma beta, using coil currents set equal to values appropriate to the reference S3 state of li383.

Three pressure profiles denoted by $p_A(s)$, $p_B(s)$, $p_C(s)$ expressed as a function of the normalized toroidal flux s were selected from a collection of measured profiles obtained on four stellarators (ATF, CHS, LHD, W7-AS) and two tokamaks (PBX-M, DIII-D) which bracket NCSX in size[1]. The selected profiles cover the plausible range of pressure peakedness/broadness that can be expected to occur in NCSX. The peaked profile, $p_A(s)$, is taken from an NBI heated L-mode discharge on DIII-D (shot 78109); the broad profile, $p_C(s)$, is taken from an NBI heated CHS discharge (shot C_MC2). It is similar to the assumed baseline li383 profile used for the NCSX design studies. The intermediate profile, $p_B(s)$ corresponds to an NBI heated discharge on PBX-M (shot 3113_1). Plots of the selected $p_j(s)$ are shown in Figure 9-3.

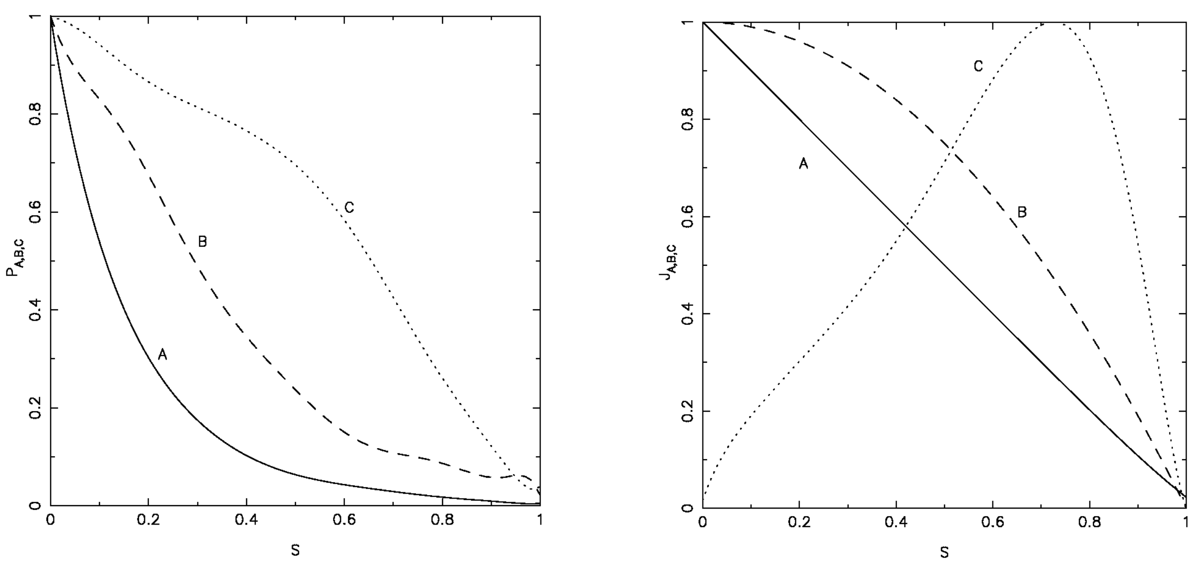

Figure 9-3. Three profiles of pressure ($p_A(s)$, $p_B(s)$, $p_C(s)$) and three profiles of parallel current by ($J_A(s)$, $J_B(s)$, $J_C(s)$) used for shape robustness calculations

Three profiles of parallel current $\mathbf{J} \bullet \mathbf{B}(s)$ denoted by $J_A(s)$, $J_B(s)$, $J_C(s)$ were also selected which cover a wide range of current peakedness/broadness. They are also shown in Figure 9-3. The peaked and intermediate current profiles have the analytic forms $J_A(s) = 1 - s$ and $J_B(s) = 1 - s^2$, respectively. The broad current profile, $J_C(s)$, is identical to the hollow li383 reference current profile.

Free-boundary equilibria were calculated for the nine possible combinations of plasma current and pressure profiles corresponding I_p = 174 kA, B_T = 1.7 T and a beta value of β = 4.2% using the coil currents shown in Table 9-1. Plasma boundaries for the nine reconstructions are shown in Figure 9-4, as are the calculated profiles of rotational transform, $\iota(s)$.

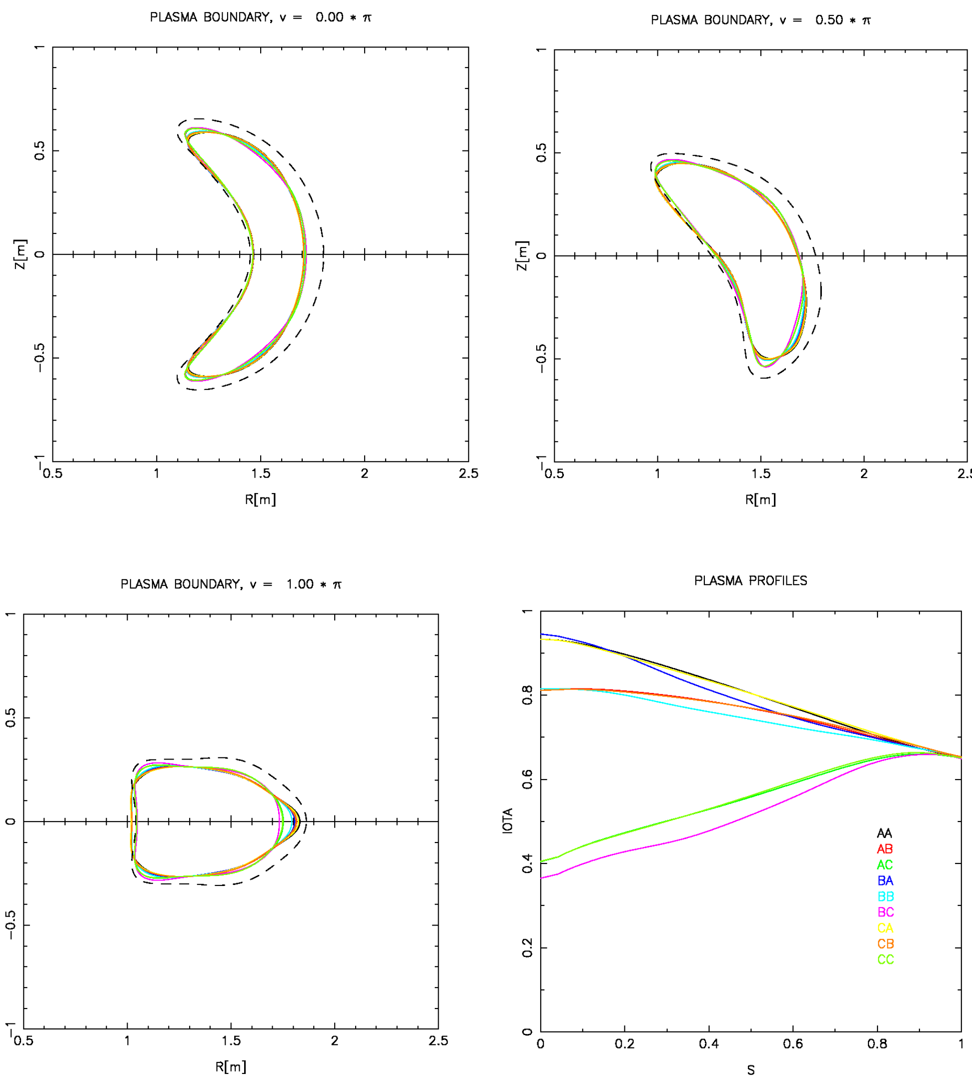

Figure 9-4. Reconstructed plasma boundaries for nine combinations of pressure and current profile with I_p = 174 kA, BT = 1.7 T, β = 4.2%, using fixed S3 (β=4.2%) coil currents. Boundaries are shown at three toroidal cross sections. The dashed curve represents the first wall boundary; it is not used as a limiter constraint in the calculations. Profiles of rotational transform are also shown.

The three groups of iota profiles correspond to the three current profiles. Members of each group differ primarily in their axis value, ι(0). Variations within each group are due to the variations in pressure profile. The first-wall boundary is shown as a dashed curve to indicate the scale of variation of the boundary shapes. However this first wall boundary was not treated as a limiter surface for the calculated equilibria. The variation in plasma shape and position for this wide range of equilibrium profiles is seen to be modest.

AUX TF [A]	MOD 1 [A]	MOD 2 [A]	MOD 3 [A]	MOD 4 [A]	PF - DIPOLE	PF - QUAD	PF - HEX	PF - OCT
0	-5.670e+5	-5.670e+5	-5.670e+5	-5.670e+5	0	0	0	0

Table 9-1. Coil currents used for shape/position robustness calculations. The auxiliary TF and PF coil currents are zero, and the modular coil currents are equal. The modular coil currents were provided by the engineering coil design code COILOPT

	$\mathbf{J_A}$	$\mathbf{J_B}$	$\mathbf{J_C}$
$\mathbf{p_A}$	$\chi^2_{BMN} = 0.032$ ε_h [%] = 1.46, 5.07, 9.70	$\chi^2_{BMN} = 0.024$ ε_h [%] = 0.71, 2.88, 6.43	$\chi^2_{BMN} = 0.020$ ε_h [%] = 0.27, 0.64, 1.44
$\mathbf{p_B}$	$\chi^2_{BMN} = 0.036$ ε_h [%] = 3.10, 5.64, 7.54	$\chi^2_{BMN} = 0.025$ ε_h [%] = 1.74, 3.63, 5.49	$\chi^2_{BMN} = 0.023$ ε_h [%] = 0.33, 0.62, 1.22
$\mathbf{p_C}$	$\chi^2_{BMN} = 0.028$ ε_h [%] = 0.93, 3.56, 7.97	$\chi^2_{BMN} = 0.022$ ε_h [%] = 0.58, 2.32, 5.74	$\chi^2_{BMN} = 0.020$ ε_h [%] = 0.26, 0.59, 1.37

Table 9-2. Measures of quasi-axisymmetry for un-optimized free-boundary equilibria with various combinations of pressure and current profile, using fixed coil currents. $\chi^2_{Bmn} = \Sigma' B^2_{mn}/B^2_{00}$ is the QA-measure used in the optimizer; ε_h is the effective helical ripple strength evaluated at normalized toroidal flux values of s= 0.25, 0.50, and 0.75

Table 9-2 presents calculated values of the quasi-axisymmetry measure $\chi^2_{Bmn} = \Sigma' B^2_{mn}/B^2_{00}$ for the un-optimized equilibria shown in Figure 9-4 (the equilibria are "un-optimized" in the sense that no attempt is made to improve the quality of the plasma parameters by allowing coil currents to vary). Also presented are values of ε_h , the effective helical ripple strength (see Chapter 8) evaluated at the three values of normalized toroidal flux s = 0.25, 0.50, and 0.75. These values of s correspond to values of normalized radius r/a of approximately 0.50, 0.70, and 0.85, respectively. The χ^2_{Bmn} values can be compared with the value 0.015 obtained for the li383 S3 reference configuration (Chapter 3, section 3.2.5) and the ε_h values can similarly be compared with the values 0.15%, 0.61%, and 1.73% for the reference fixed boundary configuration. A large degradation in quasi-axisymmetry occurs when the current profile becomes more peaked.

A mild degradation in QA-ness occurs as the pressure profile is peaked. A correlation between χ^2_{Bmn} and ε_h is seen, but it is less than perfect. For example, the degradation in χ^2_{Bmn} between the profile combination p_B, J_C and p_B, J_B is mild, yet the degradation in values of ε_h is substantial. In subsequent sections of this Chapter, we will therefore quote values of the calculated effective ripple amplitude, and omit quotation of χ^2_{Bmn}.

Figure 9-5 compares plasma boundaries for reconstructed plasmas using reference profiles but different values of β and I_p. Coil currents are again fixed at li383 reference S3 values. The boundary shown in black corresponds to an S3 state with I_p = 174 kA, β = 4.2%. The other two boundaries correspond to imagined disruptions where the plasma is assumed to have instantaneously lost all of its β or all of its current: The plasma boundary shown in red corresponds to the case of a post β-collapse I_p = 174 kA, β = 0.0%, while the boundary shown in green corresponds to the even more extreme limit where all the plasma current is lost; I_p = 0kA, β = 4.2%. The position/shape changes seen in Figure 9-5 can be contrasted with the behavior of tokamaks under equivalent changes of I_p and/or β where the loss of positional equilibrium would be much more severe. In the actual NCSX experiment, radial loss of equilibrium will be opposed by provision of an increased vertical (e.g., dipole) field.

• Case	• QA-ness measures
I_p = 174 kA, β = 4.2%	χ^2_{BMN} = 0.020 ε_h [%] = 0.27, 0.67, 1.57
I_p = 174 kA, β = 0.0%	χ^2_{BMN} = 0.068 ε_h [%] = 0.33, 0.59, 2.12
I_p = 0 kA, β = 4.2%	χ^2_{BMN} = 0.043 ε_h [%] = 0.34, 1.24, 2.95

Table 9-3. Quasi-axisymmetry measures χ^2_{Bmn} and ε_h for equilibria with various plasma current and beta values

It should be noted that each of the un-optimized equilibria corresponding to the data in Table 9-2 is unstable to kink modes at the given values of β. Even when we add to each equilibrium a sufficient dipole field to maintain radial position, the equilibria are found to be unstable. In NCSX, as in tokamaks, we must expect to change the plasma shape in response to changes in coil currents if we are to maintain stability as β, plasma current, I_p, or profile shapes (e.g., internal inductance ℓ_i) are changed.

In the following Sections, we investigate the performance of plasmas whose profiles and/or beta and net toroidal current differ from their reference forms and/or values. Coil currents are allowed to vary in such a way that χ^2_{Bmn} is minimized while kink and ballooning stability are enforced and plasmas are constrained to be limited by the first wall boundary. We will show that in spite of these constraints, stable plasmas with good quasi-axisymmetry can be obtained for a wide range of assumed plasma conditions.

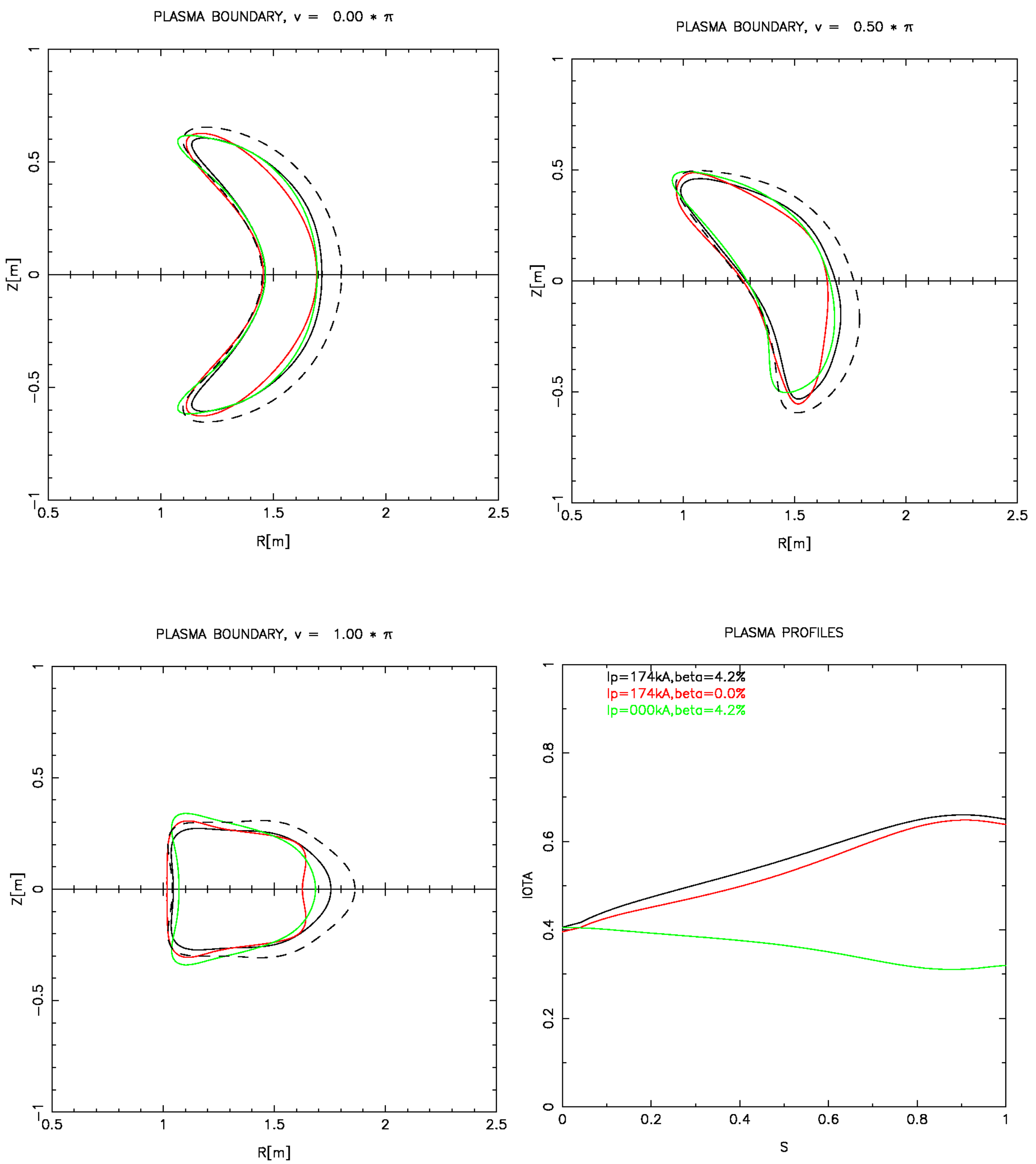

Figure 9-5. Overlay of plasma boundaries for reconstructed equilibria with reference profiles and various I_p, β values: (I_p, β) = (174 kA, 4.2%), (174 kA, 0.0%), and (0 kA, 4.2%). As in Figure 9-4, no limiter constraint was imposed

9.3 Robustness of Performance as β and I_p are Varied

In Chapter 10, discharge simulations are presented as a sequence of free-boundary equilibria corresponding to the "evolution" of an NCSX plasma from a particular S1 state where β = 0.0% to a final S3 state where β = 4.2%. Pressure profile evolution is consistent with a 1-D transport model. The evolution from initial to final states can be represented as a curve on an I_p - β plane. Each point on the curve is associated with a particular profile of plasma current and pressure.

In this section, we explore the robustness of performance of NCSX plasmas produced with M1017 coils. The free-boundary optimizer is run for a range of values of β and I_p using reference S3 profiles of current and pressure (Figure 9-2). In each case coil currents were varied to produce shape deformations of the plasma that lead to the minimization of a linear combination of χ^2_{Bmn} and the (square of the) growth rates for kink and ballooning modes. The average toroidal field was constrained to be constant, with B_T = 1.7 T at R=1.4 m.

Results are presented in Table 9-4. In each block is listed the kink and ballooning mode stability characteristics of the optimized configuration, as well as the effective helical ripple strength, ε_h[%], evaluated on the s=0.25, s=0.5, and s=0.75 magnetic surfaces. Stable free-boundary equilibria were found for nearly every case in the calculated I_p - β plane. All equilibria were stable to ballooning modes; nearly all equilibria were stable to kink modes. For Ip = 174 kA the free-boundary equilibrium with β = 5.0% was stable to both ballooning and kink modes. This β value is substantially higher than the reference li383 fixed boundary β-limit. We have not yet made a full exploration of the maximum β-limit using the M1017 coils. However, for a related modular coilset, named M0907, stable free-boundary equilibria were found through β = 6.5% (without allowing for the luxury of optimizing profiles). In four cases the kink modes were not completely stabilized by the optimizer. These appear in the yellow blocks of Table 9-4 and correspond to Ip = 130.5 kA, β = 2.0%, Ip = 130.5 kA, β = 2.0%, Ip = 174 kA, β = 1.0%, and Ip = 174 kA, β = 2.0%. It is likely that by adjusting the relative weights of χ^2_{Bmn} and χ^2_K in the physics objective function used by the optimizer the four slightly unstable equilibria of Table 9-4 can be stabilized at some modest cost to the QA-ness. With regard to the QA-ness, ε_h values displayed in Table 9-4 were never greater than 2.1% for the s=0.5 surface. Typical values are less than 1.5%. As discussed in Chapter 8, it is expected that for this magnitude of ripple amplitude, and with standard conditions of plasma temperature and density, the helical ripple transport will be small compared with axisymmetric neoclassical transport

Using reference profiles, we conclude there is a substantial region of stability with good QA-ness in the I_p - β plane.

An overlay of the plasma boundaries and calculated iota profiles for the optimized equilibria obtained in the I_p - β scan are presented in Figure 9-6. The range of variation for the coil currents which produce the optimized configurations of the I_p - β scan are presented in

Table 9-5. For the modular coil currents this variation is less than 15% of the nominal S3 currents (Table 9-1).

β[%] **Ip[kA]**	**0.0**	**1.0**	**2.0**	**3.0**	**4.0**	**5.0**
0						
43.5		$\lambda^K_{0,1}$ = S λ^B = S ε_h [%] = 0.64 2.11 5.39	$\lambda^K_{0,1}$ = S λ^B = S ε_h [%] = 0.36 1.30 3.21	$\lambda^K_{0,1}$ = S λ^B = S ε_h [%] = 0.44 1.30 2.90	$\lambda^K_{0,1}$ = S λ^B = S ε_h [%] = 0.23 0.86 2.17	
87		$\lambda^K_{0,1}$ = S λ^B = S ε_h [%] = 0.36 1.56 4.26	$\lambda^K_{0,1}$ = S λ^B = S ε_h [%] = 0.38 1.60 4.08	$\lambda^K_{0,1}$ = S λ^B = S ε_h [%] = 0.41 1.28 3.04	$\lambda^K_{0,1}$ = S λ^B = S ε_h [%] = 0.23 0.86 2.18	
130.5		$\lambda^K_{0,1}$ = S λ^B = S ε_h [%] = 0.21 0.77 2.11	λ^K_0 = -6.0e-5 λ^K_1 = -2.7e-5 λ^B = S ε_h [%] = 0.23 0.84 2.21	λ^K_0 = -8.8e-6 λ^K_1 = -2.2e-5 λ^B = S ε_h [%] = 0.50 1.14 2.66	$\lambda^K_{0,1}$ = S λ^B = S ε_h [%] = 0.20 0.67 1.49	
174	$\lambda^K_{0,1}$ = S λ^B = S ε_h [%] = 0.33 0.79 2.45	λ^K_0 = -1.9e-5 λ^K_1 = -2.0e-5 λ^B = S ε_h [%] = 0.34 0.81 1.97	λ^K_0 = -2.3e-5 λ^K_1 = -2.3e-5 λ^B = S ε_h [%] = 0.44 1.43 3.32	$\lambda^K_{0,1}$ = S λ^B = S ε_h [%] = 0.23 0.79 2.03	$\lambda^K_{0,1}$ = S λ^B = S ε_h [%] = 0.39 1.29 3.18	$\lambda^K_{0,1}$ = S λ^B = S ε_h [%] = 0.93 1.66 3.50

Table 9-4. NCSX plasma performance for various β, I_p values. The kink eigenvalues for the n=0 and n=1 family of kink modes are denoted by λ^K_0 , λ^K_1, respectively, and are tabulated if the mode is found to be unstable. In the case of kink stability, the notation $\lambda^K_{0,1}$ = S is used. λ_B = S => no unstable ballooning modes were found. Yellow blocks denote configurations which are found to be unstable to either kink or ballooning modes. The effective helical ripple strength, ε_h, is calculated for the s=0.25, s=0.5, and s=0.75 magnetic surfaces

It is interesting to contrast the free-boundary optimization results shown in Table 9-4 with corresponding fixed-boundary results shown in Table 9-6. Here, the stability of plasmas with different I_p, β values is calculated in the fixed li383 S3-state stellarator boundary. The plasma boundary shape is not allowed to change as β and I_p vary. We see that for the fixed-boundary runs there are many more unstable cases than in the free-boundary runs, and choosing a stable path from low β, low I_p to a final state defined as β = 4.0%, I_p = 174 kA is problematic. The freedom allowed in the free-boundary runs of adjusting the 3D shape to accommodate MHD stability is clearly significant and will be explored in subsequent sections.

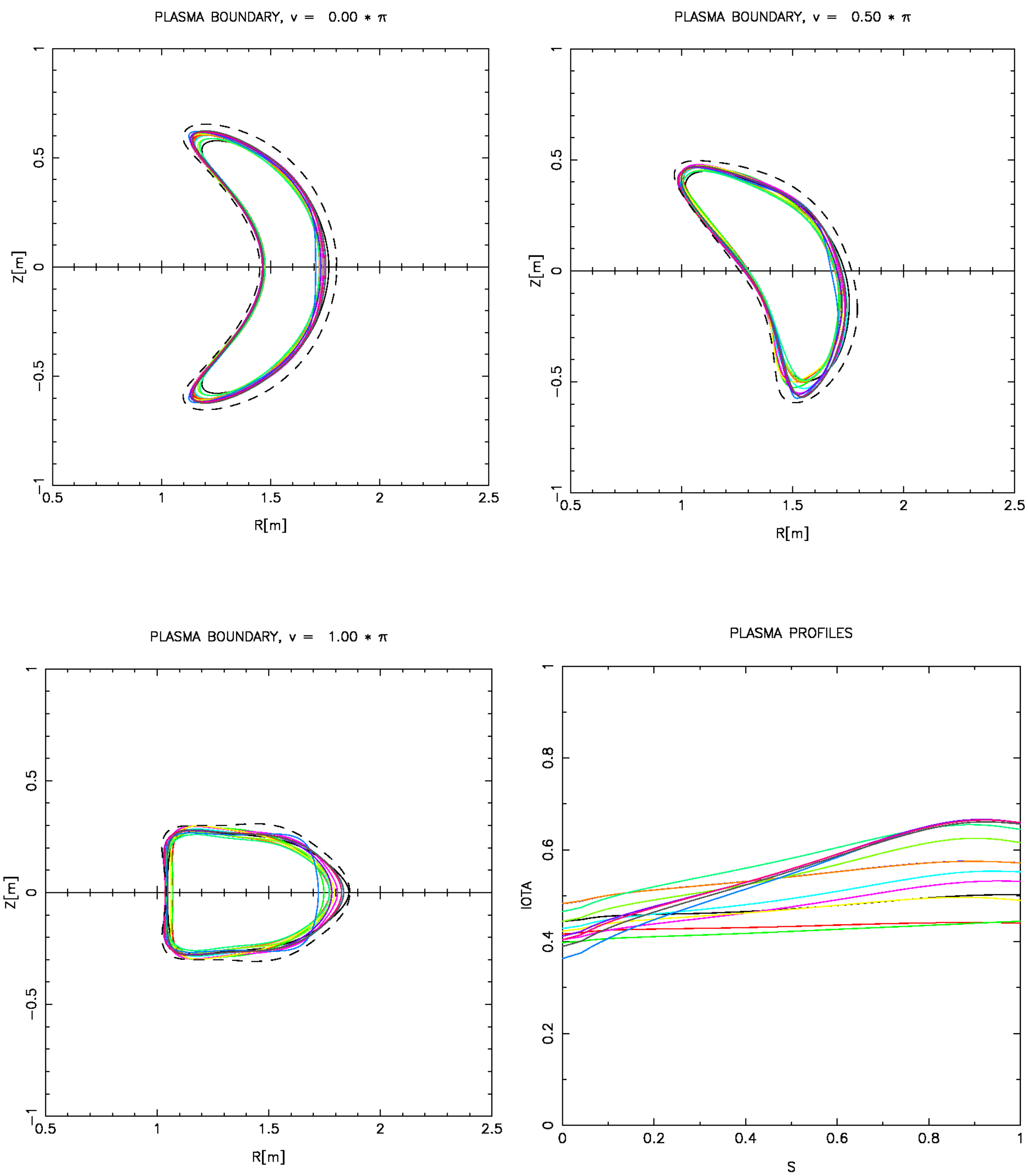

Figure 9-6. Overlay of plasma boundaries, and calculated iota profiles for stable optimized equilibria obtained of the optimized free-boundary I_p - β scan. Note the wide range of iota profiles (shear and edge iota values) for which plasmas were found to be stable

	MIN. I_C [A]	CASE	MAX. I_C [A]	CASE
Aux TF [A]	-7.172e+5	i0870b40	+7.088e+3	i1305b40
Mod 1 [A]	-6.110e+5	i0435b40	- 5.577e+5	i1305b40
Mod 2 [A]	-6.311e+5	i0435b40	- 5.566e+5	i0870b20
Mod 3 [A]	-6.157e+5	i0870b40	- 5.268e+5	i0435b10
Mod 4 [A]	-6.350e+5	i0435b10	- 4.811e+5	i1305b30
PF Dipole	+6.478e-2	i0435b40	+ 5.868e-1	i0435b10
PF Quad	- 1.234e-1	i0435b30	+ 9.444e-1	i1305b30
PF Hex	- 6.159e-1	i0435b10	+ 2.142e-0	i0870b30
PF Oct	- 7.319e-0	i1740b10	+ 1.564e-0	i0435b30

Table 9-5. Maximum and Minimum coil currents for the set of optimized configurations in the I_p - β scan experiments. For each case an identifier of the form "ixby" is given, where x/10 is the value of the current in kA, and y/10 is the value of plasma beta in %

β[%] I_P[KA]	0.0	1.0	2.0	3.0	4.0	5.0
0.0	$\lambda^K_{0,1}$ = S λ^B = S					
43.5	$\lambda^K_{0,1}$ = S λ^B = S	$\lambda^K_{0,1}$ = S λ^B = S	$\lambda^K_{0,1}$ = S λ^B = S	λ^K_0 = S λ^K_1 = -3.5e-4 λ^B = U_{13-16}	λ^K_0 = S λ^K_1 = -1.5e-3 λ^B = U_{9-18}	
87	λ^K_0 = S λ^K_1 = -1.4e-4 λ^B = S	$\lambda^K_{0,1}$ = S λ^B = S	$\lambda^K_{0,1}$ = S λ^B = S	$\lambda^K_{0,1}$ = S λ^B = S	λ^0_K = S λ^1_K = -7.8e-4 λ^B = U_{46-47}	
130.5	λ^K_0 = -1.7e-3 λ^K_1 = -3.8e-4 λ^B = S	λ^K_0 = -1.1e-3 λ^K_1 = S λ^B = S	λ^K_0 = -7.2e-4 λ^K_1 = S λ^B = S	λ^K_0 = -6.1e-4 λ^K_1 = S λ^B = U_{47-47}	λ^K_0 = -6.8e-4 λ^K_1 = -2.7e-4 λ^B = U_{46-48}	
174	λ^K_0 = -5.5e-4 λ^K_1 = -5.1e-4 λ^B = S	λ^K_0 = -4.9e-5 λ^K_1 = -4.5e-5 λ^B = S	λ^K_0 = -3.7e-5 λ^K_1 = -2.4e-5 λ^B = S	$\lambda^K_{0,1}$ = S λ^B = S	λ^K_0 = -1.2e-4 λ^K_1 = -1.9e-4 λ^B = U_{46-47}	λ^K_0 = -1.0e-3 λ^K_1 = -1.5e-3 λ^B = U_{45-48}

Table 9-6. Fixed-boundary stability results in the I_p, - β plane. Orange blocks indicate unstable cases. The $\lambda^K_{0,1}$ are kink unstable eigenvalues for the n=0 and n=1 families. $\lambda^K_{0,1}$ = S => kink stability. $\lambda^B = U_{i-j}$ => ballooning modes on surface numbers i - j (out of 49) are unstable. λ^B = S => ballooning stability. There are many unstable cases, and no stable path to I_p = 174 kA, β = 4.0%

9.4 Robustness of Performance as Plasma Profiles are Varied

For the results presented so far, the current and pressure profiles have had the same form as the reference li383 profiles. Now we investigate the effect on plasma performance of choosing plasma profiles that are different from the reference profiles. First, we examine the performance of plasmas supported by NCSX coils for a range of current profiles, with the pressure profile held fixed equal to the reference form shown in Figure 9-2. The effect of varying the current profile in the core region of the plasma is considered separately from the effect of varying the current profile in the edge region. In another set of experiments the effect of varying the pressure profile is considered, with the current profile held fixed equal to its reference form, also shown in Figure 9-2. We will show that good plasma performance is obtained for a wide range of current and pressure profiles. This allays any concern that the optimization methods used for designing the plasma configuration and coil system have produced only a narrow operating space of good performance plasmas.

9.4.1 Variation of the Current Profile in the Core Region

Here we examine the performance of plasmas supported by NCSX coils for current profiles which differ from the reference form mainly in the core region. A 1-parameter family of current profiles, J_α, is conveniently defined by

$$J_\alpha (s) = (1-\alpha)\, J^{ref}(s) + \alpha\, J^{peaked}(s), \qquad (9.4\text{-}1)$$

where $0 \le \alpha \le 1$, and J(s) denotes the surface averaged parallel current profile $\mathbf{J \bullet B}$. As α ranges from zero to one, J_α undergoes a substantial change in shape, from the reference hollow current profile, J^{ref} , to a peaked current profile defined as $J^{ref} = 1 - s^2$. A plot of the J_α used in this study is shown in Figure 9-7.

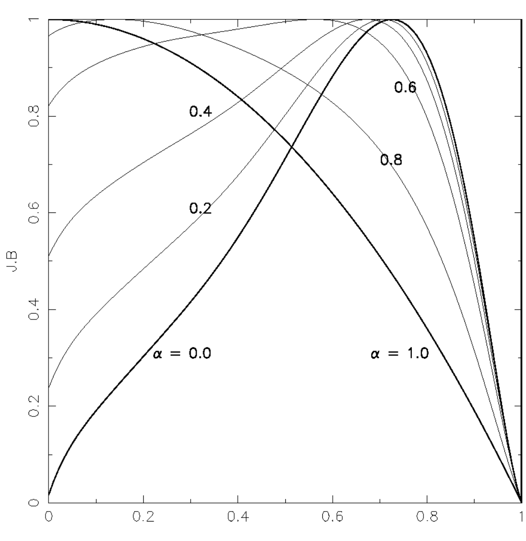

Figure 9-7. 1-parameter family of current profiles which vary mainly in the core region . The stable range of current profiles is $0 \le \alpha \le 0.5$. For this range of α, the internal inductance ℓ_i of an equivalent tokamak with the same average elongation, triangularity, and aspect ratio ranges from 0.30 to 0.54

With α = 0.0, $J_\alpha = J^{ref}$ and the plasma configuration is identical to the reference configuration. As discussed in Section 9.3, the free-boundary β-limit for these profiles is at least β = 5.0%. We execute a sequence of free-boundary optimizer runs, increasing α from 0.0 in steps of 0.2, to determine the range of values of α (i.e., range of current profiles) for which NCSX plasmas are stable at β = 3.0%. For each run, the plasma current was held fixed at Ip = 174 kA, and the average toroidal field at R = 1.4 m is B_T = 1.7 T.

Table 9-7 shows a summary of the kink and ballooning stability properties for the various optimized configurations, including values of the effective ripple ε_h. It is seen that current profiles with $0 \le \alpha \le 0.5$ are stable to kink and ballooning modes, with quasi-axisymmetry measure ε_h < 1.3% at s=0.5.

α	**0.0**	**0.1**	**0.2**	**0.3**	**0.4**	**0.5**	**0.6**	**0.7**
λ^K_0 λ^K_1	S S	S S	S S	S S	S -1.5e-5	S -2.8e-5	-7.3e-4 -5.1e-5	-9.1e-4 -8.0e-5
λ_B	S	S	S	S	S	S	S	S
ε_h[%]	0.44 1.29 2.97	0.37 1.16 3.11	0.22 0.90 2.39	0.21 0.88 2.24	0.33 1.32 3.84	0.36 1.27 3.63	0.38 1.13 3.11	0.34 1.05 2.71
TF [A]	-1.952e+5	-1.570e+5	-4.396e+4	-9.608e+4	-7.743e+4	-1.508e+5	-6.672e+4	-3.516e+4
Mod 1 [A]	-5.701e+5	-5.692e+5	-5.679e+5	-5.711e+5	-5.687e+5	-5.788e+5	-5.920e+5	-5.794e+5
Mod 2 [A]	-5.730e+5	-5.695e+5	-5.553e+5	-5.617e+5	-5.580e+5	-5.668e+5	-5.599e+5	-5.845e+5
Mod 3 [A]	-6.002e+5	-5.915e+5	-5.809e+5	-5.850e+5	-5.985e+5	-5.839e+5	-5.878e+5	-5.894e+5
Mod 4 [A]	-5.384e+5	-5.492e+5	-5.659e+5	-5.580e+5	-5.373e+5	-5.576e+5	-5.435e+5	-5.446e+5
PF Dipole	+2.434e-1	+3.467e-1	+2.152e-1	+2.254e-1	+2.878e-1	+3.218e-1	+2.606e-1	+2.423e-1
PF Quad	+1.097e-1	+6.088e-2	-7.816e-2	-1.420e-1	-2.717e-1	-4.003e-1	-3.071e-1	-4.889e-1
PF Hex	+1.515e+0	+2.813e+0	+1.995e+0	+2.910e+0	+2.050e+0	+3.275e+0	+3.185e+0	+4.122e+0
PF Oct	-9.098e+0	-8.298e+0	-1.682e+0	-2.132e+0	-4.230e+0	-4.626e+0	-3.256e+0	-1.588e+0

Table 9-7. Maximum growth rates for kink and ballooning modes ($\lambda^K_{0,1}$, λ^B), optimized values of effective ripple (ε_h[%]) at the s=0.25, s=0.5, and s=0.75 surfaces, and coil currents for various current profiles parameterized by the peakedness parameter α. All equilibria correspond to β = 3.0%. Unstable cases are shown as yellow

For reasons of computational speed, the TERPSICHORE stability calculations in the optimizer which led to the eigenvalues tabulated in Table 9-7 used 49 radial grid points and 91 modes to represent the perturbation. To gain confidence that the reported range of stable current profiles really is truly defined by $0 \le \alpha \le 0.5$, we have re-optimized the configurations using artificial multipliers for the kink and ballooning terms in δW (see Chapter 5) with COEC=COEP=1.05. The new configurations are minimally modified and have similarly small eigenvalues (actually smaller for the re-optimized α=0.5 configuration). Further convergence tests will be made using more radial grid points and a greater number of perturbation modes but the main findings are expected to remain valid.

Figure 9-8 shows an overlay of plasma boundaries and calculated iota profiles for the $\alpha < 0.5$ stable configurations. The onset of instability may be correlated with a lack of adequate shear in the iota profile for $\alpha > 0.5$.

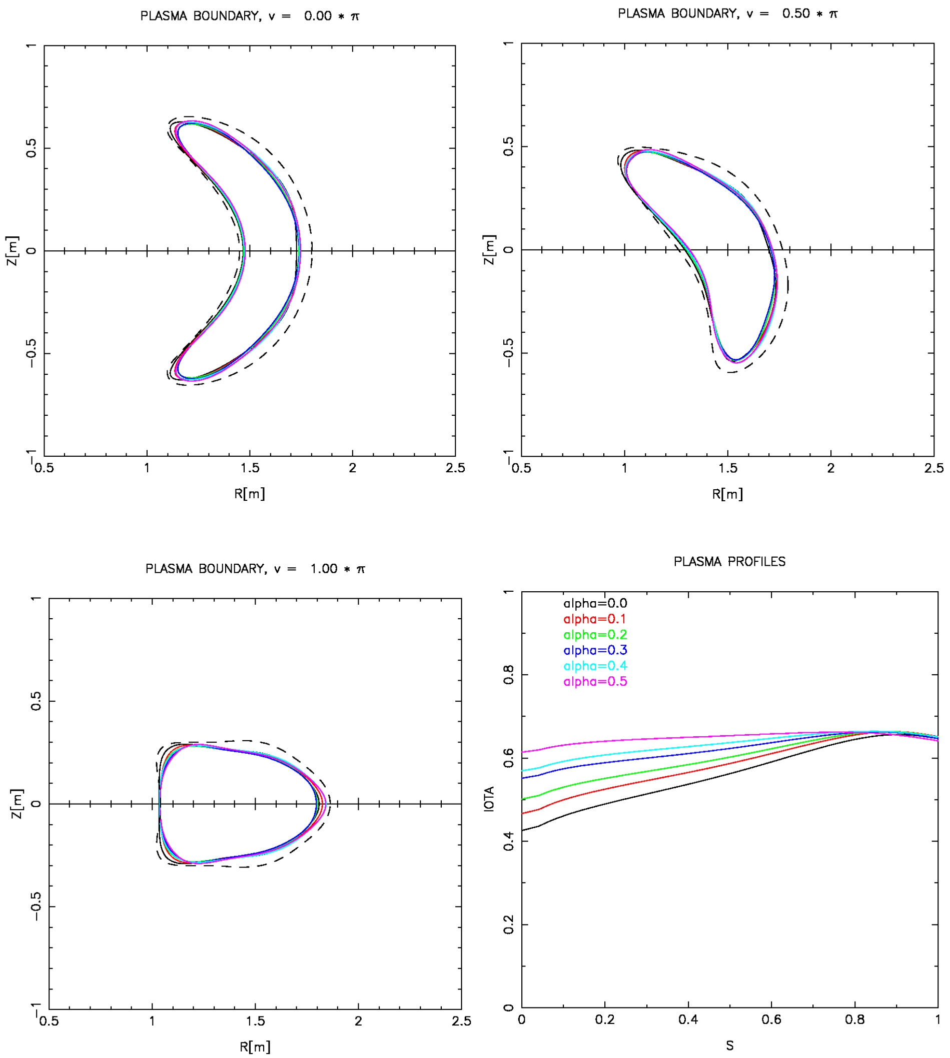

Figure 9-8. Overlay of plasma boundaries for stable equilibria at β = 3.0% for the J_α sequence of current profiles (where J • B is varied un the core region). The calculated iota profiles are also shown.

9.4.2 Variation of the Current Profile in the Edge Region

We now explore the effect of varying the current profile in the edge region. In particular we consider the family of current profiles, J_δ, shown in Figure 9-9 where

$$J_\delta\,(s) \propto J^{ref}(s) + \delta\, J^{edge}(s), \qquad (9.4\text{-}2)$$

and $J^{edge}(s) = s^8$ gives a sizeable contribution to the current profile near the plasma edge. The values of δ shown in Figure 9-9 represent the magnitude of J_δ at the plasma edge relative to the maximum value of $J_\delta\,(s)$. δ varies from 0.0 to 0.5 in steps of 0.1.

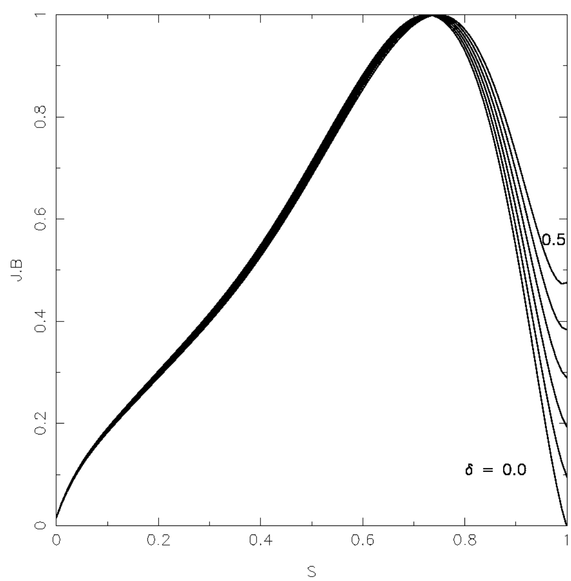

Figure 9-9. Family of current profiles $J_\delta\,(s)$ which vary mainly in the edge region. Stability may be enhanced as the edge current builds due to an increase in the global shear.

Whereas in Section 9.4.1 we considered free-boundary equilibrium reconstructions at β = 3.0%, in this section we explore the stability characteristics of free-boundary plasmas with finite edge current at β = 5.0%, a value which exceeds the reference fixed-boundary β-limit for li383.

Already the I_p - β scan presented in Table 9-4 has shown a stable configuration with I_p = 174 kA, β = 5.0%. Coil currents for this case are shown in Table 9-8. Using the same coil currents the free-boundary VMEC code was used to obtain free-boundary equilibria for each of the six current profiles shown in Figure 9-9. For each equilibrium I_p = 174 kA, β = 5.0%, and the pressure profile was fixed equal to the reference form.

For each current profile the calculated equilibrium was stable to kink and ballooning modes.

AUX TF [A]	MOD 1 [A]	MOD 2 [A]	MOD 3 [A]	MOD 4 [A]	PF - DIPOLE	PF - QUAD	PF - HEX	PF - OCT
+2.053e+3	-5.658e+5	-5.767e+5	-5.555e+5	-5.498e+5	+1.212e-1	+4.957e-2	+3.075e-1	-5.400e-1

Table 9-8. Coil currents corresponding to the stable configuration with I_p = 174kA, β = 5.0% presented in Table 9-4. These currents are used in free-boundary equilibrium reconstructions which vary the edge current density.

The robust stability for the sequence of equilibria with different edge current densities can be understood in terms of the effect on the iota profile of adding successive current layers to the plasma edge region. Figure 9-10 shows overlays of the plasma boundaries and profiles of $\iota(s)$ for the six equilibria. In particular it should be noted that as more edge current is included, the shear $\iota'(s)$ in the edge region of the plasma is increased with no change to the edge iota. Such an increase in shear is known to be stabilizing for current-carrying stellarators (see Ref. [2] and results presented in Chapter 5).

An increase in current density near the plasma edge is an expected consequence of a transition from L-Mode to H-Mode profiles. In view of the observations made above, there is an interesting possibility that such a transition will have beneficial effects on MHD stability. Future calculations should calculate β-limits for realistic models of H-mode profiles in NCSX.

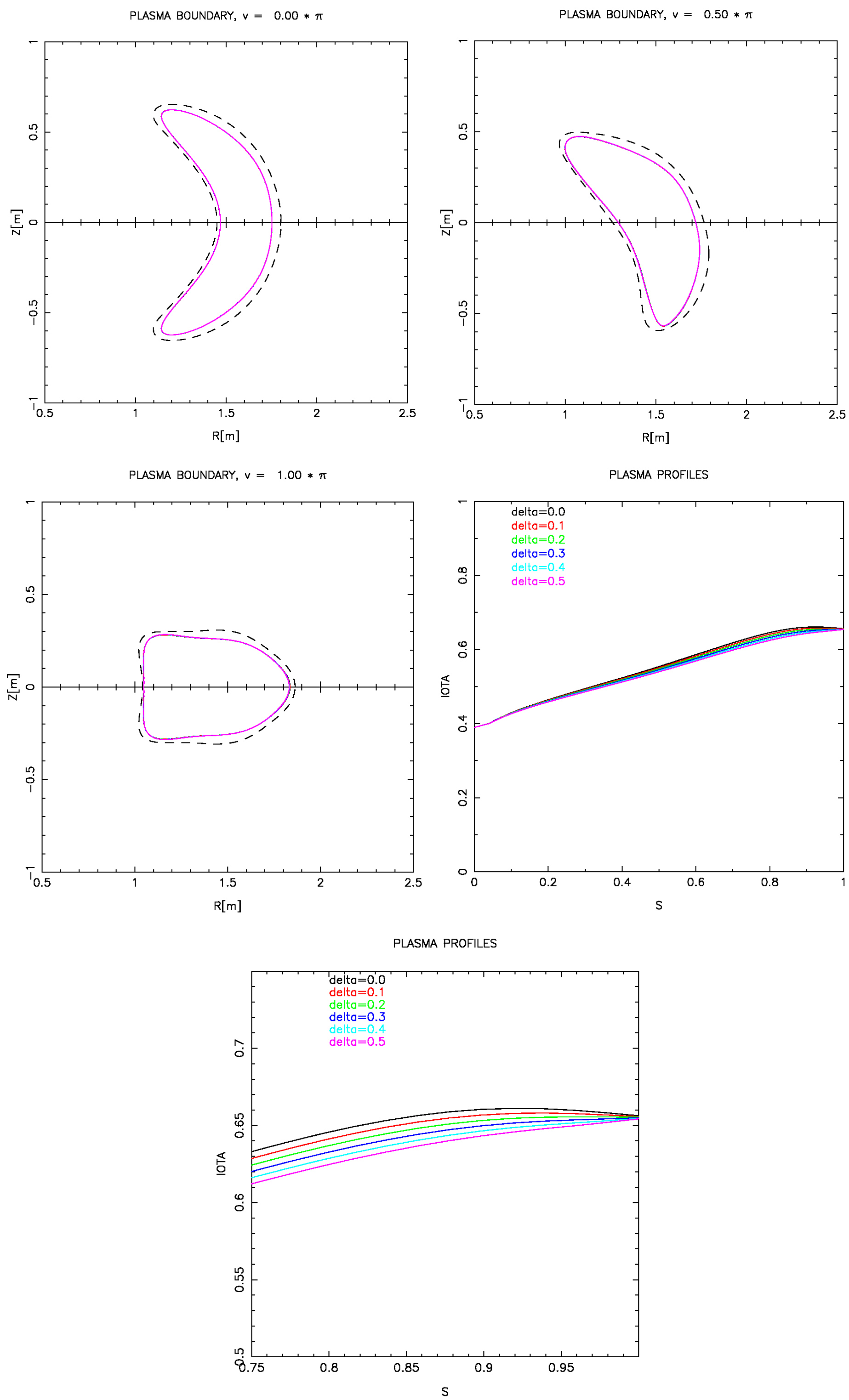

Figure 9-10. Overlay of plasma boundaries for six stable equilibria with varying edge current densities and I_p = 174 kA, β = 5.0%. The coil currents are the same in all cases. The plasma boundaries vary little. Also shown are the $\iota(s)$ profiles (shown plotted in two frames, the second of which is a blow-up of the first). As the edge current is increased, the shear increases, which is a stabilizing effect

9.4.3 Variation of the Pressure Profile

As a third set of numerical experiments we examine the performance of plasmas supported by NCSX coils for a range of pressure profiles. The current profile shape is held fixed equal to the reference form. A 1-parameter family of pressure profiles is defined by

$$P_\gamma(s) = (1 - \gamma)\, P^{ref}(s) + \gamma\, P^{peaked}(s), \qquad (9/4\text{-}3)$$

where $0 < \gamma < 1$, and P denotes the pressure profile p(s). As γ ranges from zero to one, P_γ undergoes a change from the (broad) reference pressure profile to a more peaked pressure profile whose analytic dependence on toroidal flux is $P^{peaked} \propto (1 - s)^2$. This "peaked" form is a good fit with the NBI heated PBX-M discharge profile denoted by p_B in Section 9.2. A plot of the P_γ for different values of γ is shown in Figure 9-11.

We execute a sequence of free-boundary optimizer runs, increasing γ from 0.0 to 1.0 in steps of 0.2 to determine the range of values of γ (range of pressure profiles) for which NCSX plasmas supported by the designed coils are stable to ballooning and kink modes with optimized QA measure χ^2_{Bmn} at $\beta = 3.0\%$. As in Section 9.4.1, we choose $I_p = 174$ kA, $\beta = 3.0\%$ with $B_T = 1.7$ T at R = 1.4 m, making no attempt to optimize β by changing I_p from this reference value.

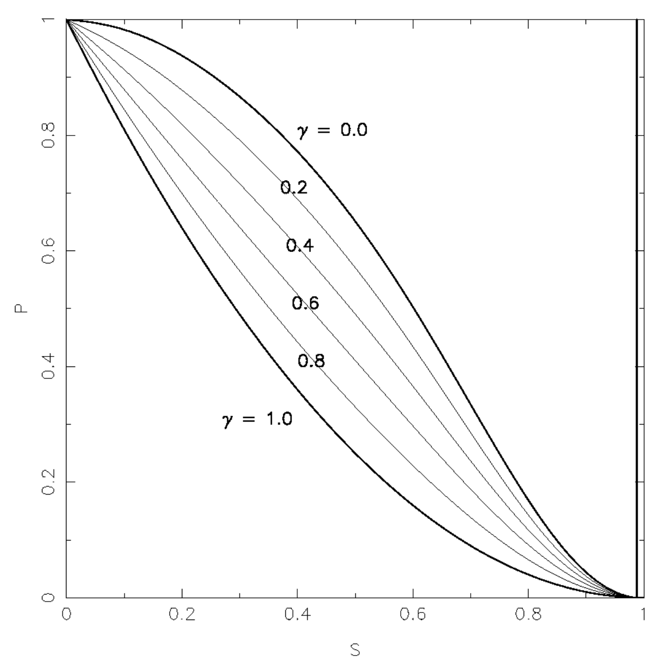

Figure 9-11. The 1-parameter family of pressure profiles, P_γ, for which plasma performance is evaluated at $\beta = 3\%$

Table 9-9 summarizes the optimizer runs as the peakedness parameter γ is varied. For the given parameterization of p(s), stable configurations with good quasi-axisymmetry (ε_h < 1.1% at s=0.5) were found for all cases except γ =1.0. For this case, we have found a stable configuration at β = 2.5%. Figure 9-12 shows an overlay of the plasmas boundaries and iota profiles for each of the stable optimized configurations with $\gamma \leq 0.8$.

The operating space of stable configurations with β = 3.0%, substantial variations in current and pressure profiles, and good quasi-symmetry appears to be quite broad. We also note that it should be possible to widen the operating space of stable profiles further by allowing the plasma current to vary in addition to the shape.

γ	**0.0**	**0.2**	**0.4**	**0.6**	**0.8**	**1.0**
λ^K_0 λ^K_1	S S	S S	S S	S S	S S	-3.0e-4 -5.4e-5
λ_B	0	0	0	0*	0*	0*
ε_h**[%]**	0.33 0.80 1.83	0.22 0.72 1.78	0.23 0.78 1.91	0.31 1.05 2.56	0.25 0.73 1.60	0.25 0.62 1.29
TF [A]	- 4.623e-1	-6.429e+1	-6.005e+1	-6.005e+1	+1.067e+3	-1.506e+4
Mod 1 [A]	-5.646e+5	-5.665e+5	-5.644e+5	-5.644e+5	-5.714e+5	-5.762e+5
Mod 2 [A]	-5.705e+5	-5.602e+5	-5.599e+5	-5.599e+5	-5.439e+5	-5.416e+5
Mod 3 [A]	-5.564e+5	-5.647e+5	-5.700e+5	-5.700e+5	-6.020e+5	-6.090e+5
Mod 4 [A]	-5.670e+5	-5.798e+5	-5.738e+5	-5.738e+5	-5.273e+5	-5.039e+5
PF Dipole	+1.250e-1	+1.235e-1	+1.326e-1	+1.326e-1	+1.043e-1	+4.353e-2
PF Quad	+2.787e-2	+2.660e-2	+7.660e-2	+7.660e-2	+2.587e-2	+3.271e-2
PF Hex	- 2.737e-2	- 4.365e-2	- 1.759e-2	- 1.759e-2	- 9.751e-3	+4.737e-3
PF Oct	- 1.017e-2	- 9.667e-3	- 9.695e-3	- 9.695e-3	- 4.849e-3	- 1.207e-2

Table 9-9. Maximum growth rates for kink and ballooning modes ($\lambda^K_{0,1}$, λ^B) , optimized values of effective ripple (ε_h[%]) at the s=0.25, s=0.5, and s=0.75 surfaces and coil currents for various pressure profiles parameterized by the peakedness parameter γ. , λ^B = 0* denotes instability on first evaluated surface (out of 49) near the magnetic axis. All equilibria correspond to β = 3.0%. Unstable cases are shown as yellow

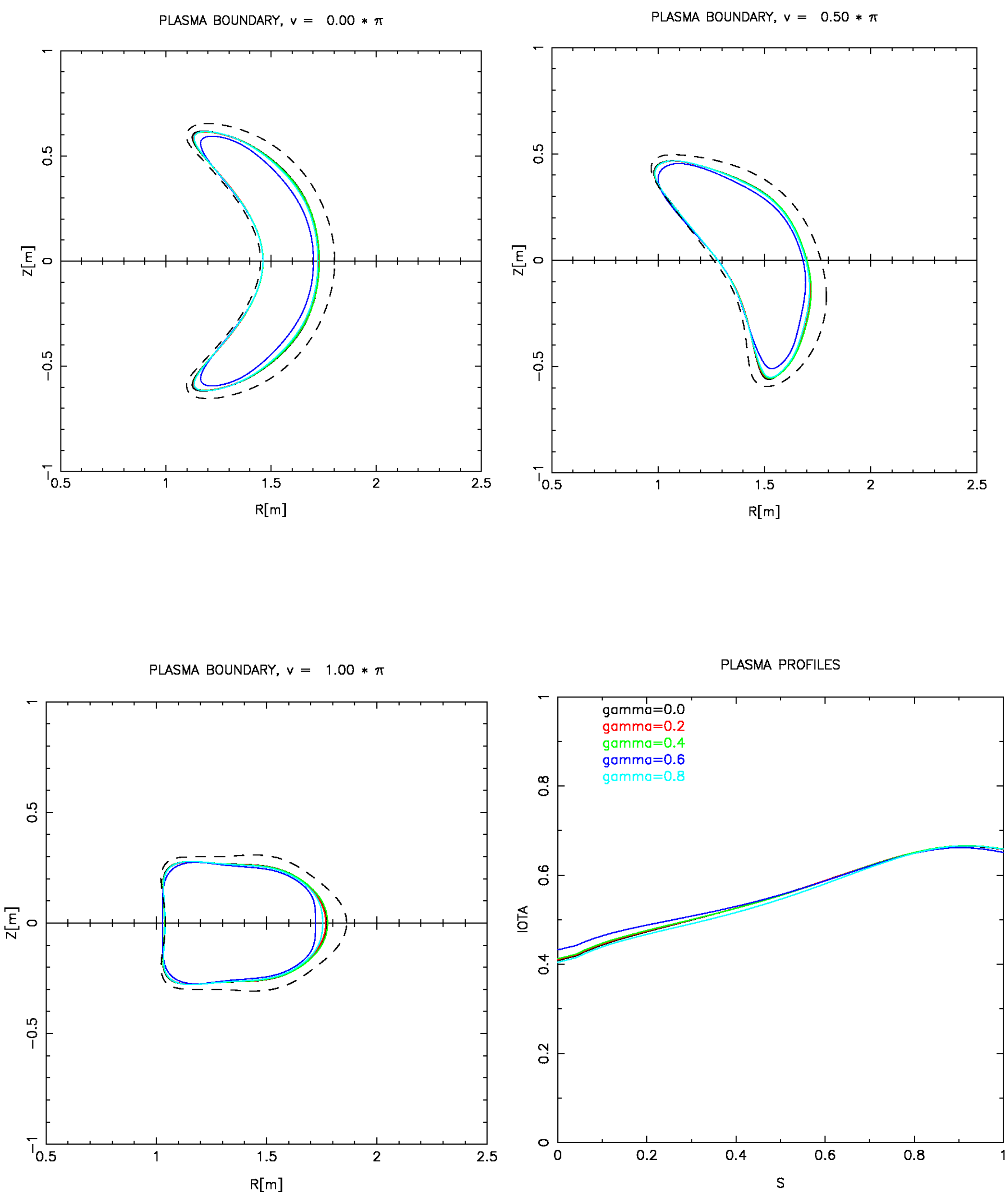

Figure 9-12. Overlay of plasma boundaries and iota profiles for stable optimized configurations of the pressure profile scan. I_p = 174 kA, β = 3.0% for all cases

9.5 Flexibility to Control the External Transform

We now demonstrate the important capability of NCSX coils to effect substantial changes in the external field contribution to ι(s). The MHD stability of stellarator plasmas can depend critically on details of the iota profile; for example on the location of the ι= 0.5 magnetic surface. The W7AS experiments reported at IAEA2000 in Sorrento [3] demonstrate cases where stability depends, not on the magnitude of the external transform ι_{ext}, but on the ability to avoid ι(1) = 0.5 during the discharge due to q=2 global tearing modes. On the other hand, the reference S3 configuration (full current, full beta) for NCSX has ι(0) = 0.44, ι(1) = 0.65, while the reference S1 "vacuum" configuration (see Chapter 10.2) has ι(s) < 0.5 for all s values. Plasma evolution from S1 to S3 implies, for the reference scenario, passage through ι(1) = 0.5. The NCSX coil currents can be chosen to evolve in such a way that 3D shaping of the plasma avoids the trigger of any kink mode. Nevertheless it is important to have the ability to control the iota profile through external shaping so that ι(1) = 0.5 can be avoided, if that is found to be necessary. In Chapter 10.4 a "high iota" startup scenario is presented, which avoids passage through ι(1) = 0.5. The ability to control ι(s) will be a very useful control knob to aid the mapping of stable/unstable boundaries for NCSX.

9.5.1 Variation of ι(s) at Fixed Shear

Here we demonstrate the ability to raise and lower ι(s) while keeping the shear essentially constant. As a baseline plasma we choose an S2 state with I_p = 174 kA, β = 0.0% that was generated from the reference li383 S3 configuration by ramping β from 4.2% to 0.0% while maintaining stability to kink and ballooning modes. The S2 state has axis and edge values of iota of ι(0) = 0.44, ι(1) = 0.65. As final preparation for the study a further optimization run was made where ι(0) and ι(1) were constrained to remain constant, the kink and ballooning constraints were turned off, and the configuration was re-optimized for χ^2_{Bmn}.

For the iota scan experiments we target desired values of ι(0) and ι(1), and optimize χ^2_{Bmn}.making no attempt to stabilize the kink and ballooning modes. The goal here is to explore coil flexibility, not plasma performance. The plasma current is held fixed at I_p = 174 kA, and the toroidally averaged B_T is held constant at 1.7 T at R = 1.4 m. (Increasing/decreasing ι(s) by changing B_T is trivial. However, changing ι(s) at fixed plasma current and toroidal field by changing the external transform using 3D shaping is not; this is the goal of the present flexibility studies). Figure 9-13 shows plasma boundaries and calculated iota profiles for cases where ι(s) was programmed to change both the axis and edge values of iota by ±0.1 and ±0.2 from the baseline S2 values. It is interesting to note the range of shapes required to produce the target iota profiles.

Table 9-10 presents a summary of the calculated coil currents and details of the calculated iota profiles. Presently NCSX plans for the auxiliary TF coils to provide ±0.3 T, corresponding to TF[A] = 2.1e+6.

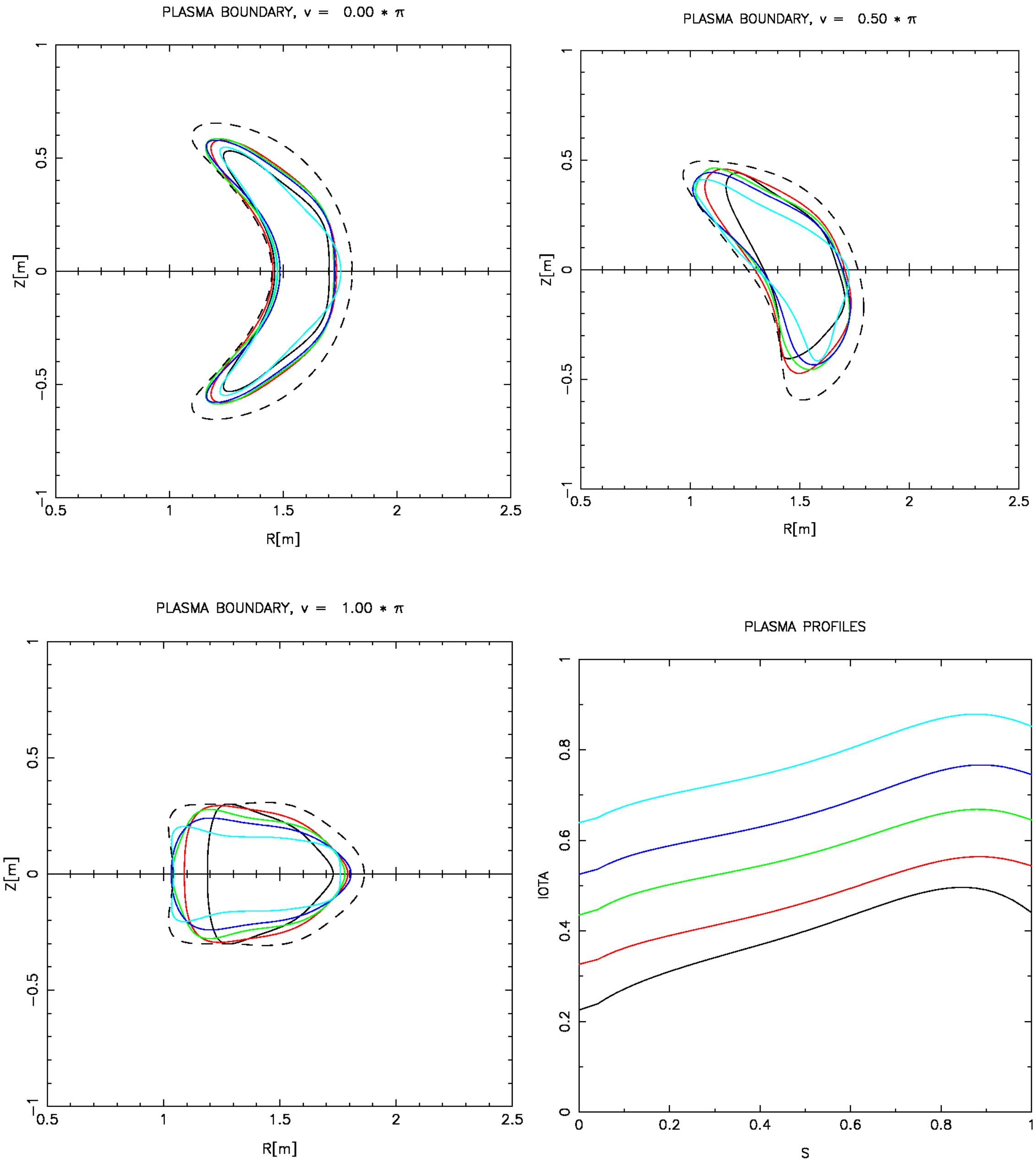

Figure 9-13. Plasma boundaries and iota profiles for iota-scan flexibility studies where coil currents are asked to change in such a way as to induce specified changes in ι(s). Here ι(s) is raised/lowered in such a way that the shear is preserved

	RUN 1	**RUN 2**	**RUN 3**	**RUN 4**	**RUN 5**
$\iota(0)$	0.23	0.33	0.44	0.53	0.64
$\iota(1)$	0.44	0.54	0.65	0.75	0.85
$\iota_{vac}(0)$	0.28	0.37	0.50	0.60	0.71
$\iota_{vac}(1)$	0.20	0.34	0.45	0.54	0.63
A	5.36	4.52	4.57	4.77	5.31
TF [A]	+2.944e+6	+1.462e+6	- 4.881e+2	- 7.960e+5	- 6.881e+5
Mod 1 [A]	- 4.156e+5	- 4.909e+5	- 5.690e+5	- 6.126e+5	- 6.217e+5
Mod 2 [A]	- 4.332e+5	- 4.954e+5	- 5.606e+5	- 5.958e+5	- 5.964e+5
Mod 3 [A]	- 4.375e+5	- 5.078e+5	- 5.906e+5	- 6.431e+5	- 5.971e+5
Mod 4 [A]	- 4.127e+5	- 4.842e+5	- 5.302e+5	- 5.428e+5	- 5.816e+5
PF Dipole	+ 7.061e-1	+ 5.370e-1	+ 4.251e-1	+ 3.880e-1	+ 1.512e-1
PF Quad	- 1.642e+0	- 2.237e-1	+ 3.553e-1	+1.000e+0	+3.019e+0
PF Hex	+1.023e+1	+4.348e+0	+3.003e+0	+3.336e+0	+2.819e+0
PF Oct	- 2.201e+1	- 8.434e+0	- 1.549e+1	- 1.695e+1	+2.068e+0

Table 9-10. Coil currents for raising/lowering $\iota(s)$ at constant shear (see Figure 9-13)

9.5.2 Variation of $\iota(s)$ at Fixed $\iota(0)$ – Changing the Shear

Figure 9-14 and Table 9-11 show results from a similar calculation, where now the axis value $\iota(0)$ is constrained to remain fixed at the nominal value $\iota(0) = 0.44$, and the edge value is increased/decreased from the nominal value of $\iota(1) = 0.65$ by ± 0.1 and ± 0.2. The effect is to change the global shear.

	RUN 6	**RUN 7**	**RUN 8**	**RUN 9**	**RUN 10**
$\iota(0)$	0.43	0.44	0.44	0.44	0.44
$\iota(1)$	0.44	0.54	0.65	0.74	0.84
$\iota_{vac}(0)$	0.27	0.51	0.50	0.51	0.53
$\iota_{vac}(1)$	0.16	0.34	0.45	0.53	0.63
A	5.23	4.87	4.57	4.72	4.88
TF [A]	- 1.257e+2	+1.630e+4	- 4.881e+2	- 1.839e+4	- 6.188e+5
Mod 1 [A]	- 5.675e+5	- 5.694e+5	- 5.690e+5	- 5.632e+5	- 5.861e+5
Mod 2 [A]	- 5.734e+5	- 5.635e+5	- 5.606e+5	- 5.554e+5	- 5.769e+5
Mod 3 [A]	- 5.757e+5	- 6.019e+5	- 5.906e+5	- 5.764e+5	- 6.016e+5
Mod 4 [A]	- 5.850e+5	- 5.230e+5	- 5.302e+5	- 5.540e+5	- 5.995e+5
PF Dipole	+ 9.995e-1	+ 6.677e-1	+ 4.251e-1	+ 4.399e-1	+ 7.193e-1
PF Quad	- 1.717e+0	- 4.195e-1	+ 3.553e-1	+ 4.468e-1	- 3.596e-1
PF Hex	+1.605e+1	+9.640e+0	+3.003e+0	- 8.239e-2	+1.519e+0
PF Oct	- 2.123e+1	- 2.161e+1	- 1.549e+1	-4.620e+0	- 3.330e-1

Table 9-11. Coil currents for increasing/decreasing shear (see Figure 9-14)

The results in this section demonstrate a substantial capability for the M1017 coil set to scale the iota profile or change the shear. We have found similar flexibility to change the ɩ(s) profile for S1 states with $I_p = 0$ kA, a flexibility that is used to control ɩ(s) in the high-iota startup scenario presented in Chapter 10.

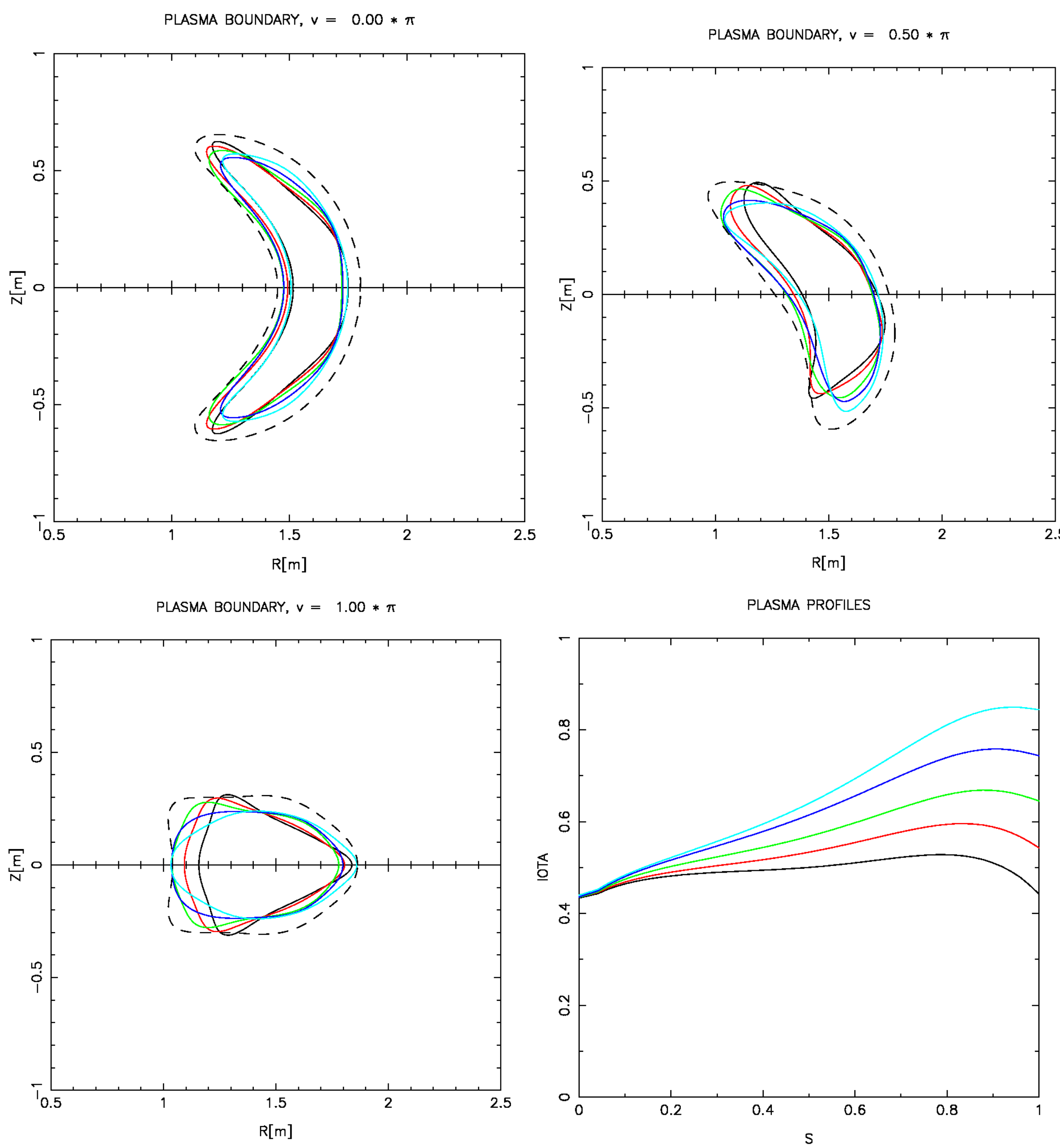

Figure 9-14. Plasma boundaries and iota profiles for iota-scan flexibility studies where coil currents are asked to change in such a way as to induce specified changes in ɩ(s). Here the shear is increased/decreased

9.6 Flexibility to Study Kink Stabilization by 3D Shaping

The free-boundary I_p - β scan numerical experiments presented in the Section 9.3 and summarized in Table 9-4 can be used to clearly demonstrate the effect of MHD stabilization by 3D shaping and to suggest controlled experiments to explore stability boundaries in NCSX.

The present measure used for stability in the free-boundary optimizer cost function is a weighted sum of the square of the maximum unstable kink mode eigenvalue and the sum (over ballooning unstable surfaces) of the maximum ballooning mode eigenvalue. It follows that any stable "final state" of the optimizer is a state of marginal stability. Consider two states from the I_p - β scan that have the same value of plasma current but different values of beta. For example the cases I_p = 43.5 kA, β = 1.0%, and I_p = 43.5 kA, β = 3.0%. The plasma shapes differ (see Figure 9-15). Each plasma is at the β-limit for its given shape.

Figure 9-15 also shows the calculated $\iota(s)$ profiles. Axis and edge iota values are:

$\iota(0)$ = 0.44, $\iota(1)$ = 0.50 for I_p = 43.5 kA, β = 1.0%;
$\iota(0)$ = 0.40, $\iota(1)$ = 0.44 for I_p = 43.5 kA, β = 3.0%.

The calculated coil currents for these two configurations are presented in the first two columns of Table 9-12.

Now consider the effect of taking the I_p = 43.5 kA, β = 1.0% configuration and raising β to 3.0% <u>while keeping the plasma boundary fixed</u>. The iota profile for this β = 3.0% "virtual" configuration is found to have $\iota(0)$ = 0.40, $\iota(1)$ = 0.50. It is strongly unstable to kink modes, with maximum eigenvalues for the n=0 and n=1 families of λ^K_0 = -5.68e-4, and λ^K_1 = -1.28e-3. Ballooning modes are also found over the range of magnetic surfaces from s = 0.14 to s = 0.33, and the ripple strength at s=0.25, s=0.5 and s=0.75 increases to ε_h = 2.10%, 5.28% and 12.9% (compared with ε_h = 0.44%, 1.30% and 2.90% - see Table 9-4). Comparing the iota profile of the fixed boundary β = 3.0% virtual configuration with the iota profiles of the free boundary β = 1.0% and free-boundary β = 3.0% configurations shows that raising beta at fixed shape has predominantly changed the transform on axis whereas the edge transform has remained unchanged. It follows that the change in shape and the change in external transform induced by the change in coil current between the I_p = 43.5 kA, β = 1.0% free-boundary configuration and the I_p = 43.5 kA, β = 3.0% free-boundary configuration are responsible for the stabilization of the higher β configuration.

We have remarked that the $\iota(s)$ profile for the I_p = 43.5 kA, β = 1.0% free-boundary configuration has $\iota(1)$ = 0.50. The question naturally arises whether the reduced β-limit of this configuration compared with the I_p = 43.5 kA, β = 1.0% free-boundary configuration, which had $\iota(1)$ = 0.44, is due to the destabilizing influence of the $\iota(1)$ = 1 / 2 rational surface. The flexibility of the NCSX modular coil set to change the iota profile (demonstrated in Section 9.5) can be used to test such a question. The free-boundary optimizer was re-run for the case I_p = 43.5 kA, β = 1.0%, with the additional constraint that the plasma shape consistent with the coil currents be such that $\iota(1)$ = 0.44. A successful solution was found with $\iota(0)$ = 0.45, $\iota(1)$ = 0.45 and ι_{max} =

0.46 at s = 0.65. The coil currents for this modified configuration are shown in the third column of Table 9-12. The constrained configuration was verified to be marginally stable by freezing the plasma boundary, increasing β, and verifying the emergence of a kink instability. If the β is increased to 3.0% in this modified configuration, we find ι(0) = 0.41, ι(1) = 0.45 and ι_{max} = 0.47 at s = 0.58. Thus the Δι due to shaping, as opposed to profile changes, is essentially zero on axis and zero at the edge. Overlays of the constrained I_p = 43.5 kA, β = 1.0% low β-limit configuration and the marginally stable I_p = 43.5 kA, β = 3.0% configuration, as well as the calculated ι(s) profiles are shown in Figure 9-16. Stabilization at the enhanced β is due to 3D shaping.

The ability to investigate the stabilizing role of 3D shaping is an important element of the experimental program of NCSX. Investigations of this type allow testing and investigation of the stability boundaries of NCSX at low β.

	I_P = 43.5 KA β = 1.0%	I_P = 43.5 KA β = 3.0%	I_P = 43.5 KA β = 1.0% ι(1) constrained
ι(0)	0.44	0.40	0.45
ι(1)	0.50	0.44	0.45
Aux TF [A]	- 3.117e+2	+6.004e+3	+6.645e+3
Mod 1 [A]	- 5.657e+5	- 5.598e+5	- 5.742e+5
Mod 2 [A]	- 5.764e+5	- 5.773e+5	- 5.638e+5
Mod 3 [A]	- 5.268e+5	- 5.717e+5	- 5.921e+5
Mod 4 [A]	- 6.350e+5	- 5.460e+5	- 5.457e+5
PF Dipole	+ 5.868e-1	+ 3.051e-1	+ 5.778e-1
PF Quad	+ 9.193e-1	- 1.234e-1	+ 9.587e-1
PF Hex	- 6.159e-1	+ 7.277e-1	+ 1.536e-1
PF Oct	+1.416e+0	+1.564e+0	- 9.332e+0

Table 9-12. Coil currents for cases illustrating MHD stabilization by 3D shaping. Units for the Auxiliary TF and Modular coil currents are amps. Poloidal field "currents" are expressed as multipole moments

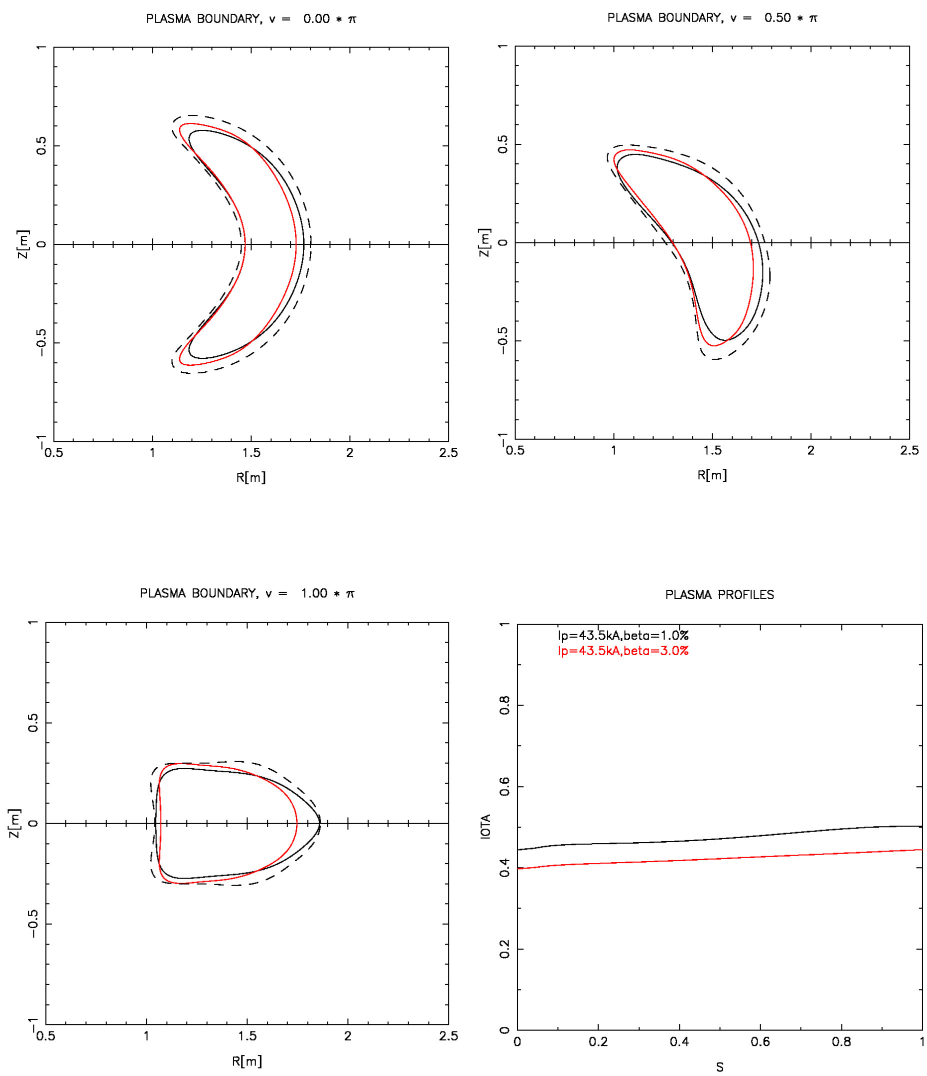

Figure 9-15. Overlay of plasma boundaries and iota profiles for the cases Ip = 43.5 kA, β = 1.0% and Ip = 43.5 kA, β = 3.0% used to illustrate MHD stabilization by 3D shaping

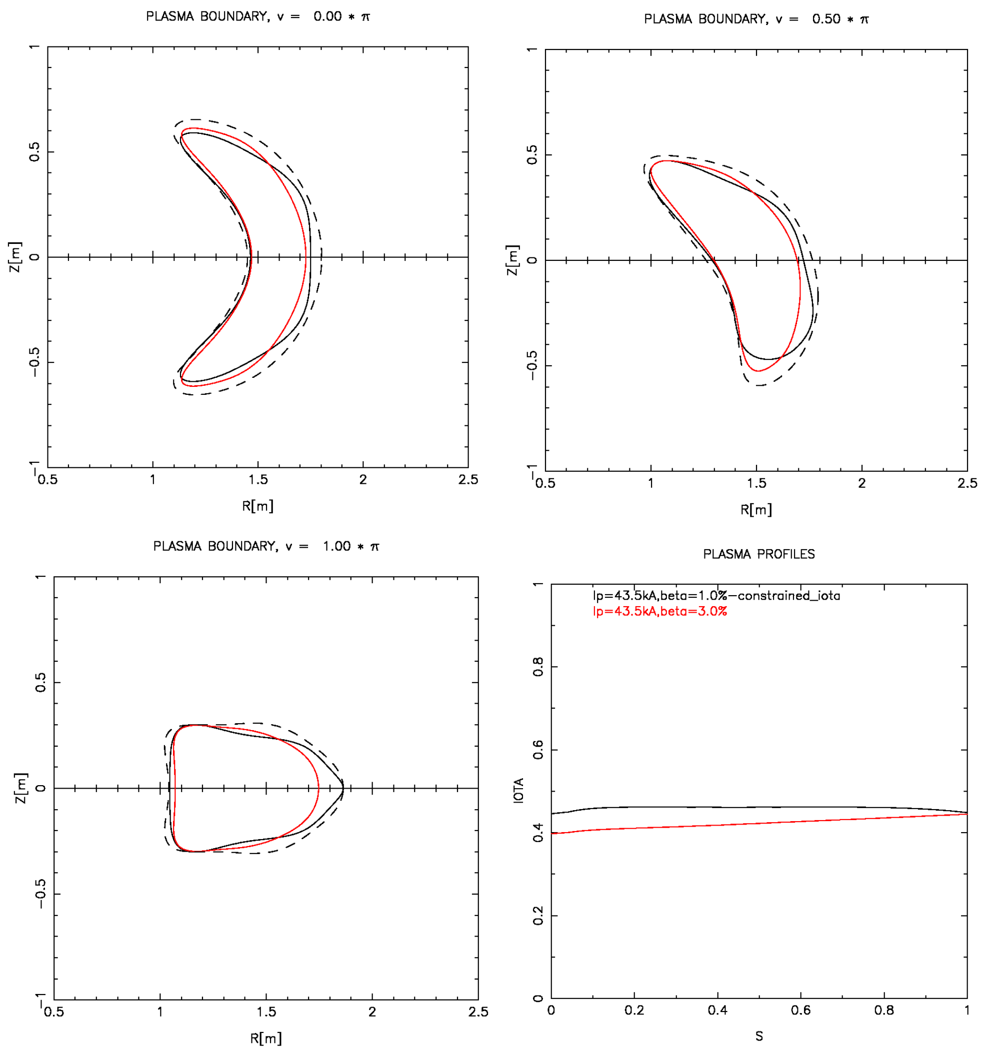

Figure 9-16. Overlay of plasma boundaries and iota profiles for the ι(1) =0.44 constrained Ip = 43.5 kA, β = 1.0% configuration and the Ip = 43.5 kA, β = 3.0% configuration. These cases are used to show that the reason the unconstrained Ip = 43.5 kA, β = 1.0% configuration has a low β-limit relative to the Ip = 43.5 kA, β = 3.0% configuration (see Figure 9-15) is not due to the proximity of ι(1) to 0.5, but rather the change in 3D shape

9.7 Flexibility to Vary the Degree of Quasi-Axisymmetry

The ability to generate configurations with good quasi-axisymmetry is an essential requirement of the NCSX design. For a systematic exploration of the role of QA in improving the transport properties of stellarator plasmas, it is necessary to have the ability to control the degree of QA-ness. In this section we demonstrate this ability, by varying NCSX modular coil currents to induce plasma shape changes that degrade/enhance the QA-ness (measured by the magnitude of the ripple amplitude, ε_h) while maintaining plasma stability to kink and ballooning modes.

Figure 9-17 shows an overlay of plasma boundaries for three configurations, each with I_p = 43.5 kA, β = 3.0%, each with the same profiles of plasma current and pressure, but each exhibiting different degrees of quasi-axisymmetry. The ripple amplitude ε_h varies by a factor of 9 at the s=0.25 surface (normalized radius r/a ≈ 0.5), and by a factor of about 4 at the s=0.5 surface. Values of ε_h and of the coil currents which support the equilibria are presented in Table 9-13. Each configuration is stable to kink and ballooning modes and was obtained using the free-boundary optimizer.

	CASE 1	CASE 2	CASE 3
ε_h[%]	0.44 1.30 2.90	2.50 3.27 5.15	3.99 5.44 8.33
Aux TF [A]	- 6.563e+2	+8.441e+3	- 4.191e+3
Mod 1 [A]	- 5.655e+5	- 5.227e+5	- 5.255e+5
Mod 2 [A]	- 5.742e+5	- 6.537e+5	- 6.562e+5
Mod 3 [A]	- 5.269e+5	- 5.510e+5	- 6.433e+5
Mod 4 [A]	- 6.351e+5	- 5.077e+5	- 2.812e+5
PF Dipole	+ 5.863e-1	+ 3.422e-1	+ 4.123e-1
PF Quad	+9.192e-1	-9.626e-2	+3.618e-2
PF Hex	-6.702e-1	+1.554e+0	+1.270e+0
PF Oct	+1.511e0	+8.322e-2	+4.653e-1

Table 9-13. Three configurations with the same profiles of plasma current and pressure, each with I_p = 43.5 kA, β = 3.0% , each stable to kink and ballooning modes, but each with different degrees of quasi-axisymmetry measured by the effective ripple ε_h measured at the s=0.25, s=0.5 and s=0.75 magnetic surfaces. CASE 1 is the optimized I_p = 43.5 kA, β = 3.0% case that appears in Table 9-4

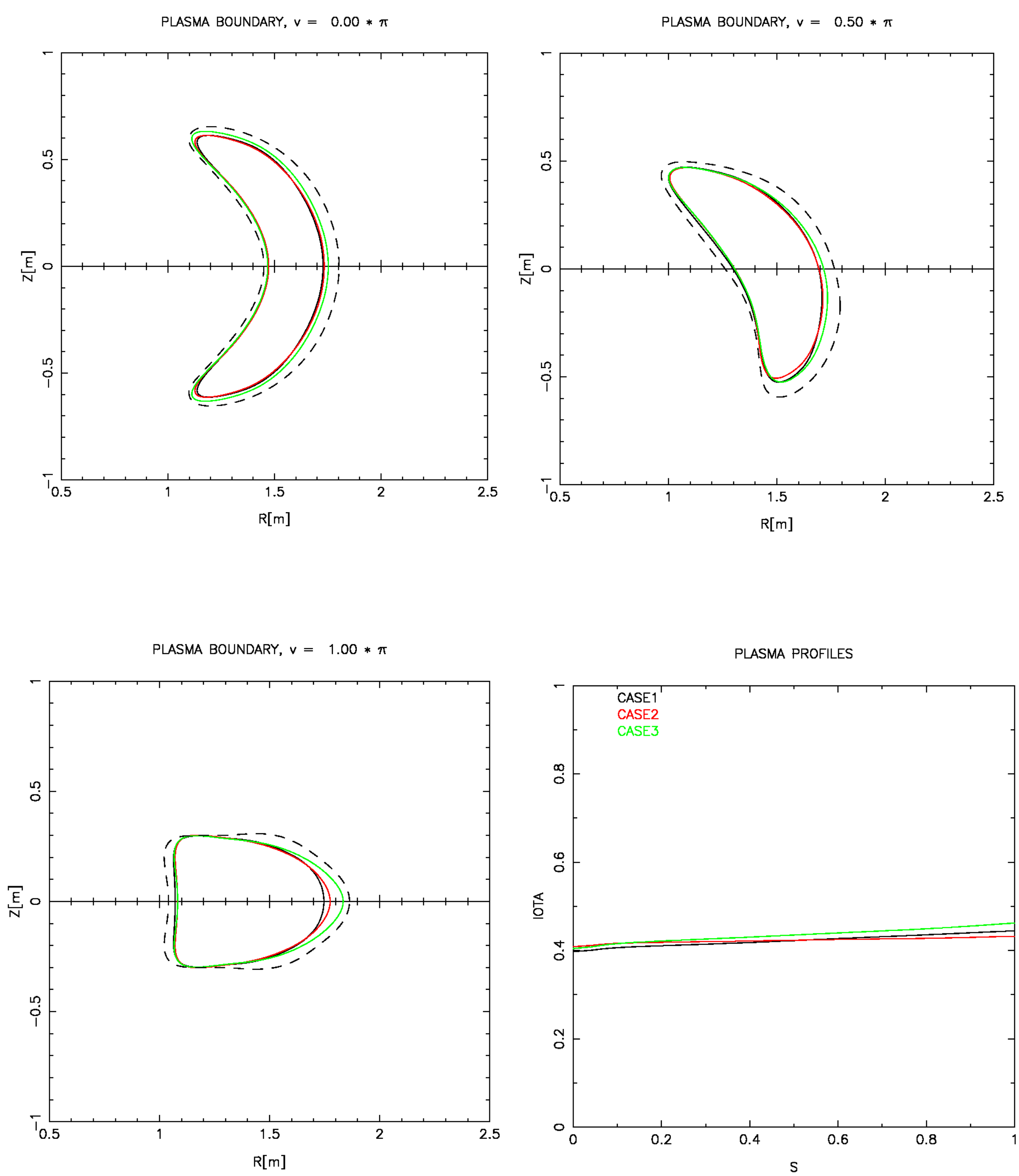

Figure 9-17. Overlay of plasma boundaries for three configurations with I_p = 43.5 kA, β = 3.0%, the same profiles of plasma current and pressure, but different levels of quasi-axisymmetry (see Table 9-13). Each configuration is stable to kink and ballooning modes

9.8 Summary

We have presented a number of numerical experiments that demonstrate the ability of NCSX coils to meet the NCSX project mission. We have shown

- The NCSX plasma shape/position is robust with respect to uncertainties in the match between plasma profiles and assumed coil currents – e.g., the plasma boundaries displayed in Figure 9-4 were obtained using a variety of assumed plasma profiles and show modest changes in shape/position, whereas Tables 9-7 and 9-9 show the variation in coil currents required for optimized plasmas with different profiles when plasmas are further constrained to be limited by the first wall boundary.

- Using reference S3 plasma profiles there is a wide operating space of I_p, β values for which plasmas supported by NCSX coils are stable to kink and ballooning modes with low helical ripple amplitude ε_h (see Table 9-4).

- NCSX plasma performance is robust with respect to substantial variations in plasma current and pressure profile shape (see Tables 9-7 and 9-9) and the discussion of finite edge current in Section 9.4.2.

- Substantial changes in the external transform $\iota(s)$ and shear $\iota'(s)$ can be induced (see Tables 9-10 and 9-11, and corresponding figures) by varying currents in the NCSX coils. This provides a significant control knob for the experimental determination of stable/unstable operating boundaries and the investigation of 3D shape stabilization.

- NCSX coils have good flexibility to stability boundaries, and to explore the role of 3D shaping in stabilizing MHD modes, see Section 9.6.

- NCSX coils have the flexibility to control the degree of quasi-axisymmetry allowing exploration of the physics of QA plasmas, see Section 9.7.

References

[1] D. Mikkelsen, "Standard Profiles for NCSX Flexibility Studies", March 1 2000 http://www.pppl.gov/ncsx/ncsxfss/Physics/physics.html

[2] M.I. Mikhailov, V.D. Shafranov, "Stable Current Profile in a Stellarator with Shear", Nucl. Fusion **30** (1990) 413-421.

[3] R. Jaenicke et al., "Operational Boundaries on the Stellarator W7-AS at the Beginning of the Divertor Experiments", 18th IAEA Fusion Energy Conference, Sorrento, Italy, 4-10 Oct 2000, Paper IAEA-CN-77/OV4/3.

Chapter 10 – Discharge Scenarios

Our objective in developing the discharge scenarios is to judge whether there are plausible and reasonable paths from vacuum fields to the desired NCSX target equilibrium. Our primary focus is the configuration li383_328. Much of the physics addressed here in pursuit of this goal is the evolution of the plasma poloidal flux. In addition to the vacuum transform, NCSX plasmas have significant toroidal current which is largely bootstrap driven. The plasma is heated by neutral beams and there is the associated neutral beam current drive. Finally, there is the directly controllable component, Ohmic current driven via a central solenoid. All contribute to the iota profile, some in competing ways. There is not a developed simulation tool for following flux evolution in 3-D; however, as the device is quasi-axisymmetric we expect the usual tokamak tools to provide an accurate guide. The discharge evolution will be followed using TRANSP, a 1 /2-D transport code with a high level of sophistication and maturity. The other major code used here is VMEC. For the most part VMEC will be used in its free-boundary mode with internal current and pressure profiles generated via TRANSP simulations, and searches for coil currents that retain attractive physics properties with these profiles.

There are four components to this task. First mapping the reference stellarator configuration into an 2-D "equivalent tokamak", called <NCSX>. Simulations are then developed to evolve the current profile from discharge initiation to the desired high beta state. Third, the profiles are mapped back into the 3-D configuration while solving the free-boundary equilibria to obtain the coil currents. Finally evaluating the physics predictions, notably kink stability, for these equilibria. Additionally, we present an alternative evolution of the plasma current buildup that avoids having the plasma edge pass through iota of 1/2.

10.1 Creating <NCSX>

As stated above the li383s configuration is the starting point for the analysis. The reference equilibrium is specified by its 3-D shape and its internal profiles (pressure and current). The first step is to remove the plasma pressure and internal current to obtain the vacuum iota. This iota is to be preserved as a current in <NCSX>. This seems the most straightforward approach, and implies the control is for essentially constant plasma shape. It is not a true requirement and an alternative is discussed in Section 10.4. It is the simplest choice. The next step is to make an axisymmetric equilibrium, retaining only the n=0 components of the reference. Here (and only here) VMEC is run in the mode where iota is preserved, rather than a current profile. As we have only axisymmetric terms this VMEC run then calculates the current profile needed to obtain this iota. This current profile is all that is needed from this calculation. This current, designated I_{EXT} is 321 kA for the R·B value of 2.05 T-m of the reference case. This transformation does not preserve aspect ratio nor plasma volume. We repeat, with a second axisymmetric calculation, keeping the n=0, m=0 term, but adjusting the n=0, m≠0 components by a single scale factor to restore the original aspect ratio, 4.37. In both cases we are keeping the value of toroidal flux at the boundary fixed at the reference equilibrium value. Since we retain the vacuum iota, the major radius, the plasma volume and the edge toroidal flux, the new <NCSX> equilibrium has a new R·B, or B since R of <NCSX> = <R> of the stellarator equilibrium. With this prescription <NCSX> has R·B=1.84 T-m and R=1.42 m. This will produce profiles with I_P, and $\Phi(\rho=1)$ values which correctly map back into the stellarator with

R·B =2.05. Since we are not able to retain the wobble of the magnetic axis, there is not a unique mapping to two dimensions. If we think of iota in terms of poloidal and toroidal currents, $\iota \propto R^2 I_{TOR} / (a^2 I_{POL}) = R I_{TOR} / (a^2 B) = R I_{TOR} / \Phi_{edge}$. Matching ι at a specified Φ_{edge} with I_{TOR} constrained, uniquely, allows for only B_ϕ as the freedom to preserve the boundary iota value. The <NCSX> equilibrium flux surfaces and current profile are shown in Figure 10-1.

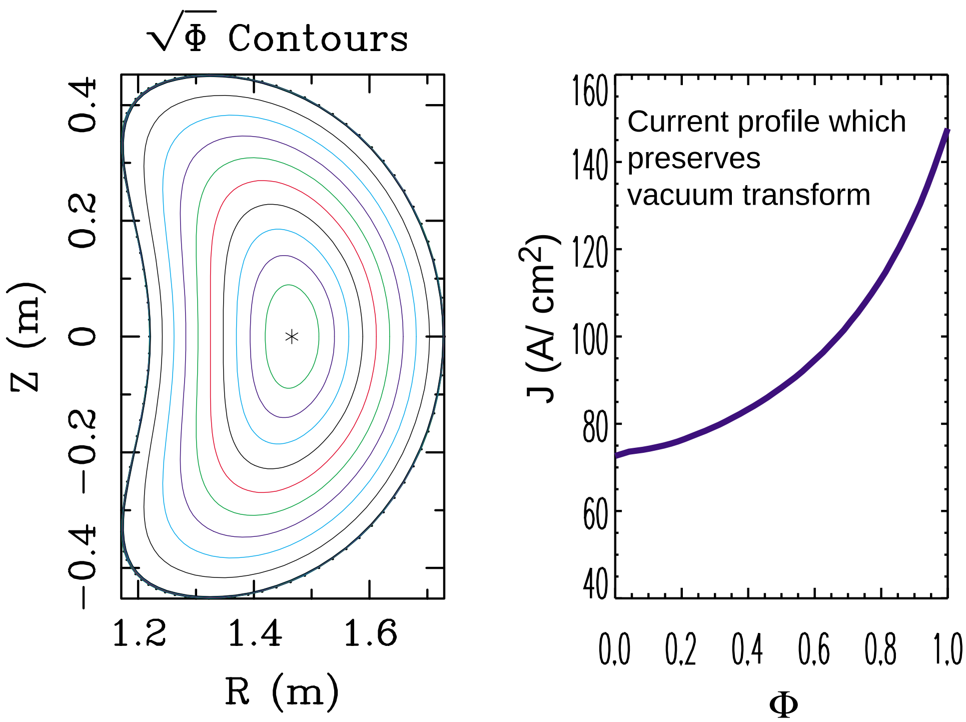

Figure 10-1 (a). Flux surfaces for the axisymmetric components of the shape of the target equilibrium, li383_328, at β=0, I_p=0 and (b). the toroidal current density required to produce the vacuum transform in the absence of 3D shaping

10.2 Discharge Evolution Modeling

The modeling of the current profile is done using TRANSP. The evolution of the plasma pressure components (T_i, T_e, n_e, and Z_{eff}) are specified in a way consistent with the predictions of Chapter 8. The plasma current has two distinct components: The 321 kA equivalent of the vacuum iota is specified to be lower hybrid driven current (LHCD). The unique aspect of LHCD is that TRANSP assumes a power source maintains this current and it does not diffuse. Other physics assumptions of importance are using the NCLASS [1] models for bootstrap current and neoclassical resistivity. The NCLASS calculations, which do more accurate (numerical) integrals of the distribution function result in about a 13 % decrease in bootstrap current, when compared to the usual analytic approximations. While neoclassical resistivity is similar outside the half-radius, near the axis the NCLASS calculation results in a 40% increase. Before proceeding we need to describe this use of TRANSP; TRANSP is an analysis code, not really a simulator. The simulations are done iteratively: do a run, look at results, change something and do it again -- very much like running a tokamak. This will be obvious in the plasma current. In order to maintain a current profile that is approximately constant in time, it is quite important to minimize the Ohmic current during startup. When the plasma is cold, the current diffuses rapidly to the core. Once the plasma heats it will take a very long time to dissipate the Ohmic flux. The plasma current waveform, $I_P(t)$, represents a number of iterations where the old waveform is replaced with a new one which is the integral of the non-Ohmic current. Of course, this changes the β_P, leading to a different bootstrap current. The change in I_P will also change the neutral beam current drive (NBCD). Additionally, the balance of the neutral beams is adjusted so that the counter losses are compensated by a lower coinjected power. This is done so the effect of NBCD on central iota is not too severe, while overall the NBCD is not too negative. While the NCSX program will include an upgrade of the neutral beams to long pulse, initially they will be limited to a pulse length of 0.3 s. It is desirable to develop a scenario consistent with initial operation - despite the long skin time of the plasma. This is not the only simulation we have done, it is the one at highest electron temperature, and thus the most difficult. The T_e profile is chosen to be roughly consistent with the confinement predictions of Chapter 8. The electron density profile is like that used in Chapter 8, but the overall magnitude is adjusted to produce the desired β_T. This differs from Chapter 8 in that the fast ion beta is about 25% of the total. The profiles are rather broad and this expectation is discussed below. Also, β_T is the convention tokamak definition, whereas in the stellarator β is $<p>$ divided by the $<B>^2$, the volume-averaged total field A typically 0.92 typical difference in NCSX is $B_{0,0}/<B> = 1.05$.

As the design goal is a quasi-axisymmetric device, it is very useful to examine <NCSX> in some detail. Usually, one would begin with the I_P waveform. However, our waveform is the resultant of the specified pressure profile, a discussed above, so we shall begin with Figure 10-2, the assumed profiles. (In the case of T_i the assumed multiplier on neoclassical transport.) The electron temperature is about 2.2 keV on axis in the high beta phase, starting from 50 eV at t=0. (Because of the care needed in initializing TRANSP at near-vacuum conditions, the plasma start is at 20 ms when the current ramp begins. The ion temperature, calculated from neo-classical conductivity with a multiplier (3) that results in the expected central value.

The density profile is consistent with observations in tokamaks and stellarators operating at this field value. As a guess, Z_{eff} is fixed at 2 in the center and the profile is set to rise modestly with time.

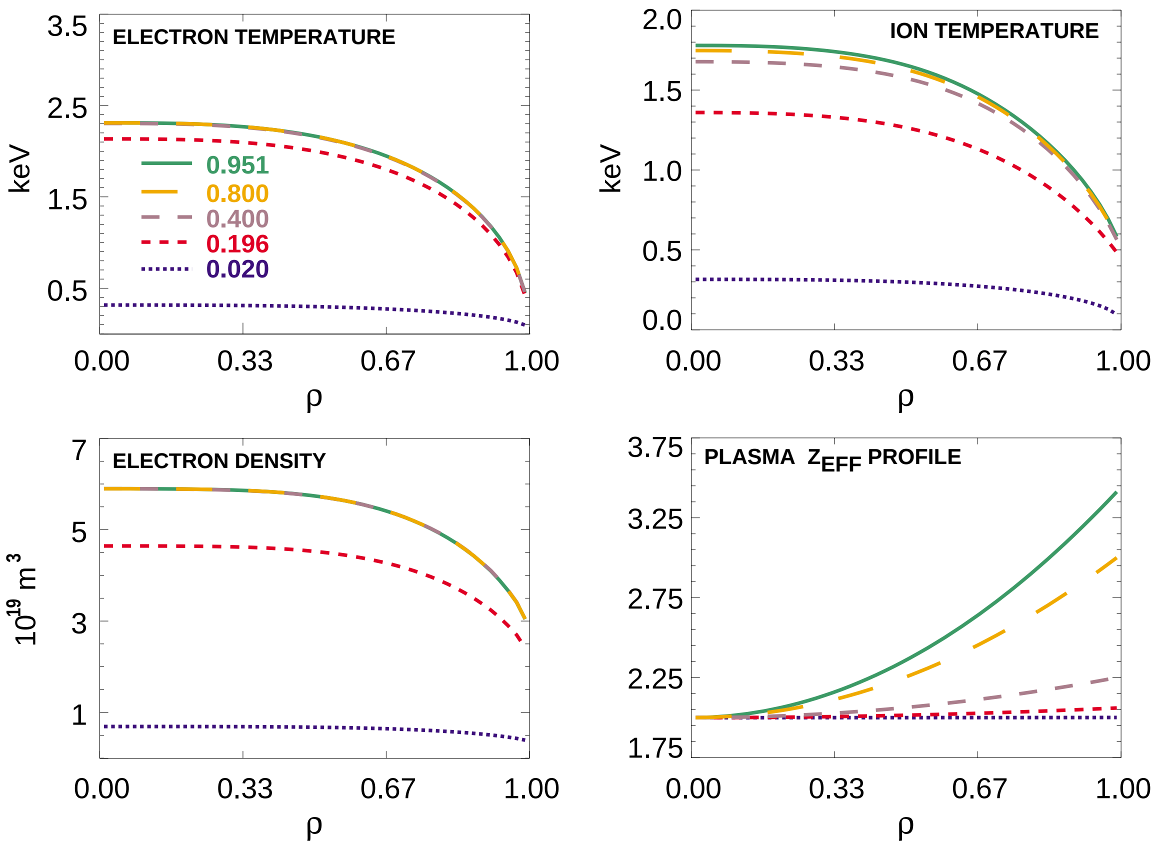

Figure 10-2. Thermal plasma components; T_e, T_i, n_e, and Z_{eff}. at selected times

The profiles along with electron collisionality determine the bootstrap current profiles. The resulting collisionalities, ν_{*i}, and ν_{*e} are shown in Figure 10-3 for the high β phase.

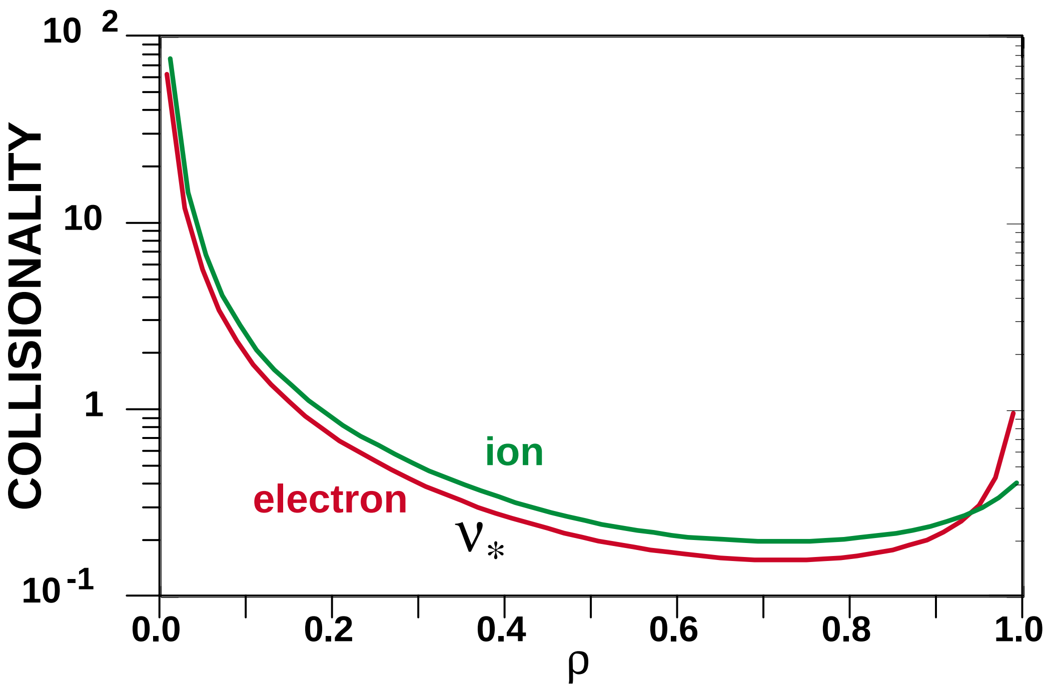

Figure 10-3. Electron and ion collisionalities at 0.4 s

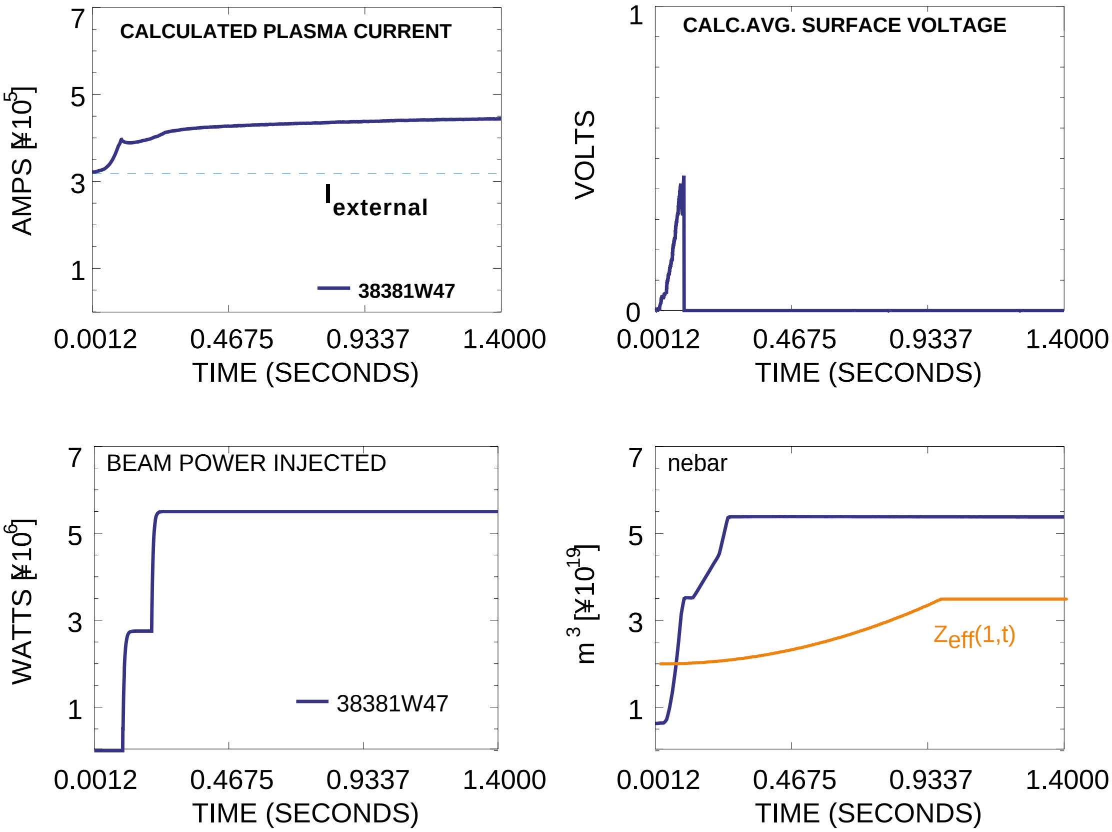

Figure 10-4. Evolution of plasma current, surface voltage, P_{inj}, density and Z_{eff}

Figure 10-4 shows the evolution of primary quantities. As already stated, the current rise is set to match the rise of driven current as closely as possible. The starting value of 321 kA is the I_{EXT} that gives the correct vacuum transform. The OH circuit is switched from current to voltage control as early as possible, near the time when NBI begins. Unlike a tokamak where there is a need to breakdown without pre-existing surfaces, this device has closed surfaces at t=0. Thus we would expect the voltage requirement to be accurately predicted here. The surface voltage only reaches a peak value of less than 1 volt, which should not present any difficulty The injected power is begun as soon as the plasma current reaches its approximate flat top in steps of 2.75 MW. The beams are paired, co & counter – unbalanced injection is not possible without severe effects on iota. The power balance is a compromise between reversing iota in the center of the plasma and minimizing the overall negative contribution of NBCD to the plasma current. Line-averaged density is programmed for the desired β.

Parenthetically, in earlier work, assuming a colder plasma (Te(0) ~ 1 keV) it was sufficient to raise the plasma current at 2 MA/s to achieve an equilibrated, bootstrap-driven plasma at similar beta in 0.4 s. This ramp rate produced an Ohmic current profile sufficiently similar to the final bootstrap current to make this possible. At the higher temperatures current equilibration is, of course much slower. Those plasmas require about twice the voltage in the current ramp as this case.

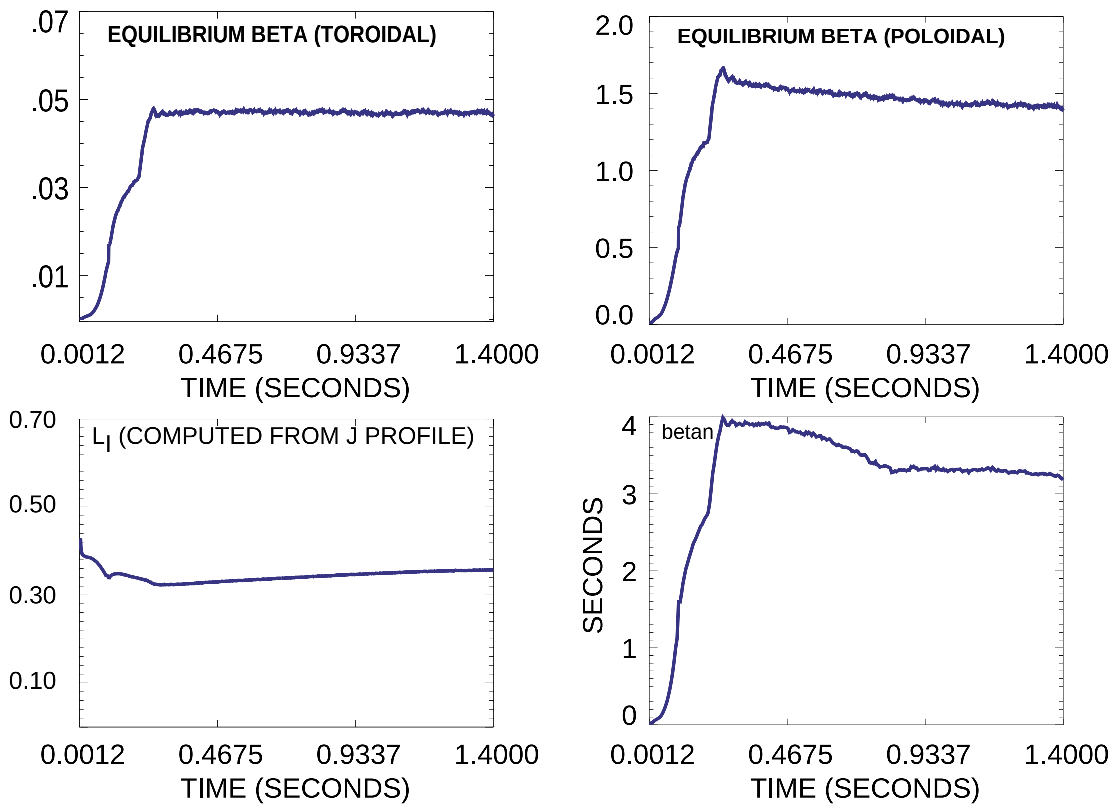

Figure 10-5. Discharge evolution; betas and plasma inductivity

β_T is chosen by control of the density to be that (4.8%) which corresponds to β=4.25 % in the stellarator. This corresponds to $\beta_P \approx 1.5$, as shown in Figure 10-5. For comparison to the tokamak, we show β_N and ℓ_i. In a tokamak, the kink stability limit (no wall) is approximately given by $\beta_N = 4 \cdot \ell_i$ Here we will obtain kink stability at $\approx 10 \cdot \ell_i$.

The calculation of the evolution of the current profile is the primary purpose of modeling the discharge evolution with TRANSP. The current profile comes quite close to being stationary in a 0.4 s pulse, consistent with the initial NB pulse length of 0.3 s, meeting the goal mentioned above. A true equilibration (flat voltage profile) would take quite a long time and require the planned beam upgrade. It is plausible, but not entirely clear, that the evolution shown hear could be achieved in practice. (We will touch on plasma control in Section 10.5.) The current densities are shown in Figure 10-6. Clearly the LHCD (external transform) is the dominant term. The bootstrap current is somewhat less than that shown in other chapters because the thermal pressure is 75% of the total (Figure 10-7) and the fast ions do not contribute significantly to the bootstrap current. While the NBCD from the “balanced” beams is small overall, it has a pronounced effect in the core, tending to increase iota because the co-injected ions are better confined. The dependence of the screening factor on Z_{eff} and aspect ratio is shown in Figure 10-8. For Z_{eff} in the expected range of 1 to 2.5 control of central iota will be an exacting task. The central value is quite important; for values less than 1.4 the effects of NBCD on central iota are negligible, whereas at central values of 2 the effects are marked and this has been the principal determinant how the NBCD and OHCD are competed, as discussed in more detail below. Co-injection orbit losses are about 18% and counter-injection losses are about 30% (Chapter 7).

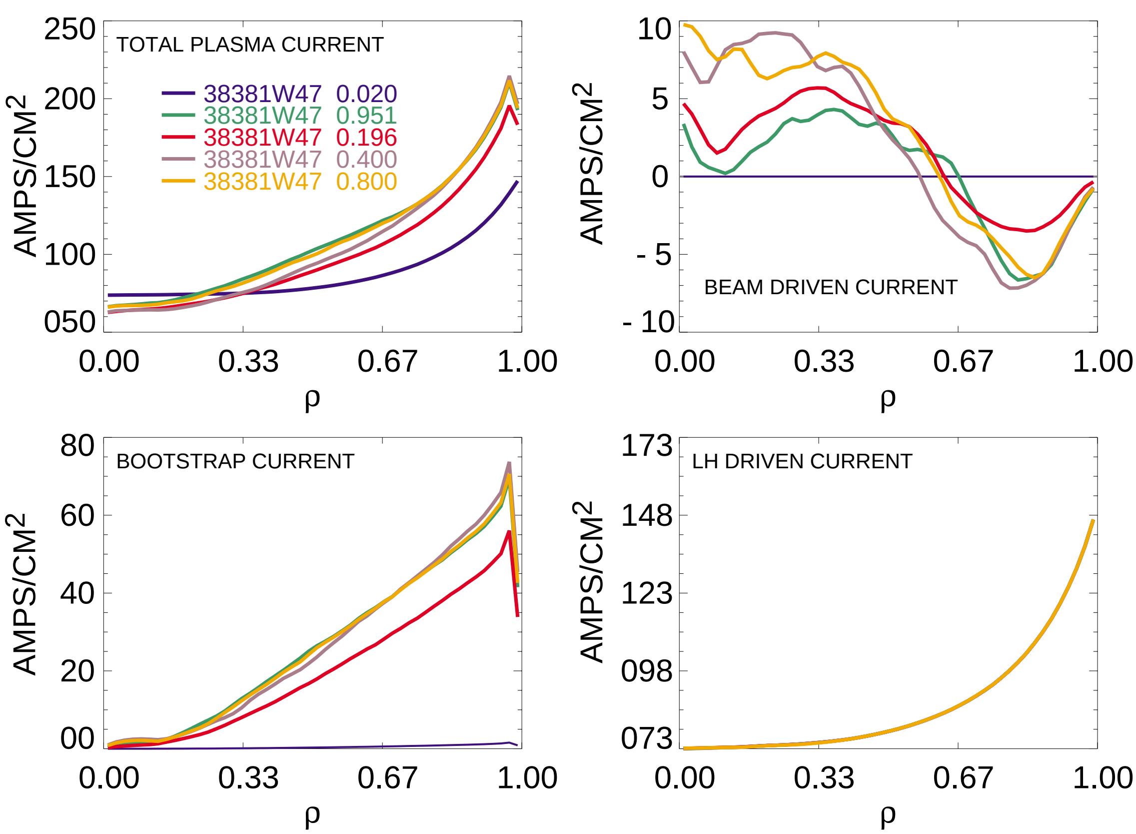

Figure 10-6. Components of the current profile at selected times

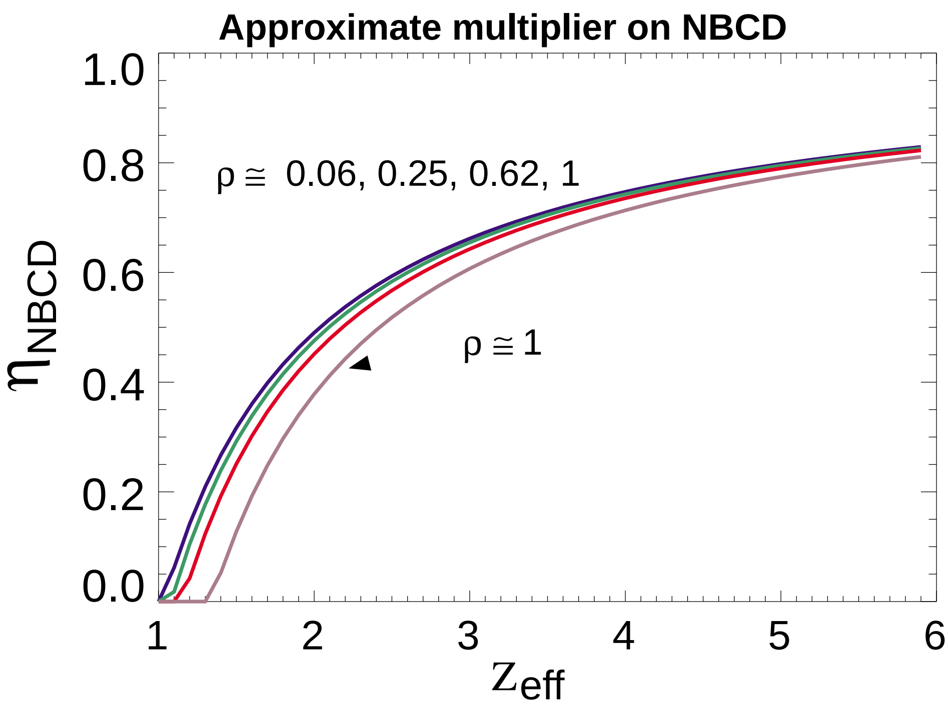

Figure 10-7. NBCD screening; $J_{NBCD} \approx n_f \ v_b \ \lambda\eta$

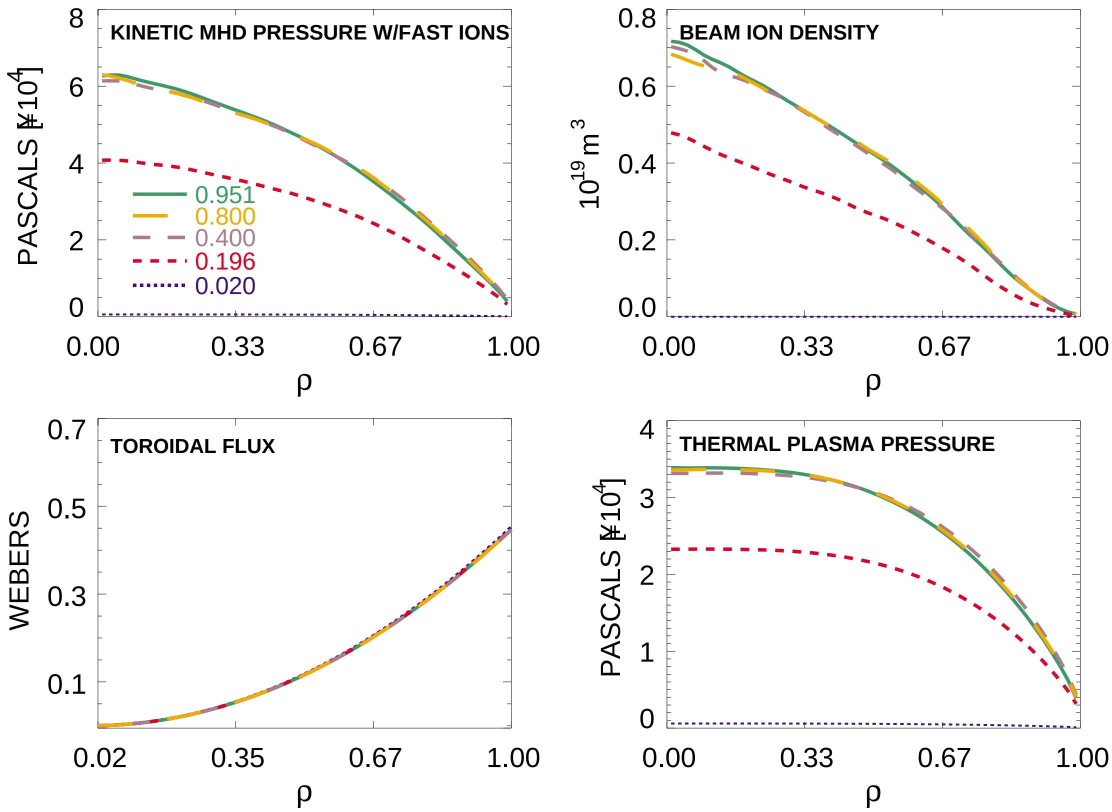

Figure 10-8. Components of the pressure profile at selected times

Our objective is to assess whether we can reasonably expect to obtain an iota profile which is reasonably consistent with the target equilibrium and to judge how much time is required to do so. The answer, in the affirmative, is shown in Figure 10-9 below. The loop voltage shows little sign of decay. Suitable averaging over the plasma cross section does show that after about 0.3 sec there is a decrease. However, the source of the voltage is the inductive reaction to internal driven currents and control of surface voltage is only a weak control on the loop voltage. The Z_{eff} profile is still changing gradually until t=1.0 s (Figure 10-5). At 1.4 s, the end of the simulation, there is still voltage churning with continuing change in iota. Recall that the plasma profiles are fixed. If the confinement depends on the plasma current, as expected, the time will be lengthened. Nevertheless, with adequate knowledge of the plasma currents and robust plasma control, maintaining a qualitatively similar iota over the beam-heating phase of a 0.4 s pulse is possible.

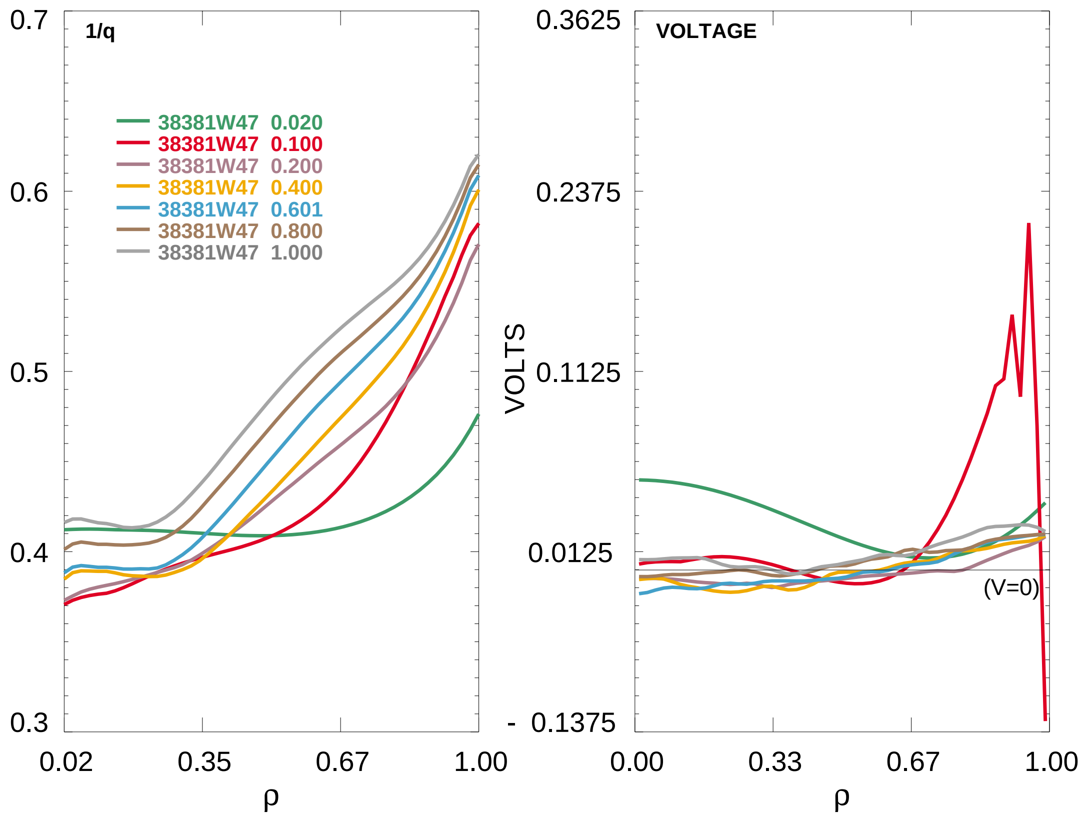

Figure 10-9. Iota and voltage profiles at selected times

While the loop voltage settles to quite a small value, there is an issue of how to define "small" when a goal is to preserve iota. To examine this we form the components of the internal voltage, $\eta \cdot J \cdot 2\pi R$ for the current components as a local (surface-averaged) quantity. Additionally we have run this simulation longer to see the decay time. These results are shown in Figure 10-10 below along with the components of total current. By 3 sec the Ohmic current has decayed virtually to zero. The integral neutral beam current is quite near zero throughout the discharge. The voltages are plotted at ρ=0.33. To allow clarity in the figure we plot the negative of the Ohmic voltage. These voltage signals are quite noisy as a result of Monte Carlo beam deposition and are heavily smoothed. The Ohmic voltage provides reasonably good cancellation of the neutral beam voltage until about 1 s. At that time, to preserve the shape of iota the co-injected beams should be reduced further eliminating the positive central current shown in Figure 10-6. This will result in a decrease of the total current by several kA.

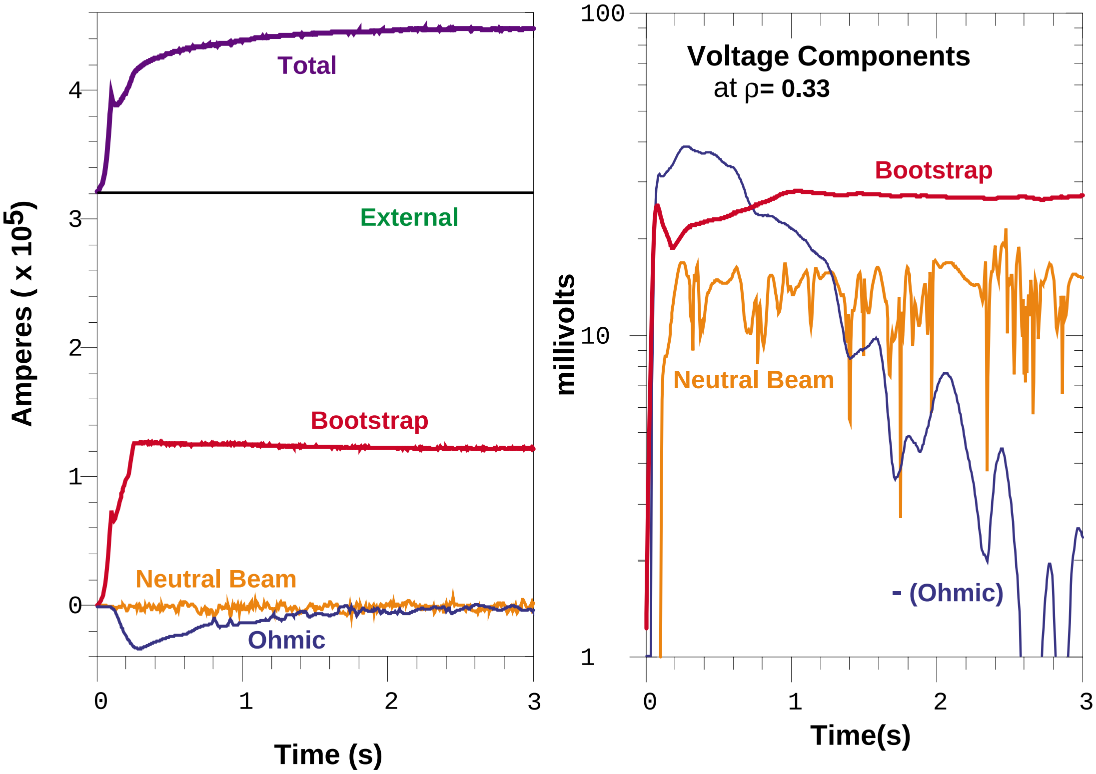

Figure 10-10. Components of toroidal l current and local toroidal voltage vs. time

Whether the confinement will be good enough to make this plasma is, of course, unknown. Beta studies may require that we operate at lower field. This would ease the problem of current control by reducing the resistive diffusion time. Estimates of confinement based on popular scaling are presented in Figure 10-11 below. τ_E^* is $(W/(P_{in}\text{-}dW/dt)$; τ_E^{D3J} is D3D-JET scaling [2]. The enhancement factors are somewhat higher than that shown in Chapter 8 as required to achieve this beta. The biggest factor is a larger $B_T = 1.4$ T (instead of 1.2 T in Chapter 8). Other factors are lower bootstrap current, resulting from the non-thermal component of beta, the difference between B_{T0} and $\langle B \rangle$ in normalization of tokamak and stellarator betas and other similar small factors. We would judge the discharge presented here as energetically plausible.

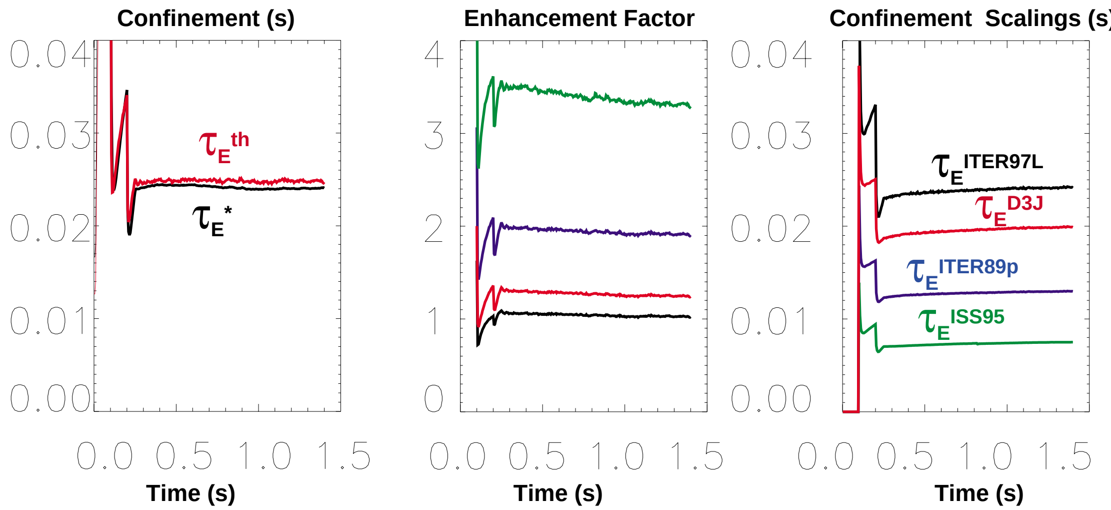

Figure 10-11. Confinement Times

10.3 Repatriation of 2-D results to the stellarator

Having obtained a self-consistent evolution of pressure and current density, we need to follow this path in a sequence of 3D free-boundary equilibria. The input profile functions for VMEC are the pressure, p(s) and flux-surface averaged current profile, I'(s), where $s=\rho^2$. $P(\rho)$, and $[\langle J\rangle(\rho) - \langle J_{LH}\rangle(\rho)]$ are extracted from the TRANSP for multiple time slices and fit to obtain the desired input functions using SVD techniques. The 3-D free-boundary equilibria are generated by an optimization process discussed in Chapter 2. We will first address the 0907a2 coil set (a2 => set of 7 PF coils). Later we will discuss progress with other coil sets that have presented difficulties.

Our first task is to obtain a converged equilibrium at any time in the discharge. The coil currents need to be reasonably consistent with the plasma. Changing beta or plasma current without changing coil currents leads to poorly converged results. This is most easily done at a time corresponding to conditions near the reference equilibrium. For each time slice we optimize as described below and then use the resulting coil currents (and magnetic axis) in the next time slice. This is repeated until all slices are done. We need a first slice with a well-converged equilibrium. After that calculation is largely an automated process of optimization with an initial guess form the previous case. A failure simply means a higher density of time slices is required.

Using the 0907a2 set also created some problem in that we could not obtain kink stability at the aspect ratio of 4.37. We did obtain good results at a lower aspect ratio, 4.12. This type of behavior is discussed in Chapter 2. This means our simulation results will be in error by about 6%, the change in the gradient scale length. In particular the bootstrap current density will be overestimated by about 6% and the integral, I_{BS} is underestimated by the same 6%. Also, the plasmas do not quite fit in the nominal plasma facing component boundary. The plasma volume was increased by about 12% by the aspect ratio change.) These details are not of concern until a coil set is finalized.

For the "W47" cases we did a full optimization over aspect ratio, R·B, quasi-symmetry, and the N=0 & N=1 families of ideal (no wall) kink instabilities. No attempt is made to regularize the coil currents or force the plasma to fit within the vessel. Results from 40 to 840 ms are presented in Table 10-1. A growth rate for the kink of $< 1 \cdot 10^{-4}$ is considered negligible, that is, with minor changes in discharge programming it can be avoided. This is satisfied for all except the 420 ms case, which comes quite close. χ^2_{Bmn} of the reference plasma is 0.015 and values less than .04 are not expected to be deleterious to confinement. The last column displays radial zones that are ballooning unstable. (1 the axis and 49 the boundary are not evaluated. Instability is restricted to a few zones near the axis and the boundary). Ballooning is evaluated on field lines beginning both at $N_{fp}\phi = 0°$ and 60°.

Time (ms)	**VV distance (m)**	**A**	**<β>**	**I_P**	**N=1 & N=0 Max ♎ $\times 10^{-5}$**	**χ^2_{Bmn}**	**Ballooning unstable zones**
0041	-0.2437	4.118	0.001	6590	3.00	0.0291	0
0061	-0.0507	4.123	0.002	18580	0	0.0303	0
0081	-0.0048	4.123	0.006	42860	0	0.0337	0
0106	-0.0109	4.123	0.016	71860	1.38	0.0327	0
0131	-0.0129	4.123	0.022	68340	8.40	0.0324	2
0151	-0.0124	4.123	0.025	69980	9.11	0.0334	2
0211	-0.0142	4.122	0.032	80700	7.52	0.0356	2,3
0315	-0.0138	4.123	0.042	100200	6.10	0.0407	2,3
0420	-0.0140	4.122	0.042	105500	10.7	0.0515	2,3
0524	-0.0160	4.122	0.042	109000	8.31	0.0378	2,3,48
0525	-0.0153	4.122	0.042	109000	7.45	0.0353	2,3
0630	-0.0131	4.123	0.042	111800	5.70	0.0300	2.3.48
0735	0.0007	4.132	0.043	114000	3.18	0.0298	2,3,48
0842	-0.0353	4.122	0.043	116900	5.74	0.0330	2,3,48

Table 10-1. Optimization Results; Case bB3.0907a2_38381W47

It is of interest to examine the plasma shapes resulting from this process. These are shown in Figure 10-12. The important point is that 12 optimizations return virtually identical shapes. The optimization at 40 ms (20 ms after the beginning of the I_P ramp) is unlikely to be of importance. The optimization at 524 ms, continued further as 525 ms is driven by ballooning stability, which is always a few zones near the axis and boundary. Again, unlikely to be of importance. The conclusion is that control of the plasma boundary will maintain the transport and stability properties. For the actual operation of the device, this is a quite favorable result.

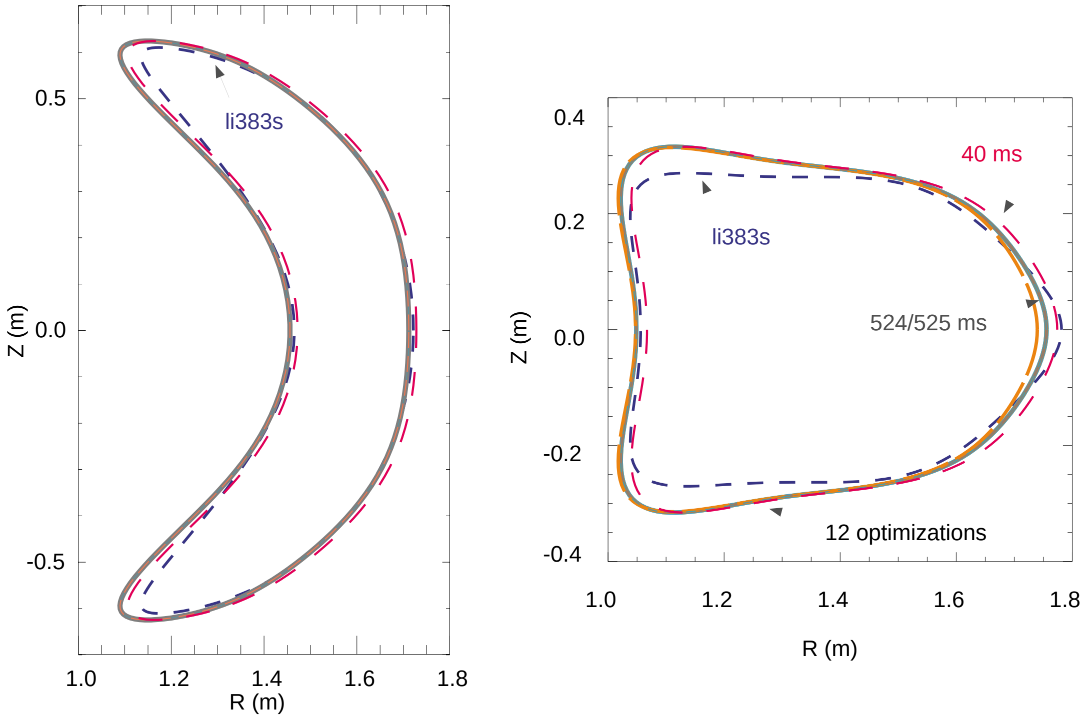

Figure 10-12. Optimized Shapes, $N_{fp}\phi$ = 0° and 180°

There has been no effort to regularize coil currents. Nevertheless, the modular coils do not make any severe excursions during 840 ms (Figure 10-13). The toroidal field does so at the first time slice, where the shape departs from the norm. This could likely be avoided, as could the large interference with the nominal PFC boundary. Beginning at 840 ms the toroidal field again departs the norm. After that we did not obtain attractive solutions. While we have not attempted to correct the situation, we think it likely that the change in central iota is the root cause of the changes in optimization results. As mentioned above, correction requires a further adjustment of the co/ctr beam balance .We should consider adding other heating such as RF after initial operation with 2 beams, to avoid additional beam-driven currents.

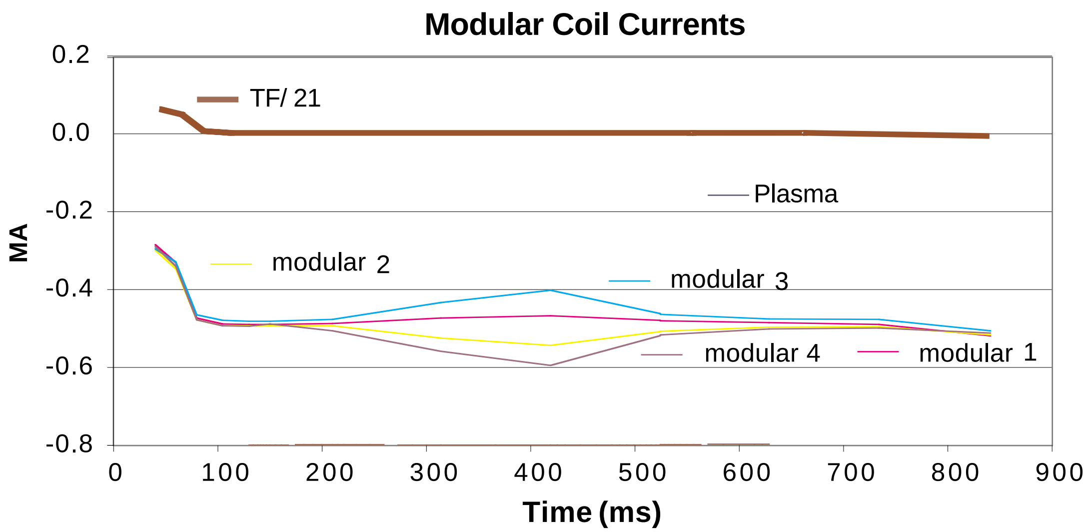

Figure 10-13. Modular Coil Currents for Optimized Shapes (0907a2)

The situation for the poloidal coils (Figure 10-14) is still less likely to be an accurate portrayal of an optimized system. This set of 7 poloidal coil pairs is simply putting them everywhere there is space, allowing them to conflict with each other, but yield favorable solutions. This is a proper starting point, but reducing the PF set and finding optimal coils requires finalizing the modular coil set, a task that is still in progress. The figure represents a part of this data set, and for this reason we include it. We do not expect it to be representative of the final design.

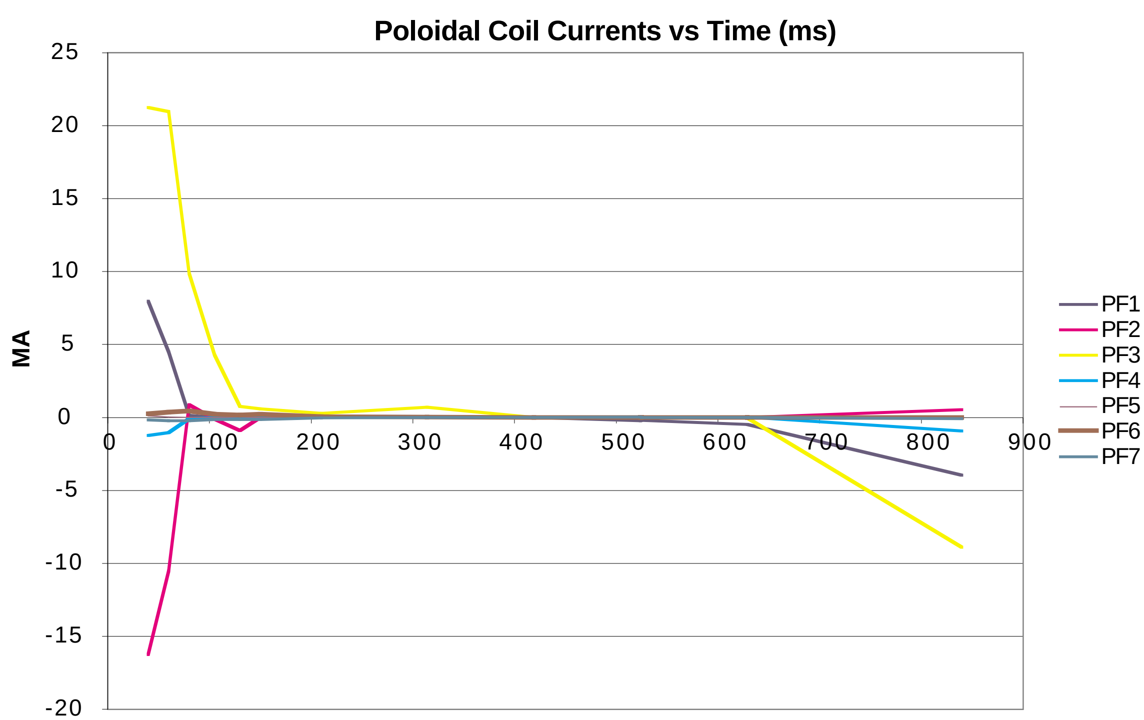

Figure 10-14. Poloidal Coil Currents for Optimized Shapes (0907a2)

The distinction between 0907a2 and other coil sets we have tried to work with is that 0907a2 does not have the outer legs of certain coils moved radially to provide neutral beam access. Our most diligent attempt was the 1017 modular coils with the a2 poloidal coil set – 1017a2. We were unsuccessful at obtaining a good solution. In particular, the stabilization of the kink family was not possible and attempting to do so drove the shape to have unattractive features. Additionally, when we tried to lower beta the coil set also produced unattractive shapes. Simply to obtain convergent VMEC solutions constraining only the target shape required a higher density of time slices than was needed for the 0907a2 coil set. With the 0907a2 coil set the methodology of either optimizing on a shape or optimizing the physics directly seems to yield good and similar results. Obtaining one good result and using this to iteratively do all the time slices works well with either It is tempting to interpret these failures as physically meaningful but this is dubious. The optimization by gradient search is prone to encountering local minima and the sensitivity to various starting points we have observed in these attempts suggests this may well be the problem. It remains a strong possibility that the methodology is simply unsuitable to coil sets other than 0907a2 and we will need to find a better approach. We have not been entirely unsuccessful, in that some solutions with satisfactory physics have been obtained. However in these cases the optimizer had managed to elude our intent and raise R·B to 2.2, lowering beta to 3.6%.

At the time of writing this final version of chapter 10, we have had the first success with the 1017a2 coil set. The procedural changes have been slight, making it very likely the entire sequence will yield stable results. This slice corresponds is 525 ms in Table 10-1The results as an addendum to Table 10-1 is

0525	-0.0133	4.122	0.0411	109000	5.87	0.0503	2,3

The kink stability is now adequate, and the quasi-symmetry a bit less than desired. These are upper bounds as the calculation is still in progress. This result does increase our confidence that the issue is methodology rather than intrinsic properties of the coil set.
Further work is required to achieve satisfactory resolution on the adequacy of these coils.

10.4 A High IOTA Startup

The evolution described in the previous section appears satisfactory. As discussed in Chapter 6, Δ' calculations (in the cylindrical limit) indicate the n/m=1/2 island width is always small, a few percent of the minor radius or less. Nevertheless there is some concern, based on W7AS results [3], that an evolution which has ɩ=1/2 passing through the plasma boundary may experience problems of resistive instability leading to disruption. An alternative is to start the plasma with a different shape. In Figure 10-15 the shapes and iota progression are shown. At 105 ms the plasma has returned to the conditions of the case discussed above. The profiles are as in the previous cases. ɩ remains always above 1/2 with a constraint that the transform not be shearless. For the most part, they fit in the vessel's notional plasma facing components. All are at R·B = 2.05 T. The quasi-symmetry and stability are shown in Table 10-2.

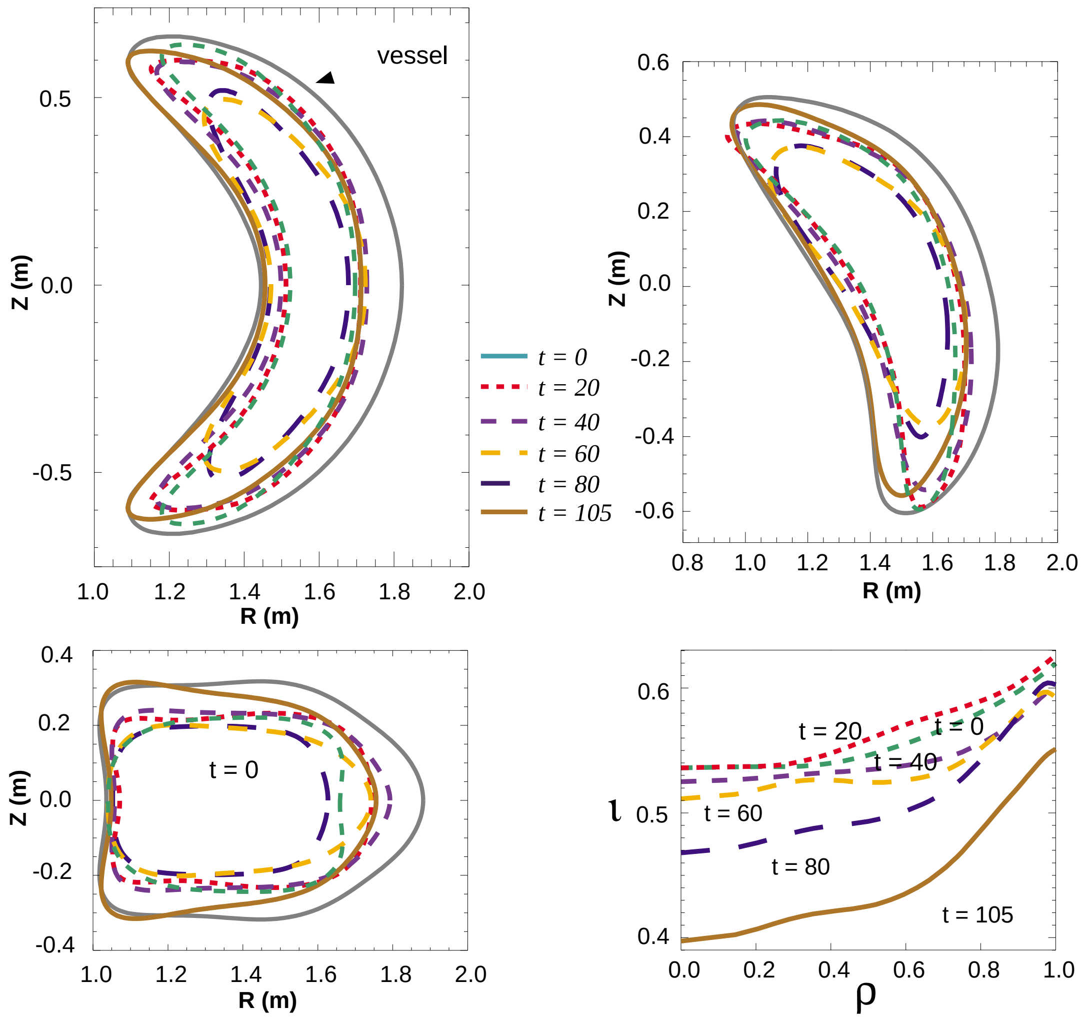

Figure 10-15. Plasma shapes at discharge initiation and during the current ramp which avoid ι=1/2 at the boundary. Shapes are shown at $N_{\phi\pi}$ ϕ= 0, $\pi/4$ and $\pi/2$

Time (ms)	**Plasma Current (A)**	χ^2_{Bmn}	$\lambda_{\kappa\iota\nu\kappa}$	**Balloon unstable zones**
0	2280	0.053	vacuum	vacuum
20	6570	0.044	~ vacuum	0
40	18500	0.032	$4.1\ 10^{-7}$	0
60	42900	0.024	$2.7\ 10^{-5}$	13 , 14
80	71900	0.019	$5.2\ 10^{-5}$	0
105	109200	0.033	$1.4\ 10^{-5}$	0

Table 10-2

This series of optimizations has led to an odd sequence of shape, but makes the point that such a startup is within the capabilities of the coil set. Currents for the modular coils are shown in Figure10-16. In spite of the shape variations, there is little change in the modular coil currents.

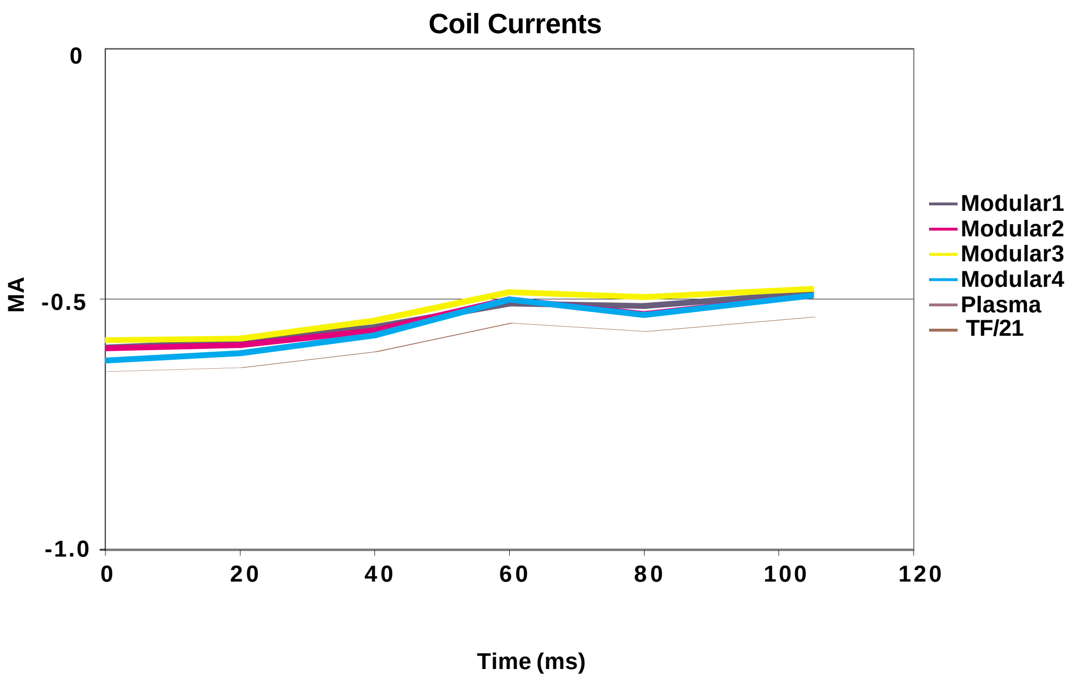

Figure 10-16. Modular Coil Currents for High iota startup

10.5 Discussion and Conclusions

Proceeding from the reference stellarator equilibrium we have constructed an “equivalent tokamak” with the vacuum transform represented as an LHCD current profile. Using this starting point in TRANSP we have evolved the plasma pressure and, along with the pressure, the self-consistent current profile to reach the target β. Such a plasma may require H-mode operation at B=1.4 T, but less confinement would be adequate at lower fields. The simulations include fast ion effects, and we find that care must be taken to account for NBCD, particularly its effect on central iota. Tailoring the $I_P(t)$ waveform and balancing the beams to account for increase losses in the counter direction achieves a nearly stationary iota profile from the start on NBI.

Analysis of the simulation profiles in 3-D yields a stable operating path to the target plasma while preserving good quasi-symmetry. These results are summarized in Table 10-2. Adequate stability to both kink and ballooning modes was found. This was done with the 0907a2 coil set. Even then, the initial aspect ratio did not yield good results and a further change from A=4.37 to A=4.12 was required. In earlier work which ranged to β~ 3% this was not necessary. This change was driven by the requirement for stability to low n modes. Optimizations such as done here don’t really exclude the 1017 coil set or the higher aspect ratio of 4.37. These optimizations can be sensitive to the exact process used, initial conditions, the order in which optimizations are done, etc. We have not find these solutions, but cannot say that they do not exist. As discussed in Section 10.3, the most recent results make us optimistic that better solutions will be found.

An alternative startup scenario, avoiding the ι=1/2 surface passing through the edge of the plasma. Cylindrical Δ' calculations indicate that the width for the m=3, n=6 island will be small, suggesting this may not be necessary (Chapter 6).

The scenario developed here assumes the existence of a rather sophisticated plasma control system and Ohmic circuit. Such a system would be a 3-D version of something like the D3D PCS. Thus it should not be viewed a radical advance, rather an extension of previous work in tokamaks. As a precursor to the control system it is necessary to undertake a study of 3-D equilibrium reconstruction. The question to be answered is how much profile information can be extracted from magnetic diagnostics and which diagnostics, and how many radial layers, are required to allow optimal control. For example, it is known that in 2-D ℓ_i cannot be determined from magnetics in a circular plasma, but configurations with elongation of the plasma cross-section allow ℓ_i to be determined from magnetics alone.

It is expected that more detailed information could be deduced in a more shaped plasma, such as a stellarator. The other-side of this argument is that the knowledge of ℓ_i is required to maintain the elongation in the shaped tokamak. This work will need to be done early in the conceptual design as many such diagnostics are often integral to the device itself and cannot be added after the fact. The results here indicate we will want to obtain an many moments as possible for the pressure and current profiles. Additionally, balanced injection is essential, otherwise, the central iota is depressed by NBCD leading to a double-valued iota profile with central iota rising above 1/2.

References:

[1] W.A. Houlberg, et.al., Phy. Plasmas **4** (1997) 3230.
[2] D.P. Schissel, et.al**.,** Nucl. Fus **31** (1991) 73.
[3] E. Sallander, et.al., Nucl. Fus **40** (2000) 1500.

Chapter 11 -- Power and Particle Handling and First Wall

11.1 Introduction and General Considerations

Experimental evidence clearly demonstrates that control of neutrals- and impurity influx is a prerequisite for enhanced plasma performance. Accordingly, the goal of the "power- and particle handling" program is to implement heat removal and particle- and impurity control consistent with enhanced plasma performance. This can be accomplished through careful design of the plasma-facing components (PFCs) and optimized plasma operation. The plasma-facing components which intercept particle- and power fluxes need to be capable of accommodating these fluxes without deleterious recycling or impurity production.

Due to their three-dimensional topology, stellarators don't necessarily have the ordered magnetic field line structure outside the separatrix found in axisymmetric tokamaks. Hence, optimized plasma-facing components also must be three-dimensional. Depending on the configuration, they can function as limiters or divertors. In a magnetic configuration with a separatrix, we define the plasma-facing component to be a "limiter" if it is located inside the last closed magnetic surface (LCMS) and intercepts closed field lines, thereby defining the plasma boundary. The same PFC can be a "divertor plate" if it is outside the LCMS and intercepts open field lines only. A fixed set of PFCs can function as a divertor or limiter by magnetically changing the configuration.

A limiter has the advantage of defining the last closed surface and can thus simplify the boundary structure by cutting off islands and ergodic regions, but the disadvantage is that it is in direct contact with the confined plasma and that it can be a strong source of recycling neutrals and impurities. A divertor, on the other hand, provides the advantage of an interface between the plasma and the solid wall which is removed from the confined plasma and buffered by the divertor plasma. However, in a stellarator, the boundary of the main plasma can be very complex, with islands and ergodic regions with short connection lengths which can themselves interact locally with the walls. Therefore, limiter operation may be more easily controllable for initial plasma operation.

With this preamble, we can state that the PFC design in NCSX is carried out with the goal to minimize the impact on plasma performance in the following sense: 1). Heat removal has to be accomplished in a way which avoids excess temperatures on the material surfaces. 2) Neutrals from recycling have to be controlled internally (baffles) and/or externally (pumps) for minimum effect on plasma performance. 3) The plasma-surface interaction has to be designed for minimum impurity generation.

The most basic task of the boundary program is the study of the field line structure outside the LCMS. This is the basis for the design of limiter- or divertor plates and, to some degree, the vacuum vessel. In a modular stellarator, such as NCSX, the plasma configuration outside the separatrix can be very complicated and detailed studies are needed, supported by modeling and experiment, before the optimum divertor can be designed. Some of the basic features can be adopted from the experience of W7-AS and the design studies for W7-X. The Wendelstein group has studied an approach for a stellarator divertor for more than a decade [1] and has developed modeling tools [2] as well as carried out divertor experiments [3]. The final phase of the Wendelstein divertor development is an island divertor in which the islands outside the LCMS are intercepted by divertor plates (open field lines) and the particles are pumped by cryo-pumps located behind baffles. Although the NCSX configuration is different from the Wendelstein configuration, there are indications that field lines outside the LCMS accumulate in the top and bottom of the bean-shaped cross sections and divertor baffles should be effective for neutrals control in these locations.

Since more modeling work and experimental experience is necessary before the ultimate divertor can be designed, we plan a phased approach for the NCSX boundary and divertor development. In the first phase the emphasis is on flexibility to accomodate different plasma configurations and this initial phase might not be optimal concerning all required functions. Adequate power handling, of course, is a prerequisite. The subsequent development will be based on further modeling, experimental feed back and model validation and will eventual lead to the final version combining optimized heat removal with good neutrals- and impurity control.

11.2 Magnetic Topology Outside the Last Closed Magnetic Surface

As indicated above, stellarators are generally thought to lack the ordered magnetic field line structure found in the scrape-off layer of axisymmetric devices. For the quasi- axisymmetric (QAS) stellarator, a tokamak-like ordering becomes evident when the first toroidal intersections of field lines with external walls are abstracted from the more numerous Poincare punctures of a given poloidal plane occuring during multiple transits of the field line around the torus. The intersection with walls limits the stochastic build up in the field line structure that would otherwise accumulate over many toroidal transits of the line. In addition, the existence of an ordered structure of external field lines launched close to the last closed magnetic surface is further revealed by applying the healing technique of Chapter 4 to any island chains just within the LCMS. For practical reasons, individual features of this boundary layer need to be considered for vacuum vessel and PFC design, with the goals of small angles of incidence of field lines and large wetted areas to distribute power loads uniformly. Additionally, some degree of configurational flexibility is required, so these loads don't vary as a result of changes in the core plasma configuration such as rotational transform, shear, beta, etc. In this study we make extensive use of a code originally developed for the design of the divertor of the W7-X stellarator, Magnetic Field Solver for Finite Beta Equilibria (MFBE), which is a new magnetic topology code developed by E. Strumberger [4], for magnetic configurations which have finite plasma pressure. Prior calculations for W7-X used vacuum magnetic fields outside LCMS. As in those calculations, vacuum magnetic fields are calculated exactly from given coil currents by the Biot-Savart law. In addition to these vacuum fields, MFBE calculates all magnetic fields of finite-beta free boundary equilibria with plasma currents on a grid whose nodes may be arbitrarily close to the plasma boundary. Unlike other stellarators, QAS configurations have a bootstrap current comparable to a tokamak with the same iota, with NCSX having an external transform fraction ranging from 60-81%. This version of MFBE is modified from the version used previously [4], by treating equilibria with toroidal current via the virtual casing principle of Shafranov-Zakharov [5].

For these scrape-off layer studies, the VMEC2000 code described in Section 4.1 is used to determine free boundary finite beta NCSX equilibria. The VMEC2000 code is an energy minimizing equilibrium code which assumes nested flux surfaces and therefore cannot be used to study islands and stochastic regions inside the LCMS. The PIES code described in Section 4.3 and HINT free boundary codes are able to treat islands and stochastic regions, but do not provide this information outside the LCMS. Coupling of the VMEC2000 and MFBE codes allows the LCMS to be found by an iteration procedure involving the toroidal flux parameter, PHIEDGE. The MFBE code obtains as input the Fourier coefficients of potential (at the boundary), flux surfaces and magnetic field from the free boundary VMEC2000. To obtain high numerical accuracy in the calculation of magnetic fields near the LCMS, the number of integration points is adaptive in the distance from the plasma boundary. Some of the interior region near the LCMS is then treated by MFBE to be consistent with external coil currents, and results which disagree with the VMEC LCMS even after iteration on PHIEDGE may be obtained, a numerical error possibly indicative of island formation just within the LCMS, a result which is further supported by the island healing results below.

Here we present calculations of the scrape-off layer field line structure (Figure11-1) for the 1017a2 modular coil design, also designated in Chapter 2 and elsewhere as M3 and which is displayed in Figure 2-4, utilizing the free-boundary VMEC reconstruction of the plasma. The 1017a2 coil set does not have island healing, and is known to have a major island chain within the LCMS from PIES calculations discussed in Chapter 4, see Figure 4-7 The modifications of the coil set to eliminate these islands, as shown by the PIES code calculation such as that illustrated in Figure 4-8 and 4-9 is accomplished by S.Hudson in the 1017c2 modular coil set. The MFBE calculation for the free boundary equilibria obtained with this island healed coil set is presented in Figure 11-2 for comparison. In both cases the VMEC2000 code with input given by li383m3.3k0.0 full current, full beta, but not optimized free boundary solution is used for "as received coils", with the resolution set at NTHETA=16, NZETA=16, MPOL=9, NTOR=5 Here a total of 30 field lines, starting at the bean shaped cross-section midplane at 2mm increments from the VMEC LCMS, are examined. Added to these plots is an approximate conformal vacuum vessel, constructed from the VMEC LCMS, but displaced 10 cm outward, which is used to calculate connection lengths.

Figure 11-1 shows two of a series of Poincaré puncture plots at the toroidal plane at zero degrees and at 60 degrees, with the starting points on the midplane. Field lines and corresponding puncture points are numbered 1 to 30 on the figure going radially outward in starting point. Each line has a color as well as a number, corresponding to the starting point. The VMEC LCMS is represented by the black solid line, the VMEC magnetic axis by the star near the center of each plot, and the conformal vessel is represented by the solid green curve. The routine plot prints out the line number of selected lines at a coordinate determined by location of the puncture point. Thus if the lines were truly ergodized, the line point number would appear randomized, that is the relative location of the starting point would not matter in determining the final position of the line. The lines are followed through 200 toroidal revolutions or until they leave the computational box (which is larger than the plot box shown here). Normally all that would be seen on a puncture plot is the accumulated punctures on the plane from all the calculated toroidal turns. But, here the puncture points which occur during the first toroidal transit of the 3 period machine are tagged with a square symbol, with the labels first, second and third intersection indicative of the period at which the puncture occurs.

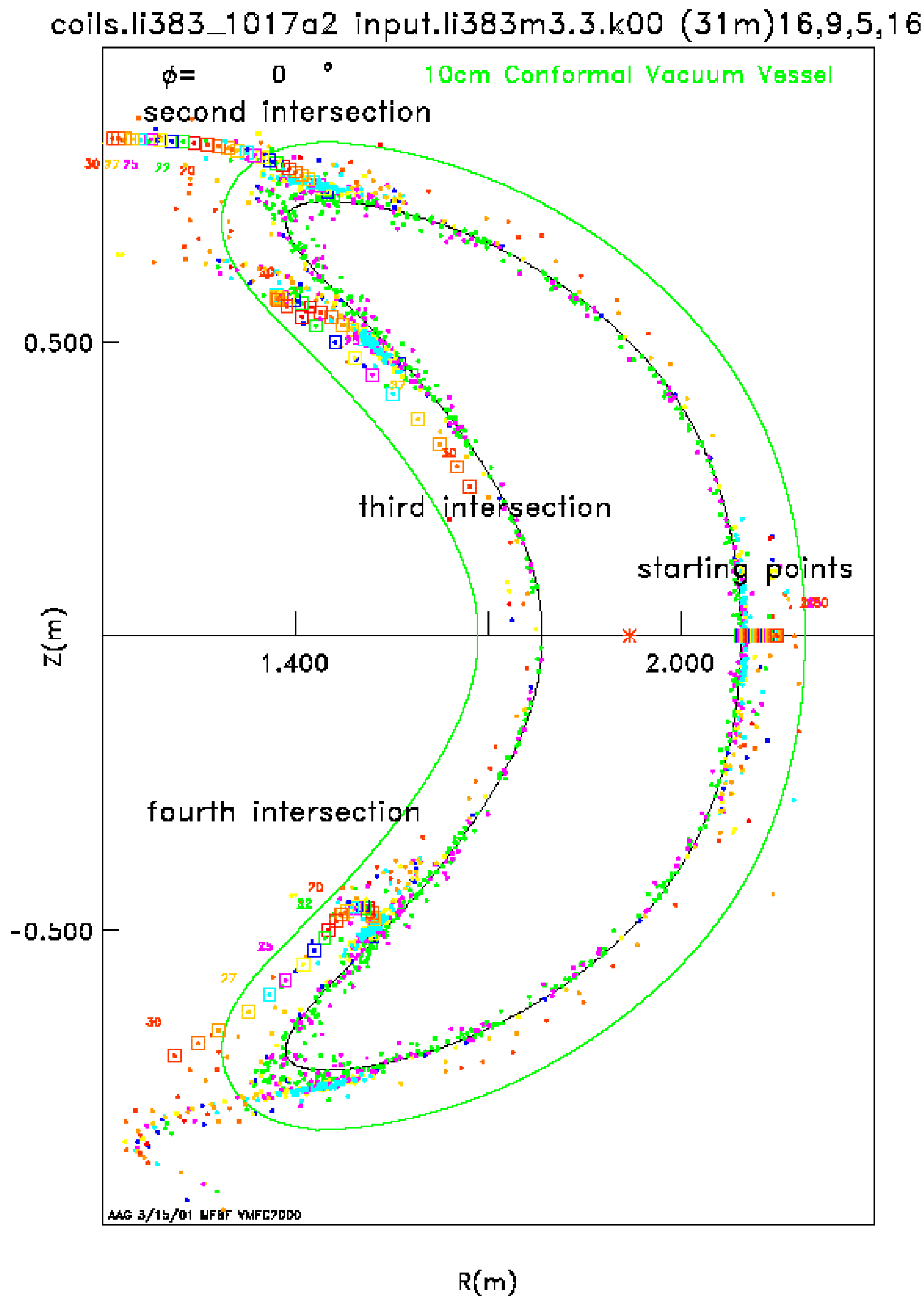

Figure 11-1a. Poincaré puncture plot for the 1017a2 coils without island healing of 30 field lines started at the midplane at a toroidal angle of $\phi = 0$ and moving out in increments of 2 mm, followed for 200 toroidal revolutions or until they leave the computational box. The solid black line is the VMEC plasma surface and the solid green contour is the conformal vacuum vessel surface at a distance of 10 cm from the plasma Punctures occuring during the first toroidal pass are highlighted by squares, and labeled by the period at which the intersection occurs

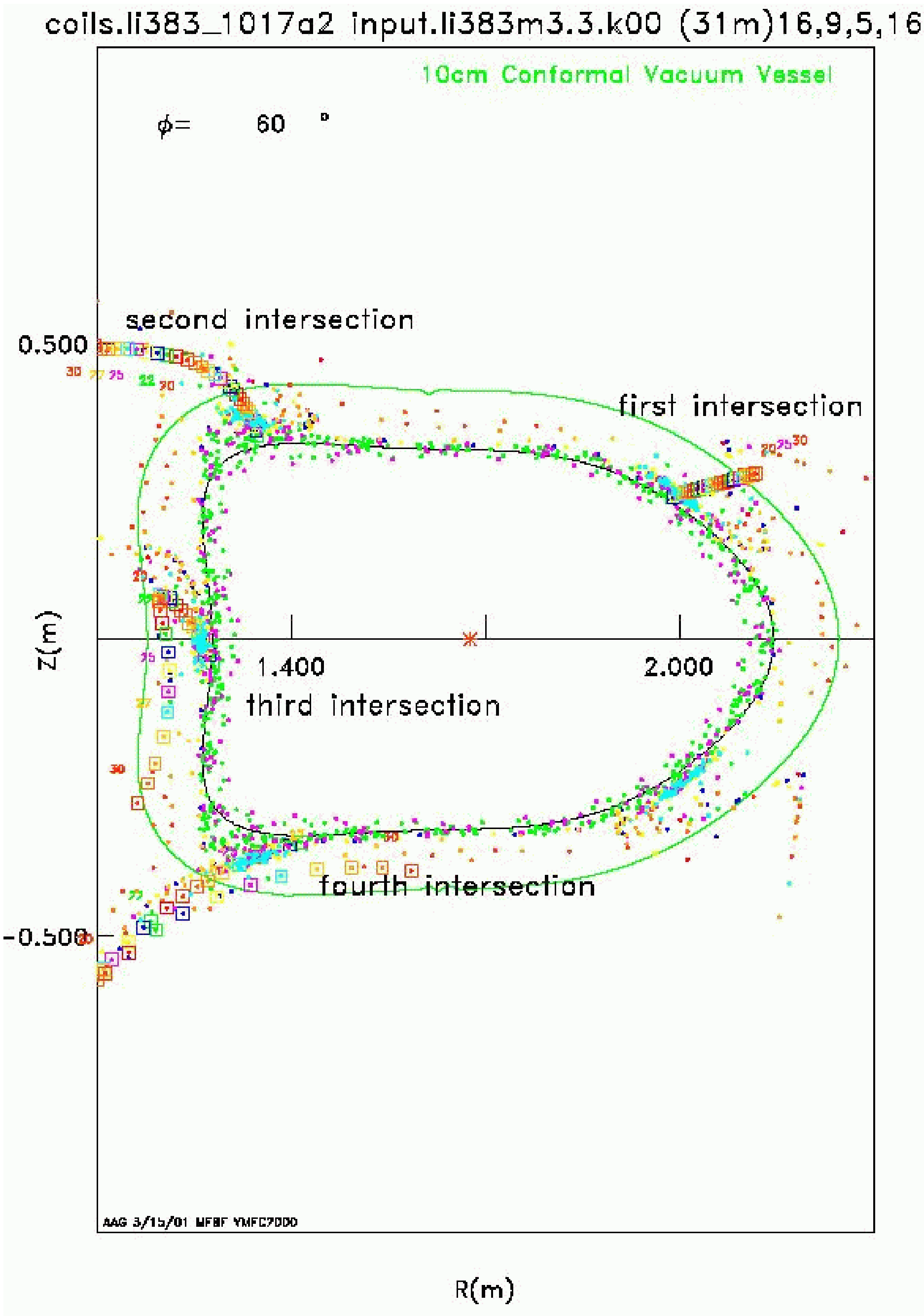

Figure 11-1b. Poincaré puncture plot at the plane located at toroidal angle ϕ =60° , with starting points shown on the midplane of Figure 11-1a, for the same 1017a2 coils without island healing

The order of the field lines continues to be preserved, at least for a single toroidal turn. The maximum excursion (and maximum flux expansion of about 5, obtained by taking the ratio of the line separation at the subsequent intersection to the separation of the starting points) of these lines occurs as the banana-shaped cross-section is approached toroidally, but is at 100 degrees rather than closer to the start of the next period (120 degrees). This maximum excursion is due to the extreme shaping needed to obtain the banana shaped cross-section, and is not a distortion of surfaces due to island structure outside the LCMS. These results do suggest there is a natural ordered-layer structure of the field lines in the edge region, and that these field lines in the edge can thus serve as the coordinate lines and provide connection lengths for plasma edge modeling of a limiter/divertor configuration. With sufficient modification of the wall to accommodate the excursion of these field lines, the diversion properties of the lines may allow a divertor concept based on this flux expansion to be developed for this compact system. Without such a modification, these plots indicate that many of the field lines will have intersected the wall in less than a full period toroidal transit, implying a relatively short connection length from the starting point to the vacuum vessel.

It is seen that there are two ergodic regions, an inner ergodic area characterized by very long connection lengths and radially clustering punctures, for starting points that are within 2 cm of the LCMS, with the closest of these actually having stayed within this region for the full 200 turns toroidally and an outer ergodic region characterized by very short connection lengths (less than a period) prevalent for field lines started beyond 2cm radially from the LCMS. These lines exhibit an ordered layer structure similar to the axisymmetric tokamak up to the first intersection with the wall. Interception by the wall does not stop the field line calculation, and they are seen to return to the region inside the vacuum vessel.

These results were obtained with some island structures observed within the LCMS. Removal of these islands, accomplished by modifying the coils as described in section 2.6, has the effect of altering the ergodicity observed in these calculations in the vicinity of the LCMS. This is illustrated in Figure 11-2 where the island healing coils set 1017c2 replaces the unhealed coils 1017a2 used to calculate Figure 11-1. The VMEC LCMS is then more accurately reproduced by the MFBE field line tracing, and the barely discernable clusters (light blue) of Poincare points outside of the LCMS of Figure 11-1 resolve into a complete chain of 5 islands (orange-red) which are shown enlarged in Figure 11-2c. The islands fit within the confines of a 10cm conformal vacuum vessel and may allow an alternative divertor concept based on island structure.

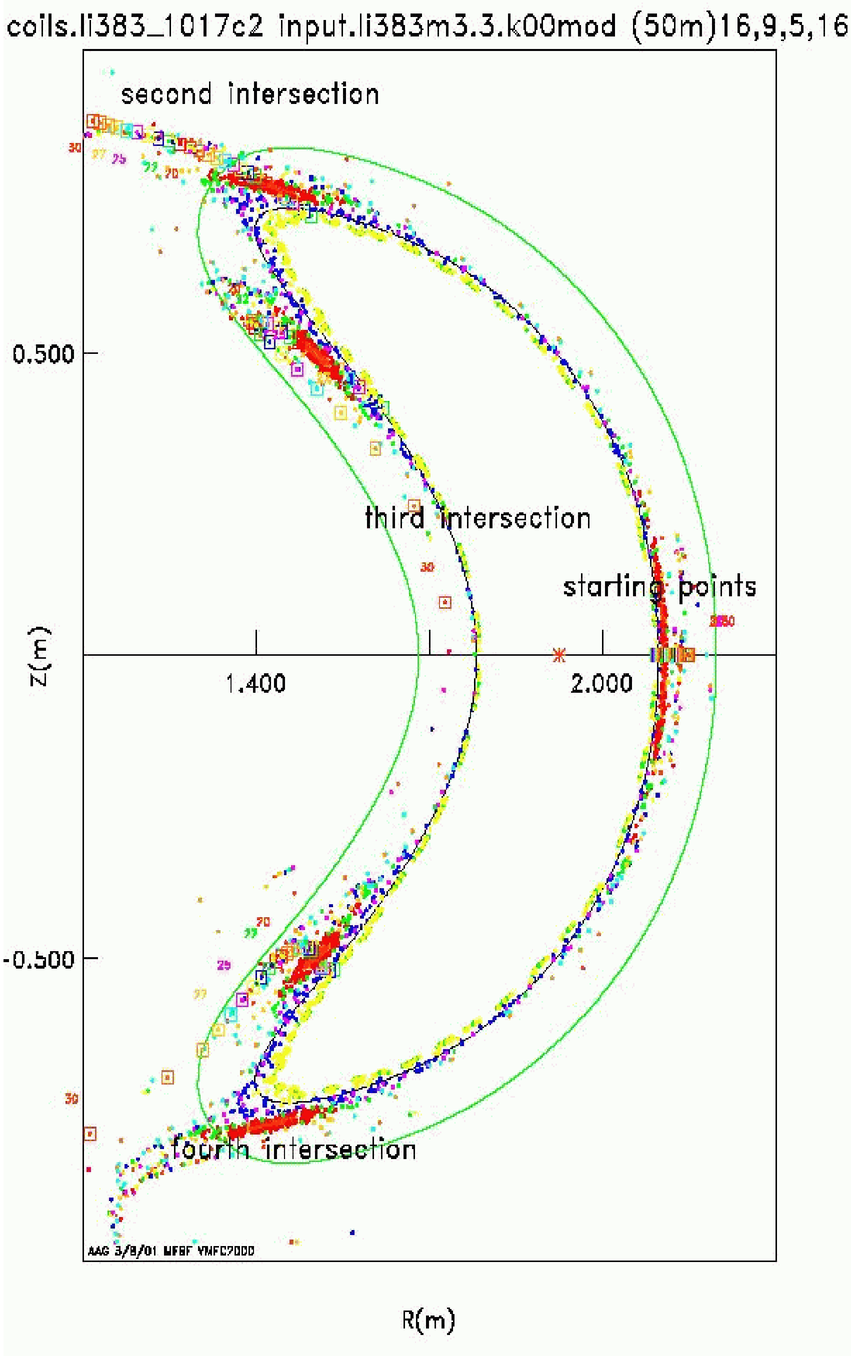

Figure 11-2a. Poincare plots with island healing implemented inside the LCMS (coils 1017c2), for the 30 field lines started at the same locations as Figure 11-1a shown for the plane at toroidal angle of $\phi = 0$ with starting points that move out from the LCMS at the midplane in increments of 2 mm. The ergodicity in the vicinity of the LCMS has now been reduced relative to Figure 11-1, and a distinct island chain is now resolvable

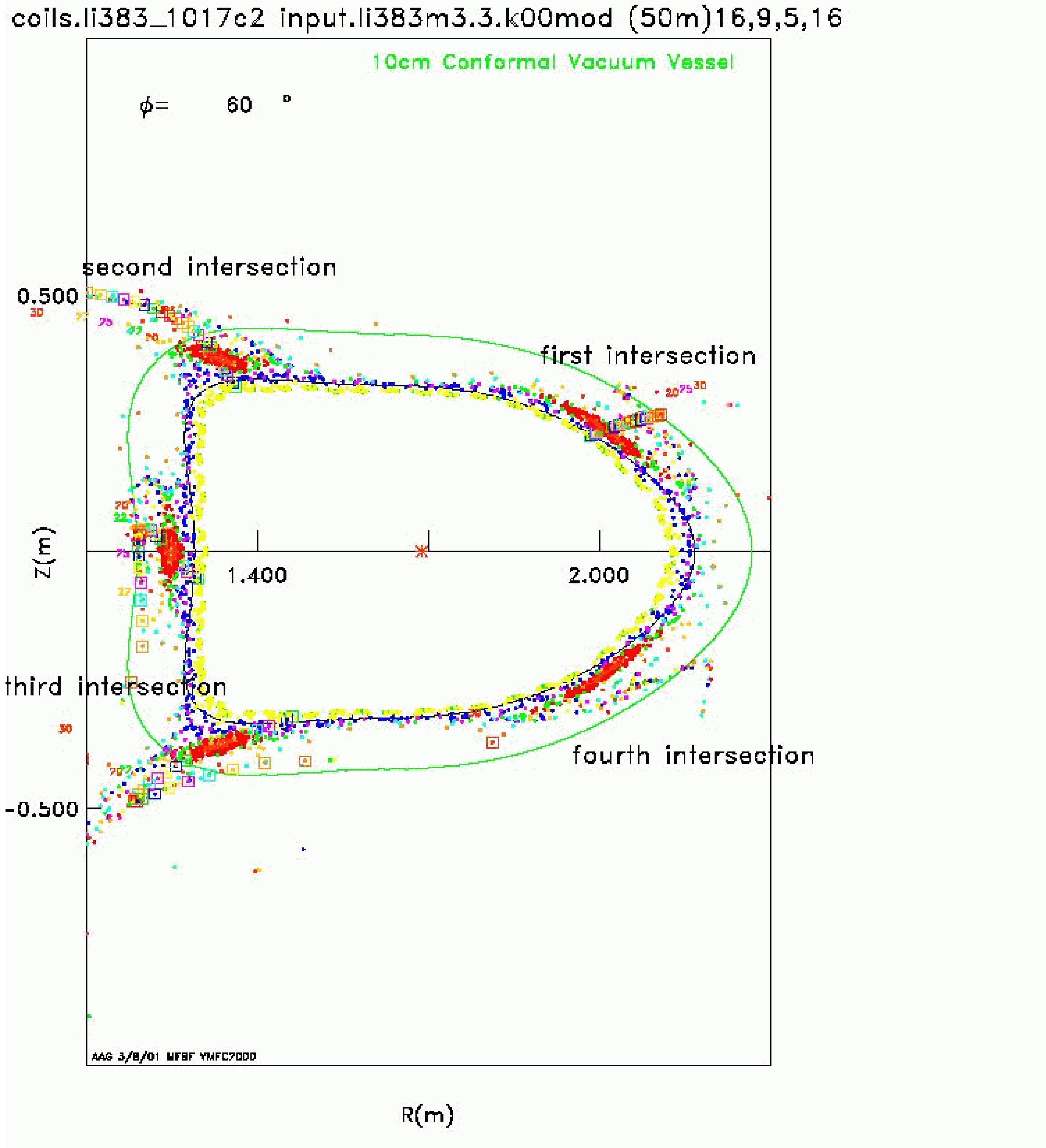

Figure 11-2b. Poincare plots with island healing implemented inside the LCMS (1017c2 coils), for the field lines started at the same locations as Figure 11-1a, with punctures shown for the plane at toroidal angle ϕ = 60°

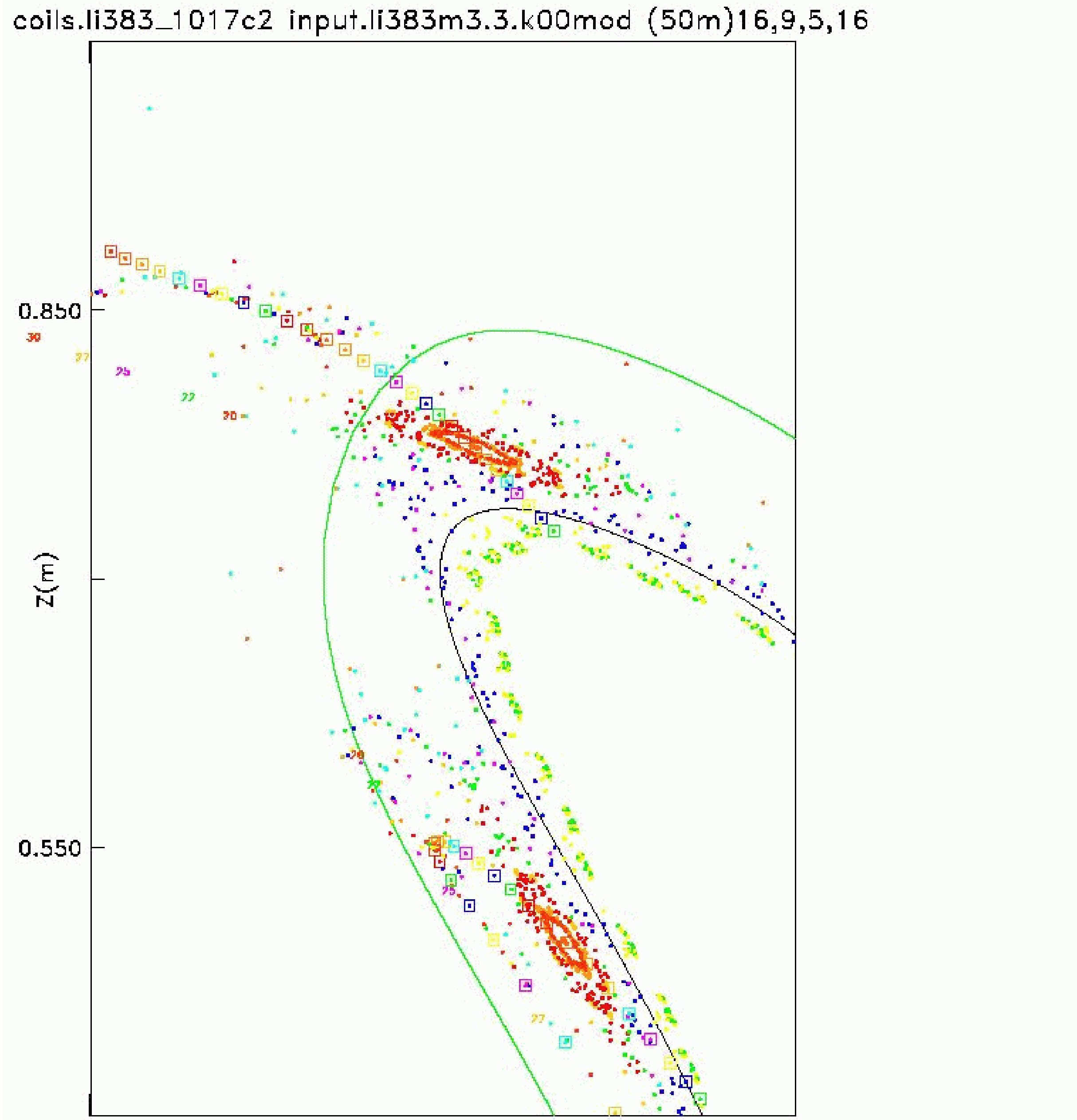

Figure 11-2c. Enlargement of Figure 11-2a region near the banana tip showing island structure between LCMS and conformal 10cm vacuum vessel wall. The squares highlight points from the Poincare puncture at the start of the second period and third period (with starting points at the midplane of the first period). The field line numbers at these highlighted points indicate the preservation of field line ordering, i.e. the field lines are still dependent on the relative position of their starting points at these early punctures, and haven't become ergodic yet. The natural island structure outside the LCMS is now clearly resolved

11.3 Fast Particles Leaving the Confined Plasma Boundary

For the initial operation NCSX will be designed for up to 6 MW of beam power in the 40 to 50 keV energy range. These beams will be injected tangentially in both the co- and counter-directions. As has been discussed above, *(Section 7.32)* the non-zero departure from perfect symmetry in stellarators will lead to enhanced levels of beam ion losses above those present in an equivalent axi-symmetric tokamak. The loss patterns of beam ions on the vacuum chamber wall might require wall armor to handle the respective heat fluxes and to minimize the generation of impurities. Within the Monte Carlo slowing-down model described in Section 7, the exit locations, exit times, pitch angles and energies of the beam ions, leaving the outermost closed flux surface, are recorded. Assuming that beam ions then move rapidly through the open outer flux region, the recorded parameters are used in estimating power loading patterns on the vacuum chamber walls.

As discussed above, some of the characteristics of a slowing-down beam for the parameters $n(0) = 6 \times 10^{19}$ m^{-3}, $T_e(0) = T_i(0) = 2.4$ keV have been calculated *(see Section 7.32)*. As an example, Figure 11-3 shows a histogram of the energy distribution of the escaping beam ions injected with 40 keV energy.

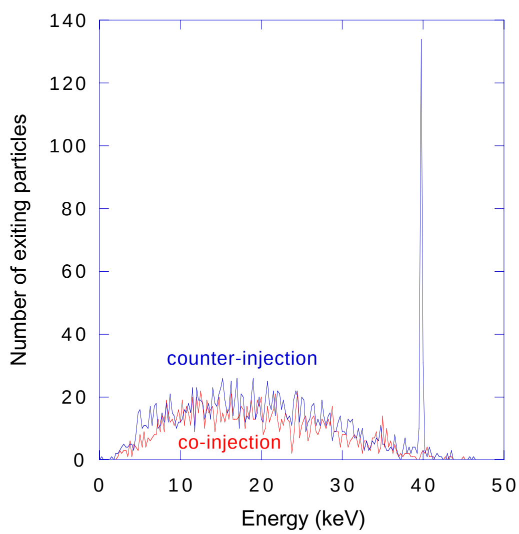

Figure 11-3. Energy spectrum of beam particles exiting the last closed magnetic surface

As can be seen, the energy losses are characterized by a broad distribution centered around 15 - 20 keV for both co- and counter- injection. The counter-injected ions also show a very sharp peak at the injection energy, presumably associated with prompt losses. It is important to know how much of the total injected energy is lost in fast particles, which is dependent on the injection energy. The result presented in Figure 11-3 has been based on 40 keV ion energy. The beams anticipated for NCSX will be capable of going up to 50 keV, but will also include lower energy components. In Figure 11-4 we investigate the variation of beam losses with injection energy as described above *(Section 7.32)*.

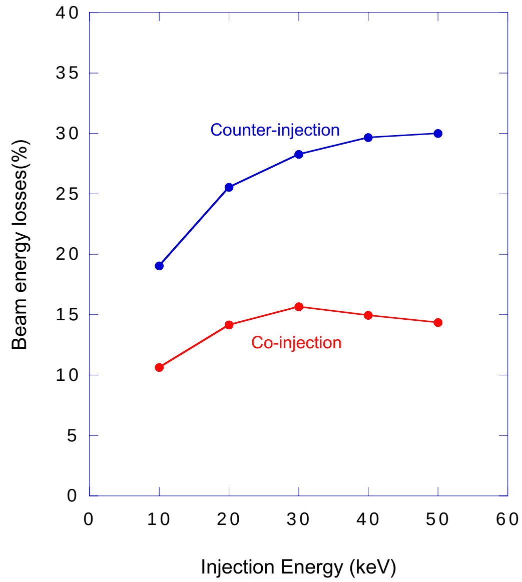

Figure 11-4. Variation of beam energy losses with injection energy for a machine design point at R_0 = 1.4 m, <B> = 1.23 T, n(0) = 8.5 x 10^{19} m^{-3}, $T_e(0) = T_i(0)$ = 1.58 keV

Based upon the current model, exit locations and energies are shown in Figure 11-5 for a typical case. Here the exit locations are plotted in Boozer poloidal and toroidal angle coordinates for the outermost flux surface. Colors are used to indicate the energy at which the fast ions leave the surface. As can be seen, most of the ions leave at intermediate energies from 10-20 keV, in similarity with Figure 11-3.

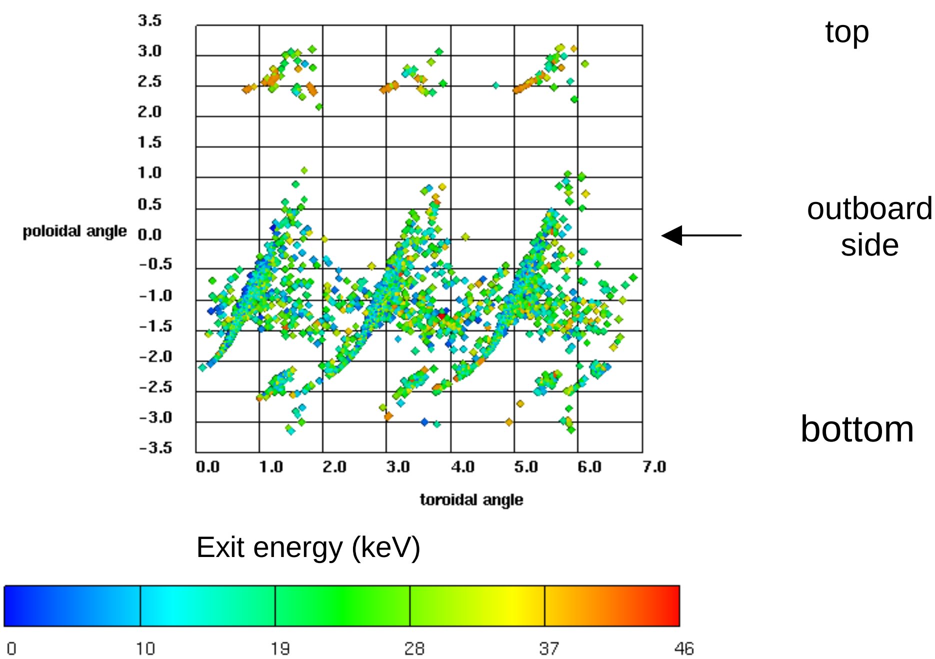

Figure 11-5. Location and energy spectrum of beam losses on outer surface in 2D Boozer coordinates

The fast ion losses are primarily concentrated in helical stripes on the bottom of the vacuum vessel with one stripe per field period (shifting to the top with reversal of the magnetic field

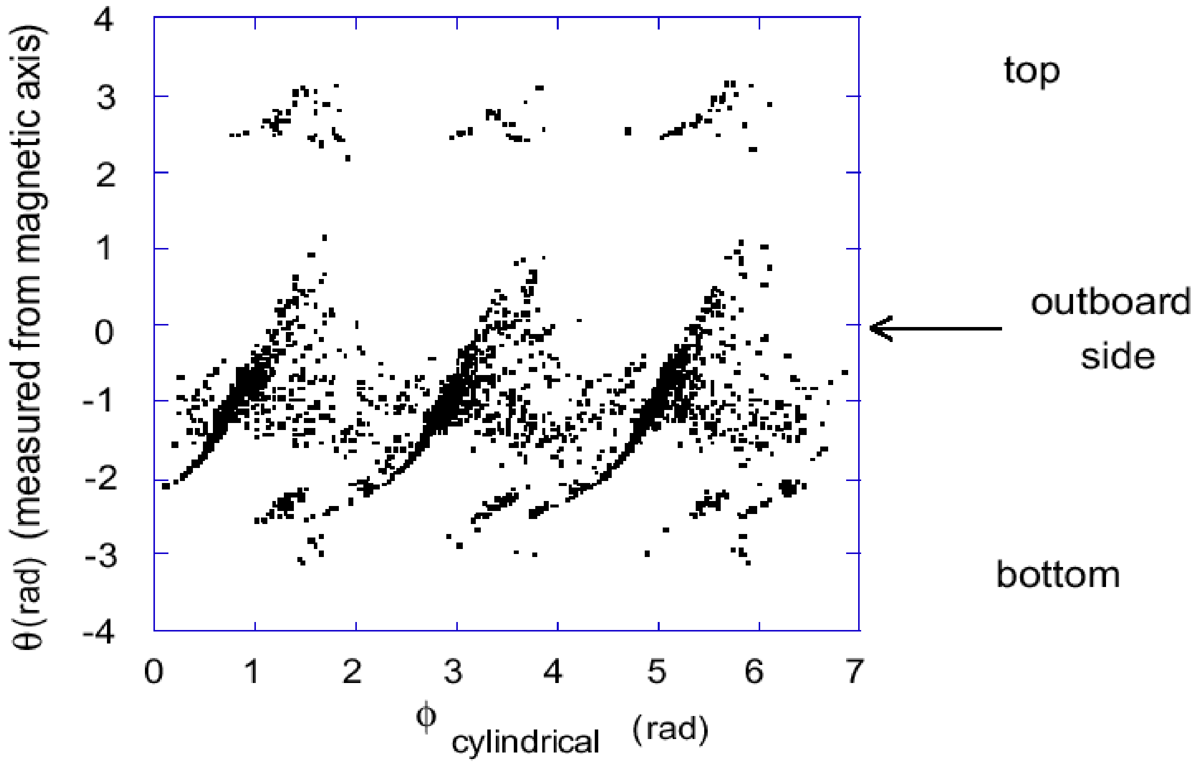

Figure 11-6. Location of beam losses on outer surface in 2D real space coordinates

direction). We have also transformed this data into real-space coordinates. In Figure 11-6 we plot the data of Figure 11-5 vs. the normal cylindrical azimuthal coordinate, $\phi_{cylindrical}$ and a poloidal angle θ, which is equal to $\tan^{-1}[z/(R-R_0)]$.

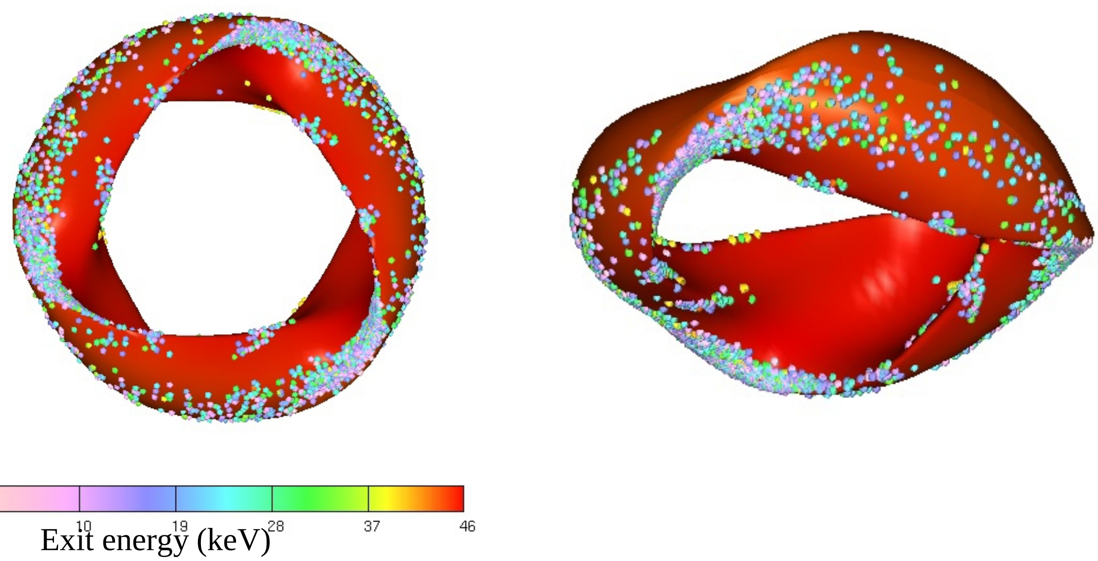

Figure 11-7. Location and energy distribution of beam losses on outer surface in 3D

Finally, we have plotted the ion loss locations on the three-dimensional outermost flux surface (Figure 11-7) as obtained from the VMEC stellarator equilibrium code. The flux surface is shown in red and the ion exit locations are color-coded according to the ion's energy at the time it passes through the flux surface. Again, it can be seen that the losses are somewhat concentrated, motivating the design of protective structures at these locations.

11.4 Heat Flux Estimates Including Cross-Field Diffusion

The initial design point for the NCSX scrape-off-layer (SOL) plasma assumes attached conditions from the last-closed-magnetic-surface (LCMS) to the material targets. This can be achieved with sufficient field-line length between the LCMS surface and the targets, $L_c > 100$ m, referred to as the connection length. Under these circumstances the SOL plasma will be at moderate to high temperature, *e.g.* , 100 - 200 eV at the LCMS and 20 - 50 eV near the targets (see below). Energy transport in a SOL at these temperatures will be dominated by electron conduction parallel to the magnetic field lines. Therefore, initial estimates of the heat flux profile on the targets can be obtained by following a sufficient number of field lines from the region of the LCMS where the power enters the SOL to where the field line strikes a surface. The density of field line strike points gives the estimate of the heat flux profile (see Section 11.2).

A heat flux estimate obtained solely from field line tracing overestimates the peak to average heat flux ratio and underestimates the radial and toroidal extent of the required high heat flux target surfaces on the wall because it ignores cross field transport in the SOL. For sufficient field line length and SOL turbulence the cross field transport can broaden the heat flux profile which finally reaches the target surface. The broadening can be both in the toroidal and the poloidal directions so this effect can have a significant impact on the required design of high heat-flux target-components. The effect of broadening of the profile compared to what would be calculated from unperturbed field line tracing has been observed experimentally on the W7-AS stellarator [7]. Of course, this broadening is enhanced by the stochastic magnetic-field layers and the magnetic island X-point structures in the SOL that are typically produced in W7-AS. However, even in the relatively ordered NCSX SOL fields, the field lines beginning close to the LCMS have sufficient connection length that some broadening of the heat flux profile is expected.

The technique used by the NCSX edgegroup to estimate the effect of cross field transport broadening of the heat flux is to couple a field line tracing algorithm with a model for "diffusion" of the field lines. The computation is set up to follow unperturbed field lines for a specified parallel distance and then displace the radial position of the field line before continuing the parallel field line tracing. The displacement distance is calculated to simulate an expected energy transport coefficient in the SOL. The displacement direction is taken from a random polar distribution in the plane perpendicular to the field line direction.

The field line tracing with diffusion technique produces substantial broadening of the strike point distribution in calculations for the W7-X stellarator design [6,7] . The setup for this example begins with the assumption that the cross-field scale width of power in the SOL is $\lambda_\perp$ =

1.5 cm. Then assuming a balance between parallel and perpendicular diffusive transport in the 2D energy balance equation, one derives that $\chi_{\|} / \chi_{\perp} \sim (\lambda_{\|} / \lambda_{\perp})^2$. If one assumes the parallel scale-length for power in the SOL is approximately L_c /4, then for an average connection length of approximately 100 m in W7-X, one obtains $\chi_{\|} / \chi_{\perp} \sim 3 \times 10^6$ as in the example of Reference 7. The code simulations for this example used 0.001 m displacements of the field lines after each 0.3 m field-line length. This implies over 300 displacements along a field line of average connection length, and 0.3 m radial displacement of the field line if all the displacements were in one direction. Even with random displacement direction it is not surprising that substantial spreading of the profile of strike points on the wall was calculated.

The computational algorithms that perform this calculation for the W7-AS and W7-X stellarator designs will be adapted to calculate the heat flux broadening for NCSX. The average field line length will be obtained from the unperturbed field line tracing results of Section 11.2. Since NCSX is a toroidal device with a combination of the properties of tokamaks and classical high aspect ratio stellarators, our knowledge of the anticipated perpendicular scale widths for power and particle flux in the SOL is quite limited. As a result we will need to do multiple simulations of field line tracing with the diffusion model for a range of perpendicular transport coefficients to scope out the requirements on the high heat flux target designs. The speed of the field-line tracing and diffusion model calculations will be increased by converting them to parallel computers so that it will be possible to trace an adequate number of lines (~1000) for a sufficient number of transport coefficient cases to guide the design requirements of the targets.

11.5 First Wall Configuration and Materials

The configuration of the first wall is to a limited degree conformal to the plasma. The reason for the vacuum vessel being only of limited conformal shape is for operational flexibility and due to the numerous ports, necessary mainly for beam injection and diagnostics, generate large deviations from conformity. This can be seen in Figure 11-8 which shows cross sections of the vacuum vessel and the plasma at $\phi = 60°$ (bullet-shaped) and $\phi = 0°$ (bean-shaped). This figure shows a typical example of how little of the bean-shaped plasma cross-section is actually surrounded by a conformal wall surface, while the situation is obviously different for the bullet-shaped cross-section. Figure 11-9 provides a plan view of the plasma and vacuum vessel that also demonstrates the large deviation of the vacuum vessel from the conformal shape.

The main material of the vacuum vessel is stainless steel and the plasma-facing components will be made of graphite or carbon-fiber composite (CFC) material. The ideal case would be to cover the whole first wall with CFCs; this would take care of neutral beam shine-through, energetic particle losses, and limiter/divertor baffles all together. But, this ideal case would be fairly expensive and also not needed for the first phase of machine operation with an input power of 3 MW for <0.30s.

To stay within the budget for the initial machine configuration, the plan is to start by covering selective areas: for neutral beam armor, inboard limiters centered at $\phi = 60°$, and neutral particle baffles centered at the $\phi = 0°$ cross-sections.

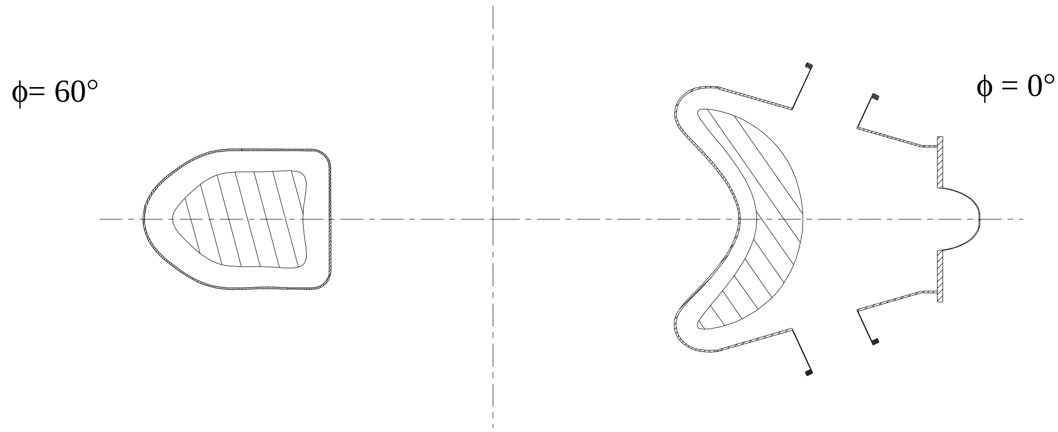

Figure 11-8. Plasma and vacuum vessel cross-section at the ϕ = 0° and ϕ = 60° cross-sections

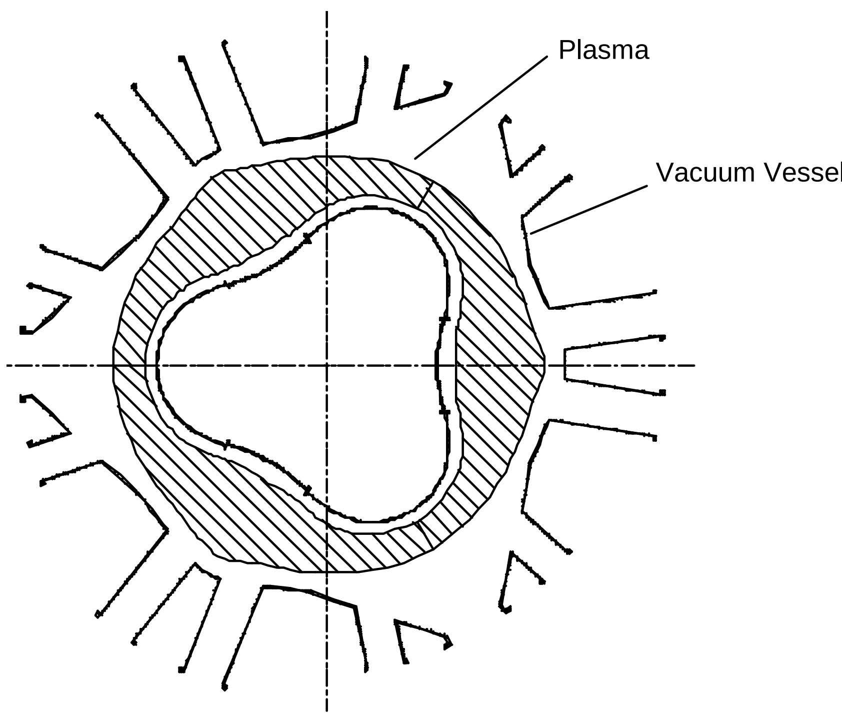

Figure 11-9. Plan view of the plasma and the vacuum vessel. It shows clearly the large deviation of the vacuum vessel from the conformal shape

11.6 Initial Power Handling System

There are several requirements that impact the NCSX limiter/divertor configuration. The power-handling requirement (i.e. power and pulse length) will be a factor in selecting the heat removal surface area. The heat load requirement for initial operation is 3 MW for a pulse length of ~0.30 sec. Data from past experiments shows that a peak heat load up to about 30 MW/m^2 can be absorbed by graphite composites. If we assume a peaking factor of three, we will require about 0.3 m^2 of heat removal area.

The need for symmetry will impact the toroidal and poloidal location of the limiters and divertors. This requirement translates to one heat removal surface per period with vertical symmetry and an area of at least 0.1 m^2 per period. In addition, the need to limit the neutral penetration to the plasma core will restrict the location of the neutral sources to broader plasma cross sections. The limiter locations will need to take into account the possible location of an RF antenna at the small major radius side of the bullet cross section.

The neutral beam injection configuration will require a system of beam armor at the locations where the beams impinge on the wall. In addition, the injection process will result in a fast ion loss as discussed in Section 11.3. The wall will need to be protected at the locations of high ion loss trajectories. The ion orbit studies indicate relatively broad regions of ion impingement on the wall.

In general, a range of options can be accommodated by the mechanical configurations being considered for NCSX. As the project progresses into more detailed design phases the local mechanical requirements for the limiters and divertor will need to be factored into the design process. We have selected a preferred limiter/divertor configuration for initial operation to demonstrate feasibility and support the costing exercise. In addition, this preferred configuration could be used to demonstrate the compatibility of the plasma facing components with the overall configuration and with physics objectives.

The preferred initial limiter/divertor configuration integrates the limiter, divertor and wall armor into one heat removal configuration. The specific approach will be to mold a range of shapes from a graphite weave to cover the required locations. We expect that the required coverage is about 50% of the first wall area. This approach can be used to mimic localized-fixed limiters by molding a shape that protrudes from the surrounding wall covering. The attraction of this option is that it can cover a multitude of heat removal and wall protection needs while minimizing performance uncertainties.

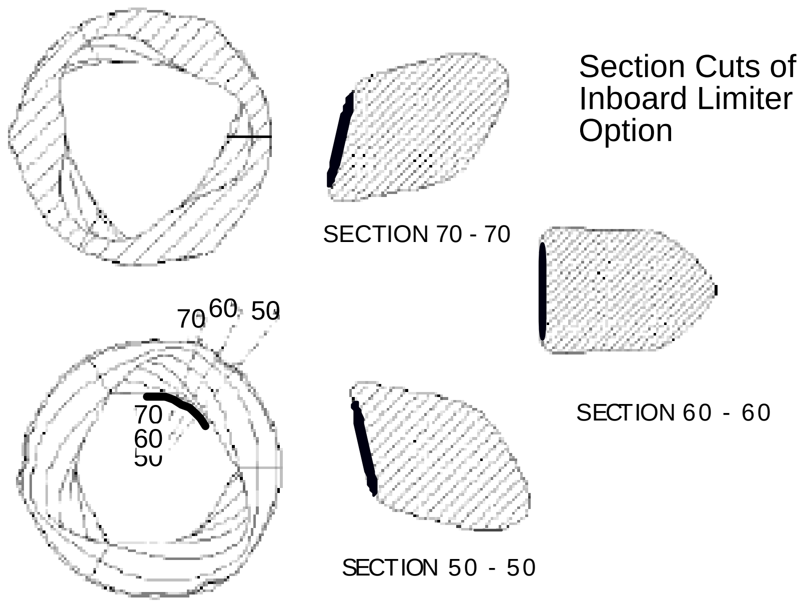

Figure 11-10. Inboard limiters 'centered' around the ϕ = 60° cross-section (one per field period)

The region selected for locating limiters is the small major radius side of the three bullet cross sections, as shown in Figure 11-10. The contact area will have the shape of a long rectangle oriented at a shallow angle to the horizontal so as contact a relatively flat surface. One attraction of this location is the existence of this flat region. A second attraction is that this location will provide reasonable neutral shielding for the plasma core. A third attraction is that this location should have reasonable magnetic shape stability. As stated above it is possible that an RF antenna will be located in this region in one magnetic period. If this is the case we will integrate the antenna power and particle protection in this period with the limiter function.

In addition to the limiters just described, we propose to locate a heat removal surface at the tips of each bean cross section (i.e. six locations). This configuration should function as a divertor. The location of heat removal surfaces near the bean tips will take advantage of the expanded flux in this region to reduce the local heat flux. An assessment is being made of whether heat removal surfaces in this location can be movable to increase flexibility. Experiments with this configuration should provide a data base to support the design of a future divertor upgrade with the potential for neutral pumping.

A research program to develop a data base for plasma facing components in this stellerator configuration will play an important role during the initial physics operations phase. This data will contribute to the design of upgrades in the plasma facing component to support higher power operation. Of particular importance will be the development of an understanding of the region outside the last closed flux surface and the geometric requirements for divertor operation.

As stated above, the location of heat removal surfaces near the bean tips will take advantage of the expanded flux in this region and provide valuable experience for future upgraded divertor implementation. An assessment is being made of whether heat removal surfaces in this location can be movable to increase flexibility. The location of a fixed limiter at the midplane of the bullet section will provide good neutral shielding behavior at a location with relatively smooth surfaces. Future studies will determine the physics flexibility to accommodate a range of plasma motion relative to the fixed limiter location. To the extent that we can move the plasma relative to the limiter without significantly degrading the physics performance we can experience the advantages of a movable limiter along with the advantages of a location at small major radius.

11.7 Divertor Upgrades

Important future improvements of the divertor/limiter system will include upgrades of the power handling capability and divertor baffling and pumping.

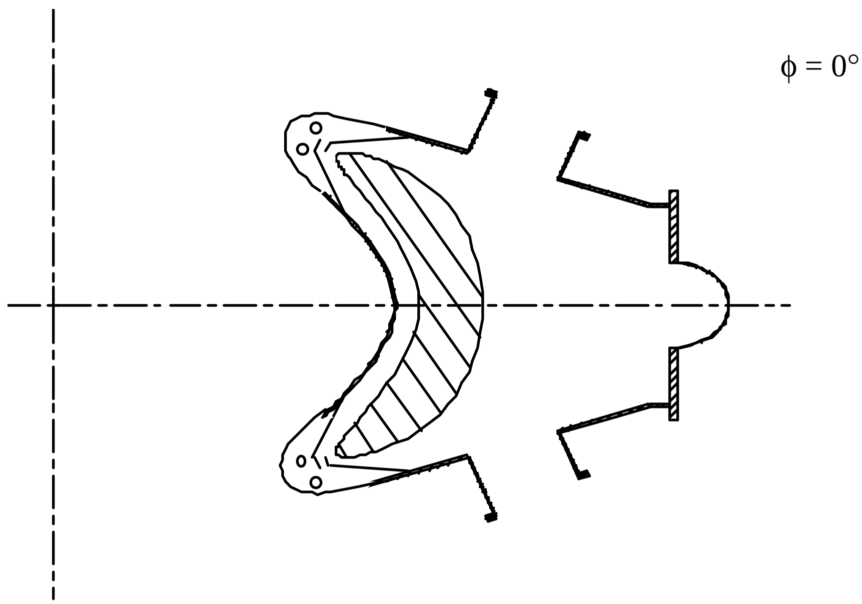

Figure 11-11. Divertor upgrade including neutrals baffles and pumping

The divertor baffles have to serve two purposes. They represent the main divertor plates, i.e. they are designed to handle about 80% of the thermal power leaving the main plasma by convection and conduction. At the same time they are designed to confine neutrals mechanically and either direct them back into the boundary plasma or guide a certain fraction behind the baffles into the divertor pumping plenum. Figure 11-11 shows a schematic view of this arrangement. Pumping could consist of titanium gettering or cryo-pumping. Note: the baffles and pumps are not toroidally continuous, but extend only over a certain toroidal length 'centered' around ϕ = 0°.The actual divertor baffle and pumping system will be designed in the future, guided by neutrals and plasma transport codes (DEGAS2, etc.).

11.8 Neutral Transport Calculations

Fully three-dimensional simulations of neutral particle behavior in NCSX will be needed in its latter design stages and as part of experimental analysis during machine operation. Although three-dimensional Monte Carlo neutral transport codes exist (e.g., DEGAS 2, EIRENE), no tools exist for easily converting external descriptions of the stellarator geometry and plasma into the data structures used inside those codes. The existence of a large effort at IPP-Greifswald to develop a three-dimensional fluid plasma code (BoRiS) provides a clear path forward for not only establishing the needed interface for the neutral transport codes, but also for setting up a coupling between them and the BoRiS code.

The near-term need (e.g., for this report) is for rough estimates of neutral penetration lengths. Tokamak experience suggests that having a significant fraction of the recycling neutral atoms and molecules reaching surfaces well inside the last-closed magnetic surface leads to unacceptably low core energy confinement times. Since the bulk of the recycled neutrals leave the surface with a cosine distribution (i.e., peaked about the normal to the material surface), the greatest penetration will be achieved in the same poloidal plane as the recycling surface. Consequently, toroidally axisymmetric neutral transport calculations can place an upper bound on the neutral penetration distance.

The DEGAS 2 Monte Carlo neutral transport code [8] is used here to perform such calculations, first with recycling at an outboard limiter and then with the recycling occurring at a divertor baffle. The setup codes used to generate the DEGAS 2 input files permit considerable, but not complete flexibility. Hence, the correspondence between the limiting and baffling structures used in DEGAS 2 and those proposed elsewhere in this document as the actual NCSX plasma facing components is less than perfect.

The plasma shape, specified in terms of a "moments" representation for R and Z, was obtained via a VMEC equilibrium for the li383 case. For the purposes of this document, the calculations use the poloidal cross-section corresponding to a toroidal angle of 0 degrees ("bean" cross section). In general, the angle used can be arbitrarily chosen. For simplicity, a uniform mesh of 30 points in the poloidal angle was assumed.

The VMEC equilibrium provided contained many more flux surfaces than were necessary for the neutral penetration calculations. The set was reduced in a semi-arbitrary manner so that the maximum distance between adjacent surfaces was 5 cm. This procedure resulted in a total of 17 surfaces for the bean cross section.

The vacuum vessel (VV) shape was likewise specified via a moments representation. To increase radial resolution between the last closed magnetic surface (LCMS) and the VV, four additional surfaces were inserted via interpolation in between.

The remaining step in establishing the geometry for neutral transport is the specification of the recycling locations. As this setup code is currently constructed, the minimum size and exact location of these surfaces is controlled by the poloidal angle mesh. One set of calculations described here uses an outboard limiter assumed to consist of two poloidal mesh segments extending from the VV to the LCMS. A second set utilizes a divertor target composed of four poloidal mesh segments centered about the bottom of the bean cross section and located just in front of the VV.

The plasma profiles used in these initial calculations (Figure 11-12) were constructed as described in Section 8.3, using an assessment of the W7-AS experimental database for the edge and scrape-off layer conditions [9].

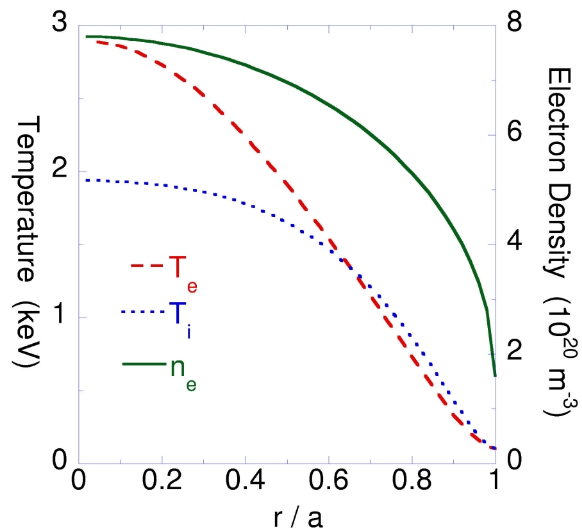

Figure 11-12. Core plasma temperature and density profiles used in the neutral transport calculations were obtained via the neoclassical transport analysis of Section 8.3

These were interpolated onto the core plasma surfaces (these calculations are in a cylindrical geometry; here, r/a is equated with the square root of the ratio of the local to LCMS toroidal flux). A scrape-off length (relative to the LCMS, locally in physical space) of 2.2 cm for both density and temperature was used. The resulting electron density and temperature profiles are shown in Figure 11-13.

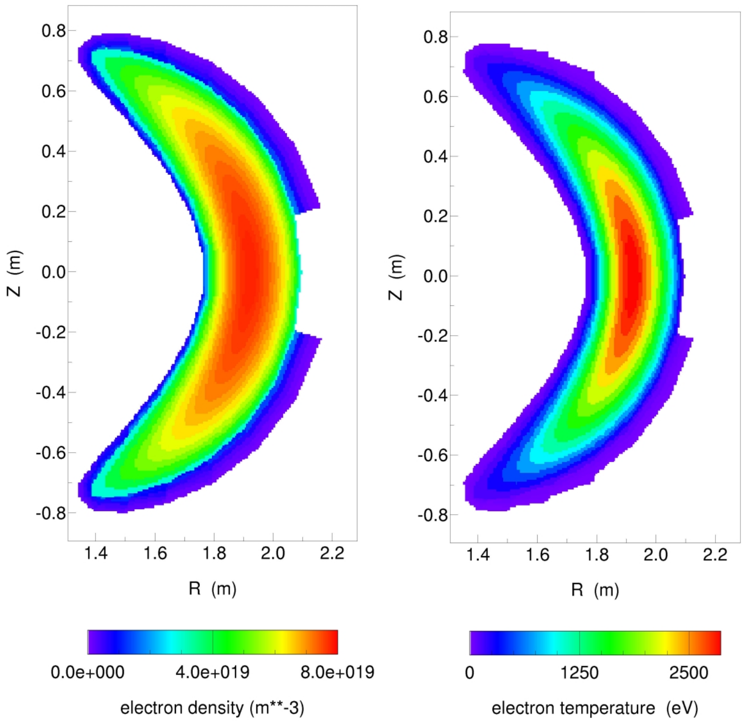

Figure 11-13. Two-dimensional plots of the electron density and temperature data used in the neutral transport calculations. These plots show the outboard limiter as the "missing" white region centered about the midplane

The white area on the right side of the cross section corresponds to the outboard limiter (this region contains plasma in the second simulation with recycling at the divertor baffle).

The atomic physics used includes D_2 dissociation and ionization, D charge exchange and ionization. All of the hardware is currently assumed to be carbon. The only plasma-material interactions used are reflection and desorption (for everything not reflected). A fixed D recycling source (2×10^{21} s^{-1}) is taken to be spread uniformly over the recycling surfaces in these two simulations.

Figure 11-14 shows the D density and D^+ ion source rate for the first simulation featuring recycling at the outboard limiter. Note that the peak neutral density and ionization source occur inside the closed flux surfaces (since the limiter is positioned at the LCMS). The scale lengths for both the density and the ion source rate in front of the limiter are about 0.8 cm. The neutral density at the magnetic axis is roughly 10^{-3} of the peak value; the ion source rate there is 3×10^{-4} of its maximum value.

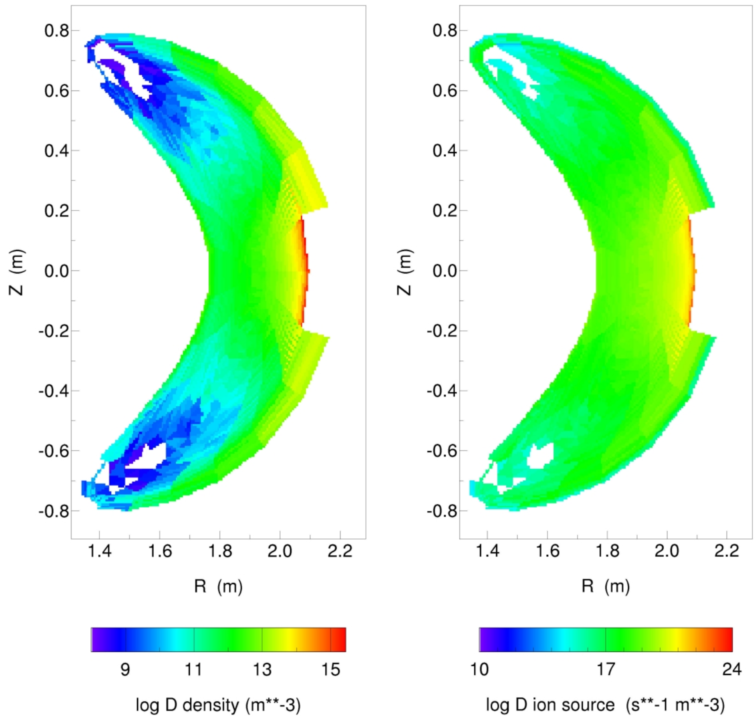

Figure 11-14. Two-dimensional plots of the log of the neutral atom density and the ion source rate obtained with recycling at an outboard limiter. To facilitate computation of the logarithm, factors of 10^9 and 10^{10}, respectively, were first added to the data

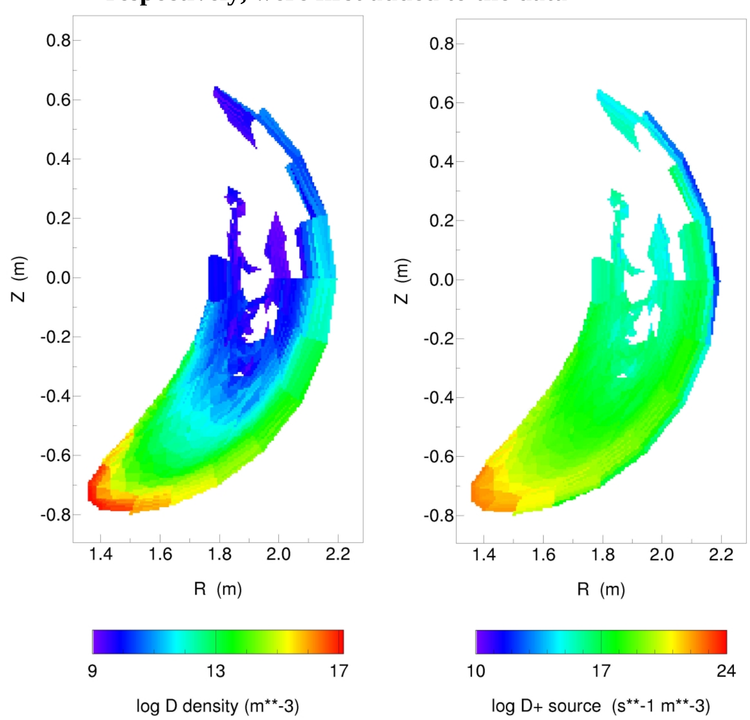

Figure 11-15. Two-dimensional plots of the log of the neutral atom density and the ion source rate obtained with recycling at lower divertor. To facilitate computation of the logarithm, factors of 10^9 and 10^{10}, respectively, were first added to the data

Figure 11-15 shows the D density and D source for the case featuring recycling at a divertor baffling surface positioned at the lower tip of the bean cross section. In this case, the density and ionization source inside the LCMS are much smaller (more than one order of magnitude) than in the limiter case. The maximum neutral density inside the LCMS is a factor of 0.09 times the overall peak value; the maximum ion source rate there is 39% of the overall peak. Both the neutral density and the ion source rate are effectively equal to zero at the magnetic axis. Thus, it is very important to ensure that recycling occurs in the peak region and not the midplane.

11.9 Edge Modeling

11.9.1 Self-Consistent Edge-Plasma Transport Modeling

Estimating high heat-flux locations and magnitudes on the vessel wall via magnetic field-line tracing is described in Section 11.4, including diffusion to model turbulent cross-field thermal transport. While these are important tools to indicate where to place protective tiles on the walls, experience with tokamaks shows that a more complete transport model of the edge plasma, including particle, momentum, and energy flows, is needed to understand the variations that are possible for the heat-flux profiles, and for the particle fueling that is related to the core density limit. The interaction between the plasma and neutrals is the key issue here. Such a model will contribute to decisions about upgrades to the NCSX power and particle handling hardware including the most effective location of baffles to control fueling. A self-consistent model will provide vital information on the type and position of edge-plasma diagnostics, and is also needed to predict the level of impurities that can enter the core.

To obtain the self-consistent description of the edge plasma and neutrals, we are collaborating with the IPP Greifswald group in the development of a 3D stellarator transport code known as BORIS. The Greifswald group, which includes 4-5 people dedicated to this task, has already designed the basic code structure and has obtained some preliminary results based on the electron and ion energy equations [10]. Our role is to provide expertise in the areas of iterative solvers, fluid neutral description, **E**x**B** drifts, and possibly parallelization. At the same time, we will adapt the code to the NCSX geometry and perform self-consistent edge-plasma calculations. We anticipate that initial results will be available for NCSX by the end of fiscal year 2001, but this modeling work and development will evolve for a number of years, finally providing a close contact between theory and experiment.

For the BORIS code, the Braginskii-like magnetized fluid equations are solved for the plasma density, parallel velocity, electron and ion temperatures, and the plasma current. The parallel transport is taken as classical, while the cross-field transport has an important turbulence component as discussed in the next section. The neutrals will initially be described by a set of flux-limited fluid equations. A finite-volume discretization is used, together with an implicit algorithm for the resulting large matrix problem.

Aside from the substantial complication associated with the 3D nature of the problem, the BORIS components are the same as we have developed in the 2D UEDGE transport code. Thus, we should be able to use this experience to great advantage while at the same time leveraging for NCSX the substantial effort being applied to this work at Greifswald. We expect to be able to characterize the edge-plasma in the same detail as we have done for tokamaks where there is generally a good correlation between models and experiments. In addition to edge-plasma characteristics and heat deposition profiles, this work will also provide the edge-plasma for Monte Carlo calculations with DEGAS2; the initial BORIS neutrals model is a fluid description and the Monte Carlo neutrals calculations will be an important refinement. Also, impurity ions will be added to the description in the next year.

We have already begun our collaborative work with the BORIS code through two visits to IPP Greifswald, and a three-week visit to LLNL last spring by two of the BORIS developers. These collaborative visits will continue in order to ensure a close connection with the code developments. This connection is further strengthened by joint work on the BOUT turbulence code described in Section 11.9.2.

A second method based on a Monte Carlo technique has also been used for advancing the plasma transport equations in 3D for stellarators [11]. This method is being developed and validated. We will monitor its progress and may collaboratively pursue it at a later time.

11.9.2 Edge-Plasma Turbulence Modeling for the NCSX

A very important component of the edge-plasma characterization is to understand, at a fundamental level, the nature of the turbulence and resulting cross-field transport. Not only does this impact the width of the scrape-off layer plasma, but it can also give rise to an edge transport barrier as in the H-mode transition for tokamaks. At the same time, the turbulence simulations need to begin with full edge-plasma profiles from two-point estimates, transport simulations, or experimental data. For the short term, turbulence simulations can give important information on the toroidal and poloidal distribution of power leaving the LCMS which can be used to improve the wall power-deposition calculations even using the field-line tracing models.

Again, the turbulence work should benefit substantially from a collaboration with IPP Greifswald, but at this time, we have the basic 3D turbulence code that has been used to describe edge-turbulence in tokamaks called BOUT [12], and the Greifswald group wants to help modify it for stellarators. To aid in this work, R. Kleiber from IPP Greifswald will visit LLNL for three months this spring (2001) to adapt BOUT to the stellarator geometry. With a successful completion of this work, extension to NCSX should be straightforward, but the computational work will be extensive.

We plan to use the results of the turbulence modeling to determine the turbulence cross-field diffusion coefficients for use in the transport code and to learn how these scale with parameters and changes to the equilibrium. In the long term (several years), we envisage a more direct coupling between the turbulence and 3D transport simulations. In addition to giving a fundamental characterization of the scrape-off layer plasma, the turbulence calculations should give an understanding of possible core transport barriers in the stellarator edge; this is of major importance to any confinement device

11.9.3 Implications of Short vs. Long SOL Connection Lengths on Core Confinement

11.9.3.1 Summary

The connection length, L_c, of field lines in the SOL outside the last closed magnetic surface (LCMS) of NCSX is an important parameter that will determine the temperature profile of the SOL plasma. Design choices under consideration now could have a dramatic effect on the magnitude of L_c. If L_c is too short, the temperature profile along the field lines could be very flat with moderate to low temperature at both the target and separatrix. This could result in poor core confinement due to low edge temperature and possibly thermal instabilities at the edge due to carbon cooling. Long connection length allows a hot separatrix temperature, significant temperature drop along field lines to reasonably low target temperature, and establishment of a high recycling regime with low impurity source at the targets. Preliminary field line tracing by Grossman [13] indicates that one key to insuring long SOL field line length is to allow sufficient gap (at least 10 cm) between the LCMS and the material boundary at the tips of the bean-shaped cross sections.

11.9.3.2 Introduction

The plasma temperature at the target surface will determine the recycling regime and impurity source rate from sputtering. The temperature upstream at the LCMS is the boundary condition for the core temperature profile. Tokamak experience has shown that this separatrix temperature sets the height of the pedestal at the edge of the core plasma. Since the temperature profiles are stiff inside the tokamak core plasma, this means that the core energy content and confinement can be very sensitive to the separatrix temperature. This may also be the case in a compact, nearly axisymmetric stellarator like NCSX.

Initial field line tracing calculations with a material boundary at 4cm conformal displacement from the LCMS showed that L_c might be as short as one field period [13]. More recent computations with Li383 version 1017a2 equilibrium fields and a conformal boundary 10 cm from the LCMS indicate that L_c may be much longer [13].

The purpose of this section is to present the implications of either short or long connection length on SOL temperature (separatrix and target) and thereby raise awareness of the possible effect these two regimes could have on core confinement, impurity source and neutral hydrogen source.

- 11.9.3.3 Basic Equations of 1D SOL Parallel Transport

Following Stangeby [14] we look for solutions to the temperature profile in a SOL flux tube assuming parallel heat conduction dominates over convection. This has been shown to be a good assumption for the dominant electron channel in tokamaks except under detachment conditions in which the temperature is very low (~1 eV) and the density is high (~1×10^{20} m^{-3}).

For non-detached SOL in NCSX, the Spitzer heat conductivity equation in the direction $s_{||}$ along the magnetic field from the LCMS to the wall is

$$d[q_{||}] / ds_{||} = d[-K_0 T^{5/2} (dT / ds_{||})] / ds_{||} = P\, G(s_{||}) / A_{||} \qquad (11.9\text{-}1)$$

where for a pure hydrogen plasma $K_{0e} \sim 2000$, $K_{0i} \sim 60$, T in [eV], and $s_{||}$ in [m]. The power from the core into the SOL is denoted as P, $G(s_{||})$ is a shape function whose $s_{||}$ integral gives unity, and $A_{||}$ is the area of the flux tube perpendicular to **B**. Thus, $q_{||} = P/A_{||}$ for $A_{||}$ constant. For $T_e \sim T_i$, electron conduction dominates the parallel energy transport in the SOL, and at sufficient collisionality, the ion power is coupled through the electron channel via energy exchange collisions.

Assuming that the power enters the flux tube at only the upstream end (outer midplane where $s_{||} = 0$) or is uniformly distributed along the flux tube only introduces a simple parameter α into the solution; $\alpha = 1$ for a localized source of $G(s_{||}) = \delta(s_{||})$ and $\alpha = 1/2$ for $G = 1/L_c$ [13]. Integrating the heat conduction equation thus gives the temperature at any point along the flux tube, $T_e(s_{||})$, in terms of either the upstream temperature, T_{eu}:

$$T_e(s_{||}) = [\, T_{eu}^{7/2} - (7\alpha/2)\, (P/A_{||})\, (s_{||}/K_{0e})\,]^{2/7}. \qquad (11.9\text{-}2)$$

Or, in terms of the target temperature, T_{et}

$$T_e(s_{||}) = [\, T_{et}^{7/2} + (7\alpha/2)\, (P/A_{||})\, (\{L_c\text{-}s_{||}\}/K_{0e})\,]^{2/7}. \qquad (11.9\text{-}3)$$

For upstream temperature at least twice the target , the upstream temperature can be well approximated by

$$T_{eu} = [\, (7\alpha/2)\, (P/A_{||})\, (L_c/K_{0e})\,]^{2/7}. \qquad (11.9\text{-}4)$$

In the evaluations given below, we set $\alpha = 1/2$, corresponding to uniform power deposition along the flux tube, but the solution does not depend very sensitively on it.

If one assumes that the sheath is the only heat sink in the SOL flux tube, *i.e.* , there are no substantial radiation losses along the tube, and that parallel pressure balance holds owing to negligible cross-field transport of parallel momentum, then stagnant flow upstream and Mach=1 flow at the target allows one to express T_{et} in terms of power and upstream density, n_u, as

$$T_{et} = (m_i/2e)\, (2q_{||}/\gamma e n_u)^2\, (7\alpha q_{||} L_c/2K_{0e})^{-4/7} \propto q_{||}^{10/7}\, n_u^{-2}\, L_c^{-4/7}. \qquad (11.9\text{-}5)$$

Here, $q_{||} = P/A_{||}$, and γ is the sum of energy sheath transmission factors for ions and electrons.

While Eq. (11.9-5) is useful for understanding the scaling trends when $T_{eu} > T_{et}$, the results presented in the examples below use the more general Eq. (11.9-3) rather than Eq. (11.9-

4), so the specialized relations in (11.9-4) and (11.9-5) do not hold if $T_{eu} \approx T_{et}$. The generalized form of Eq. (11.9-5) for the target temperature is

$$T_{et} = (m_i/2e)\,(2q_{||}/\gamma e n_u T_{eu})^2 \qquad (11.9\text{-}6)$$

which is solved numerically for T_{et} using Eq. (11.9-3) evaluated at $s_{||} = 0$.

- **11.9.3.4 NCSX Examples**

For estimating the NCSX target and upstream temperatures we use K_{0e}=2000, γ = 7 and the following assumptions:

Maximum input power to the core = 12 MW
Core radiation fraction = 0.2
Power entering the SOL = 12 x 0.8 = 9.6 MW
SOL power scale width, $\lambda_{q\perp}$ = 2 cm
Effective Major and minor radii, R_{eff} = 1.4 m, a_{eff} = 0.28 m
$A_{||}(SOL) = 4\pi R\, \lambda_{q\perp}(B_\theta/B)$ (extra factor of 2 accounts for two ends)
$(B_\theta/B) \sim 0.13$ for $iota_{edge} \sim 0.65$

This leaves L_c, n_u, the ion species and the injected power as parameters. Note also that the target temperature in Eq. (11.9-5) scales as the SOL power scale width, $\lambda_{q\perp}$ to the -10/7 power, through $q_{||}^{10/7}$, so this is an important unknown parameter for NCSX. In the examples below we have used $\lambda_{q\perp}$ = 2 cm as inferred from measurements on W7-AS [9].

- Target and Separatrix Temperatures vs. L_c and P_{inj}:

Initial results from Grossman indicated that if the material boundary was 4 cm from the LCMS up near the tips of the bean cross section then the field lines within 1 cm of the LCMS at the midplane would strike the wall within one field period. In this case, L_c ~ 5m. More recent results with 10 cm conformal gap between the LCMS and the wall including at the bean tips showed that the field lines very near the LCMS might remain inside the boundary for over 100 toroidal transits, L_c ~ 1000 m. The field line length was reduced sharply for field lines starting at the midplane farther out radially. The target and separatrix temperatures as functions of injected power are plotted for L_c = 5 m and L_c = 100 m in Figures 11-15 and 11-16 respectively.

To achieve low target sputtering and a high recycling regime in tokamaks one usually tries to minimize the plasma temperature near the targets while keeping the plasma from detaching. This means T_{et} in the range of 10-20 eV. From Figure 11-15 this low target temperature is reached in a deuterium plasma for the short L_c case only at very low input power, P_{inj} ~ 1 - 2 MW. Figure 11-16 then shows that the upstream temperature will be about 30 - 40 eV. Higher input power raises the upstream temperature but the target temperature also increases. For the full 12 MW case in NCSX the separatrix and target temperatures are almost equal. At low separatrix density (3e19 m^{-3}) the target temperature is much too high for considerations of plate sputtering and at higher separatrix density (6e19 m^{-3}) the separatrix temperature is too low for good core confinement (see sections below).

Long connection length , L_c ~ 100 m, allows substantial temperature drop in the SOL flux tube as shown in Figures 11-16 and 11-17. At the high input power of 10 MW, deuterium solutions with T_{et} ~ 20 eV and T_{sep} ~ 120 eV are possible at separatrix density of 6e19 m-3 (Figure 11-16). Even at lower density, 3e19 m-3, solutions with T_{et} ~30 eV and T_{sep} > 100 eV are possible with 5 MW of input power (Figure 11-17).

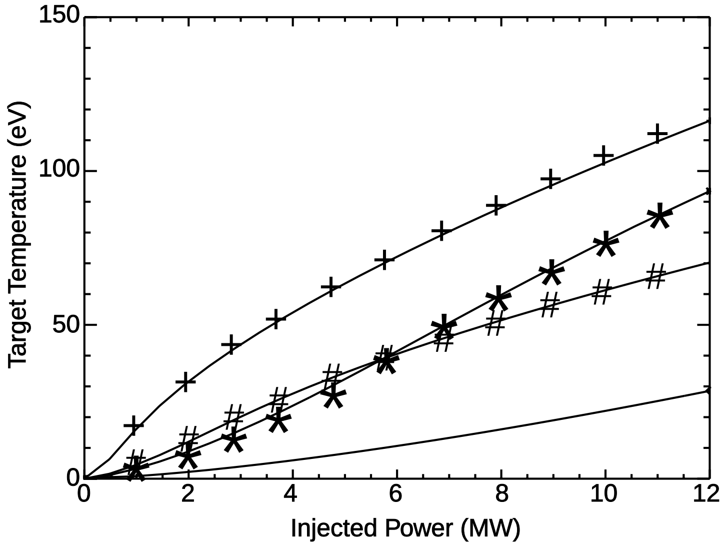

Figure 11-16. Target temperature vs injected power for four deuterium plasma cases: (a) (+) symbols use L_c = 5 m, n_u = 3.e19, (b) (#) symbols use L_c = 5 m, n_u = 6.e19, (c) (*) symbols use L_c = 100 m, n_u = 3.e19 and (d) plain line uses L_c =100m, n_u =6 e19

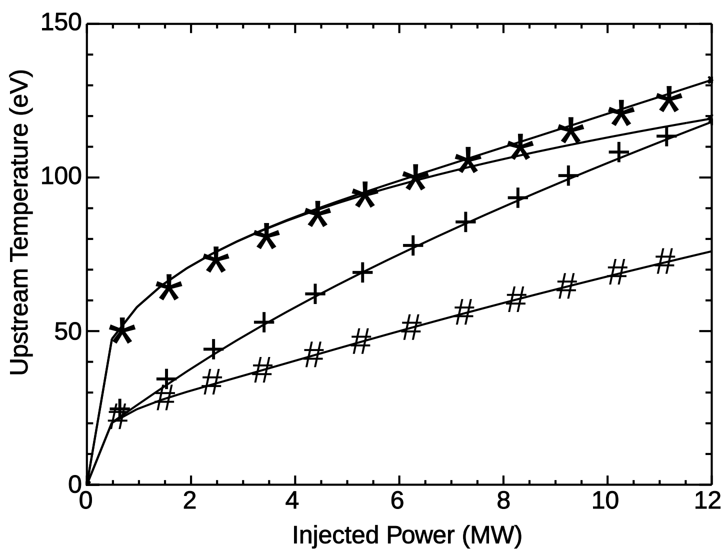

Figure 11-17. Upstream temperature vs injected power for four deuterium plasma cases: (a) (+) symbols use L_c = 5 m, n_u = 3.e19, (b) (#) symbols use L_c = 5 m, n_u = 6.e19, (c) (*) symbols use L_c = 100 m, n_u = 3.e19 and (d) plain line uses L_c =100m, n_u =6 e19

11.9.3.6 Implications of Short vs. Long Connection Length

Separatrix T_e in the 40 eV range with carbon impurity can lead to thermal instability. The carbon cooling curve increases sharply with decreasing T_e from 40 eV down to about 7 eV (see Figure11-18).

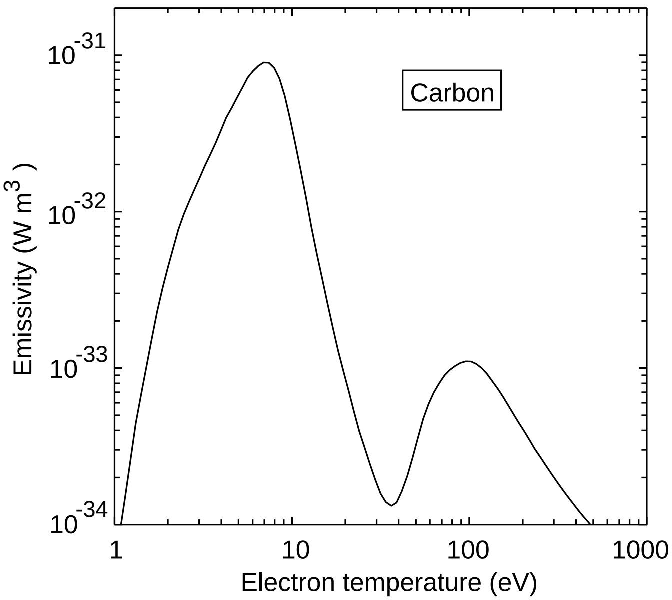

Figure 11-18. Carbon emissivity (ε) vs. electron temperature showing emissivity increase with decreasing temperature in the range $7 < T_e < 40$ eV. Radiated power is $\varepsilon n_e n_c$

If this instability occurs around the LCMS the expected result is a high density, low temperature mantle which is strongly radiating at the edge of the core plasma. If the temperature profile of the core plasma is stiff, as it is in tokamaks, then low separatrix temperature will produce low core confinement.

In diverted tokamaks the effect of this carbon thermal instability is observed in experiments with heavy gas injection to high density [15]. As the density in the SOL increases the temperature drops and the carbon radiation in the SOL increases somewhat with no appreciable decrease in core confinement. However, when the temperature at the separatrix is reduced to about 40 eV, the carbon radiation is observed to move rapidly inside the separatrix and the core confinement is reduced by a factor of two.

Long connection length allows a substantial temperature difference to be established between upstream separatrix temperature and target temperature. The separatrix temperature can be consistent with good core confinement while at the same time the target temperature can be consistent with low physical sputtering of carbon targets. The physical sputtering curve for deuterium on carbon is given in Ref. 2, p. 119. For the long L_c solution at P_{inj} = 6 MW and n_u = 5e19, T_{et} ~ 10 eV and the carbon sputtering is a factor of three less than would be the case with short L_c and T_{et} ~ 40-60 eV.

Another advantage of long connection length is that most of the temperature drop occurs near the target (see Ref. 14 p.190 cf. for discussion) so the core plasma is screened from incoming neutrals by ionization in the hot plasma not far from the target. This leads to high recycling conditions near the target at moderate core density and can even lead to detachment and substantial reduction of the heat flux on the target at higher core density.

Strong temperature gradients near the target can lead to transport of impurities away from the targets by the ∇T_i force. However the high recycling solution typically also generates sufficient flow toward the targets that the drag force on impurities balances the ∇T_i force and impurities are reasonably well entrained near the target surface. Shaping of structures in the vicinity of the targets can help to entrain the impurities.

11.9.3.7 Ideas for Achieving Long L_c

The basic tool for calculating L_c is the field line tracing code suite (VMEC, MFBE, Gourdon code) used by Art Grossman. If these calculations continue to show that field lines tend to wander radially as they transit toroidally and poloidally then a purely conformal material boundary is not the optimum for achieving long connection length. One approach would be to try to extend the material boundary outward in specified toroidal and poloidal locations where the field lines move radially outward. Present calculations indicate that most of the stretching of the material boundary should be done in the bean tips region. Depending on the engineering design this might necessitate re-optimization of the coil set somewhat to accommodate a non-conformal first wall.

11.9.3.8 Conclusions:

A two-point model of 1D energy transport in the SOL of a magnetically confined plasma has shown that for NCSX parameters, a connection length of order 5 m is insufficient to produce the desired high separatrix temperature and low target temperature needed for good core confinement and low target impurity sputtering. A connection length of order 100m would be sufficient to produce large temperature drop along SOL flux tubes from separatrix to target. Long connection length may be achievable in the NCSX design by selected perturbations of the material wall boundary away from a conformal shape about the LCMS. In particular, field line tracing calculations to date indicate that extension of the boundary farther away for the LCMS in the banana tip regions could produce the desired connection length.

11.10 Vacuum Requirements and Wall Conditioning

11.10.1 Torus Vacuum Pumping Requirements

NCSX requires sufficient wall conditioning and pumping speed to achieve base pressures of at least 2-3 x 10^{-8} torr and to recover from discharges sufficiently to allow about a 5 minute discharge repetition rate. The legacy Turbomolecular Pumping system (TMP) from PBX-M consisting of four Leybold Heraeus, 1500 l/s pumps is available for NCSX. This pumping system, together with Ti gettering, was used on the unbakeable PDX, PBX, and PBX-M vessel to achieve base pressures of ~2-3 x10^{-8} torr, and was able to recover vessel pressures from plasma discharges sufficiently rapidly to allow 3 to 5 minute discharge repetition rates, in spite of extensive internal hardware. The present plan is to mount a TMP on each of the high conductance NBI Transition Ducts, thus the application of this TMP system to NCSX will involve pump duct conductances comparable to or possibly greater than those encountered on PBX-M. In addition, if 100 Kl/s LHe Cryopumping capability is restored to the front end of each Neutral Beamline as planned, NCSX will have considerable extra pumping speed. After the initial pumping of atmospheric components is completed, the remaining partial pressure contributions will come mainly from H_2O, CO, CO_2 and hydrocarbons. The planned NCSX Bakeout, Glow Discharge Cleaning (GDC), and Boronization capability will greatly accelerate the cleanup of these impurities.

11.10.2 Vessel Bakeout

There is considerable agreement in the international fusion community regarding the desirability of baking fusion devices with graphite plasma facing components to about 350°C as the first step toward achieving optimum wall conditions. The physics basis for baking graphite to 350°C is discussed extensively in the ITER Report prepared from the draft titled "Considerations for Bakeout and Conditioning Specifications for In-vessel Components in ITER" prepared by D. Post, ITER JCT, Jan. 20, 1995 Revised May 2, 1995. This report lists the conditioning experience of major tokamaks. The final report was reviewed by the contributors from the major tokamaks. Their interesting verbatim comments/suggestions are given in the report and form a compendium of experience that will be adopted for NCSX wall conditioning.

11.10.3 Glow Discharge Cleaning

NSTX presently uses two fixed GDC anodes; other experiments (e.g., DIII-D, JT-60U) use 2 or more GDC anodes. Given uncertainties about GDC initiation and performance in the NCSX geometry, the Helium Glow Discharge Cleaning (HeGDC) design plans for 3 ports with 4.5 inch O.D. flanges equally spaced toroidally for fixed wall anodes. These anodes will be used for both GDC and gaseous boronization. The poloidal angle of these ports is not critical although symmetrical placement will facilitate monitoring and performance analysis. In addition to the anode ports, it is desirable to have 3 ports with 4.5 inch OD flanges located near to the anode ports (preferably within line-of-sight) for Pre-ionization Filaments to facilitate GDC breakdown at the actual operating pressure and voltage. On NSTX, Pre-ionization Filaments are used routinely to initiate HeGDC between discharges, and in conjunction with ECE, to initiate plasma discharges [16,17].

11.10.4 Boronization

The NCSX Boronization method should be sufficiently convenient and economical to be an operational tool that can be applied quickly and as often as required. It should also have minimal environmental, health, and safety impact when used in the NCSX Test Cell. The NCSX Boronization method could be able to use hydrogenated or deuterated boron compounds depending on subsequent plasma operations.

A suitable and effective candidate compound for NCSX boronization is Trimethylboron [$B(CH_3)_3$ or $B(CD_3)_3$] which is presently in use at PPPL on NSTX about every 3 weeks. Trimethylboron (TMB) is about a 1000 times less toxic than diborane and nonexplosive. TMB Boronization was first tested on TEXTOR where it was found to be comparable in effectiveness to Diborane and considerably safer [18]. In addition to TEXTOR, TMB Boronization has been applied extensively on COMPASS [19], Phaedrus [20], MAST [21], and NSTX [22].

The TMB Boronization procedure consists of using the regular NCSX Gas Injection and Torus Vacuum Pumping Systems. Using one Turbomolecular pump of the Torus Vacuum Pumping System, a standard HeGDC is applied for 10 min at about 4mTorr, ~450V, ~1A per each of 3 anodes. A mixture of 90% He and 10% TMB [$B(CH_3)_3$ or $B(CD_3)_3$] containing 10 grams of TMB is injected into the HeGDC until consumed (~160 minutes). This application is followed by a 2 hr HeGDC to remove the co-deposited hydrogen or deuterium from the ~ 100 nm, B/C film. In addition to the TEXTOR results which found TMB comparable to Diborane [18], work on Phaedrus with TMB [$B(CH_3)_3$], O-Carborane [$B_{10}C_2H_{12}$], and Decaborane [$B_{10}H_{14}$] found that core oxygen concentrations were lowest for TMB (B/C = 0.33). O-carborane (B/C = 5) had twice the oxygen as TMB and Decaborane (C = 0) had nearly 3 times [20].

11.10.5 Lithiumization

Lithium wall conditioning is considered an attractive future upgrade of the NCSX wall conditioning system. Lithium pellet injection has been found to significantly improve TFTR plasma performance [23,24]. This involved using a Lithium Pellet Injector with a capacity of 270 pellets to inject up to four 3 mg lithium pellets per discharge at velocities of about 500 m/sec to near-core regions. A Lithium Pellet Injector will be a useful tool for initial NCSX lithium wall conditioning studies. However, this approach has both plasma and hardware limitations. Slow injection velocities are preferred because high injection velocities cause near-core deposition and perturbation. In addition, a small pellet size and a small number of pellets per injection may be required to prevent excessive perturbation of plasma conditions. Consequently, using lithium deposition via conventional pellet injection for plasma surface conditioning can require many discharges and is inefficient; however, other pellet injection methods might avoid these difficulties [25]. At this time, the optimum lithium characteristics have not been found, and little is known about the detailed plasma surface physics and chemistry of lithium deposited on graphite limiter surfaces [26]. The ability to increase the quantity of lithium deposition while minimizing perturbations to the plasma would provide NCSX with interesting experimental and operational options. Previous experience with Low Velocity Pellet Injection into discharges [25], Lithium Effusion Oven for deposition between discharges [27] and LASER induced ablation during discharges [28] may be of interest to the NCSX Experimental Program. The planned port access will accommodate these options.

References

[1] J. Nuehrenberg et al., IAEA Conference , Wuerzburg (1992) 449.

[2] Y. Feng et al., J. Nucl. Mater. 266-269 (1999) 812.

[3] R.W.T. Koenig, et al., 14th PSI Conference, Rosenheim, May 2000.

[4] E. Strumberger et al., Nucl Fusion, **37** (1997) 19.

[5] V.D. Shafranov, L.E. Zakharov, Nucl. Fusion **12** (1972) 599.

[6] E. Strumberger, "SOL Modeling for the W7-X Ergodic Divertor Concept," Proc. 20th EPS Conf. On Controlled Fusion and Plasma Physics, Lisboa, V.**17C**, Part II (1993) 791.

[7] J. Kisslinger *et al.*, "Island Divertor for the Stellarator Wendelstein 7-X, " Proc. 21st EPS Conf. On Controlled Fusion and Plasma Physics, Montpeiller, V.**18B**, Part II (1994) 368.

[8] D.P. Stotler and C.F. F. Karney, Contrib. Plasma Phys. **34** (1994) 392.

[9] K. McCormick et al., Proc. 12th Int. Stellarator Conference, Madison 1999.

[10] R. Schneider, M. Borchardt, J. Riemann, A. Mutzke, and S. Weber, Contrib. Plasma Phys., Vol. **40** (2000) 340.

[11] Y. Feng, F. Sardei, and J. Kisslinger, J. Nucl. Mater., Vol. **266-269** (1999) 812.

[12] X. Xu, R.H. Cohen, T.D. Rognlien, and J.R. Myra, Phys. Plasmas, Vol. **7** (2000) 1951.

[13] A. Grossman, private communication, NCSX Project Meeting presentation, Jan. 2001

[14] P. C. Stangeby, "The plasma Boundary of Magnetic Fusion Devices", IoP Publishing, 2000, pp 187 cf. and pp 221 cf.

[15] T. W. Petrie et al., J. Nucl. Mater. 241-243 (1997) 639.

[16] "NSTX Filament Preionization And Glow Discharge Cleaning Systems", H. W. Kugel, et al., PPPL Report-3381, November 1999, Proc. of the 18th Symposium On Fusion Engineering, Albuquerque, NM, October 25-29, 1999 (IEEE,1999) 296.

[17] "Overview of Impurity Control and Wall Conditioning in NSTX", H. W. Kugel, et al., Proc. of the 14th Int. Conf. on Plasma Surface Interactions In Controlled Fusion Devices, May 22-26, 2000. (To be published in J. Nucl. Mtrl.)

[18] "Borontrimethyl $B(CH_3)_3$ - A Less Hazardous Substance for Boronization", J. Winter, et. al. J. Nucl. Mater. 176 &177 (1990) 486.

[19] "Boronization of Compass", H. G. Esser et al, J. Nucl. Mater., **186** (1992) 217.

[20] "Boronization Effects on Phaedrus-T Rf Operation", M. Doczy, et al., Bull. Am. Phys. Soc. **39** (7) (1994) 1631.

[21] Private Communication, S. Fielding, Culham Science Centre, May 2000.

[22] "Intial Boronization of NSTX and the Effect On Plasma Performance", H. W. Kugel, et al., Bull. Am. Phys. Soc. **45** (7) (2000) 251.

[23] D. K. Mansfield, *et al*., "Enhancement of Tokamak Fusion Test Reactor Performance by Lithium Conditioning", *Phys. Plasmas* **3**, 1892 (1996).

[24] J. A. Snipes, *et al*., "Wall Conditioning With Impurity Pellet Injection on TFTR", *J. Nucl. Mater*., 196-198 (1992) 686.

[25] H. W. Kugel, et al., "Low Velocity Boron Micro-Pellet Injector For Edge And Core Impurity Transport Measurements", Unviersity, PPPL Report No. PPPL-3306, July 1998, Proceedings of 12th Topical Conference on High-Temperature Plasma Diagnostics, Princeton, NJ, June 7-11, 1998, Rev. Sci. Instrumen. **70** (1) (1999) 493.

[26] J. Hogan, C. Bush, and C.H. Skinner, "Lithium Effects In Plasmas, Summary Of The Workshop, PPPL, 17-18 October 1996", *Nuc. Fus*., in press.

[27] H. W. Kugel, et al., "Development of Lithium Deposition Techniques for TFTR", PPPL-3270, October 1997, Proceedings of 17th IEEE/NPSS Symposium on Fusion Engineering, 6-10 October, 1997, San Diego CA.

[28] D. K. Mansfield, et al., "DOLLOP: Improved Plasma Performance Using a New Concept for Mitigating the Plasma-Wall Interaction in Fusion Devices", Bull. Am. Phys. Soc. **42**(10) (1997) 1972, and D. K. Mansfield et al., "Observations Concerning the Injection of a Lithium Aersol into the Edge of TFTR Discharges", submitted to Nucl. Fus.

Chapter 12 -- Diagnostics

A capable array of diagnostics is planned to make the plasma physics measurements necessary to accomplish program goals. The facility will be equipped with an initial set of diagnostics to support shakedown of major machine systems and the first few phases of physics operation: first-plasma, electron-beam mapping of flux surfaces, Ohmic plasma experiments, and initial heating experiments. Experimental results from the initial operating phases will help optimize the selection of upgrade systems and their design characteristics. An implementation plan for upgrade diagnostics has been developed based on experience with other projects for use as a reference for design purposes. It is used in the ongoing design process to set port access requirements and ensure that a feasible solution exists for all required measurements.

During conceptual design, the project emphasis will be on the design of the stellarator core device, including the coils, vacuum vessel, and plasma-facing components. A systematic analysis of the access constraints and tradeoffs for both baseline and upgrade diagnostics will be an important element of the conceptual design activity. Diagnostic considerations have played a prominent role in the preconceptual design development of the NCSX. As a result, a large number of ports (about 87) is provided and many specific diagnostic needs have been taken into account, however the task of providing adequate diagnostic access has only begun. At this stage, the available access is marginal, and providing good diagnostic access will be an important design goal for the conceptual design phase.

As a matter of definition, and based on historical precedent, diagnostic systems as a category include the set of sensors and instrumentation used for general plasma research. It does not include measurement instrumentation used with specific NCSX auxiliary systems. For example, Residual Gas Analyzers and ion gauges are included with the machine vacuum system. Rogowski's to measure coil currents are part of the magnet and power supply systems, *etc*. The exception to this rule for this report is the e-beam and fluorescent mesh instrumentation that is needed for the early field mapping effort on NCSX. This instrumentation is included in the baseline set of diagnostics

12.1 Baseline Diagnostics

The baseline set of research diagnostics represents the minimum component needed to accomplish the initial mission, including first plasma, shakedown of all major machine systems, electron-beam flux surface mapping, Ohmic experiments, and initial heating experiments. Included in this set is the instrumentation needed for e-beam mapping of the magnetic field. The diagnostic systems planned for the first plasma campaign and for field mapping are listed in Table 12-1, along with a summary of machine, infrastructure, and data acquisition interfaces required.

In the current plan, the first run campaign would start with a "first plasma" demonstrating that the machine can create and confine a plasma with all major systems operational. Following this first plasma demonstration, there will be a short campaign to characterize the important global quantities of the plasma. These include the plasma current, the basic equilibrium which yields the stored energy, the radiated power fraction, the line average density, crude

Table 12-1 Baseline Diagnostics and Interfaces

Diagnostic System	comments	rack	window	shutter	valve	vac	digit. channel	Speed S/M/F	frame grabber
Magnetics	100 channels	2					100	M/F	
Visible Cameras	3 cameras	1	3	3					3
Interferometer	single chord	1	1	1			4	M	
UV Spectroscopy	single sightline	1			1	1			1
Visible Spectroscopy	several fibers	1	1	1					1
Visible Filterscopes	3 views,10 fibers	1	3	3			10	M	
SXR Arrays	3 arrays	1			1		60	M/F	
e-Beam Mapping	e-beam probe, screen , CCD	1	2	2	1				2
	total	**9**	**10**	**10**	**3**	**1**	**170**		**5**

measurements of the electron temperature and Z_{eff}, and initial indications of MHD. Following this initial characterization, there will be a campaign to map the magnetic field with an electron beam.

The magnetic sensors include a diamagnetic loop, flux loops, Rogowski coils and B-coils which will provide signals to measure the magnetic flux change in the many geometries necessary to determine the internal magnetic field geometry using an equilibrium reconstruction code. Because of the strong shaping in NCSX plasmas, such a magnetic reconstruction can provide important information on profiles of plasma pressure and toroidal current.

A typical magnetic channel consists of a high temperature sensor coil mounted between the carbon first wall and the vacuum vessel with high temperature leads to a vacuum feedthrough. The signal is transmitted via field cables to a junction box and then to an integrator, and finally to a digitizer to provide flux vs time. Many of the signals will also be inputs to the plasma control computer, which will use them to control the coil currents, which determine the plasma size and shape as well as the toroidal plasma current. A detailed analysis to ascertain the optimum number and placement of different sensors will be part of the conceptual design.

Visible camera will be used initially to view all three periods of the plasma with three identical ‘tangential views’. One camera will be moderately fast with a full frame rate of at least 250 Hz to permit viewing of the startup evolution. Because of plans for wall conditioning and bakeout, shutters will be needed to protect the viewing windows from coating. The light from the plasma will be coupled through a viewing lens into a coherent fiber bundle. The fast camera will be located outside of the cryostat and will view the images through an interference filter. The viewing lens and fiber bundle may need cooling to protect them during bakeout. A PC with frame grabber will be used to control the camera, and to capture and store the data. Initially, standard frame rate, compact CCD cameras will be used at the other two locations. Ultimately, there will be dedicated, fast cameras on each of the three views.

An interferometer will be used to monitor the line density on a single line of sight through the core of the plasma during the initial plasma run. A low cost, uncompensated 1 mm microwave system is under consideration, with solid state source and mixer, similar to systems currently in use at DIII-D and Pegasus. The vacuum interface will consist of a quartz window with shutter. Optics will guide the beam through the window to a machined PFC surface on the vessel wall opposite the input port. Refraction may limit usefulness of such a system at high densities due to resulting degradation in the return signal. This effect is dependent on plasma shape and density profile shape, and on the detailed geometry of the beam, the plasma, and the reflecting PFC surface. Once candidate port geometries are defined in the conceptual design phase, ray tracing can be used to quantify the refraction limitations.

A concern with the initial shakedown of any device is unfavorable plasma interaction with the wall leading to the influx of impurities. This can be caused by poor control of the plasma, or by failure of some internal mechanical component, possibly leading to material ablation due to plasma contact. Among the first signs of such problems is an increase in the radiated power. There is also a large increase in specific impurity emission lines, which can help to identify the sources of the problem.

Most of the line radiation is in the vacuum UV and a spectrometer/detector system capable of surveying this region of the spectrum will be purchased to provide these measurements along a single sightline. This system will need a vacuum connection to NCSX, with an interface valve and a dedicated vacuum system. A visible survey spectrometer capable of simultaneously monitoring several lines of sight will also be purchased. This instrument will view the plasma through a quartz or sapphire window for near UV measurements. In addition, it will simultaneously view several quartz fibers relaying light from sightlines at 3 other shuttered windows around NCSX.

At one of these locations there will be lens imaging the plasma onto an array of ~10 large (~1 mm) quartz fibers. The fibers from these windows will be routed to a remote optical table, where interference filter/detector assemblies will be used on selected views to monitor selected impurity lines and H (D) recycling lines with high time resolution. Ultimately, there will be fiber arrays at all three locations.

Internal MHD activity can greatly influence the behavior of the plasma particularly as plasma startup control is first being established. While magnetic coils can detect disturbances that propagate to the plasma edge, a soft x-ray imaging array that spatially resolves x-ray emissivity along a fan array of sightlines with good time response is very useful to detect internal MHD activity. Ultimately a large set of such fan arrays will be needed for tomographic reconstruction of the dynamics of magnetic islands at several toroidal positions. For the first plasma run, a single 16 channel array will be installed.

The proposed array will use a compact, integrated, 16 channel linear AXUV diode array behind a pinhole. Metal foils of known thickness can be used to provide crude energy resolution. The high sensitivity and speed of these detectors make them ideally suited for fast MHD measurements in the temperature and density range expected for NCSX. It is proposed that these sensors be cooled to enhance sensitivity. The proposed system is similar to those being developed by Johns Hopkins for use on NSTX. They will fit within a reentrant head with a diameter of < 4", smaller than many of the diagnostic access ports on NCSX.

In addition to detection of MHD activity, this array can provide other data useful for early NCSX operation. Because foils and detectors are absolutely calibrated, using reasonable assumptions about the impurity content of the plasma and comparisons with modeling results, one can put significant constraints on the electron temperature using this diagnostic. This will be valuable, since, at the low TF fields and high densities expected for early NCSX operation, plasmas are overdense for ECE measurements of T_e, and Thomson scattering measurements of T_e will not be available for the first plasma run. In addition, operation of this array without a filter can provide crude measurements of the total radiated power profile. The precision of such measurements is limited due to the non-uniform spectral response of these detectors at low energy.

The field mapping hardware consists of a probe drive with an electron gun at its tip, which can be accurately positioned along a line through the nominal cross-section. The axis of the gun also needs to be adjustable for alignment with the local field. During field mapping the electron beam from the gun will intercept a fluorescent screen as it repeatedly transits the device. The light from the strike points will be imaged by a high resolution CCD camera. Careful metrology will reference screen positions to machine coordinates. Strike points will be compared to expectations of a code, which will compute the beam trajectory for given coil currents. Magnetic island structures will be investigated near reference equilibrium conditions. The influence of trim coil currents will be assessed.

12.2 Schedule for Diagnostics Upgrades

As shakedown of the many NCSX auxiliary systems proceeds, and control of the plasma becomes more routine, attention will shift toward the research goals of NCSX, and progressively more diagnostic capability will be required. Figure 12-1 shows a proposed implementation schedule for diagnostic upgrades, and how this schedule is related to the proposed research campaigns. This schedule will be further refined during the conceptual review process.

Those diagnostics needed for the first plasma campaign are grouped at the top of the list, with development listed as TPC (included in the Total Project Cost for the NCSX Construction Project). The shading specifies estimated duration for the design and installation phase, the debugging phase, and the operating phase of each diagnostic system. It is assumed that there will be approximately 6 months of 'outage' time available each year, with in-vessel access, for the installation of diagnostics and other hardware. Many calibration and alignment tasks will also occur during these outages.

As this implementation plan indicates, there is a continuing effort throughout the project to improve diagnostic capability to support program needs. Some of the diagnostics needed for the second run campaign require approximately two years to develop, and so significant effort in these areas is needed at the same time that the baseline diagnostics are being developed and installed.

As a general strategy, diagnostic development will shift from basic monitoring of global quantities and impurities during the first plasma run to local measurements of n_e, T_e, T_i and v_ϕ in the core and edge. In this plan, these local measurements become available during the second half of the 'Plasma Heating and Transport' run. More detailed profile information becomes available in the third research run. Diagnostics for measuring MHD activity, fast ion behavior, and edge and divertor characteristics will see a steady improvement in capability. Turbulence measurements become available early at the plasma edge and then in the core toward the end of the plan proposed above.

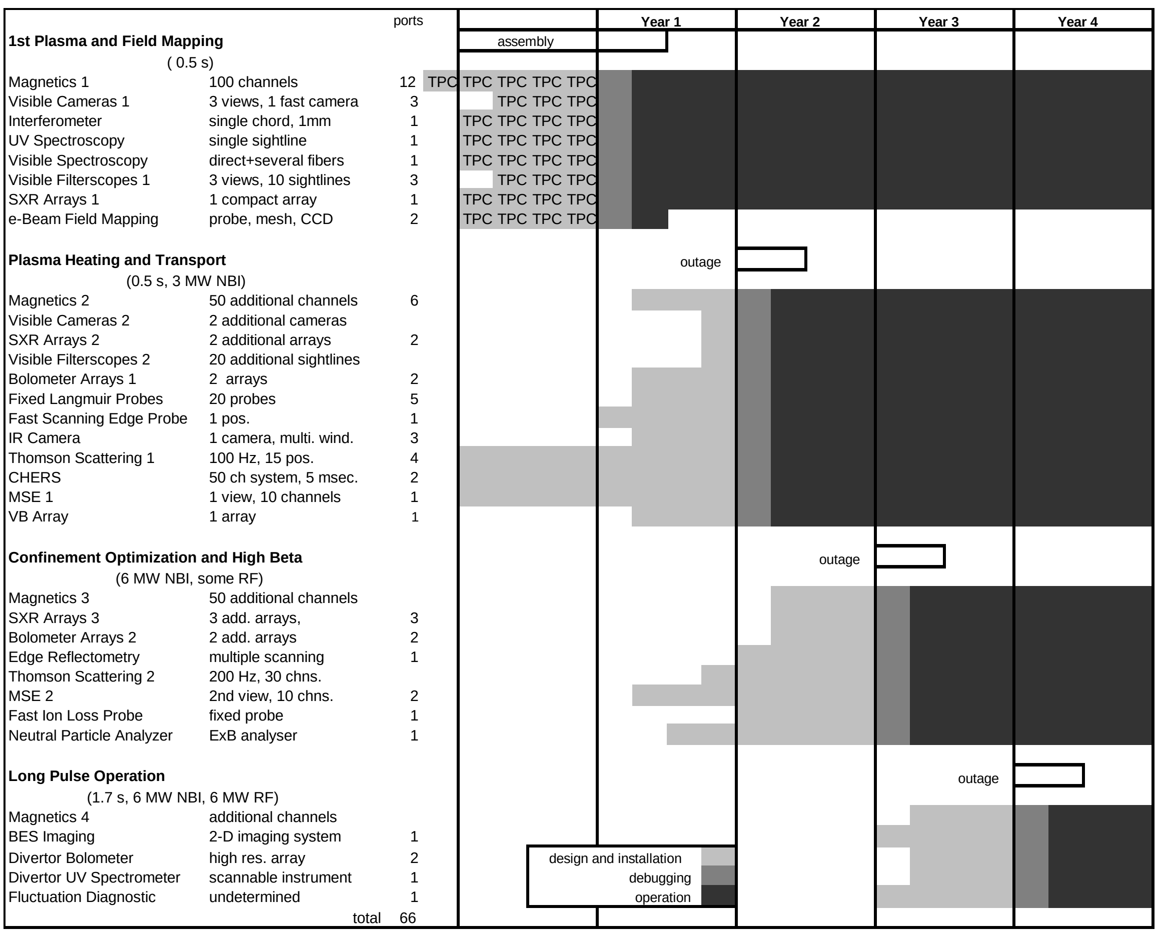

Figure 12-1 Diagnostic Implementation Plan

Since two neutral beam injectors will be operational in the "Plasma Heating and Transport Phase," it is proposed that beam based spectroscopy be used early on to obtain valuable profile information. A CHarge Exchange Recombination Spectrometer (CHERS) system is proposed to measure T_i and v_ϕ. profiles.

A Motional Stark Effect (MSE) Polarimeter is also proposed to obtain profiles of the internal magnetic field pitch angle. A second MSE system is included later in the plan to permit determination of both E_r and J(r). A diagnostic neutral beam may be needed for these measurements.

Another important profile diagnostic that will be essential for early transport experiments is a Multi-Pulse Thomson Scattering System (MPTS) which provides snap shots of the T_e and n_e profiles along a laser beam.. Similar to systems in use on many devices, the proposed system would utilize high repetition rate (100hz) Nd:YAG lasers and filter polychromator/APD detectors. The system would start with one laser and ~ 15 spatial positions, but it's design would accommodate additional lasers and spatial positions to be added as time and resources permit.

A staged approach is seen for several diagnostics in the plan outline in Figure 12-1. It is envisioned that additional or upgraded magnetics sensors will be added periodically through the life of the project, as experience is gained and as new physics or control needs arise. Multiple sets of SXR arrays for monitoring MHD activity, and bolometer arrays to measure radiated power are similarly staged in the plan.

12.3 Adequacy of NCSX Diagnostic Access

Given the plans outlined above for equipping NCSX with a comprehensive diagnostic set, the adequacy of access available for diagnostics is a legitimate concern. Such access must, in most cases, penetrate the PFC's, the vacuum vessel, the modular coil shells and their supporting plates, and the cryostat. The constraints imposed by these various boundaries severely limit the number and size of diagnostic access ports, and typically place the ports themselves at the end of rather long vacuum extensions. These long extensions pose challenges for diagnostics requiring wide angled views of the plasma.

A systematic analysis of the access constraints and tradeoffs for each diagnostic in Table 12-1, along with a discussion of how well the projected measurement accuracy matches the physics goals of NCSX, are both clearly needed in the conceptual design phase of NCSX. As an example of the geometrical constraints and their impact, consider tomography. In the present design, there are no unobstructed views in a poloidal plane common with any of the six symmetry planes. Tomographic techniques such as multi-camera bolometry and multi-camera soft x-ray arrays benefit from geometrical symmetry to reconstruct profiles. Lack of symmetry means that more cameras will be needed for equivalent spatial resolution in independent reconstructions.

As currently designed, there are 87 ports on NCSX listed in Table 3-6, including the ports used by neutral beams. There will be many other systems requiring port access, for example, feedthroughs for PFC cooling and thermocouples, for gas puffers, for wall conditioning instrumentation such as glow probes and filaments, for current and cooling leads for trim coils, as well as diagnostics. Included in Figure 12-1 is a listing of the number of ports anticipated for each diagnostic in the plan, with a total of 66. Thus, even without consideration of specific geometrical constraints for diagnostics and without any allowance for future diagnostic needs, not to mention the needs of other systems, the port availability is tight, considering the variety of measurements desired.

The only way to get a better feel for the adequacy of access is to begin looking at the needs of specific diagnostic systems. Initial studies have thus far been done for a radial Thomson scattering system, and for the beam-based CHERS systems.

The ideal geometry for the multipulse Thomson scattering system would place the laser beam at the horizontal midplane of the bullet symmetry plane. In this way, one can probe the magnetic axis for all configurations, and the flux surfaces are spread out along the beam, which optimizes the tradeoff between spatial resolution and sensitivity. Unfortunately, this geometry is impossible to achieve in the current design, because this symmetry plane is at the joint between vacuum vessel segments. However, it appears feasible that a modification to the planned port layout could provide small ports (~ 3" dia.) for the laser input and output at the midplane, as shown in Figure 12-2. In this scheme the beam would enter close to the joint on the outside, and exit on the inside on the other side of the joint. Viewing could either be from the large midplane port next to the beam, or from the top on a somewhat smaller port. For efficient design, the viewing port would need to be angled towards the magnetic axis at the symmetry plane, as shown in Figure 12-3.

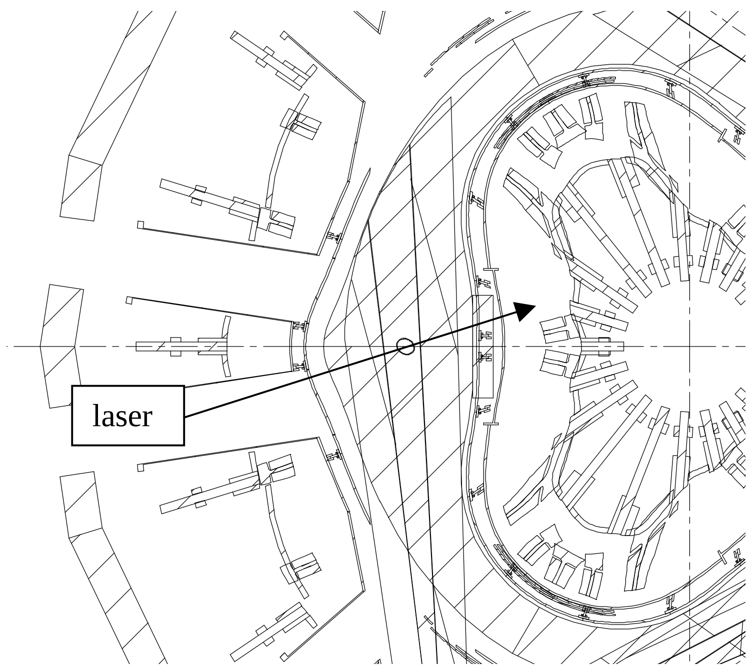

Figure 12-2 Possible path for the Thomson scattering laser

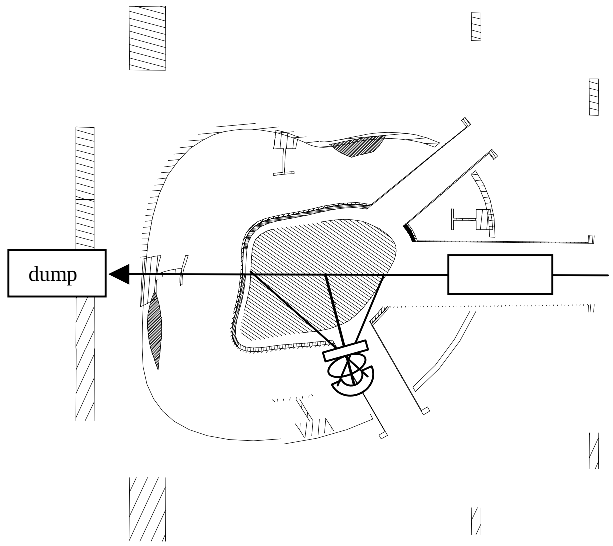

Figure 12-3 Possible viewing geometry for Thomson scattering

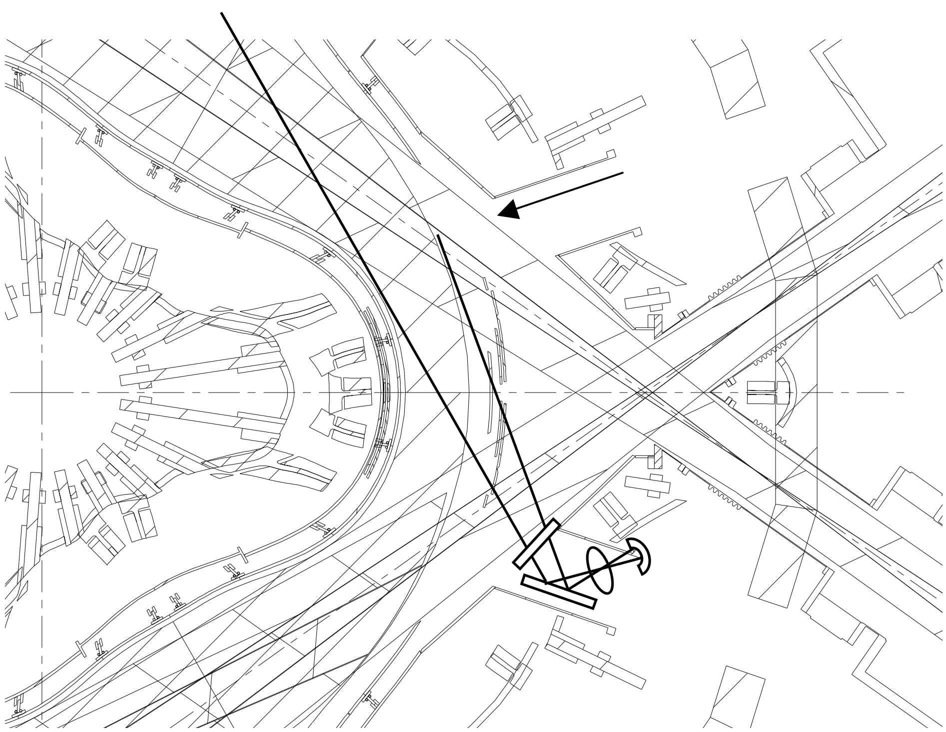

Figure 12-4 Possible viewing geometry for CHERS

Beam based spectroscopy techniques, such as CHarge Exchange Recombination Spectroscopy (CHERS) have traditionally achieved optimum spatial resolution by having sightlines that intercept the beam at points where they are tangent to plasma flux surfaces. This is the case for the sightline in Figure 12-4 at the outer edge of the plasma, if one considers, for the moment, only injecting the bottom right neutral beam. For other sightlines in this geometry, the intersection with the beam spans a large range of flux surfaces. This means that to interpret data from such a view, a spatial inversion will be necessary to derive an ion temperature and toroidal velocity profile. This inversion will likely need input from the calculated equilibrium to account for changes in the flux geometry along the sightline, as well as a calculation of the beam deposition. While such inversions have been done in a tokamak geometry with reasonable precision, uncertainties introduced by the 3-D nature of the NCSX plasma have not been predicted. Note that if one had a diagnostic beam injecting along the arrow shown in the figure, this problem would be much less severe.

The optics shown schematically in Figure 12-4 may have to extend into the path of the beam injecting from the upper right, particularly if it needs to avoid interference with the trim coils or the PFCs in this area. Thus, the choice of beam placement is clearly linked to the spatial constraints of beam-based diagnostics.

As indicated by these initial access considerations for MPTS and CHERS, there are many details to be worked out for each diagnostic, which will strongly affect its ultimate measurement capabilities. The proposed port layout needs modifications to optimize access for these two systems. Such modifications appear feasible for these two cases, provided that sufficient flexibility is maintained in the design process for the various major machine systems to accommodate the modifications. Because it is clear that port allocation will be very tight, the most must be made of each port. The adequacy of the final port configuration will depend critically on the attention given to access needs for specific diagnostics during the NCSX design process.

12.4Diagnostic Integration Plan

Diagnostic development for NSTX faces significant technical challenges. As described above, the interface between the NCSX device and the associated diagnostics is complex. Adding to the complexity of the access issue is the 3-D nature of the plasma, and the need to probe different toroidal phases. Thermal excursions for diagnostic instrumentation within the cryostat during routine operation and during the plasma facing component (PFC) bakeout will also be an issue. The difficulty of manned access inside the NCSX vacuum vessel will complicate diagnostic installation and calibration. For these and other reasons, as NCSX proceeds from pre-conceptual through detailed design, integration of diagnostics with the other machine components will be an ongoing and critical activity, and it is an explicit component of the project plan.

The proposed research plan for NCSX motivates a relatively aggressive schedule for diagnostic development. As indicated in Figure 12-1, development for several profile diagnostics planned for the first research phase must begin well before the end of the construction project. The diagnostic integration task will give special emphasis to planning for this development.

Opportunities for reuse of diagnostic equipment on NCSX will be considered on a case-by-case basis, weighing reliability and maintainability. As in other machines, the bulk of the costs associated with diagnostics are expended in providing the machine-specific interfaces and infrastructure, and therefore savings associated with component reuse are often relatively insignificant. Current planning assumes no reuse of equipment.

12.5 Opportunities for Collaborations in Diagnostics Development

Diagnostic instrumentation and analysis are specialist's fields, often reflecting the state of the art in physics understanding and technical capability. In addition, the operation of the NCSX device is not directly dependent on the operation of many of the diagnostics. An individual researcher at another institution installing a diagnostic on NCSX needs to know relatively few interface details to mount his diagnostic, and to contribute data quickly to the research program. If a collaborator is not at the site and his diagnostic fails, and is producing no data, other experiments can typically be scheduled to make productive use of the facility until the problem is resolved. Because of these and other factors, diagnostic development and operation is an area with many opportunities for collaborations.

As is the case on other collaborative programs, contributions of particular important measurements on NCSX will open doors of opportunity to the collaborating researcher for notable contributions to the physics of the device. These will typically be driven, in turn, by a wide array of operational, measurement, and analysis tools made available by the entire NCSX research team.

Chapter 13 -- Project Plans and Management

13.1 Project Schedule

13.1.1 Current Status

The NCSX project efforts leading up to this review have produced the physics basis for the NCSX proof-of-principle experiment. The scientific mission has been identified and physics requirements consistent with that mission have been developed. Pre-conceptual engineering design efforts, which have complemented the physics efforts during this phase, have produced a reference pre-conceptual design illustrating the existence of a practical machine concept that satisfies physics requirements and can be used in predicting cost and schedule ranges. The design has not been fully analyzed nor has it been optimized; these tasks will be accomplished in the next phase, conceptual design. At this stage, a significant portion of the engineering effort is devoted to the study of alternative design solutions aimed at identifying ways to reduce the cost or risk, or to improve the schedule.

13.1.2 Completing the Design, R&D, and Construction

Following this review, the review findings and recommendations will be incorporated into the project's plans for developing the design and research program. The next step will be to update the reference NCSX design, incorporating improvements identified from completed and ongoing trade studies. That update, scheduled for September, 2001, will be the basis on which the conceptual design will be developed. A conceptual design review (CDR) is currently planned for April, 2002. It is expected that the CDR will formally establish the baseline design, cost, and schedule for NCSX, with changes thereafter being subject to more rigorous control. Approval to construct NCSX would depend on a successful outcome of the CDR.

R&D and physics activities will be important to support the design development. The R&D activities will range from small-scale tests to establish design criteria to large-scale prototypes to establish manufacturing approaches and costs. Manufacturability input from industry will continue to be a feature of the design process. Physics analyses (e.g., coil-set design and flexibility, operating scenarios, boundary physics) will continue in support of the design process. Although the project's activities will become more engineering-oriented, it is expected that a stellarator theory and experimental collaboration program will continue outside the project.

Detailed engineering design is proposed to begin in FY 2003 with fabrication activities starting in FY 2004. After completing machine assembly and pre-operational testing, first plasma will be achieved, marking the completion of the project. For planning purposes, a target of the end of FY 2006 has been established.

13.2 Project Cost

Cost has been a prime consideration in establishing the design parameters for NCSX. The machine size (1.4 m) and maximum toroidal field (approximately 2 T) were established to keep the project cost at the target value of $55M (in FY 1999 dollars) while meeting the mission objectives. This project has been categorized by DOE as a Major Item of Equipment (MIE) activity and the project cost defined accordingly.

The first step in developing the estimate was to determine and document the scope of work. A Work Breakdown Structure (WBS) was established to facilitate definition of the scope of work and tabulate cost. The criteria for determining the scope of work in the Project Cost were as follows:

- The device must be fully capable of supporting initial experimental objectives.
- The device must be fully capable of accommodating required upgrades.

The subsystem managers developed the cost estimate for their subsystems based on their scope of work. A series of internal reviews were held, first to assure a clear understanding of the scope of work, and second to assure the estimates were of a quality and accuracy consistent with this phase of the design process. Where appropriate the subsystems designers solicited input from industrial fabricators to improve the quality of the design and the estimate. Some ancillary systems benefited from recent experience with NSTX and its actual cost data. These factors provided a measure of confidence that the estimate is as complete and as free of duplication and unnecessary scope as possible within the limits of current understanding.

Guidelines were established for estimating contingency. Technical, schedule, and cost risk factors were considered for each WBS element. The technical risk factor was based on the current state and level of the design. The schedule risk factor was based on criticality to the overall schedule. The cost risk factor was based on the estimating methodology used. The overall contingency added up to ~27% of the total without contingency.

The cost estimate was based on a four-year period from the start of Preliminary Design (Title I) until first plasma. R&D activities prior to the start of Preliminary Design were also included in the cost estimate. A summary of the Project Cost by WBS element is provided in Table 13-1. The overall cost is $55.0M (FY99$) including contingency. When inflated to the expected years of expenditure this cost becomes approximately $65M.

Table 13-1. Cost summary by WBS element

WBS		Description	FY1999K$
1		**Fusion Core Systems**	**$18,032.9K**
	11	Plasma Facing Components	$1,492.6K
	12	Vacuum Vessel	$2,512.2K
	13	TF Coils	$1,388.1K
	14	PF Coils	$955.7K
	15	Cryostat	$529.5K
	16	Machine Support Structure	$1,234.1K
	17	Modular Coils	$8,947.6K
	18	Trim Coils	$973.0K
2		**Auxiliary Systems**	**$2,225.5K**
	21	Fueling Systems	$114.9K
	22	Vacuum Pumping Systems	$229.9K
	23	Wall Conditioning Systems	$142.2K
	24	RF Heating Systems	$0.0K
	25	Neutral Beam Heating	$1,738.5K
3		**Diagnostic Systems**	**$2,529.7K**
4		**Power Systems**	**$4,828.5K**
5		**Central I&C & Data Acquisition Systems**	**$3,346.4K**
6		**Site & Facilities**	**$3,764.8K**
	61	Facility Modifications & Test Cell Preparations	$1,766.7K
	62	Heating & Cooling Systems	$880.7K
	63	Cryogenic Systems	$1,067.3K
	64	Utility Systems	$50.1K
7		**Machine Assembly**	**$3,791.2K**
8		**Project Oversight & Support**	**$4,002.0K**
9		**Preparations for Operations**	**$443.0K**
		Subtotal Without Contingency	**$43,293.9K**
		Contingency (~27%)	**$11,706.1K**
		TOTAL	**$55,000.0K**

In conceptual design, a bottoms up schedule will be developed. The cost will be re-estimated consistent with that schedule and any design changes that occur during the course of conceptual design.

13.3 Management and Organization

13.3.1 Institutional Arrangements

The NCSX is jointly proposed by Princeton Plasma Physics Laboratory and Oak Ridge National Laboratory in partnership. These two national laboratories are collaborating in the design, construction, operation, possible enhancements, and physics research for the NCSX project. PPPL has the lead responsibility for project execution. A management organization for the Project (Figure 13-1) is established within the PPPL organization, reporting to the Department of Energy through the PPPL Director. ORNL provides major support, including leadership in key physics and engineering areas.

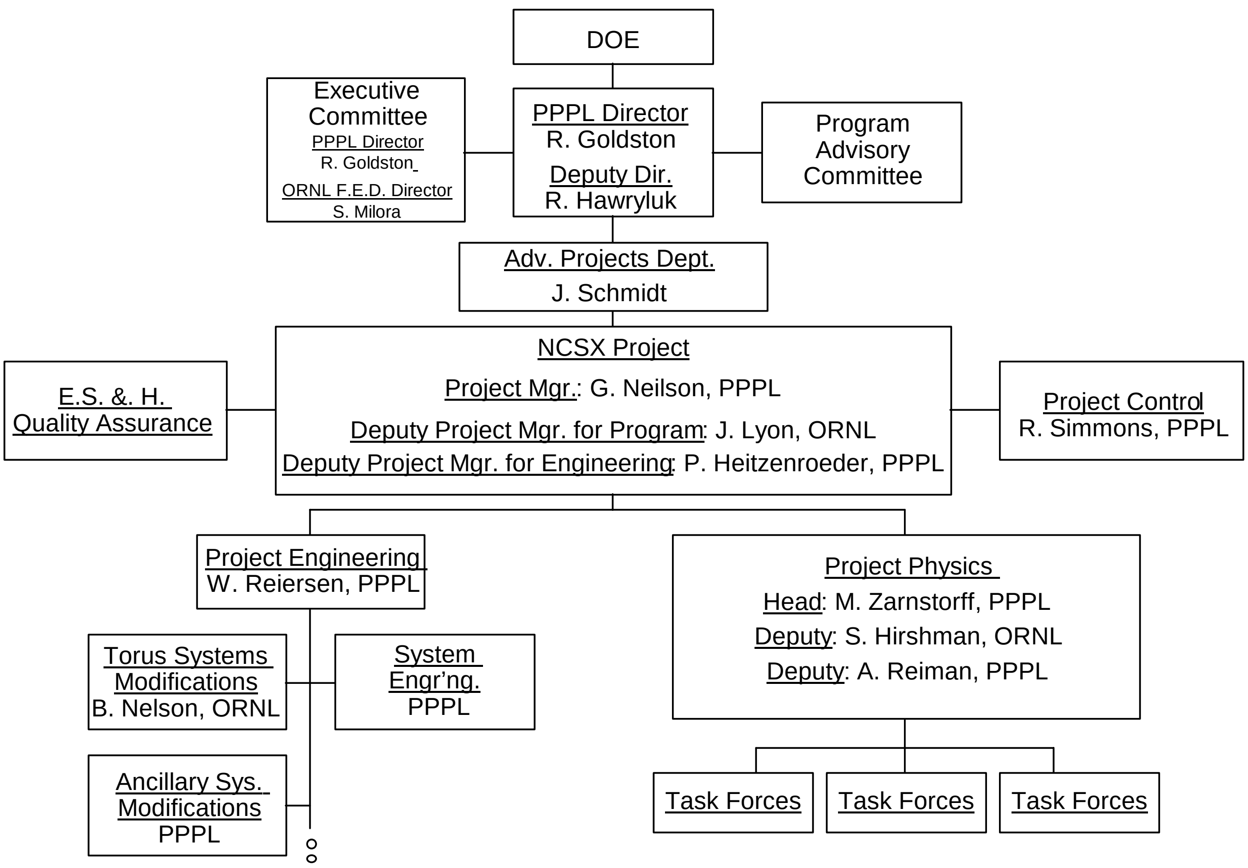

Figure 13-1. NCSX Project Organization

The physics and concept development phase of the NCSX project has been carried out by an integrated national team, led by PPPL and ORNL, with participants from several universities (to date, the University of Texas at Austin, Columbia University, University of California at San Diego, Massachusetts Institute of Technology, Auburn University, University of Montana, University of Wisconsin) and two other laboratories (Lawrence Livermore National Laboratory and Sandia National Laboratories–Albuquerque). The work has benefited from strong collaborations with foreign stellarator researchers (in Germany, Australia, Switzerland, Japan, and Russia) and has been guided by an advisory committee of distinguished U.S. and foreign scientists. This national team approach has facilitated cost-effective knowledge transfer and resource sharing within the DOE system of laboratories and been effective in broadening national participation in the program. Good communication is maintained cost-effectively through frequent teleconference meetings and web-based data sharing, with little need for travel. The success of this approach is best measured by the products it has delivered, namely a scientific knowledge base for compact stellarators and pre-conceptual designs for both the NCSX proof-of-principle experiment and the complementary QOS concept exploration experiment proposed by ORNL (currently under separate review). These constitute the scientific and technical foundations for the proof-of-principle program.

The national team model will be continued as the project moves forward. In carrying out the design and construction phases of the NCSX, PPPL will lead the project management team and be responsible for all procurement, fabrication, installation, testing, and commissioning. ORNL has the lead responsibility for designing the stellarator core (the coils, support structure, vacuum vessel, and cryostat) and will provide on-site engineering support at PPPL for the installation and relevant testing of those systems. Following the integrated team model, PPPL will support ORNL-led activities and vice versa. Both laboratories will continue to be supported in their efforts by other collaborators based on project needs.

The NCSX Project is well supported by the PPPL management and appears in the Laboratory’s institutional plan as a major initiative. The NCSX is the largest activity in the Advanced Projects Department, which leads the project, and also receives strong support from the Theory, Experiment, and Engineering Departments. Project status and issues are reviewed with the Laboratory Director and Deputy Director on a weekly basis. The PPPL and ORNL Directors have jointly written to the Department of Energy to express their strong support for NCSX and the compact stellarator program.

13.3.2 Project Organization

The lead laboratories, PPPL and ORNL, have assembled a leadership team of senior physicists and engineers for the NCSX project. Collectively they have extensive experience in stellarators and in other fusion projects of NCSX scale and larger. The key personnel and their responsibilities are:

Management

- Hutch Neilson, PPPL (Project Manager): overall project execution.
- Jim Lyon, ORNL (Deputy Project Manager for Program): project management support, emphasizing programmatic issues.
- Phil Heitzenroeder, PPPL (Deputy Project Manager for Engineering): project management support, emphasizing engineering issues.
- John Schmidt, PPPL (Advanced Projects Dept. Head): project management guidance.

Physics

- Mike Zarnstorff, PPPL (Physics Head): physics design and research
- Allan Reiman, PPPL (Deputy Physics Head): stellarator theory, plasma configurations.
- Steve Hirshman, ORNL (Deputy Physics Head): stellarator theory, coils.
- Ed Lazarus, ORNL: experimental physics, scenarios.
- Peter Mioduszewski, ORNL: power and particle handling.

Engineering

- Wayne Reiersen, PPPL (Engineering Head): overall engineering design and construction.
- Brad Nelson, ORNL (Stellarator Core Manager): stellarator core design.
- Charles Neumeyer, PPPL (Power Systems Manager): power systems design.

The project is guided by an informal Program Advisory Committee, reporting to the PPPL Director, which provides advice on technical matters. The Committee, which is composed of senior U.S. and foreign fusion researchers with broad expertise, has met four times since 1998. It has played an important role in developing the physics basis and design requirements for the NCSX. Members who have served on the committee to date are:

Prof. David T. Anderson, *University of Wisconsin*
Prof. Ira B. Bernstein, *Yale University*
Prof. Allen H. Boozer (chair), *Columbia University*
Dr. Paul R. Garabedian, *New York University*
Prof. Jeffrey H. Harris, *The Australian National University, Australia*
Prof. Richard D. Hazeltine, *University of Texas at Austin*

Prof. Chris C. Hegna, *University of Wisconsin*
Prof. Stephen F. Knowlton, *Auburn University*
Dr. James F. Lyon, *Oak Ridge National Laboratory*
Dr. Earl S. Marmar, *Massachusetts Institute of Technology*
Prof. K. Matsuoka, *National Institute for Fusion Science, Japan*
Dr. William M. Nevins, *Lawrence Livermore National Laboratory*
Dr. Peter A. Politzer, *General Atomics*
Dr. David W. Ross, *University of Texas at Austin*
Dr. Edmund Synakowski, *Princeton Plasma Physics Laboratory*
Prof. Friedrich Wagner, *Max Planck Institute for Plasma Physics, Germany*
Prof. Harold Weitzner, *New York University*

Chapter 14 -- Reactor Potential of Compact Stellarators

14.1 Quasi-Axisymmetric Compact Stellarator Reactor Configurations

Compact stellarators [1] may combine the best features of tokamaks (moderate A_p, good confinement, and high $\langle\beta\rangle$) and currentless stellarators (steady-state operation without external current drive or disruptions, stability against external kinks and vertical displacement events without a close conducting wall or active feedback systems, and low recirculating power in a reactor). The earlier Stellarator Power Plant Study (SPPS) reactor [2] with average major radius R = 14 m was calculated to be cost competitive with the R = 6 m ARIES-IV and R = 5.5 m ARIES-RS tokamak reactors with higher wall power densities largely due to SPPS's low recirculated power [3]. A more compact stellarator reactor could retain the cost savings associated with the low recirculated power of the SPPS reactor, and benefit from smaller size and higher wall power density (hence lower cost of electricity) than was possible in the SPPS reactor.

Although the NCSX configuration was not optimized as a reactor configuration, it is instructive to explore the potential of QA configurations as reactors. The analysis discussed here is only a preliminary examination of the possibilities that compact stellarators offer as reactors to see if a more detailed study is warranted. Two types of low-A_p QA compact stellarators [4] with volume-average beta $\langle\beta\rangle$ = 4-6% were examined. Figure 1 shows the last closed flux surface and the $|B|$ contours on that surface for these cases; here magenta indicates the lowest $|B|$ value and red the highest. The configuration in Figure 14-1(a) is the li383 configuration chosen for NCSX and that in Figure 14-1 (b) is 2101 configuration.

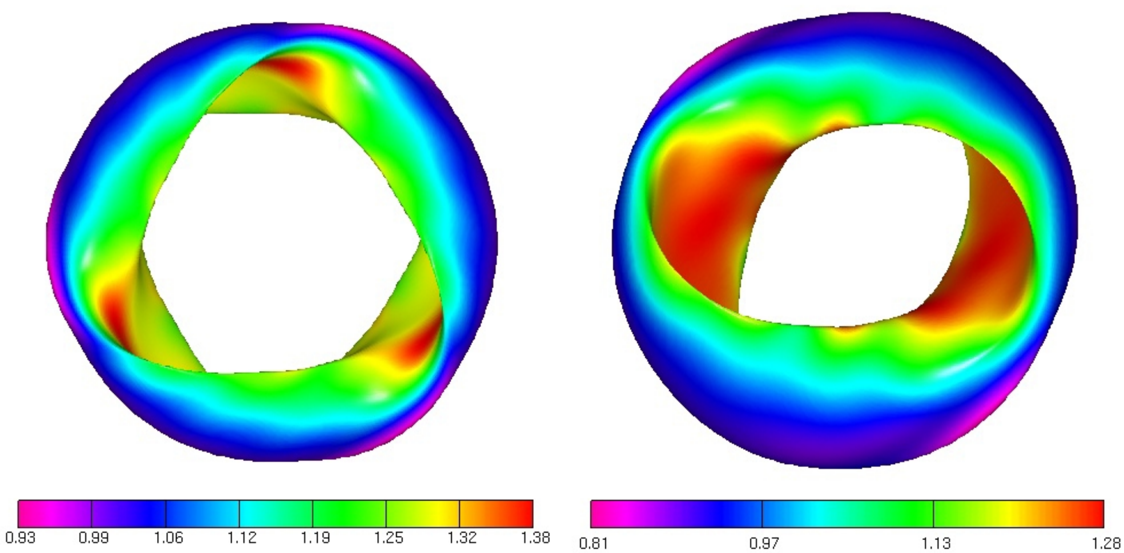

Figure 14-1

(a) QA#1: M = 3, A_p = 4.4. ***(b) QA#2: M = 2, A_p = 2.96.***

The coils that create these configurations are characterized by $A_\Delta = R/\Delta$ and B_{max}/B_0 where Δ is the minimum distance between the plasma edge and the centerline of the coils for a given R, B_{max} is the maximum field on the coils, and B_0 is the average on-axis magnetic field. These ratios depend on the specific coil design and are important because the minimum reactor size is set by $R_{min} = A_\Delta(d + ct/2)$ where d is the limiting (inboard) space needed for the plasma-wall distance, first wall thickness, blanket, shield, vacuum vessel, structure, and assembly

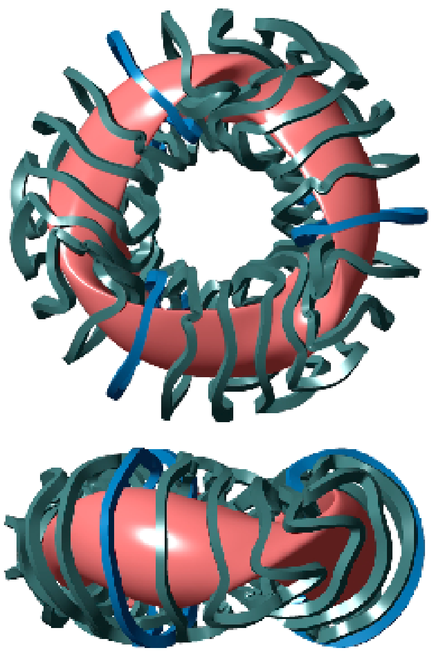

Figure 14-2. A modular coil set for the QA plasma configuration shown in Figure 14.1(a

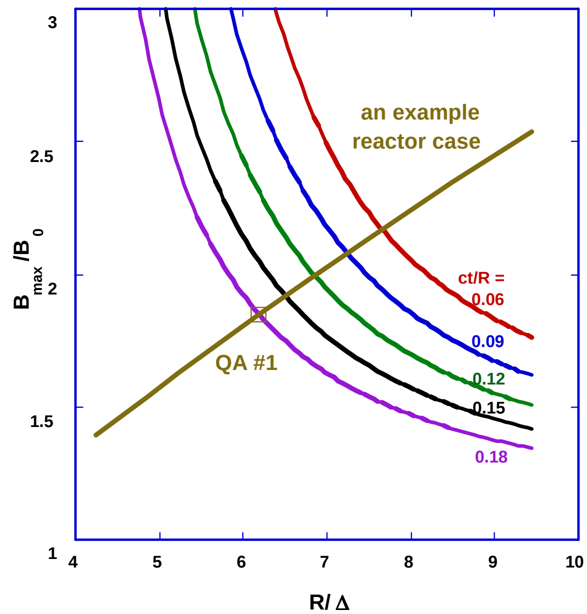

Figure 14-3 Variation of B_{max}/B_0 wit for the QA plasma configuration h R/Δ shown in Figure. 14-1(a).

gaps. From Ampere's law and the definitions of R_{min} and the average current density over the modular coil cross section, the half radial depth of the modular coils is given by

$$ct/2 = A_\Delta B_{max}/(16 N_{coil}\, j_{coil} k B_{max}/B_0)[1 + \{1 + 32\, N_{coil}\, j_{coil} kd(B_{max}/B_0)/(A_\Delta B_{max})\}^{1/2}]$$

where N_{coil} is the number of coils, j_{coil} is the current density averaged over the coil cross section in kA cm^{-2}, and k is the ratio of toroidal width to radial depth of the coils. A 20-cm thick cryostat surrounds the reactor core. For these studies, j_{coil} = 3 kA cm^{-2}, k = 2, and d = 1.12 m (similar to that for ARIES-AT [5]); the value corresponding to d on the outboard side is 1.30 m. The other reference reactor assumptions are also similar to those for ARIES-AT; *e.g.*, a thermal conversion efficiency η = 59%. A 16-T value is assumed for B_{max} (as was used for the ARIES-IV, ARIES-RS, and SPPS reactor studies), which may be more relevant for a QA reactor than the 12-T value for B_{max} used in the ARIES-AT study.

14.2 Results for the Scaling Model

The parameters that characterize a particular coil configuration in the expression for ct/2 are A_Δ, B_{max}/B_0, and N_{coil}. Figure 14-2 shows a particular modular coil set for the QA#1 plasma configuration shown in Figure 14-1(a). Rather than calculating actual coils for a large number of possible coil-plasma distances and coil cross sections, an approximate model was used for a scaling study. The NESCOIL code [6] was used to calculate B_{max}/B_0 at a distance ct/2 radially in from a current sheet (at a distance Δ from the plasma edge) that reproduced the last closed flux surface. The value of B_{max}/B_0 was increased by 15% to simulate effects due to a smaller number of coils from experience in the SPPS study. Figure 14-3 shows the tradeoff between minimizing B_{max}/B_0, which increases the field in the plasma for a given B_{max} on the coils, and maximizing Δ to allow a smaller R for a reactor with a given d, for the QA#1 case shown in Figure 14-1(a). Similar calculations were done for the QA#2 case in Figure 14-1(b). Because the fusion power P_{fusion} (and hence the net electric power generated, $P_{electric}$) $\propto \beta^2 B_0{}^4 V_{plasma}$, the value of B_{max}/B_0 needed for a given $P_{electric}$ and d is proportional to $(R/\Delta)^{3/4}$, as indicated by the "example reactor" line in Figure 14-3.

Using this model, the minimum value for R was calculated for M = 2 and M = 3 QA reactors for each ct/R value subject to several constraints: $P_{electric}$ = 1 GW, $\Gamma_n > 4$ MW m^{-2}, a plasma-coil distance 7 1.11 m, $j_{coil} > 3$ kA cm^{-2}, H-95 > 3.5, $\langle n\rangle/n_{Sudo} > 1$, and $\langle\beta\rangle > \beta_{limit}$ (4.2% for QA#1 and 4% for QA#2). Here $n_{Sudo} = 2.5[PB/Ra^2]^{1/2}$ [7] and H-95 = $\tau_E/\tau_E{}^{ISS95}$ where $\tau_E{}^{ISS95} = 0.079 a_p{}^{2.21} R^{0.65} P^{-0.59} n^{0.51} B^{0.83} \iota^{-0.4}$ [8] with R and a_p in m, B in T, n in 10^{19} m^{-3}, and P in MW. The value for Γ_n is an important figure of merit for reactor economics because it relates to the power generated per unit wall area and the costs of the main reactor core elements (blankets, shield, and coils) are proportional to the wall area. The coil parameters obtained in this way are A_Δ = 6.18, B_{max}/B_0 = 1.85, and N_{coil} = 21 for the three-field-period QA#1 configuration and A_Δ = 4.84, B_{max}/B_0 = 1.93, and N_{coil} = 14 for the two-field-period QA#2 configuration .

Table 14-1. Scaled 1-GW QA Compact Stellarator Reactors with $\langle\beta\rangle$ β_{limit}, H-95 3

	B_{max} = 12 T		B_{max} = 16 T	
	QA#1	**QA#2**	**QA#1**	**QA#2**
Average major radius R (m)	**9.77**	**8.22**	**9.15**	**7.28**
Average plasma radius a_p (m)	2.22	2.78	2.08	2.46
Plasma volume V_{plasma} (m^3)	950	1250	780	870
On-axis field B_0 (T)	**5.65**	**5.41**	**7.53**	**7.21**
Energy confinement time τ_E (s)	2.35	2.69	2.13	2.25
$\tau_E/\tau_E{}^{ISS95}$ multiplier H-95	**2.65**	**2.65**	**2.27**	**2.45**
ITER-89P confinement multiplier	1.50	1.44	1.17	1.18
Volume average beta $\langle\beta\rangle$ (%)	**4.20**	**4.00**	**2.61**	**2.70**
Vol.-average density $\langle n\rangle$ (10^{20} m^{-3})	1.54	1.31	1.55	1.33
$\langle n\rangle/\langle n\rangle_{Sudo}$	1.00	1.00	0.79	0.73
Density-aver. temperature $\langle T\rangle$ (keV)	10.9	11.1	11.9	13.1
Neutron wall load Γ_n (MW m^{-2})	**1.41**	**1.34**	**1.61**	**1.71**

Table 14-1 shows the results for the two QA cases for $\langle\beta\rangle$ > the nominal β_{limit} (4.2% for QA#1 and 4% for QA#2) and B_{max} = 12 T value, and the result if B_{max} is increased to 16 T. The values for R range from 7.28 m to 9.77 m, considerably smaller than the R = 14 m value obtained in the SPPS study or the R = 18-22 m values obtained in the HSR studies [9]. The required multiplier on the ISS-95 confinement time is modest; H-95 ranges from 2.27 to 2.65. The minimum values for R and H-95 are obtained with $\langle n\rangle/n_{Sudo} = 1$ and $\langle\beta\rangle = \beta_{limit}$ for B_{max} = 12 T. However, the $P_{electric}$ = 1 GW limit is reached for $\langle n\rangle/n_{Sudo} < 1$ and $\langle\beta\rangle < \beta_{limit}$ when B_{max} is increased to 16 T; $P_{electric} \propto \beta^2 B_0{}^4 V_{plasma}$ and the factor 3.16 increase in $B_0{}^4$ does not allow taking advantage of the β_{limit}. The value of V_{plasma} can not decrease enough to allow $\langle\beta\rangle = \beta_{limit}$ because the value of R is constrained by $R_{min} = A_\Delta(d + ct/2)$. Operation at the β limit in these cases would produce substantially more than 1 $GW_{electric}$.

Table 14-2 shows the result if the β_{limit} is increased to 5% or 6% with B_{max} = 12 T. This leads to smaller values for R as shown in Table 14.2. The higher $\langle\beta\rangle$ values allow reducing R to R_{min}, R = 8.80 m for QA#1 and R = 6.99 m for QA#2 versus R = 9.77 m for QA#1 and R = 8.22 m for QA#2 in Table 14-1. The ISS-95 confinement multipliers H-95 have had to increase to keep $P_{electric}$ = 1 GW to compensate for the smaller plasma volumes. Table 14-3 shows the same analysis with $P_{electric}$ = 2 GW. Higher values of $\langle\beta\rangle$ are now useful; a value of 6% can be accommodated with B_{max} = 12 T but not with B_{max} = 16 T. The value for Γ_n is approximately double that for the $P_{electric}$ = 1 GW cases in Table 14-1 because there is little change in R.

Table 14-2. 1-GW QA Reactors with B_{max} = 12 T, β_{limit} = 5% and 6%, H-95 3

	β_{limit} = 5%		β_{limit} = 6%
	QA#1	**QA#2**	**QA#2**
Average major radius *R* (m)	**8.80**	**7.08**	**6.99**
Average plasma radius a_p (m)	2.00	2.39	2.36
Plasma volume V_{plasma} (m^3)	700	800	770
On-axis field B_0 (T)	**5.65**	**5.41**	**5.41**
Energy confinement time τ_E (s)	2.01	2.16	2.11
τ_E/τ_E^{ISS95} multiplier H-95	**2.82**	**2.90**	**2.95**
ITER-89P confinement multiplier	1.61	1.61	1.62
Volume average beta $\langle\beta\rangle$ (%)	**4.91**	**5**	**5.1**
Vol.-average density $\langle n\rangle$ (10^{20} m^{-3})	1.80	1.64	1.65
$\langle n\rangle/\langle n\rangle_{Sudo}$	1.00	1.00	0.98
Density-aver. temperature $\langle T\rangle$ (keV)	10.8	11.1	11.3
Neutron wall load Γ_n (MW m^{-2})	**1.74**	**1.81**	**1.86**

Table 14-3. Scaled 2-GW Compact Stellarator Reactors with ⟨β⟩ 6%, H-95 3

	B_{max} = 12 T		B_{max} = 16 T	
	QA#1	**QA#2**	**QA#1**	**QA#2**
Average major radius *R* (m)	**9.71**	**7.90**	**9.15**	**7.28**
Average plasma radius a_p (m)	2.21	2.67	2.08	2.46
Plasma volume V_{plasma} (m^3)	930	1110	780	870
Energy confinement time τ_E (s)	1.65	1.80	1.51	1.59
τ_E/τ_E^{ISS95} multiplier H-95	**2.80**	**2.65**	**2.38**	**2.34**
ITER-89P confinement multiplier	1.50	1.46	1.17	1.16
Volume average beta ⟨β⟩ (%)	**6.00**	**6.00**	**3.69**	**3.82**
Vol.-ave. density ⟨*n*⟩ (10^{20} m^{-3})	1.59	1.65	1.61	1.65
$\langle n \rangle / \langle n \rangle_{Sudo}$	0.72	0.84	0.58	0.64
Density-aver. temperature ⟨*T*⟩ (keV)	15.0	13.2	16.2	15.0
Neutron wall load Γ_n (MW m^{-2})	**2.86**	**2.91**	**3.23**	**3.43**

The same assumptions were used with the plasma and coil configurations corresponding to the W7-X based HSR, the LHD based MHR-S [10], and SPPS reactors for comparison with these reactor studies. The modified HSR* had *R* = 17.4 m (instead of 22 m because B_{max} was increased from 10.6 T to 12 T), H-95 = 3.06, ⟨β⟩ = 4.9%, and Γ_n = 1.24 MW m^{-2}. The modified MHR-S* had *R* = 18.6 m (instead of 16.5 m because of the ARIES-AT blanket and shield assumptions), H-95 = 2.87, ⟨β⟩ = 5%, and Γ_n = 0.62 MW m^{-2}. The modified SPPS* had *R* = 20.8 m (instead of 14.0 m because B_{max} was decreased from 16 T to 12 T), H-95 = 3.13, ⟨β⟩ = 5%, and Γ_n = 0.60 MW m^{-2}. Thus, for the same modeling assumptions, the compact stellarator configurations lead to reactors with a factor of 2 to 3 smaller major radius and a factor of 1.4 to 3 higher wall power loading.

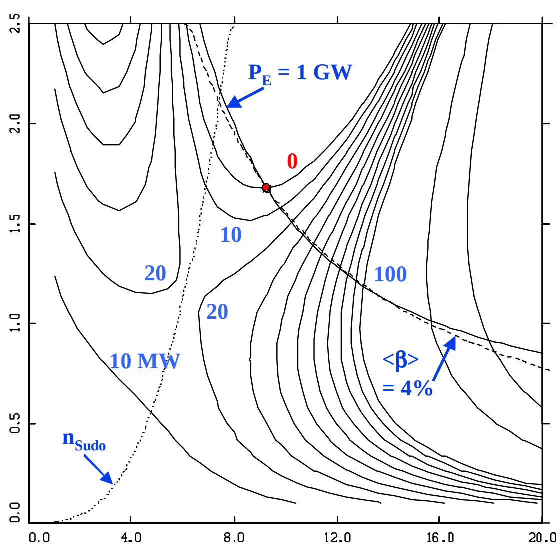

Figure 14-4. Operating space for a QA#2 reactor.

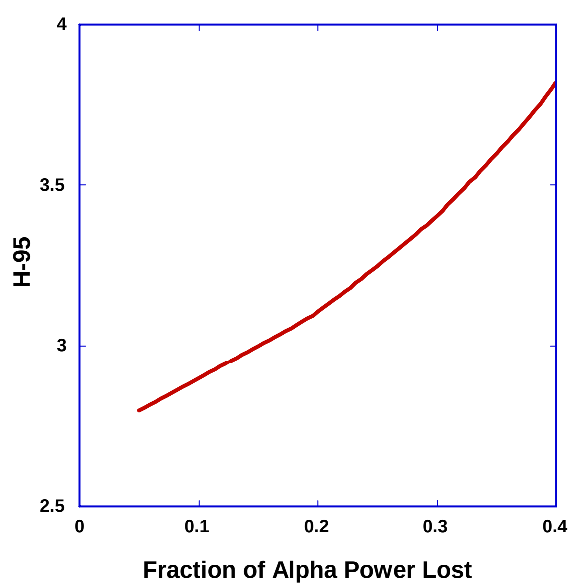

Figure 14-5. Effect of alpha-particle power loss

14.3 Results for a Reference Compact Stellarator Reactor Case

Figure 14-4 shows a POPCON plot of the operating space (⟨*n*⟩ and ⟨*T*⟩) for a QA#2 reactor with R = 7.1 m and B_0 = 5.4 T. The numbers label contours of constant auxiliary heating power in MW, "0" indicates ignition, and the curves indicate constant levels of $\langle\beta\rangle$, $P_{electric}$, and the Sudo density "limit". The red dot marks the thermally stable 1-$GW_{electric}$ operating point. The reference reactor assumptions are A_Δ = 4.84, B_{max} = 12 T, ARIES-AT inboard blanket and shield, and P_{fusion} = 1.69 GW [$P_{electric}$ = 1 GW (net)]. The reference plasma assumptions are broad ARIES-AT density profiles with $n_e > n_{Sudo}$, peaked ARIES-AT temperature profiles, τ_{He}/τ_E = 6, and an alpha-particle energy loss fraction = 0.1. The plasma parameters at the operating point are $\langle n\rangle = 1.7 \times 10^{20}$ m^{-3}, $\langle T\rangle$ = 9.3 keV, $\langle\beta\rangle$ = 4.04%, H-95 = 2.90, n_{DT}/n_e = 0.82, n_{He}/n_e = 5.9%, and Z_{eff} = 1.48. The saddle point in Fig. 14.4 determines the startup power required to reach ignition. Plasma parameters at the saddle point are $\langle n\rangle = 1.1 \times 10^{20}$ m^{-3}, $\langle T\rangle$ = 5.4 keV, $\langle\beta\rangle$ = 1.5 %, and P_{aux} = 20 MW. The confinement improvement required increases if the alpha particle power lost increases. Figure 14-5 indicates the effect of alpha-particle losses on the confinement required. The allowable alpha-particle energy loss varies from 5% at H-95 = 2.8 to 40 % at H-95 = 3.8.

14.4. Conclusions

QA configurations have the potential for a more attractive stellarator reactor. Using the ARIES-AT model with B_{max} = 12 T on the coils gives compact stellarator reactors with R = 7-8.8 m, a factor of 2-3 smaller in R than other stellarator reactors for the same assumptions. The two-field-period configuration leads to smaller reactors because of their lower plasma aspect ratios and smaller values for R/Δ. For either configuration, only modest values of H-95 are required. Further study, e.g. by the ARIES group, is warranted to fully assess the reactor potential of these configurations.

References

[1] NEILSON, G.H. et al., *Phys. Plasmas* **7** (2000) 1911.
[2] Stellarator Power Plant Study, UCSD-ENG-004 (1997).
[3] LYON, J.F., et al., Plasma Physics and Controlled Nuclear Fusion Research 1994, Seville 1994, Vol. 2, 655 (IAEA Vienna 1985); also LYON, J.F., et al., *Fusion Engineering and Design* **25** (1994) 85.
[4] ZARNSTORFF, M.C. et al., 18th IAEA Fusion Energy Conference, Sorrento, Italy, Oct. 2000.
[5] NAJMABADI, F. et al., 18th IAEA Fusion Energy Conference, Sorrento, Italy, Oct. 2000.
[6] MERKEL, P., *Nucl. Fusion* **2**7 (1987) 867.
[7] SUDO, S., et al., *Nucl. Fusion* **30** (199) 1063.
[8] STROTH, U., et al., *Nucl. Fusion* **36** (1996) 11.
[9] BEIDLER, C., et al., Fusion Energy 1996, Vol. 3, 407 (IAEA, Vienna 1997).
[10] YAMAZAKI, K., et al., Fusion Energy 1996, Vol. 3, 421 (IAEA, Vienna 1997).